Bitlis Eren Üniversitesi
Fen Bilimleri Dergisi

Bitlis Eren University
Journal of Science

ISSN : 2147-3129
e-ISSN : 2147-3188

Cilt / *Volume*: 11 Sayı / *Number*: 2 Yıl / *Year*: 2022

Yazışma Adresi

Bitlis Eren Üniversitesi
Lisansüstü Eğitim Enstitüsü
13000, Merkez, Bitlis/TÜRKİYE
Tel: 0 (434) 2220071

https://dergipark.org.tr/tr/pub/bitlisfen

BEU FBD

Bitlis Eren Üniversitesi Fen Bilimler Dergisi

Bitlis Eren University Journal of Science

Yıl/*Year:* 2022 - Cilt/*Volume:* 11 - Sayı/*Number:* 2

Sahibi / *Owner*
Prof. Dr. Necmettin ELMASTAŞ

Sorumlu Müdür / *Director*
Doç. Dr. Mehmet Bakır ŞENGÜL

Baş Editör / *Editor in Chief*
Dr. Öğr. Üyesi Ufuk KAYA

Editörler / *Editors*
Dr. Öğr. Üyesi Yunus SAYAN
Dr. Öğr. Üyesi Nuray YAVUZKANAT
Dr. Öğr. Üyesi Fatih AVCIL
Arş. Gör. Dr. Mehmet Akif YERLİKAYA

Dil Editörleri / *Language Editors*
Dr. Öğr. Üyesi Murat PARLAKPINAR (Türkçe)
Öğr. Gör. Murat ÇAN (İngilizce)

Dizgi / *Typographic*
Dr. Öğr. Üyesi Ufuk KAYA

Dergi Sekreteri / *Journal Secretary*
Ahmet UĞUR

Editör (Yayın) Kurulu / *Editorial Board*

Prof. Dr. Zekeriya YERLİKAYA	Kastamonu Üniversitesi
Doç. Dr. Ali ÇAKMAK	Bitlis Eren Üniversitesi
Doç. Dr. Yunus Levent EKİNCİ	Bitlis Eren Üniversitesi
Doç. Dr. Engin YILMAZ	Bitlis Eren Üniversitesi
Doç. Dr. Kesran AKIN	Bitlis Eren Üniversitesi
Doç. Dr. Tuncay TUNÇ	Mersin Üniversitesi
Doç. Dr. Ayşegül Demir YETİŞ	Bitlis Eren Üniversitesi
Doç. Dr. Ramazan KATIRCI	Sivas Bilim ve Teknoloji Üniversitesi
Dr. Sajad KHORSANDROO	North Carolina Agricultural and Technical State University
Dr. Öğr. Üyesi Zehra Nur KULUÖZTÜRK	Bitlis Eren Üniversitesi
Dr. Öğr. Üyesi Halil YETGİN	Bitlis Eren Üniversitesi
Dr. Öğr. Üyesi Erdal AKIN	Bitlis Eren Üniversitesi
Dr. Öğr. Üyesi Faruk ORAL	Bitlis Eren Üniversitesi
Dr. Öğr. Üyesi Necla ÖZDEMİR	Bitlis Eren Üniversitesi
Dr. Nadjet LAOUET	Constantine 1 University
Arş. Gör. Dr. İsmet SÖYLEMEZ	Abdullah Gül Üniversitesi

Danışma Kurulu / *Advisory Board*

Prof. Dr. Atilla ARSLAN	Selçuk Üniversitesi
Prof. Dr. Nurtaç ÖZ	Sakarya Üniversitesi
Prof. Dr. Saim ÖZDEMİR	Sakarya Üniversitesi
Prof. Dr. Soner ÖZGEN	Fırat Üniversitesi
Prof. Dr. Hasan SEVGİLİ	Ordu Üniversitesi
Prof. Dr. Mahmut BÖYÜKATA	Kırıkkale Üniversitesi
Prof. Dr. Esvet AKBAŞ	Van Yüzüncü Yıl Üniversitesi
Prof. Dr. Mikail ET	Fırat Üniversitesi
Prof. Dr. Özdemir ADIZEL	Van Yüzüncü Yıl Üniversitesi
Prof. Dr. Orhan Taner CAN	Bursa Teknik Üniversitesi
Doç. Dr. Bayram GÜNDÜZ	Malatya Turgut Özal Üniversitesi
Doç. Dr. Sait İZGİ	Siirt Üniversitesi
Doç. Dr. Murat ÇELTEK	Trakya Üniversitesi
Doç. Dr. Cem KOŞAR	Gaziantep Üniversitesi
Doç. Dr. Tarkan YORULMAZ	Çankırı Karatekin Üniversitesi
Dr. Öğr. Üyesi Serhat Berat EFE	Bandırma Onyedi Eylül Üniversitesi
Dr. Öğr. Üyesi Mehmet Can BALCI	Batman Üniversitesi

Dergi Hakkında / *About Journal*

Bitlis Eren Üniversitesi Fen Bilimleri Dergisi, mühendislik ve temel bilimler alanlarındaki gelişmeleri ve yenilikleri takip etmek, meslek kuruluşlarının, araştırmacıların ve bireylerin ulusal ve uluslararası gelişimlerine katkıda bulunmak ve bu alanlarda elektronik bir kaynak oluşturmak amacıyla yayımlanmaktadır. Derginin yazım dili Türkçe veya İngilizcedir. Fen Bilimleri Dergisi, Bitlis Eren Üniversitesi Lisansüstü Eğitim Enstitüsü yayını olup, 2012 yılından bu yana ücretsiz ve açık erişimli olarak yayın hayatına devam etmektedir. Mühendislik ve temel bilimlerin bilgi tabanına ve teknolojik gelişmelere ışık tutması amacıyla bu alanlarda yapılmış deneysel ve teorik ilerlemeleri konu alan özgün araştırma makalelerine yer verilmektedir. Dergiye gönderilen çalışmaların benzerlik oranı %15'i geçmemelidir. Yazım kurallarına uymayan makaleler, hakemlere gönderilmeden önce düzeltilmek üzere yazara geri gönderilir. Bu nedenle, derginin yazım kuralları dikkate alınmalıdır. Ayrıca, editörlerden yazarlara iletilen düzeltmelere veya taleplere 30 gün içerisinde cevap verilmediği takdirde ilgili makaleler reddedilir. Makaleler şekiller ve tablolar dâhil 20 sayfayı geçmemelidir. Dergiye yayın için gönderilen makaleler en az iki hakem tarafından değerlendirilir. Yazarlardan hakem önerisi talep edilmemektedir. Makalelerin dergide yayımlanabilmesi için hakemler tarafından olumlu görüş bildirilmesi gerekmektedir. Dergi Editör Kurulu, hakem raporlarını (*en aziki hakemin değerlendirmeleri geldikten sonra*) dikkate alarak makalelerin yayımlanmak üzere kabul edilip edilmemesine karar verir. Fen Bilimleri Dergisi, yılda dört defa (*Mart, Haziran, Eylül, Aralık*) yayımlanmaktadır. **Dergimiz Tübitak-Ulakbim Mühendislik ve Temel Bilimler Veri Tabanı Dergi Listesinde taranmaktadır.**

B.E.Ü. Fen Bilimleri Dergisi 11(2), 2022 / *B.E.U. Journal of Science 11(2), 2022*
İÇİNDEKİLER / *CONTENTS*

Bitlis Eren Üniversitesi Fen Bilimleri Dergisi
BİTLİS EREN UNIVERSITY JOURNAL OF SCIENCE
ISSN: 2147-3129/e-ISSN: 2147-3188
VOLUME: 11 NO: 2 PAGE: 393-399 YEAR: 2022
DOI: 10.17798/bitlisfen.956944

Effect of Temper Rolling Reduction Ratio on Microhardness and Microstructure of DC04 Grade Sheet Material

Batuhan ÖZAKIN[1*], Naci KURGAN[2]

[1]*Kavak Vocational School, Samsun University, Samsun, Turkey*
[2]*Mechanical Engineering Department, Ondokuz Mayıs University, Samsun, Turkey*
(ORCID: 0000-0003-1754-949X) (ORCID: 0000-0001-7297-7249)

Keywords: Temper rolling (skin-pass rolling), Reduction ratio, Microhardness, Microstructure, DC04 grade sheet materials.

Abstract
With temper rolling, which is the final stage of the cold rolling manufacturing process, to the surface of sheet metal materials is transferred roughness with specially roughened rolls. In this study, microhardness and microstructural evolution occurring in the section along the thickness of DC04 grade sheet materials temper rolled with various reduction ratios were investigated. As a result, it was concluded that the microhardness distribution taken from the section along the thickness increases with the increase of reduction ratio and the microhardness distribution from the surface to the center in the section decreases. In the temper rolling process with a reduction ratio of 250 µm and 500 µm an increase of approximately 5% and 15% has occurred, respectively compared to before the temper rolling process. It was also concluded that with the increase in reduction ratio, the grains in the section along the thickness elongated and thinned on the surface and this change in the center compared to the regions close to the surface was less.

1. Introduction

DC04 grade sheet materials are often preferred in automotive applications (auto body panel) due to their good formability, high strength and high amount of ductility [1, 2]. Because of these advantages, the surfaces of DC04 grade sheet materials which are used extensively in automotive applications should have a standard range of roughness for painting and shaping [3].

Temper rolling (skin-pass rolling) is the rolling process used in the final forming stage of automotive sheets [4]. In the temper rolling process, the surface roughness profile is transferred to the materials through rolls with a special texture [5]. Thanks to the surface roughness profile obtained, the forming ability and paint adhesion of sheet materials are improved. [4]. Surface roughness transferred to sheet materials by rough rolls in temper rolling is affected by many rolling parameters (roll parameters, rolling speed, reduction ratio, rolling force, elongation, lubricant conditions, etc.) [6, 7]. Among these parameters in temper rolling, the reduction ratio is one of the most effective parameters to obtain the desired surface roughness on the surface of sheet materials [8]. As the reduction ratio rises, the roughness transferred to the surface of the sheet material increases [9, 10]. At the same time, the rise in the reduction ratio causes an increase in the rolling force [7]. Since the reduction ratio in temper rolling is miserable, the pressure in areas close to the surface is higher [11]. Temper rolling differs from cold rolling in that it takes place along a high friction and a large contact arc [12]. There are many studies characterizing the microstructure and microhardness in cold rolling, but there is a large gap in the literature on this subject in temper rolling. Grassino et al. investigated the surface microstructure and along thickness microhardness behavior in temper rolled materials with three different C content (low-C steel, ultra-low C steel, zinc coated C mild steel). In all three steels, the microhardness value was slightly higher in the parts close to the surface. They observed that the microhardness profile took an almost flat shape as a result of rolling elongation of more than 2% in the zinc coated C mild steel [13]. On the other hand, Koh

*Corresponding author: batuhan.ozakin@samsun.edu.tr
Received: 24.06.2021, Accepted: 11.03.2022

et al. investigated the effect of the reduction ratio on the microstructural behavior of IF (Interstitial) and AK (Aluminum-killed) steels in the temper rolling process. They observed that while the middle layer of IF steel was less deformed than AK steel, there was more change in the surface layer [14]. There is limited literature that characterizes the microhardness and microstructure changes in the sheet material cross-section in temper rolling. This study was carried out to eliminate the lack of scientific study in the characterization of microstructure and microhardness in sheet material cross-section roughened by temper rolling. The results can be used in research and development studies. As well as there is a large gap in the literature, it was observed that the microhardness and microstructural behavior of DC04 grade material, which is one of the mild steels used extensively in the automotive field, has not been investigated.

In this study, to fill the gap in the literature, microhardness and microstructural evolution occurring in the section along the thickness of DC04 grade sheet materials temper rolled with various reduction ratios were investigated.

2. Material and Methods

2.1. Material

DC04 grade sheet material specimens were sliced from a 1.5 mm thickness plate in 30 mm width and 200 mm length. The chemical composition of the material studied was determined by Spectrolab brand optical emission spectrometer. The chemical composition of the material (in wt.%) consists of 0.027 C, 0.006 Si, 0.152 Mn, 0.015 P, 0.013 S, 0.033 Cr, 0.031 Ni, 0.044 Cu, 0.005 Mo, 0.045 Al, 99.629 Fe elements. The tensile properties of DC04 grade sheet material were determined by carrying out a tensile test with the help of an Instron brand universal tensile test machine on standard test specimens prepared in parallel to the rolling direction. The yield strength of DC04 grade sheet material was determined as 154±8 MPa, tensile strength 270±8 MPa and total elongation 39.2±0.3%. The arithmetic average roughness (R_a) value of the surface of DC04 grade sheet material before temper rolling is 0.890 μm.

2.2. Methods

Temper rolling experiments were carried out at room temperature with the help of a laboratory type rolling mill (2-high roll). All experiments were carried out under 10 rpm rolling speed, 75 mm roll diameter, 4.4 μm (R_a) roll average roughness and dry conditions. Two different reduction ratios are 250 μm and 500 μm. Details of the experimental study are shown in Figure 1a.

In order to examine the microhardness and microstructure evolution in the section along the thickness of the material, the specimen before temper rolling, the temper rolled specimens in 250 μm and 500 μm reduction ratios were cut 10 mm × 10 mm and then the bakelite was taken. Before microhardness measurements, the specimens were grinded with 1000, 1200 and 2400 grit SiC abrasive paper and then polished with a diamond solution. Figure 1b shows the points where microhardness measurement was taken from the section along the thickness of the DC04 grade sheet material specimen. In the microstructure studies, the specimens were etched in 2% nital solution after the grinding and polishing processes were repeated. Vickers microhardness measurements were determined by applying a 50 g load for 10 seconds using Struers Duramin-50 test device. Microstructural images were obtained with Jeol JSM-7001F field emission scanning electron microscope (SEM) operated at 20 kV.

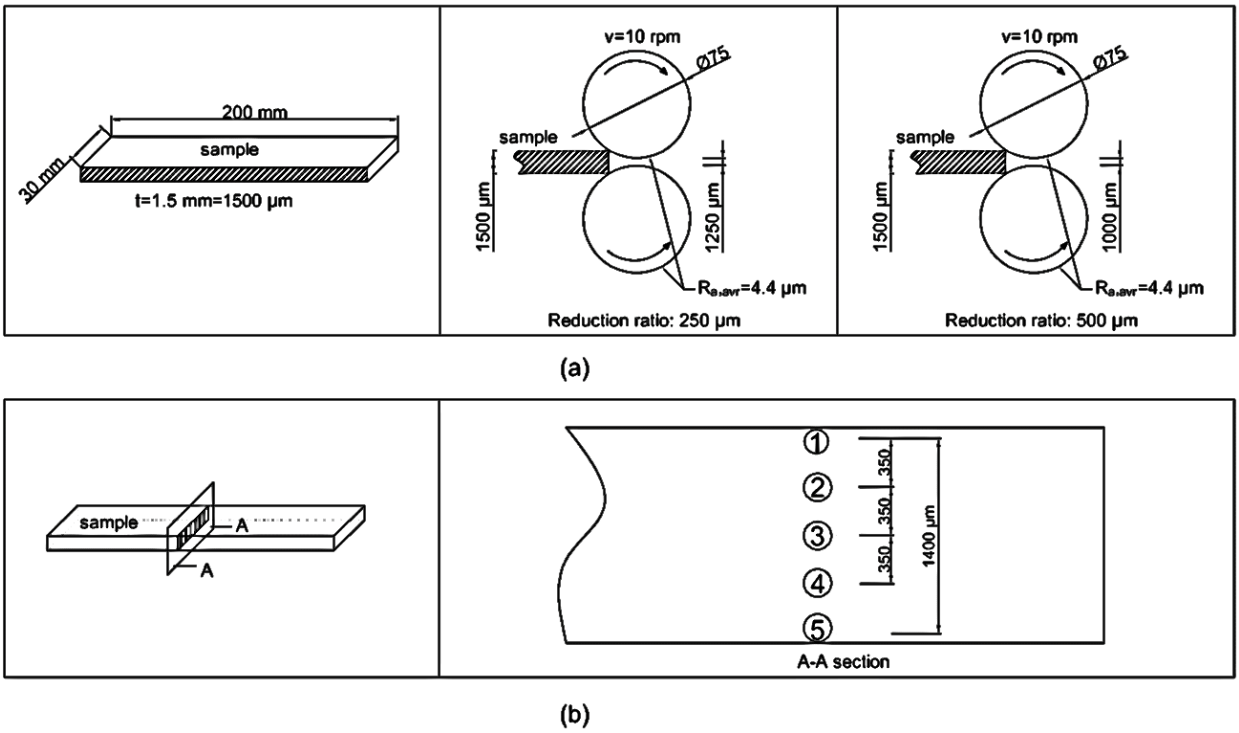

Figure 1. (a) Details of the experimental study, (b) the points where microhardness measurement was taken from the section along the thickness of the DC04 grade sheet material specimen

3. Results and Discussion

Figure 2 shows the graphical relationship obtained from Vickers microhardness ($HV_{0.05}$) measurements taken from the point numbers specified in the section along the thickness in Figure 1b.

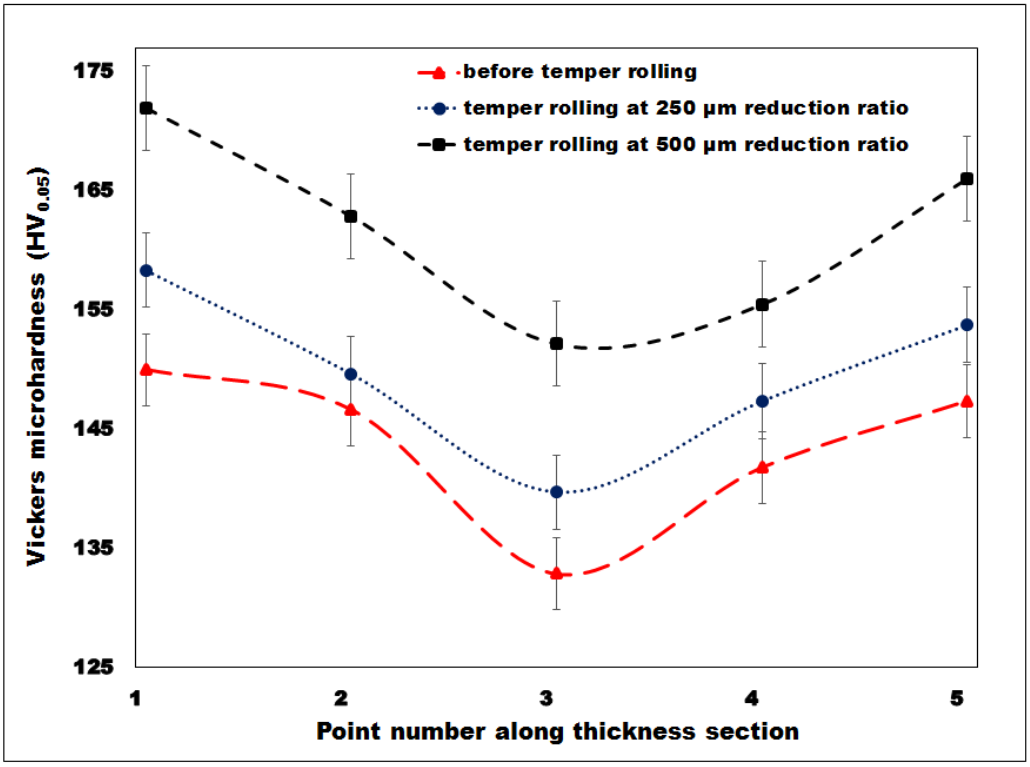

Figure 2. The graphical relationship obtained from Vickers microhardness ($HV_{0.05}$) measurements taken from the point numbers specified in the section along the thickness

In all the experiments performed in before temper rolling and skin-passed with 250 µm and 500 µm reduction ratios was observed that the microhardness value was higher at the points close to the surface and less values at the points near the center. In the formation of this situation, it was found that during the hot processing of the material, a finer-grained region was formed on the surfaces due to the faster cooling of the parts close to the surface compared to the center [13]. As the reduction ratio increased was observed that the microhardness value increased. While this increase was less (about 5-10 $HV_{0.05}$) than before temper rolling at 250 µm reduction ratio, it was observed more (about 15-20 $HV_{0.05}$) than before temper rolling at 500 µm reduction ratio. In the temper rolling process with a reduction ratio of 250 µm, an increase of approximately 5% has occurred compared to before the temper rolling process. In the temper rolling process with a reduction ratio of 500 µm, an increase of approximately 15% has occurred compared to before the temper rolling process. Therefore, it can be said that more thickness reduces at 500 µm reduction ratio and there is a similarity with the increase in the amount of thickness reduction in the occurrence of this situation. Indeed, Ko et al. stated that the most important factor in increasing the hardness value of the thickness reduction is due to the evolution of a fine grain microstructure and the formation of low angle grain boundaries [15]. At the same time, it can be said that the high hardness in the near-surface regions occurs due to the increase in dislocation density and the reduction in grain size, making the dislocation movement of the grain boundaries more difficult [16].

In order to examine the microstructure evolution as a result of the temper rolling, the scanning electron microscope (SEM) images taken from the section along the thickness of DC04 grade sheet material in before temper rolling and skin-passed with 250 µm and 500 µm reduction ratios are evaluated. The average grain size of the sheet material is about 20 µm [17]. In Figure 3a, the SEM images taken from region close to the surface in the section along the thickness of the DC04 grade sheet material before the temper rolling and in Figure 3b from the central region are seen. Before temper rolling, it is seen that the shape of the grains in the near surface and central regions has a spherical form.

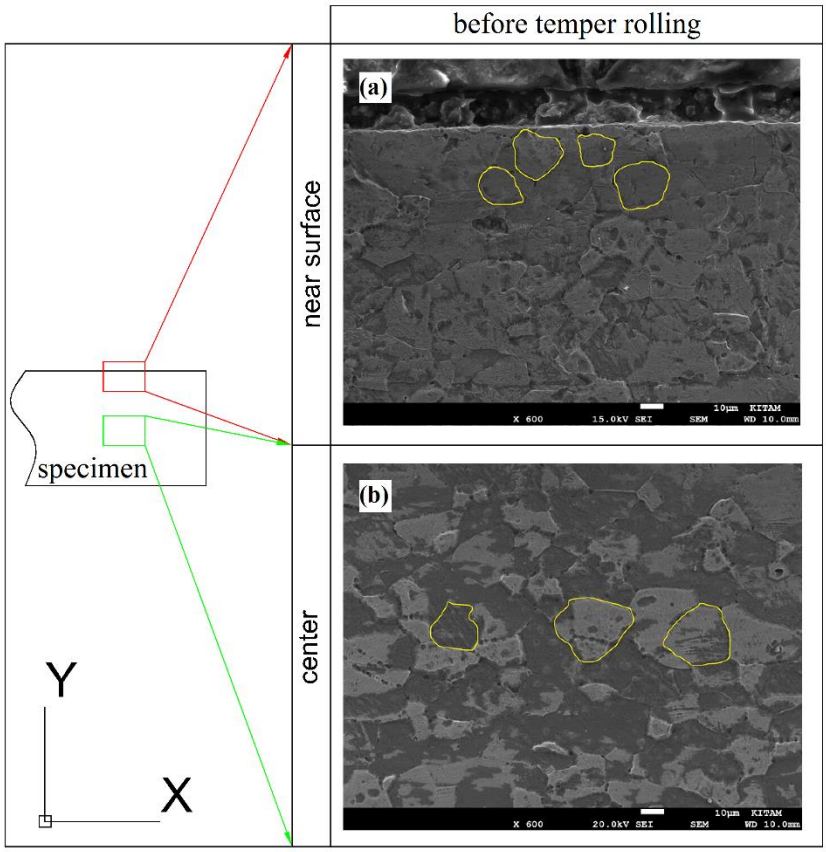

Figure 3. The SEM images taken from the section along the thickness of DC04 grade sheet material in before temper rolling; a) from region close to the surface, b) from the central region

In Figure 4a, the SEM images taken from region close to the surface in the section along the thickness of the DC04 grade sheet material with temper rolling at 250 µm reduction ratio and in Figure 4b from the central region are seen. In the temper rolling made with 250 µm reduction ratio, it is seen that the grains start to elongation in the "X" direction and the grains begin to shortening in the "Y" direction in the region close to the surface. In the central region, it can be said that this situation seen in regions close to surface has not yet fully formed.

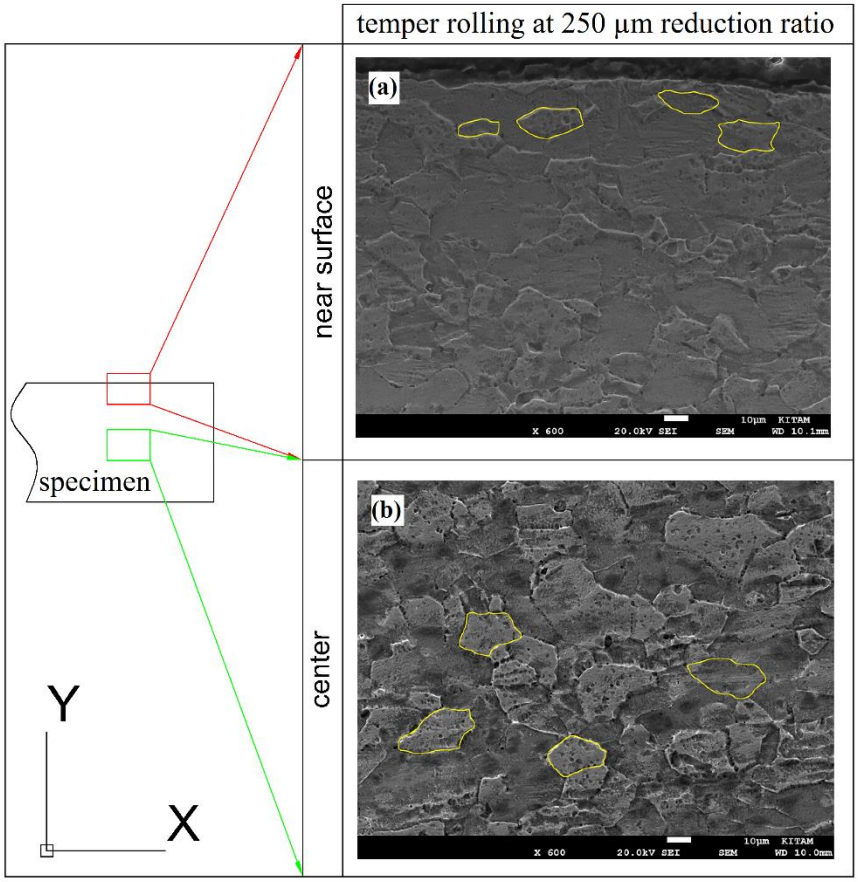

Figure 4. The SEM images taken from the section along the thickness of DC04 grade sheet material with temper rolling at 250 µm reduction ratio; a) from region close to the surface, b) from the central region

In Figure 5a, the SEM images taken from region close to the surface in the section along the thickness of the DC04 grade sheet material with temper rolling at 500 µm reduction ratio and in Figure 5b from the central region are seen. It is observed that in the region close to the surface, elongation of the grains in the "X" direction and the shortening of the grains in the "Y" direction occur in a very high amount in temper rolling with 500 µm reduction ratio. In the central region, it can be said that the elongation of the grains in the "X" direction and the shortening of the grains in the "Y" direction are less than the elongation and shortening in the region near the surface. In line with this informations, it can be concluded that as the reduction ratio increases, the grains are elongated and thinned in the regions close to the surface, and this change is less in the center compared to the regions close to the surface. Engler [18] found that the deformation of the grains increases with increasing the temper rolling degree. Koh et al. [14], on the other hand, found that in the regions close to the surface, the grains were elongated compared to the middle layer, and in the middle layer, due to heterogeneous deformation, full conduction could not be achieved and deformation did not occur to a large extent.

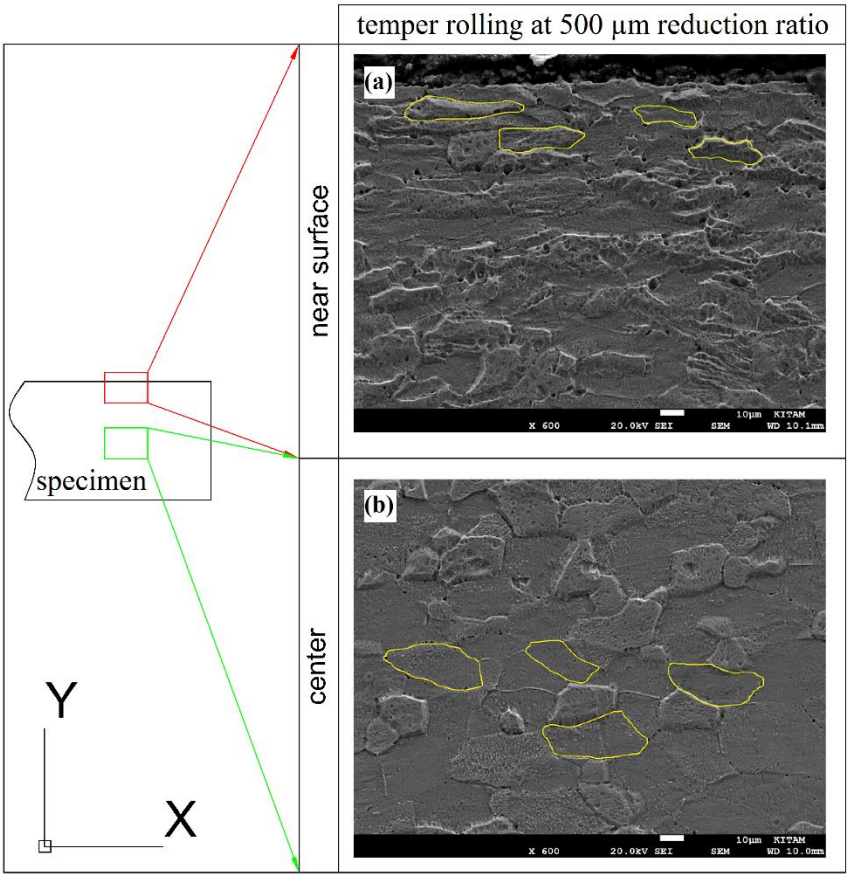

Figure 5. The SEM images taken from the section along the thickness of DC04 grade sheet material with temper rolling at 500 µm reduction ratio; a) from region close to the surface, b) from the central region

4. Conclusions

In this experimental study was investigated microhardness and microstructural evolution occurred along the thickness section of the sheet material as a result of temper rolling with different reduction ratios on DC04 grade sheet materials. The results of the investigation are presented below.

- With temper rolling process on DC04 grade sheet materials was concluded that the microhardness distribution taken from the section along the thickness rises with the increase of the reduction ratio and the Vickers microhardness ($HV_{0.05}$) distribution from the surface to the center in the section decreases.
- In temper rolling process to the DC04 grade sheet materials was concluded that with the increase in the reduction ratio the grains elongated and thinned on the surface along the thickness and this change is less in the center compared to the areas close to the surface.
- It was concluded that the findings obtained from this study can contribute to both the literature and the producers.

Acknowledgment

The authors thank for the support provided by Ondokuz Mayıs University [PYO. MUH.1904.19.013] the project number and [TÜBİTAK 2211-C], the laboratory support of "Faculty of Technology of Karabük University" and the material donations of "Ereğli Iron and Steel Factories".

Contributions of the authors

The contributions of each author to the article should be indicated.

Conflict of Interest Statement

There is no conflict of interest between the authors.

Statement of Research and Publication Ethics

The study is complied with research and publication ethics.

References

[1] A. Kocańda, and C. Jasiński, "Extended evaluation of erichsen cupping test results by means of laser speckle," *Archives of Civil and Mechanical Engineering*, vol. 16, pp. 211-216, 2016.

[2] A. Mulay, B. S. Ben, S. Ismail, A. Kocanda, and C. Jasiński, "Performance evaluation of high-speed incremental sheet forming technology for AA5754 H22 aluminum and DC04 steel sheets," *Archives of Civil and Mechanical Engineering*, vol. 18, pp. 1275-1287, 2018.

[3] D. K. Aspinwall, M. L. H. Wise, K. J. Stout, T. H. A. Goh, F. L. Zhao, and M. F. El-Menshawy, "Electrical discharge texturing," *International Journal of Machine Tools and Manufacture*, vol. 32, no. 1-2, pp. 183-193, 1992.

[4] K. Hilgenberg, and K. Steinhoff, "Texturing of skin-pass rolls by pulsed laser dispersing," *Journal of Materials Processing Technology*, vol. 225, pp. 84-92, 2015.

[5] C. Xia, X. Zhang, J. Zhang, H. Li, and S. Jia, "Evolution on topography of textured work rolls and steel strips during cold rolling and temper rolling," *Steel Research International*, vol. 88, no. 9, pp. 1600469, 2017.

[6] M. Burdek, "The change of work roll surface topography during skin pass rolling of steel sheets," *Industrial Lubrication and Tribology*, vol. 67, pp. 606-611, 2015.

[7] B. Çolak, and N. Kurgan, "An experimental investigation into roughness transfer in skin-pass rolling of steel strips," *The International Journal of Advanced Manufacturing Technology*, vol. 96, no. 9-12, pp. 3321-3330, 2018.

[8] C. Wu, L. Zhang, P. Qu, S. Li, and Z. Jiang, "A new method for predicting the three-dimensional surface texture transfer in the skin pass rolling of metal strips," *Wear*, vol. 426, pp. 1246-1264, 2019.

[9] C. Wu, L. Zhang, P. Qu, S. Li, and Z. Jiang, "A simple approach for analysing the surface texture transfer in cold rolling of metal strips," *The International Journal of Advanced Manufacturing Technology*, vol. 95, no. 1-4, pp. 597-608, 2018.

[10] B. Ma, A. K. Tieu, C. Lu, and Z. Jiang, "An experimental investigation of steel surface characteristic transfer by cold rolling," *Journal of Materials Processing Technology*, vol. 125, pp. 657-663, 2002.

[11] H. Yu, C. Lu, K. Tieu, H. Li, A. Godbole, X. Liu, and C. Kong, "Microstructure and mechanical properties of large-volume gradient-structure aluminium sheets fabricated by cyclic skin-pass rolling," *Philosophical Magazine*, vol. 99, no. 18, pp. 2265-2284, 2019.

[12] H. Kijima, "Influence of roll radius on contact condition and material deformation in skin-pass rolling of steel strip," *Journal of Materials Processing Technology*, vol. 213, no. 10, pp. 1764-1771, 2013.

[13] J. Grassino, M. Vedani, G. Vimercati, and G. Zanella, "Effects of skin pass rolling parameters on mechanical properties of steels," *International Journal of Precision Engineering and Manufacturing*, vol. 13, no. 11, pp. 2017-2026, 2012.

[14] Y. H. Koh, M. H. Lee, and S. K. Kim, "Texture evolution in low-C flat rolled steels on the physical properties," *International Journal of Precision Engineering and Manufacturing*, vol. 11, no. 3, pp. 445-452, 2010.

[15] Y. G. Ko, U. M. Chaudry, and K. Hamad, "Microstructure and mechanical properties of AA6061 alloy deformed by differential speed rolling," *Materials Letters*, vol. 259, pp. 126870, 2020.

[16] D. Fuloria, N. Kumar, S. Goel, R. Jayaganthan, S. Jha, and D. Srivastava, "Tensile properties and microstructural evolution of zircaloy-4 processed through rolling at different temperatures," *Materials & Design*, vol. 103, pp. 40-51, 2016.

[17] K. Komerla, A. Naumov, C. Mertin, U. Prahl, and W. Bleck, "Investigation of microstructure and mechanical properties of friction stir welded AA6016-T4 and DC04 alloy joints," *The International Journal of Advanced Manufacturing Technology*, vol. 94, no. 9, pp. 4209-4219, 2018.

[18] O. Engler, "Nucleation and growth during recrystallisation of aluminium alloys investigated by local texture analysis," *Materials Science and Technology*, vol. 12, no. 10, pp 859-872, 1996.

Bitlis Eren Üniversitesi Fen Bilimleri Dergisi
BİTLİS EREN UNIVERSITY JOURNAL OF SCIENCE
ISSN: 2147-3129/e-ISSN: 2147-3188
VOLUME: 11 NO: 2 PAGE: 400-410 YEAR: 2022
DOI: 10.17798/bitlisfen.984473

Karma Lif Takviyeli KYB Karışımlarının İşlenebilirlik ve Mühendislik Özelliklerinin Araştırılması

Kazım TÜRK[1*], Metin KATLAV[1], Paki TURĞUT[1]

[1]*İnönü Üniversitesi, Mühendislik Fakültesi, İnşaat Mühendisliği Bölümü, Malatya, Türkiye*
(ORCID: 0000-0002-6314-9465) (ORCID: 0000-0001-9093-7195) (ORCID: 0000-0002-3711-4605)

Anahtar Kelimeler:
Karma lif, Kendiliğinden yerleşen beton, İşlenebilirlik, Mühendislik özellikleri.

Öz

Bu çalışmada, benzer işlenebilirliğe sahip farklı boyut (makro ve mikro) ve narinlikteki çelik lif takviyeli kendiliğinden yerleşen beton (KYB) karışımların mühendislik ve işlenebilirlik özellikleri araştırılmıştır. Bu amaçla, lifsiz, sadece makro lif ve karma lif içeren KYB olmak üzere toplamda üç adet karışım tasarlanmıştır. Lifli KYB karışımları, EFNARC (2002) komitesi tarafından önerilen kriterlere göre mümkün olan benzer işlenebilirlik esas alınarak elde edilmiştir. Bu sebeple, çökme-yayılma, t_{500} ve J-halkası işlenebilirlik testleri yapılmıştır. Elde edilen lifli KYB karışımlarından 3, 28 ve 90 günlük basınç, yarmada çekme ve eğilmede çekme dayanımlarının belirlenmesi için numuneler hazırlanmış ve standartlara uygun şekilde test edilmiştir. Sonuç olarak, karışıma hem tekli hem de karma lif ilave edilmesi, karışımların işlenebilirlik özelliklerini olumsuz etkilemiştir. Bunun yanında, KYB karışımlarına narinliği 87 olan düz mikro çelik liflerin ilave edilmesinin basınç ve yarmada çekme dayanımlarında, narinliği 65 olan kancalı uçlu makro çelik liflerin ilave edilmesinin ise eğilmede çekme dayanımı değerlerinde olumlu bir etkiye sahip olduğu bulunmuştur.

Investigation of Workability and Engineering Properties of Hybrid Fiber Reinforced SCC Mixtures

Keywords:
Hybrid fiber, Self-compacting Concrete, Workability, Engineering properties.

Abstract

In this study, the engineering and workability properties of different size (macro and micro) and aspect/ratio steel fiber reinforced self-compacting concrete (SCC) mixtures with similar workability was investigated. For this purpose, a total of three SCC mixtures were designed: control with no fiber, only macro and hybrid fiber reinforced SCC. Based on possible similar workability, fiber reinforced SCC mixtures were obtained according to criteria recommended by the EFNARC (2002) committee. Therefore, slump-flow, t_{500} and J-ring workability tests were performed. Specimens obtained from SCC mixtures with fiber were prepared for 3, 28 and 90-day and compressive, splitting tensile and flexural tensile strengths tests were carried out. In conclusion, the inclusion of both single and hybrid fiber to SCC mixtures negatively affected the workability properties of the mixtures. Besides, it was found that the addition of straight micro steel fibers with an aspect ratio of 87 to mixtures had a positive effect on the compressive and splitting tensile strengths while the addition of hook-end macro steel fibers with an aspect ratio of 65 had a positive effect on the flexural tensile strength values.

*Sorumlu yazar: kazim.turk@inonu.edu.tr
Geliş Tarihi: 18.08.2021, Kabul Tarihi: 06.04.2022

1. Giriş

Kendiliğinden yerleşen beton (KYB), dünyada ilk defa 20. yüzyılın sonlarına doğru Japon bilim insanı Okamura [1] tarafından Japonya'da özellikle deprem bölgelerindeki yapı elemanlarında çok sık aralıklarla atılan donatılardan dolayı betonun kalıplara yerleştirilmesi esnasında ortaya çıkabilecek sorunları çözmek amacıyla geliştirilmiştir. Buna ilaveten KYB, kesitlere yerleşmesi sırasında her hangi bir dahili ve harici sıkıştırma işlemine gerek kalmadan kendi ağırlığı altında akabilen ve yerleşebilen inovatif bir betondur [2]. Bir beton karışımın KYB olması için EFNARC 2002 [3] komitesinin önerdiği işlenebilirlik deneylerine (Çökme-yayılma, t_{500}, J-halkası, L-kutusu, U kutusu gibi) ait sınır koşullarına sağlaması gerekmektedir. Bunun yanında, birçok üstün özelliklere sahip olan KYB'nin gevrek özelliğinden dolayı çekme dayanımı ve eğilme performansı düşüktür. Bu gibi dezavantajlarını ortadan kaldırılması amacıyla tekli ve karma lif takviyeli KYB ile ilgili birçok çalışmalarda yürütülmektedir [11-13,14,38,39]. Lif takviyeli beton ile ilgili ilk çalışmalar 20. yüzyılın ortalarında çelik lif takviye edilen betonun mekanik davranışını incelemek amacıyla yapılmıştır [4]. Bilindiği üzere, betonun çekme dayanımı basınç dayanımına göre oldukça düşüktür. Bu da özellikle yalın betonda ilk çatlak oluştuktan sonra betonun ani olarak kırılmasına ve oluşan çatlaklardan dolayı çevresel etkilere maruz kalmasına sebebiyet verir. Buna karşın, betonun çekme dayanımını artırmak için ilave edilen lifler matriste oluşturduğu bağ kuvvetleri sayesinde, betonda oluşan çatlakların başlamasını, yayılmasını ve ilerlemesini kontrol ederek betonun çekme dayanımı ve sünekliğini arttırmaktadır. Buna ilaveten, birden çok süreksiz lif tipinin betona ilave edilmesiyle elde edilen karma lif takviyeli betonların [5,6] daha ilgi çekici mühendislik özellikler sunacağı açıktır. Çünkü beton karışımına tek tip lif takviye edilmesi durumunda, betonun mekanik ve geçirimsizlik özelliklerini iyileştirmede sınırlı seviyede performans beklenebilir. Karma lif takviyeli kompozitte ise, farklı boy ve özelliklerdeki liflerin karma bir şekilde matrise ilave edilmesiyle, mikro lifler, mikro boyuttaki çatlakların başlamasını ve yayılmasını kontrol ederek betonda yüksek çekme dayanımına sebep olurlar. Daha sonra, mikro lifler, çatlağın ilerlemesini sağlayan gerilme enerjisini karşılamada yetersiz kaldığında mikro çatlaklar birleşerek makro çatlakları oluştururlar. Bu esnada devreye giren büyük makro lifler makro çatlakları kontrol ederek yapı elemanlarının, hem eğilme performansını hem de çatlak genişliklerinin sınırlandırılmasıyla çevresel etkilere karşı dayanıklılığını geliştirirler [7]. Böyle bir karma lif takviyeli kompozitin istenen performansa ulaşmada daha etkin olacağı açıktır [8,9]. Türk ve Kına (2017) [10] tarafından çimento esaslı kompozit karışımlarda karma lif kullanımı ile ilgili kapsamlı bir literatür araştırması yapılmış ve farklı boyut, narinlik ve işlevselliğe sahip liflerin betona dahil edilmesinin betonun özelliklerinden daha etkili yararlanabilme ve betonarme elemanların mekanik performansını arttırma imkanı sunduğu sonucuna varılmıştır. Bunun yanında, bu konuda yapılan bazı çalışmalarda [11-13], makro ve mikro çelik liflerin karma olarak uygun oranlarda geleneksel ve kendiliğinden yerleşen betona takviye edilmesi durumunda, eğilmeye maruz elemanların çoklu çatlak oluşumuna sebep olan sehim-sertleşmesi davranışı sergilediği gözlemlenmiştir. Diğer taraftan, makro ve mikro çelik lif ile birlikte sentetik liflerin betonda karma olarak kullanılmasının özellikle kendiliğinden yerleşen betonda meydana getirdiği işlenebilirlik sorunları dikkate alınarak, çimento yerine farklı tip mineral katkıların ikili, üçlü ve dörtlü kullanımlarının etkileri araştırılmış. Sonuçta, karma lif takviyeli betonlar için işlenebilirlik açısından en iyi harmanlamanın çimentoyla yer değiştirilen uçucu kül, yüksek fırın cürufu ve kireç taşı tozundan oluştuğu bulunmuştur [14]. Bu çalışmada farklı boy ve narinlikteki çelik lif içeren KYB'nin işlenebilirlik ve mühendislik özellikleri araştırılmıştır.

2. Deneysel Çalışma

2.1. Malzemeler

Bu çalışmadaki tüm karışımlarda bağlayıcı malzeme olarak, ÇİMKO Çimento ve Beton Sanayi A.Ş firması ürünü CEM I 42.5 R tipli Portland Çimento (PÇ) ile Sugözü Termik Santralinin baca atığı olan F sınıfı uçucu kül (UK) kullanılmıştır. Bağlayıcılara ait kimyasal ve fiziksel özellikler Tablo 1'de verilmiştir. Buna ilaveten 0-4 ve 4-16 mm elek aralığına sahip iki farklı tipte agrega kullanılırken, 0-4 ve 4-16 mm agregalarına ait su emme değerleri sırasıyla, %0,7 ve %0,5 ve doygun yüzey kuru özgül ağırlık değerleri ise sırasıyla, 2,43 ve 2,62 olarak bulunmuştur. Agregaların elek analizleri Tablo 2'de verilmiştir. Ayrıca, tüm karışımlar için yaklaşık benzer işlenebilirlik sağlamak amacıyla Sika Yapı Kimyasalları A.Ş.'den temin edilen özgül ağırlığı 1,06 olan ViscoCrete Hi-Tech 51 hiperakışkanlaştırıcı kullanılmıştır. Tüm lifli karışımlarda makro çelik lif olarak Kemerli Metal San. ve Tic. A.Ş. firmasına ait KMX 65/60 BG ve mikro çelik lif olarak da Bekaert A.Ş. firması

tarafından üretilen Dramix OL 13/.16 tercih edilmiştir. Bu liflere ait özellikler Tablo 3'de sunulmuştur.

Tablo 1. Çimento ve uçucu küle ait kimyasal ve fiziksel bileşenler

Kimyasal Kompozisyon	**PÇ (%)**	**UK(%)**
CaO	64,3	1,07
SiO_2	19,40	63,09
Fe_2O_3	3,79	6,77
Al_2O_3	5,36	21,63
MgO	2,25	-
SO_3	2,47	0,10
Na_2O	0,09	2,79
K_2O	0,90	-
Kızdırma kaybı	1,44	2,68
Fiziksel Özellikler		
Özgül Yüzey (Blaine)	3480 cm^2/g	2900 cm^2/g
Özgül Ağırlık	3,15	2,30

Tablo 2. Çalışmada kullanılacak agregalara ait elek analiz sonuçları

Agrega	**Elek boyutu (mm) - % Geçen**							
	16	**8**	**4**	**2**	**1**	**0.5**	**0.25**	**0.125**
Kırma Kum	100	100	96,55	62,9	39,4	15,8	14,2	7,35
Kırma Taş	100	19,71	1,48	0,62	0,18	0	0	0

Tablo 3. Liflere ait mekanik ve fiziksel özellikler

Lif Tipi	**Boy (mm)**	**Narinlik**	**Çekme Dayanımı (MPa)**	**Elastisite Modülü (GPa)**	**Yoğunluk (g/cm^3)**
KMX 65/60	60	65	1300	200	7,80
OL 13/.16	13	87	3000	200	7,20

2.2. Karışım Oranları

Yapılacak deneysel çalışma için, işlenebilirlik testleri açısından EFNARC'ın (2002) KYB'ler için belirlenen şartları göz önüne alınarak karışımlara ait reçete hazırlanmıştır. Bunun yanında, liflerin işlenebilirlik üzerindeki olumsuz etkisini ortadan kaldırmak ve liflerin matris tarafından sürüklenebilmesini mümkün kılacak viskoziteyi elde etmek için toplam bağlayıcı miktarı 900 kg/m^3 ve su/bağlayıcı (S/B) oranı 0.25 olarak sabit tutulmuştur. Agrega olarak %70 ve %30 oranlarında sırasıyla, 0-4 mm kırma kum ve 4-16 mm kırma taş kullanılmıştır. Lifli karışımlarda makro lif hacimce %1 ve %0,8 oranlarında ve mikro lif ise hacimce % 0,2 oranında kullanılmıştır. Bir adet kontrol karışımı, bir adet; sadece makro lif takviyeli tek lifli ve bir adet de karma lif takviyeli karışım olmak üzere toplam 3 adet KYB karışımı tasarlanmıştır. Tablo 4'de agregaların doygun yüzey kuru (DYK) olarak alındığı beton karışım oranları verilmiştir.

Tablo 4. Karışım oranları (kg/m^3)

KARIŞIM ADI	**PÇ**	**UK**	**SU**	**S/B***	**HA****	**AGREGA**		**ÇELİK LİF**	
						(0-4) mm	**(4-16) mm**	**KMX 65/60**	**DRMX OL 13/.16**
KONTROL	550	350	223	0,25	4,50	768,2	328,5	-	-
%1MAK	550	350	223	0,25	5,00	750,3	320,9	78,5	-
%0.8MAK_%0.2MİK	550	350	223	0,25	5,25	749,9	320,7	62,8	14,5

S/B*: Su/Bağlayıcı oranı
HA:** Hiperakışkanlaştırıcı
Bu karışımlara ait isimlendirmede kullanılan ifadelerin ne anlama geldiği şu şekildedir;
KONTROL: Kendiliğinden yerleşen lifsiz beton
MAK: Makro çelik lif (65/60)
MİK: 13 mm uzunluğundaki mikro çelik lif (OL 13/.16)
MAK ve MİK'in sol tarafına yazılan rakamlar karışıma takviye edilen liflerin hacimce miktarlarını ifade etmektedir. Örneğin; %0.8MAK_%0.2MİK şeklinde isimlendirilen karışım, %0.80 oranında makro çelik lif, %0.20 oranında mikro çelik lifi içermektedir.

2.3. Yöntem

Bu çalışmada tüm karışımların benzer işlenebilirlirliğe sahip olması hedeflenerek, çökme yayılma değerleri EFNARC (2005) [15] komitesinin önerdiği SF2 (660mm-750mm) sınıfı esas alınarak belirlenmiştir. Bu amaçla, karışımlardan elde edilecek numunelerin mühendislik özelliklerinin lif tipi ve kombinasyonun etkisini araştırmak için tüm karışımlarda sadece akışkanlaştırıcı miktarı değişken olarak alınmıştır. Hazırlanan karışımlara uygulanacak testler sırasıyla, işlenebilirlik (çökme-yayılma çapı, t_{500} süresi ve J-halkası yükseklik farkı (ΔH)) ve sertleşmiş beton testleri olarak iki bölümde gerçekleştirilmiştir. KYB karışımlarının 3, 28 ve 90 günlük basınç, yarmada çekme ve eğilme dayanımlarının belirlenmesi amacıyla her karışım için 3 adet olmak üzere sırasıyla, 100mm × 100mm × 100mm küp, ϕ100 × 200mm silindir ve 100mm × 75mm × 400mm prizmatik numuneler üretilmiş ve test edilmiştir. KYB karışımları hazırlanırken, 35 dm^3 hazneye sahip düşey eksenli mikser kullanılmıştır ve karışımların hazırlanmasında sırasıyla şu işlemler uygulanmıştır:

- İlk olarak iri ve ince agregalar ile varsa makro lifler ve karışım suyunun 2/3'ü düşey eksenli miksere eklenerek 3 dakika boyunca karıştırma işlemi yapılmıştır.
- Daha sonra bağlayıcı malzemeler ile karışım suyunun geriye kalan kısmı ve akışkanlaştırıcı miksere eklenerek 8 dakika daha karıştırma işlemi devam edilmiştir. Mikro lifler de, bu esnada miksere topaklanmayı engellemek amacıyla azar azar eklenmiştir. Böylece tüm karışımlar için toplamda 11 dakika karıştırma süresi uygulanmıştır (Şekil 1).

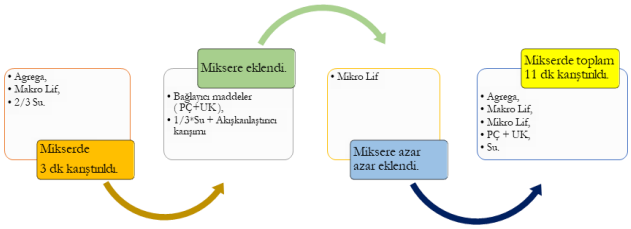

Şekil 1. Karışımların hazırlanmasında takip edilen adımları

2.3.1. İşlenebilirlik Testleri

İşlenebilirlik testleri EFNARC (2002) Komitesi'nin belirlediği öneriler doğrultusunda gerçekleştirilmiştir. Bu amaçla KYB karışımlarının her biri için çökme-yayılma, t_{500} ve J-halkası deneyleri yapılmıştır.

2.3.1.1. Çökme-yayılma, t_{500} ve J-halkası deneyi

KYB'nin doldurma kabiliyeti ve stabilitesinin ölçüldüğü çökme-yayılma testinde, deney aparatları deney öncesinde hafif ıslak bir bezle temizlendikten sonra, yeterli miktarda ve homojen olacak şekilde taze beton karışımı kesik koni şeklindeki Abrams hunisine doldurulmuştur. Abrams hunisi doldurulduktan sonra, 30 saniye zarfında koni yukarı doğru dikey olarak kaldırılmış ve Şekil 2'de de görülebileceği gibi KYB karışımının tabla üzerinde yayılması sağlanmıştır. Abrams hunisinin kaldırıldığı an ile betonun tabla üzerindeki 500 mm yayılma çapına ulaştığı an arasında geçen süre t_{500} olarak kaydedilmiştir. Karışımın yayılması bittikten sonra birbirine dik doğrultudaki çaplar ölçülüp aritmetik ortalaması alınarak karışımın çökme-yayılma değeri belirlenmiştir.

Lifli KYB'nin dar kesitler ve engeller arasındaki geçiş kabiliyetini tayin etmek için yapılan J-halkası deneyinde, halkanın merkezi ile hemen dışındaki 4 nokta arasındaki yükseklik farklarının ortalaması alınarak J-halkası yükseklik farkı (ΔH) belirlenmiştir. Aynı zamanda, betonun tabla üzerindeki 500 mm yayılma çapına ulaştığı t_{500j} süresi ve birbirine dik olacak çapların aritmetik ortalaması alınarak J-halkası yayılma çapı belirlenmiştir (Şekil 3).

Şekil 2. Çökme-yayılma deneyi

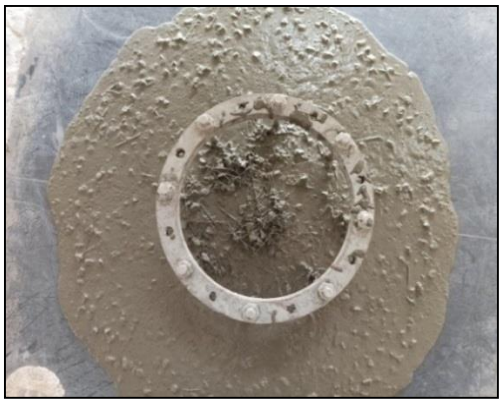

Şekil 3. J-halkası deneyi

2.3.2. Mühendislik Özellikleri

Karışımların 3, 28 ve 90 günlük mekanik özelliklerini belirlemek amacıyla, basınç, yarmada çekme ve eğilmede çekme dayanımı testleri yapılmıştır. Basınç dayanımının belirlenmesi için her bir seride 3 adet 100mm × 100mm × 100mm küp numune hazırlanmış, ASTMC39 (2018) [16] standardına uygun olarak test edilmiştir. Yarmada çekme dayanımı testi, ASTM C496 (2017) [17] standardına uygun olarak üretilmiş 3 adet ϕ100 × 200 mm silindir numuneler kullanılarak gerçekleştirilmiştir. Dört noktalı eğilme dayanımı için ise, her bir seride 2 adet 100mm × 75mm × 400mm prizmatik numune hazırlanarak ASTM C1609 (2019) [18] standardına uygun bir şekilde dört noktalı eğilme testi yapılmıştır. Ayrıca lifli karışımlardan elde edilecek yük-sehim eğrileri yardımıyla karışımlara ait eğilme toklukları, JSCE-SF4 (1984) [19] standartına göre belirlenmiştir. Şekil 4'te üretilmiş numunelere ait geometrik özellikler görülmektedir

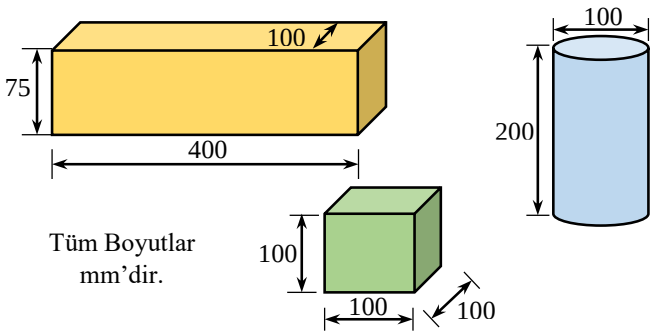

Şekil 4. Numune şekilleri ve boyutları

3. Bulgular ve Tartışma

3.1. Karışımların İşlenebilirlik Özellikleri

Lifsiz, tek ve karma lifli KYB karışımlarına ait çökme-yayılma, t_{500}, J-halkası, J-halkası çökme-yayılma ve J-halkası 500 mm'ye ulaşma süresi (t_{500j}) işlenebilirlik test sonuçları Şekil 5 ve 6'da verilmiştir. Tablodan görüldüğü gibi tüm karışımlara ait işlenebilirlik değerleri EFNARC (2002) komitesinin önerdiği sınır değerleri arasında kalmaktadır. Ayrıca şekillerden görüldüğü gibi, tüm karışımlara ait işlenebilirlik değerleri yaklaşık benzer olup, çökme-yayılma değerleri 730±5 mm, t_{500} değerleri 3±1.1 sn, J-halkası çökme-yayılma değerleri 707.5±2.5 mm ve t_{500j} değerleri ise 5±1 sn aralığında değişkenlik göstermişlerdir.

3.1.1. Çökme-yayılma ve J-halkası deneyi

Şekil 5'te görüldüğü gibi, KYB karışımlarına lif ilave edilmesiyle birlikte akışkanlaştırıcı miktarı artmasına rağmen lifsiz karışıma kıyasla lifli karışımların çökme-yayılma değerlerinin azaldığı ve t_{500} sürelerinin de arttığı tespit edilmiştir. Bunun yanında, mikro lif içeren karma lifli KYB karışımı sadece makro lif içeren tek lifli karışıma göre daha fazla akışkanlaştırıcı içermesine rağmen, her iki karışımında yaklaşık benzer çökme-yayılma ve t_{500} sürelerine sahip olduğu görülmüştür. Bu sonuçlar karışıma dahil edilen liflerin agregaya kıyasla özgül ağırlıklarının büyük olmasına ve liflerin narinliklerine dayandırılabilir. Çünkü mikro liflerin narinliklerinin makro life göre daha düşük ve özgül yüzeylerinin daha fazla olması karışımların işlenebilirliklerini olumsuz etkilemektedir. Oliveira vd. (2013) [20] tarafından yapılan deneysel çalışmada da, çelik liflerin beton karışımı içerisindeki oranı arttıkça yayılma çapının azaldığı tespit edilmiştir. Literatürde yer alan bazı

araştırmalarda [13,21,22] da benzer sonuçlar bulunmuştur.

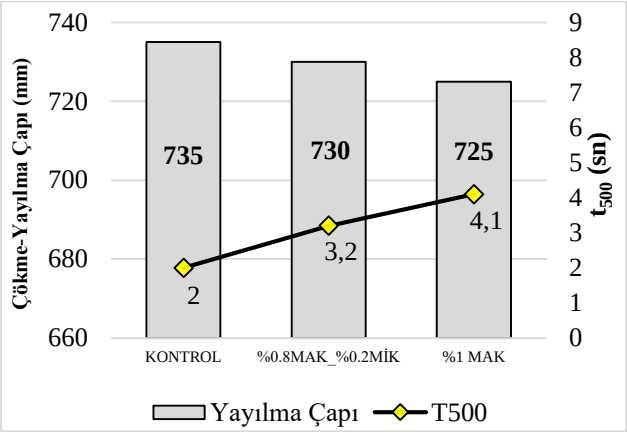

Şekil 5. Karışımlara çökme-yayılma ve t_{500} değerleri

J-halkası yükseklik farkı ve çökme-yayılma değerleri incelendiğinde, hem tek hem de karma lifli KYB karışımların lifsiz karışımlara kıyasla ΔH değerlerinde artış ve çökme yayılma değerlerinde ise azalma görülmüştür (Şekil 6). Çünkü lif geometrisi esas alındığında, özellikle mikro liflerin topaklanmaya olan eğiliminin fazla olması karışımların geçiş kabiliyeti ve aynı zamanda akıcılığını azaltabilir [23,24]. Ayrıca, Şekil 5'te görüldüğü gibi, KYB karışımlara ilave edilen makro lif miktarı artıkça karışımların engeller arasından geçiş kabiliyetinin azaldığı görülmüştür. Bununla birlikte, KYB karışımlarında makro çelik lif yerine mikro çelik lif kullanılması taze betonun J-halkası içindeki ve dışındaki yükseklik farkı (ΔH) değerlerinde artışa sebep olduğu tespit edilmiştir.

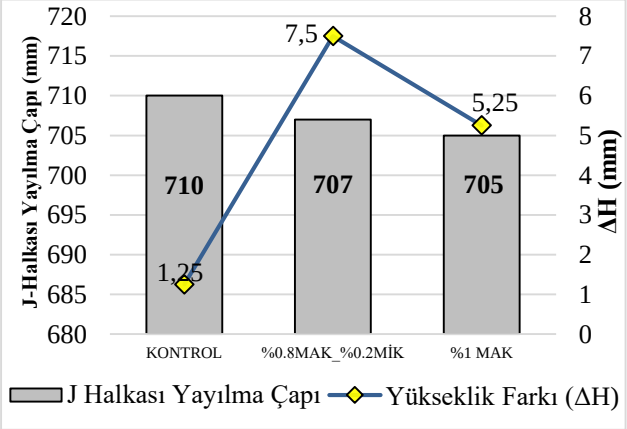

Şekil 6. Karışımlara ait J-halkası yükseklik farkı ve Çökme-yayılma değerleri

3.2. Karışımların Mühendislik Özellikleri

Lif takviyeli KYB karışımlarının basınç dayanımları Şekil 7'de verilmiştir. Şekilden görüldüğü üzere, lif takviyeli karışımlara ait basınç dayanımlarının genelde kontrol karışımına kıyasla daha düşük olduğu tespit edilmiştir. Bunun nedeni olarak makro veya mikro liflerin KYB karışımlarının işlenebilirlik özelliklerini azalttığı ve buna bağlı olarak karışımların doluluk oranının düşmesi olarak gösterilebilir. Literatürde de betona çelik lif takviyesinin betonun basınç dayanımını lifsiz betona kıyasla %±25 oranında değiştirebileceği belirtilmiştir [25, 26]. Kür süresinin artmasıyla, basınç dayanımının arttığı görülmektedir. Tüm karışımlar dikkate alındığında, 90 günlük basınç dayanımı değerleri, uçucu külün puzolanik etkisiyle 28 günlük basınç dayanımına kıyasla %6-11 arasında artmıştır. Ayrıca, sadece lif takviyeli KYB'ler dikkate alındığında, karma lif takviyeli karışımın sadece 28 ve 90 günlük basınç dayanımı değerlerinin tek tip makro lif takviyeli karışıma kıyasla daha yüksek olduğu tespit edilmiştir. Çünkü mikro liflerin daha etkili çatlak köprüleme ve dolayısıyla çatlak oluşum ve yayılımını engelleyip geciktirmesi matrisin yaşına bağlıdır. Literatürde de yapılan bazı çalışmalarda, karma lif takviyeli betonda mikro liflerin çatlak köprülemede etkili olmasının, matrisin nihai dayanım ile ilişkili olduğu ortaya koyulmaktadır [13,27,28].

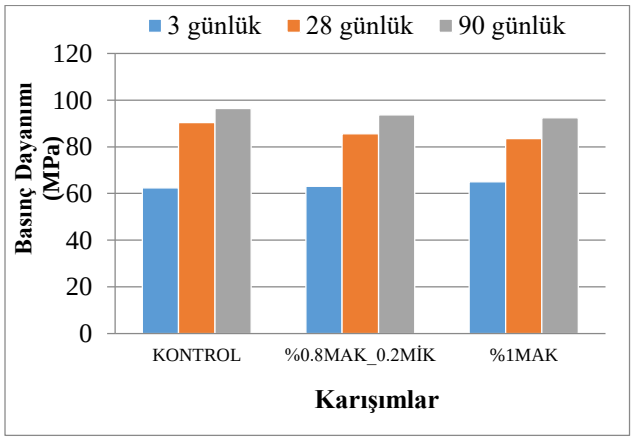

Şekil 7. Karışımlara ait basınç dayanımı değerleri

Çalışma kapsamında üretilen lifsiz, tek ve karma lif takviyeli KYB numuneleri üzerinde 3, 28 ve 90 gün sonunda yapılan yarmada çekme deneylerine ait sonuçlar Şekil 8'de verilmiştir. Şekilden görüldüğü gibi, lif takviyesi tüm kür yaşları için lifsiz kontrol numunelerine kıyasla yarmada çekme dayanımını artırırken, karma lif takviyeli KYB numunelerinin yarmada çekme dayanımı

değerlerinin genelde daha yüksek olduğu tespit edilmiştir. Literatürde bazı araştırmacılar [28-32] tarafından da bulunduğu gibi, betona tek tip lif yerine karma lif takviyesinin betonun yarmada çekme dayanımını daha çok iyileştirdiği belirtilmektedir. Ayrıca, Şekil 8'de görüldüğü gibi, tüm KYB karışımları değerlendirildiğinde, 28 günlük numunelere kıyasla, 90 günlük numunelerin yarmada çekme dayanımlarında, uçucu külün puzolanik etkisi sebebiyle %7-20 arasında bir artış olmuştur.

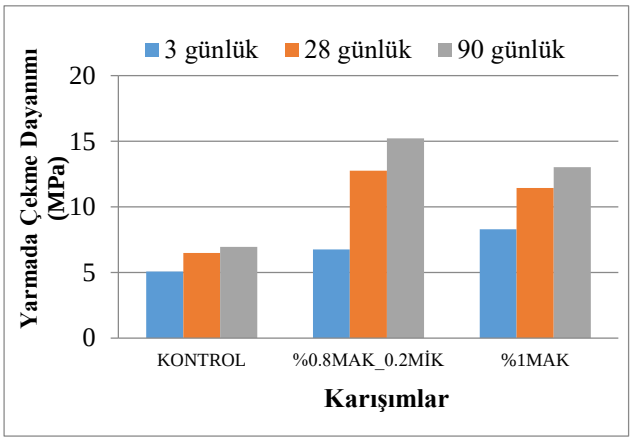

Şekil 8. Karışımlara ait yarmada çekme dayanımları

Tüm KYB karışımlarının, 3, 28 ve 90 günlük eğilmede çekme dayanımlarını belirlemek amacıyla hazırlanan prizmatik numuneler test gününde dört noktalı eğilme deneyine tabi tutulmuştur. Elde edilen sonuçlar Şekil 9'da verilmiştir. Şekilden de görülebileceği gibi, lif içeren tüm KYB karışımlarının eğilmede çekme dayanımı değerleri, lifsiz KYB karışımına kıyasla daha yüksektir. Bunun nedeni, liflerin, etkili çatlak köprülemesinin yanı sıra çatlak başlamasını, büyümesini ve geciktirmesini kontrol ederek enerji yutma kapasitesi daha yüksek bir mekanizma oluşturmasıdır [30]. Bu durum, aynı zamanda, kür yaşının ilerlemesiyle birlikte lif-matris arayüz özelliklerinin iyileşmesi karışımların eğilmede çekme dayanımlarında artış meydana gelmesine ve matris dayanımının artmasıyla özellikle mikro liflerin eğilmede çekme dayanımı üzerindeki etkilerinin daha belirgin olmasına dayandırılabilir. Ayrıca, karışıma mikro çelik lif ilave edilmesinin tek lifli karışıma kıyasla, eğilmede çekme dayanımını azalttığı tespit edilmiştir. Literatürde mevcut olan bazı çalışmalarda [27,33,34] da bu durumu destekleyici sonuçlar bulunmuştur. Bunlara ilaveten, puzolanik bir malzeme olan uçucu kül daha uzun kür şartlarında hidratasyon reaksiyonları sergilediğinden, numunelerin 90 günlük eğilmede çekme dayanımı değerlerinin, 28 günlük tüm KYB numunelerine kıyasla %7,4-15,3 arasında arttığı tespit edilmiştir.

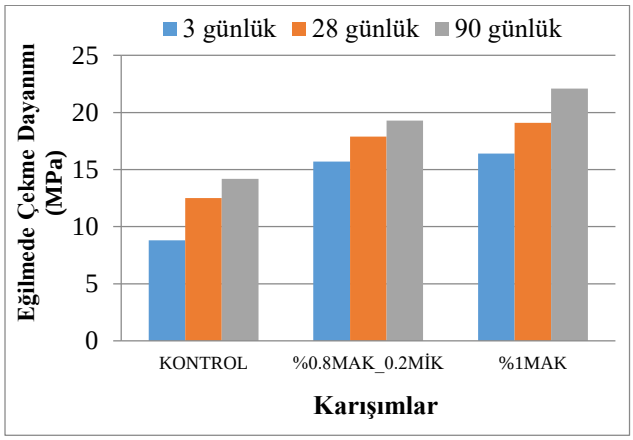

Şekil 9. Karışımlara ait eğilmede çekme dayanımları

Ayrıca, dört noktalı eğilme deneyine tabi tutulan lif takviyeli numunelere ait tokluk değerleri, yük-sehim eğrilerindeki L/150 (2 mm) sehim değerine kadar olan eğrinin altındaki alandan ($A_{(L/150)}$) faydalanılarak bulunmuştur. Daha sonra elde edilen tokluk değeri JSCE-SF4 standardının önerdiği Denklem 3.1'de yerine yazılarak eğilme tokluğu faktörü (FT) hesaplanmıştır**.** Elde edilen bulgular Tablo 5'de verilmiştir

$$FT = \frac{A_{(L/150)} \times L}{(L/150) \times b \times h^2} \quad (3.1)$$

Burada;
FT: Eğilme Tokluğu Faktörü (N/mm^2)
$A_{(L/150)}$: Yük-sehim eğrisinin altında kalan alan (N.mm)
L : Alt mesnetler arası mesafe (mm)
b, h : Numune boyutları (mm)

Tablo 5. Karışımlara ait tokluk ve eğilme tokluğu faktörü değerleri

Karışımlar	Tokluk (N.m)			Eğilme Tokluğu Faktörü (MPa)		
	3 gün	28 gün	90 gün	3 gün	28 gün	90 gün
%0.8MAK_ %0.2MİK	64,48	89,33	89,58	17,27	23,82	23,89
%1MAK	96,49	101,46	105,48	25,73	27,05	28,10

Tüm lif takviyeli karışımlara ait 3, 28 ve 90 günlük JSCE-SF4 standardına göre hesaplanan eğilme faktörü değerleri Şekil 10'da verilmiştir. Sonuçlar incelendiğinde karışıma mikro çelik lif ilave edilmesiyle eğilme tokluğunun azaldığı tespit edilmiştir. Ayrıca numunelerin eğilme tokluğu değerleri üzerinde liflerin etkili çatlak köprülemesinin daha etkin olduğu tespit edilmiştir. Ancak, nihai kür yaşında, liflerin çatlak köprülemesi

esnasından kopması sebebiyle, 28 günlük numunelerin eğilme tokluğu değerlerine kıyasla eğilme tokluğu değerleri artışında azalma görülmüştür. Literatürde yer alan bazı çalışmalarda [35-40] da bulguları destekleyen sonuçlar bulunmuştur.

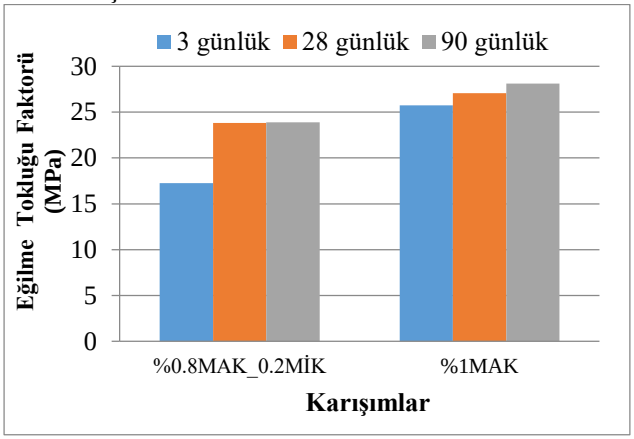

Şekil 10. Karışımlara ait eğilme tokluğu faktörü değerleri

Lifli KYB numunelerine ait eğilme deneylerinden elde edilen yük-sehim eğrileri Şekil 11'de gösterilmiştir. Lif takviyeli tüm numunelerin, tüm kür yaşları için sehim sertleşmesi davranışı sergilediği görülmüştür. Ayrıca, numunelerin eğilme davranışı incelendiğinde, makro çelik lif takviyesinin, yük taşıma kapasitesi üzerinde daha olumlu bir etkisi olduğu tespit edilmiştir. Bu durum mikro çelik lifler sadece mikro çatlakları köprülemede etkin olmasına ve tepe noktası sonrasındaki davranış üzerinde çok ciddi bir etkiye sahip olamamasına dayandırılabilir. Literatürde yer alan birçok çalışmada [13,27,36,38,41,42,43] karma lif takviyeli KYB karışımlarında mikro çelik lif oranı arttıkça, taşıma kapasitesi değerlerinde azalma olduğu tespit edilmiştir.

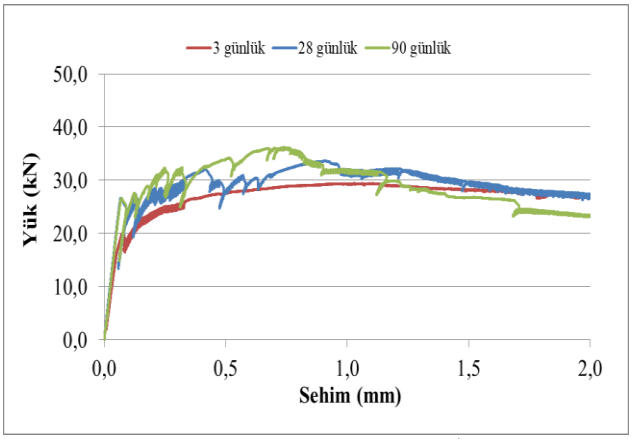

a) %0.8MAK_%0.2MİK

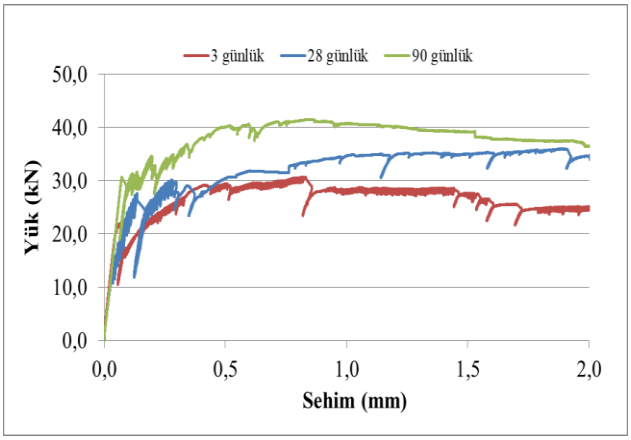

b) %1MAK

Şekil 11. Karışımlara ait 3, 28 ve 90 günlük yük-sehim eğrileri

4. Sonuçlar

Bu çalışmada, lifsiz, tek ve karma lif takviyeli olarak üretilen KYB karışımları üzerinde işlenebilirlik (Çökme-yayılma, t_{500} ve J-halkası) ve mekanik (basınç, yarmada çekme ve eğilmede çekme dayanımı) özelliklere ait deneyler yapılmıştır. Yapılan deneysel çalışmadan aşağıdaki sonuçlar bulunmuştur:

- Lifsiz kontrol karışımına göre, karışıma hem tekli hem de karma lif takviye edilmesi, karışımların çökme-yayılma çapı değerlerinde azalmaya, J-halkası yükseklik farkı (ΔH) ve yayılma sürelerinde (t_{500}) ise artışa neden olmuştur.
- Karışıma makro ve mikro çelik liflerin ilave edilmesi basınç dayanımında azalmaya neden olurken, yarmada çekme ve eğilmede çekme dayanımlarında ise artışa neden olduğu tespit edilmiştir. Lifli karışımlar içerisinde yarmada çekme dayanımlarında en fazla artış, karma lifli KYB numunelerinde görülürken, eğilmede çekme dayanımında ise en fazla artışın sadece makro lif içeren karışımda olduğu tespit edilmiştir.
- Tek ve karma lif takviyeli karışımların 3, 28 ve 90 günlük kür yaşlarından elde edilen yük-sehim eğrilerinin tümünde sehim sertleşmesi davranışı gözlemlenmiştir.
- Çelik lif takviyeli KYB karışımlarına ait eğilme tokluğu değerlerinde en iyi performansı, tüm kür yaşları için tek tip makro çelik lif takviyeli karışımdan elde edilmiştir. Ayrıca, numunelerin kür yaşının artmasına bağlı olarak matris kırılganlığının artması ve liflerin matristen sıyrılarak çıkma davranışlarının azalmasından

dolayı eğilme tokluğu değerlerindeki artışta azalma gözlemlenmiştir.

Teşekkür

Bu çalışma, Türkiye Bilimsel ve Teknolojik Araştırma Kurumu (TÜBİTAK) 1002 Hızlı destek Programı (MAG-121M024) ve İnönü Üniversitesi Bilimsel Araştırma Projesi Birimi (Proje numarası: FYL-2020-2298) tarafından desteklenmiştir. Verdikleri finansal destekten ötürü teşekkür ederiz.

Yazarların katkısı

Yazarlar makaleye eşit oranda katkı sağlamışlardır.

Çıkar çatışması beyanı

Yazarlar arasında herhangi bir çıkar çatışması bulunmamaktadır.

Araştırma ve yayın etiği beyanı

Yapılan çalışmada araştırma ve yayın etiğine uyulmuştur.

Kaynaklar

[1] H. Okamura, "Self-compacting high-performance concrete," *Concrete international*, vol. 19 no. 7, pp. 50-54, 1997.
[2] M. Nehdi, M. Pardhan, and S. Koshowski, "Durability of selfconsolidating concrete incorporating high-volume replacement composite cements," *Cement and Concrete Research,* vol. 34, pp. 2103-2112, 2004.
[3] EFNARC, "Specification and guidelines for self-compacting concrete," *European project group, UK, 2002.*
[4] D. J. Hannant, *Fiber cements and fiber concrete*, Chichester, UK: Wiley, 1978.
[5] Y. N. Ding, Z. You, S. Jalali, "Hybrid fiber influence on strength and toughness of RC beams," *Composite Structures,* vol. 92, pp. 2083–2089, 2010.
[6] P. Sukontasukkul, P. Jamsawang, "Use of steel and polypropylene fibers to improve flexural performance of deep soil–cement column," *Construction and Building Materials,* vol. 29, pp. 201–205, 2012.
[7] S. Mindess, *Thirty years of fibre reinforced concrete research at the UWM British*, Colombia, 2007.
[8] P. Rossi, P. Acker, Y. Malier, "Effect of steel fibres at two different stages: the material and the structure," *Materials and Structures*, vol. 20, no. 1, pp. 436-439, 1987.
[9] B. Mobasher, Y. L. Cheng, "Mechanical properties of hybrid cement based composites," *American Concrete Institute Materials Journal,* vol. 93, no. 3, pp. 284-292, 1996.
[10] K. Türk and C. Kına, "Çimento Esaslı Kompozitlerde Karma Lif Kullanımı," *Pamukkale Üniversitesi Mühendislik Bilimleri Dergisi,* vol. 23 no. 6, pp. 671-678, 2017.
[11] K. Türk and E. Atalay, "The Properties of Hybrid Fiber Reinforced Self-Compacting Concrete with Different Type Micro Fiber," *4th International Energy Engineering Congress, Gaziantep, Türkiye, pp.1040-1051,2019.*
[12] K. Türk ve M. Başsürücü, "Effect of Curing Conditions on the Mechanical Properties of Conventional Concrete with Hybrid Fiber," in *4th International Energy Engineering Congress,* Gaziantep, Türkiye, 2019, pp. 244-257.
[13] K. Turk, E. Oztekin, and C. Kina, "Self-compacting concrete with blended short and long fibres: experimental investigation on the role of fibre blend proportion," *European Journal of Environmental and Civil Engineering,* vol. 26. no. 3, pp. 905–918, 2022.
[14] K. Türk ve İ. Dönmez, "Some Properties Of Hybrid Fiber Reinforced Self-Compacting Concrete Containing Binary And Ternary Mineral Admixture," *4th International Energy Engineering Congress,* Gaziantep, Türkiye, 2019, pp.1052-1065.
[15] EFNARC, "European Guidelines for Self-Compacting Concrete," *Specification and Production and Use Association, 2005.*
[16] ASTM C39, "Standard Test Method for Compressive Strength of Cylindrical Concrete Specimens," *ASTM International, West Conshohocken, PA, 2018.*
[17] ASTM C496 / C496M-17, "Standard Test Method for Static Modulus of Elasticity and Poisson's Ratio of Concrete in Compression," *ASTM International, West Conshohocken, PA, 2017.*

[18] ASTM C1609 / C1609M-19. 2019. "Standard Test Method for Flexural Performance of Fiber-Reinforced Concrete," *ASTM International, West Conshohocken, PA, 2019.*
[19] JSCE, "Method of Test for Flexural Strength and Flexural Toughness of Fibre Reinforced Concrete," *JSCE Standard SF-4,1984.*
[20] L. A. Pereira de Oliveira, J. P. Castro Gomes, M. M. M. Bernardo and L. F. A Ramos, "Evaluation of dry mortar ratio as mix design parameter for steel fibre reinforced self compacting concrete," *Construction and Building Materials,* vol. 40, pp. 642-649, 2013.
[21] X. Liu, T. Wu, X. Yang and H. Wei, "Properties of self-compacting lightweight concrete reinforced with steel and polypropylene fibers," *Construction and Building Materials,* vol. 226, pp. 388–398, 2019.
[22] H. Ghanem and Y. Obeid, "The Effect of Steel Fibers on the Rhyological and Mechanical Properties of Self Compacting Concrete," *European Scientific Journal,* vol. 11. no. 21, pp. 1857–1881, 2015.
[23] B. Akcay ve M.A. Tasdemir, "Mechanical behaviour and fibre dispersion of hybrid steel fibre reinforced self-compacting concrete," *Construction and Building Materials,* vol. 28 pp. 287–293, 2012.
[24] R. Yu, P. Spiesz and H.J.H. Brouwers, "Mix design and properties assessment of ultra-high performance fibre reinforced concrete (UHPFRC)," *Cement Concrete Research,* vol. 56 pp. 29–39, 2014.
[25] U. Nyström and K Gylltoft, "Comparative numerical studies of projectile impacts on plain and steel-fibre reinforced concrete," *Int. J. Impact Eng.,* vol. 38 pp. 95–105, 2011.
[26] M. Sarı, "Farklı Tipteki Liflerin Betonun Mekanik Davranışına Etkisi," Yüksek Lisans Tezi, İstanbul Teknik Üniversitesi, İstanbul, 2013.
[27] N. Haddadou, R. Chaid, Y. Ghernouti, and N. Adjou, "The effect of hybrid steel fiber on the properties of fresh and hardened self-compacting concrete," *J. Build. Mater. Struct,* vol. 1, no. 2, pp. 65–76, 2014.
[28] M. Sahmaran, A. Yurtseven, and I. Ozgur Yaman, "Workability of hybrid fiber reinforced self compacting concrete," *Building and Environment,* vol. 40, no. 12, pp. 1672–1677, 2005.
[29] M. Hsiea, C. Tu and P.S. Song, "Mechanical properties of polypropylene hybrid fiber-reinforced concrete," *Materials Science and Engineering A,* vol. 494, pp. 153–157, 2008.
[30] R. Yu, P. Spiesz and H.J.H. Brouwers, "Development of Ultra-High Performance Fibre Reinforced Concrete (UHPFRC): Towards an efficient utilization of binders and fibres," *Construction and Building Materials,* vol. 79, pp. 273-282, 2015.
[31] J. Blunt and C. P. Ostertag, "Performance-Based Approach for the Design of a Deflection Hardened Hybrid Fiber-Reinforced Concrete," *Journal Of Engıneerıng Mechanics,* vol. 135, pp. 978-986, 2009.
[32] A. Bentur and S. Mindess, *Fiber Reinforced Cementitious Composites,* CRC press, 2006.
[33] F. Aslani, F. Hamidi, A. Valizadeh, and A. T. N. Dang, "High-performance fibre-reinforced heavyweight self-compacting concrete: Analysis of fresh and mechanical properties," *Construction and Building Materials,* vol. 232, pp. 117230, 2020.
[34] H. Mazaheripour, S. Ghanbarpour, S. H. Mirmoradi and I. Hosseinpour, "The effect of polyproplene fibers on the properties of fresh and hardened lightweight self-compacting concrete," *Construction and Building Materials,* vol. 25, no.1, pp. 351-358, 2011.
[35] J. J. Li, C. J. Wan, J. G. Niu, L. F. Wu, and Y. C. Wu, "Investigation on flexural toughness evaluation method of steel fiber reinforced lightweight aggregate concrete," *Construction and Building Materials,* vol. 131, pp. 449-458, 2017.
[36] P. Rashiddadash, A. A. Ramezanianpour, and M. Mahdikhani, "Experimental investigation on flexural toughness of hybrid fiber reinforced concrete (HFRC) containing metakaolin and pumice," *Construction and Building Materials,* vol. 51, pp. 313-320, 2014.
[37] H.R. Pakravan, M. Latifi and M. Jamshidi "Hybrid short fiber reinforcement system in concrete: A review," *Construction and Building Materials* vol. 142, pp. 280–294, 2017.
[38] K. Turk, C. Kina and E. Oztekin, "Effect of macro and micro fiber volume on the flexural performance of hybrid fiber reinforced SCC," *Advances in Concrete Construction,* vol. 10, no. 3, pp. 257-269, 2020.

[39] K. Turk, M. Bassurucu and RE. Bitkin, "Workability, strength and flexural toughness properties of hybrid steel fiber reinforced SCC with high-volume fiber," *Construction and Building Materials*, vol. 266, pp. 120944, 2021.
[40] J.J. Li, C.J. Wan, J.G. Niu, L.F. Wu, and Y.C. Wu, "Investigation on flexural toughness evaluation method of steel fiber reinforced lightweight aggregate concrete," *Construction and Building Materials*, vol. 131, pp. 449-458, 2017.
[41] M. Pajak and T. Ponikiewski "Flexural behavior of self-compacting concrete reinforced with different types of steel fibers," *Construction and Building Materials,* vol. 47, pp. 397-408, 2013.
[42] Z. Wu, C. Shi and W. He, " Effects of steel fiber content and shape on mechanical properties of ultra high performance concrete," *Construction and Building Materials,* vol. 103, pp. 8-14, 2016.
[43] R.E. Bitkin, "Basınç Donatısız KYB'den Üretilmiş Kirişlerin Eğilme Performansına Karma Lif Takviyesinin Etkisi," Yüksek Lisans Tezi, İnönü Üniversitesi, Fen Bilimleri Enstitüsü, Malatya, 2020.

Bitlis Eren Üniversitesi Fen Bilimleri Dergisi
BİTLİS EREN UNIVERSITY JOURNAL OF SCIENCE
ISSN: 2147-3129/e-ISSN: 2147-3188
VOLUME: 11 NO: 2 PAGE: 411-420 YEAR: 2022
DOI: 10.17798/bitlisfen.998006

Design of a 3D Printed Open Source Humanoid Robot

Levent PARALI[1] , Ali SARI[2*], Mehmet ESEN[3]

[1]*Manisa Celal Bayar University, Electronics & Automation Department, Turgutlu Vocational School, Manisa / Turkey*
[2]*Manisa Celal Bayar University, Electrical and Energy Department, Turgutlu Vocational School, Manisa / Turkey*
[3]*Robfly Robotics, Information Technologies and Software Inc, Manisa / Turkey*
(ORCID: 0000-0002-4462-7628) (ORCID: 0000-0002-8928-2512) (ORCID: 0000-0002-6800-3801)

Keywords: 3D printing, Humanoid robot, Skillful hand, Raspberry pi 3

Abstract
Nowadays, humanoid robots with great capabilities used in a variety of purposes to serve humans have become an integral part of our lives. In this study, we have developed a low-cost humanoid robot that can be fabricated with an open-source 3D printer. Firstly, the 3D-CAD model of the humanoid robot was created using source codes of the "InMoov" project which is originated by Gael Langevin who works as a designer on his project since 2012. The humanoid robot involves approximately 685 parts built from the PLA (Poly-Lactic Acid) raw material. After that, a new electronics system based on the embedded controllers which have been controlled with the python programming language has been designed. This robotic platform controlled with the help of voice commands has the capability to communicate with people. Furthermore, a skilled prosthetic hand controlled according to the commands from a smart glove, can grasp and holds objects, have been specially developed in this study. When comparing to the existing commercial humanoid robots, this humanoid robot developed as specific has a substructure which is not only low cost but also open to new improvements as well.

1. Introduction

The automatically operated machines named "Robot" can replace human activities, perform functions in a human-like manner, although it may not resemble human beings in appearance [1]. Humanoid robots have been built as similar to humans and are able to mimic human movements. The production of a robot usually covers the challenging design and construction processes for researchers in science and engineering fields [1, 2]. Especially, humanoid robots which have dual arms and resourceful hands demonstrate great significance in the home environments, health, and care service areas. They can be used for many services to human beings such as accompanying person, surgery operations, manipulation, and material handling etc. [3]. Recently, artificial intelligence studies about humanoid robots have become the most impressive field for clever robotics systems. Therefore, many large scientific research universities, institutions, and private sector delegates continue to work as intensely in this area.

Many humanoid robots have been fabricated in recent years. Some of them are ranked WABIAN-RV [4], ASIMO [5], HRP [6], NAO [7], "Pepper Robot" [8], KHR-1 [9], and Robot H10 [10] according to various categories.

However, some humanoid robots are too expensive or can often be bulky due to their non-optimized structure. In order to interact with humans easily, the robots with the light-weight structure are needed to equilibrate their energy efficiently. High accuracy humanoid robots with flexible structure need a lightweight and high stiffness structures controlled by the actuators [11]. As humanoid robots with heavy components cause to spend high power consumption it decreases battery life. Therefore,

*Corresponding author: ali.sari@cbu.edu.tr
Received: 20.09.2021, Accepted: 31.03.2022

battery-based most humanoid robots are designed as lightweight due to the fact that they will help working longer [12,13]. Characteristically, there is a lot of production methods with a lightweight design. One of them is a 3D printing method which is also known as additive manufacturing (AM). AM is defined as the process of joining materials to create objects from 3D model data [14, 15]. The modern AM is occurred by the main current 3D printing techniques, namely fused deposition modeling (FDM), stereolithography and laser sintering processes from the late 1980ies. AM patents have been ranked between 1979 and 2000 [16].

3D printers build objects using an AM process. Material layers by placing on top of each other occur to form the base for the next layer. Most 3D printers use thermoplastic inks based on polymer. These polymers become soft and flexible under a certain temperature range. When the printing process is finished, they are re-solidify.

Commands for positioning the nozzle of the 3D printer are received by means of a print file format. There are many print file formats in use. Various CAD (Computer-Aided Design) programs such as AutoCAD, Solid Works, and Fusion 360 have been used to produce files. Nowadays, new design tools, cameras, laser scanners can directly generate a print file by capturing photos that have various angles from 3D objects [17].

In this study, it is aimed the design and development of a humanoid robotic project by using the 3D printer technology with the purpose of achieving research and educational targets for universities. Furthermore, a speech recognition system is roughly described on the humanoid robot as well as.

Section 2 and Section 3 introduce the material selection, fabrication of the various robot parts using the 3D printer according to the stereolithography file-formats obtained from the original “InMoov” project, and the creation of the upper body by assembling 3D printed parts, respectively. Section 4 gives detailed information about hardware designs of the humanoid robot such as main control system, servo motors, skillful hand, head, shoulder, elbow control, and theirs the electrical connections between each other.

2. Material and Method

Generally, PLA (polylactic acid) which is a kind of polymerized from natural sources is used in desktop printers [18]. PLA has a larger strength and lower fragility than the traditional ABS (acrylonitrile butadiene styrene). PLA parts obtained via 3D printers have often been very used in the medical field applications due to their biocompatibility properties as well [19].

Table 1 shows the 3D print file formats in use. The humanoid robot in this project is created using the Stereo-Lithography (.STL) format. The 3D fabrication system creates a 3D printed object using additive processes for one extruder. In an additive process, an object is fabricated by layer by layer until the object is created.

Nowadays, as printers developed, both open-source and registered 3D file formats will be developed. For example, the 3D Manufacturing Format (*.3MF) was pronounced in 2015. The 3MF format is tailor-made for additive manufacturing and provides valuable benefits such as Full-Color Support, Build Tray Support, Unicode -Human Readable, etc. to additive manufacturing workflows that other formats lack [20].

Table 1. Some 3D Print File Formats

File Format	Description
*.STL	Stereo lithography; 3D single color.
*.WRL	Virtual Reality Modeling Language for multi-color 3D printing (at least two extruder)
*.OBJ	Image format with 3D coordinates
*.X3G	Used by Makerbot Replicator
*.PLY	Polygon format for scanners
*.3MF	XML based data format

Figure 1 indicates additive manufacturing method through the 3D printing process. Figure 2 and Figure 3 show the photos of varies parts which are 3D printed according to obtained *.stl file formats from original “InMoov” project, respectively [21].

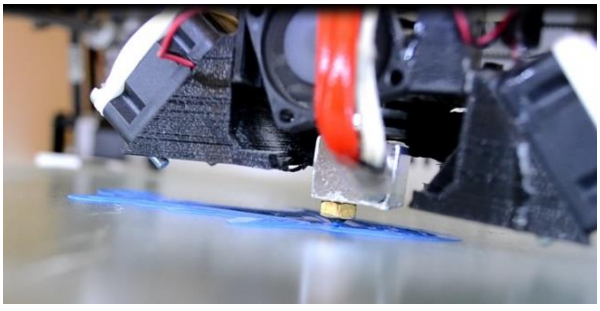

Figure 1. Additive manufacturing with 3D

3. The Completely 3D Printed Upper Body

The first open-source robot "InMoov" can be printed in 3D, compounded, and programmable. The InMoov project has been launched in 2012 by French sculptor and designer Gaël Langevin. It has been developed ever since by a worldwide community of robotics enthusiasts [21].

All parts of this humanoid robot which has the biodegradable PLA-based filament structure can be built by using the 3D printer. The 3D printer which has a working area of 200x300x180 mm has been chosen for the production of robot parts. The humanoid robot's "skin," joints, gears, and many other pieces have been 3D printed. Some of the robotic parts, its head design, and the upper body obtained by assembling 3D printed parts are shown in Figure.2, Figure.3, and Figure 4, respectively in detail.

Figure 2. InMoov open source humanoid robotic parts

Figure 3. InMoov open source humanoid robot head design

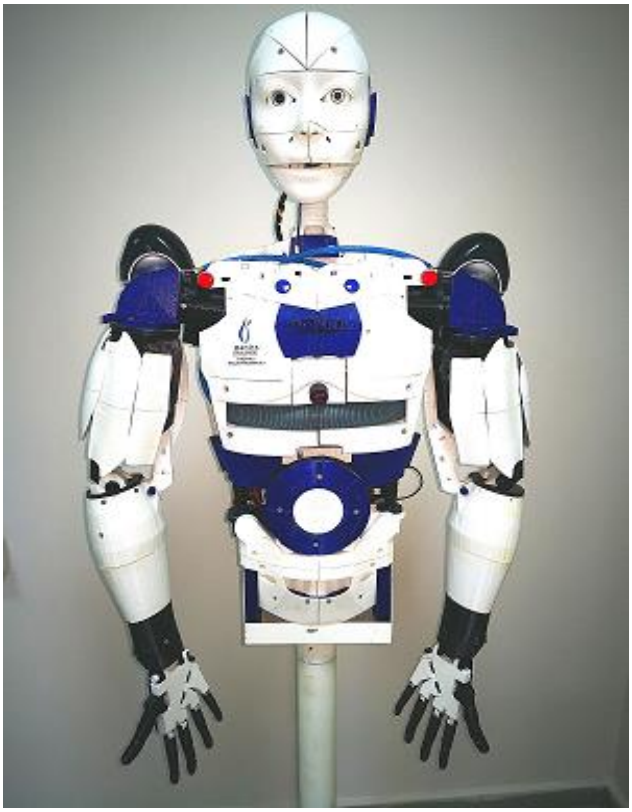

Figure 4. The front view of the humanoid robot

4. Hardware Design of the Humanoid Robot

4.1. Control System

In this study, it has been used a Raspberry Pi 3 Model B for hardware design of the humanoid robot. The Raspberry Pi with open-source code is an inexpensive, and can be used by connection it to a monitor, and using a standard mouse and keyboard. Table 2 indicates specific parameters of the Raspberry Pi 3 Model B [22].

The Raspberry Pi B model has a Cortex-A53 processor that applies the ARMv8-A architecture. This processor can be between one and four cores, it includes an L1 memory system for each and a single shared L2 cache.

Two 5V pins and two 3.3V pins are to be presented on the board, while OV is ground pins that are not configurable. The remaining all pins have 3.3V values. It means outputs are set to 3.3V and inputs are 3.3V-tolerant.

Both input and output pins of the GPIO are designated as high-3.3V or low-0V. This situation can be realized as easily with the use of internal pull-up or pull-down resistors. Pull-up resistors have been fixed for Pins GPIO2 and GPIO3, however, other pins can be configured with software.

The Cortex-A53 processor controls both static and dynamic power dissipation. The Cortex-A53 process with individual cores support four main levels of power management such as power domains, power modes, event communications and power management controller with communication [23].

The most important one of the Raspberry Pi's main parts is the GPIO (General Purpose Input Output) which has 40 pins are indicated in Figure 5.

Furthermore, the GPIO pins can be used as alternatively for various functions. Some of them are available on all pins, others on specific pins. The GPIO pins are ranked as four categories such as PWM - Pulse Width Modulation, SPI - Serial Peripheral Interface, I^2C - Inter-Integrated Circuit, Serial Communication Ports-TX/RX.

Table 2. Specific parameters of the Raspberry Pi3 Model B

SoC	BCM2835/2837
CPU	A53 @ 1.2 GHz.
Instruction Set	ARMv8-A
GPU	400 MHz
RAM	1GB SDRAM
Storage	Micro-SD
Ethernet	10/100
Wireless	802.11n/Bluetooth h4.0
Video Output	HDMI/Composite
Audio Output	HDMI/Headphones
GPIO	40

4.2. Servo Motors

Servo motors are used as two type generally to motion control of the humanoid robot such as head, shoulder, elbow, wrist, skillful hand etc. Two type servo motors are chosen for this study. One of them is MG996 type servo motor which controls both the left and the right skillful hand together. The MG996 servo has a metal gearing system resulting in extra high 10 kg stalling torque in a tiny package. It has some properties which are shown Figure 6, and Table 3 [24].

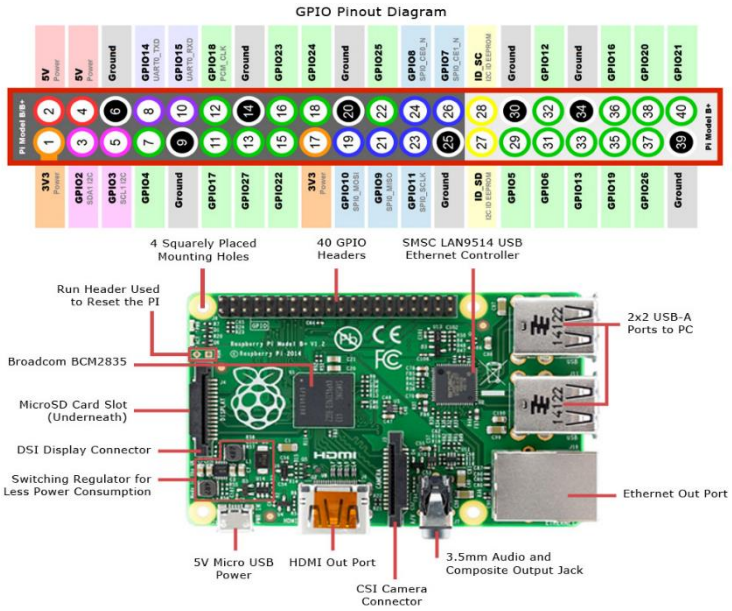

Figure 5. Raspberry Pi B model and its GPIO Pinout Diagram [22]

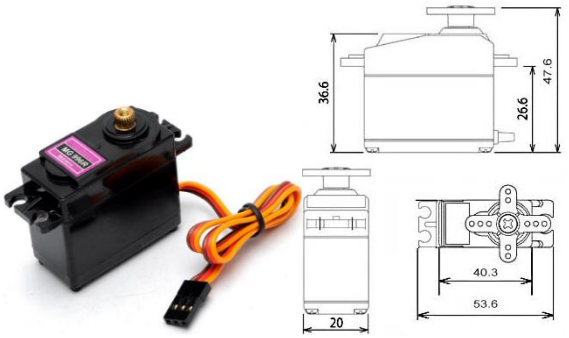

Figure 6. Real view of MG996 servo motor with its dimensions drawing

Table 3. Specifications of the MG996 type servo motor

Rotation	180 °
Weight	55gr.
Sizes	40.7 x 19.7 x 42.9 mm
Stop Torque and Current	9.4 kgf/cm at 4.8V, 11kgf/cm (2.5A) at 6V
Working Voltage Ranges	4.8V – 6.6V
Current Drawn	500 mA – 900 mA (6V)
Dead Bandwidth	1 µs
Wire Length	300mm
Temperature range	0 – 55 ºC

Another type servo motor is the Hitec HS805BB which has been used for the control of humanoid robot arms and its head. Some properties of the Hitec HS805BB are shown as detailed in Figure 7, and Table 4 [25].

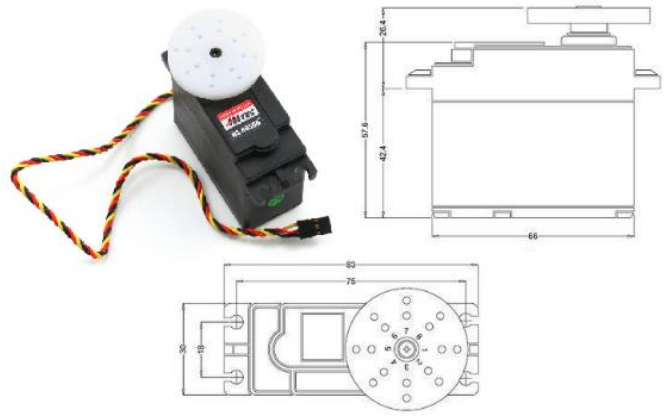

Figure 7. Real view of HS-805BB servo motor with its dimensions drawing

Table 4. Specifications of the HS-805BB type servo motor

Rotation	180 º
Control System	Pulse Width Control 1500 µs Neutral
Weight	152gr.
Sizes	Around 66 x 30 x 57.6 mm
Stop Torque and Current	19.8kgf/cm at 4.8V, 24.7kgf/cm (2.5A) at 6V
Operating Angle	45º/One Side Pulse Traveling 400 µs
Direction	Clock Wise/Pulse Trav. 1500-1900 µs
Working Voltage Ranges	4.8V – 6.0V
Current Drain	8 mA/IDLE – 700 mA No Load.
Dead Bandwidth	8 µs
Wire Length	300mm
Temperature range	-20 - 60 ºC

4.3. Skillful Hand

The left or right dexterous hand has five fingers and a wrist joint, respectively. The fingers are moved with the aid of the rope through five servo motors (MG966). It uses two ropes for each finger. One of them bends finger while other provides to come back to straight. When the left or right-hand touches an object, the fingers can clutch automatically it. Furthermore, it needs another servo motor-MG966 for the wrist joint. The wrist joint has back and forth rotation capabilities via the servo motor.

To improve various applications such as prosthesis, the skillful hand can be controlled by a data glove. As shown in Figure 8, the skillful hand can grip and grab some objects through data glove. When a human wears the data glove, it can be controlled simultaneously the prosthesis hand by moving own healthy fingers into the glove.

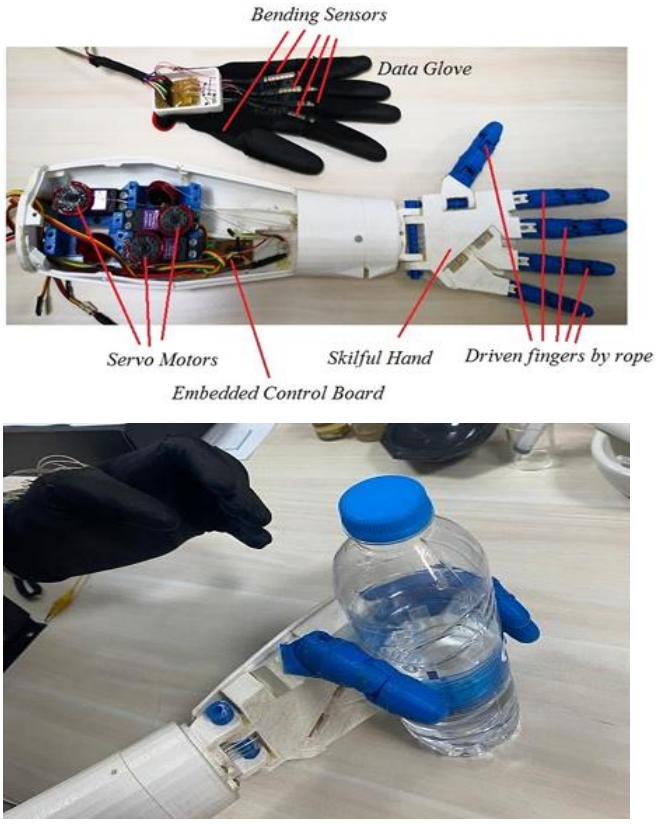

Figure 8. Left skillful hand of the humanoid robot and its control by the glove

Each of the five bending sensors are placed bonded on the top of every finger on the data glove. The bending sensors' resistance values are changed according to finger motions. In order to evaluate the change of the hand motions by bending sensor, an Arduino UNO card is used. The changes in the hand gesture convert to a series of voltage through a resistance voltage divider circuit. The bending angle and motion can be defined by using voltage signals associated with various resistance values.

The pseudo-code between the glove and the skillful hand is indicated in Figure.9.

sketch_dec12a.ino

```
#include <Servo.h>
const int pot1=A0;
const int pot2=A1;
const int pot3=A2;
const int pot4=A3;
const int pot5=A4;
Servo servo1;
Servo servo2;
Servo servo3;
Servo servo4;
Servo servo5;
int flexdurum1=0;
int flexdurum2=0;
int flexdurum3=0;
int flexdurum4=0;
int flexdurum5=0;
int pos1=0;
int pos2=0;
int pos3=0;
int pos4=0;
int pos5=0;
void setup() {
  // put your setup code here, to run once:
Serial.begin(9600);
servo1.attach(3);
servo2.attach(5);
servo3.attach(6);
servo4.attach(9);
servo5.attach(10);
}
void loop() {
flexdurum1=analogRead(pot1);
pos1=map(flexdurum1,0,1023,0,180);
{
  servo1.write(pos1);
}
flexdurum2=analogRead(pot2);
pos2=map(flexdurum2,0,1023,0,180);
{
  servo2.write(pos2);
}
flexdurum3=analogRead(pot3);
pos3=map(flexdurum3,0,1023,0,180);
{
  servo3.write(pos3);
}
flexdurum4=analogRead(pot4);
pos4=map(flexdurum4,0,1023,0,180);
{
  servo4.write(pos4);
}
flexdurum5=analogRead(pot5);
pos5=map(flexdurum5,0,1023,0,180);
{
  servo5.write(pos5);
}
}
```

Figure 9. The pseudo-code between the glove and the skillful hand

4.4. Head, Shoulder and Elbow Control

Head, jaw, shoulder, and elbow control sections have been driven by the Hitec HS805BB servos. The control modules consist of totally nine servo motors as three pieces on the head section including the jaw control, four pieces for two shoulders, and two pieces for elbows. The shoulder control section of the humanoid robot is shown in Figure 10.

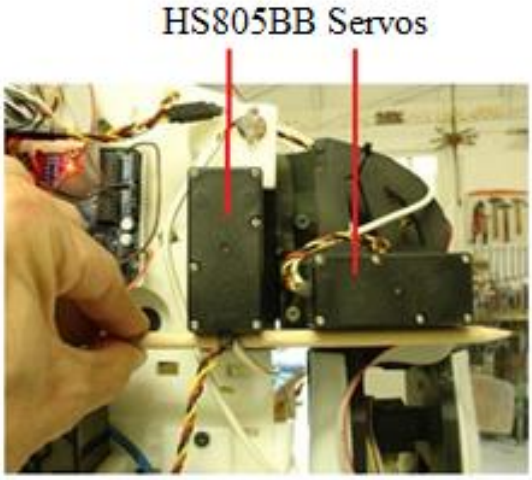

Figure 10. Shoulder joint of the humanoid robot [21]

4.5. Pulse Width Modulation (PWM) Control

Generally, a servo motor's electronics circuitry is built right inside the motor unit and has a positioning shaft with a variable, which usually is fitted with a gear. Most servo motors have three pins in which two of these are voltage terminals and the other is the signal terminal. The control signal is a pulse-width modulation (PWM) which is a way to control analog devices with a digital signal output. The servo motor's angular position owing to a high pulse is shown in Figure11.

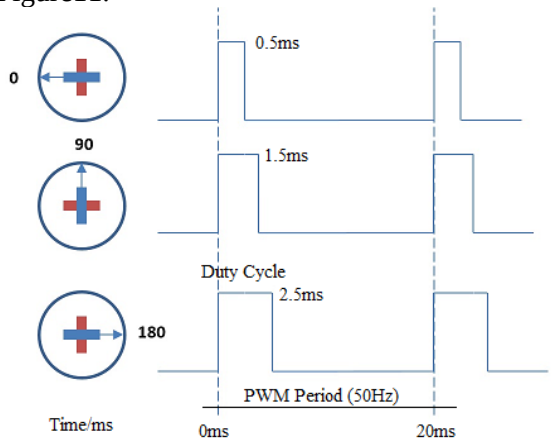

Figure 11. The duty-cycles of the square control signal

Typically, servo motors require a PWM signal with a 20 msn period and a pulse width between 0.5–2.5 msn. 0.5 msn equals to the minimum rotation angle, while 2.5 msn coincides with the maximum rotation angle. The middle position is almost 1.5 msn as the average of the pulse widths. The MG996 and HS805BB type servo motors have same maximum angle of 180°.

The desired position is controlled by the obtained PWM signal from the Raspberry Pi 3 Model B. The servo motor's speed changes according to the difference between the actual position and the desired position. If the motor is near the requested position, it will turn slowly, otherwise, it will turn fast to reach the desired position. This automatic speed control is provided by proportional control. To obtain the requested position, servos motors are controlled as continually [26].

4.6. The Electrical Connection of the 3D Printed Humanoid Robot Platform

The whole system is divided into five sub-modules as the left hand, the left arm, the right hand, the right arm, and the head. These mentioned five parts are directly controlled by the Raspberry Pi 3 Model B controller. The humanoid robot's electrical connection diagram is presented as detailed in Figure 12. Furthermore, for human-robot interactions, the microphone provides hearing of the humanoid robot, while the loud-speaker enables its speaking. Also, the mentioned system allows of the use of the various camera for image processing and face recognition applications, too.

Furthermore, in order to improve various applications on the humanoid robot, it may use in several programming languages such as Linux, Python, C, HTML5, CSS, Scratch, and JavaScript. Especially, for human-robot interaction based on speech recognition systems, it can be used Google Voice and various speech API services through an internet connection in the Raspberry Pi 3 Model B.

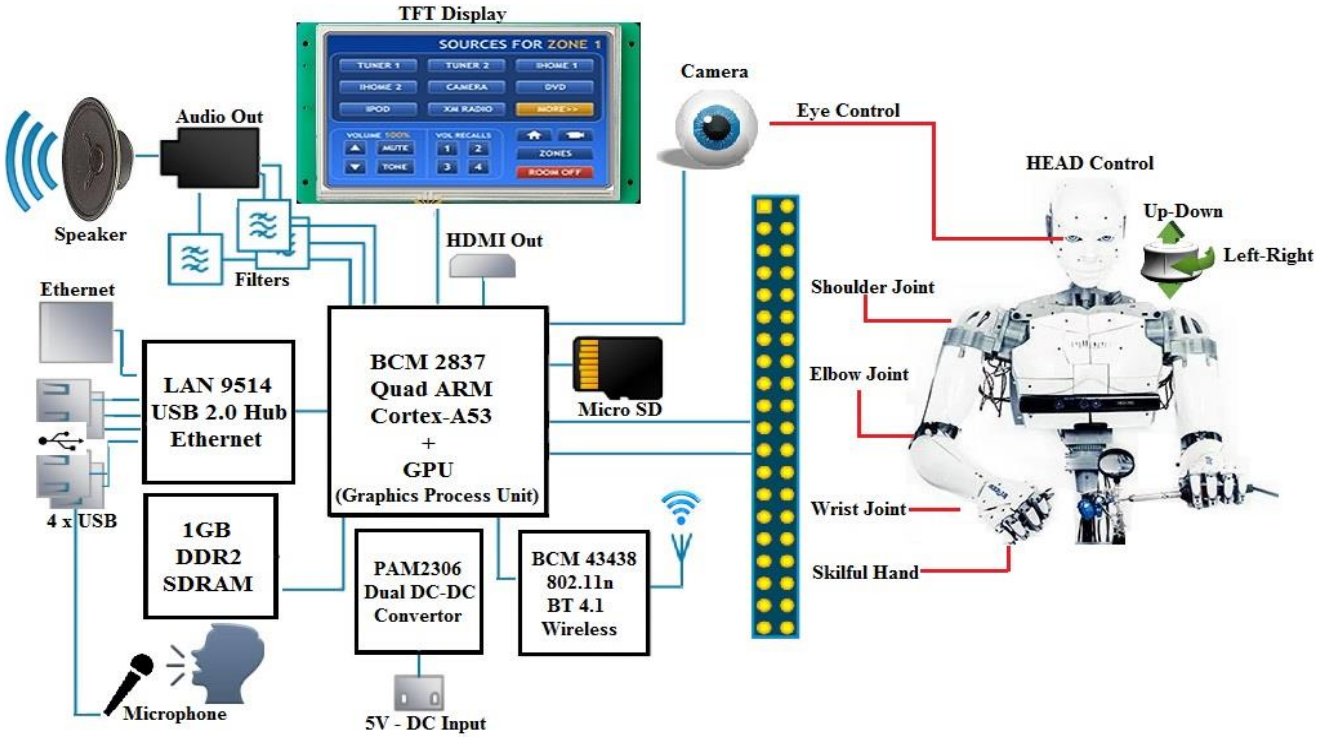

Figure 12. Connection of humanoid robot to peripherals

5. Conclusion and Suggestions

In this study, a fully functional low-cost 3D printed dual-arm humanoid robot was successfully fabricated using the open-source codes of the 3D printed humanoid robot based on "InMoov". The main control design of the humanoid robot was built on the architecture of the Raspberry Pi 3 Model B. Head, jaw, shoulder, and elbow control sections associated with the humanoid robot were driven by modules consisting of nine servo motors. Additionally; in order to realize various applications based on the prosthesis, the skillful hand which can be controlled simultaneously with a data glove was also carried out in this study. For human-robot interaction based on speech recognition systems, Google Voice and various speech API services were used via an internet connection in the Raspberry Pi 3 Model B. The python programing language has a flexible and efficient substructure that can support many speech recognition engines.

This humanoid robot fabricated for educational purposes covers also a few scientific areas which support a well-rounded mechatronics experience for a team of students that have different majors. For instance, it involves CAD-CAM works for mechanical engineering students; electronic circuits (resistors, transistors, capacitors, inductors, diodes, integrated circuits, microcontroller), sensors, and data acquisition systems for electrical and electronics engineering students; as well as potential programming works are suitable for computer science students. Furthermore, this humanoid robot system can be used to simulate human intelligence through some methods such as Artificial Intelligence (AI), Machine Learning, and Deep Learning, too.

Contributions of the authors

Levent Paralı : Drafted and wrote the manuscript, provided technical support, and performed the experimental analyses and performance evaluations.

Mehmet Esen : Wrote the software of realized humanoid robot using the python programming language.

Ali Sarı: Performed some experiments on the humanoid robot, and prepared its working algorithm.

Conflict of Interest Statement

The authors state that did not have conflict of interests

Statement of Research and Publication Ethics

The study is complied with research and publication ethics

References

[1] N. Rodriguez, G. Carbone, M. Ceccarelli, "Antropomorphic design and operation of a new low-cost humanoid robot", in *The 1st IEEE/RAS-EMBS International Conference on Biomedical Robotics and Biomechatronics*, Pisa, Italy, 2006.

[2] F. Kaplan, "Who is Afraid of the Humanoid? Investigating Cultural Differences in the Acceptation of Robots". *International Journal of Humanoid Robotics*, vol.1, no. 3, pp. 465-480, 2004.

[3] H. Cheng, G. Ji, "Design and Implementation of a Low Cost 3D Printed Humanoid Robotic Platform". *The 6th Annual IEEE International Conference on Cyber Technology in Automation, Control and Intelligent Systems (CYBER)*, Chengdu, China, 2016.

[4] G. Carbone, H.O. Lim, A. Takanishi, M. Ceccarelli, "Numerical and experimental estimation of stiffness performances for the humanoid robot WABIAN-RV". *IEEE/ASME International Conference on Advanced Intelligent Mechatronics (AIM 2003)*, Port Island, Kobe, Japan, 2003.

[5] Y. Sakagami, R. Watanabe, C. Aoyama, S. Matsunaga, N. Higaki, K. Fujimura, *The intelligent ASIMO: system overview and integration, Intelligent Robots and Systems*, Lausanne, Switzerland, 2002.

[6] K. Kaneko, F. Kanehiro, S. Kajita, K. Yokoyama, K. Akachi, T. Kawasaki, S. Ota, T. *Isozumi. Design of prototype humanoid robotics platform for HRP, Intelligent Robots and Systems*, Lausanne, Switzerland, 2002.

[7] D.L Recio, L.M. Segura, E.M Segura, A. Waern, "The NAO models for the elderly". *8th ACM/IEEE International Conference on Human-Robot Interaction (HRI)*, Tokyo, Japan, 2013.

[8] J. Lafaye, D. Gouaillier, P.B. Wieber, "Linear model predictive control of the locomotion of pepper, a humanoid robot with omnidirectional wheels". *IEEE-RAS International Conference on Humanoid Robots, Madrid*, Spain, 2014.

[9] J.H. Kim, J.H.Oh, "Torque Feedback Control of the Humanoid Platform KHR-1", *3rd IEEE International Conference on Humanoid Robots*, Karlsruhe and Munich, Germany, 2003

[10] M. Hackel, S. Schwope, "A Humanoid Interaction Robot for Information, Negotiation and Entertainment Use". *International Journal of Humanoid Robotics*, vol. 1, no. 3, pp. 551-563, 2004.

[11] D. Ye, S. Sun, J. Chen, M. Luo M, "The lightweight design of the humanoid robot frameworks based on evolutionary structural optimization". *IEEE International Conference on Robotics and Biomimetics (ROBIO 2014)*, Bali, Indonesia, 2014.

[12] T. Lens, O. Stryk, "Design and Dynamics Model of a Lightweight Series Elastic Tendon-Driven Robot Arm". *IEEE International Conference on Robotics and Automation (ICRA)*, Karlsruhe, German, 2013.

[13] H Hagenaha, W. Böhma, T. Breitsprecherb, M. Merkleina, S. Artzackba, "Modelling, Construction and Manufacture of a Lightweight Robot Arm", *Procedia CIRP Intelligent Computation in Manufacturing Engineering*, 12:211 – 216, 2013.

[14] N. Bhattacharjee, A. Urrios, S. Kang, A. Folch, "The Upcoming 3D-printing revolution in microfluidics", *Lab on a Chip*; vol. 16, no.10, pp. 1720 –1742, 2016.

[15] K. Takagishi, S. Umezu, "Development of the Improving Process for the 3D Printed Structure", *Scientific Reports*, vol. 7, no. 39852, 2017.

[16] L. Bechthold, V. Fischer, A. Hainzlmaier, D. Hugenroth, L. Ivanova, K. Kroth, B. Römer, E. Sikorska, V. Sitzmann, V, "3D printing: A qualitative assessment of applications, recent trends and the technology's future potential". Commission of Experts for Research and Innovation; 17:120, Berlin, 2015.

[17] M. Christiano, "Introduction to 3D Printing: History, Processes, and Market Growth", *https://www.allaboutcircuits.com/news/introduction-to-3d-printing-history-processes-and-market-growth.* [Accessed: 20-May-2020]

[18] M.F. Ashby, K. Johnson, Materials and Design, *The Art and Science of Material Selection in Product Design, Butterworth-Heinman*: Oxford, UK, 2013.

[19] D. Drummer, S. Cifuentes-Cuéllar, D. Rietzel, "Suitability of PLA/TCP for fused deposition modeling", *Rapid Prototyping Journal*, vol. 18, no. 6, pp. 500-507, 2012

[20] C. K. Chua, C. H. Wong, W.Y. Yeong, *Standards, Quality Control, and Measurement Sciences in 3D Printing and Additive Manufacturing*, Academic Press: Elsevier, 2017.

[21] Inmoov, "Open-source 3D printed life-size robot". *http://inmoov.fr/build-yours* [Accessed: 20-May-2020]

[22] The Raspberry Pi Model B Card Datasheets, *https://www.raspberrypi.org/documentation/hardware/raspberrypi*. [Accessed: 20-May-2020]
[23] Arm Cortex-A53 MPCore Processor Technical Reference Manual *http://infocenter.arm.com/help/index.jsp?topic=/com.arm.doc.ddi0500j/CHDDCDDG.html*. [Accessed: 20-May-2020]
[24] MG-996 High Speed Metal Gear Dual Ball Bearing Servo Motor Datasheet. *http://www.towerpro.com.tw/product/mg995-robot-servo-180-rotation.* [Accessed: 20-May-2020]
[25] HS-805BB Servo Motor Datasheet. *https://www.servocity.com/hs-805bb-servo* [Accessed: 20-May-2020]
[26] R. Firoozian, *Servo Motors and Industrial Control Theory*, Springer: Berlin, Germany, 2014.

Bitlis Eren Üniversitesi Fen Bilimleri Dergisi
BİTLİS EREN UNIVERSITY JOURNAL OF SCIENCE
ISSN: 2147-3129/e-ISSN: 2147-3188
VOLUME: 11 NO: 2 PAGE: 421-428 YEAR: 2022
DOI: 10.17798/bitlisfen.1014488

Development of a Machine Learning Based Control System for Vehicle Active Suspension Systems

Ali Rıza KALELİ[1], Halil İbrahim AKOLAŞ[2*]

[1]*Department of Electrical-Electronics Engineering, Faculty of Engineering, Samsun University, Samsun 55080, Turkey*
[2]*Vocational School of Balıkesir, University of Balıkesir, Balıkesir Turkey*
(ORCID: 0000-0002-3234-5922) (ORCID 0000-0002-3153-8044)

Keywords: Vehicle Active Suspension system, Machine Learning Methods, Linear Quadratic Optimal Control, Random Road Profile.

Abstract
In this paper, the Gaussian process (GP) algorithm, which is one of the machine learning methods, is designed to control the vehicle active suspension system (VASS). Experimental data were used to create the supervised learning method (regression method). The data was obtained from an optimal linear quadratic controller tuned based on a full state feedback optimal control approach. The results demonstrated that the proposed machine learning based (GPR) ML controller outperforms the optimal controller under uncertainties in terms of reducing the oscillation in spring mass position, vehicle body acceleration, and suspension deflection with 39.08%, 52.18%, 58.10%, and 17.81%, 15.63%, and 21.64% improvement for bump and sine sweep road conditions, respectively.

1. Introduction

The road irregularities that affect passenger comfort are one of the main sources of vibration in vehicles. Vehicle vibrations and undesirable noise have negative effects on human health, especially on the spinal cord and nervous systems [1]. Therefore, the improvement in road comfort is very important, and it is possible by designing active vehicle suspension systems (AVSS).

In the active suspension system, there are nonlinear components such as springs and dampers to generate force for adaptation to unknown road profiles. Owing to uncertain nonlinear dynamics and unknown road disturbances, it is difficult to design active suspension systems. Therefore, it is necessary to focus on advanced control techniques for these systems. Until today, the design of controller problems in AVSS has been widely discussed in the literature. For the sake of simplicity, researchers attempted to overcome these uncertainties by designing PID [2] and linear–quadratic (LQ) controllers [3]. However, these approaches are not satisfactory because the parameters of both controllers are determined based on linearized models. Due to the nonlinear nature of the system, adaptive backstepping control considering the model uncertainties and actuator delays was discussed in [4]. In another study, five different continuous sliding-mode controllers were used to avoid the chattering effect, and the effectiveness of the proposed controllers was compared to the linear control approach [5]. Adaptive backstepping control for AVSS with hard constraints was proposed to ensure the stabilizing attitude of the vehicle under road disturbance driving conditions in [6]. Robust control structure studies [7] using adaptiveness contain a lot of complex mathematical expressions, and the designing processes of the controller are therefore difficult to formalize. To improve performance against disturbance effects or uncertainties, robust controllers such as H_∞ control [8], gain scheduling, linear parameter varying control [9] were designed for active suspension systems to improve performance against disturbance effects or uncertainties. Also, a robust H infinity controller was investigated for an active suspension under

*Corresponding author: halil.akolas@balikesir.edu.tr
Received: 25.10.2021, Accepted: 06.06.2022

non-stationary operating conditions [10]. On the other hand, model-free approaches were applied to compensate for vehicle vibrations, unlike model-based approaches. For this purpose, data-driven approaches such as fuzzy logic and neural-networks were applied to deal with the nonlinear and time-varying characteristics of AVSS for improving the controller performance. In the experimental investigation of a multiple-input single-output fuzzy logic controller on an AVSS was compared with passive and classical fuzzy logic controllers [11]. An adaptive network based fuzzy inference (ANFIS) controller was designed by using the training data obtained from the system [12]. The performance of the designed controller was tested using an experimental setup and it was observed to have satisfactory closed loop performance. In [13], the neural network adjusts its weight parameters and learns from sliding mode control to prevent vibrations from vehicles due to ride irregularities. Besides, data-based methods are used to tune the parameters of different control structures. A back propagation neural network (BPN) was applied to determine the gain parameters of a PID controller for AVSS [14]. Data driven modeling methods are based on a machine learning approach. These techniques are applied in many different fields, like engineering, finance, and optimization problems, and they provide the ability to predict the complex dynamic behavior of systems [15].

As can be seen from the literature reviews above, data-driven methods can estimate the unknown system dynamics and external disturbances and improve control performance. Therefore, the main purpose of this research paper is to investigate the Gaussian process (GP) machine learning controller design for AVSS considering road disturbance conditions and system uncertainties. Besides, bump and sine sweep of the road profile are used to define road deterioration and irregularities as input to AVSS. Then, the performance of the designed controller is compared with conventional control methods in terms of wheel deflection, suspension deflection, and vehicle displacement. Finally, validation results of the proposed learning-based control scheme are given to show the effectiveness of the designed controller.

2. Material and Method

We start in this section with an explanation of the physical background of active suspension systems and the test set-up, which enable us to understand the vehicle suspension properties and the designing of the controller problems.

2.1. AVSS System

The configuration of the VASS is sketched in Figure 1. As seen this Figure 1, m_s and m_{us} are the vehicle body (spring mass) and wheel (unsprung mass) masses. k_s and b_s are stiffness and damper elements that support the vehicle body over the wheel. The k_{us} spring and b_{us} damper represent stiffness and the damping of the tire in contact with the road. The force F stands for the active damper.

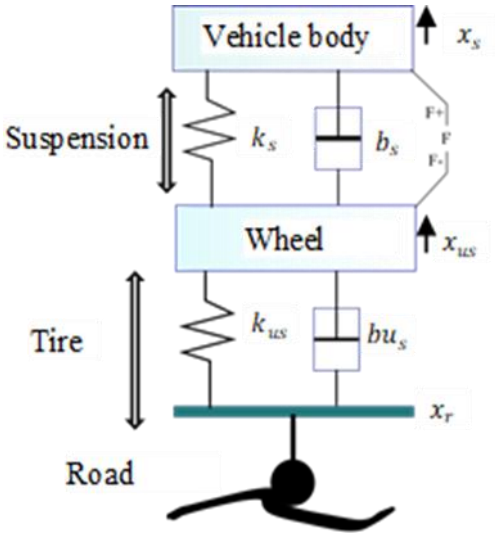

Figure 1. The active suspension system

The state space definition of VAAS is given as follows [16]

$$\dot{x} = Ax + B_1u + B_2f$$
$$y = Cx + Du + Ef$$

$$x = \begin{bmatrix} x_s - x_{us} \\ \dot{x}_s \\ x_{us} - x_r \\ \dot{x}_{us} \end{bmatrix}, u = F, f = \dot{x}_r, \quad (1)$$

$$y = \begin{bmatrix} x_s - x_{us} \\ \ddot{x}_s \end{bmatrix}$$

where, x is the state variables vector, u is the control inputs and f denotes the vector of external

inputs and disturbances and y is the output vectors. $x_s - x_{us}$ state stands for suspension travel, while $x_{us} - x_r$ defines the tire travel and the fourth state is wheel velocity.

$$A = \begin{bmatrix} 0 & 1 & 0 & -1 \\ -\frac{k_s}{m_s} & -\frac{b_s}{m_s} & 0 & \frac{b_s}{m_s} \\ 0 & 0 & 0 & 1 \\ \frac{k_s}{m_{us}} & \frac{b_s}{m_{us}} & -\frac{k_{us}}{m_{us}} & -\frac{b_s + b_{us}}{m_{us}} \end{bmatrix}$$

$$B_1 = \begin{bmatrix} 0 \\ \frac{1}{m_s} \\ 0 \\ -\frac{1}{m_s} \end{bmatrix}, \quad B_2 = \begin{bmatrix} 0 \\ 0 \\ -1 \\ \frac{b_{us}}{m_s} \end{bmatrix}, \qquad (2)$$

$$C = \begin{bmatrix} 1 & 0 & 0 & 0 \\ -\frac{k_s}{m_s} & -\frac{b_s}{m_s} & 0 & \frac{b_s}{m_s} \end{bmatrix}$$

$$D = \begin{bmatrix} 0 \\ \frac{1}{m_s} \end{bmatrix}, E = \begin{bmatrix} 0 \\ 0 \end{bmatrix}$$

2.2. GP machine Learning Approach

The Gaussian process (GP) is a nonparametric kernel-based probabilistic modeling approach [17]. The GP approach is widely used in engineering applications such as modeling, prediction, and optimization [18]. The GP is one of the machine learning methods, and the main goal of this technique is to define a mathematical relationship between input and output variables depending on the experimentally obtained data.

In recent years, the GP technique has been used as a modeling tool in the machine learning area. The most important feature of the GP approach compared to other machine learning methods is the determination of the covariance matrix defined by the independent variables. Other methods use algebraic relationships between these variables. Therefore, much less input-output system data are required while creating the GP model [19].

A GP can be a collection of random variables that is determined with average $\mu(x)$ and covariance matrix $\kappa(x, \hat{x})$ as follows.

$$\mu(x) = \mathbb{E}[y(x)] \qquad (3)$$

$$\kappa(x, \hat{x}) = \mathbb{E}[(y(x) - \mu(x))(y(\hat{x}) - \mu(\hat{x}))]$$

$$f(x) \sim GP\big(\mu(x), \kappa(x, \hat{x})\big)$$

where, $\mu(x)$ and β stand for the mean of the input data and estimated coefficient, $\kappa(x, \hat{x})$ kernel function. The function is parameterized according to the generation of a set of hyperparameters. In the machine learning literature, there are several types of kernel functions with different features that are used to fit actual data and model output. Squared exponential, rational quadratic, and exponential are the best known kernel functions. The appropriate kernel function is determined according to the characteristics of the experimental data.

The output estimation with GP is derived by Equations (4) by using Eq. (3):

$$\bar{y}^* = \mu(x^*) + \kappa(x^*, x)\kappa_y^{-1}(y - \mu(x)) \qquad (4)$$

where, $\kappa_y = \kappa + \sigma_n^2 I$ and the $g(x)^T\beta + f(x)$ model is considered. $g(x)^T$ is a basic function and the covariance matrix is obtained by a set of hypermeters. In the GPR modeling process, the vehicle body velocity of the vehicle was applied as input data to the GPR while the actuator force signal was applied as target data.

3. Results and Discussion

The controller algorithm applying GP by using the unsprung mass velocity as the feedback signal of the ML-based control scheme is conducted. The proposed control scheme is shown in Figure 2.

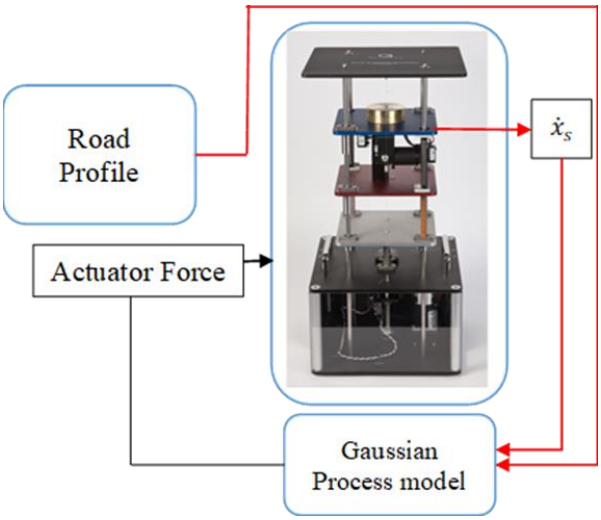

Figure 2. The active suspension system

To construct the GP model, training data was generated from the scaled Quanser VASS test setup shown in Figure 3. A fast response DC electric motor is used as an active suspension element, and an accelerometer exists in the test rig. The position and velocity of the sprung mass, the tire, and the wheel travel are measured using three quadrature encoder sensors. The VASS test set up for mechanical components and sensor properties is given in Table 1.

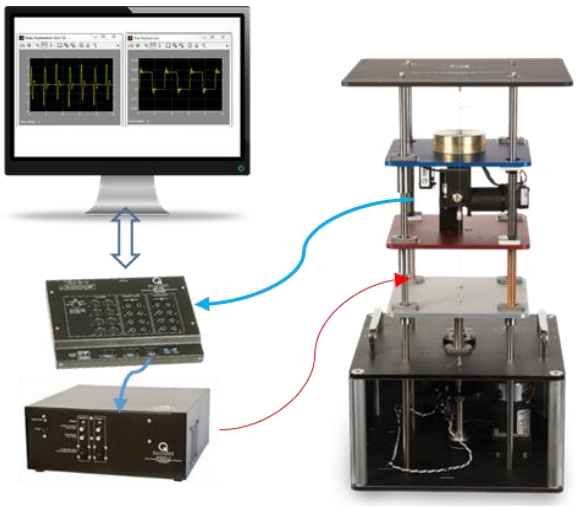

Figure 1. The experimental test rig

Table 1. VASS parameters

Symbol	Description	Value
	Structure Total Height	0.53 m
M_s	Sprung mass	2.45 kg
M_{us}	Unsprung mass	1 kg
k_s	Suspension Passive	900 N/m
k_{us}	Tire Linear Stiffness	2500 N/m
b_s	Inherent Suspension	7.5 N-
b_{us}	Inherent Tire Damping	5 N-s2/m
	Suspension Motor	0.115 N-
	Suspension Motor Shaft	0.006 m
	Suspension Encoder	942 ×

The data from the ASS system was obtained by using LQR full state feedback control. In this study, two road disturbance profiles were applied to investigate the suspension control system: bump-type road disturbance and random road disturbance. The bump road disturbance was simulated to represent bad road quality with discontinuities in the asphalt for a short time. This disturbance input has the most peak of 12 cm as shown in Figure 4.

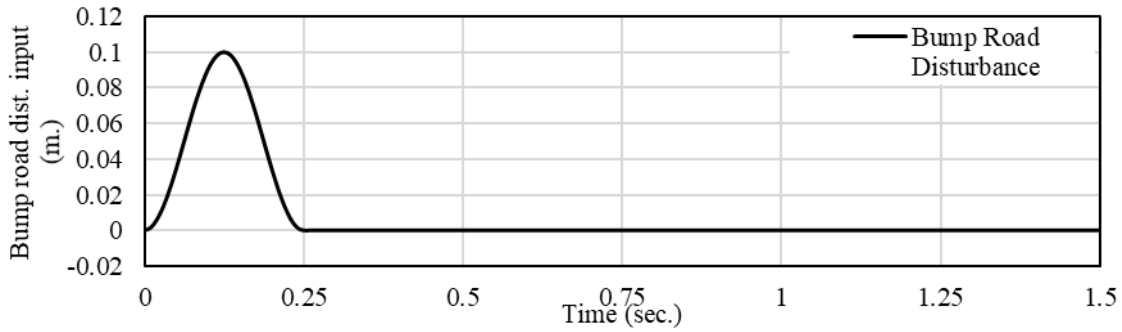

Figure 2. The applied bump disturbance input

The results for the 10 cm bump road disturbance input are shown in Figure 5. ML and LQR controllers are implemented for suspension travel (deflection), vehicle body acceleration, and vehicle body travel states as shown in the Figure 5, 6, and 7, respectively.

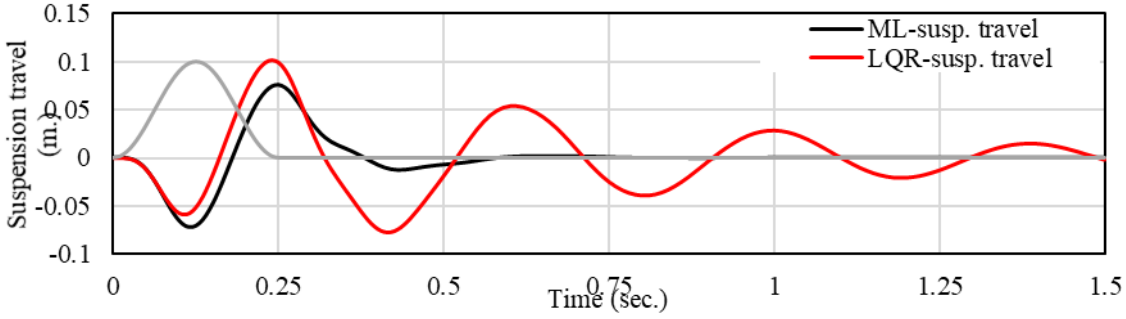

Figure 3. Comparison of suspension travel for LQR and ML based GPR controller (Bump dist.)

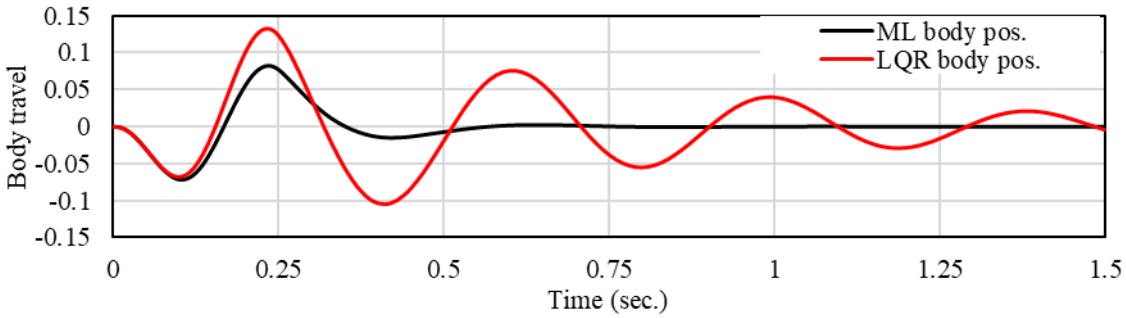

Figure 4. Comparison of vehicle body travel for bump disturbance input

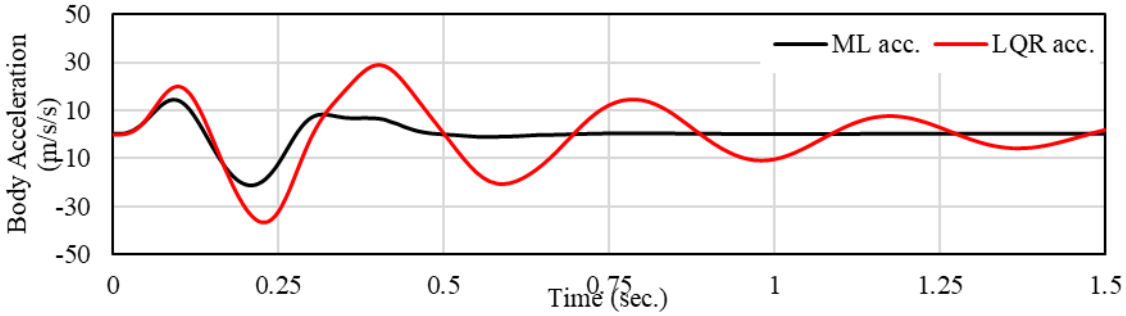

Figure 5. Comparison of vehicle body acceleration for bump road disturbance

As can be seen from Figure 5-7, an ML-based GPR controller is better to suppress the fluctuations around the reference signal than a classical LQR control structure. Figure 8 compares the results obtained from the applied actuator force. When the data in Figure 8 is analyzed, it is clear that the amplitude of the force is larger under the proposed controller. The result is significant because of effectively reduces the oscillations. The actuator force must be applied opposite direction against the road vibrations. Therefore, the actuator gives an instantaneous response.

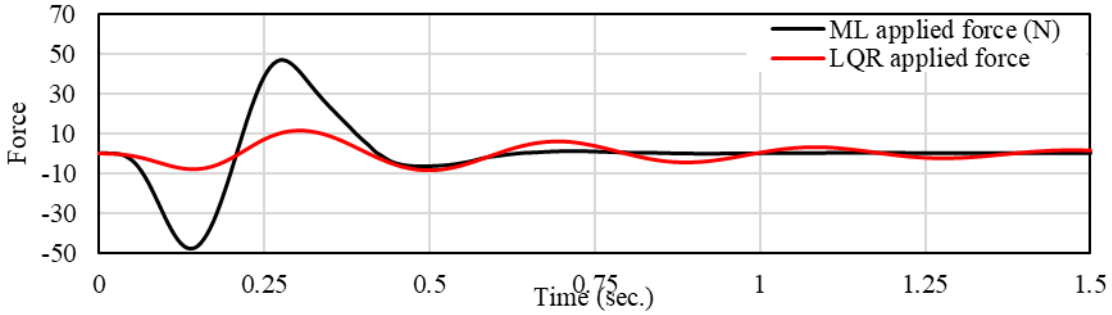

Figure 6. Comparison actuator forces of LQR and ML based controller under bump road disturbance

When the Figure 5-7 were examined, the spring mass position was significantly influenced by the road profile. Therefore, the sine sweep irregularity road profile is used to evaluate the performance of the designed controller as shown in Figure 9 in the second test. The sine sweep disturbance signal is applied to test vehicle suspension systems in all automotive industries.

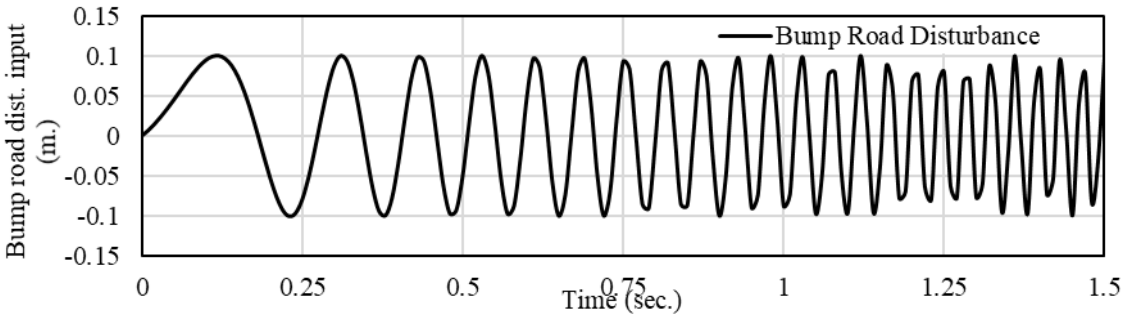

Figure 7. The generated sine sweep road disturbance profile

The tracking performances of developed ML and LQR controllers are demonstrated according to sprung mass positions, suspension travel, and body acceleration in Figure 10-12. It can be clearly seen from the figures that the proposed approach is effective in tracking both spring and non-spring mass position errors. From the graph, the amplitude of sprung mass position oscillation was also reduced in comparison to the classical systems. In this way, passenger comfort can be improved by reducing the impact of road vibrations.

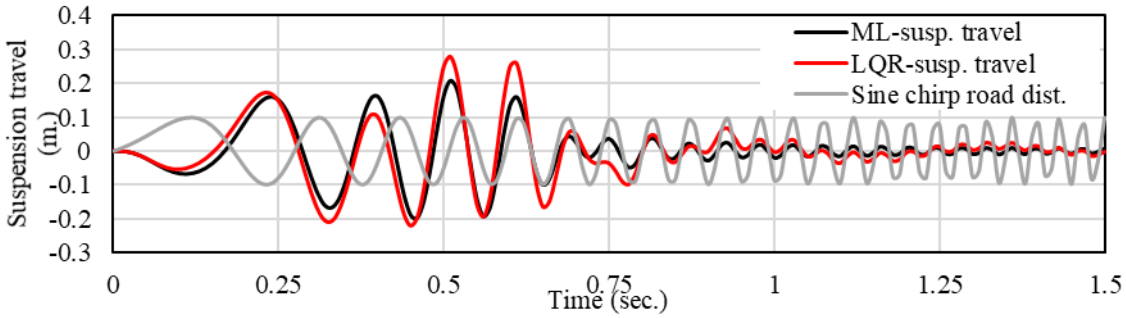

Figure 8. Comparison of suspension travel for LQR and ML based GPR controller (sine sweep road dist.)

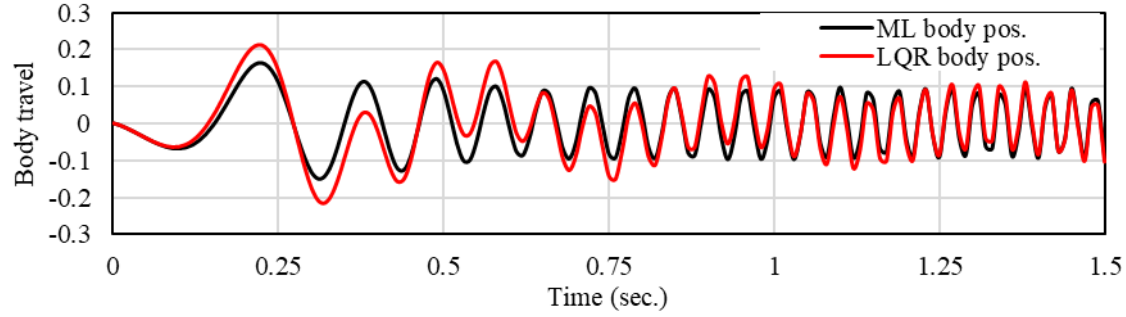

Figure 9. Comparison of vehicle body travel for sine sweep disturbance input

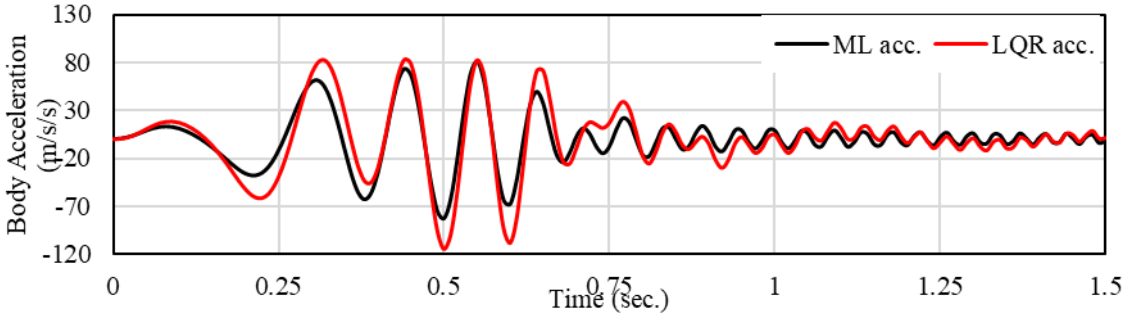

Figure 10. Comparison of vehicle body acceleration for sine sweep road disturbance

As can be seen in Figure 13, the applied actuator force changes rapidly to reduce the variable frequency vibrations in the PSD road profile conditions. From this data in Figure 13, there is an amplitude difference between LQR and ML-based GPR controllers in applied force. Interestingly, the amplitude of force for the proposed method is greater than the classical LQR control to suppress the vibration.

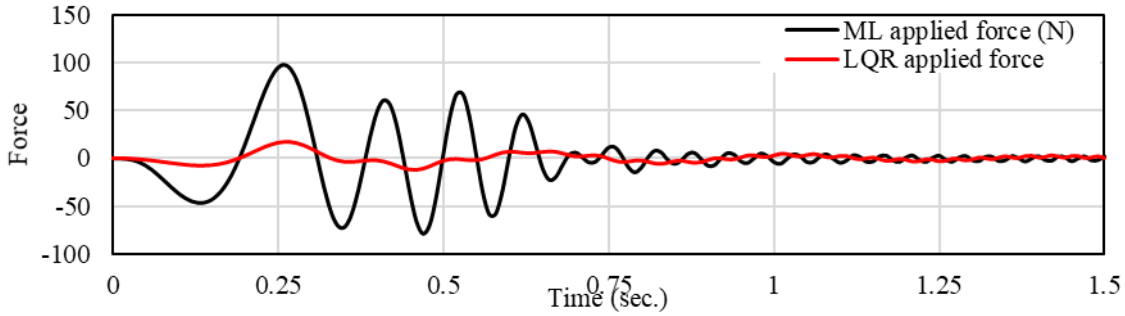

Figure 11. Comparison actuator forces of LQR and ML based controller under sine sweep road profile

The numerical values of VASS output for controlling vehicle body travel, suspension deflection, and body acceleration for two road disturbances are depicted in Table 2. It can be seen from the data in Table 2 that the ML controller shows the best performance according to RMS improvement percentage values in the bump and sine sweep road disturbances.

Table 2. RMS values for LQR and ML controllers and improvement percentage

	Bump road disturbance			Sine sweep road disturbance		
	LQR	ML	Improvement percentage	LQR	ML	Improvement percentage
Vehicle Body travel	0.0371	0.0226	39.08%	0.0887	0.0729	17.81%
Suspension deflection	0.0504	0.0241	52.18%	0.0902	0.0761	15.63%
Vehicle body acceleration	13.5918	5.695	58.10%	35.2248	27.1138	23.03%

4. Conclusion

This study set out to determine the ML-based GPR control method for VASS. The optimal structure of the GPR model was determined by using the trial and error method. Real experimental data was used in the training process of the ML model. Then, the performance of the proposed controller was compared with the classical LQR control according to applied actuator force. In this study, it was designed to investigate the effect of vibrations caused by unevenness on the road surface on passenger comfort. One of the striking findings of the study is the direct control of a mechanical system with ML-based control approaches. The performance of the used proposed and classical control methods is compared in terms of the oscillations in the sprung part of the VASS. Therefore, it has been shown that the proposed ML-based control method outperforms the LQR controller with 39.08%, 52.18%, 58.10%, and 17.81%, 15.63%, 23.03% reductions in both bump and sine sweep profile conditions.

Contributions of the authors

All authors contributed equally to the study.

Conflict of Interest Statement

There is no conflict of interest between the authors.

Statement of Research and Publication Ethics

The study is complied with research and publication ethics.

References

[1] L. Sitnik, M. Magdziak-Tokłowicz, R. Wróbel, and P. Kardasz, "Vehicle Vibration in Human Health," *J. KONES. Powertrain Transp.*, vol. 20, no. 4, pp. 411–418, 2015, doi: 10.5604/12314005.1137854.

[2] Y. Shahid and M. Wei, "Comparative analysis of different model-based controllers using active vehicle suspension system," *Algorithms*, vol. 13, no. 1, Jan. 2020, doi: 10.3390/a13010010.

[3] J. Watton, K. M. Holford, and P. Surawattanawan, "The application of a programmable servo controller to state control of an electrohydraulic active suspension," *Proc. Inst. Mech. Eng. Part D J. Automob. Eng.*, vol. 218, no. 12, pp. 1367–1377, Dec. 2004, doi: 10.1243/0954407042707650.

[4] H. Pang, X. Zhang, J. Yang, and Y. Shang, "Adaptive backstepping-based control design for uncertain nonlinear active suspension system with input delay," *Int. J. Robust Nonlinear Control*, vol. 29, no. 16, pp. 5781–5800, Nov. 2019, doi: 10.1002/rnc.4695.

[5] L. Ovalle, H. Ríos, and H. Ahmed, "Robust Control for an Active Suspension System via Continuous Sliding-Mode Controllers," *Eng. Sci. Technol. an Int. J.*, 2021, doi: 10.1016/j.jestch.2021.06.006.

[6] W. Sun, H. Gao, and O. Kaynak, "Adaptive backstepping control for active suspension systems with hard constraints," *IEEE/ASME Trans. Mechatronics*, vol. 18, no. 3, pp. 1072–1079, 2013, doi: 10.1109/TMECH.2012.2204765.

[7] N. Yagiz and Y. Hacioglu, "Backstepping control of a vehicle with active suspensions," *Control Eng. Pract.*, vol. 16, no. 12, pp. 1457–1467, Dec. 2008, doi: 10.1016/j.conengprac.2008.04.003.

[8] S. Kilicaslan, "Control of active suspension system considering nonlinear actuator dynamics," *Nonlinear Dyn.*, vol. 91, no. 2, pp. 1383–1394, Jan. 2018, doi: 10.1007/S11071-017-3951-X.

[9] I. Fialho and G. J. Balas, "Road adaptive active suspension design using linear parameter-varying gain-scheduling," *IEEE Trans. Control Syst. Technol.*, vol. 10, no. 1, pp. 43–54, Jan. 2002, doi: 10.1109/87.974337.

[10] L.-X. Guo, L.-P. Zhang, L.-X. Guo, and L.-P. Zhang, "Robust H∞ control of active vehicle suspension under non-stationary running," *JSV*, vol. 331, no. 26, pp. 5824–5837, Dec. 2012, doi: 10.1016/J.JSV.2012.07.042.

[11] Y. Taskin, Y. Hacioglu, and N. Yagiz, "Experimental evaluation of a fuzzy logic controller on a quarter car test rig," *J. Brazilian Soc. Mech. Sci. Eng.*, vol. 39, no. 7, pp. 2433–2445, Jul. 2017, doi: 10.1007/s40430-016-0637-0.

[12] U. Rashid, M. Jamil, S. O. Gilani, and I. K. Niazi, "LQR based training of adaptive neuro-fuzzy controller," in *Smart Innovation, Systems and Technologies*, 2016, vol. 54, pp. 311–322, doi: 10.1007/978-3-319-33747-0_31.

[13] S. J. Huang and W. C. Lin, "A neural network based sliding mode controller for active vehicle suspension," *Proc. Inst. Mech. Eng. Part D J. Automob. Eng.*, vol. 221, no. 11, pp. 1381–1397, Nov. 2007, doi: 10.1243/09544070JAUTO242.

[14] M. Heidari and H. Homaei, "Design a PID controller for suspension system by back propagation neural network," *J. Eng. (United Kingdom)*, vol. 2013, 2013, doi: 10.1155/2013/421543.

[15] S. L. Brunton and J. N. Kutz, "Data Driven Science & Engineering - Machine Learning, Dynamical Systems, and Control," p. 572, 2017, Accessed: Sep. 06, 2021. [Online]. Available: databook.uw.edu.

[16] "Active Suspension - Quanser." https://www.quanser.com/products/active-suspension/ (accessed Sep. 08, 2021).

[17] G. Kopsiaftis, E. Protopapadakis, A. Voulodimos, N. Doulamis, and A. Mantoglou, "Gaussian process regression tuned by Bayesian optimization for seawater intrusion prediction," *Comput. Intell. Neurosci.*, vol. 2019, 2019, doi: 10.1155/2019/2859429.

[18] J. Zhang, W. Li, L. Zeng, and L. Wu, "An adaptive Gaussian process-based method for efficient Bayesian experimental design in groundwater contaminant source identification problems," *Water Resour. Res.*, vol. 52, no. 8, pp. 5971–5984, Aug. 2016, doi: 10.1002/2016WR018598.

[19] X. Chen, Y. Tian, T. Zhang, and J. Gao, "Differential Evolution Based Manifold Gaussian Process Machine Learning for Microwave Filter's Parameter Extraction," *IEEE Access*, vol. 8, pp. 146450–146462, 2020, doi: 10.1109/ACCESS.2020.3015043.

Bitlis Eren Üniversitesi Fen Bilimleri Dergisi
BİTLİS EREN UNIVERSITY JOURNAL OF SCIENCE
ISSN: 2147-3129/e-ISSN: 2147-3188
VOLUME: 11 NO: 2 PAGE: 429-435 YEAR: 2022
DOI: 10.17798/bitlisfen.1016122

Tıbbi Önemi Olan *Hyoscyamus niger* L.: Fenolik Madde İçeriği ve in vitro Antiproliferatif Aktiviteleri

Yusuf ALAN[1], Murat KÜRŞAT[2*]

[1]*Moleküler Biyoloji ve Genetik Bölümü, Fen Edebiyat Fakültesi, Muş Alparslan Üniversitesi*
[2] *Biyoloji Bölümü, Fen Edebiyat Fakültesi, Bitlis Eren Üniversitesi*
(ORCID: 0000-0003-0007-0212) (ORCID: 0000-0002-0861-4213)

Keywords: *Hyoscyamus niger*, Antiproliferatif, Fenolik madde, in vitro.

Abstract
Tıbbi önemi olan bitkiler, zengin bileşenleri nedeniyle kanser de dahil çeşitli hastalıkların tedavisinde en önemli ilaç kaynaklarından birini temsil etmektedirler. Bu çalışmanın amacı, *Hyoscyamus niger* bitkisinin toprak üstü kısımlarının metanol (HNM) ve su (HNS) ekstraktlarının 17 farklı fenolik madde içeriğini araştırmak, *in vitro* antiproliferatif aktivitesini değerlendirmektir. Bu amaçla ekstraktların 17 farklı fenolik madde içeriği HPLC ile belirlendi. Antiproliferatif aktivite ise, karaciğer kanseri hücre hattı (Hep G2), osteosarkoma hücre hattı (U-2 OS) ve sağlıklı fare fibroblast (L-929) hücre hatlarına karşı MTT testi ile tayin edildi. Ekstraktlarda en fazla miktarda askorbik asit belirlendi. HNM ekstraktı içerik yönünden HNS ekstraktından daha zengindi. Antiproliferatif aktivite sonuçlarına göre en güçlü etkiyi HNM ekstraktı, özellikle Hep G2'ye karşı gösterdi. Genel olarak değerlendirildiğinde HNM ekstraktının fenolik madde içeriği ve antiproliferatif aktivite bakımından daha iyi olduğu belirlendi. Bitki ekstraktlarının aktif bileşenlerinin izole edilerek daha fazla *in vivo* ve *in vitro* çalışmaların yapılması önem arz etmektedir.

Hyoscyamus niger L. of Medical Importance: Phenolic Substance Content and *in vitro* Antiproliferative Activities

Keywords: *Hyoscyamus niger*, Antiproliferative, Phenolic substance, in vitro.

Abstract
Medically important plants represent one of the most important sources of drugs in the treatment of various diseases, including cancer, due to their rich components. The aim of this study was to investigate the content of 17 different phenolic substances of methanol (HNM) and water (HNS) extracts of the aerial parts of the *Hyoscyamus niger* plant and to evaluate the in vitro antiproliferative activity. For this purpose, the content of 17 different phenolic substances of the extracts was determined by HPLC. Antiproliferative activity was determined by MTT assay against osteosarcoma cell line (U-2 OS), liver cancer cell line (Hep G2) and healthy mouse fibroblast cell (L-929) cell lines. The highest amount of ascorbic acid was determined in the extracts. HNM extract was richer in content than HNS extract. According to the antiproliferative activity results, HNM extract showed the strongest effect, especially against Hep G2. When evaluated in general, it was determined that HNM extract was better in terms of phenolic content and antiproliferative activity. By isolating the active components of plant extracts. It is important to conduct more *in vivo* and *in vitro* studies.

*Sorumlu yazar: botanikkursat@gmail.com
Geliş Tarihi: 28.10.2021, Kabul Tarihi: 23.03.2022

1. Giriş

Tıbbi amaçla kullanılan bitkiler tarih boyunca birçok hastalığın tedavisinde önemli bir role sahip olmuşlardır. Birçok önemli tıbbi bitkiyi bünyesinde bulunduran, tabiatta 85 cins ve 2200 den fazla türü barındıran Solanaceae familyasıdır. Bu familyanın ülkemizde doğal olarak yayılış gösteren 9 cins ve 31 türü bulunmaktadır. Eczacılıkta kullanım alanı olan ve zehir etkisi yapan tropan alkoloitleri bu familyaya ait türlerde bulunmaktadır. Sebze olarak kullanılan bitkiler (Domates, Biber, Patlıcan vs.) yönünden de önemli bir familyadır [1]. Bu familyaya ait olan *Hyoscyamus* cinsinin Türkiye florasında *H. niger, H. albus, H. reticulatus, H. aureus, H. pusillus* ve *H. leptoclyx* olmak üzere altı türü bulunmaktadır [2]. *Hyoscyamus niger* yaygın olarak henbane, siyah henbane veya kokuşmuş it üzümü olarak bilinen zehirli bir bitkidir [3].

Kanser, modern çağın en yaygın ve ölümcül hastalığıdır [4]. Bitki bazlı ilaçlar, kemoterapötik ilaçlar için birincil kaynak olarak iyi bir etki potansiyeline sahiptir. Kolorektal, lösemi ve göğüs kanseri gibi hastalıkların tedavisinde şu anda kullanılan kemoterapötik ajanlardan bazıları başlangıçta bitkilerden türetilmiştir [5,6]. Bu nedenle, bitkiler antitümör bileşikleri bulundurdukları için iyi kaynaklardır. Bazı *Hyoscyamus* türlerinden elde edilen tropan alkaloidleri hyoscyamine ve scopolamine'nin analjezik olduğunu göstermiştir [7,8]. *H. niger*, sentezlediği alkaloidlerin dışında, canlılarda son derece etkili rollere sahip saponinler, lignanlar, kumarinolignanlar ve fenolik bileşikleri bünyesinde sentezlemektedir [9]. Bitkisel kaynaklı fenolik bileşikler insan vücudunda kanser ve önemli kalp hastalıklarına karşı koruyucu aktivite göstermelerinin yanı sıra, antioksidan, antienflamatuvar, anti-allerjik, antimikrobiyal aktiviteleri de bulunmaktadır [10]. Ayrıca önemli bir fenolik bileşik grubu olan flavonoidlerin antioksidan özellikleri sayesinde insan bünyesinde çeşitli kalp rahatsızlıkları ve kanser gibi tehlikeli hastalıklara karşı koruyucu rolleri bulunmaktadır [11]. Tibet Tıbbı'nda *H. niger* antihelmintik, antitümöral ve antipiretik olarak kullanılmaktadır [12].

Literatürde birçok bitki türünün kimyasal bileşimi ve biyolojik aktiviteleri bilinmesine rağmen, bileşiklerin seviyesi ve kalitesi ile biyolojik aktiviteleri coğrafi köken ve yetiştirme koşullarına göre önemli ölçüde değişebilmektedir [13]. Bu nedenle bu araştırma, 1600 m rakıma sahip Ağrının Patnos ilçesinde toplanan *H. niger* bitkisinin fenolik bileşik miktarı ve antikanser aktivitelerini değerlendiren ilk çalışmadır. Bu bitkiden elde edilen metanol ve su ekstraktlarının 17 fenolik madde miktar tayini Yüksek Basınçlı Sıvı Kromatografisi (HPLC) ile yapıldı. Ayrıca ekstraktların karaciğer kanseri hücre hattı (Hep G2), osteosarkoma hücre hattı (U-2 OS) ve sağlıklı fare fibroblast hücre (L-929) hatları üzerindeki antiproliferatif aktiviteleri araştırıldı.

2. Material and Metot

2.1. Bitki Örneklerinin Toplanması ve Ekstraksiyonu

H. niger bitkisi Ağrı ili Patnos ilçesinde toplandı. Toplanan bitki örneklerinin Türkiye Florasına göre tanımlanması yapıldı [2]. Bitki örnekleri herbaryum materyali haline getirilerek Muş Alparslan Üniversitesi, Araştırma Laboratuvarlarında saklanmaktadır. Bitkinin toprak üstü kısımları gölgede kurutulmaya bırakıldı. *H. niger* metanol (HNM) ve su (HNS) ekstraktları daha önce tarafımızca yapılan çalışmada olduğu gibi hazırlandı [14].

2.2. HPLC ile Fenolik Madde Analizi

Fenolik madde miktarının belirlenmesi amacıyla, vanilin, gallik asit, askorbik asit, 3,4-dihidroksibenzoik asit, kafeik asit, mirisetin, absisik asit, kersetin, apigenin, kaempferol, kurkumin, katekol, trans-p-kumarik asit, sinnamik asit, 4-hidroksibenzoik asit, rosmarinik asit ve salisilik asit standartları kullanıldı. Standartların son konsantrasyonları 10 mg/ml olacak şekilde tartılıp 50 ml'lik balon jojeler içine konuldu. Hazırlanan standartlar %1'lik asetik asit ile 1/9 oranında asetonitril ilave edilerek çözelti hazırlandı. Çözeltiye 1/1 oranında metanol ilave edilerek standartları çözmek için gerekli olan stok çözelti hazırlandı. Stok çözeltilerden 5 farklı oranda (100 mM, 75 mM, 50 mM, 25 mM ve 10 mM) olacak şekilde numuneler hazırlandı [15]. *H. niger* bitkisinden elde edilen su ve metanol ekstraktları HPLC'ye yüklemek için 20 mg/ml olacak şekilde stok çözeltiyle seyreltilerek, 0,45 µm'lik membran filtreden geçirilerek filtre edildi. Bileşiklerin miktarlarının tespit edilmesinde bileşiklere ait HPLC kromatogramlarından elde edilen entegre alanlar ve standart maddelerin ara stok çözeltileri ile hazırlanan kalibrasyon eğrilerinden yararlanıldı. Fenolik madde analizinde Agilent Technologies 1260 Infinity II HPLC cihazı (Agilent, USA) kullanıldı. Mobil faz olarak solvent A için; %1 asetik asit, B için ise; asetonitril kullanıldı. HPLC konfügürasyonu 1260 DAD WR dedektör (272, 280 ve 310 nm) , 1260 Quat Pump

VL pompa (1 ml/dk akış hızı), 1260 Vialsampler (20 µl enjekte) ve G7130A kolon fırınından (28 °C) oluşmaktadır. Analiz için kullanılan analitik kolon ACE 5 C18 (250x4.6 mm id)'dir.

2.3. Ekstraktların Antiproliferatif Aktivitesi

Çalışmamızda, karaciğer kanseri hücre hattı (Hep G2), osteosarkoma hücre hattı (U-2 OS) ve sağlıklı fare fibroblast hücre (L-929) hatları kullanıldı. Hücre hatları Muş Alparslan Üniversitesi Araştırma Laboratuvarlarından temin edildi. Bu hücre hatları için besiyeri ortamı olarak RPMI (Sigma) kullanıldı. *H. niger* ekstraktları RPMI'da 25, 50 ve 100 µg/ml konsantrasyonlarda hazırlanarak sitotoksisitelerinin belirlenmesinde 3-(4,5-dimethyl-thiazol-2-yl)-2,5-diphenyltetrazolium bromide (MTT) testi uygulandı [16]. Hücre hatlı besi ortamı ve ekstrakt içermeyen kuyucuklar kontrol grubu olarak kullanıldı. Bu kuyucukların mikroplate okuyucuyla (Thermo scientific MULTISKAN GO, Finland) okutulduktan sonra alınan absorbans sonuçları %100 canlı hücre olarak değerlendirildi. Hücrelerin % inhibisyon oranları aşağıdaki formül yardımıyla hesaplandı.

$$\%\ \text{inhibisyon} = 1 - \left(\frac{\text{OD}_{\text{Örnek}}}{\text{OD}_{\text{Kontrol}}}\right) \text{x} 100$$

2.4. İstatistiksel Analiz

Verilerimiz % ortalama ve ortalamanın standart sapması (Mean +- SEM) olarak verildi. Hücre kültürü ve fenolik madde miktarları kendi aralarında One Way ANOVA'yı takiben t testi kullanılarak kıyaslandı. $p<0.05$ olanlar istatistiksel yönden önemli kabul edildi ve istatistiki önemlilik dereceleri "*" sembolü ile belirtildi. Buna göre PP<0.05 *(önemli); P<0.01 **(çok önemli); P<0.001*** ve P<0.0001**** (yüksek derecede önemli); P>0.05 ns (önemsiz) gösterildi.

3. Bulgular ve Tartışma

3.1. HPLC Analizi ile Fenoliklerin Miktarları

H. niger HNM ve HNS ekstraktlarının fenolik madde miktarları Tablo 1'de verildi. HPLC ile fenolik madde miktarlarına bakıldığında en fazla miktarda askorbik asitin HNS'de (8.13±0,57 µg/ml), en az miktarda sinnamik asitin HNM ekstraktında (0.75±0.01 µg/ml) olduğu tespit edildi. HNM ve HNS karşılaştırıldığında 4-hidroksibenzoik asit, trans-p-kumarik asit, mirisetin, absisik asit ve sinnamik asit miktarlarında yüksek derecede anlamlı fark tespit edildi. Her iki ekstraktta askorbik asit, 4-hidroksibenzoik asit, trans-p-kumarik asit ve katekol var iken, HNM ekstraktında ayrıca mirisetin, absisik asit ve sinnamik asit'in olduğu belirlendi. Toplam fenolik miktarı HNM ekstraktında (15.03±0,05 µg/ml) daha fazla miktarda olup, HNS ekstraktına karşı yüksek derecede anlamlı farkın olduğu gözlendi.

H. niger yaprak, kök ve tohumlarında hiyosiyamin, atropin, tropan ve skopolamin gibi alkaloidler bulunmuştur [17-19]. Ma ve ark., (2002) alkoloid olmayan birleşiklerin varlığını tespit etmişlerdir [20]. Ayrıca *H. niger* bitkisinin alkaloidlere ek olarak, witanolidler, flavonoidler, lignanlar, kumarinolignanlar, saponinler, gliseritler, glikozitler ve fenolikler içerdikleri bildirilmiştir [12]. Aynı bitkinin fenolik içeriği Folin-Ciocalteu yöntemi ile belirlenmiştir [21]. Yapılan başka bir çalışmada ise, klorojenik asit, rutin ve kuersetin miktarları belirlenmiştir. Çalışmada, Klorojenik asit 0.4±0.0 mg/g, rutin 9.2±0.5 mg/g ve kuersetin ise 1.1±0.1 mg/g olarak kaydedilmiştir [22]. Çalışmamızda ise, kuersetin varlığı tespit edilmedi. HNM ekstraktının HNS ekstraktından daha fazla fenolik madde içerdiği belirlendi. Bu çalışmaya benzer şekilde *H. niger* bitkisinden elde edilen ekstraktların fenolik içerikleri ile ilgili çalışmalar yok denecek kadar azdır.

3.2. Ekstraktların Hücre Hatlarına Karşı Antiproliferatif Aktivitesi

Ekstraktların üç farklı konsantrasyona sahip çözeltisi (25, 50 ve 100 µg/ml) bir gün boyunca Hep G2, U 2 OS ve L-929 hücreleri ile muamele edildi ve absorbansları ölçüldü. Elde edilen absorbans sonuçları ile hücre hatlarının % inhibisyon ve IC_{50} değerleri hesaplandı. Hücre hatlarına ait IC_{50} değerleri Tablo 2'de, % inhibisyon grafikleri ise Şekil 1'de verildi.

MTT testi ile ekstraktların %50 gelişme inhibisyonu gösteren IC_{50} değerleri hesaplandı. MTT testi sonuçlarına göre Hep G2 (66.76 µg/ml), U 2 OS (532,59 µg/ml) ve L-929 (201.76 µg/ml) hücreleri ile en düşük IC_{50} değeri HNM ekstraktına ait olarak belirlendi. Hep G2 ve L-929 hücre hatlarına karşı farklı konsantrasyonlardaki (25, 50 ve 100 µg/ml) HNM ekstraktı, HNS'ye göre yüksek derecede anlamlı fark gösterdi. Ayrıca HNM ekstraktı U

2 OS hücre hattına karşı 50 µg/ml konsantrasyonda uygulandığında, antiproliferatif özelliğinin HNS ekstraktından yüksek derecede anlamlı fark sergilediği tespit edildi. 25 ve 100 µg/ml konsantrasyonlarda ise HNM ekstraktı HNS'ye karşı çok önemli fark gösterdi.

Tablo. 1. *H. niger* ekstraktlarının fenolik madde miktarları (µg/ml)

Fenolikler	Miktarlar (µg/ml)	
	HNS	HNM
Askorbik asit	8.13±0,57^{c}	6.10±0,31
Gallik asit	0.00±0.00^{a}	0.00±0.00
3,4-Dihidroksibenzoik asit	0.00±0.00^{a}	0.00±0.00
4-Hidroksibenzoik asit	2.12±0.03^{e}	2.38±0.01
Trans-p-kumarik asit	1.36±0.01^{e}	1.70±0.03
Mirisetin	0.00±0.00^{e}	1.85±0.01
Absisik asit	0.00±0.00^{e}	1.28±0.01
Kuersetin	0.00±0.00^{a}	0.00±0.00
Apigenin	0.00±0.00^{a}	0.00±0.00
Kaempferol	0.00±0.00^{a}	0.00±0.00
Kurkumin	0.00±0.00^{a}	0.00±0.00
Katekol	1.20±0.08^{a}	0.97±0.02
Vanilin	0.00±0.00^{a}	0.00±0.00
Kafeik asit	0.00±0.00^{a}	0.00±0.00
Sinnamik asit	0.00±0.00^{e}	0.75±0.01
Rosmarinik asit	0.00±0.00^{a}	0.00±0.00
Salisilik asit	0.00±0.00^{a}	0.00±0.00
Toplam fenolik	12.80±0.04^{e}	15.03±0.05

Tablo.2. *H. niger* ekstraktlarının hücre hatları üzerindeki IC50 değerleri

Hücreler	HNM (IC_{50} µg/ml)	HNS (IC_{50} µg/ml)
Hep G2	66,76	98,00
U- 2 OS	532,59	576,52
L929	201,76	253,62

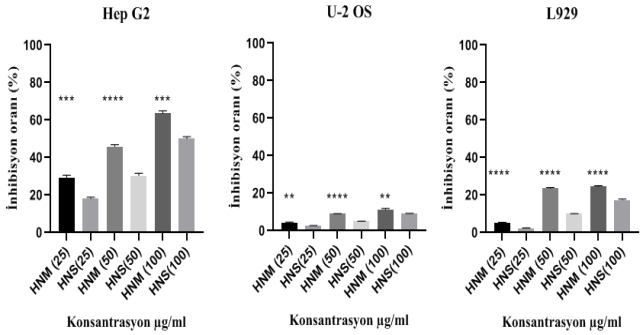

Şekil. 1. *H. niger* ekstraktlarının % inhibisyon grafikleri.

Polifenolik bileşikler açısından zengin olan tıbbi bitkiler, antioksidan ve antisitotoksik aktiviteleri nedeniyle kanser tedavisinde kullanılan en önemli ilaç kaynaklarından birini temsil etmektedir. Bu nedenlerle, kanser tedavisi ve onkolojik araştırmalar için çok önemli bir portal oluşturan bitkilerden yeni antikanser ajanlar ve bileşikler elde edilmeye çalışılmaktadır. Bitki kaynaklı tümör inhibitörleri, kanser hücrelerinin tipine ve bitki türlerinin yanı sıra kullanılan ekstrakta da bağlıdır. Çoğu kemo önleyici bileşik ve bunların analogları veya türevleri başlangıçta bitki kökenlidir ve çeşitli *in vitro* ve *in vivo* test sistemlerinde kendiliğinden ve kimyasal mutajenezi inhibe eder [23]. Hyoscyamus cinsine ait bitki ekstraktının Hep G2 hücreleri üzerindeki antikanser aktivitesi incelenmiş ve hücre proliferasyonunun inhibisyon yüzdesinin %97 olduğu belirlenmiştir [24]. *H. albus* yapraklarından hazırlanan MeOH ekstresinin farklı hücre dizileri üzerinde güçlü sitotoksik aktiviteye sahip olduğu belirlenmiştir [25]. *H. niger* ekstraktı, tüm zaman dilimlerinde Hep G2 kanser hücre dizisine karşı sitotoksik aktivite sergilemiştir. Aynı ekstrakt, RD ve AMN-3

hücre hatları üzerinde orta derecede sitotoksik etkiye sahip iken, normal hücre hatları üzerinde hiçbir etki göstermemiştir [26]. Ayrıca *H. niger* ekstraktı LNCaP insan prostat kanseri hücrelerinde orta derecede sitotoksisite sergilemiştir [20]. Başka bir çalışmada ise, *H. niger* yaprak ve tohum ekstraktlarının kanser hücre hatları üzerindeki sitotoksik etkileri değişkenlik göstermiştir. Bazı hücre dizilerinde sitotoksik reaksiyona neden olurken, diğerlerinde hücre proliferasyonunu indüklemiştir. *H. niger* ekstraktlarının sitotoksisite aralığının, çeşitli kanser hücre hatlarında %7 ile %30 arasında değiştiği ve bu bitkinin antikanser bileşikleri içermediğini düşündürmüştür [13]. Kaempferol, kuersetin, antosiyanlar, kumarik asit ve ellagik asit gibi bazı bileşiklerin meme hattı hücreleri (MCF-7), oral (KB,CAL-27), kolon (HT-29, HCT-116) ve prostat (LNCaP, DU-145) gibi insan kanser hücrelerinin büyümesini engelleyebileceği bildirilmiştir [27,28].

Bu çalışmada, özellikle metanol ekstraktı konsantrasyon artışına bağlı olarak en iyi antiproliferatif aktiviteyi Hep G2 hücre hattına karşı gösterdi. Ayrıca ekstraktların U 2 OS ve L929'a karşı düşük antiproliferatif aktivite gösterdiği belirlendi. Bu durum konsantrasyon, kullanılan çözücü ve hücre hatlarına bağlı olarak antiproliferatif aktivitenin değişkenlik gösterebileceği bilgisini doğrulamaktadır. Aynı zamanda ekstraktların kaempferol ve kuersetin gibi fenolikleri içermemelerinden dolayı U 2 OS hücre hattına karşı iyi antiproliferatif aktivite göstermediği düşünülmektedir. Bununla birlikte metanol ekstraktında daha fazla miktarda kumarik asit bulunmasından dolayı, daha iyi antiproliferatif aktivite sergilemesi literatürdeki bilgileri doğrulama niteliğindedir. Ayrıca, toprak yapısı, ekolojik faktörler, genotipler ve iklim koşullarının bitki türlerindeki biyokimyasal içeriklerde farklılıklara yol açtığı bilinmektedir [29]. Bu nedenle bu çalışma ile önceki çalışmaların antiproliferatif aktivite sonuçlarının değişkenlik göstermesinin nedeni bitkilerin toplandığı bölgedeki farklılıklardan kaynaklanabilir. Elde edilen sonuçlar, farklı bölgelerdeki bitkilerin biyolojik aktiviteler üzerindeki etkileri ile ilgili çalışmalara katkı sunmaktadır.

4. Sonuç ve Öneriler

Kanser, yüksek morbidite ve mortalitesi nedeniyle tüm dünyada önemli bir sağlık sorunu olarak kabul edilmektedir. Doğal olarak elde edilen antikanser bileşikleri nispeten daha az yan etkiye sahiptir, bu nedenle araştırma için ana odak noktası olmaya devam etmektedir. *H. niger* bitkisinin toprak üstü kısımlarından elde edilen saf su ve metanol ekstraktlarının fenolik madde içerikleri ve antiproliferatif aktivitesi araştırıldı. HPLC analiz sonuçlarına göre, en fazla oranda askorbik asit varlığı belirlendi. HNM ekstraktı içerik bakımından HNS ekstraktından daha zengindi. Ekstraktların antikanser aktivite sonuçlarına göre en güçlü etkiyi HNM ekstraktı, özellikle Hep G2'ye karşı gösterdi. Bu durumun nedeninin, ekstraktların içerdiği bileşiklerin farklılığından kaynaklandığı düşünülmektedir. Gelecekteki çalışmalar, aktif bileşenleri izole etmeyi ve saflaştırmayı ve bunların daha farklı kanser hücreleri üzerindeki etkisini araştırmayı amaçlayacaktır. Bununla birlikte, aktif bileşenlerin tam etki modunu keşfetmek için daha fazla *in vivo* ve *in vitro* çalışmaya ihtiyaç vardır.

Yazarların Katkısı

Bu çalışmada tüm katkı yazarlara aittir.

Çıkar Çatışması Beyanı

Bu çalışmada yazarlar arasında herhangi bir çıkar çatışması bulunmamaktadır.

Araştırma ve Yayın Etiği Beyanı

Yapılan çalışmada araştırma ve yayın etiğine uyulmuştur.

Kaynaklar

[1] N. Tanker, M. Koyuncu and M. Coşkun, *Solanaceae*, Farmasötik Botanik Üniversitesi Eczacılık Fakültesi Yayınları, Ankara, 2007.

[2] P. H. Davis, *Flora of Turkey and the East Aegean Islands*, Edinburgh University Press, Edinburgh, 1975.

[3] O. Kennedy David, *The Deliriants-The Nightshade (Solanaceae) Family. Plants and the Human Brain*,.Oxford University Press, New York,, 2014.

[4] R. Siegel, D. Naishadham and A. Jemal, "Cancer statistics" *CA: A Can. J. for Clin.*,vol. 62, pp. 10-29, 2012.

[5] T. Huang, W. H. Gong, X. C. Li, C. P. Zou, G. J. Jiang, X. H. Li and D. P. Feng, "Induction of apoptosis by a combination of paclitaxel and carboplatin in the presence of hyperthermia", *Asian Pac. J. of Can. Prev.*, vol. 13, pp. 81-85, (2012).

[6] H. J. Park, M. J. Kim, E. Ha and J. H. Chung, "Apoptotic effect of hesperidin through caspase3 activation in human colon cancer cells", *SNU-C4. Phytomedi*., vol. 15, pp. 147-151, 2008.

[7] M. Uzun and A. Kaya, "Traditional medicinal plants used for oral and dental diseases in Turkey", *Bio. Divers. and Con.*, vol.12, no. 1, pp. 138-148, 2019.

[8] L. Mateus, S. Cherkaoui, P. Christen and J. L. Veuthey, "Capillary electrophoresis for the analysis of tropane alkaloids: Pharmaceutical and phytochemical applications", *J. of Pharmac. and Biome. Analy.*, vol. 18, pp. 815-825, 1998.

[9] A. M. J. Aljibouri, K. W. Al-samarraei, A. S. Abd, D. M. Magee and A. J. A. Ali, "Alkaloids production from callus of *Hyoscyamus niger* L. in vitro", J. of Life Scien., vol. 6, no. 8, pp. 874, 2012.

[10] N. B. Tuncel and N. Yılmaz, "Kaz Dağları'ndan toplanan bazı bitkilerin fenolik asit kompozisyonlarının yüksek performanslı sıvı kromatografisi ile belirlenmesi", *Akad. Gıda*, vol. 8, no. 3, pp. 18-23, 2010.

[11] B. Stavric, "Role of chemopreventers in human diet", *Clinic. Bioch.*, vol. 27, no. 5, pp. 319-332. (1994).

[12] A. S. Begum, "Bioactive non-alkaloidal secondary metabolites of *Hyoscyamus niger* Linn. seeds: A review", *Res. Jour. of Seed Scien.*, vol. 3, pp. 210–217, 2010.

[13] D. Uğur, H. Güneş, F. Güneş and R.Mammadov, "Cytotoxic activities of certain medicinal plants on different cancer cell lines", *Turk. J. of Pharmac. Sci*., vol. 14, no. 3, pp. 222-230, 2017.

[14] Y. Alan and N. Yılmaz, "Phenolic substance contents and biological activities of *Verbascum Insulare* Boıss. & Heldr", *Extrac., Farmacia*, vol. 67, no. 4, pp. 641-647, 2019.

[15] S. Tapan, "Quantitative HPLC analysis of phenolic acids, flavonoids and ascorbic acid in four different solvent extracts of two wild edible leaves, Sonchus Arvensis and Oenanthe Linearis of north-eastern region in India", *J. Appl. Pharm. Sci*., vol. 6, pp. 157-166, 2016.

[16] E. Alkış, Ü. Keleştemür, Y. Alan, N. Turan and Buldurun, "Cobalt and ruthenium complexes with pyrimidine based schiff.base: Synthesis, characterization, anticancer activities and electrochemotherapy efficiency", *Jour. of Mol. Struct.*, vol. 1226, pp. 129402, 2021.

[17] D. Frohne and H. J. Pfander, *A Colour Atlas of Poisonous Plants*, Wolfe Publishing, London, UK., 1983.

[18] M. Ghorbanpour, M. Hatami and M. Hatami, "Activating antioxidant enzymes, hyoscyamine and scopolamine biosynthesis of *Hyoscyamus niger* L. plants with nano-sized titanium dioxide and bulk application", *Acta agricul. Slove*., vol. 105, pp. 23-32, 2015.

[19] E. K. Akkol, M. Ilhan, E. Kozan, F. Tuğçe, G. Dereli, M. Sak, "Sobarzo-Sánchez EInsecticidal Activity of *Hyoscyamus niger* L. On Lucilia sericata Causing Myiasis", *Plants*, vol. 9, pp. 655, 2020.

[20] C. Y. Ma, W. K. Liu and C. T. Che, "Lignanamides and nonalkaloidal components of *Hyoscyamus niger* seeds", *Jour. of Nat. Prod*., vol. 65, no. 2, pp. 206-209, 2002.

[21] K. Hajipoor, A. M. Sani and A. Mohammad, "In vitro antioxidant activity and phenolic profile of Hyoscyamus niger", *IJBPAS*, vol. 4, no. 7, pp. 4882-4890, 2015.

[22] A. R. Jassbi, R. Miri, M. Masroorbabanari, M. Asadollahi, M. Attarroshan and I. T. Baldwin, "HPLC-DAD-ESIMS analyses of *Hyoscyamus niger* and *H. reticulatus* for their antioxidant constituents". *Austin Chromatogr*, vol. 1, no. 5, pp. 1022, 2014.

[23] W. U. Xifeng, G. Jian and M. Spitz, "Mutagen sensitivity; Genetic predisposition factor for cancer", *Canc. Res*., vol. 67, pp. 3493–3495, 2007.
[24] S. E. Bassem, F. Walid, M. Khaled, M. Salwa and E. May, "Screening of natural products for therapeutic activity against solid tumors", *Ind. J. of Experim. Bio.*, vol. 48, pp. 258-284, 2010.
[25] M. Yahia, M. Yahia, A. Benhouda and H. Haba, "New Biological Anticancer Activities of Atropine Isolated From Algerian Hyoscyamus albus's Leaves", *Pharmacologyonline*, vol. 3, pp. 286-296, 2018.
[26] A. O. Ismeel, "Cytogenetic and cytotoxic studies on the effect of phytoinvestigated active compounds of Hyoscyamus niger (in vivo and ex vivo) ", PhD thesis, Al-Nahrain University- College of Science, Iraq, 2011.
[27] K. Murota and J. Terao, "Antioxidative flavonoid Q: implication of its intestinal absorption and metabolism", *Arch. Biochem. Biophys*., vol. 417, pp. 12–17, 2003.
[28] Y. Massinissa, Y. Mouloud and A. Benhouda, "Antitumor Activity of Methanolic Fractions Extracted From the Aerial Part of Algerian Hyoscyamus albus and apoptotic cell aspect screening", *Ind. J. of Pharmac. Educa. and Res.*, vol. 52, pp. 1-21, 2018.
[29] H. Servi, B. Eren Keskin, S. Çelik, U. Budak and B. Kababıyık, "Essential oil and fatty acid composition of endemic *Gypsophila laricina* Schreb. from Turkey", *Turk J Pharm Sci.*, vol. 16, no. 2, pp. 220-226, 2019.

Bitlis Eren Üniversitesi Fen Bilimleri Dergisi
BİTLİS EREN UNIVERSITY JOURNAL OF SCIENCE
ISSN: 2147-3129/e-ISSN: 2147-3188
VOLUME: 11 NO: 2 PAGE: 436-448 YEAR: 2022
DOI: 10.17798/bitlisfen.1017804

Deneysel Tasarım Yöntemleri ile bir Santrifüj Pompa Çarkında Dengeleme Deliği Tasarım Optimizasyonu

Selahattin SEFACI[1*], Osman BABAYİĞİT[2], Saim KOÇAK[3]

[1]*Sempa Pompa Makina A.Ş.*
[2]*Karamanoğlu Mehmetbey Üniversitesi Makine Mühendisliği Bölümü*
[3]*Konya Teknik Üniversitesi Makine Mühendisliği Bölümü*
(ORCID: 0000-0002-7696-6202) (ORCID: 0000-0003-3788-7787) (ORCID: 0000-0003-0342-7408)

Anahtar Kelimeler: Dengeleme delikleri, Eksenel kuvvet, Optimizasyon, Pompa verimi, Taguchi.

Öz

Bu çalışmanın amacı, rulmanlara gelen eksenel kuvvetleri azaltarak rulman ömrünü uzatmak için pompa çarkına açılacak en uygun dengeleme deliğinin belirlenmesidir. Çalışmada eksenel kuvvetlerin azaltılmasının yanı sıra pompa veriminde meydana gelen değişiklikler de dikkate alınmıştır. Bu çalışma için 1480 rpm hız, 350 m^3/h debi ve 51 m basma yüksekliğine sahip tek kademeli santrifüj pompa seçilmiştir. Seçilen pompa çarkı üzerindeki dengeleme deliğinin tasarım optimizasyonu, deneysel tasarım metodu ve Hesaplamalı Akışkanlar Dinamiği (HAD) kullanılarak gerçekleştirilmiştir. HAD analizleri için Ansys Fluent programı kullanılmıştır. Optimum sonuca ulaşmak amacıyla dengeleme deliklerinin çark içerisindeki; delik merkezi açısı, delik çapı, delik merkezi çapı ve adedini belirleyen dört parametre tespit edilmiş ve Çok Amaçlı Taguchi Yöntemi kullanılarak optimizasyon çalışması gerçekleştirilmiştir. Amaçlar; düşük eksenel yük ve yüksek pompa verimi olarak kabul edilmiştir. HAD sonuçları, varyans analizi (ANOVA) ve sinyal/gürültü (S/N) oranına göre değerlendirilmiştir. Yapılan çalışmalar sonucunda; delik çapının amaçlar üzerinde en etkili parametre olduğu tespit edilmiştir. Optimum tasarımın; belirlenen dört parametre için sırasıyla 0°, 12 mm, 100 mm ve 6 adet olduğu belirlenmiştir.

Design Optimization of Balancing Hole in a Centrifugal Pump Impeller by using Experimental Design Methods

Keywords: Balancing holes, Axial force, Optimization, Pump efficiency, Taguchi.

Abstract

The aim of this study is to determine the optimal balancing hole to be drilled into the pump impeller in order to extend the bearing life by reducing the axial forces exposed on the bearings. In this study, as well as reduction of the axial forces, the changes in the pump efficiency are also considered. For this study, a single-stage centrifugal pump having a 1450 rpm speed, 350 m^3/h flow rate and 51 m head is chosen. It is foreseen to optimize the design optimization of the balancing holes on the selected pump impeller is implemented by using the method of experimental design and Computational Fluid Dynamics (CFD). Ansys Fluent software is used for CFD analysis. In order to reach the optimum results, four parameters including the hole center angle, hole diameter, hole center diameter and number of balancing holes in the impeller are selected, and the optimization study is carried out by using Multi-Objective Taguchi Method. Low axial force and high pump efficiency are accepted as objectives. CFD results are evaluated according to the ANOVA and signal/noise (S/N) ratio. As a result, it is determined that the hole diameter is the most effective parameter on these objectives. The optimum design parameters are

*Sorumlu yazar: s.sefaci@sempapompa.com
Geliş Tarihi: 02.11.2021, Kabul Tarihi: 07.04.2022

found to be 0º, 12 mm, 100 mm and 6 for the parameters given above, respectively.

1. Giriş

Santrifüj pompalarda çarkın ön ve arka yüzlerinde meydana gelen basınç farkı nedeniyle eksenel kuvvetler birbirini dengeleyememektedir. Bu durum çark ve pompa mili vasıtasıyla çarka bağlı diğer pompa organlarının pompanın emme ağzına itilmesine neden olmaktadır. Dengelenmemiş eksenel kuvvetler nedeniyle rulmanlar aşırı ısınmakta ve ilerleyen zamanda pompa yataklarında ciddi hasarlar meydana gelebilmektedir.

Bilimsel çalışmalarda ve endüstriyel uygulamalarda santrifüj pompalarda oluşan eksenel yükleri dengelemek için farklı yöntemler kullanılmaktadır. Bu yöntemler içerisinde en pratik ve maliyet açısından en uygun yöntem çarkların arka yüzüne dengeleme deliği delinmesidir.

Dengeleme delikleri yönteminde çarkın arka yüzünde bulunan yüksek basınçlı akışın dengeleme delikleri sayesinde çarkın düşük basınçlı bölgesine geçmesi sağlanır (Şekil 1. a). Çarkın arka yüzündeki basınç azaltılarak çarkın arka yüzü ile ön yüzü arasındaki basınç farkı azaltılmış olur (Şekil 1. b). Ancak dengeleme delikleri santrifüj pompalarda kayıp-kaçak akış miktarını artırması nedeniyle pompa verimini azaltmaktadır.

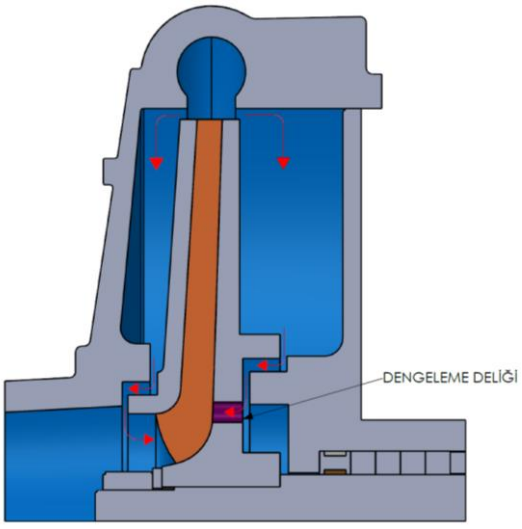

(a)

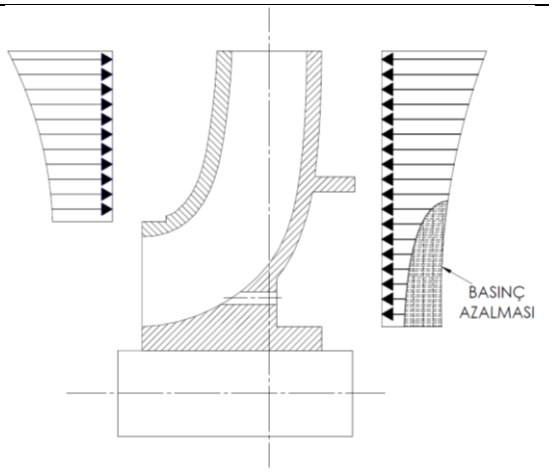

(b)

Şekil 1. Çarkına dengeleme deliği açılan bir pompada meydana gelen akış yönleri (a), çarkın ön ve arka yüzeylerinde meydana gelen basınç dağılımı (b)

Literatürde santrifüj pompalarda pompa performansının artırılması ile ilgili çalışmalar yapan araştırmacılar bulunmaktadır [1-4]. Bazı araştırmacılar eksenel yüklerin tespiti ve dengeleme yöntemleri ile ilgilenmişlerdir [5-10]. Yapılan çalışmaların büyük bir bölümünde araştırmacılar sayısal ve deneysel yöntemleri kullanmış ve bu yöntemleri birbirleri ile kıyaslamışlardır. Literatürde yapılan bazı çalışmalar aşağıda ifade edildiği gibidir:

Bruus ve ark., çok kademeli santrifüj bir pompada oluşan eksenel yükleri incelemişlerdir. Çalışmalarında zamandan tasarruf edebilmek amacıyla analitik hesapların ve HAD analizlerinin birlikte çalıştığı hibrid bir metot geliştirmişlerdir. Çalışmalarının sonucunda hibrid metodu ile HAD sonuçlarını kıyasladıklarında sonuçların birbirine yakın olduğunu fakat bununla birlikte gerçek ölçüm değerlerine göre farklılıklar meydana geldiğini ifade etmişlerdir [11].

Szlaga, santrifüj pompalarda eksenel yükleri azaltmak amacıyla kullanılan yöntemlerden biri olan pompa çarkının arka yüzeyine kanat yerleştirme yöntemini incelemiştir. Çalışmasında analitik, HAD ve deneysel olmak üzere üç ayrı yöntem kullanarak elde ettiği sonuçları karşılaştırmıştır. Karşılaştırma sonucunda; analitik, HAD ve deneysel yöntemle elde edilen sonuçların, arka kanatlarda herhangi bir işlem yapılmadığında birbirine yakın olduğunu, arka kanatlar tornalandığında ise sonuçların farklılık gösterdiğini tespit etmiştir. Ayrıca arka kanatların şekil ve pozisyonunun enerji kayıplarını azaltabileceğini ifade etmiştir [12].

Watanabe ve ark., üç kademeli pompada kayıp kaçak akışlarının pompada meydana gelen

eksenel yüklere etkisini incelemek amacıyla HAD çalışması yapmışlardır. Çalışmalarında HAD sonuçları ve ölçüm değerleri kıyaslandığında pompa basma yüksekliği, pompa verimi ve eksenel yük değerlerinin birbiri ile uyumlu olduğunu belirlemişlerdir [13].

Babayiğit ve ark., iki kademeli santrifüj pompada dengeleme deliklerinin ve kayıp kaçakların pompa performansına etkisini incelemek amacıyla çalışma yapmışlardır. Çalışmalarında farklı HAD modellerini ve deneysel çalışma sonuçlarını kıyaslamışlardır. Çalışmada realizable k-ε türbülans modelini kullanmışlardır. Pompa çalışma noktası için HAD ve deneysel sonuçlar arasındaki farkın yaklaşık %1 olduğunu belirleyerek bu yöntemin uygunluğunu ortaya koymuşlardır. Pompa çarkına dengeleme deliği açılmasının pompa çarkı yüzeylerinde meydana gelen eksenel yük farkını azalttığını fakat kayıp kaçak akış oranını artırması nedeniyle pompa performansını olumsuz etkilediğini ifade etmişlerdir [14].

Parlak ve ark., tek kademeli santrifüj pompada dengeleme deliklerinin, aşınma halkalarının ve çark arka yanak yüzeyi ile salyangoz duvarı arasındaki mesafenin (ara mesafe) eksenel yükler üzerindeki etkisini sayısal ve deneysel olarak incelemişlerdir. Yaptıkları çalışma ile, eksenel yükler üzerinde aşınma halkalarının ve dengeleme deliklerinin ara mesafeye göre daha etkili olduğunu tespit etmişlerdir. Dengeleme deliği, aşınma halkası ve ara mesafe değişikliği ile gerçekleştirilen farklı tasarımlar neticesinde eksenel yük değerinde yaklaşık %60 azalma elde edilirken pompa veriminde yaklaşık %5 azalma meydana geldiğini belirlemişlerdir [15].

Fathi ve ark., tek kademeli santrifüj pompada dengeleme deliklerinin pompa performansına etkisini sayısal ve deneysel olarak incelemişlerdir. HAD analizleri ve deneysel çalışma sonuçlarının birbiri ile uyumlu olduğunu ifade etmişlerdir. Çalışmada 5 mm çaptan büyük dengeleme delikleri kullanıldığında basma yüksekliğinin ve pompa veriminin sırası ile yaklaşık %6 ve %3 azaldığını, ayrıca dengeleme delik çapının eksenel yükleri üzerinde oldukça etkili olduğunu belirtmişlerdir. Çalışmanın sonunda optimum dengeleme deliği çapında toplam eksenel yükün %56 azaldığını belirlemişlerdir [16].

Boitel ve ark., tek kademeli yarı açık çarka sahip santrifüj pompada salyangoz ve çarkın arasındaki ön tip açıklığının pompa performansına ve eksenel yüke etkisini tespit etmek amacıyla farklı özgül hızlara sahip pompalarda HAD çalışması yapmışlardır. Çalışmalarında ön tip açıklığı azaldıkça pompanın basma yüksekliği ve pompa veriminin arttığını ve bu durumun düşük özgül hızlarda daha etkili olduğunu ifade etmişlerdir. Bununla birlikte bütün özgül hızlardaki pompalarda ön tip açıklığının en az, arka tip açıklığının en fazla olduğu durumda eksenel yükün en yüksek değere ulaştığını tespit etmişlerdir [17].

Zhou ve ark., çok kademeli dalgıç tip pompa çarkında eğik tornalamanın pompa performansına ve eksenel yüklere etkisini tespit etmek amacıyla sayısal ve deneysel çalışma yapmışlardır. Çalışmada beş farklı arka yüz çapına sahip çark kullanmışlardır. Çalışmalarının sonucunda arka yüz çapının azalmasıyla birlikte eksenel yüklerin azaldığını fakat pompa performansının önemli ölçüde azaldığını tespit etmişlerdir. Yaptıkları karşılaştırmalar neticesinde kullanılan çark ve benzerleri için eğik tornalama açısının 20° olmasını tavsiye etmişlerdir [18].

Nataraj ve ark., tek kademeli santrifüj pompa performansını iyileştirmek için çark tasarım parametrelerini Taguchi Deneysel Tasarım Yöntemini (TDTY) kullanarak optimize etmeyi amaçlamışlardır. Çalışmalarını hem HAD yöntemi ile hem de deneysel olarak gerçekleştirmişlerdir. Çalışmada L8 ortagonal dizisi ile parametre olarak çark genişliği, çark giriş çapı, kanat sayısı ve kanat çıkış açısını kullanmışlardır. HAD ve deneysel çalışma sonuçlarının birbiri ile uyumlu olduğunu, bununla birlikte fiziksel olarak prototip üretilmemesi nedeniyle HAD çalışmalarının daha avantajlı olduğunu belirtmişlerdir. Çalışmalarının sonucunda pompa performansında çark giriş çapının çark çıkış genişliğine göre çok daha etkili olduğunu ifade etmişlerdir [19].

Dong ve ark., santrifüj bir pompada, tasarım noktasında, altı farklı çapa sahip dengeleme deliği değeri ile çark arka bölmesindeki akış özelliklerini ve disk sürtünme kaybını incelemişlerdir. Arka bölmedeki türbülanslı sınır tabakasının sızıntı akışından büyük ölçüde etkilendiği sonucuna ulaşmışlardır. Dengeleme deliği çapının; tasarım değerinden daha büyük olduğu durumda arka bölmenin disk sürtünme kaybının değişmediğini, tasarım değerinden daha küçük olduğu durumda ise, delik çapı küçüldükçe arka bölgedeki diskin sürtünme kaybının arttığını tespit etmişlerdir [20].

Cheng ve ark., yüksek hızlı santrifüj pompanın kavitasyon performansına dengeleme deliği özel alanının etkisini sayısal yöntemle incelemişlerdir. İlk kavitasyon aşamasında, özel alanın artmasıyla birlikte pompanın basma yüksekliğinin ve veriminin azaldığını tespit

etmişlerdir. Dengeleme deliğinin özel alanının, rotor eksenel kuvvetinin büyüklüğünü ve yönünü değiştirebileceğini ifade etmişlerdir. Özel alanın artmasıyla, pompanın anti-kavitasyon performansının zayıfladığını, dengeleme deliği bölgesinde meydana gelen kavitasyonun pompa çarkı göbeğinin yakınında yoğunlaştığını belirtmişlerdir [21].

Dönen tüm elemanlarda olduğu gibi santrifüj pompa çarklarında da eksenel kaçıklık, balans ve titreşim konusu büyük önem arz etmektedir [22]. Bu nedenle pompa çarkına dengeleme deliği uygulanmasında eksenel kaçıklık ve balans hususunda dikkat etmek gerekir.

Santrifüj pompalarda eksenel yüklerin dengelenmesi konusunda birçok çalışma bulunmasına rağmen uygulanan metotlarda pompalardaki kayıp kaçakların artması veya gereğinden fazla güç tüketimi nedeniyle pompa verimlerinin düşmesinin önüne geçilememiştir. Bununla birlikte birçok endüstriyel uygulamada dengeleme delikleri tahmini yollarla delinmektedir. Dengeleme deliklerinin oluşturduğu kayıp kaçakların verim azalmasına sebep olması nedeniyle tasarım parametrelerine ait seviyelerin uygun kombinasyonları belirlenip incelendikten sonra dengeleme deliğinin uygulanması gerekmektedir.

Çalışmada en iyi sonucun elde edilebilmesi için kullanılan her bir parametre seviyesinin farklı kombinasyonlarında bir dizi deneylerin yapılması gerekmektedir. Yapılan deneyler sonucunda elde edilen veriler değerlendirilerek parametrelerin optimum değerleri tespit edilmektedir. Uygun kombinasyonun belirlenmesinde klasik olarak çalışma yapılırken her seferinde bir parametre seviyesi değiştirilerek diğer parametreler sabit tutulmaktadır. Bu sayede değiştirilen parametrenin sisteme olan etkisi araştırılmaktadır. Ancak klasik yöntem zaman kaybına ve ekonomik olarak zorluklara neden olmaktadır [23].

TDTY zaman ve ekonomik tasarrufları amaçlayarak deneylerin verimli bir şekilde yapılması ve sonuçların yorumlanmasını sağlamaktadır. Kısacası TDTY optimizasyon problemlerinin çözümünde başarılı bir metot olarak ortaya çıkmaktadır [24]. TDTY kullanılarak farklı alanlarda birçok çalışma yapılmıştır [25-29].

Bu çalışmada, hem yüksek pompa verimi elde etmek hem de pompa çarkına etki eden eksenel yük farkını azaltmak amacıyla tek kademeli santrifüj pompa çarkında dengeleme deliklerine ait parametrelerin tek ve çok amaçlı TDTY kullanılarak sayısal yöntemle optimizasyonu gerçekleştirilmiştir. İşletmelerde eksenel yükü azaltmak amacıyla pompa çarklarında gelişi güzel açılan dengeleme deliklerinin pompa verimini nasıl etkileyebileceği araştırılmıştır.

2. Materyal ve Metot

Çalışma için SEMPA firmasında üretilmekte olan tek kademeli santrifüj bir pompa seçilmiştir. Pompanın katı modelleri ve akış hacimleri Solidworks ve ANSYS programları kullanılarak tasarlanmıştır. Pompanın sayısal analizleri ANSYS-Fluent paket programı ile yapılmıştır. Çalışmada TDTY uygulanmıştır.

2.1. Sayısal Çalışma

Santrifüj pompa tasarımında pompa debisi, pompa basma yüksekliği ve pompa devri olmak üzere üç parametrenin belirlenmesi gerekmektedir. Bu çalışmada pompa için belirlenen tasarım parametreleri Tablo 2.1'de verilmiştir.

Tablo 1. Pompa Tasarım Parametreleri

Parametre	Değer
Debi (m^3/h)	350
Basma Yüksekliği (m)	51
Devir (d/d)	1480

Ansys-Fluent programı kullanılarak santrifüj pompalarla ilgili basma yüksekliği, pompa gücü, pompa verimi, eksenel ve radyal yükler gibi bir çok önemli kavram hesaplanabilmektedir. Santrifüj pompalarla ilgili sayısal çalışma yapılırken izlenecek yol aşağıdaki gibidir:

- Pompa katı modelinin tasarımı,
- Çark, salyangoz, giriş ve çıkış kısımlarının akış hacimlerinin oluşturulması,
- Akış hacimleri üzerinde uygun ağ yapısının oluşturulması,
- Belirlenen sınır şartlarına göre HAD analizlerinin gerçekleştirilmesi.

2.1.1. Katı Model, Akış Hacimleri ve Mesh Yapısı

Çalışmada ticari olarak üretilmekte olan santrifüj pompanın çark, salyangoz ve salmastra kutusu Solidworks programında tasarlanmıştır. Tasarlanan katı modellerin, Ansys Design Modeler programında akış hacimleri tasarlanarak pompaya giriş ve çıkış hacimleri eklenmiştir (Şekil 2).

Çalışmada sayısal çözüm ağ yapısı oluşturulurken Ansys-Meshing programı kullanılmıştır. Akış hacimleri içerisinde kayıp kaçak bölgeleri dörtgensel, diğer bölgeler ise üçgensel ağ

yapısı kullanılarak oluşturulmuştur (Şekil 3). Analizlerin ağ yapısından bağımsız hale gelmesi için yapılan çalışmada ağ sayısı yaklaşık 4.2 milyon iken, maksimum çarpıklık değeri 0.94 olarak elde edilmiştir.

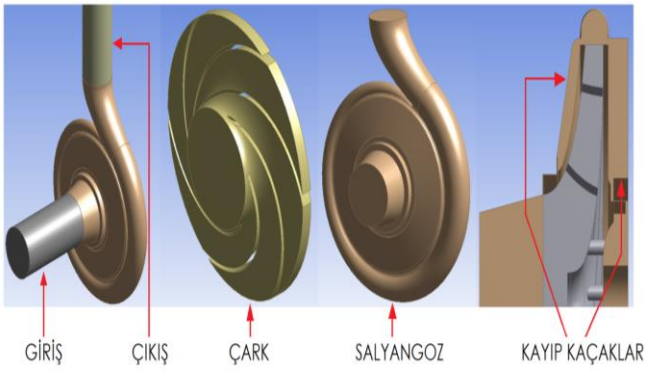

Şekil 2. Sayısal analizlerde kullanılmak için oluşturulan santrifüj pompa akış hacimleri

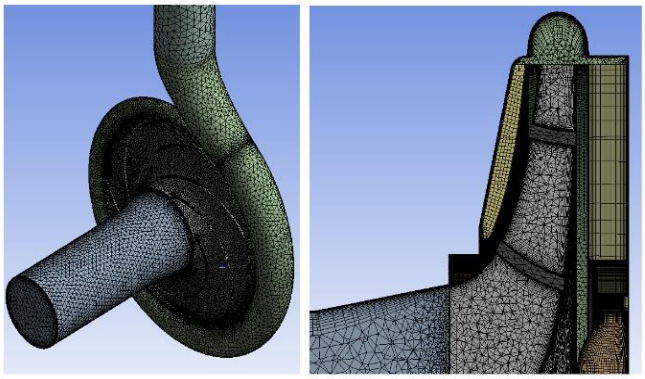

(a) (b)

Şekil 3. Santrifüj pompa akış hacimleri üzerinde oluşturulan çözüm ağ yapısı (a) ve ağ yapı detay kesit görünümü (b)

2.1.2. Sayısal Analiz

HAD ile yapılan uygulamalarda kullanılabilecek farklı türbülans modelleri bulunmaktadır. Santrifüj pompalarla ilgili yapılan bazı sayısal çalışmalarda RNG k-ε, SST k-ω ve Realizable k-ε gibi türbülans modelleri birbiri ile karşılaştırılmıştır. Realizable k-ε modelinin diğer modellere göre deneysel sonuçlarla daha uyumlu sonuçlar verdiği görülmüştür [30-31]. Bu çalışmada türbülans modeli olarak Realizable k-ε modeli kullanılmıştır. Daha kısa sürede sonuç almak amacıyla çözücü olarak coupled algoritma tercih edilmiştir [32]. Uygulanan pompa sınır koşulları Tablo 2'de gösterilmiştir.

Tablo 2. Pompa sayısal analizleri için kullanılan sınır şartları

Konum	Sınır Şartı
Giriş	Giriş Basıncı (Pressure Inlet)
Çıkış	Çıkış Debisi (Mass Flow Outlet)
Duvarlar	Ölçeklenebilir Duvar Fonksiyonu (Scalable Wall Function)
Çark	Dönen Referans Parça (Rotating Reference Frame)

Analiz esnasında akışın sabit olduğu kabul edilerek pompanın çalışma şartlarına uygun olarak girişinde statik basınç, çıkışında ise kütlesel debi tanımlanmıştır. Doğru çözüm elde edebilmek amacıyla sınır tabakaya yakın mesafelerde boyutsuz sınır tabaka mesafesi (y^+) değerlerinin kabul edilebilir sınırlar arasında elde edilmesi ve uygun duvar fonksiyonu seçilmesi gerekmektedir. Standart wall function, enhanced wall treatment ve scalable wall function gibi birçok duvar fonksiyonu k-ε türbülans modelinde kullanılmaktadır. Sınır tabakasının laminer ve tampon akış bölgesinde hatalı modellemeyi engellemesi nedeniyle scalable wall functions duvar fonksiyonu tercih edilmiş ve HAD çalışmaları $y^+ < 300$ olacak şekilde gerçekleştirilmiştir [32].

Pompa içerisinde modellenen akış hacimleri için 3 farklı denklemin çözümü yapılmaktadır. Bunlar:

- Süreklilik Denklemi
- Momentum Denklemi
- Transport denklemleridir.

Sıkıştırılamaz akış için süreklilik ve momentum denklemi sırasıyla aşağıdaki gibidir [32]:

$$\nabla \vec{V} = 0 \qquad (1)$$

$$\rho\nabla(\vec{v}\vec{v}) = -\nabla P + \mu\nabla^2\vec{V} + \rho\vec{g} + \vec{F} \qquad (2)$$

Realizable k-ε modeli için transport denklemleri aşağıdaki gibidir:

$$\frac{\partial}{\partial t}(\rho k) + \frac{\partial}{\partial x_i}(\rho k u_j) = \frac{\partial}{\partial x_i}\left[\left(\mu + \frac{\mu_t}{\sigma_k}\right)\frac{\partial k}{\partial x_j}\right] + G_k + G_b - \rho\varepsilon - Y_M + S_k \qquad (3)$$

$$\frac{\partial}{\partial t}(\rho\varepsilon)+\frac{\partial}{\partial x_i}(\rho\varepsilon u_j) = \frac{\partial}{\partial x_i}\left[\left(\mu+\frac{\mu_t}{\sigma_\varepsilon}\right)\frac{\partial \varepsilon}{\partial x_j}\right] + \rho C_1 S\varepsilon - \rho C_2 \frac{\varepsilon^2}{k+\sqrt{v\varepsilon}} + C_{1\varepsilon}\frac{\varepsilon}{k}C_{3\varepsilon}G_b + S_\varepsilon \quad (4)$$

Burada;

$$C_1 = max\left[0.43, \frac{\eta}{\eta+5}\right] \quad (5)$$

$$\eta = S\frac{k}{\varepsilon} \quad (6)$$

$$S = \sqrt{2S_{ij}S_{ij}} \quad (7)$$

Yukarıda ifade edilen denklemlerde G_k terimi, ortalama hız gradyanları ile üretilen türbülans kinetik enerjiyi ifade etmektedir. G_b terimi kaldırma kuvveti nedeniyle meydana gelen türbülans kinetik enerji üretimini ifade etmektedir. Y_M terimi sıkıştırılabilir akışlar için çalkantılı dilatasyon katsayısıdır. C_2 ve $C_{1\varepsilon}$ sabit katsayılar, σ_k ve σ_ε; k ve ε için Prandtl sayısı, S_ε ve S_k kaynak terimlerdir. Çalışmada denklemlerdeki sabitler için standart değerler ($C_{1\varepsilon} = 1.44,\ C_2 = 1.9, \sigma_k = 1.0$ ve $\sigma_\varepsilon = 1.2$) kullanılmıştır. Denklem (3) ve (4)'te kullanılan türbülans viskozitesi (μ_t) Prandtl-Kolmogorov ilişkisi kullanılarak hesaplanmaktadır [32].

$$\mu_t = \rho C_\mu \frac{k^2}{\varepsilon} \quad (8)$$

Sayısal çalışmaların sonunda pompaya gelen yükler, pompa giriş çıkış basınçları ve dönen yüzeylerde oluşan tork değerleri belirlenmiştir. Belirlenen değerlere göre pompaya ait hidrolik verim aşağıdaki gibi hesaplanmaktadır [33].

$$P_h = \frac{\rho * g * Q * H_m}{1000} \quad (9)$$

$$P_{mil} = \frac{\tau * \omega}{1000} \quad (10)$$

$$\omega = \frac{2 * \pi * n}{60} \quad (11)$$

$$\eta_h = \frac{P_h}{P_{mil}} \quad (12)$$

2.2. Deneysel Tasarım

Deneysel tasarım teknikleri istatistiksel bir yaklaşımın yanı sıra tüm araştırma-geliştirme faaliyetlerinde kullanılabilecek, kaliteyi artıran, maliyetleri düşüren, sonuçların güvenilirliğini sağlayan, tüm diğer kalite tekniklerini destekleyen ve tamamlayan tekniklerdir [24].

Deneysel tasarım diğer bilimsel disiplinlere benzer kendine özgü terminoloji ve metodolojiye sahiptir. Deneyler laboratuvar ortamında pilot uygulama, tam uygulama ya da klinik olarak yapılabilmektedir. Deney çalışmaları bilimin merkezinde yer almaktadır. Deney tasarımı sebep ve etki ilişkisini belirlemek için planlanmış bir yaklaşımdır [23]. Deneysel çalışmalarda amaca yönelik parametreler belirlenerek parametrelere ait uygun seviyelerde çalışmalar sürdürülür. Bu çalışmada santrifüj pompanın, mekanik dayanım açısından çark yüzeyleri üzerine etki eden net eksenel yükünün düşük olması ve aynı zamanda mümkün olan en yüksek verime de sahip olması istenmektedir. Bu sebeple ulaşılmak istenilen amaca yönelik çark tasarımına ait parametrelerin bir kısmının sabit seviyelerde, bir kısmının ise değişken olarak belirlenmesi gerekmektedir. Çark tasarımı için bu çalışmada belirlenen parametreler Şekil 4'te detaylı olarak gösterilmiştir.

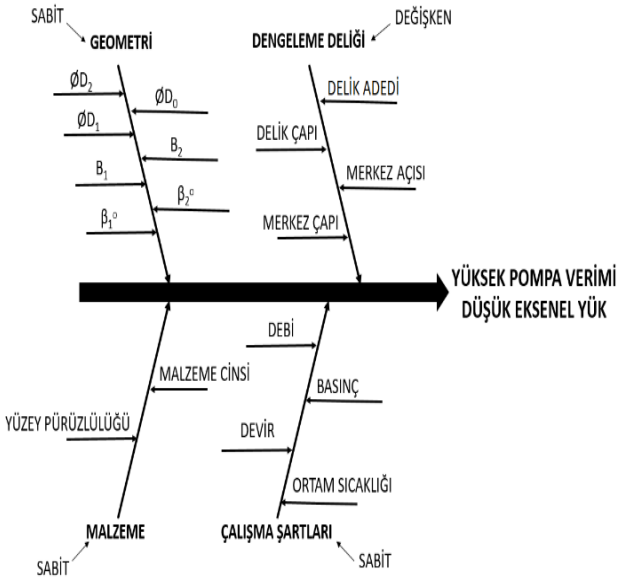

Şekil 4. Pompa çarkı tasarım parametrelerine ait balık kılçığı diyagramı

Çalışmada pompa çarkı üzerinde delinecek olan dengeleme delikleri için dört farklı parametre tanımlanmıştır. Tanımlanan bu parametreler ve değerleri Tablo 3 ve Şekil 5'te gösterilmektedir.

Tablo 3. Dengeleme deliği tasarım optimizasyonunda kullanılan parametrelerin değerleri

Parametreler	1. Seviye	2. Seviye	3. Seviye	4. Seviye
Merkez Çapı (ØA) (mm)	100	110	120	130
Delik Çapı (ØB) (mm)	6	8	10	12
Merkez Açısı (θ) (°)	0	7.5	15	22.5
Delik Adedi (n)	3	6		

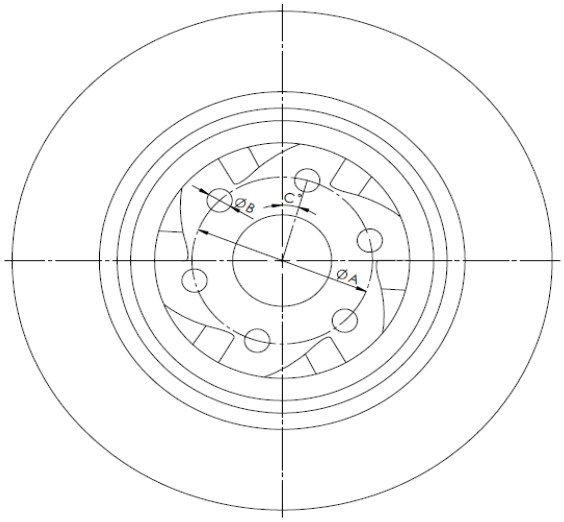

Şekil 5. Dengeleme deliği tasarım optimizasyonu için seçilen parametreler

Dengeleme deliklerinin delinmesinde seçilen parametre seviyeleri çark üzerinde dengeleme deliklerinin imalat açısından uygunluğu dikkate alınarak minimum ve maksimum değer aralıklarını kapsayacak şekilde tespit edilmiştir. Pompa çarkının arka aşınma halkası ve çark arka göbek çapının oluşturduğu sınırlandırma neticesinde merkez çapı ve delik çapı minimum ve maksimum olarak sırasıyla 100-130 mm ve 6-12 mm olarak tespit edilmiştir. Kanat geometrisi ve kanat adedinin oluşturduğu sınırlandırma neticesinde merkez açısı ve delik adedi minimum ve maksimum olarak sırasıyla 0°-22.5° ve 3-6 adet olarak belirlenmiştir.

Belirlenen parametreler ve farklı seviyeleri ile deneysel çalışma yapılırken klasik yöntemlerle parametrelerin tüm kombinasyonları kullanıldığında, 128 adet deneme yapılması gerekmektedir. Klasik yöntemlerle yapılan deneysel çalışmalarda takip edilen yol Şekil 6'da incelenmektedir [23]. Tüm çalışmalarda bir parametre değişken olarak belirlenir ve diğer bağımsız parametreler sabit tutulur.

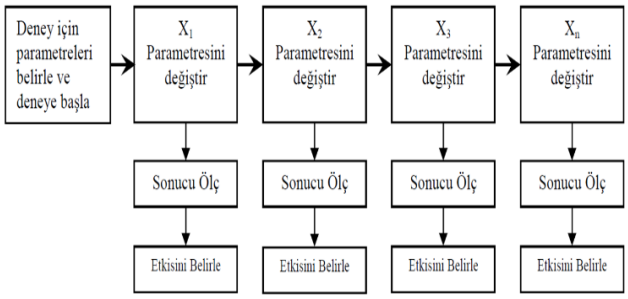

Şekil 6. Klasik deney yönteminde izlenen yol

Klasik yöntemlerle yapılan deneysel çalışmaların ciddi maliyet problemi oluşturmasının yanı sıra parametre ve seviye sayılarına bağlı olarak deneylerin tamamlanması çok uzun zaman gerektirmektedir.

TDTY, klasik yöntemlerin aksine birden fazla parametrenin aynı anda farklı kombinasyonlarını kullanarak daha az deneyle en uygun sonucun elde edilmesini sağlamaktadır. Japon bilim adamı Dr. Genichi Taguchi tarafından geliştirilen bu istatistiksel deney tasarım yöntemi sayesinde kaliteye ulaşmada çok daha az deneme ile daha iyi sonuç alma imkânı elde edilmektedir.

TDTY, gürültü oranı veya kayıp fonksiyonu olarak bilinen üç farklı amaca uygun olarak değerlendirilmektedir [34]. Bunlar;

İstenilen sonucun en büyük en iyi olduğu durumda:

$$S/N = -10 \log\left(\frac{1}{n}\sum_{i=1}^{n}\frac{1}{y_i^2}\right) \qquad (13)$$

En düşük en iyi olduğu durumda:

$$S/N = -10 \log\left(\frac{1}{n}\sum_{i=1}^{n} y_i^2\right) \qquad (14)$$

Normal en iyi olduğu durumda:

$$S/N = 10 \log\left(\frac{\overline{y}^2}{n}\right) \qquad (15)$$

Burada:

$$\overline{y} = \frac{1}{n}\sum_{i=1}^{n} y_i \qquad (16)$$

$$S^2 = \frac{1}{n-1}\sum_{i=1}^{n}(y_i - \overline{y})^2 \qquad (17)$$

Burada;

y_i, i. denemede elde edilen sonucu, n=1, denemedeki test sayısını, $\overline{y}$, sonuçların ortalamasını, S^2, sonuçların varyansını ifade etmektedir.

Çalışmada belirlenen parametreler ve seviyelere göre L16 ortagonal dizisi kullanılarak çalışma gerçekleştirilmiş ve hesaplanan eksenel yük ve verim değerleri ayrıntılı olarak Tablo 4'te verilmiştir.

Tablo 4. L16 ortagonal dizisi kullanılarak gerçekleştirilen çalışmada kullanılan parametrelere bağlı elde edilen eksenel yük ve verim değerleri

	Parametreler				Sonuçlar	
Deney	Delik Çapı (mm)	Merkez Çapı (mm)	Merkez Açısı (°)	Delik Adedi	Verim (%)	Eksenel Yük (N)
1	6	100	0	3	79.35	5653.15
2	6	110	7.5	3	79.37	5599.31
3	6	120	15	6	79.02	3402.71
4	6	130	22.5	6	78.97	3594.64
5	8	100	7.5	6	78.91	1558.13
6	8	110	0	6	78.78	1640.48
7	8	120	22.5	3	79.11	3474.05
8	8	130	15	3	78.96	3661.5
9	10	100	15	3	78.96	2191.27
10	10	110	22.5	3	79.02	2379.3
11	10	120	0	6	78.75	1135.09
12	10	130	7.5	6	78.54	1271.11
13	12	100	22.5	6	78.61	742.479
14	12	110	15	6	78.83	895.981
15	12	120	7.5	3	78.77	1819.38
16	12	130	0	3	78.83	1615.87

3. Bulgular ve Tartışma

Pompalarda oluşan eksenel yük farkını azaltmak amacıyla kullanılan dengeleme delikleri yöntemi, kayıp kaçak akış artışına sebep olması nedeniyle pompa veriminde önemli oranda azalmaya neden olabilmektedir. Bu çalışmada, meydana gelebilecek bu verim azalmasının asgari düzeye indirilmesi için, dengeleme deliklerini oluşturan parametrelerin optimize edilmesi amaçlanmıştır. Elde edilen sonuçlar TDTY ile analiz edilmiştir. Kayıp fonksiyonu olarak eksenel yük için en düşük en iyi fonksiyonu, pompa verimi için en yüksek en iyi fonksiyonu seçilmiştir. Kayıp fonksiyonlarına göre parametrelerin optimum seviyelerindeki değerler Denklem 18 ile tahmin edilmiştir [26].

$$\eta_{opt} = m + \sum_{j=1}^{n}\left[\left(m_{i,j}\right)_{max} - m\right] \qquad (18)$$

Burada: η_{opt}, tahmin edilen optimum değeri, m, η değerinin 16 denemeye göre genel ortalamasını, $\left(m_{i,j}\right)_{max}$, parametrelerin optimum seviyelerinde elde edilen değeri, n, parametre sayısını ifade etmektedir.

Kayıp fonksiyonları çok amaçlı olarak değerlendirilirken Denklem 19 kullanılmıştır [26].

$$S/N_{opt} = \left(W_{eksenel\ yük}\, S/N_{eksenel\ yük}\right) + \left(W_{verim}\, S/N_{verim}\right) \qquad (19)$$

Burada $W_{\text{eksenel yük}}$ ve W_{verim} değerleri eksenel yük ve verime ait ağırlık değerleridir. Bu değerler tecrübe, müşteri talebi ve diğer ihtiyaçlara göre belirlenen değerlerdir. Bu çalışmada eksenel yük ve verime ait ağırlık değerleri eşit kabul edilmiştir.

3.1. Tek Amaçlı Sonuçların Analizi

Çalışmada TDTY kullanılarak eksenel yük ve pompa verimi için dengeleme deliği parametreleri analiz edilmiştir. Her bir parametre seviyesine göre eksenel yük (Tablo 5) ve pompa verimi (Tablo 6) S/N değerleri elde edilmiştir. Elde edilen optimum seviyelere göre oluşacak eksenel yük ve pompa verimi tahmin edilmiştir (Tablo 7). Bununla birlikte elde edilen sonuçlar ANOVA analizi ile değerlendirilerek parametrelerin sonuçlar üzerindeki katkısı tespit edilmiştir. Tablo 8 ve Tablo 9'da sırasıyla eksenel yük ve pompa verimi için ANOVA analizleri incelenmektedir. Eksenel yük için parametrelerin etkisi önem sırasına göre delik çapı, delik adedi, merkez çapı ve merkez açısı için sırasıyla %67.23, %31.02, %1.04 ve %0.31 olarak elde edilmiştir. Pompa verimi için ise parametrelerin etkisi önem sırasına göre delik çapı, delik adedi,

merkez çapı ve merkez açısı için sırasıyla %50.50, %27.45, %13.58 ve %2.4 olarak elde edilmiştir. İki amaç için hatanın katkısı sırasıyla %0.41 ve %6.07 olarak hesaplanmıştır.

Tek amaçlı olarak gerçekleştirilen çalışmada hem eksenel yük hem de pompa verimini etkileyen parametrelerin önem sırasının; delik çapı, delik adedi, merkez çapı ve merkez açısı olmak üzere aynı olmasına rağmen, bu parametrelerin eksenel yük ve pompa verimi üzerindeki etki derecelerinin oldukça farklı olduğu açıkça görülmektedir (Tablo 8 ve Tablo 9).

Tablo 5. Farklı parametre seviyelerinde elde edilen eksenel yük S/N oranları

Seviye	Delik Çapı (dB)	Merkez Çapı (dB)	Merkez Açısı (dB)	Delik Adedi (dB)
1	-72.93	-65.78	-66.15	-69.47
2	-67.56	-66.45	-66.52	-63.69
3	-64.38	-66.93	-66.94	
4	-61.45	-67.15	-66.71	
Delta	11.48	1.37	0.78	5.78
Rank	1	3	4	2

Tablo 6. Farklı parametre seviyelerinde elde edilen pompa verimi S/N oranları

Seviye	Delik Çapı (dB)	Merkez Çapı (dB)	Merkez Açısı (dB)	Delik Adedi (dB)
1	37.97	37.95	37.94	37.95
2	37.94	37.95	37.94	37.93
3	37.93	37.94	37.94	
4	37.93	37.93	37.95	
Delta	0.04	0.02	0.01	0.02
Rank	1	3	4	2

Tablo 7. Eksenel yük ve pompa verimi için tespit edilen optimum parametre değerleri

Amaç	Optimum Seviye	Tahmin Edilen S/N	Tahmin Edilen Değer
Eksenel Yük	A4B1C1D2	-57.33 dB	476.95 N
Pompa Verimi	A1B1C4D1	38 dB	79.34%

Tablo 8. Eksenel yük için ANOVA analizi

Kaynak	SS	DOF	Variance	F -Ratio	C %
Delik Çapı	289.95	3	96.65	276.35	67.23
Merkez Çapı	4.47	3	1.49	4.26	1.04
Merkez Açısı	1.34	3	0.45	1.28	0.31
Delik Adedi	133.77	1	133.77	382.49	31.02
Hata	1.75	5	0.35		0.41
Toplam	431.27	15			100

Tablo 9. Pompa verimi için ANOVA analizi

Kaynak	SS	DOF	Variance	F - Ratio	C %
Delik Çapı	0.0042	3	0.0014	13.87	50.50
Merkez Çapı	0.0011	3	0.0004	3.73	13.58
Merkez Açısı	0.0002	3	0.0001	0.66	2.40
Delik Adedi	0.0023	1	0.0023	22.61	27.45
Hata	0.0005	5	0.0001		6.07
Toplam	0.0084	15			100

3.2. Çok Amaçlı Sonuçların Analizi

Belirlenen parametrelerin farklı seviyeleri için elde edilen eksenel yük ve pompa verimi değerleri çok amaçlı TDTY kullanılarak analiz edilmiştir. Elde edilen optimum seviyelere göre eksenel yük ve pompa verimi değerleri tahmin edilmiştir (Tablo 10). Çok amaçlı olarak elde edilen optimum S/N oranları Tablo 11'de verilmiştir. Parametre seviyelerine göre optimum S/N oranları Tablo 12'de verilmiştir. Bununla birlikte elde edilen sonuçlar ANOVA analizi ile değerlendirilerek parametrelerin sonuçlar üzerindeki katkısı tespit edilmiştir. Tablo 13'te optimum S/N oranları için ANOVA analizleri incelenmektedir. Optimum S/N oranları için parametrelerin etkisi önem sırasına göre delik çapı, delik adedi, merkez çapı ve merkez açısı için sırasıyla %67.22, %30.98, %1.07 ve %0.31 olarak elde edilmiştir. Hatanın katkısı %0.42 olarak hesaplanmıştır.

Tablo 10. Çok amaçlı TDTY'ye göre optimum parametre seviyesinde tahmin edilen eksenel yük ve pompa verimi değerleri

Amaç	Optimum Seviye	Tahmin Edilen Değer		
		S/N (dB)	Eksenel Yük (N)	Pompa Verimi (%)
Eksenel Yük ve Pompa Verimi	A4B1C1D2	-9.7	476.95	78.68

Tablo 11. Çok amaçlı TDTY'ye göre elde edilen S/N oranları

Deney	S/N $_{Eksenel\ Yük}$ (dB)	S/N $_{Verim}$ (dB)	S/N$_{opt}$ (dB)
1	-75.04	37.99	-18.52
2	-74.96	37.99	-18.48
3	-70.63	37.95	-16.34
4	-71.11	37.94	-16.58
5	-63.85	37.94	-12.95
6	-64.29	37.92	-13.18
7	-70.81	37.96	-16.42
8	-71.27	37.94	-16.66
9	-66.81	37.94	-14.43
10	-67.52	37.95	-14.78
11	-61.10	37.92	-11.58
12	-62.08	37.90	-12.09
13	-57.41	37.93	-9.73
14	-59.04	37.93	-10.55
15	-65.19	37.92	-13.63
16	-64.16	37.93	-13.11

Tablo 12. Farklı parametre seviyelerine göre elde edilen optimum S/N oranları

Seviye	Delik Çapı (dB)	Merkez Çapı (dB)	Merkez Açısı (dB)	Delik Adedi (dB)
1	-17.48	-13.91	-14.10	-15.75
2	-14.80	-14.25	-14.29	-12.87
3	-13.22	-14.49	-14.49	
4	-11.76	-14.61	-14.38	
Delta	5.72	0.69	0.39	2.87
Rank	1	3	4	2

Tablo 13. Optimum S/N oranları için ANOVA analizi sonuçları

Kaynak	SS	DOF	Variance	F - Ratio	C%
Delik Çapı	71.96	3	23.99	268.96	67.22
Merkez Çapı	1.15	3	0.38	4.29	1.07
Merkez Açısı	0.33	3	0.11	1.24	0.31
Delik Adedi	33.17	1	33.17	371.90	30.98
Hata	0.45	5	0.09		0.42
Toplam	107.05	15			100

3.3. Sonuçların Değerlendirilmesi

TDTY kullanılarak düşük eksenel yük ve yüksek pompa verimi elde etmek amacıyla L16 dizisine uygun olarak HAD çalışmaları yapılmıştır. Sonuçlar eksenel yüklere ve pompa verimine göre önce tek amaçlı olarak, daha sonra çok amaçlı olarak değerlendirilmiştir. Elde edilen S/N oranlarına göre Minitab 19 programı kullanılarak her bir parametre seviyesinde eksenel yük ve pompa veriminde meydana gelen değişiklikler Şekil 7 - Şekil 9'da verilmiştir.

Verilen bu şekillerde x ekseni parametrelere ait seviyeleri, y ekseni ise seviyelere göre elde edilen S/N oranlarını göstermektedir. Şekil 7 incelendiğinde, delik çapı ve delik adedi arttıkça, merkez çapı ve merkez açısı ise azaldıkça eksenel yükün azaldığı görülmektedir. Şekil 8 incelendiğinde ise; delik çapı, delik adedi ve merkez çapı azaldıkça, merkez açısı ise arttıkça pompa veriminin arttığı tespit edilmektedir. Hem düşük eksenel kuvvet hem de yüksek pompa verimi için çok amaçlı olarak değerlendirildiğinde; delik çapı ve delik adedi arttıkça, merkez çapı ve merkez açısı azaldıkça optimum değere ulaşıldığı anlaşılmaktadır (Şekil 9).

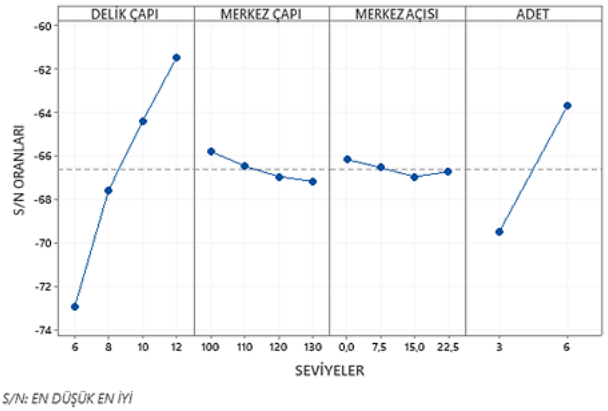

Şekil 7. Parametrelerin farklı seviyelerinde eksenel yük için hesaplanan S/N oranları

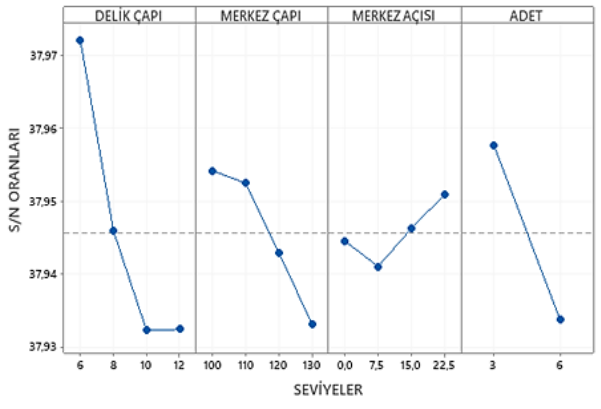

Şekil 8. Parametrelerin farklı seviyelerinde pompa verimi için hesaplanan S/N oranları

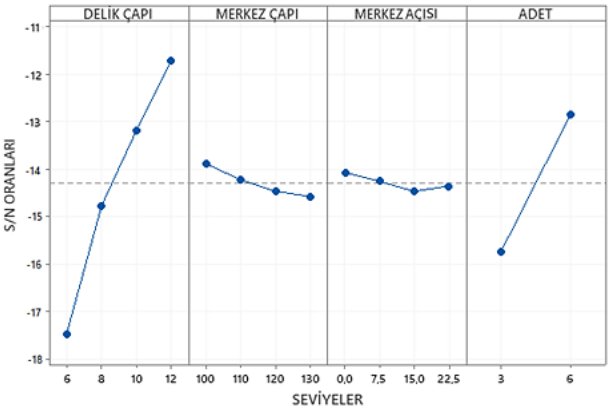

Şekil 9. Parametrelerin farklı seviyelerinde eksenel yük ve pompa verimi birlikte değerlendirilerek (çok amaçlı) hesaplanan S/N oranları

Santrifüj pompalarla ilgili yapılan birçok çalışmada HAD ve deneysel çalışma sonuçlarının birbirine uyumlu olduğu görülmüştür [1-2]. İmalatta pompa çarkına dengeleme deliği açılırken yalnızca delik çapı ve delik adedi kullanılmakta, delik merkez çapı ve merkez açısı bilinmemektedir. İmalat esnasında delik çapı ve delik adedi en iyi sonucu verecek şekilde seçilmiş olsa bile delik merkez çapı ve merkez açısı bilinmeden rastgele dengeleme deliği açılmaktadır. Bu çalışmada çok amaçlı optimizasyon ile elde edilen verilere göre; çarkına optimize dengeleme deliği açılmış pompa, rastgele dengeleme deliği açılan pompa (delik çapı ve delik adedi aynı, merkez çapı ve merkez açısı farklı) ve dengeleme deliği açılmayan pompa için aynı şartlarda ayrı ayrı HAD analizleri gerçekleştirilmiş ve sonuçlar karşılaştırmalı olarak Tablo 14'te gösterilmiştir.

Tablo 14. Farklı dengeleme deliği şartlarında HAD analiz sonuçlarında elde edilen değerler

Değer	Dengelemee Deliksiz Pompa	Optimize Dengeleme Delikli Pompa	Rastgele Dengelemee Delikli Pompa
Basma Yüksekliği (m)	51.2	50.7	50.2
Verim (%)	80.8	78.7	77.44
Eksenel Yük (N)	8860	802	1045.2

Tablo 14 incelendiğinde çarklarında dengeleme deliği açılan pompalarda eksenel yük değerlerinde çok önemli oranda azalma elde edilirken aynı zamanda basma yüksekliği ve verim değerlerinde de bir miktar azalma meydana geldiği görülmektedir. Dengeleme deliksiz pompaya göre; optimize dengeleme delikli ve rastgele dengeleme delikli pompalarda eksenel yük, pompa verimi ve basma yüksekliği değerlerinde sırasıyla yaklaşık %91/%88, %2.6/%4.1 ve %1/%2 azalma meydana geldiği tespit edilmiştir. Bu sonuçlar optimize dengeleme delikli pompa ile rastgele dengeleme delikli pompaya göre daha düşük eksenel yük ve daha yüksek verim elde edilebileceğini açıkça göstermektedir.

4. Sonuç ve Öneriler

Pompa yataklarında, eksenel yük farkı nedeniyle aşırı ısınma ve yıpranma problemleri meydana gelmektedir. Bu nedenle eksenel yük farkını azaltmaya yönelik uygulamalardan bir tanesi ve en yaygın olanı ise pompa çarkına dengeleme deliği açılmasıdır. Bu çalışma, pompa çarklarına açılacak olan dengeleme deliklerinin farklı durumlarda ne tür sonuçlar ortaya çıkaracağını belirlemek ve optimum sonuca ulaşmak amacıyla gerçekleştirilmiştir. Enerji tüketiminin son derece önemli olduğu düşünüldüğünde pompa çarklarına açılacak olan dengeleme deliği için elde edilen eksenel yük azalmasının yanı sıra pompa veriminde meydana gelebilecek azalmanın da dikkate alınması gerekmektedir.

Belirlenen parametrelerin hem eksenel yük hem de pompa verimi üzerindeki etki sırası aynı gerçekleşmiştir. Delik çapı ve delik adedinin delik merkez çapı ve merkez açısına göre çok daha etkili olduğu tespit edilmiştir. Eksenel yük bakımından değerlendirildiğinde önemli olan parametrelerin delik çapı ve delik adedi olduğu, delik merkez çapı ve merkez açısının göz ardı edilebileceği anlaşılmaktadır. Pompa verimi bakımından değerlendirildiğinde ise delik çapı ve delik adedinin önemli parametreler olmasına rağmen eksenel yüke göre daha düşük oranda etkili olduğu görülmektedir. Pompa verimi için delik merkez açısı göz ardı edilebilecek olmasına rağmen delik merkez çapı dikkate alınması gereken bir parametre olarak karşımıza çıkmaktadır.

Delik çapı ve delik adedinin artması eksenel yükü azaltırken pompa verimini de azaltmaktadır. Özellikle delik merkez çapının eksenel yük bakımından ihmal edilebilecek olması pompa veriminin daha yüksek elde edilebilmesi için değerlendirilebilecek bir parametre olarak ortaya çıkmaktadır. Optimize dengeleme delikli ve rastgele dengeleme delikli pompalar için elde edilen sonuçlar da bunun açık bir göstergesidir.

Bu çalışma için belirlenen pompada parametre ağırlıklarının eksenel yük için daha baskın

olması nedeniyle tek amaçlı ve çok amaçlı eşit ağırlıklı TDTY sonucunda aynı optimum geometri elde edilmiştir. Gelecek çalışmalarda aynı pompada farklı ağırlıklı TDTY ve farklı pompalarda aynı yöntemlerde denemeler gerçekleştirilerek elde edilen sonuçların karşılaştırılması planlanmaktadır.

Teşekkür

Çalışmanın gerçekleştirilmesinde paylaşım ve izin katkılarından dolayı SEMPA POMPA firmasına teşekkür ederiz.

Yazarların Katkısı

Selahattin SEFACI, yüksek lisans tezi kapsamında bu çalışmayı gerçekleştirerek verileri elde etmiş ve makalenin taslak yapısını oluşturmuştur.

Osman BABAYİĞİT, aktif olarak SEMPA firmasının akademik danışmanlığını yürütmekte ve çalışma konularını belirlemektedir. Önceki çalışmalarından elde ettiği bilgiler doğrultusunda parametrelerin belirlenmesinde, sonuçların değerlendirilmesinde ve makalenin yazılmasında katkıda bulunmuştur.

Saim KOÇAK, Selahattin SEFACI'nın danışman öğretim üyesi olarak, konunun belirlenmesinde, çalışmanın yönlendirilmesinde, bilgi paylaşımı ve sonuçların değerlendirilmesi kapsamında katkıda bulunmuştur.

Çıkar Çatışması Beyanı

Yazarlar arasında herhangi bir çıkar çatışması bulunmamaktadır.

Araştırma ve Yayın Etiği Beyanı

Yapılan çalışmada araştırma ve yayın etiğine uyulmuştur.

Kaynaklar

[1] R. Spence and J. Amaral-Teixeira, "A CFD parametric study of geometrical variations on the pressure pulsations and performance characteristics of a centrifugal pump," *Comput. Fluids*, vol. 38, no. 6, pp. 1243–1257, 2009.

[2] S. R. Shah, S. V. Jain, R. N. Patel, and V. J. Lakhera, "CFD for centrifugal pumps: A review of the state-of-the-art," *Procedia Eng.*, vol. 51, pp. 715–720, 2013.

[3] M. G. Patel and A. V. Doshi, "Effect of Impeller Blade Exit Angle on The Performance of Centrifugal Pump," *Int J. Emerging Technology and Advanced Engineering*, vol. 3, no. 1, pp. 91–99, 2013.

[4] L. Tan, B. Zhu, S. Cao, H. Bing, and Y. Wang, "Influence of blade wrap angle on centrifugal pump performance by numerical and experimental study," *Chin. J. Mech. Eng.*, vol. 27, no. 1, pp. 171–177, 2014.

[5] I. Pavlenko, J. Trojanowska, O. Gusak, V. Ivanov, J. Pitel, and V. Pavlenko, "Estimation of the reliability of automatic axial-balancing devices for multistage centrifugal pumps," *Period. Polytech. Mech. Eng.*, vol. 63, no. 1, pp. 52–56, 2018.

[6] P. S. Bolade, S. J. Madki, and kirloskar brothers limited, "Analysis of hydraulic thrusts in centrifugal pump to increase te bearing life," *Int. J. Eng. Res. Technol. (Ahmedabad)*, vol. V4, no. 08, 2015.

[7] S. Budea, "Axial Balance in Centrifugal Pumps-Back Labyrinth Versus Dorsal Vanes," *Hidraulica*, vol. 1, pp. 19–24, 2015.

[8] B. Mary and F. Cerru, "Axial force modelling and measurement in a single stage centrifugal pump," in *13th European Conference on Turbomachinery Fluid Dynamics and Thermodynamics*, 2019.

[9] H. Miyashiro and K. Takada, "Axial hydraulic thrust caused by pump starting," *J. Basic Eng.*, vol. 94, no. 3, pp. 629–635, 1972.

[10] S. D. Gatta, S. Salvadori, P. Adami, and L. Bertolazzi, "CFD Study for Assessment of Axial Thrust Balance in Centrifugal Multistage Pumps," in *The 13th International Conference on Fluid Flow Technologies*, 6-9 September, Budapest, 2006.

[11] K. A. J. Bruurs, B. P. M. van Esch, M. S. van der Schoot, and E. J. J. van der Zijden, "Axial thrust prediction for a multi-stage centrifugal pump," in *Volume 1A, Symposia: Keynotes; Advances in Numerical Modeling for Turbomachinery Flow Optimization; Fluid Machinery; Industrial and Environmental Applications of Fluid Mechanics*, Pumping Machinery, 2017.

[12] M. Szlaga, Balancing Axial Force in Centrifugal Pumps with Pump Out Vanes. *E3S Web of Conferences*, 2019.

[13] H. Watanabe, T. Yamashita, S. Watanabe, and Y. Hara, CFD Analysis of Axial Thrust in Three Stages Centrifugal Pump at Design and Partload Conditions, in *Asme/Jsme/Ksme 2015 Joint Fluids Engineering Conference*, Seoul, 2015.
[14] O. Babayigit, M. Ozgoren, M. H. Aksoy, and O. Kocaaslan, "Experimental and CFD investigation of a multistage centrifugal pump including leakages and balance holes," *dwt*, vol. 67, pp. 28–40, 2017.
[15] H. Pehlivan, Z. Parlak, "Investigation of parameters affecting axial load in an end suction centrifugal pump by numerical analysis," *J. Appl. Fluid Mech.*, vol. 12, no. 5, pp. 1615–1627, 2019.
[16] M. Fathi, M. Raisee, S. A. Nourbakhsh, and H. A. Arani, "The effect of balancing holes on performance of a centrifugal pump: numerical and experimental investigations," *IOP Conf. Ser. Earth Environ. Sci.*, vol. 240, p. 032017, 2019.
[17] G. Boitel, D. Fedala, and N. Myon, "Tip clearance effects on loads and performances of semi-open impeller centrifugal pumps at different specific speeds," *IOP Conf. Ser. Earth Environ. Sci.*, vol. 49, p. 032013, 2016.
[18] L. Zhou, W. Shi, W. Li, and R. Agarwal, "Numerical and experimental study of axial force and hydraulic performance in a deep-well centrifugal pump with different impeller rear shroud radius," *J. Fluids Eng.*, vol. 135, no. 10, p. 104501, 2013.
[19] M. Nataraj and V. P. Arunachalam, "Optimizing impeller geometry for performance enhancement of a centrifugal pump using the Taguchi quality concept," *Proc. Inst. Mech. Eng. A: J. Power Energy*, vol. 220, no. 7, pp. 765–782, 2006.
[20] W. Dong, Z. Liu, H. Zhang, G. Zhang, H. Jiang, and P. Li, "Effects of the balance hole diameter on the flow characteristics of the rear chamber and the disk friction loss in the centrifugal pump," *Processes (Basel)*, vol. 10, no. 3, p. 613, 2022.
[21] X. Cheng, Z. Chang, and Y. Jiang, "Study on The Influence of The Specific Area of Balance Hole on Cavitation Performance of High-Speed Centrifugal Pump," *Journal of Mechanical Science and Technology*, vol. 34, no. 8, pp. 3325–3334, 2020.
[22] H. Saruhan and M. Kam, "Experimental Spectral Analysis of Split Sleeve Bearing Clearance Effect on A Rotating Shaft System," *Makine Teknolojileri Elektronik Dergisi*, vol. 13, no. 4, pp. 1–8, 2016.
[23] B. Gökçe and S. Taşgetiren, "Kalite İçin Deney Tasarımı," *Makine Teknolojileri Elektronik Dergisi*, vol. 6, pp. 71–83, 2009.
[24] M. Savaşkan, Y. Taptık, and M. Ürgen, "Deney Tasarımı Yöntemi İle Matkap Uçlarında Performans Optimizasyonu," *İTÜ DERGİSİ/d*, 2010.
[25] R. Surace, L. A. C. De Filippis, A. D. Ludovico, and G. Boghetich, "Application of Taguchi method for the multi-objective optimization of aluminium foam manufacturing parameters," *Int. J. Mater. Form.*, vol. 3, no. 1, pp. 1–5, 2010.
[26] M. Kaladhar et al., "Application of Taguchi approach and Utility Concept in solving the Multi-objective Problem when turning AISI 202 Austenitic Stainless Steel," *J. Eng. Sci. Technol. Rev.*, vol. 4, no. 1, pp. 55–61, 2011.
[27] İ. Asiltürk and S. Neşeli, "Multi response optimisation of CNC turning parameters via Taguchi method-based response surface analysis," *Measurement (Lond.)*, vol. 45, no. 4, pp. 785–794, 2012.
[28] T.-S. Lan, "Taguchi Optimization of Multi-Objective CNC Machining Using TOPSIS," *Inf. Technol. J.*, vol. 8, no. 6, pp. 917–922, 2009.
[29] M. A. Mohamed, Y. H. P. Manurung, and M. N. Berhan, "Model development for mechanical properties and weld quality class of friction stir welding using multi-objective Taguchi method and response surface methodology," *J. Mech. Sci. Technol.*, vol. 29, no. 6, pp. 2323–2331, 2015.
[30] O. Babayigit, M. Ozgoren, M. H. Aksoy, and O. Kocaaslan, "The effect of balance holes to centrifugal pump performance," *AIP Conference Proceedings*, vol. 1863, no. 1, pp. 030004, 2017.
[31] L. Xian-Hua, Z. Shu-Jia, Z. Bao-Lin, and H. Qing-Bo, "The Study of The k-e Turbulence Model for Numerical Simulation of Centrifugal Pump," *7th International Conference on Computer-Aided Industrial Design and Conceptual Design*, vol. IEEE, pp. 1–5, 2006.
[32] A.N. S. Y. Fluent, "ANSYS fluent theory guide 15.0," ANSYS, 2013.
[33] Centrifugal Pumps. Berlin, Heidelberg: Springer Berlin Heidelberg, 2008.
[34] E. U. Mullins, "Recent developments in quality control: An introduction to "Taguchi Methods"," *Niger. J. Technol.*, vol. 15, no. 1, pp. 1–15, 1991.

Bitlis Eren Üniversitesi Fen Bilimleri Dergisi
BİTLİS EREN UNIVERSITY JOURNAL OF SCIENCE
ISSN: 2147-3129/e-ISSN: 2147-3188
VOLUME: 11 NO: 2 PAGE: 449-458 YEAR: 2022
DOI: 10.17798/bitlisfen.1020207

The New Wave Solutions in the Field of Superconductivity

Özlem KIRCI[1*], Tolga AKTÜRK[2], Hasan BULUT[3]

[1]*Department of Mathematics, Faculty of Arts and Sciences, Kırklareli University, Turkey*
[2]*Departments of Mathematics and Science Education, Faculty of Education, Ordu University, Turkey*
[3]*Department of Mathematics, Faculty of Science, Fırat University, Turkey*
(ORCID: 0000-0003-2986-952X) (ORCID: 0000-0002-8873-0424) (ORCID: 0000-0002-6089-1517)

Keywords: Landau-Ginzburg-Higgs (LGH) equation, The modified exponential function method, Wave solutions.

Abstract
In this study, the Landau-Ginzburg-Higgs (LGH) equation, which has the physically important wave solutions, is considered. This equation is discussed via the modified exponential function method (MEFM) to describe superconductivity. Some new solutions are discovered in the form of rational, hyperbolic, and trigonometric functions when compared with the ones taking part in the literature. The functions which are candidates to be the exact solutions of the nonlinear equation are tested by the Mathematica program at the end of the steps of the method and it is observed that they satisfy the LGH equation. Additionally, the 2-D and the 3-D graphs accompanying the density and contour plots are illustrated.

1. Introduction

Having an active role and the profound employment of the nonlinear partial differential equations (NLPDEs) in various fields such as fluid dynamics, electromagnetism, acoustic, optics, DNA vibration dynamics, electrical lines and etc., the exact solutions for understanding and interpretation of the nonlinear phenomenon become crucial. For instance, the Korteweg-de Vries equation used in fluid dynamics, aerodynamics, and continuum mechanics as a model for shock wave formation, solitons, turbulence, boundary layer behavior, and mass transport. The nonlinear Schrödinger equation describes the propagation of optical pulses in optic fibers. The Zakharov–Kuznetsov equation arises in number of scientific models including fluid mechanics, astrophysics, solid state physics, plasma physics, chemical kinematics, chemical chemistry, optical fiber and geochemistry [1]-[3]. Due to its significant role in applied sciences, it is very important to obtain the solution of an NLPDE which allows us to analyze the phenomenon modeled via such equations. Therefore, various methods have been proposed to find exact solutions to NLPDEs, such as the $(G'/G, 1/G)$-expansion method [4], He's variational methods [5], $\exp(-\varphi(\xi))$-expansion method, and sine-cosine method [6], the Bernoulli sub-equation function method [7], the modified (G'/G^2)-expansion approach [8], the extended Sinh-Gordon equation expansion method [9], the extended rational sinh-cosh method [10], the improved modified extended tanh-function method [11], the modified F-expansion method [12], sine-Gordon expansion method and $\left(m + (G'/G)\right)$-expansion method [13], and so on.

The LGH equation which is one of the common values of mathematics and applied sciences is utilized for comprehending the notions in superconductivity and cyclotron waves which have many usage areas such as medicine, plasma physics, chemistry, biology, electricity-electronic, transportation, and so on. The interpenetration of such essential applications and the LGH equation has turned the focus of this study to analyze the exact wave solutions. This equation is given by

$$u_{tt} - u_{xx} - m^2 u + n^2 u^3 = 0, \qquad (1)$$

where $u(x,t)$ is the electrostatic potential of the ion-cyclotron wave, m and n are real parameters, and x and t define the spatial and temporal coordinates [14]. The executed methods in the literature for observing the soliton solutions of the LGH equations are

*Corresponding author: ozlem.isik@klu.edu.tr
Received: 07.11.2021, Accepted: 05.05.2022

appeared in [14]-[20]. In this study, the MEFM is put to use which is not applied before. For this purpose the progress of the paper is as follows; in section2 the processes of the MEFM are given, the application of the method to the LGH equation comes immediately together with the graphical results in section3 and finally, the conclusion takes part at the end.

2. Materials and Method

The starting point of the MEFM is to convert an NLPDE into a nonlinear ordinary differential equation (NLODE) by the wave transform $\xi = k(x - ct)$ where k and c represent the wave height and the wave frequency. Let the following NLPDE

$$Q(U, U_x, U_t, U_{xx}, U_{xt}, U_{tt}, U_{xxtt}, \dots) = 0, \quad (2)$$

contains the highest order derivatives and the nonlinear terms. As mentioned above after the wave transform $\xi = k(x - ct)$, the related derivatives in equation (2) are evaluated and substituted into equation (2) to obtain the following NLODE

$$N(U, U^2, U', U'', \dots) = 0, \quad (3)$$

According to MEFM the solution of equation (3) is assumed to be

$$U(\xi) = \frac{\sum_{i=0}^{N} A_i[\exp(-\Omega(\xi))]^i}{\sum_{j=0}^{M} B_j[\exp(-\Omega(\xi))]^j} = \frac{A_0 + A_1\exp(-\Omega(\xi)) + \cdots + A_n\exp(-n\Omega(\xi))}{B_0 + B_1\exp(-\Omega(\xi)) + \cdots + B_m\exp(-m\Omega(\xi))}, \quad (4)$$

where $A_i, B_j, (0 \le i \le N, 0 \le j \le M)$ are constants with $A_N \neq 0, B_M \neq 0$ and will be determined by using a ready-made package program. Besides the coefficients, the upper bounds N, M, and the function $\Omega(\xi)$ are required to expand equation (4). N and M are discovered by the balancing rule which enables a relation between them taking into account the highest order derivative and the highest order nonlinear term in equation (3). Finally, the $\Omega(\xi)$ function is the solution of the ordinary differential equation given below

$$\Omega'(\xi) = exp(-\Omega(\xi)) + \mu exp(\Omega(\xi)) + \lambda. \quad (5)$$

The process goes on with the substitution of equation (4) into equation (3) taking into account equation (5) which leads to a system of algebraic equations. In this system, the coefficients are specified via Mathematica.

The MEFM offers five families for the solutions, hence after writing the stated coefficients in equation (4) five classes are obtained for each case. These families are given in [21] as in the following.

Family 1: When $\mu \neq 0, \lambda^2 - 4\mu > 0$,

$$\Omega(\xi) = \ln\left(\frac{-\sqrt{\lambda^2-4\mu}}{2\mu}\tanh\left(\frac{\sqrt{\lambda^2-4\mu}}{2}(\xi + E)\right) - \frac{\lambda}{2\mu}\right). \quad (6)$$

Family2: When $\mu \neq 0, \lambda^2 - 4\mu < 0$,

$$\Omega(\xi) = \ln\left(\frac{\sqrt{-\lambda^2+4\mu}}{2\mu}\tan\left(\frac{\sqrt{-\lambda^2+4\mu}}{2}(\xi + E)\right) - \frac{\lambda}{2\mu}\right). \quad (7)$$

Family3: When $\mu = 0,\ \lambda \neq 0$ and $\lambda^2 - 4\mu > 0$,

$$\Omega(\xi) = -\ln\left(\frac{\lambda}{exp(\lambda(\xi+E))-1}\right). \quad (8)$$

Family4: When $\mu \neq 0,\ \lambda \neq 0$ and $\lambda^2 - 4\mu = 0$,

$$\Omega(\xi) = \ln\left(-\frac{2\lambda(\xi+E)+4}{\lambda^2(\xi+E)}\right). \quad (9)$$

Family5: When $\mu = 0,\ \lambda = 0$ and $\lambda^2 - 4\mu = 0$,

$$\Omega(\xi) = \ln(\xi + E), \quad (10)$$

where $A_0, A_1, \dots, A_n, B_0, B_1, \dots, B_m, E, \lambda, \mu$ are constants.

2.1. Application of the Method to LGH Equation

Equation (1) is reduced to the following NLODE

$$(k^2c^2 - k^2)U'' - m^2U + n^2U^3 = 0, \quad (11)$$

by the wave transform $\xi = k(x - ct)$. The balancing rule reveals the relation between N and M as $M + 1 = N$. Therefore, it can be considered as $N = 2$ and $M = 1$. Thus, the assumed solution (4) of the equation (11) is in the form of

$$U(\xi) = \frac{A_0 + A_1e^{-\Omega(\xi)} + A_2e^{-2\Omega(\xi)}}{B_0 + B_1e^{-\Omega(\xi)}}. \quad (12)$$

A system of algebraic equation is derived when the required derivative terms are obtained from equation (12) and substituted in equation (11). Then by solving this system with the help of the package program, it is encountered with many possibilities for the coefficients. We have just given some of them starting with case1 as follows,

$$A_0 = \frac{\lambda A_2 B_0}{2B_1},\ A_1 = \frac{1}{2},\ A_2 = \left(\lambda + \frac{2B_0}{B_1}\right),$$

$$n = -\frac{i\sqrt{2(-1+c^2)}kB_1}{A_2}, m = -\frac{ik\sqrt{(\lambda^2-4\mu)(-1+c^2)}}{\sqrt{2}}, \quad (13)$$

where $i = \sqrt{-1}$. These coefficients are substituted in equation (12) and it was confirmed that this traveling wave solution function provides equation (11), by getting support from Mathematica.

The coefficients in equation (13) and the families stated above in equations (6-10) are substituted in equation (12), respectively. Thus, the following situations are presented for the solution functions of equation (1). Besides, the graphs are shown under the related solutions by giving appropriate values to the variables in the resulting equations.

Family 1

The solution $U_{1,1}$ and the relevant graphs in Figure1 are obtained for case1/family1:

$$U_{1,1} = \frac{A_2(\lambda^2-4\mu+\lambda\omega)}{2B_1(\lambda+\omega)}, \quad (14)$$

where $\omega = \sqrt{\lambda^2 - 4\mu}\mathrm{Tanh}[\frac{1}{2}(\mathrm{EE} + \xi)\sqrt{\lambda^2 - 4\mu}]$ and $\xi = k(-ct + x)$.

Family 2

The solution $U_{1,2}$ and the relevant graphs in Figure2 are obtained for case1/family2:

$$U_{1,2} = \frac{A_2(\lambda^2-4\mu-\lambda\theta)}{2B_1(\lambda-\theta)}, \quad (15)$$

where $\theta = \sqrt{-\lambda^2 + 4\mu}\mathrm{Tan}[\frac{1}{2}(\mathrm{EE} + \xi)\sqrt{-\lambda^2 + 4\mu}]$ and $\xi = k(-ct + x)$.

Family 3

The solution $U_{1,3}$ and the relevant graphs in Figure3 are obtained for case1/family3:

$$U_{1,3} = \frac{\lambda Coth[\frac{1}{2}(EE+\xi)\lambda]A_2}{2B_1}. \quad (16)$$

Family4

The solution $U_{1,4}$ and the relevant graphs in Figure4 are obtained for case1/family4:

$$U_{1,4} = \frac{\lambda A_2}{(2+\mathrm{EE}\lambda+\xi\lambda)B_1}. \quad (17)$$

Family 5

The solution $U_{1,5}$ and the relevant graphs in Figure5 are obtained for case1/family5:

$$U_{1,5} = \frac{A_2}{(\mathrm{EE}+\xi)B_1} \quad (18)$$

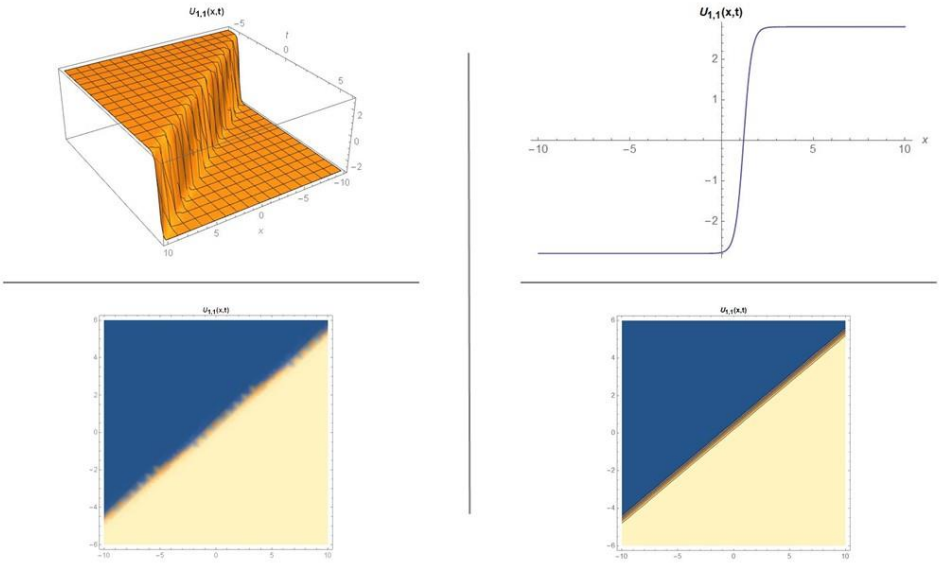

Figure 1. The three dimensional, density and contour graphs of solution (14) for the values $\lambda = 3, \mu = 1, A_2 = 0.5, B_1 = 0.2, k = 2, B_0 = 1, A_0 = 3.75, A_1 = 3.25, c = 2, EE = 0.75$ and two-dimensional graph for $t = 1$

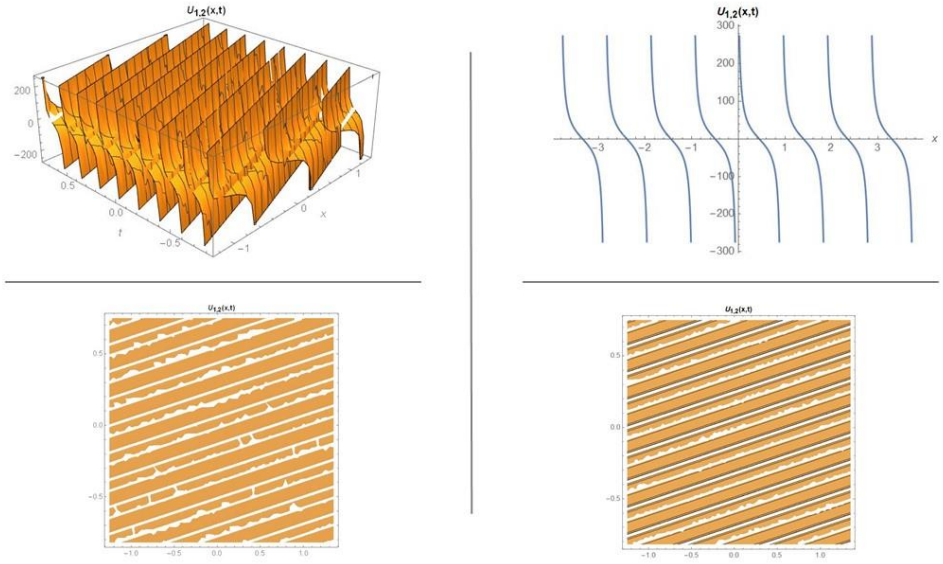

Figure 2. The three dimensional, density and contour graphs of solution (15) for the values $\lambda = 1, \mu = 3, A_2 = 0.5, B_1 = 0.02, k = 2, B_0 = 1, A_0 = 12.5, A_1 = 25.25, c = 5, EE = 0.75$ and two-dimensional graph for $t = 1$

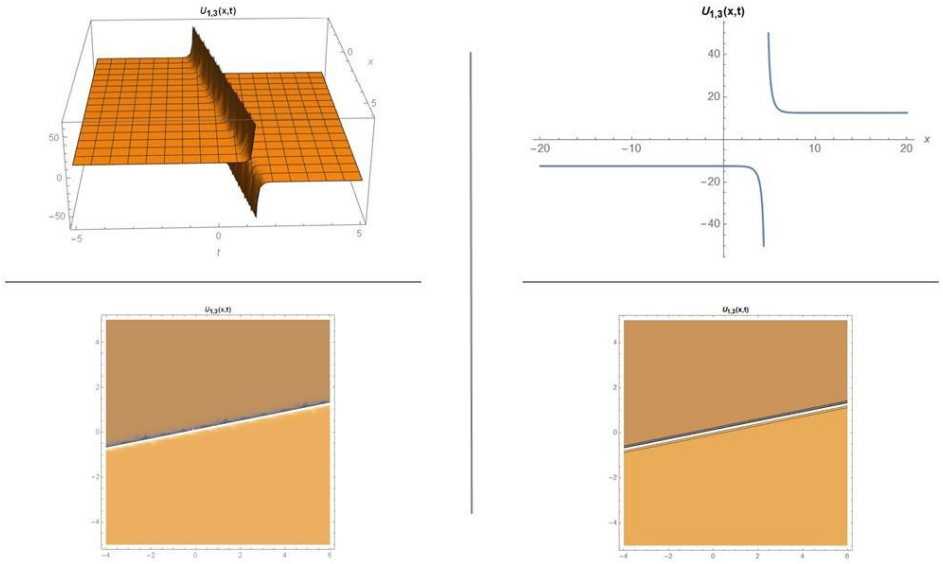

Figure 3. The three dimensional, density and contour graphs of solution (16) for the values $\lambda = 1, \mu = 0, A_2 = 0.5, B_1 = 0.02, k = 2, B_0 = 1, A_0 = 12.5, A_1 = 25.25, c = 5, EE = 0.75$ and two-dimensional graph for $t = 1$

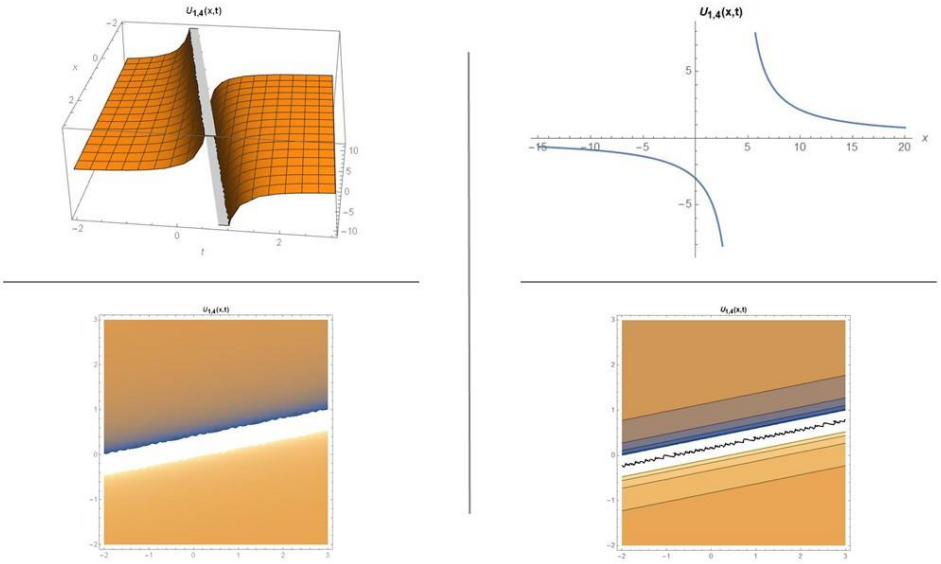

Figure 4. The three dimensional, density and contour graphs of solution (17) for the values $\lambda = 2, \mu = 1, A_2 = 0.5, B_1 = 0.02, k = 2, B_0 = 1, A_0 = 25, A_1 = 25.25, c = 5, EE = 0.75$ and two-dimensional graph for $t = 1$

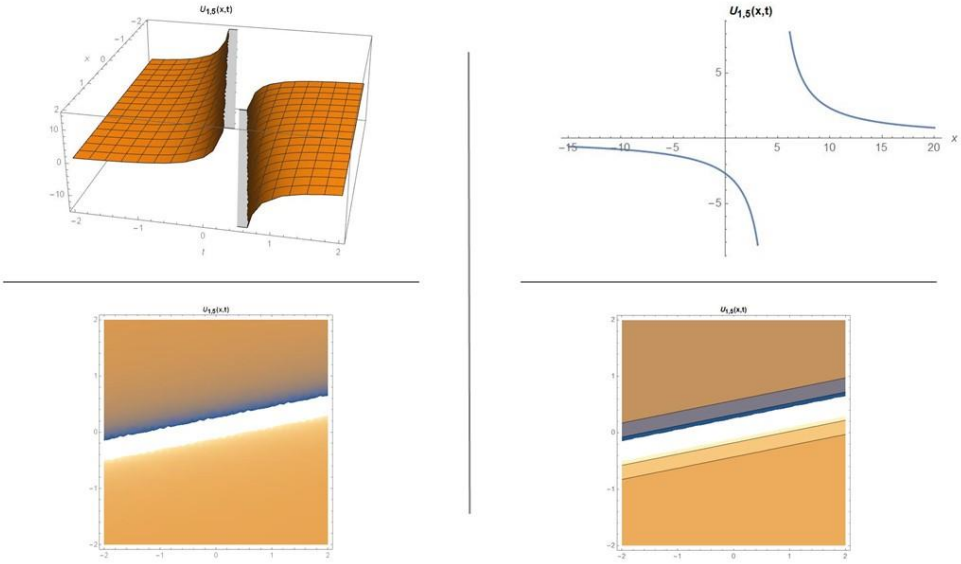

Figure 5. The three dimensional, density and contour graphs of solution (18) for the values $\lambda = 0, \mu = 0, A_2 = 0.5, B_1 = 0.02, k = 2, B_0 = 1, A_0 = 0, A_1 = 25, c = 5, EE = 0.75$ and two-dimensional graph for $t = 1$

We have discussed another possible coefficient group case2 below,

$$A_0 = -\frac{\sqrt{(1-c^2)k^2}\lambda B_0}{\sqrt{2}n}, A_1 = \frac{\lambda A_2}{2} - \frac{\sqrt{2(1-c^2)k^2}B_0}{n},$$
$$B_1 = -\frac{nA_2}{\sqrt{2(1-c^2)k^2}}, m = -\frac{\sqrt{(1-c^2)k^2(\lambda^2-4\mu)}}{\sqrt{2}}. \quad (19)$$

The parameters in equation (19) are substituted in equation (12) regarding the five $\boldsymbol{\Omega}(\boldsymbol{\xi})$ options as given in equations (6-10).

Family 1

The solution $U_{2,1}$ and the relevant graphs in Figure6 are obtained for case2/family1:

$U_{2,1} =$

$$-\frac{\frac{\sqrt{(1-c^2)k^2}\lambda B_0}{\sqrt{2}n}-\frac{4\mu^2 A_2}{(\lambda+\omega)^2}+\frac{\mu\left(n\lambda A_2-2\sqrt{2}\sqrt{(1-c^2)k^2}B_0\right)}{n(\lambda+\omega)}}{B_0+\frac{\sqrt{2}n\mu A_2}{\sqrt{(1-c^2)k^2(\lambda+\omega)}}}, \quad (20)$$

where $\omega=\sqrt{\lambda^2-4\mu}\mathrm{Tanh}[\frac{1}{2}(\mathrm{EE}+\xi)\sqrt{\lambda^2-4\mu}]$ and $\xi=k(-ct+x)$.

Family 2

The solution $U_{2,2}$ and the relevant graphs in Figure7 are obtained for case2/family2:

$$U_{2,2}=-\frac{\frac{\sqrt{(1-c^2)k^2}\lambda B_0}{\sqrt{2}n}-\frac{4\mu^2 A_2}{(\lambda-\theta)^2}+\frac{\mu\left(n\lambda A_2-2\sqrt{2}\sqrt{(1-c^2)k^2}B_0\right)}{n(\lambda-\theta)}}{B_0+\frac{\sqrt{2}n\mu A_2}{\sqrt{(1-c^2)k^2(\lambda-\theta)}}}, \quad (21)$$

where $\theta=\sqrt{-\lambda^2+4\mu}\mathrm{Tan}[\frac{1}{2}(\mathrm{EE}+\xi)\sqrt{-\lambda^2+4\mu}]$ and $\xi=k(-ct+x)$.

Family 3

The solution $U_{2,3}$ and the relevant graphs in Figure8 are obtained for case2/family3:

$$U_{2,3}=-\frac{\sqrt{(1-c^2)k^2}\lambda\mathrm{Coth}[\frac{1}{2}(\mathrm{EE}+\xi)\lambda]}{\sqrt{2}n}. \quad (22)$$

Family 4

The solution $U_{2,4}$ and the relevant graphs in Figure9 are obtained for case2/family4:

$$U_{2,4}=-\frac{\sqrt{2(1-c^2)k^2}\lambda}{n(2+\mathrm{EE}\lambda+\xi\lambda)}. \quad (23)$$

Family 5

The solution $U_{2,5}$ and the relevant graphs in Figure10 are obtained for case2/family5:

$$U_{2,5}=-\frac{\sqrt{2}\sqrt{2(1-c^2)k^2}}{\mathrm{EE}n+\xi n}. \quad (24)$$

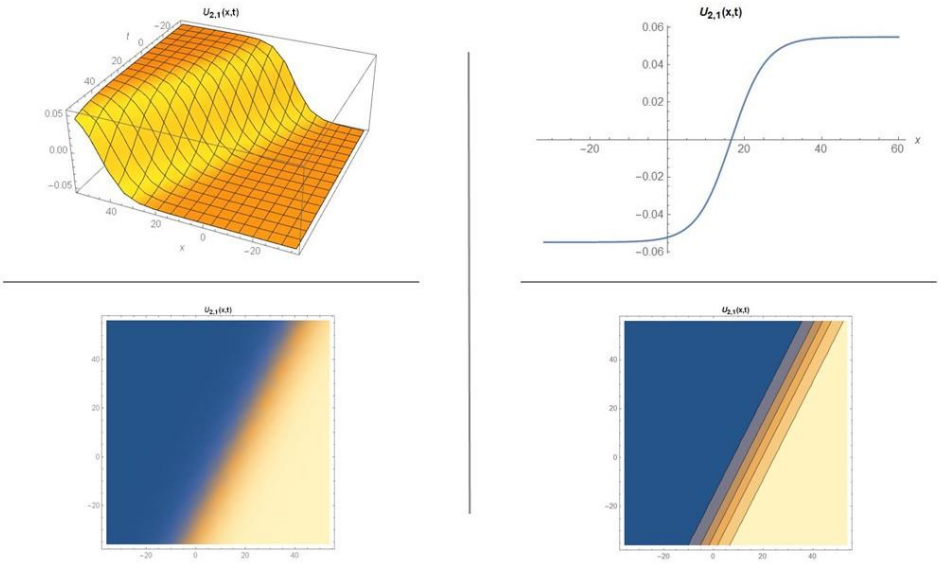

Figure 6. The three dimensional, density and contour graphs of solution (20) for the values $\lambda=3,\mu=1,n=2.5,A_2=0.25,B_1=-5.1031,k=-0.1,B_0=1,A_0=-0.0734847,A_1=0.32601,c=0.5,EE=0.75,m=-0.136931$ and two-dimensional graph for $t=1$

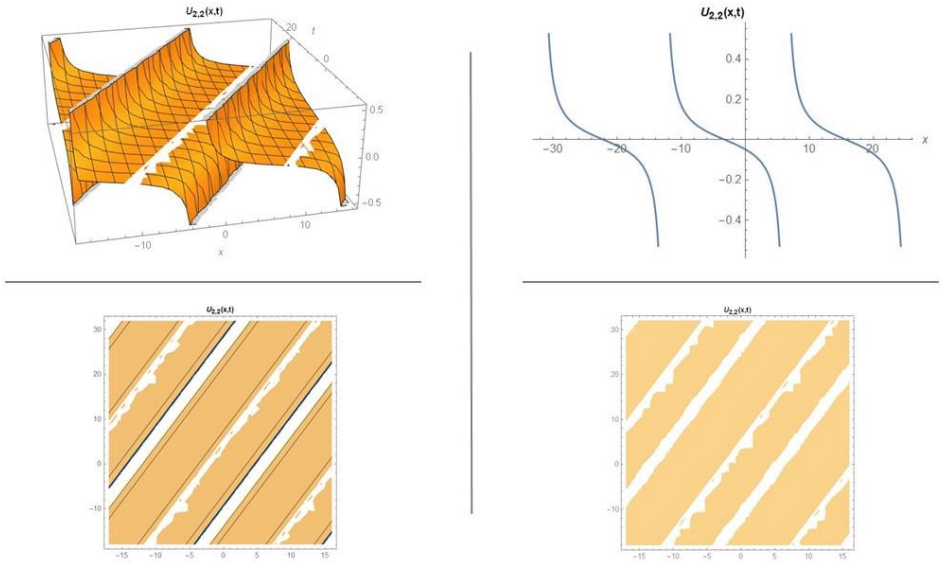

Figure 7. The three dimensional, density and contour graphs of solution (21) for the values $\lambda = 1, \mu = 3, n = 2.5, A_2 = 0.25, B_1 = -5.1031, k = -0.1, B_0 = -1, A_0 = 0.0244949, A_1 = 0.17399, c = 0.5, EE = 0.75, m = -0.203101i$ and two-dimensional graph for $t = 1$

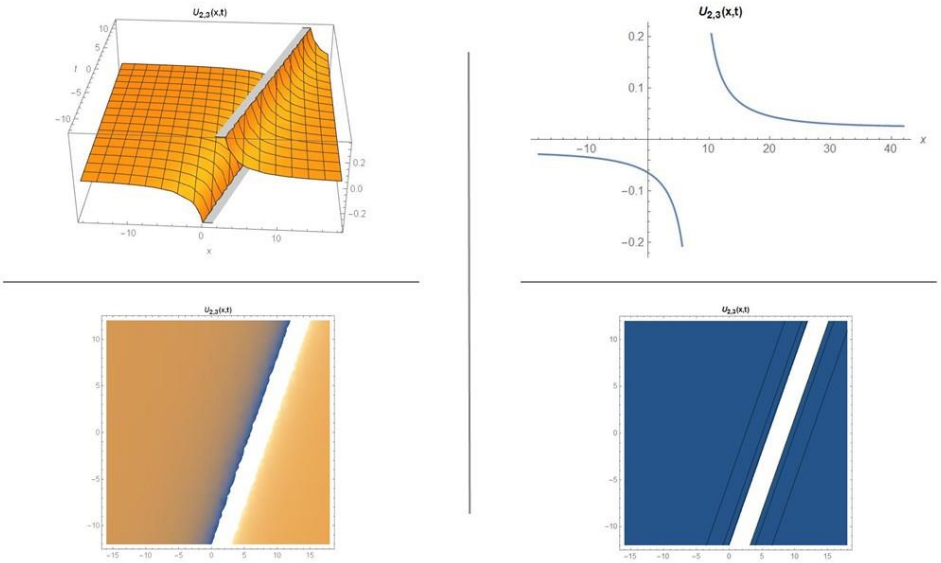

Figure 8. The three dimensional, density and contour graphs of solution (22) for the values $\lambda = 1, \mu = 0, n = 2.5, A_2 = 0.25, B_1 = -5.1031, k = -0.1, B_0 = -1, A_0 = 0.0244949, A_1 = 0.17399, c = 0.5, EE = 0.75, m = -0.0612372$ and two-dimensional graph for $t = 1$

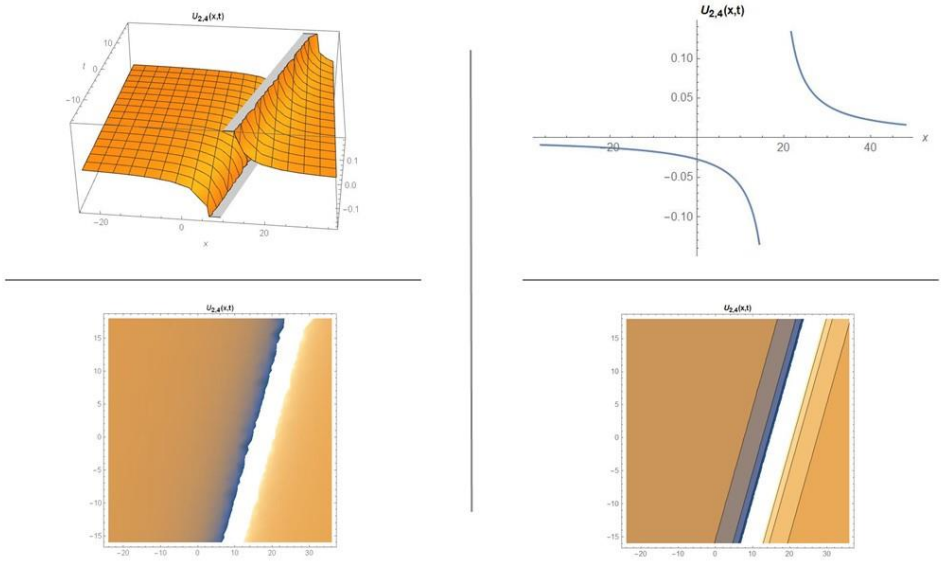

Figure 9. The three dimensional, density and contour graphs of solution (23) for the values $\lambda = 2, \mu = 1, n = 2.5, A_2 = 0.25, B_1 = -5.1031, k = -0.1, B_0 = -1, A_0 = 0.0489898, A_1 = 0.29899, c = 0.5, EE = 0.75, m = 0$ and two-dimensional graph for $t = 1$

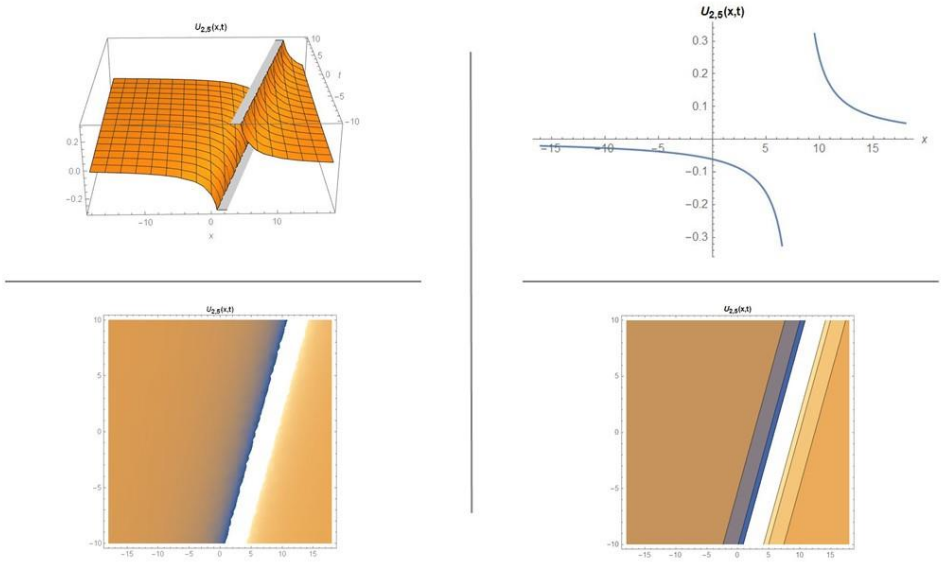

Figure 10. The three dimensional, density and contour graphs of solution (24) for the values $\lambda = 0, \mu = 0, n = 2.5, A_2 = 0.25, B_1 = -5.1031, k = -0.1, B_0 = -1, A_0 = 0, A_1 = 0.0489898, c = 0.5, EE = 0.75, m = 0$ and two-dimensional

3. Results and Discussions

The several solution forms of the LGH equation are illustrated above in Figures1-10. The kink type, singular kink type, and the periodic type solutions are observed. The solutions and the related graphics are different when compared to ([14]-[20]). Interpretation of these fresh solutions can put a new complexion on the applications of the LGH equation.

4. Conclusion

We have determined the new exact solution forms of the LGH equation as hyperbolic, trigonometric, and rational functions via the modified exponential function method, which is an effective and functioning method. The application of the MEFM method for this equation is not encountered in the literature. The process of plotting the graphs and the computations is overcome with the aid of Mathematica. The LGH equation is used in superconductivity, which has a wide application area, as mentioned in Section1. Therefore, the newly obtained wave solutions may be helpful to widen the knowledge in the related field and may develop new ideas.

Contributions of the authors

The authors confirm that the contribution is equally for this paper.

Conflict of Interest Statement

There is no conflict of interest between the authors.

Statement of Research and Publication Ethics

The study is complied with research and publication ethics.

References

[1] T. Xiang, "A Summary of the Korteweg-de Vries Equation", *Institute for Mathematical Sciences, Renmin University of China, Beijing*, 100872, 2015.

[2] E. M. E. Zayed, K. A. E. Alurrfi, "On solving two higher-order nonlinear PDEs describing the propagation of optical pulses in optic fibers using the $(G'/G\,, 1/G)$-expansion method", *Ricerche di Mathematica*, vol. 64, no. 1, pp. 167–194, 2015.

[3] S. T. Mohyud-Din, M. Noor Aslam, K.N. Inayat, "Exp-function method for traveling wave solutions of modified Zakharov-Kuznetsov equation", *Journal of King Saud University (Science)*, vol. 22, no. 4, pp. 213-216, 2010.

[4] S. Duran, "Extractions of travelling wave solutions of (2 + 1)-dimensional Boiti–Leon–Pempinelli system via (G′/G, 1/G)-expansion method", *Optical Quantum Electronics*, vol. 53, 299, 2021.

[5] K. J. Wang, G. D. Wang, "Solitary and periodic wave solutions of the generalized fourth-order Boussinesq equation via He's variational methods", *Mathematical Methods in the Applied Sciences*, vol. 44, no. 7, pp. 5617-5625, 2021.

[6] M. A. E. Abdelrahman, M. A. Sohaly, "On the new wave solutions to the MCH equation", *Indian Journal of Physics*, vol. 93, no. 7, pp. 903-911, 2019.

[7] H. M. Baskonus, J. F. Gomez-Aguilar, "New singular soliton solutions to the longitudinal wave equation in a magneto-electro-elastic circular rod with M-derivative", *Modern Physics Letters B*, vol. 33, no. 21, 2019.

[8] S. Behera, N. H. Aljahdaly, J. P. S. Virdi, "On the modified (G'/G^2)-expansion method for finding some analytical solutions of the traveling waves", *Journal of Ocean Engineering and Science*, 2021, doi: https://doi.org/10.1016/j.joes.2021.08.013.

[9] A. S. Bezgabadi, M. A. Bolorizadeh, "Analytic combined bright-dark, bright and dark solitons solutions of generalized nonlinear Schrödinger equation using extended Sinh-Gordon equation expansion method", *Results in Physics*, vol. 30, 104852, 2021.

[10] H. Rezazadeh, A. Korkmaz, M. M. A. Khater, M. Eslami, D. Lu, R. A. M. Attia, "New exact traveling wave solutions of biological population model via the extended rational sinh-cosh method and the modified Khater method", *Modern Physics Letters B*, vol. 33, no. 28, 2019.

[11] W. B. Rabie, H. M. Ahmed, "Dynamical solitons and other solutions for nonlinear Biswas– Milovi equation with Kudryashov's law by improved modified extended tanh-function method" *Optik*, vol. 245, 167665, 2021.

[12] A. R. Seadawy, D. Lu, N. Nasreen, "Construction of solitary wave solutions of some nonlinear dynamical system arising in nonlinear water wave models", *Indian Journal of Physics*, vol. 94, pp. 1785–1794, 2020.

[13] H. F. Ismael, H. Bulut, H. M. Baskonus, "Optical soliton solutions to the Fokas–Lenells equation via sine-Gordon expansion method and $\left(m+(G'/G)\right)$-expansion method", *Pramana- Journal of Physics*, vol. 94, no. 35, 2020.

[14] H. K. Barman, M. A. Akbar, M. S. Osman, K. S. Nisar, M. Zakarya, A. H. Abdel-Aty, H. Eleuch, "Solutions to the Konopelchenko-Dubrovsky equation and the Landau-Ginzburg-Higgs equation via the generalized Kudryashov technique", *Results in Physics*, vol. 24, 104092, 2021.

[15] Md. E. Islam, M. A. Akbar, "Stable wave solutions to the Landau-Ginzburg-Higgs equation and the modified equal width wave equation using the IBSEF method", *Arab Journal of Basic and Applied Sciences*, vol. 27, no. 1, pp. 270-278, 2020.

[16] H. K. Barman, M. S. Aktar, M. H. Uddin, M. A. Akbar, D. Baleanu, M. S. Osman, "Physically significant wave solutions to the Riemann wave equations and the Landau-Ginsburg-Higgs equation", *Results in Physics*, vol. 27, 104517, 2021.

[17] B. Ghanbari, J. F. Gomez-Aguilar, "Optical soliton solutions of the Ginzburg-Landau equation with conformable derivative and Kerr law nonlinearity", *Revista Mexicana de Fisica*, vol. 65, pp. 73-81, 2019.

[18] A. Bekir, O. Unsal, "Exact solutions for a class of nonlinear wave equations by using the first integral method" *International Journal of Nonlinear Science*, vol. 15, no. 2, pp. 99–110, 2013.

[19] A. Iftikhar, A. Ghafoor, T. Jubair, S. Firdous, S. T. Mohyud-Din, "The expansion method for travelling wave solutions of (2+1)-dimensional generalized KdV, sine Gordon and Landau-Ginzburg-Higgs equation", *Scientific Research and Essays*, vol. 8, no. 28, pp. 1349–1859, 2013.

[20] M. E. Islam, M. A. Akbar, "Stable wave solutions to the Landau-Ginzburg-Higgs equation and the modified equal width wave equation using the IBSEF method", *Arab Journal of Basic and Applied Sciences*, vol. 27, no. 1, pp. 270–8, 2020.

[21] H. Bulut, H. M. Baskonus, "New Complex Hyperbolic Function Solutions for the (2+1)-Dimensional Dispersive Long Water–Wave System", *Mathematical and Computational Applications*, vol. 21, no. 2, 2016.

Bitlis Eren Üniversitesi Fen Bilimleri Dergisi
BİTLİS EREN UNIVERSITY JOURNAL OF SCIENCE
ISSN: 2147-3129/e-ISSN: 2147-3188
VOLUME: 11 NO: 2 PAGE: 459-468 YEAR: 2022
DOI: 10.17798/bitlisfen.1025334

h- Stability of Functional Dynamic Equations on Time Scales by Alternative Variation of Parameters

Halis Can KOYUNCUOĞLU[1*], Nezihe TURHAN TURAN[1]

[1]*Izmir Katip Celebi University, Faculty of Engineering and Architecture, Department of Engineering Sciences, Izmir, Turkey*
(ORCID: 0000-0002-8880-1552) (ORCID: 0000-0002-9012-4386)

Keywords: h-Stability, Time scale, Uniform boundedness, Alternative variation of parameters.

Abstract

In this paper, we concentrate on nonlinear functional dynamic equations of the form

$$x^{\Delta}(t) = a(t)x(t) + f\big(t, x(t)\big), \quad t \in \mathbb{T}$$

on time scales and study h-stability, which implies uniform exponential stability, uniform Lipschitz stability, or uniform stability in particular cases. In our analysis, we use an alternative variation of parameters, which enables us to focus on a larger class of equations since the dynamic equations under the spotlight are not necessarily regressive. Also, we establish a linkage between uniform boundedness and h-stability notions for solutions of dynamic equations under sufficient conditions in addition to our stability results.

1. Introduction

The theory of time scales, which was initiated by S. Hilger in 1988 (see [1]), has taken noticeable attention in pure and applied mathematics in the last decades. The main objective of this theory is three-fold: unification, extension, and discretization of conventional calculus. Since the theory of time scales avoids the disjoint study of continuous and discrete mathematical structures, it has become a hot topic for researchers, and time scale analogs of existing theories have been reconstructed on hybrid time domains, namely time scales. Furthermore, recent studies in this field indicate that it is possible to establish a linkage between dynamical equations on time scales and other disciplines such as economics, physics, biology, or engineering sciences. We refer to readers [2]-[10] in order to polish the application potential of time scales in different fields.

Stability theory of differential and difference equations is one of the landmark topics of qualitative theory of dynamical equations in applied mathematics. Since the theory of time scales enables researchers to analyze differential and difference equations in a joint framework, researchers established a unified stability theory for dynamic equations defined on time scales for various stability types. By a quick literature review, one may easily find pioneering papers on the stability, asymptotic stability, or exponential stability of dynamic equations on time scales (see [11]-[15]). However, it should be pointed out that the stability analysis of nonlinear equations is grueling, especially when the equation is constructed on arbitrary time domains. For example, it is challenging and sometimes impossible to design a controller for a nonlinear system that ensures exponential stability. Hence, the utilization of the h-stability notion has opened a new window into stability analysis by providing a generalized approach. The concept of h-stability is first introduced by M. Pinto in [16] as an extension of notions of exponential stability and uniform Lipschitz stability. As it is discussed in [17], the following relationship holds between the well-known stability types

h -stability ⇒ uniform exponential stability ⇒ uniform Lipschitz stability ⇒ uniform stability.

*Corresponding author: haliscan.koyuncuoglu@ikcu.edu.tr
Received: 18.10.2021, Accepted: 21.03.2022

As a consequence of the above-given implications, this topic has taken prominent attention in a small duration of time, and mathematicians have studied h-stability for solutions of dynamic equations on continuous, discrete, and hybrid time domains. We refer to readers [16]-[25] as inspiring papers on this topic.

In this research, we focus on the following nonlinear abstract dynamic equation defined on an arbitrary time scale $\mathbb{T}$,

$$x^{\Delta}(t) = a(t)x(t) + f\big(t, x(t)\big),\ t \in \mathbb{T}, \qquad (1)$$

and obtain a stability analysis based on the h-stability concept. The abstract equation (1) has tremendous application potential, and its particular forms can be found in numerous papers in different fields. For example, one may easily observe that equation (1) turns into

- A single artificial effective neuron with dissipation model

  $$x'(t) = -a(t)x(t) + \mathrm{b}(t)\tanh\big(x(t)\big) + I(t),$$

  for all $t \in \mathbb{R}$,

- Continuous-time Lasota-Wazewska model on the survival of red blood cells

  $$x'(t) = -rx(t) + \eta(t)e^{-\gamma x(t)},$$

  for all $t \in \mathbb{R}$,

- Discrete-time Clark's model in population dynamics without delay

  $$\Delta x_n = (\gamma - 1)x_n + F(x_n),$$

  for all $t \in \mathbb{N}_0$,

under particular choices of a, f, and $\mathbb{T}$ (see [26]-[28], respectively). From our mathematical point of view, it is reasonable to study the abstract equation (1) on arbitrary time scales since the obtained stability results might be used for several real-life models under sufficient conditions. The analogy between the nonlinear abstract dynamic equation (1) and the specific nonlinear models in the applied sciences reveals the application potential of outcomes of the paper on a wide range of disciplines. Moreover, we shall highlight that the concept of regressivity is essential for the theory of dynamical equations on time scales since it is inevitable to define generalized exponential function. By regressiveness of a dynamic equation

$$x^{\Delta}(t) = a(t)x(t),\ t \in \mathbb{T},$$

we mean $1 + \mu(t)a(t) \neq 0$ for all $t \in \mathbb{T}^k$ where μ and the set $\mathbb{T}^k$ are defined as in the next section. Even though every function is regressive when $\mathbb{T} = \mathbb{R}$, regressivity becomes a restrictive condition for classes of dynamic equations when $\mathbb{T}$ has discrete structures. This issue is pointed out by the authors of [21], and their outcomes indicate that without regressivity assumption, it is still possible to study h-stability for dynamic equations on time scales. In this manuscript, we aim to study h-stability for scalar-valued dynamic equations on time scales without assuming regressivity. Motivated by the papers [29]-[32], we use a regressive auxiliary function to invert an alternative variation of parameters to achieve this task. Thus, the regressivity condition becomes redundant for the main equation of the manuscript. Furthermore, our approach does not only provide an alternative tool for h-stability analysis but also improves the current literature since it enables us to construct comparative results regarding the h-stability and boundedness for dynamic equations on time scales.

The organization of the paper is as follows: The next section is devoted to preliminaries of time scales calculus for the readership. In Section 3, we present the main results of the manuscript, and in the last section, we provide an elaborative conclusion.

2. Time Scales Essentials

We give the following introductory information for the readers who are not familiar with time scale calculus. The following definitions, results, and examples are given due to the pioneering book [33].

A time scale denoted by $\mathbb{T}$, which inherits the standard topology on $\mathbb{R}$, is an arbitrary, nonempty, closed subset of real numbers. We define the forward jump operator $\sigma: \mathbb{T} \to \mathbb{T}$ by $\sigma(t) \coloneqq \inf\{s \in \mathbb{T},\ s > t\}$, while the backward jump operator $\rho: \mathbb{T} \to \mathbb{T}$ is defined as $\rho \coloneqq \sup\{s \in \mathbb{T},\ s < t\}$ for $t \in \mathbb{T}$. Also, the graininess (step-size) function $\mu(t): \mathbb{T} \to [0, \infty)$ is given by $\mu(t) = \sigma(t) - t$. A point $t \in \mathbb{T}$ is said

to be right-dense if $\mu(t) = 0$ or equivalently $\sigma(t) = t$; otherwise, it is called right-scattered. In a similar fashion, a point $t \in \mathbb{T}$ is said to be left-dense if $\rho(t) = t$, or else it is called left-scattered. By the notation $[s,t)_{\mathbb{T}}$, we mean the intersection $[s,t) \cap \mathbb{T}$, and the intervals $[s,t]_{\mathbb{T}}$, $(s,t)_{\mathbb{T}}$, and $(s,t]_{\mathbb{T}}$ can be defined in the same manner. A function $f: \mathbb{T} \to \mathbb{R}$ is said to be rd-continuous if it is continuous at right dense points and its left-sided limit exists at left dense points. Besides, C_{rd} stands for all rd-continuous functions defined on $\mathbb{T}$. The set $\mathbb{T}^k$ is given in the following way: If $\mathbb{T}$ has a left-scattered maximum m, then $\mathbb{T}^k = \mathbb{T} - \{m\}$; otherwise $\mathbb{T}^k = \mathbb{T}$.

Delta-derivative of a function $f: \mathbb{T} \to \mathbb{C}$ at $t \in \mathbb{T}$ is given by

$$f^{\Delta}(t) = \begin{cases} \lim\limits_{s \to t} \dfrac{f(t) - f(s)}{t - s}, & \mu(t) = 0 \\ \dfrac{f\big(\sigma(t)\big) - f(t)}{\mu(t)}, & \mu(t) > 0 \end{cases}$$

provided the limit exists. For $f \in C_{rd}$ and $s, t \in \mathbb{T}$ we define delta-integral as

$$\int_s^t f(\tau)\Delta\tau = F(t) - F(s),$$

where $F^{\Delta} = f$ on $\mathbb{T}^k$.

Table 1 illustrates the main characteristics of three essential time scales.

A function $f: \mathbb{T} \to \mathbb{R}$ is said to be regressive if $1 + \mu(t)f(t) \neq 0$ for all $t \in \mathbb{T}^k$ and f is called positively regressive if $1 + \mu(t)f(t) > 0$ for all $t \in \mathbb{T}^k$. The notations $\mathcal{R}$ and $\mathcal{R}^+$ indicate the set of all regressive functions, and the set of all positively regressive functions, respectively. For $h > 0$, we introduce $\mathbb{C}_h \coloneqq \{z \in \mathbb{C}: z \neq -1/h\}, \mathbb{J}_h \coloneqq \{z \in \mathbb{C}: -\pi/h < Im(z) < \pi/h\}$, and $\mathbb{C}_0 \coloneqq \mathbb{J}_0 \coloneqq \mathbb{C}$. For $h \geq 0$ and $z \in \mathbb{C}_h$, the cylinder transformation $\xi_h: \mathbb{C}_h \to \mathbb{J}_h$ is defined by

$$\xi_h(z) \coloneqq \begin{cases} z, & h = 0 \\ \dfrac{1}{h} Log(1 + zh), & h > 0 \end{cases}$$

Then the unified exponential function $e_p(.,s)$ on a time scale $\mathbb{T}$ is defined by

$$e_p(t,s) \coloneqq \exp\left\{\int_s^t \xi_{\mu(\tau)}\big(p(\tau)\big)\Delta\tau\right\} \text{ for } s,t \in \mathbb{T}.$$

Moreover, the exponential function $e_p(.,s)$ is the unique solution to the initial value problem

$$\begin{cases} x^{\Delta}(t) = p(t)x(t), & t \in \mathbb{T}^k \\ x(s) = 1 \end{cases},$$

and if $p \in \mathcal{R}^+$, then $e_p(t,s) > 0$ for all $t \in \mathbb{T}^k$.

In Table 2, we give some examples of exponential functions on specific time scales. In the sequel, we present the following results as groundwork for the outcomes of the manuscript.

Theorem 1 (Variation of Constants [33, Theorem 2.77])**.** Let $t_0 \in \mathbb{T}$ and $x_0 \in \mathbb{R}$. The unique solution of the regressive initial value problem

$$\begin{cases} x^{\Delta}(t) = p(t)x(t) + f(t) \\ x(t_0) = x_0 \end{cases}$$

is given by

$$x(t) = e_p(t,t_0)x_0 + \int_{t_0}^t e_p\big(t,\sigma(\tau)\big)f(\tau)\Delta\tau.$$

Theorem 2 ([33, Theorem 6.1])**.** Let $x, f \in C_{rd}$ and $p \in \mathcal{R}^+$. Then

$$x^{\Delta}(t) \leq p(t)x(t) + f(t) \text{ for all } t \in \mathbb{T}$$

implies

$$x(t) \leq x(t_0)e_p(t,t_0) + \int_{t_0}^{t} e_p\big(t,\sigma(\tau)\big)f(\tau)\Delta\tau,$$

for all $t \in \mathbb{T}$.

Theorem 3 (Gronwall's inequality [33, Theorem 6.4])**.** Let $x, f \in C_{rd}$ and $p \in \mathcal{R}^+$, $p \geq 0$. Then

$$x(t) \leq f(t) + \int_{t_0}^{t} x(\tau)p(\tau)\Delta\tau$$

for all $t \in \mathbb{T}$ implies

$$x(t) \le f(t) + \int_{t_0}^{t} e_p\big(t,\sigma(\tau)\big) f(\tau) p(\tau) \Delta\tau \quad \text{for all } t \in \mathbb{T}.$$

Table 1. Three essential time scales

$\mathbb{T}$	$\mathbb{R}$	$\mathbb{Z}$	$q^{\mathbb{Z}} \cup \{0\}, q > 1$
$\rho(t)$	t	$t-1$	$\frac{t}{q}$
$\sigma(t)$	t	$t+1$	qt
$\mu(t)$	0	1	$(q-1)t$
$f^{\Delta}(t)$	$f'(t)$	$\Delta f(t)$	$D_q f(t) = \frac{f(qt)-f(t)}{(q-1)t}$
$\int_0^t f(\tau)\Delta\tau$	$\int_0^t f(\tau)d\tau$	$\sum_{\tau=0}^{t-1} f(\tau), (0<t)$	$\int_1^t f(\tau) d_q\tau = (q-1)\sum_{\tau=0}^{n-1} q^{\tau} f(q^{\tau}), t = q^n$

Table 2. Examples of exponential functions

$\mathbb{T}$	$\mathbb{R}$	$\mathbb{Z}$	$h\mathbb{Z}$	$q^{\mathbb{N}_0}$	$\frac{1}{n}\mathbb{Z}$
$e_\alpha(t,t_0)$	$e^{\alpha(t-t_0)}$	$(1+\alpha)^{t-t_0}$	$(1+\alpha h)^{\frac{(t-t_0)}{h}}$	$\prod_{s\in[t_0,t)} [1+(q-1)\alpha s]$	$\left(1+\frac{\alpha}{n}\right)^{n(t-t_0)}$

3. Main Results

We start this section by bringing the abstract functional dynamic equation (1) into the spotlight which is defined as

$$x^{\Delta}(t) = a(t)x(t) + f\big(t,x(t)\big), t \in \mathbb{T}$$

where $a: \mathbb{T} \to \mathbb{R}$, $f: \mathbb{T} \times \mathbb{R} \to \mathbb{R}$ belong to C_{rd} and $f(t,0) = 0$.

Firstly, we introduce the notion of h-stability in the light of [20, Definition 2.2].

Definition 1. The nonlinear dynamic equation (1) is said to be an h-equation if there exist a positive function $h: \mathbb{T} \to \mathbb{R}$, a constant $c \ge 1$, and $\delta > 0$ such that

$$|x(t,t_0,x_0)| \le c|x_0|\frac{h(t)}{h(t_0)}, t \ge t_0$$

if $|x_0| < \delta$. Moreover, if h is a bounded function, then (1) is called h-stable.

Remark 1. Since the time scale exponential function $e_p(.,s)$ can be regarded as a solution of the homogeneous dynamic equation $x^{\Delta}(t) = p(t)x(t)$, then the solution of the regressive initial value problem

$$\begin{cases} x^{\Delta}(t) = p(t)x(t), & t \in \mathbb{T}^k \\ x(t_0) = x_0 \end{cases} \tag{2}$$

is h-stable if there exist a positive, bounded function $h: \mathbb{T} \to \mathbb{R}$ and a constant $c \ge 1$ such that

$$\big|e_p(t,t_0)\big| \le c\frac{h(t)}{h(t_0)}, \ t \ge t_0. \tag{3}$$

Additionally, we provide the following definition for constructing the last result of the manuscript, which establishes a linkage between boundedness and h-stability.

Definition 2 ([34])**.** A solution x to a dynamical equation

$$x^{\Delta}(t) = f(t,x)$$

is said to be globally uniformly bounded if for every $\delta > 0$, there exists $c := c(\delta)$ such that $|x(t_0)| \leq \delta$ implies $|x(t)| \leq c$ for all $t, t_0 \in \mathbb{T}$ with $t \geq t_0 \geq 0$.

We present the following lemma due to [32, Lemma 3.1].

Lemma 1. The nonlinear dynamic equation (1) has a solution x if and only if

$$x(t) = x(t_0)e_p(t,t_0) + \int_{t_0}^{t} e_p\big(t,\sigma(\tau)\big)\Big([a(\tau) - p(\tau)]x(\tau) + f\big(\tau,x(\tau)\big)\Big)\Delta\tau, \tag{4}$$

for all $t \in [t_0,\infty)_{\mathbb{T}}$, where $p:[t_0,\infty)_{\mathbb{T}} \to \mathbb{R}$ is regressive.

Now, we are ready to give the first stability result of the manuscript.

Theorem 4. Consider the following initial value problem

$$\begin{cases} x^{\Delta}(t) = a(t)x(t) + f\big(t,x(t)\big), \ t \in \mathbb{T} \\ x(t_0) = x_0 \end{cases} \tag{5}$$

where $a, f \in C_{rd}$, $f(t,0) = 0$, and a is not necessarily regressive. Also, we introduce the following auxiliary regressive initial value problem

$$\begin{cases} x^{\Delta}(t) = p(t)x(t) \\ x(t_0) = x_0 \end{cases}. \tag{6}$$

Assume that the following conditions hold:

C1: Solution of (6) is h-stable.

C2: There exists a function g such that

$$|f(t,x) - f(t,y)| \leq g(t)|x - y|.$$

C3: There exists $M > 0$ such that

$$\int_{t_0}^{t} \frac{h(\tau)}{h\big(\sigma(\tau)\big)}\big(|a(\tau) - p(\tau)| + g(\tau)\big)\Delta\tau \leq M.$$

Then, (5) is h-stable.

Proof. Suppose that conditions **C1-C3** are satisfied. By (4), we obtain the inequality

$$|x(t)| \leq |x_0|\big|e_p(t,t_0)\big| + \int_{t_0}^{t} \big|e_p\big(t,\sigma(\tau)\big)\big|\,(|a(\tau) - p(\tau)||x(\tau)| + \big|f\big(\tau,x(\tau)\big)\big|)\Delta\tau.$$

Then we use the condition **C1** together with (3) and get

$$|x(t)| \leq \mathrm{c}|x_0|\frac{h(t)}{h(t_0)} + \int_{t_0}^{t} \mathrm{c}\frac{h(t)}{h\big(\sigma(\tau)\big)}(|a(\tau) - p(\tau)||x(\tau)| + \big|f\big(\tau,x(\tau)\big)\big|)\Delta\tau$$

$$= \mathrm{c}|x_0|\frac{h(t)}{h(t_0)} + \mathrm{c}\frac{h(t)}{h(t_0)}\int_{t_0}^{t} \frac{h(t_0)}{h\big(\sigma(\tau)\big)}(|a(\tau) - p(\tau)||x(\tau)| + \big|f\big(\tau,x(\tau)\big)\big|)\Delta\tau$$

$$\leq \mathrm{c}|x_0|\frac{h(t)}{h(t_0)} + \mathrm{c}\frac{h(t)}{h(t_0)}\int_{t_0}^{t} \frac{h(t_0)}{h\big(\sigma(\tau)\big)}(|a(\tau) - p(\tau)||x(\tau)| + g(\tau)|x(\tau)|)\Delta\tau$$

by the adoption of **C2** in the last step.

Next, we set

$$z(t) = \int_{t_0}^{t} \frac{h(t_0)}{h\big(\sigma(\tau)\big)}(|a(\tau) - p(\tau)||x(\tau)| + g(\tau)|x(\tau)|)\Delta\tau$$

and observe

$$z^{\Delta}(t) = \frac{h(t_0)}{h\big(\sigma(t)\big)}(|a(t) - p(t)||x(t)| + g(t)|x(t)|)$$

$$\leq \frac{h(t_0)}{h\big(\sigma(t)\big)}\Big[|a(t) - p(t)|\Big(\mathrm{c}|x_0|\frac{h(t)}{h(t_0)} + \mathrm{c}\frac{h(t)}{h(t_0)}z(t)\Big) + g(t)\Big(\mathrm{c}|x_0|\frac{h(t)}{h(t_0)} + \mathrm{c}\frac{h(t)}{h(t_0)}z(t)\Big)\Big]$$

$$= \mathrm{c}|x_0|\frac{h(t)}{h\big(\sigma(t)\big)}\big(|a(t) - p(t)| + g(t)\big)$$

$$+\left(\mathrm{c}\frac{h(t)}{h(\sigma(t))}\big(|a(t)-p(t)|+g(t)\big)\right)z(t).$$

Consequentially, we deduce the inequality

$$z^{\Delta}(t) \le \varphi(\mathrm{t})z(t)+\psi(t),$$

where

$$\varphi(t)=\mathrm{c}\frac{h(t)}{h(\sigma(t))}\big(|a(t)-p(t)|+g(t)\big), \qquad (7)$$

and

$$\psi(t)=|x_0|\varphi(t). \qquad (8)$$

One may easily observe that $\varphi \in \mathcal{R}^{+}$, and then Theorem 2 implies

$$z(t) \le z(t_0)e_{\varphi}(t,t_0)+\int_{t_0}^{t} e_{\varphi}\big(t,\sigma(\tau)\big)\psi(\tau)\,\Delta\tau$$
$$=\int_{t_0}^{t} e_{\varphi}\big(t,\sigma(\tau)\big)\psi(\tau)\,\Delta\tau \qquad (9)$$

since $z(t_0)=0$. If we write the inequality (9) explicitly, then we have

$$z(t) \le \int_{t_0}^{t} \mathrm{c}|x_0|\frac{h(\tau)}{h(\sigma(\tau))}(|a(\tau)-p(\tau)|+\ g(\tau))$$
$$\exp\left(\int_{\sigma(\tau)}^{t}\xi_{\mu(s)}\big(\varphi(s)\big)\Delta s\right)\Delta\tau$$

where

$$\xi_{\mu(t)}\big(\varphi(t)\big)=\frac{1}{\mu(t)}Log\left(1+c\mu(t)\frac{h(t)}{h(\sigma(t))}\big(|a(t)-p(t)|+g(t)\big)\right)$$

when $\mu>0$, and

$$\xi_{\mu(t)}\big(\varphi(t)\big)=c\frac{h(t)}{h(\sigma(t))}\big(|a(t)-p(t)|+g(t)\big)$$

when $\mu=0$.

Here we get

$$z(t) \le \int_{t_0}^{t} \mathrm{c}|x_0|\frac{h(\tau)}{h(\sigma(\tau))}\big(|a(\tau)-p(\tau)|+g(\tau)\big)$$
$$\exp\left(\int_{\sigma(\tau)}^{t} c\frac{h(s)}{h(\sigma(s))}\big(|a(s)-p(s)|+g(s)\big)\Delta s\right)\Delta\tau$$

which yields to

$$|x(t)| \le \mathrm{c}|x_0|\frac{h(t)}{h(t_0)}$$
$$+\mathrm{c}^2|x_0|\frac{h(t)}{h(t_0)}\int_{t_0}^{t}\frac{h(\tau)}{h(\sigma(\tau))}(|a(\tau)-p(\tau)|+$$
$$g(\tau)\big)\exp\left(\int_{\sigma(\tau)}^{t} c\frac{h(s)}{h(\sigma(s))}(|a(s)-p(s)|+\right.$$
$$\left.g(s)\big)\Delta s\right)\Delta\tau.$$

By using **C3**, we write

$$|x(t)| \le \mathrm{c}|x_0|\frac{h(t)}{h(t_0)}+\mathrm{c}^2|x_0|\frac{h(t)}{h(t_0)}Me^{cM}$$
$$=|x_0|\frac{h(t)}{h(t_0)}(\mathrm{c}+\mathrm{c}^2Me^{cM})$$

which shows x is h-stable. The proof is complete. □

Next, we present an inequality that is crucial for establishing a comparative stability result.

Lemma 2 ([21, Lemma 3.25])**.** Suppose that $m \in C_{rd}(\mathbb{T}\times\mathbb{R}^{+},\mathbb{R})$ is non-decreasing in the second argument x for each fixed $t \ge t_0$ with the property

$$x(t)-\int_{t_0}^{t} m\big(\tau,x(\tau)\big)\Delta\tau \le y(t)-\int_{t_0}^{t} m\big(\tau,y(\tau)\big)\Delta\tau,$$

for $t \ge t_0 \in \mathbb{T}$ and $x,y \in C_{rd}(\mathbb{T},\mathbb{R}^{+})$. If $x(t_0)<y(t_0)$, then $x(t)<y(t)$ for all $t \ge t_0 \in \mathbb{T}$.

Theorem 5. Suppose that there exists a function $k \in C_{rd}(\mathbb{T}\times\mathbb{R}^{+},\mathbb{R}^{+})$ so that

$$|f(t,x)| \le k(t,|x|), \qquad (10)$$

where k is increasing with respect to its second argument. We set

$$m(t,x) = |a(t) - p(t)|x(t) + k\big(t, x(t)\big), \qquad (11)$$

and also assume $p \in \mathcal{R}^+$. Consider the following auxiliary equation

$$\begin{cases} u^{\Delta}(t) = p(t)u(t) + m\big(t, u(t)\big) \\ u(t_0) = u_0 \end{cases}. \qquad (12)$$

If (12) is h-stable, then (5) is also h-stable whenever $u_0 = |x_0|$.

Proof. Suppose that the inequality (10) holds, and (12) is h-stable. We fix $u_0 = |x_0|$ and observe that the function m given in (11) is increasing with respect to its second term. By (4), (10), and (11), we have

$$\begin{aligned} |x(t)| &\le |x_0|e_p(t,t_0) \\ &\quad + \int_{t_0}^{t} e_p\big(t,\sigma(\tau)\big)\big(|a(\tau) \\ &\quad - p(\tau)||x(\tau)| + \big|f\big(\tau, x(\tau)\big)\big|\big)\,\Delta\tau \\ &\le |x_0|e_p(t,t_0) \\ &\quad + \int_{t_0}^{t} e_p\big(t,\sigma(\tau)\big)\big(|a(\tau) \\ &\quad - p(\tau)||x(\tau)| + k(\tau,|x|)\big)\,\Delta\tau \\ &\le |x_0|e_p(t,t_0) \\ &\quad + \int_{t_0}^{t} e_p\big(t,\sigma(\tau)\big)m(\tau,|x(\tau)|)\,\Delta\tau, \end{aligned}$$

which yields to

$$\begin{aligned} &|x(t)| - \int_{t_0}^{t} e_p\big(t,\sigma(\tau)\big)m(\tau,|x(\tau)|)\,\Delta\tau \\ &\le |x_0|e_p(t,t_0) \\ &= u(t) - \int_{t_0}^{t} e_p\big(t,\sigma(\tau)\big)m(\tau,|u(\tau)|)\,\Delta\tau. \end{aligned}$$

Subsequently, we have $|x(t)| < u(t)$ due to Lemma 2. Hence,

$$|x(t)| < u(t) \le cu_0\frac{h(t)}{h(t_0)} = c|x_0|\frac{h(t)}{h(t_0)},$$

and this proves our assertion. □

The following result focuses on boundedness and h-stability.

Theorem 6. Suppose that the auxiliary regressive initial value problem given in (6)

$$\begin{cases} x^{\Delta}(t) = p(t)x(t) \\ x(t_0) = x_0 \end{cases}$$

is h-stable with an increasing function h. Also, consider the dynamic equation given in (5), which is

$$\begin{cases} x^{\Delta}(t) = a(t)x(t) + f\big(t, x(t)\big) \\ x(t_0) = x_0 \end{cases}$$

with condition **C2** of Theorem 4. Then, the solution of the nonlinear equation (5) is globally uniformly bounded whenever

$$e_{\kappa}(t,t_0) \le \omega \qquad (13)$$

where

$$\kappa(t) = |a(t) - p(t)| + g(t). \qquad (14)$$

Proof. Assume that (6) is h-stable with an increasing function h, and **C2** and (13) hold. In the light of (4) and **C2**, one may easily obtain the inequality

$$\begin{aligned} |x(t)| &\le |x_0|\big|e_p(t,t_0)\big| + \int_{t_0}^{t}\big|e_p\big(t,\sigma(\tau)\big)\big|(|a(\tau) \\ &\quad -p(\tau)||x(\tau)| + \big|f\big(\tau,x(\tau)\big)\big|)\Delta\tau \\ &\le |x_0|\big|e_p(t,t_0)\big| + \int_{t_0}^{t}\big|e_p\big(t,\sigma(\tau)\big)\big|(|a(\tau) \\ &\quad -p(\tau)||x(\tau)| + g(\tau)|x(\tau)|)\Delta\tau \\ &\le \mathrm{c}|x_0|\frac{h(t)}{h(t_0)} + \int_{t_0}^{t} c\frac{h(t)}{h\big(\sigma(\tau)\big)}(|a(\tau) \\ &\quad -p(\tau)||x(\tau)| + g(\tau)|x(\tau)|)\Delta\tau. \end{aligned}$$

Hereby monotonicity of h, we get

$$h^{-1}(t)|x(t)| \le c|x_0|h^{-1}(t_0) + c\int_{t_0}^{t} h^{-1}\big(\sigma(\tau)\big)(|a(\tau)-p(\tau)| |x(\tau)|+g(\tau)|x(\tau)|)\Delta\tau$$

$$\le c|x_0|h^{-1}(t_0) + c\int_{t_0}^{t} h^{-1}(\tau)|x(\tau)|(|a(\tau)-p(\tau)|+g(\tau))\Delta\tau. \quad (15)$$

Then, we set $u(t) = h^{-1}(t)|x(t)|$ and rewrite (15) as follows:

$$u(t) \le cu(t_0) + c\int_{t_0}^{t} u(\tau)\big(|a(\tau)-p(\tau)|+g(\tau)\big)\Delta\tau.$$

Here, Theorem 3 implies $u(t) \le cu(t_0)e_\kappa(t,t_0)$, where κ is as in (14). Then we have

$$|x(t)| \le c\frac{h(t)}{h(t_0)}e_\kappa(t,t_0)|x_0| \le c^*\frac{h(t)}{h(t_0)}|x_0|,$$

for $c^* = c\omega \ge 1$. The proof is complete. □

4. Concluding Comments

This study focuses on functional dynamic equations of the form (1) on time scales and provides a detailed analysis regarding h-stability. In the setup of the paper, an alternative variation of parameters formula is used via an auxiliary regressive function p. This approach does not only elicit a new point of view but also relaxes a compulsory condition, namely regressivity, from the dynamic equation of interest. Therefore, contrary to Theorem 1, we do not assume the regressiveness of the main equation for the inversion of the solution.

This study consists of three main results. In Theorem 4 and Theorem 5, we propose sufficient conditions for h-stability of (1) via an h-stable and regressive auxiliary dynamic equation; for instance, see **C1** of Theorem 4. Note that one may easily write the following identity for the generalized exponential function

$$\big|e_p(t,t_0)\big| = \big|e_p(t,\theta)\big|\big|e_p(\theta,t_0)\big| = \frac{\big|e_p(t,\theta)\big|}{\big|e_p(t_0,\theta)\big|}$$

for $t_0 \le \theta \in \mathbb{T}$, by utilizing [33, Theorem 2.36]. Then, h-stability of the linear equation in (2) is straightforward by setting $h(t) = \big|e_p(t,\theta)\big|$, if $e_p(t,\theta)$ is bounded. By [32, Remark 3.8] (see also [35, Example 1]), we have $e_p(t,\theta) \to 0$ as $t \to \infty$ for any negative-valued function p satisfying $|p(t)| \le \eta$ for all $t \in \mathbb{T}$ where $\sup\mathbb{T} = \infty, \eta > 0$ and $-\eta \in \mathcal{R}^+$. This indicates $e_p(t,\theta)$ is bounded. Thus, we shall point out that the h-stability assumption we made for the auxiliary system is a checkable condition. Moreover, the additional conditions introduced in Theorem 4 and 5 are foreseeable since we convert (1) to an integral equation. In the last main result of the manuscript, namely Theorem 6, the connection between uniform boundedness and h-stability notions is highlighted similarly to Theorem 4 and 5.

The outcomes of the manuscript are not only a unification but also a significant extension for the established literature since they allow us to consider h-stability of functional dynamical equations on general domains not restricted to $\mathbb{T} = \mathbb{R}$ or $\mathbb{T} = \mathbb{Z}$.

Contributions of the authors

All authors contributed equally to the study.

Conflict of Interest Statement

There is no conflict of interest between the authors.

Statement of Research and Publication Ethics

The authors declare that this study complies with Research and Publication Ethics.

References

[1] S. Hilger, "Ein Maßkettenkalkül mit Anwendung auf Zentrumsmannigfaltigkeiten", Ph.D. Dissertation, Universität Würzburg, Institut für Mathematik, Würzburg, Germany, pp. 1-141, 1988.

[2] F. M. Atıcı, D. C. Biles, and A. Lebedinsky, "An application of time scales to economics", *Math. Comput. Model*., vol. 43, no. (7-8), pp. 718-726, 2006, https://doi.org/10.1016/j.mcm.2005.08.014.

[3] F. M. Atıcı and N. Turhan, "Sequential decision problems on isolated time domains", *J. Math. Anal. Appl*., vol. 388, no. 2, pp. 753-759, 2012, https://doi.org/10.1016/j.jmaa.2011.09.068.

[4] J. Y. Chen and Y. Zhang, "Time-scale version of generalized Birkhoffian mechanics and its symmetries and conserved quantities of Noether type", *Adv. Math. Phy*., vol. 2021, 2021, Article ID 9982975, https://doi.org/10.1155/2021/9982975.

[5] A. K. Abraehim, A. K. Jaber, and R. Al-Salih, "Flow optimization in dynamic networks on time scales", *J. Phys. Conf. Ser.*, vol. 1804, no. 1, 7 pages, 2021, https://doi.org/10.1088/1742-6596/1804/1/012025.

[6] M. Bohner, S. Streipert, and D. F. M. Torres, "Exact solution to a dynamic SIR model", *Nonlinear Anal. Hybrid Syst.*, vol. 32, pp. 228-238, 2019, https://doi.org/10.1016/j.nahs.2018.12.005.

[7] X. Chen, C. Shi, and D. Wang, "Dynamic behaviors for a delay Lasota-Wazewska model with feedback control on time scales", Adv. *Difference Equ.*, vol. 17, 13 pages, 2020, https://doi.org/10.1186/s13662-019-2483-8.

[8] E. Pawłuszewicz, "Observability of Nonlinear Control Systems on Time Scales-Sufficient Conditions". in: *Mathematical Control Theory and Finance*, Edited by Sarychev A., Shiryaev A., Guerra M., Grossinho MR., Springer, Berlin, Heidelberg, pp. 325-335, 2008. https://doi.org/10.1007/978-3-540-69532-5_18.

[9] Ö. Öztürk and H. M. Güzey, "Optimal control of quadrotor unmanned aerial vehicles on time scales", *Int. J. Difference Equ., vol. 13, no. 1, pp. 41-54, 2018.*

[10] D. R. Poulsen, J. M. Davis, and I. A. Gravagne, "Optimal control on stochastic time scales", *IFAC-PapersOnLine*, vol. 50, no. 1, pp. 14861-14866, 2017, https://doi.org/10.1016/j.ifacol.2017.08.2518.

[11] C. Hoffacker and C. C. Tisdell, "Stability and instability for dynamic equations on time scales", *Comput. Math. Appl.*, vol. 49, no. 9-10, pp. 1327-1334, 2005, https://doi.org/10.1016/j.camwa.2005.01.016.

[12] H. Wu and Z. Zhou, "Stability for first order delay dynamic equations on time scales", *Comput. Math. Appl*., vol. 53, no. 12, pp. 1820-1831, 2007, https://doi.org/10.1016/j.camwa.2006.09.011.

[13] J. Zhang and M. Fan, "Boundedness and stability of semi-linear dynamic equations on time scales", *Progress in Qualitative Analysis of Functional Equations*, 1786, pp. 45-56, 2012.

[14] E. Akın-Bohner, Y. N. Raffoul, and C.C. Tisdell, "Exponential stability in functional dynamic equations on time scales", *Commun. Math. Anal*., vol. 9, no 1, pp. 93-108, 2010.

[15] A. C. Peterson and Y. N. Raffoul, "Exponential stability of dynamic equations on time scales", *Adv. Difference Equ.*, vol. 2005, no. 2, 2005, Article ID 858671, https://doi.org/10.1155/ADE.2005.133.

[16] M. Pinto, "Perturbations of asymptotically stable differential systems", *Analysis*, vol. 4, no. 1-2, pp. 161-175, 1984.

[17] S. K. Choi, N. J. Koo, and R. S. Ryu, "h-stability of differential systems via t_∞-similarity". *Bull.* Korean *Math. Soc*., vol. 34, no. 3, pp. 371-383, 1997.

[18] H. Damak, M. A. Hammmami, and A. Kicha, "h-stability and boundedness results for solutions to certain nonlinear perturbed systems", *Mathematics for Applications*, vol. 10, pp. 9-23, 2021, https://doi.org/10.13164/ma.2021.02.

[19] S. K. Choi, N. J. Koo, and S. M. Song, "h-stability for nonlinear perturbed difference systems", *Bull. Korean Math. Soc*., vol. 41, no. 3, pp. 435-450, 2004, https://doi.org/10.4134/BKMS.2004.41.3.435.

[20] S. K. Choi, N. J. Koo, and D. M. Im, "h-stability for linear dynamic equations on time scales", *J. Math. Anal. Appl*., vol. 324, no. 1, pp. 707-720, 2006, https://doi.org/10.1016/j.jmaa.2005.12.046.

[21] S. K. Choi, Y. H. Goo, and N. Koo, "h-stability of dynamic equations on time scales with nonregressivity", *Abstr. Appl. Anal*., vol. 2008, 2008, Article ID 632473, https://doi.org/10.1155/2008/632473.

[22] S. K. Choi, Y. Cui, and N. Koo, "Variationally stable dynamic systems on time scales", *Adv. Difference Equ*., vol. 2012, no. 1, 2012, Article ID 129, https://doi.org/10.1186/1687-1847-2012-129.

[23] B. B. Nasser, M. Djemai, M. Defoort, and T. M. Laleg-Kirati, "Time scale state feedback h-stabilization of linear systems under Lipschitz-type disturbances", *Internat. J. Systems Sci*., vol. 52, no. 8, pp. 1719-1729, 2021, https://doi.org/10.1080/00207721.2020.1869345.

[24] B. Neggal, K. Boukerrioua, B. Kilani, and I. Meziri, "h-stability for nonlinear abstract dynamic equations on time scales and applications", *Rend. Circ. Mat. Palermo (2)*, vol. 69, no. 3, pp. 1017-1031, 2020, https://doi.org/10.1007/s12215-019-00452-x.

[25] B. B. Nasser, K. Boukerrioua, M. Defoort, M. Djemai, M. A. Hammmami, and T. M. Laleg-Kirati, "Sufficient conditions for uniform exponential stability and h-stability of some classes of dynamic equations on arbitrary time scales", *Nonlinear Anal. Hybrid Syst*., vol. 32, pp. 54-64, 2019, https://doi.org/10.1016/j.nahs.2018.10.009.

[26] A. Gopalsamy and S. Sariyasa, "Time delays and stimulus dependent pattern formation in periodic enviroments in isolated neurons", *Dyn. Contin. Discrete Impuls. Syst. Ser. B Appl. Algorithms*, vol. 9, pp. 39-58, 2002.

[27] S. N. Chow, "Existence of periodic solutions of autonomous functional differential equations", *J. Differential Equations*, vol. 15, pp. 350-378, 1974.

[28] C. W. Clark, "A delayed- recruitment model of population dynamics, with an application to baleen whale populations", *J. Math. Biol*., vol. 3, pp. 381-391, 1976, https://doi.org/10.1007/BF00275067.

[29] Y. N. Raffoul, "Stability and boundedness in nonlinear and neutral difference equations using new variation of parameters formula and fixed point theory", *Cubo*, vol. 21, no. 3, pp. 39-61, 2019, https://doi.org/10.4067/s0719-06462019000300039.

[30] Y. N. Raffoul, "Nonlinear functional delay differential equations arising from population models", *Adv. Dyn. Syst. Appl*., vol. 14, no. 1, pp. 67-81, 2019..

[31] A. Larraín-Hubach and Y. N. Raffoul, "Boundedness, periodicity and stability in nonlinear delay differential equations", *Adv. Dyn. Syst. Appl*., vol. 15, no. 1, pp. 29-37, 2020.

[32] H. C. Koyuncuoğlu, "Some qualitative results for functional delay dynamic equations on time scales", *Turkish J. Math*., vol. 45, no. 1, pp. 1985-2007, 2021, https://doi.org/10.3906/mat-2102-106.

[33] M. Bohner and A. C. Peterson, *Dynamic Equations on Time Scales: An Introduction with Applications*, Birkhäuser, Boston, 2001.

[34] H. K. Khalil, *Nonlinear Systems*, Prentice Hall, New York, 1-734, *2002*.

[35] M. Adıvar and Y. N. Raffoul, "Stability and periodicity in dynamic delay equations". *Comput.* Math. *Appl*., vol. 58, no. 2, pp. 264-272, 2009, https://doi.org/10.1016/j.camwa.2009.03.065.

Bitlis Eren Üniversitesi Fen Bilimleri Dergisi
BİTLİS EREN UNIVERSITY JOURNAL OF SCIENCE
ISSN: 2147-3129/e-ISSN: 2147-3188
VOLUME: 11 NO: 2 PAGE: 469-477 YEAR: 2022
DOI: 10.17798/bitlisfen.1024236

Sinaptik Etkinlik Fonksiyon Tabanlı Sızdıran Entegre ve Ateşleme Nöron Modelini Kullanarak İnsan Ses Sinyallerinde Cinsiyet Tespiti

Vedat TÜMEN[1*]

[1]*Bitlis Eren Üniversitesi, Mühendislik-Mimarlık Fakültesi, Bilgisayar Mühendisliği Bölümü (ORCID: 0000-0003-0271-216X)*

Anahtar Kelimeler: Ani sivri uçlu ağlar, Cinsiyet tespiti, Derin öğrenme, Sinyal işleme.

Abstract

Günümüzdeki teknolojik gelişmeler, insanların bir ses sinyalinden konuşmacının cinsiyetini belirlemesi mümkün kılmıştır. Frekans türleri, spektral ve entropi gibi sayısal nitelikli veriler ses sinyallerinin akustik bilgilerini oluşturmaktadır. Son zamanlarda, yüksek başarı oranlarına sahip yapay zekâ tabanlı öğrenme modelleri çeşitli alanlarda ilgi görmeye başladı. Ses sinyalleri üzerinde derin öğrenme modelleri ile ilgili birçok çalışma bulunmaktadır. Bu çalışmada, derin öğrenme modellerinden esinlenerek tasarlanmış ve farklı bir mimari yapısı olan ani sivri uçlu sinir ağları kullanılmıştır. Çalışmada kullanılan veri kümesi, insan konuşmalarını ve seslerini içeren akustik bilgiye dayalı parametrelerden oluşmaktadır. Belirlenen bir veri seti kullanılarak ani sivri uçlu sinir ağı modeli eğitilmiş ve cinsiyet tespitinin gerçekleştirilmesi sağlanmıştır. Önermiş olduğumuz bu çalışmada sonuç olarak, sınıflandırma sürecinde %98,84 genel doğruluk başarısı elde edilmiştir. Bu çalışmada gerçekleştirilen deneysel analizler ile ani sivri uçlu sinir ağı modelinin başarılı bir şekilde çalıştırıldığı, yüksek başarımlar elde edildiği gözlemlenmiştir.

Gender Determination in Human Voice Signals using Synaptic Efficacy Function-based Leaky Integrate and Fire Neuron Model

Keywords: Spiking network, Gender detection, Deep learning, Signal processing

Abstract

Today's technological advances have made it possible for people to determine the gender of the speaker from an audio signal. Numerical data such as frequency types, spectral and entropy constitute acoustic information of audio signals. Recently, artificial intelligence-based learning models with high success rates have started to attract attention in various fields. There are many studies on deep learning models on audio signals. In this study, spiked neural networks with a different architectural structure, inspired by deep learning models, were used. The dataset used in the study consists of parameters based on acoustic information including human speech and voices. By using the determined data set, the spiked neural network model was trained and gender determination was achieved. As a result, 98.84% overall accuracy success was achieved in the classification process in this proposed study. With the experimental analyses carried out in this study, it was observed that the spiked neural network model was successfully run and high performances were obtained.

1. Giriş

Erkek ve kadın bireylerin cinsiyetlerini fark etmede kullanılan parametrelerden biri de ses sinyalleridir. Sesin kaynağından çıkış anına kadar geçen süreçte, cinsiyet farkındalığını ölçen akustik özellikler vardır. Bu özellikler, genelde sesin entropisi veya temel frekans ile baskın frekans değerleri arasında farklılıkların oluşmasına sebep olur. Temel frekans değerleri kaynağın boyutu ile ters orantılıdır ve kolaylıkla ölçülebilmektedir [1]. Erkek yetişkin bireylerde temel frekans değeri genelde düşüktür ve

*Sorumlu yazar: vtumen@beu.edu.tr

Geliş Tarihi: 01.12.2021, Kabul Tarihi: 05.04.2022

bayan yetişkin bireylerde ise bu frekans değeri genelde yüksektir. Erkek yetişkinlerde frekans değeri 120 hertz kabul edilirken, bayan yetişkinlerde ise 200 hertz olarak kabul edilir [2]. Fakat temel frekans değerleri her zaman için bu sonucu doğrulamayabilir. Bu sebeple cinsiyet belirlemede diğer akustik özelliklerine de gereksinim duyulmaktadır. Ses sinyalleri üzerinde cinsiyet sınıflandırılması üst düzey bir bilişsel çalıştırma gerektiren bir durumdur [3,4]. İnsan-makine etkileşimi gün geçtikçe daha da artmaktadır ve bilişim tabanlı cinsiyet tanıma sistemleri karmaşık bir yapıya sahiptir. Bu tür sistemlerin kendi içerisinde problemleri ve sınırlamaları vardır. Sesin karmaşıklığını artıran nedenlerden bazıları sıralanırsa; gürültülü ortamda konuşmak, sıkıştırılmış ses verileri, telefon görüşmeleri, farklı konuşma dillerinin kullanılması şeklinde ifade edilebilir. [5,6]. Neticede, karmaşıklık akustik özelliklerin çıkartılmasını olumsuz etkileyebilmektedir. Bu tür problemleri minimize edebilmek için yapay zekâ tabanlı sistemlere ihtiyaç duyulmaktadır [7].

Literatürde ses sinyallerini işleyerek konuşmacının cinsiyetini belirleyen birçok çalışma yer almaktadır. Bunlardan bazıları incelenirse; G. S. Archana ve ark. çalışmasında ses sinyallerini kullanarak cinsiyet tespitini gerçekleştirmişler. Onlar, veri eğitiminde yapay sinir ağlarını (YSA) ve sınıflandırma sürecinde destek vektör makinelerini (DVM) kullanmışlar. Onların sınıflandırma sürecinde elde ettikleri genel doğruluk oranı %80 olmuştur [8]. S.C. İleri ve ark. deneysel analizlerde konuşma sinyalleri üzerinde cinsiyet tespitini gerçekleştirmişlerdir. Onlar, veri kümesinde mel - frekans spektral katsayıları (MFSK) tekniğini kullanarak özellikler çıkarılmış ve bu özellikleri temel bileşenler analizi yöntemi (TBA) ile daha verimli çıkarımlar elde edilmiştir. Daha sonra bu çıkarımlar her bir özellik değerini normalleştirme adımından geçirerek, DVM yöntemi ile sınıflandırmışlar. Sınıflandırma sürecinde elde ettikleri genel doğruluk başarısı %98.18 olmuştur [9]. David Doukhan ve ark. Fransızca konuşma sinyallerinden oluşan veri kümesini kullanarak cinsiyet tespitini gerçekleştirmişler. Onlar, veri kümesi için ön işlem adımı olarak gauss karışım modelleri (GKM), i-vektörler yöntemini kullanmışlar ve ardından tasarladıkları evrişimsel sinir ağları (ESA) ile veri kümesini eğitip, sınıflandırmışlar. Onların, sınıflandırma sürecinde elde ettikleri en iyi genel doğruluk başarısı %96.52 olmuştur [10]. Ping Wang ve ark. Elektro Ensefalo Grafiği (EEG) sinyallerini kullanarak cinsiyet tespitini gerçekleştirmişlerdir. Onlar, rastgele orman (RO) ve lojistik regresyon (LR) makine öğrenme yöntemlerini melezleştiren bir model önermişlerdir. Sınıflandırma sürecinde çapraz doğrulama yöntemi ile elde ettikleri en iyi genel doğruluk başarısı %99.82 olmuştur [11].

Çalışmalar incelendiğinde farklı veri türlerinden yapay zeka teknikleri ve algoritmaları kullanarak cinsiyet analizinin yapıldığı tespit edilmiştir. Bu çalışmada, insanların konuşma ve ses sinyallerinden cinsiyet tespitinin gerçekleştirilmesi amaçlanmıştır.

Ani sivri uçlu sinir ağları (ASUSA) tasarlanan bir sinir ağı modelinde nöronların sivri uçları aracılığı ile biyolojik bilgi iletimi sağlamaktadır. Sinir hücrelerinde meydana gelen ani artış stereotipik olaylar olduğu varsayıldığından burada oluşan veri iki temel adımda işlenmektedir. Ani atışın zamansal değeri ve frekans değerlerinin uyarıcı veya engelleyici olup olmadığının tespiti oldukça yüksek performans göstermiştir [12]. ASUSA'lar ayrıca, üçüncü nesil sinir ağları olarak kabul edilir ve kendilerini, büyük ağların çok hızlı gerçek zamanlı simülasyonuna ve düşük bir hesaplama maliyetine izin vererek, beynin davranış ve öğrenme potansiyelini modellemek için en başarılı yaklaşımlardan biri olarak ortaya koymuştur [13]. Daha kapsamlı ASUSA ağları geliştirilerek daha karmaşık görevleri çözebiliriz. Bu nedenle, geleneksel derin öğrenme modellerine göre kıyaslandığında daha karmaşık eğitim yöntemlerinin bilgi işlem platformlarındaki verimsiz artış simülasyonları nedeniyle eğitim süresinde oluşabilecek bir darboğazı önlemektedir. Bu önemli sorunların giderilmesi için farklı bir model yapısı olan ASUSA modeli ile eğitimin başarılı bir şekilde gerçekleştirilmesi hedeflenmektedir.

Bu makalede materyal ve metot bölümünde veriseti ve önerilen yöntem ve parametreler yer almaktadır. Bölüm 3'te bulgular bölümünde çalışmanın deneysel analizlerine ve elde edilen sonuçlara yer verilmiştir. Bu çalışmadaki performans değerleri ile literatürde bulunan yüksek başarımlı sonuçlar Bölüm 4'te karşılaştırılmıştır. Son olarak bölüm 5'te sonuçlar tekrar değerlendirilmiş ve gelecek çalışmalar hakkında öneriler verilmiştir.

2. Materyal ve Metod

2.1. Veriseti

Veri kümesi, konuşma ve ses sinyallerinin akustik özelliklerine dayalı olarak bir sesi erkek veya kadın olarak tanımlamak için oluşturulmuştur. Veri kümesi, herkesin erişebileceği ".csv" uzantılı dosyadan oluşmaktadır ve 22 akustik özellik içermektedir [14]. Bu akustik özellikler Tablo 1'de verilmiştir.

Veri kümesi, erkek ve kadın konuşmacılardan toplanan 3168 kayıtlı ses örneğinden oluşmaktadır. Ses örneklerinin eşit olarak 1584 âdeti erkek konuşmacılardan ve 1584 âdeti kadın konuşmacılarından oluşmaktadır. Ses kayıtlarında gerçekleşen konuşma dili İngilizcedir. Ses örneklerinin frekans aralığı (0-280) Hz olarak işlenmiştir ve önceden işlenmiş WAV dosyaları bir CSV dosyasına dönüştürülmüştür [14]. Ek olarak, bu çalışmanın analizinde veri kümesinin %30'u test verisi ve %70'i eğitim verisi olarak ayrıldı.

Tablo 1. Veri kümesini oluşturan akustik özellikler

No	Özellik	Açıklama
1	Meanfreq	Ortalama frekans (kHz cinsinden)
2	Sd	Frekansın standart sapması
3	Median	Medyan frekans (kHz cinsinden)
4	Q25	İlk nicelik (kHz cinsinden)
5	Q75	Üçüncü nicelik (kHz cinsinden)
6	IQR	Çeyrekler arası aralık (kHz cinsinden)
7	Skew	Çarpıklık
8	Kurt	Basıklık
9	Sp.ent	Spektral Entropi
10	Sfm	Spektral düzlük
11	Mode	Mod frekansı
12	Centroid	Frekans sentroid
13	Peakf	En yüksek enerjili frekans (Tepe frekansı)
14	Meanfun	Akustik sinyalde ölçülen ortalama temel frekans
15	Minfun	Akustik sinyalde ölçülen minimum temel frekans
16	Maxfun	Akustik sinyalde ölçülen maksimum temel frekans
17	Meandom	Akustik sinyalde ölçülen ortalama baskın frekans
18	Mindom	Akustik sinyalde ölçülen minimum baskın frekans
19	Maxdom	Akustik sinyalde ölçülen maksimum baskın frekans
20	Dfrange	Akustik sinyalde ölçülen baskın frekans aralığı
21	Modindx	Modülasyon indeksi (Temel frekansların bitişik ölçümleri arasındaki birikmiş mutlak farkın frekans aralığına bölünmesiyle hesaplanır)
22	Label	Etiket (Erkek veya Kadın)

2.1. Ani Sivri Uçlu Sinir Ağları ile Önerilen Yaklaşım

Ani sivri uçlu sinir ağları (ASUSA), nöron ve sinaptik durumları zaman kavramı ile birleştiren ve doğal sinir yapılarını tek tek inceleyen bir ağ modelidir. ASUSA yapılarındaki nöronların yayılma döngülerinde tetiklenmemesi, bu nöronların öz kalitelerini belirli bir seviyeye yükseltmelerine olanak sağlar. Bir nöron tetiklendiğinde, etrafındaki diğer nöronların sinyal potansiyelini artıran veya azaltan bir durum yaratır. Nöronların aktivasyonunu gerçekleştirmek için belirli bir eşik değeri kullanır. Nöronlardan gelen tetikleme değeri bu eşik değerini aşarsa, tetikleyici denilen olay meydana gelir; aksi durumda nöron için bozulma denilen olay meydana gelir [15]. Belirli periyotlarla çıkan veya azalan tetiklenen çizgiler ve bunların aralıkları, gerçek değer sayısını temsil eder. Bu sayıların yorumlanması, ASUSA modelinin yapısında kullanılan kodlama ve kod çözme yöntemleri ile yapılır. Ani sivri uçlu (ani darbeli) nöronlar, model içinde meydana gelen her geçici sinyali hesaba katar ancak hemen işlemez. Sinyalin işlenmesi için belirli bir eşiğin aşılması, sivri uçlu nöronların onu beklemesi ve eşik aşılır aşılmaz sinyali işlemesi gerekir. Sonuç olarak, artan veya azalan bir sinyal çıkışı üretir. Böylece, artan veya azalan sinyaller kodlama şemaları oluşturulur [15,16]. Sinyallerin hem darbe (sivri uçlu) frekansı hem de darbe aralığı dikkate alınır ve kodlar bir sayı dizisine karşılık gelecek şekilde yorumlanarak kod çözme olayı gerçekleşir. Darbelerin hesaplanmasında ASUSA modeli, sızdıran entegre ve ateşleme (SEA / LIF) yöntemlerini kullanılır. SEA yöntemi için kullanılan integral formül Denklem 1'de verilmiştir. Denklem 1'deki değişkenler; I: akım, V: volt, C: kondansatör, R: direnç ve t: zaman değerini temsil eder [17].

$$(t) - \frac{V_m(t)}{R_m} = C_m \frac{\partial Vm(t)}{\partial t} \qquad (1)$$

ASUSA, YSA modeline benzer derin katmanlar ve gizli ağ yapılarından oluşmaktadır; fakat YSA modeli gibi sürekli bir çıktı üretmeyen karmaşık yapılardır. Bu model YSA modellerine göre daha masraflıdır. Çünkü ASUSA modeli sinirsel durumları simülasyon olarak yorumlayabilmektedir (Ör; NEST, BindsNet, Brian ve GENESIS) [18]. ASUSA, genel olarak; giriş katmanı, gizli katmanlar ve çıkış katmanından oluşmaktadır ve bu durum Şekil 1'de gösterilmiştir. Burada, giriş katmanı girdi olarak aldığı görüntüyü önceden işler ve özellikler çıkarır. Özellik kümesi daha sonra gizli katmanlara aktarılır ve özellikler gizli katmanlara yayıldıkça, daha karmaşık bir eğitim sürecine girerler. ASUSA karmaşık yapıyı çözümleyebilmek için her bir döngüde ağırlık güncellemeleri yapar ve geri yayılım yaklaşımını kullanır. Sınıflandırma sürecinde, kolayca yorumlanamayan bir ikili çıktı üretir ve her bir nöronun yalnızca yakındaki nöronlarla ilgilendiğini gösteren, sivri uçlu nöronların uzaysal öğrenimini artırır. Bu çalışmada kullanılan sınıflandırma yöntemi, Sinaptik etkinlik fonksiyon tabanlı sızdıran entegre ve ateşleme nöronu (SEFRON)'dur [19].

SEFRON, popülasyon yaklaşımı ile tasarlanmış ve geçici kodlamaların yer aldığı bir sınıflandırıcı modeldir. SEFRON, ani artış sayacı kullanmaz bunun yerine en erken atış süresini kullanır. Ayrıca, giriş ve çıkış nöronları arasında zamanla değişen ağırlıkları (tek bir ağırlık değil) eğitim sürecinde kullanır. SEFRON, öğrenmeyi kolaylaştırmak ve sınıflandırma sürecine katkı sağlaması için spike-timed plasticity (STDP) öğrenme kurallını yapısında kullanır. STDP, ASUSA modelinin giriş ve çıkış nöronlarının zamana dayalı bağlantı ayarlarını gerçekleştirir. En erken atış süresini gerçekleştiren girdi verisi çıkış sınıfı ile etiketlendirilir [19]. ASUSA, ani bir tepki modeli olarak görünür ve her nöron, periyodu boyunca yalnızca bir kez ateşlenir. Ateşleme oranı dağılımı Denklem 2 'ye göre hesaplanır. Bu denklemde, x girdi katmanı, y = f (x) çıktı katmanı, N nöron sayısıdır. R_{max}, ateşleme hızını; XX koordinatındaki nöronlara bitişik nöronların sayısını ve δ sabit bir değerini temsil eder. ASUSA' da her gecikme süresi, ön-sinaptik ateşlendiği zaman ile son-sinaptik yükselmeye başladıktan sonraki zaman arasındaki fark olarak tanımlanır. Ek olarak, bu modelde öğrenme hızı, ön-sinaptik ve son-sinaptik ateşleme zamanı arasındaki fark gecikmeyi değiştirme işlemidir [19,20].

$$f_x(x') = R_{max} e^{\frac{cos(\frac{2\pi}{N}(XX))}{\delta^2}} \qquad (2)$$

ASUSA modeli Jeyasothy ve ark.'nın SEFRON adı verdikleri açık kaynak kodları kullanılarak tasarlanan bir yaklaşımdır. Bu çalışmada tüm analizler SEFRON modelinin açık kaynak kodları güncellenerek gerçekleştirilmiştir [19].

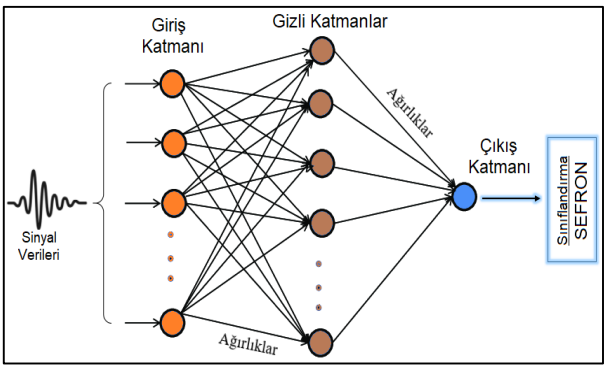

Şekil 1. ASUSA modelinin genel adımları; giriş katmanı, gizli katmanlar ve çıktı katmanı

Şekil 1 incelendiğinde sayısal değerler içeren sinyal verileri hazırlanan modelin giriş katmanına verilir ve buradaki nöronlar, ağırlık parametreleri içeren gizli katmanlar ile eşleştirilerek hesaplanır ve aktivasyon fonksiyonlarından geçirilerek çıkış katmanına ulaştırılır. Çıkış katmanındaki özellikler SEFRON modeli ile taşıdığı değere göre sınıflandırılır. Önerilen yaklaşımın genel tasarımı Şekil 2'de verilmiştir.

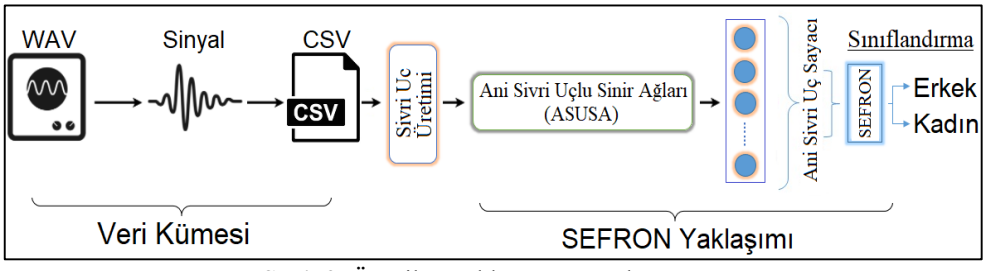

Şekil 2. Önerilen yaklaşımın genel tasarımı

Şekil 2 incelendiğinde ses aygıtlarından alına ses verileri csv formatına dönüştürülür. Bu verilerden daha sonra sivri uç üretimi yapılır ve ASUSA ağına verilir. Bu ağda elde edilen özellik parametreleri SEFRON yaklaşımı kullanılarak sınıflandırılır. Tablo 2'de kullanılan SEFRON modelinin parametre değerleri görülmektedir.

Tablo 2. Veri kümesini oluşturan akustik özellikler

Özellik	Açıklama
Popülasyon kodlama şemasındaki alıcı alan nöron sayısı	18
Ön-sinaptik artış aralığı (ms)	3
Son-sinaptik artış aralığı (ms)	4
Son-sinaptik ateşleme süresi (ms)	2
Zaman adım hassasiyeti	0,01
Ağırlık güncellemesinin öğrenme oranı	0,56
Zamanla değişen ağırlıktaki çekirdeğin sigması (ms)	0,5
Ani tepki fonksiyonunun zaman sabiti (ms)	3
Maksimum devir (dönem) sayısı	100
STDP öğrenme penceresinin zaman sabiti Label	1,8

Tablo 2' incelendiğinde SEFRON modelinin en önemli parametre değerlerinden olan alıcı nöron sayısı sınıf sayısının 2 olması ve veri sayısının da yüksek olmaması nedeniyle 18 olarak ayarlanmıştır. Farklı nöron sayıları ile denemeler yapılmış en uygun sayının 18 olduğu tespit edilmiştir. Kadın ve erkek seslerinin tespiti için önerilen bu modelde sinaptik artışı 2 ila 4 ms aralığında denemeler yapılarak seçilmiştir. Maksimum 100 dönem sayısıyla önerilen modelin tepkileri incelenmiştir.

3. Bulgular

Çalışmanın analiz süreci MATLAB 2020 yazılımı kullanılarak gerçekleştirildi. Donanımsal gereksinimler; işlemci Intel® Core i5 4200M 2.5 GHz, grafik kartı belleği 2 GB, geçici bellek 6 GB ve 64 bitlik Windows 10 işletim sistemi kullanılmıştır. Deneysel analizlerin sonuçlarını elde edebilmek için karışıklık matrisi kullanılmıştır ve bu matrisin metrik parametreleri şunlardır; duyarlılık, özgüllük, hassasiyet, f-skor ve doğruluktur. Metrik değerlerinin hesaplanmasında Denklem 3 ile Denklem 7 arasındaki formüller kullanıldı. Bu denklemlerde kullanılan değişkenler; doğru pozitif (DP), doğru negatif (DN), yanlış pozitif (YP), yanlış negatif (YN) anlamına gelmektedir [21–24].

$$\text{Duyarlılık (Duy.)} = \frac{DP}{DP + YN} \tag{3}$$

$$\text{Özgüllük (Özg.)} = \frac{DN}{DN + YP} \tag{4}$$

$$\text{Hassasiyet (Has.)} = \frac{DN}{DN + YP} \tag{5}$$

$$\text{F} - \text{skor (f} - \text{skr)} = \frac{2xDP}{2xDP + YP + YN} \tag{6}$$

$$\text{Doğruluk (Dğr.)} = \frac{DP + DN}{DP + YN + YP + DN} \tag{7}$$

Çalışmanın deneysel analizinde ses sinyallerinden oluşan veri kümesi, "csv" uzantılı dosya formatına dönüştürüldü. Ardından veri kümesi %30'u test verisi olarak ve %70'i eğitim verisi olarak iki gruba ayrıldı. Eğitim ve test verileri önerilen yaklaşım modeli ile eğitildi. Eğitim için devir (dönem) sayısı 100 seçildi. Model eğitimi, her bir devir sayısı için yaklaşık 121 saniye sürdü ve toplam da önerilen modelin eğitimi 12100 saniyede tamamlandı. Eğitim ve test verilerinin eğitim grafikleri Şekil 3'te gösterildi. Önerilen modelin kayıp grafikleri Şekil 3(a)'da ve genel doğruluk grafikleri ise Şekil 3(b)'de gösterildi.

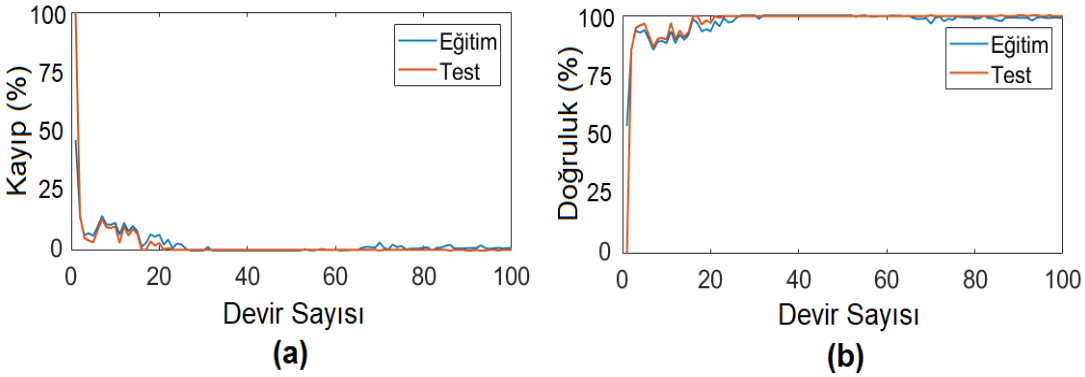

Şekil 3. Önerilen yaklaşımın eğitim ve test grafikleri; a) kayıp grafikleri, b) genel doğruluk grafikleri

Deneysel analizde eğitim ve test verilerinden elde edilen karışıklık matrisler Şekil 4'te gösterilmiştir. Test verilerinin karışıklık matris değerleri Şekil 4(a)'da ve eğitim verilerinin karışıklık matris değerleri Şekil 4(b)'de verilmiştir.

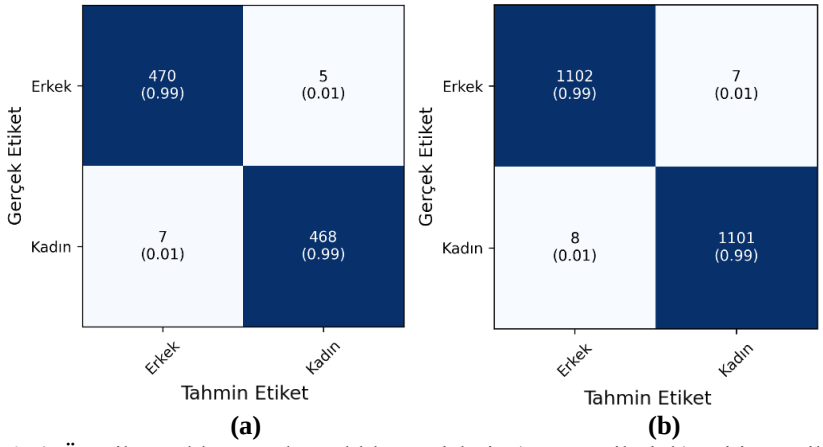

Şekil 4. Önerilen yaklaşımın karışıklık matrisleri; a) test verileri, b) eğitim verileri

Test verilerinin karışıklık matris değerleri kullanılarak elde edilen metrik tabanlı analiz sonuçları Tablo 3'te verilmiştir. Eğitim verilerinin analiz sonucunda elde edilen genel doğruluk başarısı %98,92 ve test verilerinin analiz sonucunda elde edilen genel doğruluk başarısı %98,84 olarak tespit edilmiştir.

Tablo 3. Önerilen yaklaşımda kullanılan SEFRON modelinin parametreleri ve değerleri

Parametre	Sınıf	Duy.	Özg.	Has.	f-skr	Genel Dğr.
Test	Erkek	98,73	98,74	98,84	98,84	98,84
	Kadın	98,73	98,94	98,95	98,84	
Eğitim	Erkek	99,01	98,83	98,83	98,92	98,92
	Kadın	98,83	99,01	99,01	98,92	

Tablo 3 incelendiğinde önerilen modelin ses tanımada yüksek başarı elde edildiği görülmektedir. Cinsiyete göre yaklaşık hemen hemen aynı oranlarda performans gösterdiği görülmektedir. Eğitim aşamasının performans ortalaması %98,92 olurken test aşaması %98,84 olarak tespit edilmiştir.

4. Tartışma

Çeşitli biyometrik verilerden çıkartılan özellikleri kullanarak bireylerin cinsiyet tespiti, teknolojik gelişmelerin paralelinde mümkün hale gelmiştir. Biz bu çalışmada, İngilizce dili konuşanlar arasından elde edilen ses sinyallerini işleyerek ani sivri uçlu ağlar ile eğitimini gerçekleştirilmiştir. ASUSA modeli derin öğrenme modellerine göre daha zahmetli bir mimari

yapısına sahiptir ve çeşitli platformlarda yazılımcılar tarafından geliştirilmektedir. ASUSA modeli ile standart veri kümeleri (MNİST, NİST, CİFAR, vb.) kullanılarak analizler gerçekleştirmişlerdir. Fakat diğer veri kümeleri (imgeler, sinyaller vb.) üzerinde literatürde çalışmalar sınırlıdır. ASUSA modeli ile cinsiyet tanıma sürecinde veri kümelerinden elde edilen akustik özellikler kullanarak başarılı bir sonuç elde edilmiştir. Aynı veri kümesini kullanarak analizler gerçekleştiren diğer çalışmalar hakkında bilgiler Tablo 4'te verilmiştir.

Tablo 4. Önerilen yaklaşımda kullanılan SEFRON modelinin parametreleri ve değerleri

Çalışma	Yıl	Model/Yöntem	Genel Dğr. (%)
Buyukyilmaz ve Cibikdiken [6]	2016	ESA / Çok Katmanlı Algılayıcı (ÇKA)	96.74
Livieris, Pintelas ve Pintelas [25]	2019	Yarı denetimli öğrenme	98.42
Kacamarga ve ark. [26]	2019	ÇKA / Sigmoid	96.80
Önerilen bu çalışma	2022	SEFRON	98.84

Büyükyılmaz ve Cibikdiken [6], ESA modeli ile ÇKA sınıflandırıcısını birlikte kullandıkları melez bir yaklaşım kullanarak %96.74 oranında başarı elde etmişlerdir. Kacamarga ve ark. [26], ÇKA modelini tam bağlantılı katmanlar ile birlikte kullanarak %96.80 oranında başarı elde etmişlerdir. İki çalışmada benzeri bir model önerdikleri için elde ettikleri başarılar yaklaşık çıkmıştır. Livieris, Pintelas ve Pintelas [25], yarı denetimli kendinden etiketli algoritma yöntemini kullanarak cinsiyet tespit başarısını %98.42'ye yükseltmiştir. Önerdiğimiz model ile ESA modellerinden farklı bir yaklaşım kullanarak cinsiyet tespit başarısı %98,84'e çıkartılmıştır. Aynı veri kümesini kullanan çalışmalarda önerilen yaklaşımlara kıyasla, ASUSA modelinin başarısı daha iyi performans sergilediği görülmüştür.

5. Sonuç ve Öneri

Ses sinyallerini kullanarak insanların özelliklerini ayırt etmek mümkündür. Bu özelliklerden biri de cinsiyet ayrımının ses sinyalleri üzerinde gerçekleştirilmesidir. Günümüzde, derin öğrenme modelleri ile insan sesinden elde edilen akustik özellikleri kullanarak istenilen bilgiyi elde etmek mümkündür. Akustik özellikler ile bireylerin cinsiyet türünün doğru bir şekilde tespit edilebilmesi ve %90 üzerinde başarılı sonuçlar alınabilmektedir. Bu çalışmada akustik özellikler kullanılarak, sivri uçlu model ile cinsiyet tespitini %98,84 başarı ile ayırt edilmesi gerçekleştirildi. Önerilen yaklaşım, performans anlamında başarılı sonuçlar üretilmiştir. Önerilen yaklaşımın dezavantajlı yönü ise, diğer ESA modellerine göre daha fazla zaman kaybı olmasıdır. Bu durum, SEFRON modelinin darbelerin (sivri uçlu) oluşmasına kadar beklenen sürelerden kaynaklanmaktadır. Ayrıca SEFRON modelinin bir diğer dezavantajlı yönü olarak Tablo 2'de belirtilen parametre değerleri farklı veri kümelerinde değişkenlik göstermesidir. Bu durum, modelin başarılı sonuç alabilmesini geciktirebilmektedir. Neticede, ASUSA modeli gelişime açık bir modeldir ve bu problemlerin minimize edilmesi yakın zamanda mümkündür.

Gelecek çalışmalarda, farklı veri kümeleri üzerinde derin öğrenme modelleri ile sivri uçlu yaklaşımlar birlikte tasarlanarak analizlerin gerçekleştirilmesi planlanmaktadır.

Araştırma ve Yayın Etiği Beyanı

Yapılan çalışmada araştırma ve yayın etiğine uyulmuştur.

Kaynaklar

[1] C. Pernet and P. Belin, "The Role of Pitch and Timbre in Voice Gender Categorization", *Frontiers in Psychology*, vol. 3, 2012. Doi: 10.3389/fpsyg.2012.00023.

[2] V. Cartei and D. Reby, "Effect of Formant Frequency Spacing on Perceived Gender in Pre-Pubertal Children's Voices", *PLoS ONE*, vol. 8, no. 12, p. e81022, 2013. Doi: 10.1371/journal.pone.0081022.

[3] M. Poon and M. Ng, "The role of fundamental frequency and formants in voice gender identification", *Speech, Language and Hearing*, vol. 18, no. 3, pp. 161-165, 2014. Doi: 10.1179/2050572814y.0000000058.

[4] V. Skuk, L. Dammann and S. Schweinberger, "Role of timbre and fundamental frequency in voice gender adaptation", *The Journal of the Acoustical Society of America*, vol. 138, no. 2, pp. 1180-1193, 2015. Doi: 10.1121/1.4927696.

[5] R. Alkhawaldeh, "DGR: Gender Recognition of Human Speech Using One-Dimensional Conventional Neural Network", *Scientific Programming*, vol. 2019, pp. 1-12, 2019. Doi: 10.1155/2019/7213717.

[6] M. Buyukyilmaz and A. Cibikdiken, "Voice Gender Recognition Using Deep Learning", *Proceedings of 2016 International Conference on Modeling, Simulation and Optimization Technologies and Applications (MSOTA2016)*, 2016. Doi: 10.2991/msota-16.2016.90.

[7] E. Salomons and P. Havinga, "A Survey on the Feasibility of Sound Classification on Wireless Sensor Nodes", *Sensors*, vol. 15, no. 4, pp. 7462-7498, 2015. Doi: 10.3390/s150407462.

[8] G. Archana and M. Malleswari, "Gender identification and performance analysis of speech signals", *2015 Global Conference on Communication Technologies (GCCT)*, 2015. Doi: 10.1109/gcct.2015.7342709.

[9] S. İleri, a. Karabina and E. KILIÇ, "Konuşmacı Cinsiyetinin Tespitinde Değişik Normalizasyon Tekniklerinin Kıyaslanması", *Mehmet Akif Ersoy Üniversitesi Uygulamalı Bilimler Dergisi*, vol. 2, no. 2, pp. 1-12, 2018. Doi: 10.31200/makuubd.410625.

[10] D. Doukhan, J. Carrive, F. Vallet, A. Larcher and S. Meignier, "An Open-Source Speaker Gender Detection Framework for Monitoring Gender Equality", *2018 IEEE International Conference on Acoustics, Speech and Signal Processing (ICASSP)*, 2018. Doi: 10.1109/icassp.2018.8461471.

[11] P. Wang and J. Hu, "A hybrid model for EEG-based gender recognition", *Cognitive Neurodynamics*, vol. 13, no. 6, pp. 541-554, 2019. Doi: 10.1007/s11571-019-09543-y.

[12] M. Pfeiffer and T. Pfeil, "Deep Learning With Spiking Neurons: Opportunities and Challenges", *Frontiers in Neuroscience*, vol. 12, 2018. Doi: 10.3389/fnins.2018.00774.

[13] J. Lobo, J. Del Ser, A. Bifet and N. Kasabov, "Spiking Neural Networks and online learning: An overview and perspectives", *Neural Networks*, vol. 121, pp. 88-100, 2020. Doi: 10.1016/j.neunet.2019.09.004.

[14] K. Becker, "Gender Recognition by Voice", *Kaggle.com*, 2022. [Online]. Doi: https://www.kaggle.com/primaryobjects/voicegender. [Accessed: 01- Apr- 2022].

[15] M. Toğaçar, B. Ergen and Z. Cömert, "Detection of weather images by using spiking neural networks of deep learning models", *Neural Computing and Applications*, vol. 33, no. 11, pp. 6147-6159, 2020. Doi: 10.1007/s00521-020-05388-3.

[16] A. Sboev, A. Serenko, R. Rybka and D. Vlasov, "Solving a classification task by spiking neural network with STDP based on rate and temporal input encoding", *Mathematical Methods in the Applied Sciences*, vol. 43, no. 13, pp. 7802-7814, 2020. Doi: 10.1002/mma.6241.

[17] A. Tavanaei, M. Ghodrati, S. Kheradpisheh, T. Masquelier and A. Maida, "Deep learning in spiking neural networks", *Neural Networks*, vol. 111, pp. 47-63, 2019. Doi: 10.1016/j.neunet.2018.12.002.

[18] M. Stimberg, R. Brette and D. Goodman, "Brian 2, an intuitive and efficient neural simulator", *eLife*, vol. 8, 2019. Doi: 10.7554/elife.47314.

[19] A. Jeyasothy, S. Sundaram and N. Sundararajan, "SEFRON: A New Spiking Neuron Model With Time-Varying Synaptic Efficacy Function for Pattern Classification", *IEEE Transactions on Neural Networks and Learning Systems*, vol. 30, no. 4, pp. 1231-1240, 2019. Doi: 10.1109/tnnls.2018.2868874.

[20] X. Wang, X. Lin and X. Dang, "A Delay Learning Algorithm Based on Spike Train Kernels for Spiking Neurons", *Frontiers in Neuroscience*, vol. 13, 2019. Doi: 10.3389/fnins.2019.00252.

[21] S. Sayyad, M. Shaikh, A. Pandit, D. Sonawane and S. Anpat, "Confusion Matrix-Based Supervised Classification Using Microwave SIR-C SAR Satellite Dataset", *Communications in Computer and Information Science*, pp. 176-187, 2021. Doi: 10.1007/978-981-16-0493-5_16.

[22] M. Toğaçar, Ergen B. Biyomedikal Görüntülerde Derin Öğrenme ile Mevcut Yöntemlerin Kıyaslanması. Fırat Üniversitesi Mühendislik Bilim Derg 2019;31:109–21.

[23] E. Basaran, Z. Comert, A. Sengur, U. Budak, Y. Celik and M. Togacar, "Chronic Tympanic Membrane Diagnosis based on Deep Convolutional Neural Network", *2019 4th International Conference on Computer Science and Engineering (UBMK)*, 2019. Doi: 10.1109/ubmk.2019.8907070.

[24] W. Alsaggaf, Z. Cömert, M. Nour, K. Polat, H. Brdesee and M. Toğaçar, "Predicting fetal hypoxia using common spatial pattern and machine learning from cardiotocography signals", *Applied Acoustics*, vol. 167, p. 107429, 2020. Doi: 10.1016/j.apacoust.2020.107429.

[25] I. Livieris, E. Pintelas and P. Pintelas, "Gender Recognition by Voice using an Improved Self-Labeled Algorithm", *Machine Learning and Knowledge Extraction*, vol. 1, no. 1, pp. 492-503, 2019. Doi: 10.3390/make1010030.

[26] M. Kacamarga, T. Cenggoro, A. Budiarto, R. Rahutomo and B. Pardamean, "Analysis of Acoustic Features in Gender Identification Model for English and Bahasa Indonesia Telephone Speeches", *Procedia Computer Science*, vol. 157, pp. 199-204, 2019. Doi: 10.1016/j.procs.2019.08.158.

Bitlis Eren Üniversitesi Fen Bilimleri Dergisi
BİTLİS EREN UNIVERSITY JOURNAL OF SCIENCE
ISSN: 2147-3129/e-ISSN: 2147-3188
VOLUME: 11 NO: 2 PAGE: 478-489 YEAR: 2022
DOI: 10.17798/bitlisfen.1033852

İçerisinde Dik Bölmeler Bulunan Trapez bir Kanalda Bölme Yüksekliğinin Akış ve Isı Transferine Etkisinin İncelenmesi

Selma AKÇAY[1*]

[1]*Çankırı Karatekin Üniversitesi, Mühendislik Fakültesi, Makine Mühendisliği Bölümü, 18100 Çankırı (ORCID: 0000-0003-2654-0702)*

Keywords: Trapez kanal, Dik bölme, Nanoakışkan, Isı transferi, Sayısal çalışma.

Öz

Bu çalışmada, üst duvarında dik bölmeler olan, alt duvarı trapez şeklinde bir kanalda, bölme yüksekliğinin akış ve ısı transferine etkisini nanoakışkan ve taban akışkan için sayısal olarak incelenmiştir. Nanoakışkan olarak TiO_2 nanopartiküllerin su içerisinde süspansiyonu kullanılmış ve partikül hacim oranı, φ=%1 sabit kalmıştır. Sayısal çalışma, Hesaplamalı Akışkanlar Dinamiği (HAD) tabanlı FLUENT 15.0 programı ile gerçekleştirilmiştir. Kanalın üst yüzeyi adyabatiktir ve alt trapez yüzeyi sabit sıcaklıkta (T_w=360K) korunmuştur. İki farklı bölme yüksekliği (t=H/2 ve t=2H/3) kullanılarak 200≤Re≤1200 Reynolds sayıları için nanoakışkanın ve taban akışkanın Nusselt sayısı (Nu), sürtünme faktörü (f) ve termo-hidrolik performansı (THP) hesaplanmıştır, ayrıca çalışma bölmesiz kanal akışı ile de karşılaştırılmıştır. Kanalda, farklı parametrelerde hız ve sıcaklık görüntüleri elde edilmiştir. Sayısal sonuçlar, trapez bir kanalda bölmelerin yüksekliğine ve nanoakışkana bağlı olarak ısı transferinin önemli ölçüde iyileştiğini, ancak sürtünmenin de bir miktar arttığını göstermiştir. En yüksek THP, bölmesiz kanalda taban akışkana göre, TiO_2-su nanoakışkanda Re=400 ve t=2H/3 bölme yüksekliğinde 1,95 olarak elde edilmiştir.

Investigation of Effects of Baffle Heights on Flow and Heat Transfer in a Trapezoidal Channel with Vertical Baffles

Keywords: Trapezoidal channel, Vertical baffle, Nanofluid, Heat transfer, Numerical study.

Abstract

In this study, the effects of baffle heights on the flow and heat transfer in a trapezoidal channel with vertical baffles on the upper wall and trapezoidal shaped the lower wall were numerically investigated for nanofluid and base fluid. The suspension of TiO_2 nanoparticles in water was used as nanofluid and the particle volume fraction was kept constant at φ = 1%. Numerical study was realized with Computational Fluid Dynamics (CFD) based FLUENT 15.0 program. The upper surface of the channel was adiabatic and the lower trapezoidal surface was kept at a constant temperature (T_w = 360K). Nusselt number (Nu), friction factor (f) and thermo-hydraulic performance (THP) of nanofluid and base fluid were calculated for 200 ≤ Re ≤ 1200 Reynolds numbers using two different baffle heights (t = H/2 and t = 2H/3) and also the study was compared to channel flow without baffles. The velocity and temperature contours were obtained in different parameters in the channel. The numerical results showed that in a trapezoidal channel, the heat transfer improved significantly depending on the height of the baffles and nanofluid, but the friction also increased slightly. The highest THP was obtained as 1.95 in the TiO_2-su nanofluid flow at Re = 400 and t = 2H/3 baffle height in the channel without baffles according to the base fluid.

*Sorumlu yazar: selmaakcay@karatekin.edu.tr
Geliş Tarihi: 07.12.2021, Kabul Tarihi: 01.06.2022

1. Giriş

Son yıllarda, termal cihazların etkinliğini düşürmeden ısı transfer hızını artırmak için pek çok araştırma yapılmaktadır. Bu çalışmalarda, pasif ve aktif ısı transferi iyileştirme yöntemlerinden yararlanılmaktadır. Aktif yöntemlerin harici bir güç gerektirmesi ve hareketli mekanik parçalar içermesi nedeniyle, daha ekonomik ve güvenli olan pasif yöntemlere olan ilgi artmıştır. Pasif yöntemler, hem maliyet hem de enerji tasarrufu sağladığı için oldukça avantajlıdır. [1-3]. Yüzey alanını artırmayı hedefleyen çeşitli dalgalı yüzey geometrileri, oldukça yaygın kullanılan pasif yöntemlerin başında gelmektedir. Bu konuda, farklı dalgalı geometriye sahip kanalların akış ve ısı transfer davranışları incelenmiştir. Yapılan çalışmalarda, dalgalı yüzeylerin kendi kendine akış salınımı meydana getirmesi ve yüzey alanını artırması nedeniyle bir miktar basınç düşüşü ile birlikte ısı transferini oldukça artırdığı bildirilmiştir [4-9].

Isı transfer performansını daha fazla iyileştirmek için birden fazla pasif yöntem birlikte kullanılmaktadır. Bunun için kanal yüzeylerine pin-fin, bölme ilavesi, bükülmüş bantlar, kanatçıklar ve girdap üreteçleri gibi uygulamalarla ısıl performansın artırılması hedeflenmiştir. Türbülatör etkisi gösteren bu uygulamaların, akış karışımını iyileştirerek ısı transferini artırdığı bildirilmektedir Bu nedenle, pasif yöntemler, ısı değiştiricileri, buharlaştırıcılar, kondansatörler, gaz türbini kanadı soğutma kanalları, nükleer reaktörler, güneş hava ısıtıcıları gibi pek çok mühendislik uygulamalarında tercih edilmektedir [10-29]. Sriromreun vd. [30] dikdörtgen bir kanalda Z tipi saptırma türbülatörlerinin ısıl performans üzerindeki etkilerini deneysel ve sayısal olarak analiz etmişler ve düz kanallarla karşılaştırıldığında Z bölmelerin ısıl performans üzerinde önemli bir etkiye sahip olduğunu göstermişlerdir. Turgut ve Kızılırmak [31] bir kanal içerisinde farklı eğim açılarına ($30^o \leq \alpha \leq 150^o$) sahip bölmelerin akış ve ısı transferini türbülanslı akış için sayısal olarak incelemişler ve en yüksek ısıl performansın $\alpha=150^o$'de elde edildiğini bulmuşlardır. Promvonge vd. [32] deneysel çalışmalarında, eğimli at nalı bölmelerinin kullanıldığı bir kanalda, ısı transfer iyileşmesinin düz kanallara kıyasla yaklaşık %92-208 oranında arttığını bunun yanında sürtünme faktörünün ise 1.76-6.37 kat arttığını bildirmişlerdir. Kumar vd. [33] çoklu V-tipi bölmeler kullanarak güneş hava kanalının ısı transfer davranışını deneysel olarak incelemişlerdir. Sahel vd. [34] yaptıkları sayısal bir çalışma ile dikdörtgen bir kanalda kullanılan farklı bölme tasarımının ısı transferini %65 oranında iyileştirdiğini bildirmişlerdir. Alnak [35] farklı açılarda yerleştirilmiş dikdörtgen bölmelere sahip çapraz oluklu üçgen kanallarda ısı transferi ve basınç düşüşünü k-ε türbülans modelini kullanarak analiz etmiştir. Çalışmanın sonucunda, Re = 6000 için 90° dikdörtgen bölmeli oluklu kanalın Nusselt sayısı, 60° değerinden %52,8 daha yüksek olduğunu, ayrıca Re = 1000 için basınç düşüşü değeri 90° bölme açısına göre 60° dikdörtgen bölme açısına sahip kanal için %65,97 daha düşük olduğunu göstermiştir. Karabulut [36] alt duvarı üçgen şeklinde dalgalı, üst duvarı düz ve üçgen bölmeler içeren bir kanalda bölme yüksekliği ve bölme açılarının ısı transfer performansına etkilerini k-ε türbülans modeli ile analiz etmiştir. Çalışma sonucunda 60^o bölme açısında Nusselt sayısının daha yüksek ve basınç düşüşünün ise daha düşük olduğunu belirtmiştir. Olfian vd. [37] güneş hava ısıtıcı kanalının alt ve üst duvarlarına yerleştirilmiş farklı açılarda dikdörtgen ve V-şeklinde bölmelerin termal etkinliğini sayısal olarak analiz etmişler ve en yüksek etkinliğin, yüksek Reynolds sayısında (Re=2000) 90^o açıda dikdörtgen bölmelerin olduğu durum için elde edildiğini bildirmişlerdir. Saha [38] dikdörtgen bir mikro kanalda düz ve elmas şeklinde olan iki farklı bölme geometrisinde hava akışının ısı transfer karakteristiğini $10000 \leq Re \leq 50000$ aralığında sayısal olarak incelemiş ve elmas şeklinde bölmeler bulunan kanalda ısı transferinin, sürtünme faktörünün ve ortalama Nusselt sayısının daha yüksek olduğunu bildirmiştir. El Habet vd. [39] dikdörtgen bir kanalda sıralı ve kademeli yerleştirilmiş delikli bölmelerin termo-hidrolik performansını türbülanslı akış şartları için deneysel ve sayısal olarak incelemişler ve sonuçta düz kanala göre yaklaşık %410 ısı transferinde iyileşme sağlandığını ve sıralı bölme durumunda daha yüksek basınç kaybı olduğunu ve en yüksek termal etkinlik oranının kademeli katı bölmelerin olduğu durumda elde edildiğini bildirmişlerdir. Salhi vd. [40] dairesel kesitli düz bir boru içerisine dikdörtgen ve üçgen kesitli uzunlamasına yerleştirilmiş bölmelerin akış ve ısı transferini k-ε türbülans modeli ile incelemişler ve sonuçta dikdörtgen kesitli bölmelerin ısı transferi açısından üçgen kesitli bölmelerden daha iyi olduğunu göstermişlerdir. Bidari vd. [41] ısı değiştiricilerinde ısı transfer performansını iyileştirmek için kullanılan farklı tipteki vorteks üreteçlerin etkilerini inceleyen bir derleme çalışması sunmuşlardır. Phu vd. [42] farklı açılarda ve mesafelerde bölmelerin bulunduğu hava kollektörlerinde akış ve ısı transfer davranışını standart k-ε türbülans modelinde iki boyutlu olarak

incelemişler ve en yüksek termal etkinliğin 90º bölme açısında elde edildiğini bildirmişlerdir.

Endüstri uygulamalarında yaygın olarak kullanılan su, etilen glikol gibi sıvılar, düşük termal özeliklere sahiptir. Bu tür geleneksel soğutma sıvılarının termo-fiziksel özeliklerini iyileştirmek için yüksek ısıl iletkenliğe sahip nano boyutlu katı parçacıkların temel akışkana ilave edilmektedir. Yapılan araştırmalarda, nanoakışkanlar ile diğer pasif teknikler birlikte kullanılmış ve akışkanın ısı taşınım katsayısının oldukça arttığı bildirilmiştir [43-51]. Heshmati vd. [52] farklı nanoakışkanlar (Al_2O_3, CuO, ZnO ve SiO_2) için değişen partikül hacim oranlarında ($0 \leq \varphi \leq 0.04$) farklı geometrilerdeki oluklu bölme ile geriye dönük bir basamak üzerinde $50 \leq Re \leq 400$ için karışık taşınım ısı transferini sayısal olarak incelemişlerdir. Sonuçta, yüksek partikül hacim oranları ve küçük nanopartikül çapına sahip nanoakışkanların ısı transferini önemli ölçüde iyileştirdiğini, ancak eğimli bölmelerin yüksek basınç düşüşüne yol açtığını bildirmişlerdir. Ajeel vd. [53] kavisli oluklu bir kanalda L şekilli bölmelerin varlığında ZnO-su nanoakışkanın akış ve ısı transferi özelliklerini türbülans akış rejiminde sayısal olarak incelemişler ve bölmelerin varlığına bağlı olarak akışta girdap oluşumunun artan türbülans etkileri ile ısı transferini arttırdığını bildirmişlerdir. Phu vd. [54] farklı eğim açılarına, yüksekliğine ve mesafelerine sahip bölmeler içeren güneş kollektör kanallarında Cu-su nanoakışkanın termohidrolik davranışını sonlu hacim metodu ile araştırmışlardır. Isı transferi ve basınç düşüşünün bölme parametrelerinden oldukça etkilendiğini ve en düşük termohidrolik performansın 30º bölme açısında elde edildiğini bildirmişlerdir. Manca vd. [55] yüzeylerine ısı akısı uygulanmış bir kanalda, farklı yiv yüksekliklerinde, %0 ila %4 nanopartikül hacim oranlarında Al_2O_3–su nanokışkanın türbülanslı akışta ısı transferini araştırmışlardır. Çalışmalarının sonucunda, Reynolds sayısı ve partikül hacim oranı arttıkça ısı transferinin iyileştiğini ve pompalama gücünün de arttığını bildirmişlerdir. Menni vd. [56] ısı değiştiricilerinin termal performansını iyileştirmek amacıyla yaptıkları çalışmada, kanal içinde farklı açılarda bölmeler kullanarak nanoakışkanların kombine etkisini dinamik ve ısıl davranışlarını türbülanslı akış şartlarında incelemişler ve en yüksek termal iyileşme faktörünün, yüksek Reynolds sayısında dik bölmelerin kullanıldığı durumda elde edildiğini belirtmişlerdir.

Literatür çalışmasından da anlaşıldığı üzere, farklı geometrilere sahip dalgalı kanallarda, ilave edilen bölmelerin farklı düzenlemelerinde ısı transferine etkisini inceleyen pek çok araştırma bulunmaktadır. Bu çalışmaların temel amacı yüksek ısı transferi elde ederken basınç düşüşünün de düşük olmasını sağlamaktır. Çok değişik dalgalı kanal geometrisinin bulunması, kanala ilave edilen bölmelerin geometrisi, bölme açısı, akış türü, akışkan yapısı, akışkan sıcaklığı, nanoakışkan parametreleri gibi incelenen parametrelerin oldukça fazla olması, en iyi parametreleri bulma yönünde araştırmaları genişletmiştir. Literatürde üst yüzeyi düz ve bölmeler ilave edilmiş, alt yüzeyi trapez şeklinde dalgalı bir kanal geometrisinin kullanılmadığı tespit edilmiş ve bu geometride bölme yüksekliğinin ve nanoakışkanların akış ve ısı transfer davranışlarını inceleyen herhangi bir çalışmaya rastlanmamıştır. Bu nedenle bu çalışmada, üst duvarı düz ve içerisine dik bölmeler ilave edilmiş, alt yüzeyi trapez şeklinde dalgalı olan bir kanalda farklı bölme yüksekliğinin ve TiO_2-su nanoakışkanın ısı transferi ve sürtünme faktörü üzerindeki etkisi laminer akış şartlarında sayısal olarak incelenmiştir.

2. Materyal ve Metod

2.1. Sayısal Model ve Kullanılan Eşitlikler

Şekil 1'de, çalışmada kullanılan kanalın geometrisi verilmiştir. Kanalın yüksekliği (H), 19 mm, trapez şeklinde dalgalı kanal uzunluğu L_2=12H, iki bölme arasındaki mesafe S=2H olarak alınmıştır. Kanal girişinde ve çıkışında, L_1=12H uzunluğunda ısıtılmamış düz bir bölüm vardır. Kanalın alt yüzeyi toplam 6 adet trapez bölümü içermektedir. Trapez kanalı oluşturan her bir kısmın uzunluğu b=H/2 ve trapez kısmın yüksekliği a=H/3 olarak alınmıştır. İki farklı bölme yüksekliği t=H/2 ve t=2H/3 kullanılmıştır. Bölmeler kanalın üst yüzeyine dik olarak yerleştirilmiş ve sayısal modeldeki diğer geometrik parametreler sabit tutulmuştur. Çözümler, Reynolds sayısının belirli bir aralığı ($200 \leq Re \leq 1200$) için uygulanmıştır.

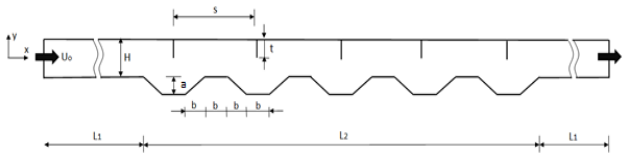

Şekil 2. Sayısal modelin geometrisi

Kanal içindeki akışkanın sıkıştırılamaz, tek fazlı ve Newtoniyen tip olduğu düşünülmüştür. Akış, daimi, iki boyutlu ve laminer akış şartlarında incelenmiştir. Akışkan olarak, TiO_2 nanopartiküllerin sudaki homojen süspansiyonu kullanılmıştır. Işınımla ısı transferi, yerçekimi ve viskoz terimler ihmal

edilmiştir. Bu kabullere göre kullanılan eşitlikler aşağıda verilmiştir.
Süreklilik denklemi:

$$\frac{\partial u_i}{\partial t} + \nabla(\rho u) = 0 \quad (1)$$

Momentum denklemi:

$$\frac{\partial u_i}{\partial t} + \frac{\partial (u_i u_j)}{\partial x_i} = -\frac{\partial p}{\partial x_i} + \frac{1}{Re}\nabla^2 u_j = 0 \quad (2)$$

Enerji denklemi:

$$\frac{\partial T}{\partial t} + u_i \frac{\partial T}{\partial x_i} = \frac{1}{PrRe}\nabla^2 T = 0 \quad (3)$$

Çalışmada geometrik parametreler dışında kullanılan diğer parametreler, akışkan hızı (Reynolds sayısı, Re), partikül hacim oranı (φ), yüzey sürtünme faktörü (f), Nusselt sayısı (Nu) ve Termo-hidrolik performans (THP) olarak belirlenmiştir. Bu parametrelere ait eşitlikler aşağıda verilmiştir.
Reynolds sayısı (Re):

$$Re = \frac{\rho u D_h}{\mu} \quad (4)$$

Yerel Nusselt sayısı (Nu_x):

$$Nu_x = \frac{h D_h}{k_f} \quad (5)$$

$$q" = h\Delta T_{lm} \quad (6)$$

$$\Delta T_{lm} = \frac{(T_i - T_o)}{ln\left(\frac{T_w - T_i}{T_w - T_o}\right)} \quad (7)$$

Ortalama Nusselt sayısı (Nu):

$$Nu = \frac{1}{L}\int_0^L Nu_x \, dx \quad (8)$$

Burada, ρ akışkan yoğunluğunu, μ dinamik viskoziteyi, D_h hidrolik yarıçapı, k_f ise akışkanın ısı iletkenlik katsayısını temsil etmektedir. u akışkanın ortalama hızını, h ısı taşınım katsayısını, q" ısı akısını, L toplam kanal uzunluğunu ve ΔT_{lm} ise logaritmik sıcaklık farkını göstermektedir. T_i, T_o ve T_w sırasıyla akışkanın kanala giriş sıcaklığını, akışkanın kanal çıkışındaki ortalama sıcaklığını ve kanalın trapez dalgalı yüzeylerinin sıcaklığını ifade etmektedir.
Isı transfer performansı (η):

$$\eta = \frac{Nu_n}{Nu_o} \quad (9)$$

Burada, Nu_n nanoakışkan için hesaplanan Nusselt sayısını, Nu_o ise taban akışkan için hesaplanan Nusselt sayısını göstermektedir.

Kanal içerisindeki bölmelerin varlığı nedeniyle ve nanopartiküllere bağlı olarak kanalda önemli basınç düşüşü meydana gelmektedir. Nanoakışkanların viskozitesinin taban akışkana göre yüksek olması nedeniyle ısı transfer iyileştirme çalışmalarında sürtünme faktörüyle birlikte değerlendirilmesi gerekmektedir.
Sürtünme faktörü (f):

$$f = \frac{2\Delta P D_h}{\rho u^2 L} \quad (10)$$

Burada, ΔP kanal giriş ve çıkışındaki basınç farkıdır. Sürtünme faktörüne bağlı olarak boyutsuz sürtünme katsayısı (Γ) tariflenmiştir.

$$\Gamma = f_n / f_o \quad (11)$$

Burada, f_n nanoakışkan için hesaplanan sürtünme faktörünü, f_o ise taban akışkan için hesaplanan sürtünme faktörünü göstermektedir. Isı transfer performansı ve boyutsuz sürtünme faktörüne bağlı olarak termo-hidrolik performans (THP) tanımlanmıştır.

$$THP = \frac{(Nu_n/Nu_o)}{(f_n/f_o)^{1/3}} \quad (12)$$

Table 1. TiO_2 nanopartikülün ve suyun termo-fiziksel özelikleri [59]

	Yoğunluk ρ [kg/m³]	Özgül ısı C [J/kgK]	Isıl iletkenlik k [W/mK]	Dinamik viskozite μ [kg/ms]
Su	997.1	4179	0.613	0.001004
TiO_2	4250	686.2	8.9538	-

Nanoakışkan olarak TiO_2-su süspansiyonu kullanılmış olup nanopartikül hacim oranı (φ=%1) sabit tutulmuştur. Nanopartiküllerin temel akışkan içine homojen bir şekilde dağıldığı kabul edilmiş ve nanoakışkanların termo-fiziksel özeliklerinden yoğunluk Eşitlik (13) ve özgül ısı Eşitlik (14) ile [57],

ısıl iletkenlik Eşitlik (15) ile viskozite Eşitlik (16) ile [58] hesaplanmıştır. Temel akışkan olarak su kullanılmıştır. TiO_2 nanopartikülün ve suyun termo-fiziksel özelikleri Tablo 1'de verilmiştir [59].

$$\rho_{nf} = (1-\varphi)\rho_{bf} + \varphi\rho_{pt} \quad (13)$$

$$C_{nf} = (1-\varphi)C_{bf} + \varphi C_{pt} \quad (14)$$

$$k_{nf} = k_{bf}\frac{\left[k_{pt} + 2k_{bf} - 2\varphi(k_{bf} - k_{pt})\right]}{\left[k_{pt} + 2k_{bf} + \varphi(k_{bf} - k_{pt})\right]} \quad (15)$$

$$\mu_{nf} = \mu_{bf}[123\varphi^2 + 7.3\varphi + 1] \quad (16)$$

2.2. Sayısal Prosedür

Problemin çözümü için Hesaplamalı Akışkanlar Dinamiği (HAD) tabanlı, FLUENT 15.0 [60] programı kullanılmıştır. Denklemlerin ayrıklaştırılmasında sonlu hacim yaklaşımı uygulanmıştır. Bu eşitlikler, SIMPLE algoritması kullanılarak çözülmüş ve taşınım ile yayınım terimleri ikinci dereceden ileri fark şeması kullanılarak ayrıklaştırılmıştır. Yakınsama kriteri olarak süreklilik ve momentum eşitliklerinde 10^{-4}, enerji eşitliği için 10^{-6} alınmıştır.

Akışkanın kanala T_i=293K sıcaklığında girdiği kabul edilmiştir. Kanal girişinde, "hız giriş" sınır şartı, çıkışında ise "dışa akış" sınır şartı tariflenmiştir. Bölmelerin bulunduğu kanalın üst yüzeyleri adyabatik olarak kabul edilmiş, trapez alt yüzeyler ise 360K eş sıcaklığında korunmuştur. Kanalın giriş ve çıkışındaki düz bölümler ile dik bölmeler için kaymaz ve adyabatik duvar sınır şartı uygulanmıştır.

Tablo 2. Hücre sayısı ile Nusselt sayısının yüzde değişimi (bölmelerin olmadığı durum için)

Hücre sayısı	Nusselt sayısı (Nu)			
	Re = 200	Değişim (%)	Re = 800	Değişim (%)
78504	2.345	-	7.612	-
125564	2.893	23.36	8.785	15.41
176432	3.274	13.17	9.538	8.57
213664	3.408	4.09	9.731	2.02
258323	3.425	0.50	9.745	0.14
310544	3.427	0.06	9.748	0.03

Sayısal modelin çizimi ve hücrelere bölme işlemi Gambit yazılımı ile yapılmıştır. Hücreler, tri/pave ağ yapısı ile oluşturulmuş ve hücre mesafe aralığı 0.3 olarak alınmıştır. Çözümlerin ağ yapısından bağımsız olduğunu belirlemek için farklı hücre sayılarında çözümler tekrarlanmış ve her bir çözüm için Nusselt sayıları hesaplanmıştır. Bu hesaplamalara göre 213664 hücre sayısından sonra Nusselt sayıları arasındaki farkın %2'den daha küçük olduğu belirlenmiştir. Bu nedenle, 213664 eleman sayısı sayısal modele uyarlanmıştır. Hücre eleman sayısı ile Nusselt sayısının yüzde olarak değişimi Tablo 2'de, eleman sayısı ile Nu değişimi ise Şekil 2 ile gösterilmiştir.

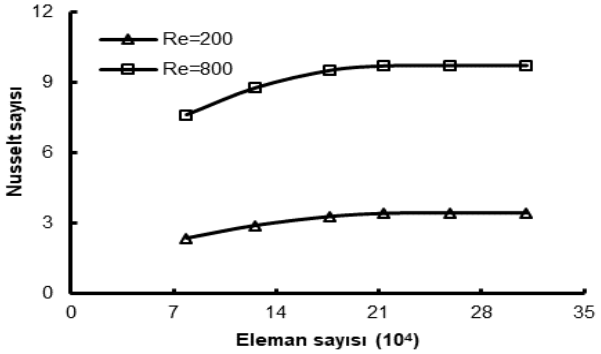

Şekil 2. Eleman sayısı ile Nusselt sayısının değişimi (bölmelerin olmadığı durum için)

3. Bulgular ve Tartışma

Sayısal çalışmanın geçerliliğini belirlemek için, yapılan çözümler Meyer ve Abolarin [61] tarafından gerçekleştirilen deneysel çalışma sonuçları ile karşılaştırılmıştır.

Tablo 3. Bu çalışmada ve Ref. [61]'de x/D mesafesi ile h, ısı taşınım katsayısının (W/m^2K) değişimi

x/D	h, ısı transfer katsayısı, Ref. [61]	h, ısı transfer katsayısı, Bu çalışma	% fark
20	402	407	1,2285
33	421	429	1,8648
46	435	454	4,1850
60	472	485	2,6804
73	504	514	1,9455
86	495	521	4,9904
100	485	545	11,0092
113	532	572	6,9930
126	552	586	5,8020
140	580	582	0,3436
153	591	582	-1,5464
166	585	586	0,1706
180	575	578	0,5190
193	581	578	-0,5190
206	576	581	0,8606
220	590	582	-1,3746
233	585	585	0,0000
246	595	595	0,0000
260	600	600	0,0000
270	640	601	-6,4892

Bunun için, D_h=19mm çapında ve yüzeylerine q" = 2kW sabit ısı akısı uygulanmış düz bir kanalda Re=1331 değeri için kanal boyunca x/D mesafeleri ile h, ısı taşınım katsayıları hesaplanmıştır. Literatüre ait deneysel sonuçlar ile bu çalışmaya ait sayısal sonuçlar, Tablo 3'te verilmiş olup, her iki çalışma sonuçları arasındaki uyum Şekil 3'te gösterilmiştir.

Bu bölümde, içerisinde dik bölmeler bulunan bir kanalda nanoakışkanın akış ve ısı transfer mekanizması üzerindeki etkileri farklı parametreler için incelenmiştir. Nanopartikül hacim oranı φ=0.01 olarak sabit tutulmuş ve Reynolds sayısı (Re) değiştirilmiştir. Kanal içerisinde iki farklı bölme yüksekliği ile bölmelerin olmadığı durumda hem nanoakışkan akışı hem de taban akışkan için Nusselt sayısı, boyutsuz sürtünme faktörü ve termo-hidrolik performans değerleri hesaplanmıştır.

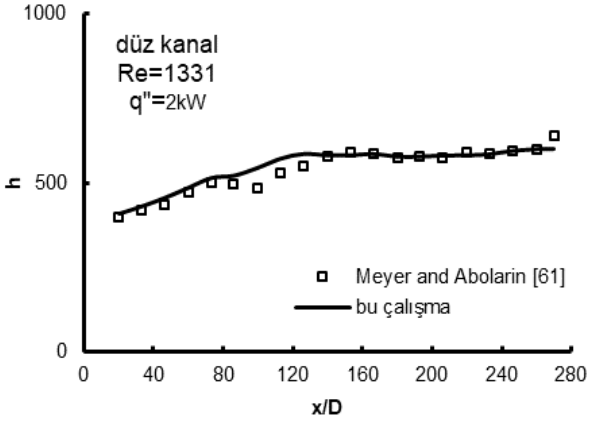

Şekil 3. Sayısal çözümün geçerliliği

Şekil 4a'da bölmesiz ve iki farklı bölme yüksekliğine sahip kanal için TiO_2-su nanoakışkanın taban akışkana göre Re ile ısı transfer performansının değişimi verilmiştir. Bölmesiz kanal ve taban akışkan akışı (t=0 ve φ=0) referans olarak gösterilmiştir. Her durum aynı geometrideki taban akışkan ile oranlanarak ısı transfer performansı hesaplanmıştır. Burada bölmeli kanaldaki nanoakışkan akışının, bölmeli kanaldaki taban akışkana göre ısı transferi incelenmiştir. Şekil 4a'dan Re arttıkça ısı transfer performansının da arttığı görülmektedir. Düşük Re'de (Re≤500) bölmesiz kanal ve t=H/2 bölme yüksekliğindeki kanal için birbirine yakın ısı transfer performansı elde edilirken en yüksek ısı transfer performansı Re=1200 için t=2H/3 bölme yüksekliğinde yaklaşık 1,12 olarak elde edilmiştir. Şekil 4b'de bölmesiz ve iki farklı bölme yüksekliğine sahip kanal için TiO_2 nanoakışkanın bölmesiz kanal için taban akışkana göre Re ile ısı transfer performansının değişimi verilmiştir. Bölmesiz kanal ve taban akışkan akışı (t=0 ve φ=0) referans olarak gösterilmiştir. Her durum için bölmesiz kanaldaki taban akışkan akışı ile oranlanarak ısı transfer performansı hesaplanmıştır. Burada hem nanoakışkan akışının ve hem de bölmelerin varlığının ısı transferine etkileri araştırılmıştır. Şekil 4b'den Re arttıkça ısı transfer performansının yaklaşık Re=600'e kadar arttığı, daha sonra hafif bir azalma eğilimi gösterdiği görülmektedir. Kanal içinde bölmelerin varlığı, bölmesiz duruma göre ısı transferini oldukça iyileştirdiği, bölme yüksekliği artıkça ısı transfer performansının da arttığı gözlenmektedir. En yüksek ısı transfer performansı Re=400 için t=2H/3 bölme yüksekliğinde yaklaşık 2,66 olarak elde edilmiştir. Şekil 4a ve 4b'den ısı transfer iyileşmesinde nanoakışkandan ziyade bölmelerin varlığının daha etkili olduğu tespit edilmiştir.

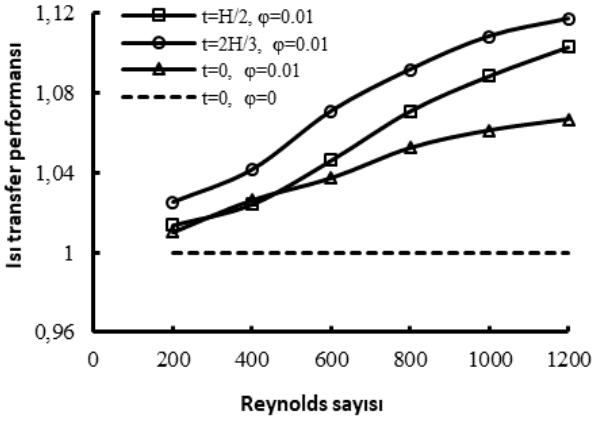

a

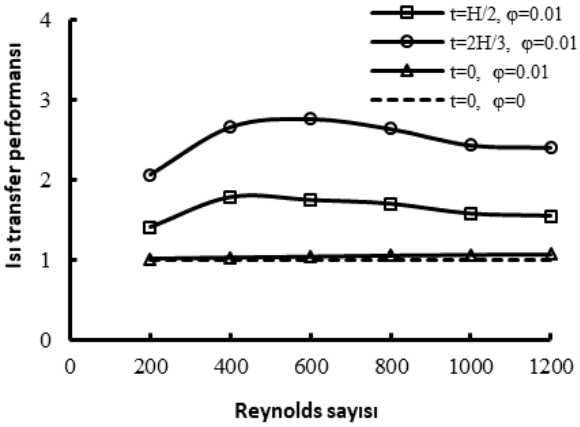

b

Şekil 4. Nonakışkanların ısı transfer performansı,
a) Bölmeli kanalda taban akışkan referans alındığında,
b) Bölmesiz kanalda taban akışkan referans alındığında

Şekil 5a'da bölmesiz ve iki farklı bölme yüksekliğine sahip kanal için TiO_2-su nanoakışkanın, taban akışkana göre Reynolds sayısı ile boyutsuz sürtünme faktörünün değişimi verilmiştir. Bölmesiz kanal ve taban akışkan akışı (t=0 ve φ=0) referans

olarak gösterilmiştir. Her durum, bölmesiz kanalda taban akışkan ile oranlanarak sürtünme faktörü hesaplanmıştır. Burada nanoakışkan akışının boyutsuz sürtünme faktörüne etkileri incelenmiştir. Şekil 4a'dan Reynolds sayısı arttıkça sürtünme faktörünün de arttığı görülmektedir. En yüksek boyutsuz sürtünme faktörü Re=1200 için t=2H/3 bölme yüksekliğinde yaklaşık 1.26 olarak elde edilmiştir.

Şekil 5b'de bölmesiz ve iki farklı bölme yüksekliğine sahip kanal için TiO_2-su nanoakışkanın bölmesiz kanal için taban akışkana göre Reynolds sayısı ile sürtünme faktörünün değişimi verilmiştir. Her durum, bölmesiz kanaldaki taban akışkan akışı ile oranlanarak boyutsuz sürtünme faktörü hesaplanmıştır. Burada hem nanoakışkan akışının ve hem de bölmelerin sürtünme faktörüne olan etkileri araştırılmıştır.

Şekil 5b'den Reynolds sayısı ve bölme yüksekliği arttıkça sürtünme faktörünün arttığı görülmektedir. Kanal içinde bölmeler ve nanoakışkan, bölmesiz duruma göre sürtünme değerini oldukça artırmaktadır. En yüksek sürtünme faktörü Re=1200 için t=2H/3 bölme yüksekliğinde yaklaşık 5,43 olarak elde edilmiştir. Şekil 5a ve 5b'den nanoakışkanın sürtünme faktörünü kabul edilebilir bir miktarda artırdığı, kanal içerisindeki bölmelerin ise çok daha fazla basınç düşüşüne neden olduğu tespit edilmiştir.

Şekil 6a'da bölmesiz ve iki farklı bölme yüksekliğine sahip kanal için TiO_2–su nanoakışkanın taban akışkana göre Reynolds sayısı ile THP değişimi gösterilmiştir. Bölmesiz kanal ve taban akışkan akışı (t=0 ve φ=0) referans olarak alınmıştır. Her durum aynı geometrideki taban akışkan ile oranlanarak THP elde edilmiştir. Burada nanoakışkan akışının THP'a etkileri araştırılmıştır. Şekil 6a'dan Reynolds sayısı arttıkça THP değerinin de arttığı görülmektedir. Bütün THP değerleri referans değerin üzerinde elde edilmiştir. Bu da kanal içerisindeki sürtünmeye rağmen ısı transferinin önemli derecede iyileştiğini göstermektedir. Bölmesiz kanalda nanoakışkan akışında (t=0 ve φ=0.01) THP eğrisi, en yüksek bölme uzunluğundaki nanoakışkan akışında (t=2H/3 ve φ=0.01) elde edilen THP eğrisi ile oldukça benzer olduğu görülmüştür. Bunun nedeni t=0 ve φ=0.01 durumuna göre t=2H/3 ve φ=0.01 durumu için kanal içerisindeki basınç düşüşünün çok daha yüksek olmasıdır. Şekil 6b'de bölmesiz ve iki farklı bölme yüksekliğine sahip kanal için TiO_2-su nanoakışkanın bölmesiz kanal için taban akışkana göre Reynolds sayısı ile THP değişimi verilmiştir. Her durum için bölmesiz kanaldaki taban akışkan akışı ile oranlanarak THP değerleri elde edilmiştir. Burada hem nanoakışkan akışının ve hem de bölmelerin, THP'a etkileri araştırılmıştır.

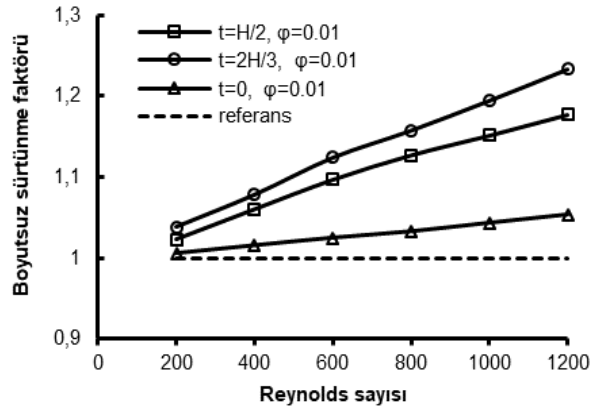

a

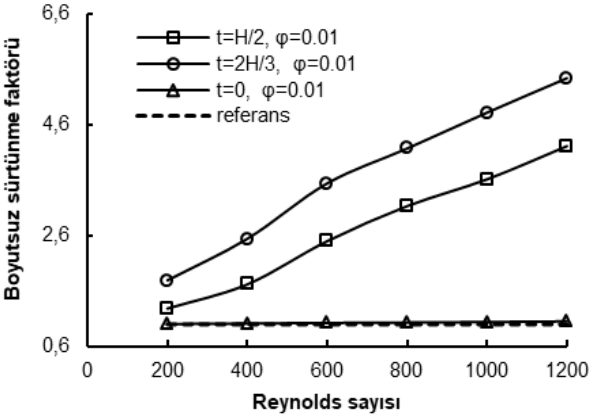

b

Şekil 5. Nanoakışkanların sürtünme faktörü,
a) Bölmeli kanalda taban akışkan referans alındığında,
b) Bölmesiz kanalda taban akışkan referans alındığında

Şekil 6b'den Re=400 değerine kadar, bölme yüksekliği arttıkça THP değeri artmaktadır. Re=400 değerinden sonra her iki bölme yüksekliği için THP eğrisi hızlı bir şekilde düşmektedir. Re≥1000 değerinden sonra t=H/2 bölme yüksekliğinde THP eğrisi referans değerin altına düşmektedir. En yüksek THP, Re=400 ve t=2H/3 bölme yüksekliğinde yaklaşık 1,95 olarak elde edilmiştir. Trapez kanalda nanoakışkanların ve bölmelerin varlığı, THP değerini bölmesiz kanaldaki taban akışkana göre oldukça artırmaktadır.

Trapez kanaldaki akış ve ısı transfer mekanizmasına farklı yükseklikteki bölmelerin etkilerini gözlemleyebilmek için çeşitli parametrelerde, kanalda hız ve sıcaklık dağılımları elde edilmiştir.

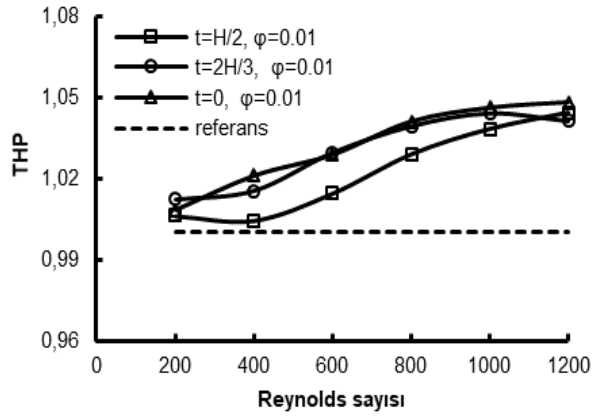

a

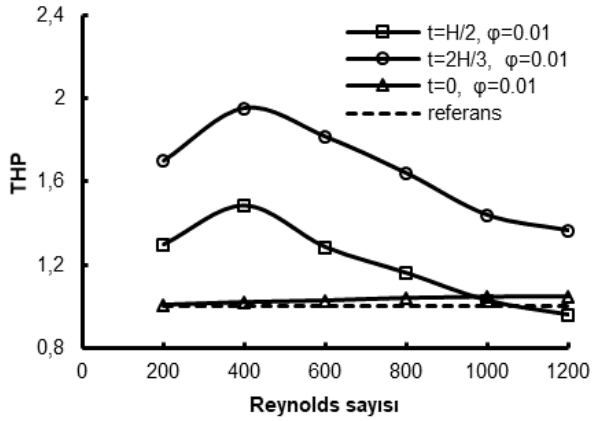

b

Şekil 6. Taban akışkana göre nanoakışkanların THP, **a)** Bölmeli kanalda, **b)** Bölmesiz kanalda

Şekil 7 ile Re=400 ve taban akışkan için bölmesiz ve iki farklı bölme yüksekliğinde hız görüntüleri (a), sıcaklık dağılımları (b) ve vorteks yapıları (c) gösterilmiştir. Şekil 7a'dan kanal içerisindeki bölmelerin trapez şeklindeki bir kanalda akış yapısını önemli derecede etkilediği gözlenmektedir. Trapez bir kanalda bölmelerin varlığı, akış salınımına neden olmaktadır. Bölmelerin yüksekliği arttıkça akış salınımları da artmaktadır. Ayrıca her bölme arasında ikincil akış döngülerinin oluştuğu ve bu döngülerin bölme yüksekliğine bağlı olarak arttığı görülmektedir. İkincil akış yapıları, akış karışımında önemli bir etkiye sahiptir. Akış karışımı ne kadar homojen olursa ısı transfer hızı da o derece artacaktır. Kanal içerisindeki bölmeler laminer alt tabakayı kırarak ısıl direnci azaltmaya yardımcı olmaktadır. Her bölmeden sonra bu durum periyodik olarak tekrar ettiğinden akışın homojen bir şekilde karışımını sağlamaktadır. Kanal yüzeyine yakın sıcak akışkanın daha soğuk akışkan ile teması, ısı transfer performansını da iyileştirecektir. Şekil 7b'de bölme yüksekliğinin sıcaklık dağılımı üzerindeki etkileri gösterilmiştir. Yüksek sıcaklığa sahip trapez yüzeylerde, bölme yüksekliği arttıkça yüzey sıcaklığının azaldığı görülmektedir. Şekil 7c'de ise bölmesiz ve farklı bölme yükseklikleri için kanal içerisinde oluşan vorteks yapıları verilmiştir. Bölme yüksekliği arttıkça akış içerisinde kopmalar meydana geldiği ve girdap yapılarının arttığı görülmektedir.

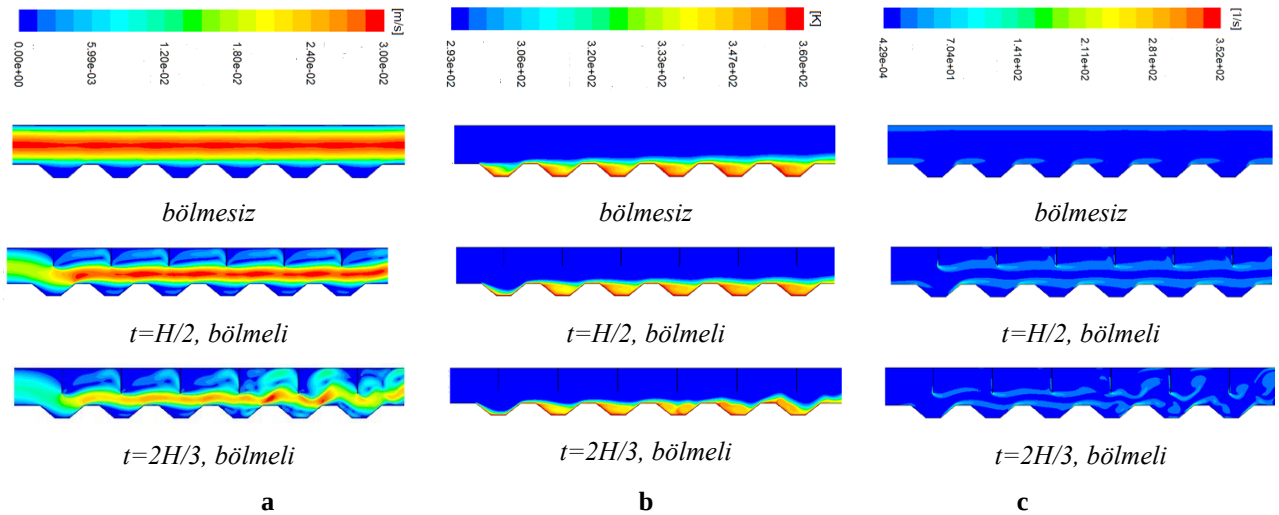

a **b** **c**

Şekil 7. Re=400'de taban akışkan için bölmesiz, t=H/2 ve t=2H/3 bölmeli trapez oluklu kanal görüntüleri, **a)** hız görüntüleri, **b)** sıcaklık dağılımları, **c)** vorteks yapıları

4. Sonuç ve Öneriler

Bu çalışmada, içerisinde dik bölmeler bulunan trapez bir kanalda farklı bölme yüksekliğinin TiO_2-su nanoakışkan ve taban akışkan akışında ısı transferine etkileri sayısal olarak incelenmiştir. Akış ve ısı transferi üzerinde, bölme yüksekliğinin, nanoakışkanın ve Reynolds sayısının etkileri analiz edilmiştir.

Sayısal çalışmada elde edilen önemli sonuçlar aşağıda listelenmiştir:

a. Akış yapısının ve sıcaklık alanlarının, kanal geometrisinden, nanoakışkandan ve Reynolds sayısından oldukça etkilendiği gösterilmiştir.
b. Bölme yüksekliği arttıkça kanal içinde akış salınımı ve ikincil akış döngülerinin arttığı gözlenmiştir.
c. Re ve bölme yüksekliğinin artmasıyla ısı transfer performansının önemli derecede arttığı, ancak sürtünme faktörünün de arttığı görülmüştür.
d. Bölmesiz kanalda taban akışkana göre, en yüksek ısı transfer performansı Re=400 değeri ve t=2H/3 bölme yüksekliği için nanoakışkan akışında yaklaşık 2.66 olarak elde edilmiştir.
e. En yüksek sürtünme faktörü Re=1200 ve t=2H/3 bölme yüksekliği için nanoakışkan akışında yaklaşık 5.43 bulunmuştur.
f. En iyi termo-hidrolik performans Re=400 ve t=2H/3 bölme yüksekliği için nanoakışkan akışında yaklaşık 1,95 olarak elde edilmiştir.

Öneriler: Kanal içerisindeki bölmelerin açısı, bölmeler arası mesafeler, akışkan hızı ve kanal geometrisi değiştirilerek farklı nanoakışkanlar ve değişen partikül hacim oranları için yeni çalışmalar yapılabilir ve bu parametrelerin akış ve ısı transferine etkileri araştırılabilir. Ayrıca, yapılan sayısal çalışma sonuçları, ileride yapılacak deneysel çalışma sonuçları ile karşılaştırılabilir.

Araştırma ve Yayın Etiği Beyanı

Yapılan çalışmada araştırma ve yayın etiğine uyulmuştur

Kaynaklar

[1] Y. G. Lei, Y. L. He, R. Li, and Y. F. Gao, "Effects of baffle inclination angle on flow and heat transfer of a heat exchanger with helical baffles," *Chem. Eng. Process*, vol. 47, no. 12, pp. 2336–2345, November 2008. doi: 10.1016/j.cep.2008.01.012

[2] O. Keklikcioglu and V. Ozceyhan, "Thermohydraulic performance evaluation for horizontal tube by using combination of modified coiled wire inserts and graphene nanoplatelet-water nanofluids," *Int. Commun. Heat and Mass Transfer*, vol. 123, Art. no. 105206, April 2021. doi: 10.1016/j.icheatmasstransfer.2021.105206

[3] U. Akdag, S. Akcay, and D. Demiral, "Heat transfer enhancement with laminar pulsating nanofluid flow in a wavy channel," *Int. Commun. Heat and Mass Transfer*, vol. 59, pp. 17–23, December 2014. doi: 10.1016/j.icheatmasstransfer.2014.10.008

[4] S. Skullong, P. Promvonge, C. Thianpong, and M. Pimsarn, "Thermal performance in solar air heater channel with combined wavy-groove and perforated-delta wing vortex generators," *Appl. Therm. Eng.*, vol. 100, pp. 611–620, May 2016. doi: 10.1016/j.applthermaleng.2016.01.107

[5] U. Akdag, S. Akcay, and D. Demiral, "Heat transfer enhancement with nanofluids under laminar pulsating flow in a trapezoidal-corrugated channel," *Progress in Computational Fluid Dynamics, An International Journal*, vol. 17, no. 5, pp. 302-312, September 2017.

[6] R. Kumar, V. Goel, and A. Kumar, "Investigation of heat transfer augmentation and friction factor in triangular duct solar air heater due to forward facing chamfered rectangular ribs: A CFD based analysis," *Renew Energy*, vol. 115, pp. 824–835, January 2018. doi: 10.1016/j.renene.2017.09.010

[7] M. E. Nakhchi, "Experimental optimization of geometrical parameters on heat transfer and pressure drop inside sinusoidal wavy channels," *Therm. Sci. Eng. Prog.*, vol. 9, pp. 121–31, March 2019. doi: 10.1016/j.tsep.2018.11.006

[8] A. Kaood and M. A. Hassan, "Thermo-hydraulic performance of nanofluids flow in various internally corrugated tubes," *Chemical Engineering & Processing: Process Intensification*, vol. 154, Art. no. 08043, August 2020. doi: 10.1016/j.cep.2020.108043

[9] Z. Li and Y. Gao, "Numerical study of turbulent flow and heat transfer in cross corrugated triangular ducts with delta-shaped baffles," *Int. J. Heat Mass Transf*., vol. 108, pp. 658–670, May 2017. doi: 10.1016/j.ijheatmasstransfer.2016.12.054

[10] R. Karwa and B. K. Maheshwari, "Heat transfer and friction in an asymmetrically heated rectangular duct with half and fully perforated baffles at different pitches," *Int. Commun. Heat and Mass Transfer*, vol. 36, pp. 264–268, March 2009. doi: 10.1016/j.icheatmasstransfer.2008.11.005

[11] S. Sripattanapipat and P. Promvonge, "Numerical analysis of laminar heat transfer in a channel with diamond-shaped baffles," *Int. Commun. Heat and Mass Transfer*, vol. 36, no. 1, pp. 32-38, January 2009. doi: 10.1016/j.icheatmasstransfer.2008.09.008

[12] S. Kwankaomeng and P. Promvonge, "Numerical prediction on laminar heat transfer in square duct with 30° angled baffle on one wall," *Int. Commun. Heat and Mass Transfer*, vol. 37, pp. 857-866, August 2010. doi:10.1016/j.icheatmasstransfer.2010.05.005

[13] K. Nanan, N. Piriyarungrod, C. Thianpong, K. Wongcharee, S. Eiamsa-ard, "Numerical and experimental investigations of heat transfer enhancement in circular tubes with transverse twisted-baffles," *Heat Mass Transfer*, vol. 52, pp. 2177–2192, October 2016. doi:10.1007/s00231-015-1728-7

[14] O. Keklikcioglu and V. Ozceyhan, "Experimental investigation on heat transfer enhancement of a tube with coiled-wire inserts installed with a separation from the tube wall," *Int. Commun. Heat and Mass Transfer*, vol. 78, pp. 88-94, November 2016. doi: 10.1016/j.icheatmasstransfer.2016.08.024

[15] P. Sriromreun, "Numerical study on heat transfer enhancement in a rectangular duct with incline shaped baffles," *Chem. Eng. Trans*., vol. 57, pp. 1243–1248, 2017. doi: 10.3303/CET1757208

[16] F. Menasria, M. Zedairia, and A. Moummi, "Numerical study of thermohydraulic performance of solar air heater duct equipped with novel continuous rectangular baffles with high aspect ratio," *Energy*, vol. 133, pp. 593-608, August 2017. doi: 10.1016/j.energy.2017.05.002

[17] S. Akcay and U. Akdag, "Parametric investigation of effect on heat transfer of pulsating flow of nanofluids in a tube using circular rings," *Pamukkale University, Journal of Engineering Sciences*, vol. 24, no. 4, pp. 597-604, 2018. doi: 10.5505/pajes.2017.70120

[18] S. Z. Tang, F. L. Wang, Y. L. He, Y. Yu and Z. X. Tong, "parametric optimization of H-type finned tube with longitudinal vortex generators by response surface model and genetic algorithm," *Appl. Energy*, vol. 239, pp. 908–918, April 2019. doi: 10.1016/j.apenergy.2019.01.122

[19] J. A. Modi and M. K. Rathod, "Comparative study of heat transfer enhancement and pressure drop for fin-and-circular tube compact heat exchangers with sinusoidal wavy and elliptical curved rectangular winglet vortex generator," *Int. J. Heat and Mass Transfer*, vol. 141, pp. 310-326, October 2019. doi: 10.1016/j.ijheatmasstransfer.2019.06.088

[20] N. T. Luan and N. M. Phu, "Thermohydraulic correlations and exergy analysis of a solar air heater duct with inclined baffles," *Case Stud. Therm. Eng*., vol. 21, Art. no. 100672, October 2020. doi: 10.1016/j.csite.2020.100672

[21] C. E. Bensaci et al., "Numerical and experimental study of the heat transfer and hydraulic performance of solar air heaters with different baffle positions," *Renew Energy*, vol. 155, pp. 1231–1244, August 2020. doi: 10.1016/j.renene.2020.04.017

[22] D. Wang et al., "Evaluation of the performance of an improved solar air heater with "S" shaped ribs with gap," *Sol. Energy*, vol. 195, pp. 89–101, January 2020. doi: 10.1016/j.solener.2019.11.034

[23] P. Promvonge, P. Promthaisong, and S. Skullong, "Experimental and numerical heat transfer study of turbulent tube flow through discrete V-winglets," *Int. J. Heat and Mass Transfer*, vol. 151, Art. no. 119351, April 2020. doi: 10.1016/j.ijheatmasstransfer.2020.119351

[24] P. Promvonge and S. Skullong, "Thermo-hydraulic performance in heat exchanger tube with V-shaped winglet vortex generator," *Appl. Therm. Eng.*, vol. 164, Art. no. 114424, January 2020. doi: 10.1016/j.applthermaleng.2019.114424

[25] Z. Sun, K. Zhang, W. Li, Q. Chen, and N. Zheng, "Investigations of the turbulent thermal-hydraulic performance in circular heat exchanger tubes with multiple rectangular winglet vortex generators," *Appl. Therm. Eng.*, vol. 168, Art. no. 114838, March 2020. doi: 10.1016/j.applthermaleng.2019.114838

[26] M. E. Nakhchi, M. Hatami, and M. Rahmati, "Experimental investigation of performance improvement of double-pipe heat exchangers with novel perforated elliptic turbulators," *Int. J. Thermal Science*, vol. 168, Art. no. 107057, October 2021. doi: 10.1016/j.ijthermalsci.2021.107057

[27] H. Xiao, P. Liu, Z. Liu, and W. Liu, "Performance analyses in parabolic trough collectors by inserting novel inclined curved-twisted baffles," *Renewable Energy*, vol. 165, pp. 14-27, March 2021. doi: 10.1016/j.renene.2020.11.068

[28] S. W. Chang and T.H. Cheng, "Thermal performance of channel flow with detached and attached pin-fins of hybrid shapes under inlet flow pulsation," *Int. J. Heat and Mass Transfer*, vol. 164, Art. no. 120554, January 2021. doi: 10.1016/j.ijheatmasstransfer.2020.120554

[29] G. Sureandhar, G. Srinivasan, P. Muthukumar, and S. Senthilmurugan, "Performance analysis of arc rib fin embedded in a solar air heater," *Therm. Sci. Eng. Prog.*, vol. 23, Art. no. 100891, June 2021. doi: 10.1016/j.tsep.2021.100891

[30] P. Sriromreun, C. Thianpong, and P. Promvonge, "Experimental and numerical study on heat transfer enhancement in a channel with Z-shaped baffles," *Int. Commun. Heat Mass Transf.*, vol. 39, no. 7, pp. 945–952, August 2012. doi: 10.1016/j.icheatmasstransfer.2012.05.016

[31] O. Turgut and E. Kızılırmak, "Effects of Reynolds number, baffle angle, and baffle distance on 3-D turbulent flow and heat transfer in a circular pipe," *Thermal Science*, vol. 19, no. 5, pp. 1633-1648, 2015. doi:10.2298/TSCI121011045T

[32] P. Promvonge, S. Tamna, M. Pimsarn, and C. Thianpong, "Thermal characterization in a circular tube fitted with inclined horseshoe baffles," *Appl. Therm. Eng.*, vol. 75, pp. 1147–1155, January 2015. doi: 10.1016/j.applthermaleng.2014.10.045

[33] R. Kumar, A. Kumar, R. Chauhan, and M. Sethi, "Heat transfer enhancement in solar air channel with broken multiple V-type baffle," *Case Stud. Therm. Eng.*, vol. 8, pp. 187–197, September 2016. doi: 10.1016/j.csite.2016.07.001

[34] D. Sahel, H. Ameur, R. Benzeguir, and Y. Kamla, "Enhancement of heat transfer in a rectangular channel with perforated baffles," *Appl. Therm. Eng.*, vol. 101, pp. 156–164, May 2016. doi: 10.1016/j.applthermaleng.2016.02.136

[35] D. E. Alnak, "Thermohydraulic performance study of different square baffle angles in cross-corrugated channel," *Journal of Energy Storage*, vol. 28, Art. no. 101295, April 2020. doi: 10.1016/j.est.2020.101295

[36] K. Karabulut, "Heat Transfer and pressure drop evaluation of different triangular baffle placement angles in cross-corrugated triangular channels," *Thermal Science*, vol. 24, no. 1A, pp. 355-365, 2020. doi:10.2298/TSCI190813466K

[37] H. Olfian, A. Z. Sheshpoli, and S. S. M. Ajarostaghi, "Numerical evaluation of the thermal performance of a solar air heater equipped with two different types of baffles," *Heat Transfer*, vol. 49, pp. 1149-1169, May 2020. doi:10.1002/htj.21656

[38] S. Saha, "Numerical study of air-flow phenomena through a baffled rectangular micro-channel," *Journal of Modeling and Optimization*, vol. 13, no. 2, pp. 51-57, 2021. doi:10.32732/jmo.2021.13.2.51

[39] M. A. El Habet, S. A. Ahmed, and M. A. Saleh "Thermal/hydraulic characteristics of a rectangular channel with inline/staggered perforated baffles," *Int. Comm. Heat Mass Tranf.*, vol. 128, Art. no. 105591, Nov. 2021. doi: 10.1016/j.icheatmasstransfer.2021.105591

[40] J. E. Salhi, T. Zarrouk, and N. Salhi, "numerical study of the thermo-energy of a tubular heat exchanger with longitudinal baffles," *Materials Today: Proceedings*, vol. 45, no. 8, pp. 7306-7313, 2021. doi: 10.1016/j.matpr.2020.12.1213

[41] M. V. Bidari, P. B. Nagaraj, and G. Lalagi, "Influence of different types of vortex generators (VGs) to enhance heat transfer performance in heat exchangers: A Review," *Int. J. Ambient Energy*, Oct. 2021, doi.org/10.1080/01430750.2021.1980740.

[42] N. M. Phu, P. B. Thao, and N.V. Hap, "Effective efficiency assessment of a solar air heater having baffles spaced with different successive ratios," *Case Studies in Thermal Engineering*, vol. 28, Art. no 101486, Dec. 2021. doi: 10.1016/j.csite.2021.101486

[43] M. Chandrasekar, S. Suresh, and A. C. Bose, "Experimental studies on heat transfer and friction factor characteristics of Al_2O_3/water nanofluid in a circular pipe under laminar flow with wire coil inserts," *Exp. Therm. Fluid Sci.*, vol. 34, no. 2, pp. 122–30, Feb. 2010. doi: 10.1016/j.expthermflusci.2009.10.001

[44] G. Huminic and A. Huminic, "Heat transfer and flow characteristics of conventional fluids and nanofluids in curved tubes: A Review," *Renew. Sustain. Energy Rev.*, vol. 58, pp. 1327–1347, May 2016. doi: 10.1016/j.rser.2015.12.230

[45] H. Fazeli, S. Madani, and P. R. Mashaei, "Nanofluid forced convection in entrance region of a baffled channel considering nanoparticle migration," *Appl. Therm. Eng*., vol. 106, pp. 293–306, August 2016. doi: 10.1016/j.applthermaleng.2016.06.010

[46] S. Akcay, "Numerical analysis of heat transfer improvement for pulsating flow in a periodic corrugated channel with discrete V-type winglets," *Int. Commun. Heat and Mass Transfer*, vol. 134, Art. no. 105991, May 2022. doi: 10.1016/j.icheatmasstransfer.2022.105991

[47] C. Qi, Y. L. Wan, C. Y. Li, D. T. Han, and Z. H. Rao, "Experimental and numerical research on the flow and heat transfer characteristics of TiO_2-water nanofluids in a corrugated tube," *Int. J. Heat and Mass Transfer*, vol. 115, pp. 1072–1084, Dec. 2017. doi:10.1016/j.ijheatmasstransfer.2017.08.098

[48] S. Akcay, "Numerical analysis of hydraulic and thermal performance of Al_2O_3-water nanofluid in a zigzag channel with central winglets," *Gazi University Journal of Science*, vol. 36, no.2, 2023, (in press), DOI: 10.35378/gujs.1012201.

[49] S. Rashidi, M. Eskandarian, O. Mahian, and S. Poncet, "Combination of nanofluid and inserts for heat transfer enhancement, gaps and challenges," *Journal of Thermal Analysis and Calorimetry*, vol. 135, pp. 437–460, January 2019. doi:10.1007/s10973-018-7070-9

[50] S. Mei, C. Qi, T. Luo, X. Zhai, and Y. Yan, "Effects of magnetic field on thermo-hydraulic performance of Fe_3O_4-water nanofluids in a corrugated tube," *Int. J. Heat and Mass Transfer*, vol. 128, pp. 24–45, January 2019. doi:10.1016/j.ijheatmasstransfer.2018.08.071

[51] S. H. H. Karouei, S.S.M. Ajarostaghi, M.G. Bandpy, and S.R.H. Fard, "Laminar heat transfer and fluid flow of two various hybrid nanofluids in a helical double pipe heat exchanger equipped with an innovative curved conical turbulator," *Journal of Thermal Analysis and Calorimetry*, vol. 143, pp. 1455–1466, January 2021. doi:10.1007/s10973-020-09425-0

[52] A. Heshmati, H. A. Mohammed, and A. N. Darus, "Mixed convection heat transfer of nanofluids over backward facing step having a slotted baffle," *Applied Mathematics and Computation*, vol. 240, pp. 368–386, August 2014. doi.org/10.1016/j.amc.2014.04.058

[53] R. K. Ajeel, K. Sopian, and R. Zulkifli, "Thermal-hydraulic performance and design parameters in a curved-corrugated channel with L-shaped baffles and nanofluid," *Journal of Energy Storage*, vol. 34, Art. no. 101996, Feb. 2021. doi: 10.1016/j.est.2020.101996

[54] N. M. Phu, P.B. Thao, and D.C. Truyen, "Heat and fluid flow characteristics of nanofluid in a channel baffled opposite to the heated wall," *CFD Letters*, vol. 13, no. 1, pp. 33-44, January 2021. doi:10.37934/cfdl.13.1.3344

[55] O. Manca, S. Nardini, and D. Ricci, "A Numerical study of nanofluid forced convection in ribbed channels," *Applied Thermal Engineering*, vol. 37, pp. 280-297, May 2012. doi: 10.1016/j.applthermaleng.2011.11.030

[56] Menni et al., "Enhancement of the turbulent convective heat transfer in channels through the baffling technique and oil/multiwalled carbon nanotube nanofluids," *Numerical Heat Transfer, Part A: Applications*, vol. 79, no. 4, pp. 311-351, Published online: 08 Dec 2020. doi.org/10.1080/10407782.2020.1842846

[57] B. Pak and Y. I. Cho, "Hydrodynamic and heat transfer study of dispersed fluids with submicron metallic oxide particles," *Exp. Heat Transfer*, vol. 11, no. 2, pp. 151–170, 1998. doi:10.1080/08916159808946559

[58] S. Kakac and A. Pramuanjaroenkij, "Review of convective heat transfer enhancement with nanofluids," *Int. J. Heat and Mass Transfer*, vol. 52, pp. 3187–3196, June 2009. doi: 10.1016/j.ijheatmasstransfer.2009.02.006

[59] E. Abu-Nada, Z. Masoud, and A. Hijazi, "Natural convection heat transfer enhancement in horizontal concentric annuli using nanofluids," *Int. Commun. Heat and Mass Transfer*, vol. 35, no. 5, pp. 657-665, May 2008. doi:10.1016/j.icheatmasstransfer.2007.11.004

[60] ANSYS Inc. *ANSYS Fluent User Guide & Theory Guide- Release 15.0*. USA, 2015.

[61] J. P. Meyer and S. M. Abolarin, "Heat transfer and pressure drop in the transitional flow regime for a smooth circular tube with twisted tape inserts and a square-edged inlet," *Int. J. Heat and Mass Transfer*, vol. 117, pp. 11-29, Feb. 2018. doi:10.1016/j.ijheatmasstransfer.2017.09.103

Bitlis Eren Üniversitesi Fen Bilimleri Dergisi
BİTLİS EREN UNIVERSITY JOURNAL OF SCIENCE
ISSN: 2147-3129/e-ISSN: 2147-3188
VOLUME: 11 NO: 2 PAGE: 490-498 YEAR: 2022
DOI: 10.17798/bitlisfen.1036026

Performance Assessment of a Combined Coal Gasification and Methanation System with Particle Swarm Optimization Method

Münür Sacit HERDEM[1], Sercan YALÇIN[2*]

[1]*Department of Mechanical Engineering, Adıyaman University, Adıyaman, 02040, Turkey.*
[2]*Department of Computer Engineering, Adıyaman University, Adıyaman, 02040, Turkey.*
(ORCID: 0000-0003-0079-0041) (ORCID: 0000-0003-1420-2490)

Keywords: Carbon dioxide hydrogenation, Particle swarm optimization, Coal gasification, Methane production

Abstract

Carbon dioxide hydrogenation is a promising method of producing alternative fuels in an environmentally friendly way. Researchers in the current literature have mainly investigated the performance of carbon dioxide hydrogenation systems that use carbon dioxide from various sources and hydrogen from water electrolysis units. In the present study, the performance of a combined coal gasification and methanation unit is investigated to produce methane and power. The carbon dioxide and hydrogen for the methanation unit are provided by the coal gasification system. A Particle swarm optimization (PSO), an optimization-based artificial intelligence method, is applied to optimize the carbon dioxide and hydrogen values here. Therefore, the water electrolysis unit, which needs high amounts of energy, effectively is removed from the system. The results from the studied system showed that it is possible to produce ~225 kilotons of methane annually by using ~946 kilotons of coal per year. In addition, the results revealed that annual carbon dioxide utilization of ~624.3 kilotons is possible. The system efficiency is estimated at around 49%.

1. Introduction

It is significantly important to investigate and develop novel and alternative energy conversion systems because of the increasing energy requirements and adverse environmental effects of fossil fuels [1], [2]. Producing alternative fuels from various sources including coal, biomass, renewable sources, etc., is one of the solutions for governments to enhance energy security, energy independence and the clean production of fuels. One of the most promising ways to produce alternative fuels from different sources is carbon dioxide hydrogenation. Various fuels, including methane, methanol, ethanol, 1-Butanol, 2-Butanol, iso-octanal, dimethyl ether, polyoxy dimethyl ether, synthetic gasoline, paraffinic diesel, and paraffinic kerosene can be produced via carbon dioxide hydrogenation [3]. Various carbon dioxide sources that are produced from coal gasification power plants, coal-fired power plants, gas-fired power plants, refineries and natural gas processing, steel mills, cement production, biogas plants, and direct air capture have been mainly used for carbon dioxide hydrogenation systems in the literature [4]. In addition, the hydrogen requirement for carbon dioxide hydrogenation has been provided by employing water electrolysis [4].

Dieterich et al. [4] reviewed the state of the art of the conversion of hydrogen and carbon dioxide to liquid fuels via power-to-liquid (PtL) processes. They investigated the feasibility of the production of methanol, dimethyl ether, and Fischer-Tropsch fuels via carbon dioxide hydrogenation and PtL processes. Schemme et al. [5] provided a comprehensive overview of the synthesis possibilities and potential of hydrogen and carbon dioxide based alternative fuels for the transport sector. They explained the promising synthesis pathways as well as the technical aspects of the adopted processes to produce alternative fuels (methanol and higher alcohols) for the transport sector. Schemme et al., in their other paper [3], conducted a study to understand the

*Corresponding author: svancin@adiyaman.edu.tr
Received: 13.12.2021, Accepted: 02.06.2022

economic feasibility of the production of various fuels via carbon dioxide hydrogenation. Herdem et al. [6] suggested a novel combined oxyfuel combustion biomass gasification and solar photovoltaic system to produce methanol in an environmentally friendly way. They used carbon dioxide hydrogenation for methanol synthesis. The hydrogen for the methanol synthesis was provided by an alkaline water electrolysis system, while the power requirement of the alkaline water electrolysis system was supplied by the solar photovoltaic and biomass gasification plants, and the remaining power was provided from the electrical grid. Furthermore, the carbon dioxide for the methanol synthesis was provided by the oxyfuel combustion biomass gasification system. Zhang et al. [7] studied the techno-economic optimization of green methanol production from the carbon dioxide hydrogenation system with an integrated solid-oxide electrolysis process. They simulated the system using Aspen Plus and used multi-objective optimization for the techno-economic optimization. Kotowicz et al. [8] performed a thermodynamic analysis of a carbon dioxide hydrogenation system for environmentally friendly methanol production. Hydrogen for the methanol synthesis was provided by water electrolysis. The power requirement of the water electrolysis was provided by a 40 MW wind farm during the night valleys. They [8] also used the captured carbon dioxide from a power plant`s flue gas for renewable methanol production. Eveloy [9] investigated a hybrid solid oxide electrolyzer and oxyfuel combustion system for methane production via carbon dioxide hydrogenation. The system was conceptually designed for synthetic natural gas (methane), power, and heat production. Eveloy developed a thermodynamic model to investigate the operation characteristics and energetic and exergetic performance of the system. Momeni et al. [10] investigated the performance of a synthetic natural gas (methane) production system based on carbon dioxide hydrogenation. They used the carbon dioxide from a natural gas power plant while employing a water electrolysis unit in the system for hydrogen production to produce synthetic natural gas. They estimated the energy and environmental performance of the system as well as the cost of the system. Synthetic fuels and electro-fuels for the transport sector have also been reviewed in terms of production processes and cost in [11] and [12]. However, the estimation of these system inputs sometimes does not produce adequate and accurate results. The use of more up-to-date mathematical models and applications has become essential to increase the efficiency of methane production. Recently, artificial intelligence technologies have been used to make effective and accurate coal gasification and methanation systems and to obtain statistical results [13], [14]. Today, with the discovery of optimization-based technologies such as genetic algorithms and PSO, artificial intelligence methods such as machine learning, artificial neural networks, and even deep learning with feature selection are frequently used for coal methaneization and gasification. In addition, it enables effective energy production and the use of alternative energy sources in life. Azarhoosh et al. [15] simulated and optimized the auto-thermal reforming of methane to synthesis gas using a genetic algorithm. Shamsi et al. [16] presented process simulation and optimization of the coal gasification process in a moving-bed reactor using Pittsburgh No. 8 coal as feed. A simulation was used to estimate solid and gas temperature status and gas composition in the reactor. The methods such as optimization methods, artificial intelligence, and machine learning are applied in many application areas such as health, agriculture, education, sport, finance as well as obtaining optimum energy sources. It has become indispensable for efficiency in various fields to produce the best information from big data or to extract the best or optimum values from energy data [17]. In addition to artificial neural networks (ANNs), machine learning algorithms, ensemble models, and hybrid models could be used to high prediction performance to assess coal gasification and methanation applications. Deep learning algorithms have also been used to predict coal methanation parameters [18]. Due to the high performance of machine learning methods in different disciplines, these methods have been used frequently in various energy fields, especially in the last decade. Researchers have used machine learning algorithms in prediction, and estimation of factors affecting match results [19].

In this study, a preliminary analysis was performed to show the energetic performance of a combined coal gasification and carbon dioxide hydrogenation unit for methane and power production using optimization based Particle Swarm Optimization (PSO). The reason for using PSO as the optimization algorithm in this study is that particle motions are suitable for the optimization of carbon dioxide and hydrogen data. Also, PSO is the most well-known of all metaheuristic methods. Adaptation of this method in this study has already allowed and validated the optimal and optimal results. In addition, a parametric study was conducted to understand the effects of various parameters on the performance of the methanation unit. The simulation of the system was conducted using Aspen Plus.

The innovative contributions and highlights of this study can be listed as follows.

- The main novelty of this study is that the hydrogen produced from the coal gasification system is used as a hydrogen source for carbon dioxide hydrogenation instead of using water electrolysis, as in the other studies in the literature.
- The carbon dioxide is also provided from the coal gasification system for the carbon dioxide hydrogenation unit.
- In this coal gasification and methaneization system, the PSO method has been applied in order to use the carbon dioxide and hydrogen data feeding the reactors in the best and balanced way. In this way, the most effective results were obtained.

The data regarding the coal gasification system was extracted from previous work [20]. The main focus of this study is to investigate the energy efficiency of the combined coal gasification and methanation system and the effects of different operation parameters on the methanation unit. The present study will be useful for researchers as a guide for developing alternative fuel production systems.

2. Material and Method

The simplified schema of the studied system is illustrated in Figure 1. The coal gasification plant is explained in detail in our previous study [20]. The system consists of a coal gasifier unit, an air separation unit, a water gas shift reactor unit, hydrogen sulfur, and carbon dioxide removal units, a pressure swing adsorption unit, an alkaline electrolyser unit, a heat recovery steam generator unit, and a power generation unit. Hydrogen is produced in the system by using the pressure swing adsorption unit, and the alkaline water electrolyser unit, which is powered by the power generation unit. In this study, it is assumed that the hydrogen is produced via the pressure swing adsorption unit; thus, the coal gasification system produces power, hydrogen, and carbon dioxide as well as sulfur as a by-product. All the produced hydrogen and a certain amount of produced carbon dioxide in the coal gasification unit are used in the methanation unit. In addition, the power requirement for the methanation unit is provided by the power generated in the coal gasification unit [21].

The methanation unit integrated into the coal gasification plant is shown in Figure 2. Methane is produced in the methanation unit via the carbon dioxide hydrogenation reaction. The carbon dioxide hydrogenation for methane production is known as the Sabatier reaction, which is given in Eq.(1) [17]. The amounts of the reactants are estimated based on the reaction stoichiometry.

$$4H_2 + CO_2 \rightarrow CH_4 + 2H_2O \; H_r^o = -206\, kJ/mol \quad (1)$$

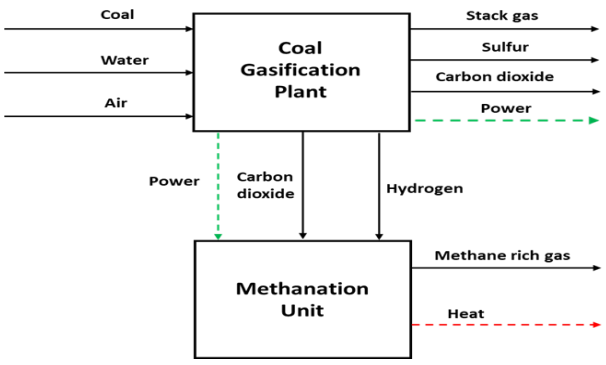

Figure 1. A simplified scheme of the studied system in this study. The coal gasification plant is explained in detail in [20]

Various types of reactors can be used for carbon dioxide hydrogenation, including multitubular reactors [22] and micro-channel reactors [23]. In this study, the effects of different parameters on the performance of carbon dioxide hydrogenation for methane production are estimated using the Gibbs free energy minimization method without considering any specific type of reactor. This method is useful in understanding the thermodynamic limits of different parameters on carbon dioxide hydrogenation. After that, the PSO method is used to optimize the carbon dioxide and hydrogen parameters and to achieve the desired limitation. PSO is a metaheuristic-optimization method in which the behavior of various birds in nature is artificially tackled to obtain a desired target or optimum value [24]. In a flock, a bird always flies towards a better position in its surroundings. Each individual in the PSO is like a bird, following various rules and interacting with other individuals around it in order to complete the final task. In a PSO algorithm, each individual in the swarm is represented as a particle. The particles follow several simple rules and benefit from the experience of neighboring particles or their own during swarm updates. They update their position to head to the destination and their speed to arrive at the destination just in a given time [24]. The velocity and position equations of the basic PSO algorithm are given in Eqs. (2) and (3).

$$v_i(t+1) = \omega v_i(t) + c_1 r_1(t)(o_b(t) - x_i(t)) + c_2 r_2(t)(g_b(t) - x_i(t)) \quad (2)$$

$$x_i(t+1) = x_i(t) + v_i(t+1) \quad (3)$$

where v_i and x_i are the velocity and position of the particle i at time t, respectively. Also, c_1 and c_2 are acceleration constants that are positive numbers used in the contribution of cognitive and social components to rate the updates. Random numbers r_1 and r_2 can take various values between 0 and 1. The inertia weight ω controls the inertia of a particle, and measures the effect of the velocity of the previous instant on the next displacement. $o_b(t)$ and $g_b(t)$ are the optimal positions calculated by the particle itself and all particles in the population, respectively. All particles know the population information. Each particle moves towards the global optimal solution and aims to find the optimal solution in the population. Before the update, the particle decides whether the reached location is better than the known location or the location known by someone else. Otherwise, the particles retain the previous optimal values and continue to move. The PSO algorithm only terminates when a successful solution is found or the iteration count reaches its maximum value.

Therefore, $(G^t)_{T,P}$ is created for fitness function $min_{n_i}(G^t)_{T,P}$ given in Eq. (4). The function is minimized until the best reactor values are selected according to this equation. In PSO, c_1 and c_2 values selected as 1 and 2, respectively. The population number was chosen as 50 in PSO method.

$$minimize_{n_i}(G^t)_{T,P} = \min_{n_i} \sum_{i=1}^{M} n_i \left(G_i^o + RTln\left(\frac{\bar{f}_i}{f_i^o}\right)\right) \quad (4)$$

In this study, four moles of hydrogen are used per one mole of carbon dioxide. The inlet conditions of the reactants are given in Table 1. The effects of reaction temperature and pressure, and reactant inlet temperature to the reactors on the carbon monoxide conversion, the amount of heat removal requirement for the first reactor and methane production are found from the simulation. The carbon dioxide conversion for the first reactor is calculated as in Eq.(5).

$$X_{CO2,R1} = \frac{\dot{n}_{CO2,4} - \dot{n}_{CO2,5}}{\dot{n}_{CO2,4}} \times 100 \quad (5)$$

where $\dot{n}_{CO2,4}$ is the mole flow rate of the carbon dioxide at stream 4 (see Figure 2) while $\dot{n}_{CO2,5}$ is the mole flow rate of the carbon dioxide at stream 5. In addition, the overall carbon dioxide conversion in the methanation unit is estimated as in Eq.(6).

Table 1. Carbon dioxide and hydrogen feed streams to the methanation unit.

Parameter	CO_2 gas	H_2 gas
Flowrate (kg/h)	71268.7	13058.6
Temperature (°C)	25	25
Pressure (bar)	1.5	20

An RGibbs reactor in Aspen Plus is used for the Gibbs free energy minimization method. The list of the chemical components used in the simulation are H_2, CO_2, CH_4, and H_2O. Thermodynamic physical properties in the simulation are estimated using the Peng-Robinson equation of state with Boston-Mathias modification (PR-BM) [21]. Two reactors for the carbon dioxide hydrogenation are used in the system illustrated in Figure 2. Note that the CO_2 and H_2 feed in Figure 2 are given as an optimized input to the system thanks to the PSO.

The first reactor is an isothermal reactor that requires heat removal to control the reactor temperature while the second reactor is an adiabatic reactor. A similar strategy (one tubular reactor and one adiabatic reactor in series) is suggested in [21] for methanation of coke oven gas to improve the system efficiency and increase the catalyst lifetime. Using a multitubular reactor and an adiabatic reactor in series can also be useful for carbon dioxide hydrogenation to decrease the system cost and increase the efficiency. The obtained results in this study can be expanded in future studies to understand the benefits of this method.

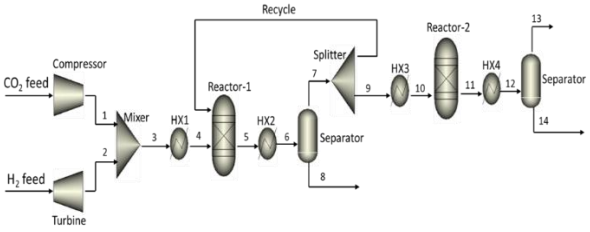

Figure 2. Methanation unit where carbon dioxide hydrogenation takes place. The figure is modified from [21].

$$X_{CO2,Overall} = \frac{\dot{n}_{CO2,4} - \dot{n}_{CO2,11}}{\dot{n}_{CO2,4}} \times 100 \quad (6)$$

where $\dot{n}_{CO2,11}$ is the mole flow rate of the carbon dioxide at stream 11. The system efficiency of the combined coal gasification and methanation system is found after the parametric analysis. The efficiency of the system is calculated as in Eq.(7).

$$\eta_{sys} = \frac{\dot{W}_{net}+\dot{m}_{H2}LHV_{H2}+\dot{m}_{CH4}LHV_{CH4}}{\dot{m}_{Coal}LHV_{Coal}} \quad (7)$$

where $\dot{W}_{net}$ is net power generation of the combined coal gasification and methanation system while LHV_i is the lower heating value of the hydrogen, methane, and coal. In addition, $\dot{m}_i$ refers to the mass flow rate of the hydrogen, methane and coal. Further explanation about the system is given in the Section 3.

3. Results and Discussion

The change in the carbon dioxide conversion for the first reactor with variation of the reactor temperature and pressure is shown in Figure 3. The reactor temperature changes from 150°C to 400°C. In addition, there are different reactor operation pressures: 3 bar, 10 bar and 50 bar which are used to understand the effect of the operation pressure on the carbon dioxide conversion. As shown in the figure, the carbon dioxide conversion increases with lower reactor temperature as expected. The methanation reaction (Eq.(1)) is highly exothermic; thus, the reaction shifts to the left with an increase in temperature according to Le Chatelier`s Principle [25].

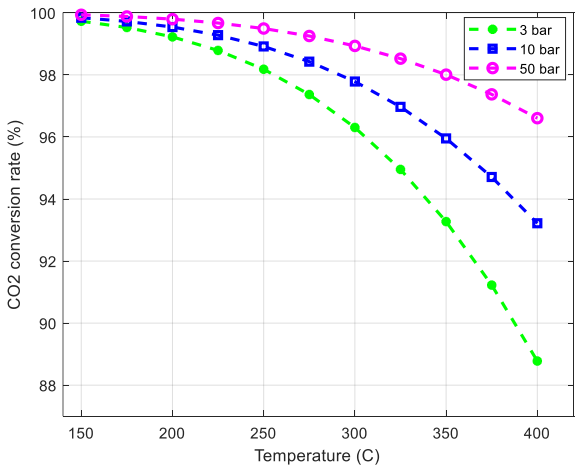

Figure 3. The change in the carbon dioxide conversion for the first reactor with variation of the reactor temperature and pressure.

The low reaction temperature is thermodynamically favourable for the carbon dioxide hydrogenation; however, the reaction kinetics and the catalyst used for carbon dioxide hydrogenation should be considered to define the optimal reaction temperature. The reactor temperature is generally higher than 280°C for carbon dioxide hydrogenation in practical applications [23]. The carbon dioxide conversion also increases with an increase in pressure. In particular, the effect of pressure on the conversion significantly increases with relatively high reactor temperature. For example, the carbon dioxide conversion is equal to ~96% at 300°C and 3 bar while it is ~99% at 300°C and 50 bar. On the other hand, the carbon dioxide conversion is equal to ~88.5% at 400°C and 3 bar while it is ~96.5% at 400°C and 50 bar. Although the carbon dioxide conversion can be increased with elevated pressures, the balance of plant of the system can also significantly increase with an elevated operation pressure. Therefore, the carbon dioxide conversion and the balance of plant of the system should both be considered to select the optimum operation pressure of the methanation unit.

One of the most important issues for carbon dioxide hydrogenation to produce methane is to control the reactor temperature because the carbon dioxide hydrogenation reaction is highly exothermic. Therefore, it is critical to understand the change in the heat removal requirement of the reactor with the variation of different parameters. The change in the amount of heat removal requirement from the reactor with variation of the reactor temperature and pressure, and the reactant inlet temperature into the reactor is shown in Figures 4 and 5, respectively.

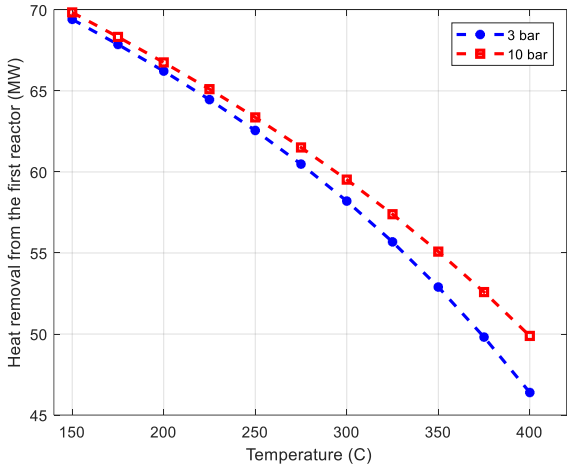

Figure 4. The change in the heat removal requirement from the first reactor with variation of the reactor temperature, pressure and reactant inlet temperature. The reactant inlet temperature is 50°C.

As seen in the figures, there is no significant effect of the operation pressure on the amount of heat removal from the reactor. The heat removal requirement increases with elevated reactor temperature as expected because carbon dioxide

conversion is higher at the elevated reactor temperatures. One of the easiest ways to control the heat removal requirement of the reactor is to manipulate the reactant inlet temperature. A heat exchanger (HX1 in Figure 2) is used to control the reactant inlet temperature. As seen from Figures 4 and 5, the heat removal requirement from the first reactor increases ~27% at 350ºC and 3 bar with variation of the reactant inlet temperature from 50ºC to 250ºC.

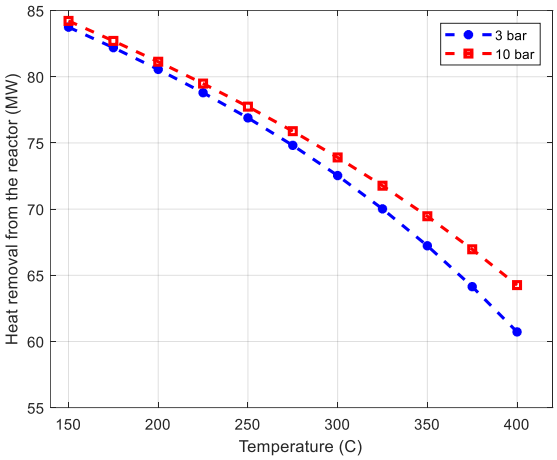

Figure 5. The change in the heat removal requirement from the first reactor with variation of the reactor temperature, pressure and reactant inlet temperature. The reactant inlet temperature is 250ºC.

The changes of the overall carbon dioxide conversion and methane production in the methanation unit variation of the first reactor temperature and the reactant inlet temperature into the second reactor are shown in Figures 6 and 7. The results are obtained for 3 bar operation temperature of the methanation unit. As illustrated in Figure 6, it is possible to achieve an overall carbon dioxide conversion higher than 96% for all parameters used in the present study. As expected, the higher overall conversion is found for the lower reactant inlet temperature of the second reactor. The reaction kinetics and hot spot formation in the reactor should be considered for the final decision of the reactor temperature and the reactant inlet temperature of the reactor. As can be shown from Figures 6 and 7, the thermodynamically maximum methane production is obtained at almost 100% carbon dioxide conversion. The maximum methane production is around 25972 kg/h at ~100% carbon dioxide conversion while it is ~25000 kg/h at ~96% carbon dioxide conversion, as seen in Figure 7. The efficiency of the combined coal gasification and methanation unit and methane production from the system are estimated for 3 bar and 20 bar operation pressure of the methanation unit after the parametric analysis and optimization method. These operation pressures are selected while considering hydrogen output pressure from the pressure swing adsorption unit and the carbon dioxide inlet pressure to the methanation unit.

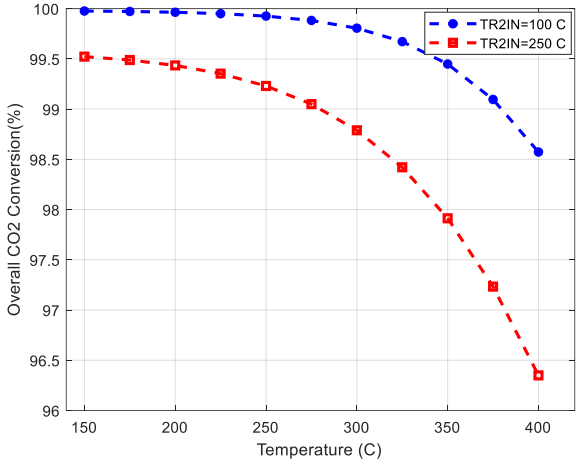

Figure 6. The change in the total carbon dioxide conversion with the variation of the temperature of the first reactor and the reactant inlet temperature of the second reactor.

The carbon dioxide inlet pressure is increased to the operation pressure of the methanation unit by using a compressor. A single compressor is used to increase the pressure of the carbon dioxide feed stream for 3 bar of the operation pressure of the methanation unit while a multistage compressor is selected to increase pressure of the carbon dioxide feed stream for 20 bar of the operation pressure of the methanation unit. In addition, a turbine is used to decrease the hydrogen pressure and produce extra power for 3 bar of the operation pressure.

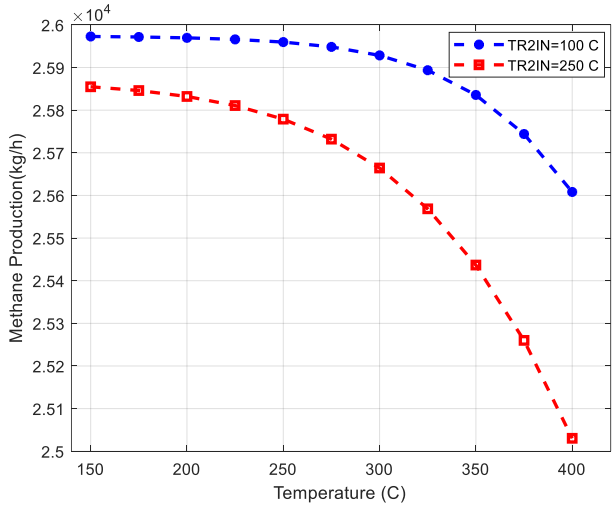

Figure 7. The change in the methane production rate with the variation of the temperature of the first reactor and the reactant inlet temperature.

The isentropic efficiency of the compressors and turbine is assumed to be 0.8. After applying the

PSO and parameters, the results for carbon dioxide and hydrogen feed streams to the methanation unit are listed in Table 2.

Table 2. Carbon dioxide and hydrogen feed streams to the methanation unit

Parameters	CO_2	H_2
Operation pressure of the methanation unit (bar)	3	20
Power generation from the coal gas gasification plant (MW)	26.1	26.1
Compressor power requirement in the methanation unit (MW)	-5.77	-10.07
Hydrogen turbine power generation in the methanation unit (MW)	5.2	0
Net power generation (MW)	25.6	15.4
Overall carbon dioxide conversion (%)	98.8	99.6
Hydrogen rate in the product (kg/h)	158.85	53.72
Methane production (kg/h)	25664	25870
System efficiency (based on LHV) (%)	49.88	48.5

As shown from the table, the increase in methane production is only 0.8% with increasing operation pressure of the methanation unit from 3 bar to 20 bar. Reactor values are optimized by PSO method. However, the compression work significantly increases with higher operation pressure of the methanation unit. Therefore, lower pressure can be preferred to increase the system efficiency. The power generation and methane production from the system are equal to ~25.6 MW and ~25664 kg/h, respectively for 3 bar operation pressure and 108000 kg/h coal input (Illinois#6 coal is used in the coal gasification system and the LHV of the coal is equal to 25.88 MJ/kg [20]).

4. Conclusion and Future Work

A novel system based on combined coal gasification and carbon dioxide hydrogenation is proposed in this study to produce power and methane using PSO method. A parametric analysis was conducted to understand the effects of various parameters on the performance of the methanation unit. In addition, the reactor feeds were optimized by applying the PSO method. The results showed that it is possible to produce ~25.6 MW of power and ~25664 kg/h methane for 108000 kg/h coal by using a combined coal gasification and methanation unit. The results also showed that the system efficiency is ~50%. This efficiency was estimated by assuming that the produced methane is directly injected into the available methane pipeline. The advantage of the PSO method here cannot be overlooked either.

In future studies, the methanation unit will be analyzed in detail by developing Multiphysics models while considering the reaction kinetics and hot spot formation in the reactors to optimize methane production. In addition, various scenarios to produce different fuels including ammonia, methanol, methane and diesel from the combined coal and biomass systems will be explored. Furthermore, deep learning techniques for techno economic assessment of the system should be performed in future studies.

Contributions of the authors

All authors contributed equally to the study.

Conflict of Interest Statement

There is no conflict of interest between the authors.

Statement of Research and Publication Ethics

The study is complied with research and publication ethics.

References

[1] C. Yılmaz and M. Kanoglu, "Investigation of hydrogen production cost by geothermal energy", *International Advanced Researches and Engineering Journal*, Vol. 1, No. 1, pp. 5-10, 2017.

[2] O. Sen and C. Yılmaz, "Thermodynamic performance analysis of geothermal and solar energy assisted power generation and residential cooling system", *International Advanced Researches and Engineering Journal*, Vol. 4, No. 1, pp. 2020.

[3] S. Schemme et al., "H2-based synthetic fuels: A techno-economic comparison of alcohol, ether and hydrocarbon production", *International journal of hydrogen energy*, Vol. 45, No.8, pp. 5395-5414, 2020.

[4] V. Dieterich et al., "Power-to-liquid via synthesis of methanol, DME or Fischer–Tropsch-fuels: a review", *Energy & Environmental Science*, Vol. 13, No. 10, pp. 3207-3252, 2020.
[5] S. Schemme et al., "Promising catalytic synthesis pathways towards higher alcohols as suitable transport fuels based on H2 and CO2", *Journal of CO2 utilization*, Vol. 27, pp. 223-237, 2018.
[6] M.S. Herdem et al., "Simulation and modeling of a combined biomass gasification-solar photovoltaic hydrogen production system for methanol synthesis via carbon dioxide hydrogenation", *Energy Conversion and Management*, Vol. 219, 113045, 2020.
[7] H. Zhang et al., "Techno-economic optimization of CO2-to-methanol with solid-oxide electrolyzer", *Energies*, Vol. 12, No. 19, 3742, 2019.
[8] J. Kotowicz, M. Brzeczek and D. Wecel, "Analysis of the work of a" renewable" methanol production installation based on h2 from electrolysis and co2 from power plants", *Energy*, 119538, 2020.
[9] V. Eveloy, "Hybridization of solid oxide electrolysis-based power-to-methane with oxyfuel combustion and carbon dioxide utilization for energy storage", *Renewable and Sustainable Energy Reviews*, Vol. 108, pp. 550-571, 2019.
[10] M. Momeni et al., "A comprehensive analysis of a power-to-gas energy storage unit utilizing captured carbon dioxide as a raw material in a large-scale power plant", *Energy Conversion and Management*, Vol. 227, 113613, 2021.
[11] S. Hanggi et al., "A review of synthetic fuels for passenger vehicles", *Energy Reports*, Vol. 5, pp. 555-569, 2019.
[12] S. Brynolf et al., "Electrofuels for the transport sector: A review of production costs", *Renewable and Sustainable Energy Reviews*, Vol. 81, pp. 1887-1905, 2018.
[13] S. Buyrukoğlu, "Promising Cryptocurrency Analysis using Deep Learning", *5th International Symposium on Multidisciplinary Studies and Innovative Technologies (ISMSIT)*, 21-23 Oct., Ankara, Turkey, 2021.
[14] S. Buyrukoğlu, F. Batmaz and R. Lock, "Increasing the similarity of programming code structures to accelerate the marking process in a new semi-automated assessment approach", *11th International Conference on Computer Science & Education (ICCSE)*, 23-25 Aug., Nagoya, Japan, 2016.
[15] M. J. Azarhoosh, H. Ale Ebrahim and S. H. Pourtarah, "Simulating and optimizing auto-thermal reforming of methane to synthesis gas using a non-dominated sorting genetic algorithm II method", *Chem. Eng. Commun.*, Vol. 203, No. 53, doi: https://doi.org/10.1080/00986445.2014.942732, 2016.
[16] M. Shamsi, H. Ale Ebrahim and S. H. Pourtarah, "Simulation and Optimization of Coal Gasification in a Moving-bed Reactor to Produce Synthesis Gas Suitable for Methanol Production Unit", *Chem. Biochem. Eng. Q.*, Vol. 33, No. 4, pp. 427–435, 2019.
[17] S. Buyrukoğlu and A. Akbaş, "Machine Learning based Early Prediction of Type 2 Diabetes: A New Hybrid Feature Selection Approach using Correlation Matrix with Heatmap and SFS", *Balkan Journal of Electrical and Computer Engineering*, Vol. 10, No. 2, pp. 110 – 117, 2022.
[18] S. Buyrukoğlu, Y. Yılmaz and Z. Topalcengiz, "Correlation value determined to increase Salmonella prediction success of deep neural network for agricultural waters", *Environ. Monit. Assess.*, Vol. 194, 373, 2022.
[19] S. Buyrukoğlu and S. Savaş, "Stacked-Based Ensemble Machine Learning Model for Positioning Footballer", *Arab J Sci Eng.*, https://doi.org/10.1007/s13369-022-06857-8, 2022.
[20] M.S. Herdem et al., "Thermodynamic modeling and assessment of a combined coal gasification and alkaline water electrolysis system for hydrogen production", *International Journal of Hydrogen Energy*, Vol. 39, No. 7, pp. 3061-3071, 2014.
[21] Z. Qin et al., "Methanation of coke oven gas over Ni-Ce/γ-Al2O3 catalyst using a tubular heat exchange reactor: Pilot-scale test and process optimization", *Energy Conversion and Management*, Vol. 204, 112302, 2020.
[22] R.T. Zimmermann, J. Bremer and K. Sundmacher, "Optimal catalyst particle design for flexible fixed-bed CO2 methanation reactors", *Chemical Engineering Journal*, Vol. 387, 123704, 2020.
[23] T. Chwola et al., "Pilot plant initial results for the methanation process using CO2 from amine scrubbing at the Łaziska power plant in Poland", *Fuel*, Vol. 263, 116804, 2020.
[24] W. Liu, Z. Wang, N. Zeng, F.E. Alsaadi and X. Liu, "A PSO-based deep learning approach to classifying patients from emergency departments", *International Journal of Machine Learning and Cybernetics*, Vol. 12, pp. 1939–1948, 2021.

[25] N. Christofides, A. Mingozzi and P. Toth, “The Vehicle Routing Problem”, *Chichester, UK: Wiley*, pp. 315–338, 1979.

Bitlis Eren Üniversitesi Fen Bilimleri Dergisi
BİTLİS EREN UNIVERSITY JOURNAL OF SCIENCE
ISSN: 2147-3129/e-ISSN: 2147-3188
VOLUME: 11 NO: 2 PAGE: 499-507 YEAR: 2022
DOI: 10.17798/bitlisfen.1036634

Deciphering the Relationship between the Mass, Size and Engine Properties of Boeing and Airbus Aircraft

Seyhun DURMUŞ[1*]

[1]*Balikesir University Edremit School of Civil Aviation, Balikesir, Turkey*
(ORCID: 0000-0002-1409-7355)

Keywords: Boeing, Airbus, Conceptual aircraft design, Thrust to weight ratio, Design point.

Abstract

In the study, it is aimed to analyze the mass, size, and engine characteristics of different Boeing and Airbus aircraft models, which are the duopoly in air transportation market, and to decipher the correlations between the conceptual design parameters of these aircraft. For this purpose, data on the production year, mass, size, and engine characteristics of 36 Boeing and 20 Airbus aircraft were collected. The fuselage length, cabin width, wingspan and wing area were considered as the size characteristics. In order to compare the mass characteristics of aircraft, the operational empty mass, engine mass and maximum take-off weight (MTOW) were examined. Since commercial jets are important in terms of aerodynamic design, that is, they determine the status of these aircraft models in the matching table, thrust weight and wing loading characteristics are also examined. Th fineness ratios decreased linearly as the wingspan/fuselage length ratios increased. Similarly, as MTOW increases, the operational empty weight/MTOW ratio tends to decrease. Both engine mass and the total thrust of the engines tended to increase linearly with MTOW. The correlations obtained on mass size and engine relations will contribute to the conceptual aircraft design and engine selection.

1. Introduction

The rivalry between Airbus and Boeing has been described as a duopoly in the commercial large-jet market since the 1990s. This duality has become increasingly prominent after a series of mergers in the global aviation industry. Airbus strengthens as a pan-European consortium, while Boeing acquires arch-rival McDonnell Douglas. Other major commercial jet manufacturers, such as Fokker and BAE systems, could not compete with Airbus and Boeing and withdraw from this market. Passenger capacity, range, engine choices, safety and quality, aircraft prices, outsourcing, technology, currency and exchange rates, and production planning are the main components of this competition [1]. Due to Airbus' sales momentum thanks to the A320neo family and Boeing's problems with the Boeing 737 MAX, the A320 family eventually surpassed the Boeing 737 to become the best-selling aircraft [2]. Statistics conducted in 2019 showed that a total of 11394 Boeing aircraft and a total of 10137 Airbus aircraft were in service [3]. The current disputes between Airbus and Boeing are based on the alleged illegal subsidies given by the governments of both countries give to their respective airlines [4]. King [5] states that the long-range Airbus A380 and Boeing 787, have lower fuel costs per passenger, and that these 2 aircraft are not alternatives to each other, but are complementary aircraft. Zeinali and Rutherford [6] suggested that aircraft design parameters (range, payload etc.) changed over time, affecting fuel efficiency, so the CO2 certification requirement had to be adjusted for specific replacement designs. Ariffin et al. [7] studied the relationship between thrust to weight ratio and maximum take-off mass. Results of that study showed that the thrust to weight ratio of narrow-body aircraft was in the range of 0.22-0.32. The claim that the Boeing 747-8I will carry almost as many passengers as Airbus's superjumbo

*Corresponding author: drmsyhn@gmail.com
Received: 16.12.2021, Accepted: 20.05.2022

(A380) and will be produced for half of Airbus's estimated investment, has triggered a competitive strategy between Boeing and Airbus [8-10]. Onishi [11] studied the preliminary design of a multi-fuselage gigantic flying boat as an alternative to Boeing 747 and A380. Curran et al. [12] applied Value Operations Methodology (VOM) theory to the Airbus A350-900 versus the Boeing 787-9. The results showed that the B787 was superior in terms of cost, while the A350 provided an advantage in terms of passenger satisfaction. Jasmine et al. [13] used seat load factor for payload optimization comparison of Airbus A330 and Boeing 777-300 ER. Raymer [14] proposed an approach to estimate fuselage lengths using maximum take-off gross mass. Raymer found a power correlation between the aircraft mass and fuselage length for different types of aircraft such as sailplanes, homebuilt, general aviation, jets. Bejan et al. [15] suggested that there is a ratio between the wingspan and fuselage length, and between fuel load and aircraft size of aircraft. In that study, the relationship between aircraft was performed on correlations between the mass, speed, engine mass, range etc. Marta [16] performed optimization of small regional jet geometry with parameters of fuselage length, fuselage diameter, wingspan, wing chord using a genetic algorithm. In current study, geometric and size properties (fuselage length, fuselage with, wingspan, aspect ratio), mass properties (OEW, MTOW, engine mass) and aerodynamic characteristics (wing loading, thrust to weight ratio) of 20 Airbus aircraft and 36 Boeing aircraft were compared. As a result of the study, it was aimed to reveal the correlations obtained from the distribution charts for use in the conceptual design of a commercial jet airliners.

2. Material and Method

In the study, data of 20 Airbus and 36 Boeing aircraft including years of first flight, operational empty weight (OEW), maximum take-off gross weight (MTOW), wingspan, fuselage length, cabin widths, wing area, wing aspect ratio, engine mass, and engine thrust are collected from Jane's All the World's Aircraft [17], technical specification data presented in the Rivals in Sky [18], Boeing commercial website [18] and Airbus Family Figures booklet [20]. Details of the studied aircraft models are given in Table 1.

Table 1. List of studied aircraft models including the years of first flight.

#	Model	Year	#	Model	Year	#	Model	Year
1	Airbus A300B4	1972	1	Boeing 707-120B	1957	21	Boeing 777-200	1994
2	Airbus A310-200	1982	2	Boeing 707-320B	1960	22	Boeing 777-200ER	1996
3	Airbus A300-600R	1985	3	Boeing 727-100	1963	23	Boeing 737-600	1997
4	Airbus A310-300	1985	4	Boeing 727-200	1967	24	Boeing 737-700	1997
5	Airbus A320-200	1987	5	Boeing 737-100	1967	25	Boeing 737-800	1997
6	Airbus A321-200	1990	6	Boeing 737-200	1968	26	Boeing 757-300	1998
7	Airbus A340-300	1991	7	Boeing 747-200B	1970	27	Boeing 767-400ER	1999
8	Airbus A330-300	1992	8	Boeing 727-200A	1971	28	Boeing 747-400ER	2001
9	Airbus A340-200	1992	9	Boeing 737-200A	1971	29	Boeing 777-300	2003
10	Airbus A319-100	1995	10	Boeing 747-100B	1979	30	Boeing 777-300ER	2003
11	Airbus A319LR	1995	11	Boeing 767-200	1981	31	Boeing 777-200LR	2005
12	Airbus A330-200	1997	12	Boeing 747-300	1982	32	Boeing 737-700 ER	2006
13	Airbus A340-600	2001	13	Boeing 757-200	1982	33	Boeing 737-900 ER	2006
14	Airbus A318-100	2002	14	Boeing 767-200ER	1983	34	Boeing 787-8	2009
15	Airbus A340-500	2002	15	Boeing 737-300	1984	35	Boeing 747-8I	2010
16	Airbus A380-800	2005	16	Boeing 767-300	1985	36	Boeing 787-9	2013
17	Airbus A350-1000	2014	17	Boeing 767-300ER	1987			
18	Airbus A350-800	2014	18	Boeing 737-400	1988			
19	Airbus A350-900	2014	19	Boeing 747-400	1988			
20	Airbus A350-900R	2014	20	Boeing 737-500	1989			

When scatter plot is created with the values given in Table 1, Fig. 1 is obtained. Boeing entered the commercial passenger aircraft market with its first aircraft, the Boeing 707, in 1957; this was followed by the Boeing 727 and 737 series in 1967. The first Airbus A300B-4 aircraft was produced in 1972, the Airbus A 310 series in 1982, and the Airbus A320 series in 1985. Boeing's first double-decker Boeing 747-200B made its first flight in 1970, while Airbus' first double-decker A380 made its first flight in 2005. Airbus' newly produced Airbus A350 aircraft has been in service since 2014, while Boeing's newly produced Dreamliner 787 has been in service since 2009.

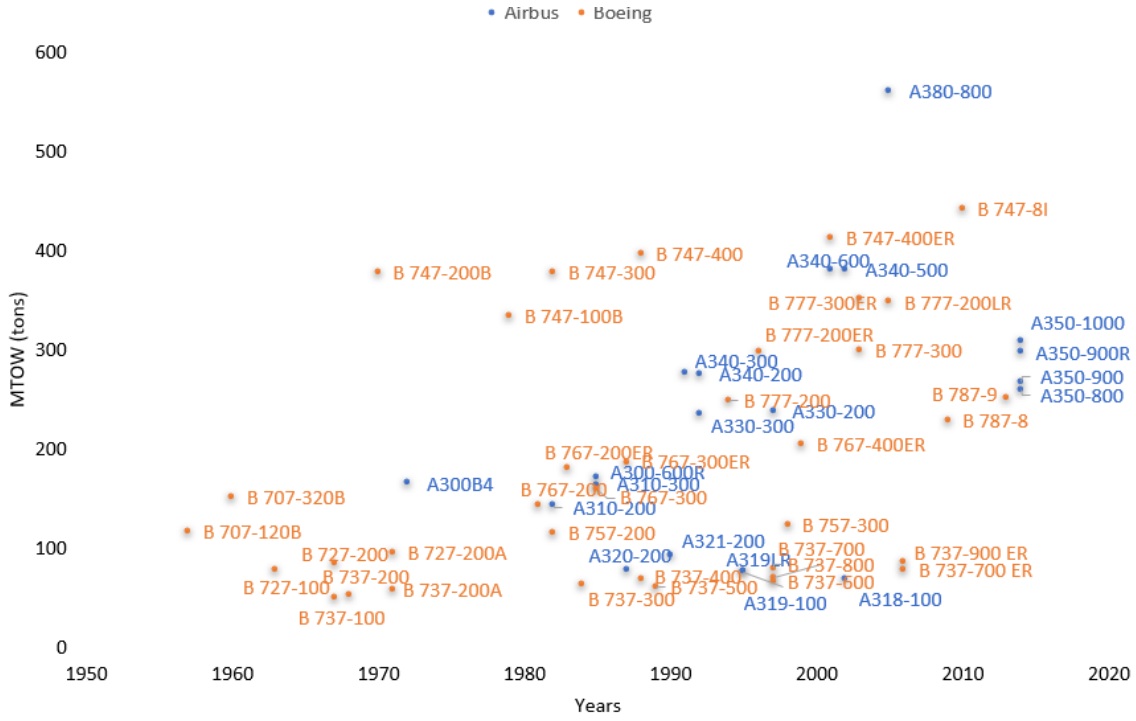

Figure 1. Distribution of MTOW data for the year of production of Airbus and Boeing aircraft

3. Results and Discussion

Various scatter plots related to the size, geometric, mass, and aerodynamic characteristics of the aircraft have been created from the compiled data. Some power and linear correlations with a high value of R-Squared (R^2, coefficient of determination) value were obtained from the distribution charts for use in the conceptual design of commercial passenger jets. In this section, first, geometric and dimensional characteristics, then mass characteristics and finally aerodynamic characteristics of Airbus and Boeing aircraft were compared, and correlations were revealed. It is known in the literature that the wingspan and fuselage length are functions of maximum take of weight (MTOW); in this study, it is explained what kind of correlation occurs with the equations obtained from the charts. Fig. 2 shows the power correlation between the fuselage length and MTOW, as well as power correlation between the wingspan and MTOW. Eq. 1 gives the correlation between fuselage length and MTOW, where length is in meters and MTOW is in kilogram. Eq. 2 gives the correlation between the wingspan and MTOW, where the length is in meters and MTOW is in kg. There is a power relationship between MTOW and length.

$$\text{Wingspan} \cong 0.26\ \text{MTOW}^{(0.43)} \quad (1)$$

$$\text{Fuselage length} \cong 0.32\ \text{MTOW}^{(0.42)} \quad (2)$$

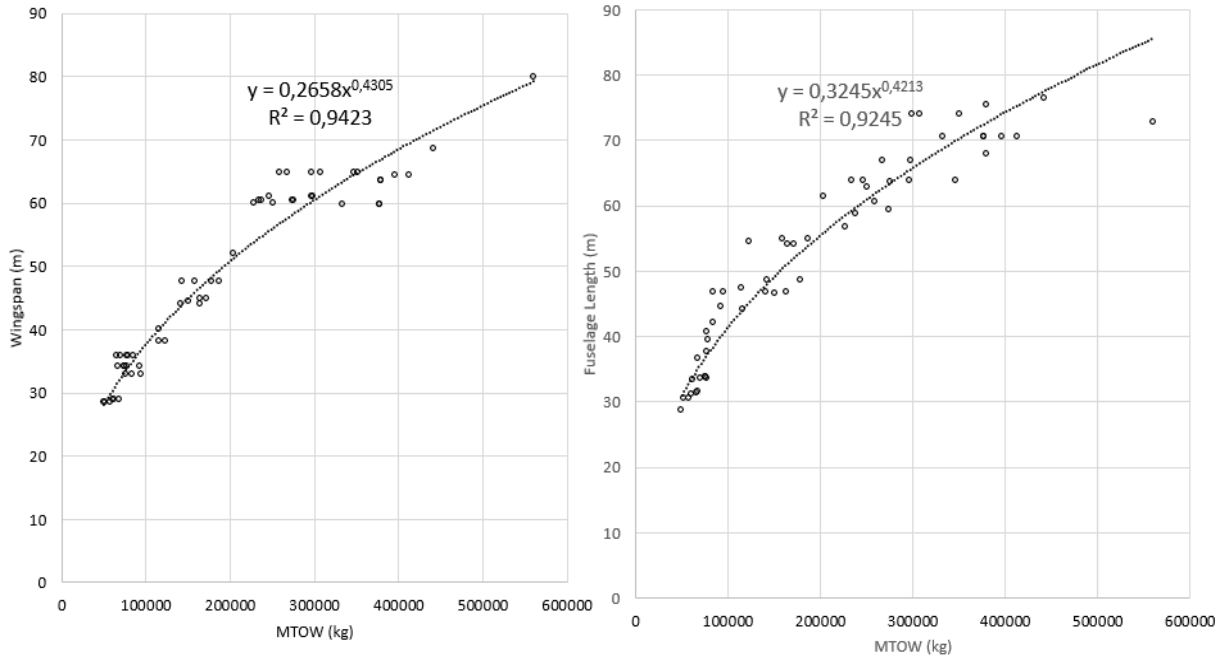

(a) (b)

Figure 2. (a) The power correlation between the wingspan and MTOW (b) The power correlation between the fuselage length and MTOW

Fineness ratio is the ratio of the fuselage length of to its maximum width X, which is a leading parameter in parasite drag of an aircraft. Fig. 3 shows the linear relationship between fineness ratios in Airbus and Boeing aircraft according to wingspan/fuselage length ratios. Airbus' fineness ratio (fuselage length/cabin width ratio) ranges from 8.3 (A310-300) to 14.1 (A340-600), while Boeing's fineness ratio ranges from 8.2 (Boeing 737-100) to 15.7 (Boeing 757-300). Since cabin widths range from 3.5 m (Boeing 727) to 6.5 m (A380) and fuselage lengths range from 31.4 m (Airbus A318-100) to 76.3 m (Boeing 747-8I), it is the fuselage lengths that determine the fineness ratio rather than the cabin width. The wingspan varies from 34.1 m (A318, A321) to 79.8 m (A380) in Airbus, and from 28.4 m (Boeing 737) to 68.5 m (Boeing 747-8I) in Boeing. The wingspan-to-fuselage-length ratio in Airbus ranges from 0.76 (A321-200) to 1.1 (A380). The wingspan-to-fuselage-length ratio in Boeing ranges from 0.69 (Boeing 757 300) to 1.14 (Boeing 737-600). The ratio of wingspan to fuselage length in Boeing varies between 0.69 (Boeing 757-300) and 1.14 (Boeing 737-600). The deviation in Airbus's slope in Fig.3 is due to the Airbus A380 aircraft.

Narrow-body aircraft have a cabin width of less than 4 meters and a single aisle. The cabin width of wide-body aircraft is more than 5 meters; exceptionally, the Boeing 767 is a wide-body aircraft with a width of 4.72 meters. Airbus's A310 and A320 series are narrow-body aircraft (3.7 m), while the A330, A340, A350 and A380 series are wide-body aircraft. Boeing's 707, 727, 737 and 757 series are narrow-body aircraft (3.5 m), while the 747, 767, 777 and 787 series are wide-body aircraft. In different types of the same models, the aspect ratio and wing area are generally same, and in general, aspect ratios are between 8-10. Airbus's wing aspect ratios range from 7.5 (A380) to 10.1 (A340), while Boeing's wing aspect ratios range from 7 (Boeing 747) to 11.1 (Boeing 787). As extreme examples, the Boeing 737-400 has a wing area of 91 m^2, the Boeing 747-8I has 554 m^2, the Airbus A-320 has 123 m^2, and the A380 has 845 m^2.

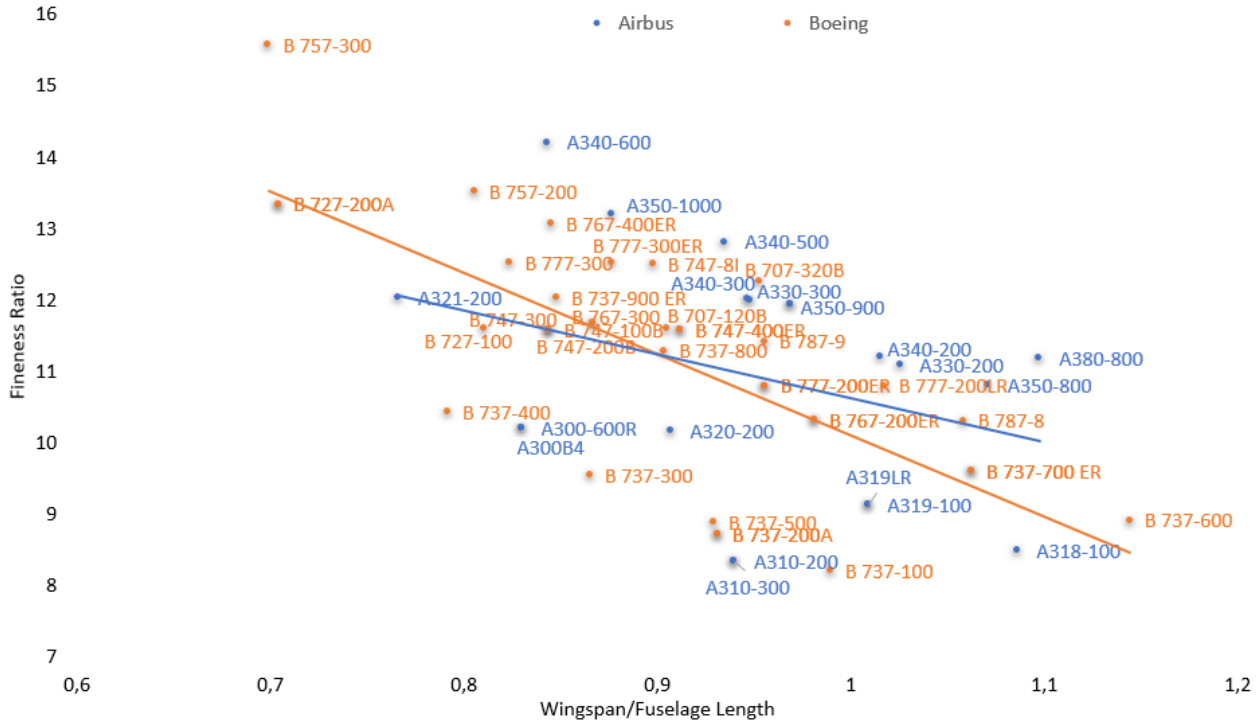

Figure 3. Distribution of fineness ratios in Airbus and Boeing aircraft according to wingspan/fuselage length ratios

From the trendline equations presented in Fig. 4, it can be said that there is a power correlation between the wing area (S_{wing}) and MTOW in commercial aircraft with a high R^2 value. Although Airbus and Boeing have similar curves in terms of wing area, it can be said that Airbus aircraft have a slightly larger wing area than Boeing aircraft. Eq. 3 and Eq. 4 gives the correlations between the MTOW and wing area where wing area is in m^2 and MTOW is in kg. Although Durmus [21] proposed a power law of 2/3(0.66) in subsonic aircraft, in this study, the power relationship between wing area and mass in large commercial aircraft was approximately 0.84 and 0.9. It can be said that the power relations obtained in Eq. 3 and Eq.4 are proportional to the square of the relations obtained in Eq. 1.

$$\text{Swing, Airbus} \cong 0.0044\ \text{MTOW}^{(0.91)} \quad (3)$$

$$\text{Swing, Boeing} \cong 0.0101\ \text{MTOW}^{(0.84)} \quad (4)$$

The ratio of operational empty weight (OEW) to MTOW is an important parameter in the payload analysis of commercial aircraft. Fig. 5 shows the distribution of the operational empty weight of the aircraft according to the MTOW ratios. OEW/MTOW ratios in Boeing aircraft range from 0.42 (Boeing 777 200 LR) to 0.61 (Boeing 737-200). The OEW/MTOW ratios in Airbus aircraft range from 0.42 dec A350-900R) to 0.58 (A318-100). Generally, the frequency range of the OEW/MTOW ratio is between 0.45 and 0.55. In general, it can be said that the OEW/MTOW ratio decreases as the aircraft mass increases according to linear relationship. Exceptionally, it can be stated that the slope of the double-decker aircraft, namely the Boeing 747 and the Airbus A380, is inconsistent with the general curve slope.

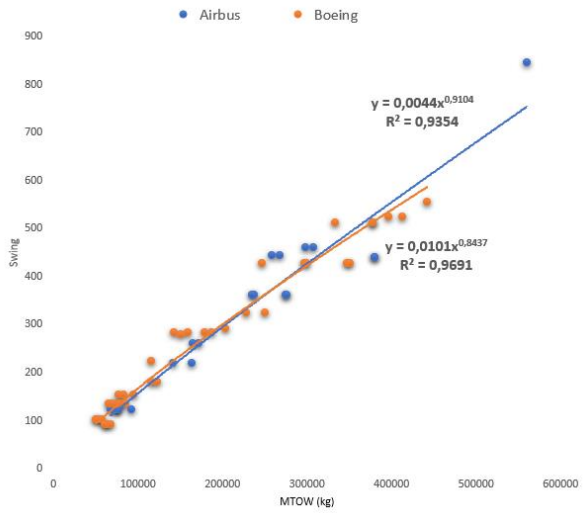

Figure 4. The correlation between wing area and MTOW in Airbus and Boeing aircraft

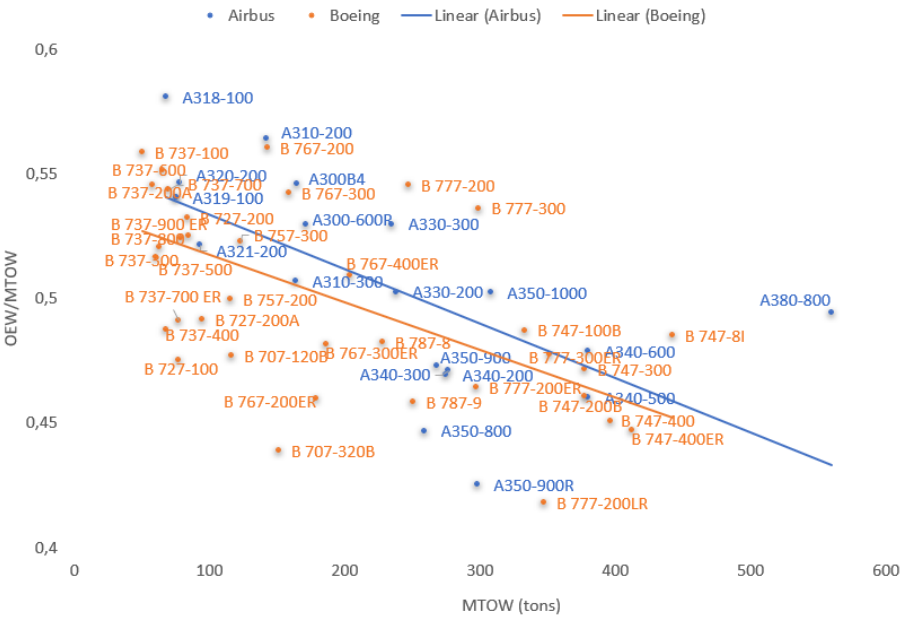

Figure 5. OEW/MTOW distribution chart with MTOW on Airbus and Boeing aircraft

Based on the results presented in Fig. 6(a) and 6(b), it can be said that there is a linear relationship between MTOW with both the engine mass and total engine thrust. On the other hand, the same engine (GE CF6-80C2) can be used in aircraft types belonging to the same series (such as Boeing 767-200, 767-300, 767 400 ER) despite their different MTOWS. Since the level of technology affects the correlations of aircraft parameters, some correlations have obtained for before and after based on the year 1990, which is the year composite materials began to be used in aircraft. The correlation results indicate that, the engine weight increases as the bypass ratio increases. Eq. 5 and Eq. 6 gives the correlations between the engine mass and MTOW, where both are in tons.

$$\text{Engine mass}_{\text{After the 1990s}} = 0.0489\ \text{MTOW} \quad (5)$$

$$\text{Engine mass}_{\text{Before the 1990s}} = 0.0477\ \text{MTOW} \quad (6)$$

A linear relationship was found between the total engine thrust and MTOW with a the R^2 is 0.99. Eq. 7 and Eq. 8 gives such correlation considering the year of first flight.

$$\text{Total Engine Thrust}_{\text{After the 1990s}} = 0.273\text{MTOW} \quad (7)$$

$$\text{Total Engine Thrust}_{\text{Before the 1990s}} = 0.281\text{MTOW} \quad (8)$$

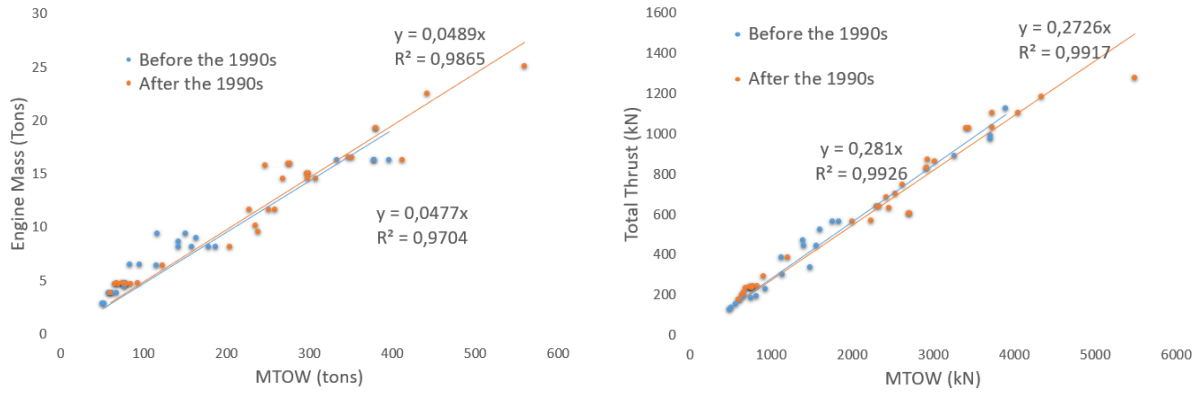

(a) (b)

Figure 6. (a) Correlation between engine mass with MTOW considering the year of first flight (b) Correlation between total engine thrust and MTOW considering the year of first flight.

The thrust-to-weight ratio (T/W) is a ratio that describes an aircraft's thrust relative to its weight. Thrust-to-weight ratios of Airbus and Boeing aircraft are given in Fig. 7. The T/W ratio is a dimensionless parameter. In general, an accumulation occurs in the range of 0.25-0.35 in medium-weight aircraft (MTOW<200 tons), while an accumulation is observed in the range of 0.25-0.30 in heavy-weight aircraft (MTOW> 200 tons).

Thrust to weight (T/W)-wing loading (WL) charts are knowns as matching charts to optimize an aircraft's aerodynamical design point by flight phases such as cruise, take-off, and landing. Low T/W and low WL limits the take-off and cruise flight phases, while high WL and high T/W limit the landing (approach) flight phase. The matching chart given in Fig. 8 indicates an idea of the design point of commercial passenger aircraft. While maximum cruise speed and gust stability increase with increasing wing loading, while short take-off landing (STOL) capability of aircraft increases with decreasing wing loading.

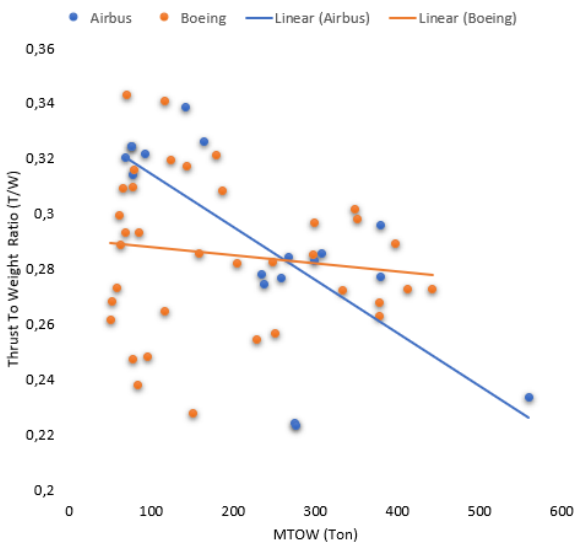

Figure 7. Correlations between thrust to weight ratio (T/W) and MTOW

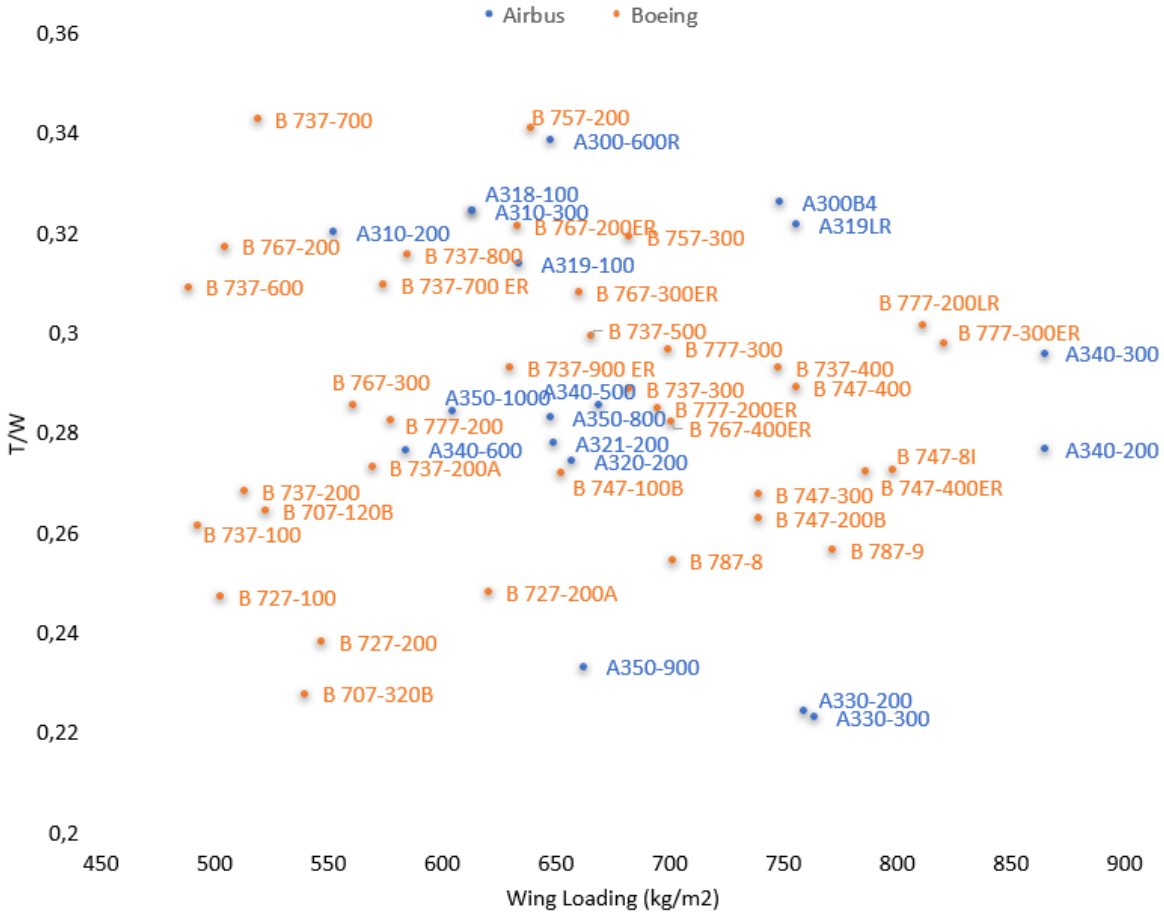

Figure 8. Aerodynamic design point of Boeing and Airbus aircraft

4. Conclusion and Suggestions

In this study, the geometric, mass, and aerodynamic characteristics of 20 Airbus and 36 Boeing aircraft were compared. A power relationship between fuselage length and MTOW, wingspan and MTOW has been deciphered. In general, fineness ratio ranges from 8.3-14.1 in Airbus, and 8.2-15.7 in Boeing. The cabin width of the narrow-body Airbus is about 3.7 m and that of Boeing is about 3.5 m. Cabin width of wide-body Airbus is 5.3-6.5 meters and that of Boeing is 5.5-6.1 meters and exceptionally, the Boeing 767 is a wide-body aircraft with a width of 4.72 meters. The length of fuselage varies between 31.4-75.3 m in Airbus and varies between 30.5-76.3 m in Boeing. The wingspan ranges from 34.1-79.8 m in Airbus, that of Boeing ranges from 28.4-68.5 m. in Airbus, the wingspan/fuselage length ratio ranges from 0.76 to 1.1 and that of ranges from 0.69 to 1.14 in Boeing. Wing area ranges from 123-845 m^2 in Airbus and 91-554 m^2 in Boeing. In general, aspect ratio values are accumulated between 8-10, although Airbus's wing aspect ratios range from 7.5 to 10.1and Boeing's wing aspect ratios range from 7 to 11.1. In general, accumulation range of OEW/MTOW ratio is from 0.45 to 0.55. OEW/MTOW ratios range from 0.42 to 0.61 in Boeing and that of range from 0.42 to 0.58 in Airbus. Engine mass is between 4.0-7.0% compared to total aircraft mass in Airbus and that of between 3.94-8.06% in Boeing. Thrust to weight (T/W) ratios of accumulated in the range of 0.25-0.35 in medium weight aircraft (MTOW<200 tons), and that of in the range of 0.25-0.30 in heavy weight aircraft (MTOW>200 tons). There is a linear relationship between wing area-MTOW and total engine thrust-MTOW with a high R-squared. Fineness ratios decreased linearly as wingspan/fuselage length ratios increased and as the MTOW increases, the operational empty weight/MTOW ratio tends to decrease. Engine mass and the total thrust of the engines have tended to increase linearly with increasing MTOW.

Statement of Research and Publication Ethics

The study is complied with research and publication ethics.

References

[1] Datamonitor, *Airlines Industry Profile: United States November* 2008: 13–14

[2] J. Flottau, *Airbus and Boeing ponder higher narrowbody production: after strong 2017, both manufacturers see upward pressure on rates; suppliers warn of potential bottlenecks,* Aviation Week & Space Technology 2018.

[3] Flight Global, *World Airline Census 2019*, Flight International.

[4] S. Chanda, *The Battle of the Big Boys: A Critical Analysis of the Boeing Airbus Dispute Before the WTO*. Available at SSRN 1944588, 2011.

[5] J. M. King, "The Airbus 380 and Boeing 787: A role in the recovery of the airline transport market," Journal of air transport management, vol. 13, no. 1, pp. 16-22, 2007.

[6] M. Zeinali and D. Rutherford, "Trends in Aircraft Efficiency and Design Parameters," *International Council on Clean Transportation*, 2010.

[7] L. M. Ariffin, A. H. Rostam and W. M. E. Shibani, "Study of Aircraft Thrust-to-Weight Ratio," *Journal of Aviation and Aerospace Technology*, vol. 1 no. 2, 2019.

[8] N. Al-Najjar, I. Aoyagi, G. Goldstein, T. Korupp, B. Liu and S. Singh, *Boeing and Airbus: Competitive Strategy in the Very-Large-Aircraft Market*, Kellogg School of Management Cases.

[9] S. E. Bodily and K. C. Lichtendahl, *Airbus and Boeing: Superjumbo Decisions* Darden Business Publishing Cases.

[10] L. B. Campos, "On the competition between Airbus and Boeing," *Air & Space Europe*, vol. 3, no. 1-2, pp. 11-14, 2001.

[11] R. Onishi, "Flying Ocean Giant: A Multi-Fuselage Concept for Ultra-Large Flying Boat,". In *42nd AIAA Aerospace Sciences Meeting and Exhibit* p. 696, 2004.

[12] R. Curran, A. Gkirgkis and C. Kassapoglou, "A Value Operations Methodology (VOM) Approach to Multi-Criteria Assessment of Similar-Class Air Vehicles: An Airbus A350 Versus the Boeing 787 Case Study," in *17th AIAA Aviation Technology, Integration, and Operations Conference*, p. 4253, 2017.

[13] A. Jasmine, A. R. Putranto, A. Charles and A. Sodikin, "Payload Optimization Comparison of Airbus 330–300 and Boeing 777–300ER Aircraft," *Journal of Physics: Conference Series*, vol. 1573, no. 1, pp. 012023, July, 2020.
[14] D. Raymer, *Aircraft design: a conceptual approach*, American Institute of Aeronautics and Astronautics, Inc.
[15] A. Bejan, J. D. Charles and S. Lorente, "The evolution of airplanes," *Journal of Applied Physics*, vol. 116 no. 4, pp. 044901, 2014.
[16] A. C. Marta, *Parametric study of a genetic algorithm using a aircraft design optimization problem*, Report Stanford University, Department of Aeronautics and Astronautics.
[17] J. Paul, *Jane's all the world's aircraft 2004-2005*, Jane's Information Group Inc, Alexandria.
[18] B. H. Dutton, *Rivals in the Sky Airbus and Boeing*, Kesley Publishing.
[19] Boeing, Technical Specs. https://www.boeing.com/commercial/ (access date: 20.08.2021).
[20] Airbus, S. A. S. *Airbus Family Figures*, Airbus, 2021.
[21] S. Durmus, "Theoretical model proposal on direct calculation of wetted area and maximum lift-to-drag ratio," *Aircraft Engineering and Aerospace Technology*, vol. 93 no. 6, pp. 1097-1103, 2021.

Bitlis Eren Üniversitesi Fen Bilimleri Dergisi
BİTLİS EREN UNIVERSITY JOURNAL OF SCIENCE
ISSN: 2147-3129/e-ISSN: 2147-3188
VOLUME: 11 NO: 2 PAGE: 508-518 YEAR: 2022
DOI: 10.17798/bitlisfen.1038966

Ransomware Detection in Cyber Security Domain

Ömer ASLAN[1*]

[1]*Bandırma Onyedi Eylül University, Department of Software Engineering, Balıkesir-Turkey (ORCID: 0000-0003-0737-1966)*

Keywords: Cyber security, Ransomware detection, Behavior-based detection, Machine learning

Abstract

In recent years, ransomware has become highly profitable cyber attacks. This is because, everyday there are several new devices attending to computer networks before testing their security strength. In addition, it is easy to launch ransomware attacks by using Ransomware-as-a-Service. This paper proposed a new method that creates the ransomware specific features by using ransomware behaviors which are performed on file, registry, and network resources. The weights are assigned to the behaviors based upon where the actions are performed. The most feasible features are selected based on the assigned weights as well as Information Gain. The selected features are classified by using ML classifiers including J48 (C4.5), RF (Random Forest), AdaBoost (Adaptive Boosting), SLR (Simple Logistic Regression), KNN (K-Nearest Neighbors), BN (Bayesian Network), and SMO (Sequential Minimal Optimization). The experiments are performed on several ransomware variants as well as benign samples. The test results show that our proposed method is feasible and effective. The *DR*, *FPR*, *f*-measure, and accuracy are measured as 100%, 1.4%, 99.4%, 99.38%, respectively.

1. Introduction

Ransomware is a type of malware (malicious software) in the cyber security domain which is designed to prevent or limit access to a computer system until some amount of ransom is paid as a cryptocurrency. There are three ways that ransomware can affect a victim machine [1]: locker, crypto, and combination of locker-crypto ransomware. In locker ransomware, accessing a computer is blocked while in crypto ransomware, files are encrypted in the computer system. In combination with locker-crypto ransomware user access to computers is blocked as well as data being encrypted. Crypto ransomware is more destructive than locker ransomware because it is difficult to decrypt data without paying the money as a cryptocurrency.

Recently, ransomware attacks have increased in both frequency and severity. Covid-19 pandemic accelerates and enlarges the attack surface because of the remote working. Cyber criminals see the pandemic as a chance to increase the number of attacks against employees who work remotely. For instance, malicious emails were increased up to 600% because of Covid-19 [2]. In addition, 37% of organizations were affected by ransomware attacks in 2020 [3]. According to the Ransomware attack statistics report [4], in the first half of 2021 the number of ransomware attacks almost doubled when compared with the previous year 2020. The destructive effect of ransomware attacks is increasing. According to the National Security Institute, ransom fees are requested by about $5000 to $200.000 in the year between 2018 to 2020 [4]. Morgan estimated that in every 11 seconds, a ransomware attack occur in 2021 [5]. It can be seen from the above statistics that ransomware is becoming dangerous for individuals as well as organizations day by day.

To decrease the disruptive consequences of the ransomware, the detection and prevention system needs to be built. There are mainly two kinds of ransomware detection systems that can be deployed including static and dynamic analysis. Static analysis examines the source code of the executable without running the actual code. In static analysis, generally

*Corresponding author: omer.aslan.bisoft@gmail.com
Received: 20.12.2021, Accepted: 28.03.2022

signature is used to define [6] and separate ransomware from cleanware. The advantages of static analysis is that it detects the ransomware before running the actual code. The cons of static analysis is that it cannot detect new ransomware which is quite different from the existing ones. This is because intelligent ransomware is using various code obfuscation techniques to prevent being analyzed correctly. On the other hand, dynamic analysis examines the behaviors of ransomware while the code of the ransomware is being executed. With dynamic analysis, known ransomware as well as zero-day ransomware can be detected. Furthermore, it is resistant to code obfuscation techniques. However, some ransomware variants are not presenting their true behaviors when running under virtual machine and Sandbox environments. In this paper we proposed a method to eliminate the shortcomings of the dynamic analysis listed above and to better detect newly created ransomware. Besides, this research aims to decrease the disruptive consequences of the ransomware attacks by providing further investigation of victim machines.

In this study, a behavioral based ransomware detection method is proposed which uses data mining and machine learning (ML) techniques in the cyber security domain. Several ransomware variants are analyzed, and behaviors are collected by using dynamic analysis tools. While behaviors are created, one or a group of system calls are converted into higher-level operations which is called behavior. The behaviors are grouped to generate features. When behaviors are converted into features, system paths and activities that are performed in the system are taken into consideration. The behaviors are divided into three categories including file, registry, and network operations. Those operations are used to generate ransomware features. Then, most effective features are selected by using feature selection algorithms as well as known Information Gain algorithms. Finally, well known machine learning classifiers are used to separate ransomware from cleanware.

The rest of the paper is organized as follows. In section 2, literature review is discussed. In this section, various types of ransomware, and ransomware spread methods are examined. In addition, leading methods, which are designed to stop or detect ransomware in the literature, are discussed. In section 3, the proposed method is explained. In this section, data collection, feature creation and selection as well as classification techniques are presented. In section 4, results and discussion are presented. Finally, in section 5 conclusion and future research direction is given.

2. Literature Review

This section is divided into three main subsections. In the first subsection, background information about ransomware including ransomware types, propagation techniques, and evolving of ransomware over the years are explained. In the second subsection, the leading methods in the literature which detect or prevent ransomware attacks are given. Finally, the evaluation, pros and cons of each study has been discussed.

2.1. Evolving of Ransomware over the Years

The first ransomware example was the AIDS Trojan which was seen in 1989 [7]. At that time, it was not as dangerous as today's ransomware. Ransomware is written for revenue generation. There are 4 common revenue generation ways including fake antivirus scams, misleading applications, crypto, and locker ransomware. At first, misleading applications as well as fake antivirus tools appeared and got attention between 2005 to 2010. Timely, locker and crypto ransomware are created. Locker ransomware got popular between 2011 to 2012. Crypto ransomware got popular from 2013 up to these days. Between 2005 to 2021, ransomware attacks evolved from a malicious floppy disk which was demanding 189 dollars to a billion dollars' businesses with sophisticated tools over the years. These days, it is easy to launch ransomware attacks because new markets offer Ransomware-as-a-Service (RaSS). Recently, ransomware related attacks are targeting critical systems including finance, oil, gas, transportation and healthcare. It is also targeting IoT (Internet of Things) and mobile devices as well as cloud computing environments.

There are mainly two types of ransomware: Locker and crypto ransomware. Locker ransomware which can be defined as a computer locker denies requests to computers or other devices. On the other hand crypto ransomware, which can be defined as a data locker, prevents accessing files and data. Both locker and crypto ransomware prevents users from accessing something important unless paying requesting money as a cryptocurrency. Locker ransomware is only blocking access to the computer interface, it does not make changes on files and data on the computer system. However, crypto ransomware generally encrypts the important files and data on the computer system which makes the crypto ransomware more destructive.

There are four main stages of ransomware: Infect the system, locking the system or data, demand ransom, and release the files. In order to infect the

victim system, the ransomware needs to spread the target machine by spam email, phishing, and other techniques. After the victim system is infected, the payload of the ransomware is executed to generate public-private key pairs to encrypt the files. Then, a ransom message pops up which shows the amount of money needed to be paid. Finally, when the requested money has been paid, attackers send required keys to the victim to decrypt the files.

There are several techniques to spread ransomware from one system to another. Traffic distribution systems, social engineering techniques, spam email, downloader, and exploit kids are well-known ransomware spreading techniques. The well-known ransomware attacks, spreading methods, and consequences from 2013 to 2021 can be seen in table 1. Email attachment, exploiting software vulnerabilities, exploiting users' trust, and credentials theft have been seen as spreading methods over the years (Table 1). Consequences can be to encrypt all the files in the victim system and can affect many countries along the globe.

After the ransomware infected the victim system, the message appeared to demand money from the victim system. Examples of typical ransomware (WannaCry) messages can be seen in figure 1. It can be seen from figure 1, the ransom should be paid as a cryptocurrency in this example Bitcoin with a specific time period. After the demanded ransom has been paid, the attackers send required keys to decrypt the files.

Figure 1. Shows WannaCry ransomware message when victim files are encrypted

Table 1. List of well-known ransomware attacks over the years

Ransomware Attack	Year	Spread Method	Consequences
CryptoLocker	2013-2014	It spread by email attachments as well as by Gameover ZeuS botnet	It encrypted files on desktops as well as network shares and demand for ransom
TeslaCrypt	2015	It lured users to click phishing email	It encrypted the files and pop up a message for asking $500 ransom as a bitcoin to decrypt the files
WannaCry	2017	It exploited a Windows vulnerability	It affected 150 countries and encrypted computer hard drive
NotPetya	2017	It exploited a vulnerability CVE-2017-0144 on Windows Server Message Block protocol	It was one of the most destructive ransomware attacks in the history and affected many industries such as banks, power companies, and airports
LockerGoga	2019	Malicious emails, credentials theft, and phishing scams	It blocked the victims' accessing to the system and lost millions of dollars
CovidLock	2020	It exploited users' trust which claims to provide statistical data about COVID-19	It affected Android devices that encrypted data and denied the accessing data
REvil (Ransomware Evil)	2021	It exploited Microsoft exchange server vulnerability	The attackers demanded 50 million dollars and also leaked some data which included bank communications, balances, and images of financial spreadsheets

2.2. State-of-the-art Studies on Ransomware

There were only a few studies which specifically detect ransomware among malware or cleanware. Different studies used different methods to separate ransomware from cleanware. The methods that have been used in the literature were examined based upon the main idea, proposed method, and obtained performances.

Detection, prevention, and cure of ransomware attacks was presented by Brewer [8]. According to the author, targeted attacks were increased which were related to ransomware. Besides, some of the mass distribution of the attacks were automated which accelerate the infection process as well as demanding more ransom. In the first place, organizations and big companies need to get ready before attacks take place. For instance, companies need to eliminate the vulnerabilities before getting infected by ransomware and take regular system back-up in the safe place. Because most of the ransomware exploited system vulnerabilities to

propagate, and delete back-up files when running ransomware payloads. When companies are affected by ransomware, they are not only losing money, but also loss of business, possibly the permanent loss of important files, and suffer the effects of lost productivity.

Sgandurra *et al.* proposed an EldeRan which used dynamic analysis and machine learning techniques to classify ransomware [9]. The proposed approach monitored the activities that were performed by ransomware during the first installation. Paper stated that these sets of characteristic features were common across families and assisted the early detection of novel variants. After the feature generation process finished, the Mutual Information criterion was used to select most significant features. Then, Regularized Logistic Regression was used as a classifier. Experimental results presented that EldeRan performance based on area under the ROC curve measured as 0.995.

Nieuwenhuizen discussed a behavioral approach to detect ransomware [1]. As stated in the paper that static analysis which relies on signatures was not resistant to code obfuscation techniques. Thus, could not detect unknown ransomware. On the other hand, combining ransomware behavioral traits with machine learning algorithms increased the detection performances and also could detect zero-day ransomware. This is because core behavioral traits are not changing among the different variants. In other words, even though the code order of the ransomware changes, most of the behaviors remain the same [10].

Vinayakumar *et al.* evaluated the deep and shallow networks to distinguish ransomware from cleanware [11]. Cuckoo Sandbox was used to collect API calls and their frequency. Extracted APIs were given to the MLP (Multi-Layer Perceptron) as well as DNN (Deep Neural Network) to gather optimal feature sets. Then, machine learning classifiers were applied to selected features to detect and classify ransomware families. Test results showed that MLP gained highest accuracy with 1.0 and classified the ransomware families with accuracy of 0.98.

Crypto ransomware detection method, which was using http traffic, on a software defined network (SDN) was proposed by Cabaj *et al.* [12]. Authors assumed that http message sequences and their content sizes were good indicators of features when detecting new CryptoWall and Locky ransomware families. At first, ransomware network traffic was gathered to generate characteristic features from the outgoing http messages and its size. CryptoWall communicated with the command and control server by using domain names instead of direct IP addresses, and it also used HTTP POST messages. Besides, it directed traffic to hacked proxy servers and used the RC4 algorithm to encrypt the data. Locky ransomware communication patterns were similar to the CryptoWall family. Then, in the second step, for each ransomware family, feature vectors were prepared and the centroid vector. Finally, data obtained from two previous steps were used for detection in SDN based solutions. The proposed method was tested on CryptoWall and Locky ransomware families traffic. The test results indicated that performance is feasible with detection rates from 97% to 98% with 4 to 5% false positives when relaying on POST triples and domains.

Almashhadani *et al.* presented a behavioral analysis of network activities for crypto ransomware specifically on locky ransomware families [13]. Locky's PCAP execution traces of the MCFP (Malware Capture Facility Project) dataset were collected. Paper emphasized that locky has many network actions which might be used in order to extract behavioral features. From the TCP, HTTP, NBNS, and DNS traffic, 18 features were extracted. These properties are common in the locky ransomware family which can distinguish this ransomware from the benign ones. After features were generated, BN, RF, and LibSVM were used for classification. As stated in the paper, the proposed method could track the ransomware network activities, specified the valid extracted features, and achieved high detection accuracy as 97.08%, while decreasing the *FPR* (False Positive Rate).

Bae *et al.* presented machine learning-based ransomware detection [14]. The proposed approach first, extracted the API sequences by using *n*-gram techniques. API sequences were used to generate features, then features were represented as a vector. Finally, six machine learning classifiers including RF, Logistic Regression (LR), NB, Support Vector Machine (SVM), KNN, and Stochastic Gradient Descent (SGD) were performed for classification. The suggested method could separate different types of ransomware, benign files, as well as other malware variants. According to experiments, the presented method detected known and unknown ransomware among other malware types.

In our previous study, we have examined the detection of ransomware as well as other malware types such as virus, worm, Trojan horse, rootkit, etc. [15]. We found that building an effective and feasible approach to recognize all malware is a very difficult task, and more novel academic studies are needed to effectively detect ransomware as well as other

malware types. Trends in malware creation techniques are changing dramatically over time while the success of malware detectors' performances are decreasing timely. Hence, combining several methods and technology together may create a more feasible detector. For instance, combining the behavioral features with deep learning in the cloud environment can build more efficient detectors in ransomware recognition.

Beama *et al*. discussed the analysis of ransomware attacks based on the challenges, recent advances as well as future research directions [16]. The paper stated that static analysis is mostly evaded by code obfuscation techniques. In addition, based on some academic papers, certain dynamic analysis methods could be eluded by obfuscation techniques. Access control and data backups could be used as a prevention techniques to reduce ransomware destructive consequences, but these techniques suffer from various deficiencies as well. This is because access control and backups can increase the overhead significantly. Furthermore, current ransomware detection systems generate high false alarms while decreasing the detection rate. Authors claim that machine learning techniques can be used for ransomware detection more efficiently. ML-based models can learn to identify the general behavior patterns by classifying suspicious behaviors. Thus, it can detect unknown malware which have not been in the wild before.

2.3. Evaluation of State-of-the-art Studies

In the literature studies, various ransomware detection techniques were examined based upon the proposed methods, the main idea, and gained performances. Few static analysis versus several dynamic analysis studies were used to create ransomware features. A summary of each ransomware detection method is given in table 2. Most of the studies were performed merely on a few ransomware files which cannot be generalized for all ransomware variants. Besides, in most studies in the literature, the feature space was pretty big and the number of features increased when more program samples were analyzed which leads to requiring more computational times for the learning process. Thus, we conclude that current ransomware detectors are not good enough to recognize and classify the unknown ransomware variants. On the other hand, our proposed method performed on different ransomware variants with high performance, decreased feature space drastically, while decreasing the computation time for learning and detection processes. In addition, our proposed method increases the DR and accuracy for known and unknown ransomware strains.

3. Materials and Methods

This section presents materials and proposed methods. We have changed our previous proposed method to detect ransomware files [10]. Figure 2 shows the extended version of our previous proposed method architecture [10]. The section is split into five parts including proposed method, data collection, feature creation and selection, detection, and performance evaluation. The ransomware samples were downloaded from online websites and analyzed under dynamic analysis tools. The execution traces of ransomware activities were obtained. Then, ransomware behaviors and features were generated from the ransomware activities. After that the most significant features were selected by using features' weights as well as Information Gain. Finally, we used well known machine learning classifiers to separate ransomware from benign samples.

3.1. Proposed Method

After the execution traces of ransomware collected, the ransomware behaviors and features were created. While creating ransomware behaviors, one or a group of system calls are converted into higher-level operations which is called behavior. To illustrate, if the order of the activities are CreateFile, WriteFile, and CloseFile; the associated ransomware behavior will be WriteFile. After ransomware behaviors are created, we perform a proposed algorithm to generate features. When behaviors are converted into features, system paths and activities that are performed in the system are taken into consideration. The behaviors are divided into three categories: file operations, registry operations, network operations. Those operations are used to generate ransomware features. When ransomware features are created, the most significant features are counted. As it can be seen in figure 3, we divided general program behaviors into 3 categories: M (Malware behaviors), B (Benign behaviors), and R (Ransomware behaviors)

$$M = x + a + b + z \quad (1)$$

$$B = \mathrm{b} + \mathrm{z} + \mathrm{y} \quad (2)$$

$$R = a + b \quad (3)$$

Table 2. Current ransomware detection methods which are represented in the literature

Paper	Year	Proposed Method	Goal/Success
Sgandurra *et al.* [9]	2016	Dynamic analysis and machine learning techniques to classify ransomware	Area under the ROC curve measured as 0.995
Vinayakumar *et al.* [11]	2017	Extracted API calls are evaluated by the MLP as well as DNN to select best feature set	Classified the ransomware families with accuracy of 0.98
Cabaj *et al.* [12]	2018	Http message sequences and their content sizes are used as features	Highest detection rate measured as 98% while FPR is measured as 5%
Almashhadani [13]	2019	Locky's PCAP execution traces of the MCFP dataset were collected	Achieved high detection accuracy as 97.08%, while decreasing the FPR
Bae *et al.* [14]	2020	API sequences by using n-gram techniques	Could separate different types of ransomware, benign files, as well as other malware variants efficiently
Proposed method	**2021**	**Ransomware specific behavioral patterns combining with ML techniques**	**Could effectively detect known and unknown ransomware with high accuracy**

We mostly consider the behaviors (*a*) that are only seen in ransomware samples. Plus, behaviors (*b*) that are seen mainly in ransomware with high frequency, while rarely seen in benign samples with less frequency. Behaviors *a* and *b* are determined by using weights assigned to where the actions are performed (Figure 2). Thus, when features are created from the behaviors, the behaviors which have smaller weights than threshold and the features that have smaller frequency are eliminated from the dataset. That way, ransomware specific behaviors are generated before classification takes place.

a) File related features: One of the most common ways for ransomware to interact with the system is through file operations. The ransomware tries to protect its existence in the system by creating files or making changes to the existing files. To create the features from the file related behaviors, the behavior itself (read, write, execute, etc.) , the location of the behaviors that are performed, and extension of the files are taken into consideration. For instance, ransomware performs more read and write behaviors, because it needs to read every file and encrypt those files or first copy the original files into different locations then encrypt the copied files. Thus, more weights are assigned to those behaviors when generating the features. Ransomware also executes behaviors generally in automatic startup file locations as well as temp locations. For those behaviors, more weights are assigned during the feature generation. The behaviors which are performed on different files are also considered, and assigned more weights. For example, sometimes ransomware injects itself into system processes such as svchost. exe, explorer. exe, etc. and inject itself into most used DLLs.

b) Registry related features: The registry is a database that hierarchically holds the operating system and application settings such as drive, startup, network, user account information, etc. Ransomware usually uses the registry to start automatically in the system. In other worlds, the ransomware can automatically run itself in the background every time the system is started. We assigned more weights on the behaviors related to registry autostart locations, access to registry keys and make changes on those keys, and some system specific registry locations.

c) Network related features: Network related behaviors are source and destination IP addresses, average packet size, port numbers that are used, the number of packets that are exchanged between the machines, etc. Ransomware mostly shows anomalous behavioral patterns. For example, generally ransomware uses the order of http packets to send required keys to the victim machine from the command and control center. Size of the packets are taken into consideration. Also, ransomware performs network operations to be able to spread in the network environment and gain unauthorized access to other systems, and there are many Windows API methods that can be used for this purpose. More weights are assigned to those network behaviors when generating network related features.

3.2. Data Collection

The ransomware samples are collected from different sources: Malshare, theZoo aka Malware DB, Tekdefense, and VirusShare [17-20]. To ensure the ransomware variants, Virustotal is used to label the samples. For the experiment, 346 ransomware samples and 304 benign are analyzed under Process Monitor to capture the activities that ransomware displayed. Instead of Process Monitor we could also use other dynamic analysis tools such as Capture BAT, Cuckoo Sandbox, API Monitor, Regshot, and Wireshark. However, we selected Process Monitor because it is an enhanced monitoring tool which shows real-time file, registry and network activities.

When ransomware make changes on important files and registry entries, Process Monitor shows these changes. Besides, filtering can be performed easily according to many categories. The dataset consists of various ransomware variants including locky, Jigsaw, ransomlock, cryptolocker, petya, Wannacry, and CTB-Locker. The benign samples are also collected from different categories: system tools, office documents, games, multimedia, and other programs.

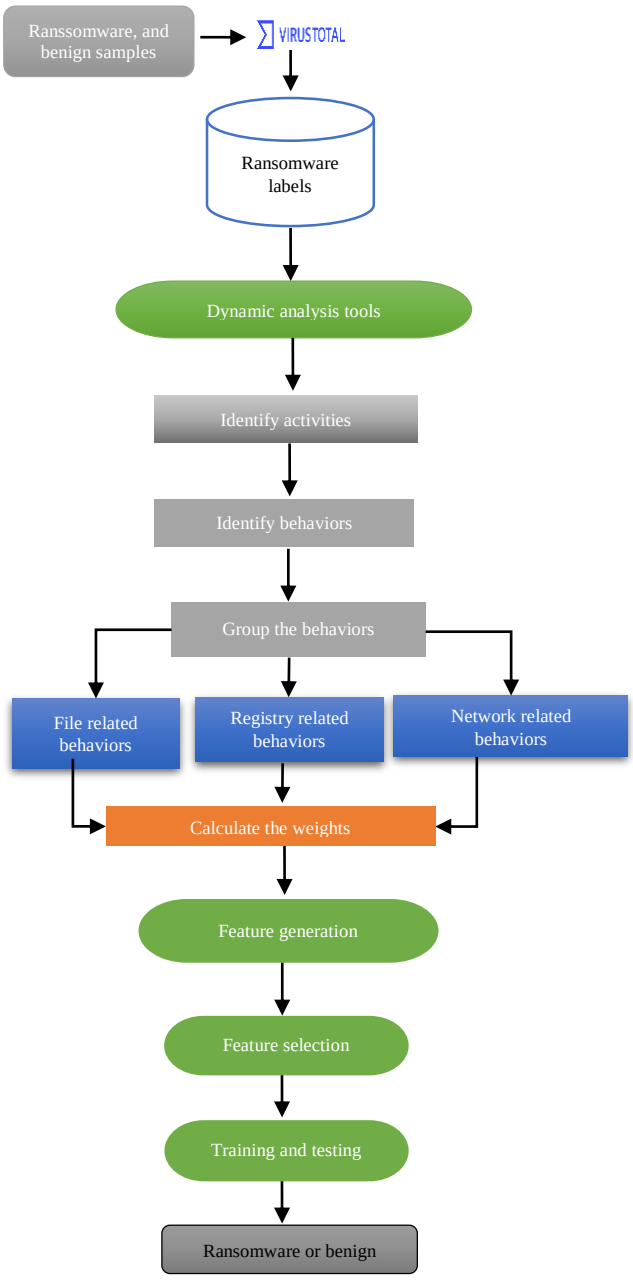

Figure 2. Proposed ransomware detection architecture

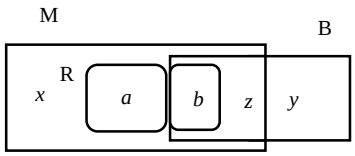

Figure 3. Shows the malware, benign and ransomware behaviors

3.3. Feature Creation and Selection

The Process Monitor is used to monitor ransomware behaviors. Collected ransomware and benign files are analyzed in virtual machines Windows 7, 8, and 10 (Figure 4). For each ransomware, the clean version of the virtual machine is used. During the feature generation, the implementation is carried out by using Python scripting language. When creating a property, following stages are followed:

Stage 1: Converting activities into behaviors

Stage 2: Separate the behaviors as file, registry, and network

Stage 3: Calculate the weights for each behavior where the action is performed and which action is performed

Stage 4: Group the behaviors based on the different system resources

Stage 4: Group the behaviors on different instances of the same resources

Stage 5: Extract the features from 1 to 5 consecutive order behaviors

Stage 7: Computing the weights for each feature

Stage 8: Calculate the frequency of each feature

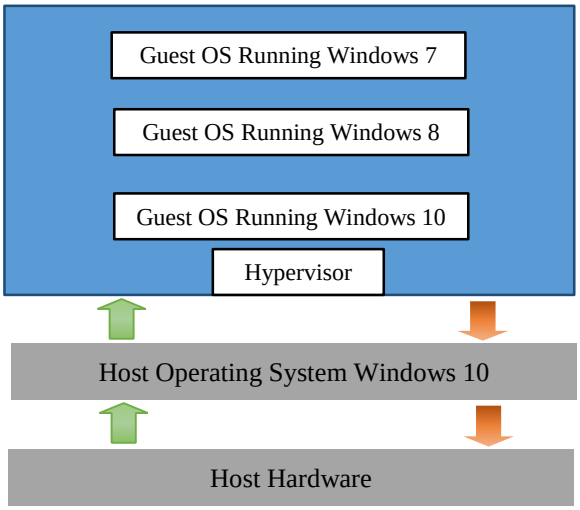

Figure 4. Ransomware analysis environment

After the features, their weights, and frequencies are obtained, the feature vector is created for each ransomware as well as benign samples. In other words, each analyzed file is represented as a feature vector. If the feature is repeated *x* times, *x* is written for frequency value. If the feature is repeated *0*, *0* is written for frequency value. For the feature selection phase, first more significant features are chosen based on the features' weights. During the weights assignment, the feature itself and the locations of features where performed is considered. In this process, the features are divided into 3 groups: file, registry and network related. Then each group is divided into subgroups. For example, if a feature about the file shows operations for the directory where the file is located, the weight will be low, if the feature creates another file and copies its own data to this file, it will be heavily weighted. Whether the feature is active or passive also affects the weight vector to be assigned. For example, if the feature is "read", the weight given is low, if it is "write", it is high. If the program frequently uses Ntdll.dll instead of Wininet.dll and kernel32.dll, or if it includes features that use high-risk methods such as NtReadProcessMemory and NtAdjustTokenPrivileges, the weight value to be assigned is high as well. After the weight assignments process is finished for each feature, the Information Gain algorithm is used to decrease the number of features further. In Information Gain, the property which has the maximum gain is chosen repeatedly when selecting the most significant features. The Information Gain can be calculated as the following for a given dataset.

Information $Gain\ (A) = Information(D) - Information_A(D)$ (4)

$Information(D) = -\sum_{j=1}^{v} pi\ log_2\ (pi)$ (5)

$Information_A(D) = -\sum_{j=1}^{v} \frac{|D_j|}{|D|} log_2\ (\frac{|D_j|}{|D|})$ (6)

$Gain(A)$ represents how much information will be obtained when splitting using the property *A*.

3.4. Detection

Although machine learning algorithms are used extensively in various areas for years, they are not used sufficiently in ransomware detection. Hence, several ML classifiers including J48, RF, AdaBoost, SLR, KNN, BN, and SMO are used in this study. We cannot say one classifier is more effective than the others since each classifier can perform better than others based on the numbers of features used, distributions of data, and association among properties. After the feature selection process is finished, the classification is performed. In this phase, selected features are given into the C4.5, RF, AdaBoost, SLR, KNN, BN, and SMO classifiers as an input and ransomware or benign is generated as an output.

3.5. Performance Evaluation

To assess the proposed method performance, detection rate (*DR*), false positive rate (*FPR*), *f*-measure, and accuracy are used. These measures are calculated by using the confusion matrix (Table 3). These measures are presented by the *TP* (The number of ransomware is marked as ransomware), *TN* (The number of benign is marked as benign), *FP* (The number of benign is mistakenly marked as ransomware), and *FN* (The number of ransomware accidentally marked as benign). By using these values, *DR*, *FPR*, f-measure, and accuracy are calculated as the following:

DR = Recall= TP/ (TP+FN) (7)

FPR = FP/ (FP+TN) (8)

Precision = TP/ (TP + FP) (9)

*F-Measure = (2 * precision * recall)/ (precision + recall)* (10)

Accuracy = TP+TN/ (TP+TN+FP+FN) (11)

Table 3. Confusion Matrix

		Predicted Class	
		Yes	No
Actual Class	Yes	TP	FN
	No	FP	TN

When training and testing is applied, holdout (75% and 25% split) as well as 10-fold cross-validation procedures are performed. At first, when a few ransomware samples were used, the performance of the holdout was less than cross-validation. However, when more ransomware samples were analyzed, the holdout performances increased.

4. Results and Discussion

This section of the paper presents the test results and interprets the proposed method performances. The results are summarized in table 4, table 5, and figure 5.

Table 4 shows the performance of ML classifiers on created ransomware dataset. Various ML classifiers as well as metrics are used to evaluate the performance. As it can be seen from table 4. except SMO, other classifiers' performances are quite high. To illustrate, J48 *DR* measured as 100%, *FPR* measured as 1.4%, *f*-measure calculated as 99.4%, and accuracy measured as 99.38%. Similar results are obtained from the classifiers RF, AdaBoost, SLR. The performances of the KNN and BN classifiers are satisfactory, too. These performance results show that our proposed method, which used to create the ransomware features, is effective and feasible to separate ransom specific features from the benign samples.

Table 4. Classifiers performances on the created ransomware

Classifier	DR (%)	FPR (%)	F-Measure (%)	Accuracy (%)
J48	100	1.4	99.4	99.38
RF	99.1	0.7	99.3	99.23
AdaBoost	98.8	0.7	99.1	99.07
SLR	97.8	1.4	98.3	98.14
KNN	91	7.9	92	91.53
BN	91.3	11.2	90.8	90.15
SMO	78.3	6.3	85.2	85.53

Figure 5 presents the accuracy results on different ML classifiers before feature selection and after feature selection. When ransomware and benign features are created by using the proposed method, the most significant features are selected by using proposed weights measures. Feature selection is also applied by using Information Gain before ML classifiers are performed. As it can be seen from the figure 5, before the feature selection the second time, the performances were quite good, but selecting features by Information Gain one more time increased the model performances. This shows that a few most significant features can lead to the conclusion of more than several hundreds of features.

The list of file-registry related features which are mostly seen in ransomware samples rather than benign in our testbed can be seen in table 5. It is observed that ransomware performs more operations on the created files and reads files' contents from one file into another. In addition, it copies itself into automatic startup locations on the registry, so it performs many registry reading and changing operations. Even though some of the listed features can be seen rarely in few benign files, the frequency of the features are quite low when compared to the frequency of features counted in ransomware. ReadFile, CreateFileReadFile, ReadFileWriteFile, WriteFileCreateFileMapping,SetBasicInformationFile, RegOpenKey, RegQueryValue, RegSetInfoKey, RegSetValue, and RegDeleteValue features are seen in ransomware samples with high frequencies in important file directories and registry locations.

Most of the current ransomware detection methods are performed only on a few ransomware samples which cannot be generalized for all ransomware families and strains. Besides, they have difficulties to detect unknown ransomware variants, and are not resistant to code obfuscation techniques. On the other hand, the proposed method could effectively perform on ransomware and benign samples. The proposed method tested on different types of ransomware, and increased the detection and accuracy rate for known and newly created ransomware. Furthermore, the proposed method decreased the number of features which can lead to separate ransomware from the cleanware as well as it is resistant to code obfuscation techniques.

Table 5. The list of file-registry related features that frequently seen in ransomware rarely seen in benign files

List of Features
ProcessStart
ThreadCreate
LoadImageReadFile
ReadFile
CreateFileReadFile
RegOpenKey
RegQueryValue
RegSetInfoKey
RegEnumValue
RegCreateKey
RegSetValue
RegDeleteValue
ReadFileWriteFile
WriteFileCreateFileMapping
SetBasicInformationFile
RegSetInfoKeyRegQueryKey
RegSetInfoKeyRegOpenKey
RegSetInfoKeyRegEnumValue
RegOpenKeyRegEnumValue
WriteFileSetBasicInformationFile
CreateFileSetBasicInformationFile
ReadFileQueryBasicInformationFile

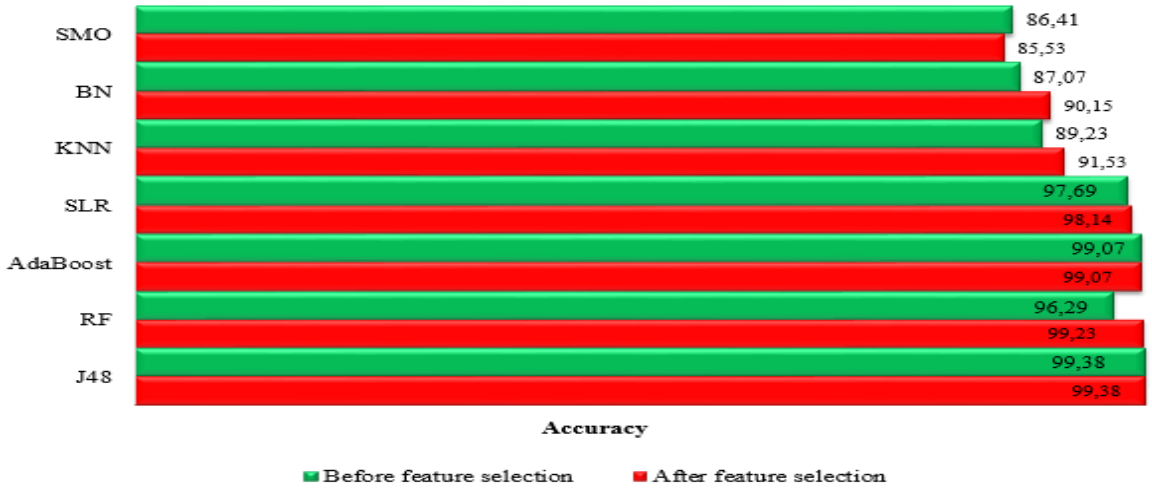

Figure 5. Proposed method performances before feature selection and after feature selection

Although the proposed method can effectively detect the several ransomware variants, there are still some limitations that need to be mentioned. The proposed method is tested on a few hundred ransomware and benign samples. The number of analyzed samples needs to be increased. Some behaviors are similar in ransomware and benign samples. Those behaviors are increased when more samples are analyzed. We need to modify our feature creation algorithm and update the threshold values for weight assignments to decrease those behaviors and associated features. In this study, the proposed method is tested on only Windows operating systems, the proposed algorithms can be modified and used for different operating systems.

5. Conclusion and Future Research Direction

Ransomware can be seen as one of the most destructive malware among the other cyber attacks. The ransomware attacks can deny access to the victim data by locker and crypto ransomware. While in crypto ransomware, files are encrypted in the computer system, in locker ransomware, accessing the computer is blocked. This paper proposed a behavioral based ransomware detection method which uses data mining and machine learning (ML) techniques. Several ransomware variants are analyzed, and behaviors are collected by using dynamic analysis tools. The behaviors are grouped into three categories including files, registries, and networks. Also, the behaviors' locations are considered when creating a feature's weights. The most effective features are selected by using our feature selection algorithm by using assigned weights as well as known Information Gain algorithm. The experiment's test results confirm that our proposed method is effective and feasible by measuring the various metrics including *DR*, *FPR*, *f*-measure, and accuracy. The best performance is measured as 100% for *DR*, 1.4% for *FPR*, 99.4% for *f*-measure, and 99.38% accuracy on the same classifier. Similar results are obtained for other used ML classifiers. As a future work, we aim to analyze more ransomware samples as well as classify the ransomware samples based on the different ransomware families. Furthermore, more dynamic analysis tools such as Wireshark, API Monitor, Regshot, and Sandboxes will be used for future studies.

Statement of Research and Publication Ethics

The study is complied with research and publication ethics

References

[1] D. Nieuwenhuizen, "A behavioural-based approach to ransomware detection," *MWR Labs Whitepaper*, 2017.
[2] Associated Press, "The Latest: UN warns cybercrime on rise during pandemic," 2020.
[3] Sophos Report, "The State of Ransomware 2021," 2021.

[4] Cognyte CTI Research Group, "Ransomware Attack Statistics 2021 – Growth & Analysis," 2021.
[5] S. Morgan, "Global Ransomware Damage Costs Predicted To Reach $20 Billion (USD) By 2021," *Cybercrime Magazine*, 2019.
[6] Ö. Aslan and R. Samet, "Investigation of possibilities to detect malware using existing Tools," in *2017 IEEE/ACS 14th International Conference on Computer Systems and Applications (AICCSA)* (pp. 1277-1284), 2017.
[7] J. P. Tailor and A.D. Patel, "A comprehensive survey: ransomware attacks prevention, monitoring and damage control," *Int. J. Res. Sci. Innov*, vol. 15, pp. 116-121, 2017.
[8] R. Brewer, "Ransomware attacks: detection, prevention and cure," *Network Security*, vol. 9, no. 5-9, 2016.
[9] D. Sgandurra, L. Muñoz-González, R. Mohsen and E. C. Lupu, "Automated dynamic analysis of ransomware: Benefits, limitations and use for detection," *arXiv preprint arXiv:1609.03020*, 2016.
[10] Ö. Aslan, R. Samet and Ö. Ö. Tanrıöver, "Using a Subtractive Center Behavioral Model to Detect Malware," *Security and Communication Networks, 2020*.
[11] R. Vinayakumar, K.P. Soman, K.S. Velan and S. Ganorkar, "Evaluating shallow and deep networks for ransomware detection and classification," in *2017 International Conference on Advances in Computing, Communications and Informatics (ICACCI)*, pp. 259-265, 2017.
[12] K. Cabaj, M. Gregorczyk and W. Mazurczyk, "Software-defined networking-based crypto ransomware detection using HTTP traffic characteristics," *Computers and Electrical Engineering*, vol. 66, pp. 353-368, 2018.
[13] A. O. Almashhadani, M. Kaiiali, S. Sezer and P. O'Kane, "A multi-classifier network-based crypto ransomware detection system: A case study of locky ransomware," *IEEE Access*, vol. 7, pp. 47053-47067, 2019.
[14] S. I. Bae, G. B. Lee and E. G. Im, "Ransomware detection using machine learning algorithms," *Concurrency and Computation: Practice and Experience*, vol. 32, no. 18, e5422, 2020.
[15] Ö. Aslan and R. Samet, "A comprehensive review on malware detection approaches," *IEEE Access*,vol. 8, pp. 6249-6271, 2020.
[16] C. Beaman, A. Barkworth, T. D. Akande, S. Hakak and M. K. Khan, "Ransomware: Recent advances, analysis, challenges and future research directions," *Computers and Security*, vol. 111, pp. 102490, 2021.
[17] Malware downloading website, https://malshare.com/, accessible in 2021.
[18] Malware downloading website, https://thezoo.morirt.com/, accessible in 2021.
[19] Malware downloading website, http://www.tekdefense.com/, accessible in 2021.
[20] Malware downloading website, https://virusshare.com/, accessible in 2021.

Bitlis Eren Üniversitesi Fen Bilimleri Dergisi
BİTLİS EREN UNIVERSITY JOURNAL OF SCIENCE
ISSN: 2147-3129/e-ISSN: 2147-3188
VOLUME: 11 NO: 2 PAGE:519-528 YEAR: 2022
DOI: 10.17798/bitlisfen.1048378

Control of Recyclable Wates and Zero Waste Project Applications: Example of Necmettin Erbakan University

Fatma KUNT[1*], Mehmet Yıldırım GÜNDÜZ[1]

[1]*Necmettin Erbakan University, Faculty of Engineering, Department of Environmental Engineering*
(ORCID: 0000-0003-2128-216X) (ORCID: 0000-0002-6221-6515)

Keywords: Waste management, Recycling, Zero waste, Environmental awareness.

Abstract

Billions of people around the world consume unconsciously every day. The resulting wastes are again left to nature by being irresponsible. Due to the rapid depletion of natural resources, humanity has entered new searches. The most important of these, waste management and recycling, dates back to B.C. Each purchased product is made available to us in a package. Well-evaluated wastes benefit the country's economy. The issue of evaluation of all wastes, especially recyclable wastes initiated with the Zero Waste Project, was initiated in our country in 2017 and was finalized in 2019 with a regulation.

In this study, the current situation of our university in terms of environmental awareness and protection of natural resources has been evaluated and it has been tried to reveal what studies have been done and what needs to be done. All activities carried out from the establishment of the Zero Waste Unit to the collection of wastes in separate classes are indicated in stages. In addition, a survey study was conducted on 306 people, in which students, academicians and administrative staff participated. According to the results of the survey, it was seen that the participants were conscious about waste management. Then, the contribution to the economy and the environment is calculated over the amount of collected waste, and the extent to which the country's economy can be contributed is emphasized with numerical values. As a result, the current level of awareness on waste management in universities was determined and information was given on how to improve it.

1. Introduction

Living beings tries to live together and continue their lives in a healthy and happy environment since their formation. Their most important needs is food and shelter. As time and technology progress, our needs are shaped and undergo many changes. During this time, fire the most important invention in human history was discovered and the greatest damage that can be given to nature has begun to be given. Fire which began to become uncontrollable caused many forests to burn. In the time until it was determined what would burn and what would put out the fire, the burning forests led to the deterioration of the first ecological order.

In the ındustrial age, the extraction of resources and the production of goods expanded to meet the ever growing consumer culture. Many consumption indexed products such as fabrics, white goods and electronic products that were once called luxury, are now becoming commonplace [1]. In proportion to these, environmental problems have emerged and environmental pollution issues have begun to enter our lives.

New strategies should be developed on waste management by considering the sociological and economic effects of the society. In this regard, states

*Corresponding author: drfatmakunt@gmail.com
Received: 27.12.2021, Accepted: 11.05.2022

should develop solutions to this situation through contracts and regulations in the international environment.

When looking at the processes carried out within the framework of waste management, which has an effective place among environmental protection policies, it is located the minimization of domestic, medical, hazardous and non-hazardous waste, separate collection at the source, intermediate storage, transportation, recovery, recycling and disposal of waste. [2].

In the light of all these developments, the importance which is given to recycling has increased considerably, espcially in recent years. Recycling is no longer viewed as just a waste collection business, but societies approach it as an initiative to raise environmental awareness and protect natural resources. [3].

In recent years, the importance of evaluating wastes with various projects around the world, even the efforts to create no waste have started. In our country, studies on waste management have gained momentum. The " Zero Waste Project" which was initiated under the auspicies of the Presidency and with the support of the Ministry of Environment and Urbanization, is the best example of this. With the Project initiated at the Ministry's service building on september 25, 2017, seperate collection, transportation and evaluation of waste at the source was initiated in all areas including public institutions, shopping malls, schools, universities, dormitories, airports, bus stations, hospitals, estates and residences. Compared to the past, recycling projects, which were left only to the volunteers of the citizens are encouraged by the state this time and they are tried to be developed through non governmental organizations, authorized organizations affiliated to the ministry, municipalities and television channels.

The Industrial Revolution started with James Watt's invention of the first steam engine in 1765, developed with the use of electricity as an input in iron production in 1870, and accelerated in 1940 with the Fordist Production System. The Flexible Production System and Informatıon Society phase, which came to the fore in the 1980's, continues today [4]. This situation has brought to the production and the use of resources used in production to an unavoidable point.

The rapid increase in the world population from the past to the present and the increase in the amount of consumption and the amount of waste generated at the same rate have led to the formation of different waste management practices and different reuse areas and sectors. Due to the rapid depletion of natural resources and the effect of damage to the environment, manufacturers have searched for different raw materials and it has been seen that many materials can be reused.

The products that we did not use as garbage for years were evaluated haphazardly and caused serious damage to the environment.

Recycling is the recycling of materials such as glass, paper, aluminum, plastic, battery, motor oil, accumulator, concrete, organic, electronic, medical, hazardous and non-hazardous wastes left after being used by people, after physical and chemical processes, and converted into raw materials and recycled. is included in the energy production process [5].

Recycling can reduce the negative effects of solid wastes on the environment, human health and the country's economy, as well as protect groundwater from pollution by eliminating pollution and destruction of natural resources. In addition, the raw materials and by-products required by the industry can be obtained from recycled products without consuming natural resources again [6].

Akçay and Dal's research aimed that determine the opinions of science teachers about sustainable development and zero waste. The sample group of the study consists of 102 science teachers working in Ağrı city center and central villages. "Opinion Form on Sustainable Development and Zero Waste" was used as data collection tool in the study. As a result of the research, it was determined that science teachers have general knowledge about the concepts related to sustainable development and zero waste, but their knowledge on some subjects is insufficient. Most of the teachers stated that sustainability means continuity and continuity, as well as investing in the future, protection of natural resources and their transfer to the future, continuous development and economic continuity [7].

Increasing concern about solid waste problems and a holistic approach to their management Pietzsch et al. (2017) developed a literature review about the subject ''Zero Waste". To that end, a systematic literature review was executed, through which 102 published articles were analyzed with the aim to, initially, comprehend the concept of Zero

Waste, and, then, map its benefits, challenges, and critical success factors [8].

In this study, our aim is to explain the level of the Zero Waste approach in the university and the municipality we are affiliated with, how our students have this awareness and how they should evaluate their waste and how we can contribute to our country's economy by offering solutions.

2. Material and Method

In this section, the researches, findings and comments related to the research problem are discussed. Figure 1 shows the graphic taken from the Higher Education Institution page, where there are 129 state universities, 74 foundation universities and 4 foundation university vocational schools affiliated to the Higher Education Institution in the 2019-2020 academic year in our country.

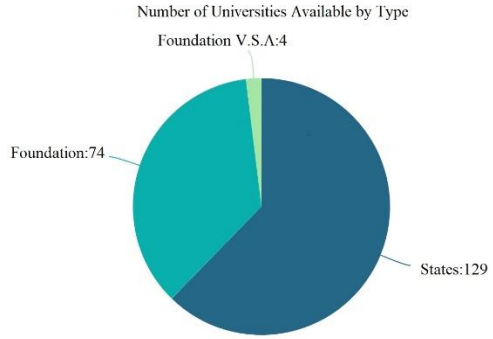

Figure 1. Number of universities in our country [9]

In Figure 2, the graph taken from the Higher Education Institution page shows that 3.002.964 people enrolled in the associate degree departments, 4.538.926 people in the undergraduate departments, 297.001 people in the graduate departments and 101.242 people in the doctorate departments of these universities in 2019-2020.

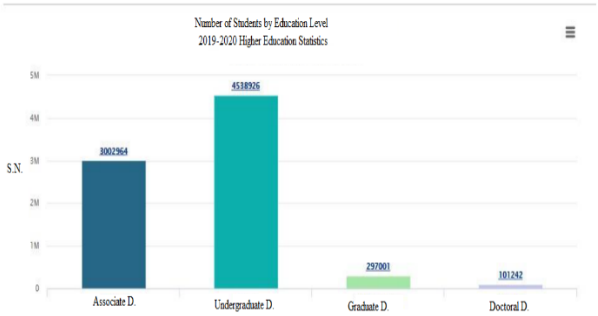

Figure 2. Total number of students [9]

There are 7.940.133 students in higher education in total across the country. Considering that each individual produces 1,17 kg/ person.day waste in a day, the amount of waste to be generated is approximately 9,289 tons. These wastes include all waste groups. If it is considered that 20% of the total waste amount is packaging waste and it is assumed that these wastes can be collected seperately at the rate of 100%, 1,857 tons of packaging waste will be generated per day. When these wastes are supported with waste management and Zero Waste projects in universities, they will make a great contribution to the country's economy and natural resources.

2.1. Working Area

University campuses can be considered " small cities" due to their size and the number of people living in the area on a daily basis and many higher education instiutions can generate significant environmental and social activities through both direct and indirect activities [10]. Universities and schools are the best places to launch awareness campaigns to raise global awareness of environmental issues, because they are essentials sources of knowledge and culture [11].
Necmettin Erbakan University which was established by being published in the Official Gazette dated 21 July 2010 and numbered 27.648, located within the borders of Meram district of Konya that is the province with the largest surface area in Turkey, has been included in our study area. There are a total of 36.334 students, including 20 faculties, 8 vocational schools, 31 research centers, 4 institutes, 8 coordinators, 27.020 undergraduate, 2.900 associate degree, 6.085 graduate and 329 pedogocial formation students throughout our university. In addition, there are 1.909 teaching staff and 1.149 administrative staff [12].

As a result of the decision taken by the university administration on 21.02.2020, faculty unit supervisors started to work within the scope of Zero Waste Management.

At the beginning of the university, recyclable wastes and organic wastes will be started and then all waste groups determined in the Waste Management Regulation will be tried to be separated.

Considering that it is a Faculty of Medicine affiliated to our university, it will be delivered to a company that has an agreement with Konya Metropolitan Municipality in order to manage the hazardous and medical wastes. In this article, only the amount of recyclable waste has been tried to be emphasized. The amounts of chemical and hazardous waste groups formed in the laboratories have not been calculated by us. Faculties have taken the necessary precautions for the chemical and hazardous wastes generated in the laboratories and they dispose of these wastes in accordance with the regulations.

For the waste codes under 20 code headings in the annexes of the Waste Management Regulation, the group starting with we 15, that is, packaging waste, is taken as basis. 15 01 01 Paper – Cardboard Packaging, 15 01 02 Plastic Packaging, 15 01 04 Metallic Packaging, 15 01 07 Glass Packaging classes are the waste codes that we will include in the calculation. We expect that paper and cardboard waste will come out of the classrooms and canteen. It is aimed to mix Plastic, Metal and Glass wastes in all waste bins left in the corridors, canteen and common areas, and then to separate them and deliver them to the municipality.

3. Results and Discussion

The Zero Waste approach is based on the 4R rule which forms the basis of awareness. Concepts such as Reduction, Reuse, Recycle, Respect are the words that make up the rule. The 4R Rule is a great way to protect our environment. That will help us for a livable world. That can be a guide for humanity to think while consuming and creating waste and what they should do to reduce the damage they cause to environment. It plays a role in changing lifestyles and teaches what they can do for future generations.

Figure 3. 4R Rule steps[13]

If we expand these terms a little more; Reduction; includes all the ways required for waste reduction. Wastes must be prevented. For global development, instead of spending our energy on the management of wastes, we can spend it on the management of wastes that do not occur or that occur less. In order to reduce waste generation, that is, non-recyclable disposable wastes, it was requested to apply a discount when the students come to buy their drinks with their own glasses by meeting with the school canteen managements.

It enables us to use durable and long lasting goods and to prefer materials that do not contain toxic substances. This concept will lead us to move away from disposable materials, produce waste-free or minimal waste, and protect natural resources.

Reuse; It means that a product that has completed the first use stage is used without changing its physical conditions, instead of being included in the waste class. We can classify the wastes that we can not reduce and that we have to produce. For instance, PET bottles will remain as waste after the product we use in them. Instead of this, it can be stored by putting food that we can consume in winter. In addition, in rural areas, tomato paste boxes or oil cans are also used by planting flowers in them.

The biggest obstacle to reuse is the ego of humanity. The concept of being new should be set aside and the understanding of reuse should be adopted.

Recycling; According to the definition in the Waste Management Regulation, is an "Any recovery process in which wastes are processed into products, materials or substances for their original use or other purposes, including the reprocessing of organic materials, excluding energy recovery and use as fuel or reprocessing of waste for filling".

In this step, after the wastes to be recycled are collected separately, new products can be obtained by breaking down and melting. While new products are

obtained by saving energy from wastes such as paper, glass, metal and plastic, more compost can be produced from organic wastes.

Respect; It is actually the most important item. Man has to respect himself. Based on this, we have to know that we are not the only ones living in the world and that we have to respect other living things as well. Henderson Island, which is located in the Pacific Ocean and is inhabited by no one, is heavily polluted by wastes which are stuck to sea creatures. No people live on this island. By indirect means, the reverse current in the oceans has been polluted by pollutants carried by attaching to the creatures that live and migrate on that island.

In other words, humanity did not show the same respect to nature that it did not feel for itself and has succeeded in polluting an island it has never lived on.

Figure 4. Zero Waste hierarchy

In accordance with the zero waste hierarchy, our primary goal is that the product we purchase should be durable, repairable and recyclable. So the important point is to consider before buying whether we really need it. Banning single-use plastic waste in canteens, cafeterias, social facilities, etc. on the campus, as well as preventing the use of plastic bags in markets and shopping centers will also help us reduce waste generation. Reusing the wastes we produce in the most appropriate form, instead of directly eliminating them, will again contribute greatly to waste management. If we have produced the waste but cannot reuse it, recycling is one of the best solutions. For this purpose, together with the commission established at the university, indoor boxes placed in faculties and social areas and outdoor piggy banks, where we will finally store the waste, were placed.

For this; In cooperation with the commission established at the university, the indoor boxes shown in Figure 7, which were placed in faculties and social areas, and the outdoor piggy banks, shown in Figure 6, where we will finally store the waste, were placed. A total of 1200 indoor boxes and 11 outdoor boxes were placed in our faculties. These boxes and piggy banks were provided by Konya Provincial Directorate of Environment and Urbanization, Konya Metropolitan Municipality and Meram Municipality. In addition, a mobile waste collection center with 4 compartments was provided to our Rectorate building through the Meram Municipality agreement company.

A meeting was held with the Ministry of Youth and Sports regarding the provision of a compost machine for organic wastes that will originate from the cafeteria and be generated as a result of student consumption. A compost machine was requested to the most suitable point for the cafeteria section through the Ministry. Due to the cost of the machine, no results have been obtained yet.

After the supply of collection materials, face-to-face training were given to 350-400 cleaning personnel and administrative personnel working in 9 faculties and the Rectorate. In addition, Environmental Awareness and Zero Waste training was given to approximately 80 participants within the scope of Necmettin Erbakan University Faculty of Nursing.

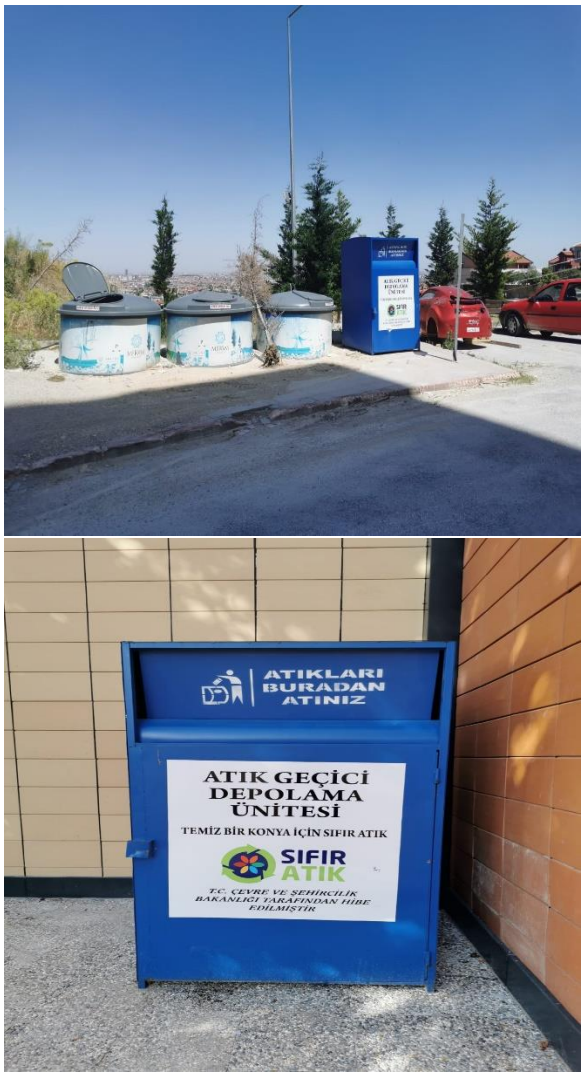

Figure 5. Waste temporary storage unit

Figure 6. Indoor boxes

Figure 7. Mobile waste collection center

Due to the pandemic period, an online survey was conducted with the participation of 213 students, 5 academicians, 13 administrative staff and 76 private sector employees. Participants were asked 18 questions. They were asked to mark the options

"Strongly Disagree - Disagree - No Idea - Agree - Strongly Agree" among the 1-5 options for their answers to the questions. The surveys were initiated by sending the web page created using the Survey Google Docs system to the participants. After the expected 15-day period, data were taken from the system as the answers are written in Table 1. It has been seen in the answers given by the participants of this survey that our students are aware of waste management and environmental awareness, but it is seen that the necessary materials are not provided to put them into practice and that environmental awareness education is not done much.

Table 1. Survey question and answer percentages

SURVEY QUESTIONS				
1. I follow the environmental problems of our country.				
5,20 %	5,90%	23,50 %	**42,20 %**	26,80%
2.I know that waste is classified.				
2,30 %	1,60%	6,20%	22,50 %	**69,00%**
3.I have information about the Zero Waste Project launched in our country.				
6,50 %	7,80%	2,90%	**28,80 %**	**37,60%**
4. I know what recyclable waste is.				
2,30 %	1,30%	7,90%	29,90 %	**59,20%**
5. Organic waste (food waste, etc.) and I accumulate recyclable waste (paper, glass, plastic, metal) separately.				
10,20 %	17,40 %	16,70 %	22,60 %	**34,10%**
6.I know at what stages the waste that I throw into the recycling bins goes through.				
5,60 %	14,40 %	**30,20 %**	22,60 %	28,90%
7. I know that I contributed to the national economy when I supported the Zero Waste Project.				
6,90 %	3,60%	9,80%	22,50 %	**58,20%**
8. I find the importance given to recycling sufficient in our country.				
28,60 %	**33,20 %**	26%	10,20 %	6,30%
9. I use the Zero Waste Bins located in the university corridors to contribute to recycling and the economy.				
3,70 %	6,30%	12,70 %	26%	**53,30%**
10. If an event (Interview-Symposium) on Zero Waste management is held at the university, I will participate.				
9,90 %	13,90 %	23,10 %	23,40 %	**31%**
11. I participate in environmental activities of Non-Governmental Organizations.				
13,50 %	22,80 %	**34,70 %**	17,50 %	15,80%
12. I would like to take part in an Environmental and Zero Waste Community to be established at the university.				
7,30 %	10,60 %	26,10 %	20,10 %	**36,60%**
13. I know that plastics have been lost in nature for many years.				
2,30 %	0%	1,30%	10,20 %	**86,50%**
14. I know that household waste is used in the production of electricity.				
6,30 %	6,90%	20,10 %	16,80 %	**51,30%**
15. I use lamps and electrical appliances when necessary.				
3,90 %	1,30%	11,10 %	25,20 %	**60%**
16. I throw the waste batteries in the waste battery box instead of throwing them in the trash.				
7,20 %	6,90%	7,20%	24,30 %	**54,80%**
17. I use cloth bags or nets instead of plastic bags in grocery stores.				
7,20 %	11,80 %	19%	23%	**40,30%**
18. I read it electronically instead of printing it out to avoid wasting paper.				
10,50 %	17,00 %	21%	18%	**34,10%**

4. Conclusion and Suggestions

After the lack of equipment and trainings, with the project we started in May 2020, the wastes started to be weighed and collected through a company which is contracted with the Municipality. The total amount of waste measured weekly with the help of a hand scale until April 2021 is presented in Table 2.

Table 2. Amount of waste collected

WASTE CODE	WASTE NAME	AMOUNT
15 01 01	Paper and Cardboard Packaging	33,408 kg
15 01 02	Plastic Packaging	22,272 kg
15 01 04	Metallic Packaging	7,424 kg
15 01 07	Glass Packaging	11,136 kg

According to the amount of waste collected, it belongs to the Ministry of Environment and Urbanization https://sifiratik.gov.tr/sifir-atik/atik-sayaci the contributions we have made to nature have been determined by the transactions made through the online system.

Our contribution to nature and economy with the 33,408 kg of paper and cardboard waste we collect;

- With the paper we collected, 567 trees were kept in nature.
- We saved 83 m3 of land in the landfills.

Figure 9. Our earnings from our paper - cardboard waste

Our contribution to nature and economy with the 22,272 kg plastic waste we collect;

- We saved 363 barrels of raw material oil.
- 913 kg of greenhouse gas emissions were prevented.

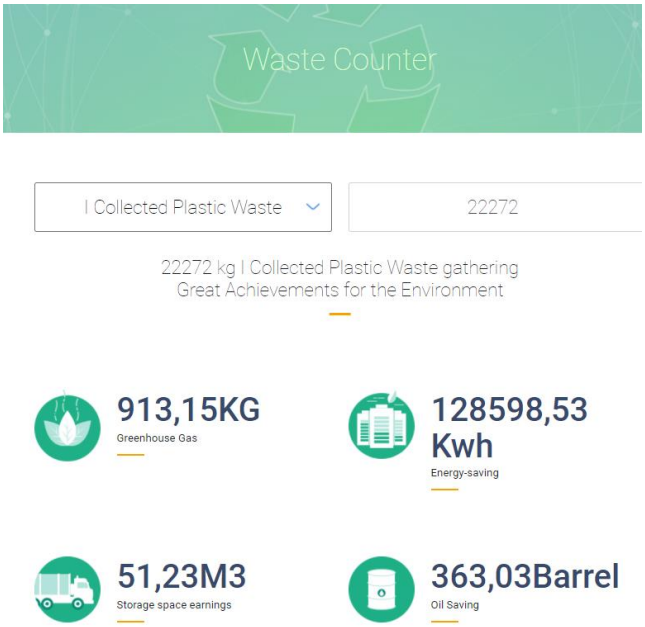

Figure 10. Our earnings from our plastic waste

Our contribution to nature and economy from the 7,424 kg of metal waste we collect;

- We saved 9 kg of raw materials used from nature.
- We prevented 705 kg of greenhouse gas emissions.

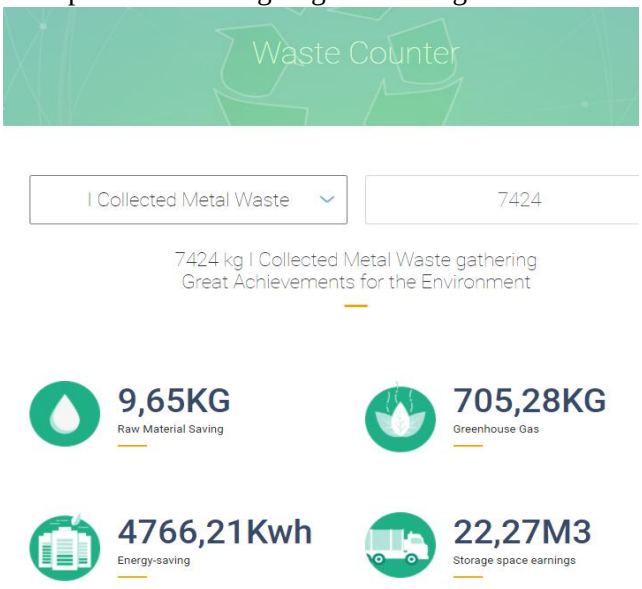

Figure 11. Our earnings from our metal waste

Our contribution to nature and economy from the 11,136 kg of glass waste we collect;

- We saved 13 kg of raw materials.
- We prevented 334 kg of greenhouse gas emissions.

Figure 12. Our earnings from our glass waste

Considering that we do not produce main materials such as cellulose and terephthalate within the borders of our country, but import them from abroad, promoting the recycling of paper and plastic bottles will enable us to use previously produced wastes instead of imported raw materials. In this way, the current account deficit in our country due to imports will be tried to be closed to some extent. In order to prevent waste with the Zero Waste Project, food waste will be prevented by the portion arrangement to be made in the cafeterias.

In addition to all the activities carried out for the development of the Zero Waste Project at universities, different suggestions can be presented.

- Environmental awareness trainings can continue continuously for all staff, academicians and students throughout the university.
- Information brochures about zero waste projects initiated at the university can be prepared for first year students who have just started university.
- Various activities can be supported by establishing a student community with volunteer students.
- Educational studies on zero waste should be carried out in established student groups and all faculties.
- Environmental awareness and zero waste training should be given to everyone, from the rector to the cleaning staff.
- Projects such as conferences, waste-free living panels, waste-free camps should be developed.
- Working areas such as non-governmental organizations, associations and foundations should be expanded.
- The responsibilities of each individual should be clearly stated.

Contributions of the authors

All authors contributed equally to the study.

Conflict of Interest Statement

There is no conflict of interest between the authors.

Statement of Research and Publication Ethics

The study is complied with research and publication ethics

References

[1] A. U. Zaman, "A Comprehensive Review Of The Development Of Zero Waste Management: Lessons Learned And Guideliners," *Journal of Clear Production*, pp. 12-15, 2015.

[2] K. Ulaşlı, Geri Kazanılabilir Atıkların Yönetimi ve Sıfır Atık Projesi Uygulamaları: Kadıköy Belediyesi, Yüksek Lisans Tezi, Hasan Kalyoncu Üniversitesi Fen Bilimleri Enstitüsü, Gaziantep, 2015.

[3] A. Gürer, and G. Sakız, "Yetişkinlerin Küresel Isınma ile İlgili Bilgi Düzeyleri ve Geri Dönüşüm Farkındalıkları," *İnsan ve Toplum Bilimleri Araştırma Dergisi*, vol. 7, no. 2, pp. 1364-1391, 2018.

[4] Z. Dinler, *İktisada Giriş*, Ekin Kitapevi Yayınları, Dokuzuncu Basım, Bursa, 2003.

[5] P. Ural Keleş, and M. İ. Keleş, "İlkokul 3. ve 4. Sınıf Öğrencilerinin Geri Dönüşüm Kavramı ile İlgili Algıları," *Erzincan Üniversitesi Eğitim Fakültesi Dergisi*, vol. 20, no. 2, pp. 481-498, 2018.

[6] S. Büyüksaatçi, T. Küçükdeniz, and Ş. Esnaf, "Geri Dönüşüm Tesislerinin Yerinin Gustafson-Kessel Algoritması – Konveks Programlama Melez Modeli Tabanlı Simülasyon ile Belirlenmesi," *İstanbul Ticaret Üniversitesi Fen Bilimleri Dergisi*, vol. 7, no. 13, pp. 1-20, 2008.

[7] Ş. Dal, and N. Okur Akçay, "Fen bilimleri öğretmenlerinin sürdürülebilir kalkınma ve sıfır atık ile ilgili görüşlerinin belirlenmesi," *e- Kafkas Eğitim Araştırmaları Dergisi*, vol. 8, no. 3, pp. 438-459, 2021. doi:10.30900/kafkasegt.862414.

[8] N. Pietzsch, J. L. D. Ribeiro, J. F. de Medeiros, "Benefits, challenges and critical factors of success for Zero Waste: A systematic literature review," *Waste Management*, vol. 67, pp. 324-353, 2017.

[9] https://istatistik.yok.gov.tr/ (Erişim Tarihi: 22.05.2021) (URL-1).

[10] R. Lukman, A. Tiwary, A. Azapagic, "Towards greeninig a university campus: The first step towards "greening" a university campus," *Resour. Conserv. Recycl*, vol. 53, pp. 639-644, 2017.

[11] E. C. Rada, C. Bresciani, E. Girelli, M. Ragazzi, M. Schiavon and V. Torretta, "Analysis and Measures to Improve Waste Management in School" *Sustainability*, vol. 8, pp. 840, 2017.

[12] https://www.erbakan.edu.tr/s/sayilarla-neu (Erişim Tarihi: 22.05.2021) (URL-2).

[13] O. Can, *İklim Değişikliği ve Atık Yönetimi*, İstaç, 2015.

Bitlis Eren Üniversitesi Fen Bilimleri Dergisi
BİTLİS EREN UNIVERSITY JOURNAL OF SCIENCE
ISSN: 2147-3129/e-ISSN: 2147-3188
VOLUME: 11 NO: 2 PAGE: 529-536 YEAR: 2022
DOI: 10.17798/bitlisfen.1051969

The Lyapunov Exponents of Thirring Instantons

Beyrul CANBAZ[1*]

[1]*Department of Occupational Health and Safety, Istanbul Yeni Yuzyil University, Istanbul, Turkey. (ORCID: 0000-0002-5633-2296)*

Keywords: Instanton, Spinor, Lyapunov exponents, Chaos theory, Nonlinear systems

Abstract

Recently, nonlinear differential equations corresponding to pure spinor instanton solutions have been obtained by using Heisenberg ansatz in the 2D Thirring Model, which is used as a subject model in Quantum field theory. In addition, the evolution of spinor type instanton solutions in phase space was investigated according to the change in the constant parameter β. Spinor instanton dynamics is a special case in which nonlinear terms play an important role. Chaos describes certain nonlinear dynamical systems that depend very precisely on initial conditions. Lyapunov exponents are an important method for measuring stability and deterministic chaos in dynamical systems. Lyapunov exponents characterize and quantify the dynamics of small perturbations of a state or orbit in state space. In this study, The chaotic behavior of spinor type instanton solutions is analyzed by numerical study of the time evolution of the Lyapunov exponents. Moreover, the Lyapunov spectrum of spinor type instanton solutions with respect to varying the parameter are plotted. As a result of the Lyapunov Spectrum, it was determined that the spinor type instanton solutions exhibit chaotic behavior at parameter value β= 2. Periodic and quasi periodic behaviors were detected when the parameter values were β<2. In cases of β>2, weak chaotic behaviors were observed. This study demonstrates that Thirring Instantons, which are spinor type instanton solutions, exhibit chaotic properties.

1. Introduction

Instantons are classical solutions that spontaneously break conformal symmetry with zero energy in finite and non-zero actions. In quantum field theories, instantons are defined as tunneling processes between vacuums with different topological structures [1]. This property plays a significant role in understanding the problems of quark confinement within particles.

The Thirring Model was proposed by Walter Thirring in 1958 as a test model for quantum field theories [2]. The model is a 2-dimensional conformal invariant pure fermionic a model [2]. In addition, the model is an important known model for fermions in (1 + 1) space-time dimensions with a nonlinear term [3]. Akdeniz–Smailagic found a class of pure spinor type instanton solutions of the Thirring Model by breaking of the conformal symmetry i.e. $\langle 0|\bar{\psi}\bar{\psi}|0\rangle \neq 0$ in 1979 [3]. Later, it was shown that the spinor type instanton solutions are stable [4]. A decade ago, nonlinear differential equations corresponding to pure spinor instanton solutions were obtained by Heisenberg ansatz in the Thirring Model [5]. Moreover, the evolution of these spinor-type instanton solutions in phase space and the role of coupling constant in this evolution were examined [5]. A few years ago, the stability of the spinor type instanton solutions was investigated by the scale index method [6]. Recently, the chaotic behavior of the spinor type instanton solutions was investigated using the General Alignment Index (GALI) method [7].

Chaos describes certain nonlinear dynamical systems that depend very precisely on initial

*Corresponding author: beyrul.canbaz@yeniyuzyil.edu.tr
Received: 31.12.2021, Accepted: 23.06.2022

conditions [8]. Instability is one of the most fundamental properties of nonlinear dynamical systems. Generally, Lyapunov exponents are characterized by exponential deviation rates of infinitesimal irregularities given an orbit. Lyapunov exponents are also known to characterize properties of chaotic systems other than instability, such as metric entropy and attractive size. Also, for large systems, the extent of chaos is defined on the basis of the spectrum of Lyapunov exponents [9].

Lyapunov exponents (LEs) are one of the most common methods for determining the degree of sensitivity of the evolution of a dynamical system to initial conditions [10]. LEs measure how the distance between orbitals with two slightly different initial conditions grows or shrinks over time Having a positive largest Lyapunov exponent (LLE) is generally considered an indication that the system is chaotic [11]. The LLE value is an indicator of chaoticity, but numerical computation can take a lot of time before they manifest themselves, especially for orbits that adhere to regular orbits for a long time. Since the chaotic behavior LLE is defined as the t → ∞ limit of the system, the time required for the system to converge to the limit value may be excessively long [12]. LLE provides more information than characterizing a trajectory as regular or chaotic, because it also quantifies the concept of chaoticity by providing a characteristic time scale for the dynamical system studied. In a detailed analysis of the time evolution of the LLE, a sloping decrease of the power-law $\lambda_1 \propto t^{-1}$ indicates regular state and any deviation from this law signifies chaos or weak chaos [12]. Also, staying constant to a positive value according to increasing time durations indicates that the system is in a chaotic or weakly chaotic state.

In this study, chaotic behavior of spinor type instanton solutions [5] is investigated by Lyapunov exponents. The chaotic behavior is analyzed by performing a numerical study of the time evolution of the Lyapunov exponents (LEs). Lyapunov exponent (LE) spectrum of system of two nonlinear ordinary differential equations corresponding spinor type instanton solutions with varying the parameters is plotted. Additionally, the behaviors in phase space and Lyapunov exponents of the spinor type instanton solutions are demonstrated comparatively.

2. Material and Method

2.1. Thirring Model

The Thirring model [2] is described by the two-dimensional pure fermionic, conformal invariant Lagrange equation.

$$L = i\bar{\psi}\sigma_\mu\partial_\mu\psi + \frac{g}{2}(\bar{\psi}\psi)^2 \quad (1)$$

Here, the positive coupling constant is g [3].The equation of motion is,

$$i\sigma_\mu\partial_\mu\psi + g(\bar{\psi}\psi)\psi = 0 \quad (2)$$

The Euclidean configuration of the Heisenberg approximation [13],

$$\psi = \left[ix_\mu\gamma_\mu\chi(s) + \varphi(s)\right]C \quad (3)$$

is given by the equation. Here C is an arbitrarily chosen spinor constant, $\chi(s)$ and $\varphi(s)$ of $s = x^2 + t^2 (x_1 \equiv x, x_2 \equiv t)$ are the real functions. Substituting equation (3) for equation (2), we get

$$\chi(s) + s\frac{d\chi(s)}{ds} + \alpha[s\chi(s)^2 + \varphi(s)^2]\varphi(s) = 0 \quad (4a)$$

$$\frac{d\varphi(s)}{ds} - \alpha[s\chi(s)^2 + \varphi(s)^2]\chi(s) = 0 \quad (4b)$$

The dimensionless form of nonlinear simple differential equation system pair (4a) and (4b),

$$2\frac{dp(t)}{dt} + \frac{1}{2}p(t) - \alpha AB(p(t)^2 + q(t)^2)q(t) = 0 \quad (5a)$$

$$2\frac{dq(t)}{dt} - \frac{1}{2}q(t) - \alpha AB(p(t)^2 + q(t)^2)p(t) = 0 \quad (5b)$$

Here, p and q are dimensionless functions of t and A, B are constants [5]. The solution of this system of equations for β=α(AB)=1 is the Thirring instantons [5]. The evolution of Thirring instantons has been investigated in phase space as seen Figure 1 [5].

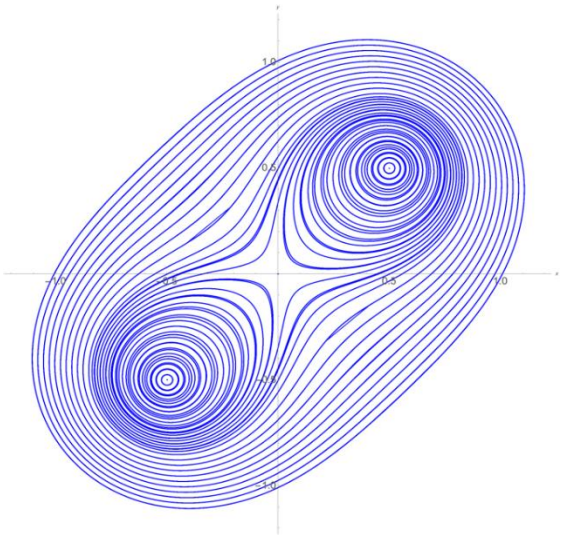

Figure 1. Phase diagram corresponding to the solutions of Thirring instantons [5].

A while ago, the stability of spinor type instanton solutions with different $\beta = \alpha(AB)$ values has been investigated by the scale index method [6]. It was determined that spinor type instanton solutions are unstable according to the scale index method for the value of $\beta = 2$ as seen Figure 2 [6].

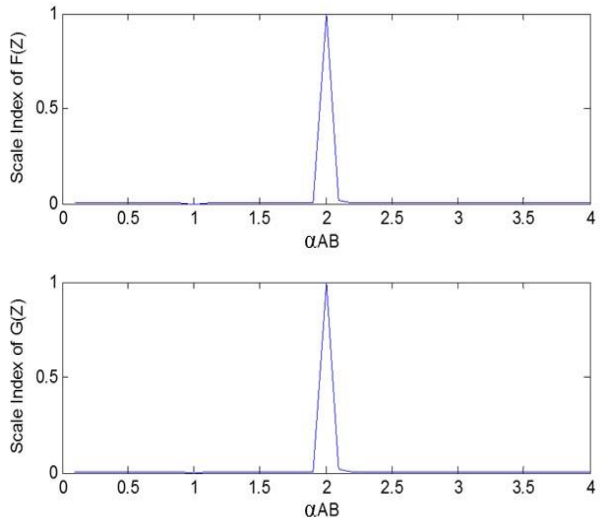

Figure 2. Scale index parameters of F(Z) and G(Z) versus αAB for the initial points: -1/2,-1/2 [6]. (In this study, Scale index parameters of *F(Z)* and *G(Z)* are *q* and *p* respectively)

2.2 Computation of Lyapunov Exponents

Lyapunov exponents are the rate of convergence or divergence of two adjacent orbits over time [14]. If the orbitals diverge slowly, they are periodic systems, and if this divergence is exponential, they are chaotic systems. The positive value of the Lyapunov exponent corresponds to the chaos, the zero value to the periodicity, and the negative value to the stable equilibrium state. In Ref. [15], a numerical technique was developed for calculating all LEs based on the time evolution of many deviation vectors kept linearly independent by a Gram-Schmidt orthonormalization procedure. In this study, the articles of Oseledec [16] and Benettin et al. [17, 18], whose theoretical results have been clearly proven, are followed.

A dynamical system can be characterized by a differential equation as

$$\dot{x} = \frac{dx}{dt} = f(x), \quad t > 0 \tag{6}$$

here f is a continuous function. The LEs can be numerically obtained as time limits of appropriately computed quantities Λ_i, which are usually referred to as the finite-time LEs, i.e.

$$\lambda_l = \lim_{t\to\infty} \Lambda_l\,, \qquad l = 1, 2, \dots, N \tag{7}$$

which can for example be evaluated by the so-called 'standard method' [12, 18]. In particular, the largest Lyapunov exponent LLE (λ_1) is estimated as the limit for $t \to \infty$ of the finite-time LLE

$$\Lambda_1(t) = \frac{1}{t} \ln \frac{\|\omega(t)\|}{\|\omega(0)\|} \tag{8}$$

Where $\omega(t) = \delta x(t) = \big(\delta q(t), \delta p(t)\big) = \big(\delta q_1(t), \dots, \delta q_N(t)\big)\,, \delta p_1(t), \dots, \delta p_N(t)$ denotes the phase space perturbation vector from the orbit $x(t) = \big(q(t), p(t)\big)$ at time *t*. In the case of regular orbits, $\lambda_1(t)$ tends to zero following the power law [12, 18]

$$\lambda_1(t) \propto t^{-1}, \tag{9}$$

while for chaotic or weakly chaotic orbits, it tends to

a non-zero positive value.

The Lyapunov exponents describe the behavior of vectors in the tangent space of the phase space and are defined from the Jacobian matrix

$$J_{i,j}(t) = \frac{df_i(x)}{dx_j}\Big|_{x(t)} \qquad (10)$$

The evolution of an initial deviation vector $\omega(0)$ is governed by the so-called variational equations [12]

$$\dot{\omega}(t) = \begin{bmatrix} \delta\dot{q}_l(t) \\ \delta\dot{p}_l(t) \end{bmatrix} = J.\omega(t), l = 1, 2, \dots, N, \qquad (11)$$

this Jacobian defines the evolution of the tangent vectors via the equation.

Jacobian matrix evaluated at the position $x(t)$ of the orbit in the system's phase space for all $i, j = 1, 2, \dots, 2N$. The elements of J matrix in (11) depend on the evolution of the orbit $x(t)$ but are independent of $\omega(t)$.

The Lyapunov exponents are calculated for a long observation time of 100000 t units and with a step size 1.0 t unit. The time evolution of the Lyapunov exponents of system (5) is shown in Fig. 6. The (+, −) nature of the Lyapunov exponents confirms the chaotic nature [19]. Numerical calculations of the Lyapunov exponents are integrated together using the tangent map of the model corresponding to the spinor type instanton solutions (5) that describe the evolution of the initial excitation of the system along with the equations of variation (11) for one or more initial perturbations (deviation vectors). method and Verner's "Most Efficient" 9/8 Runge–Kutta solver with tight fault tolerances [20]. The algorithm was implemented on top of the DynamicalSystems.jl software library, which was written entirely in the Julia programming language [21, 22].

3. Results and Discussion

The phase diagram corresponding to the spinor type instanton solutions found in the previous study [5] is given in Figure 1. As can be seen from the phase diagram, the stable points are (-0.5, -0.5) and (0.5,0.5). For β =α(AB) =1, the solution of this system of equations is the Thirring instantons given in Ref. [5]. Based on these stable points of the Thirring instantons, the Lyapunov spectrum of the spinor type instanton solutions (5) with varying parameter β =α(AB) for (q, p) = (0.5,0.5) fixed are examined. Figures 3 and 4 shows LLE spectrum of the spinor type instanton solutions (5), plotted in the interval (0, 100] and (0, 10) respectively by increasing the parameter β by 0.01 for initial condition (q, p) = (0.5, 0.5) fixed. t = 10^5 time units are used for numerical solution.

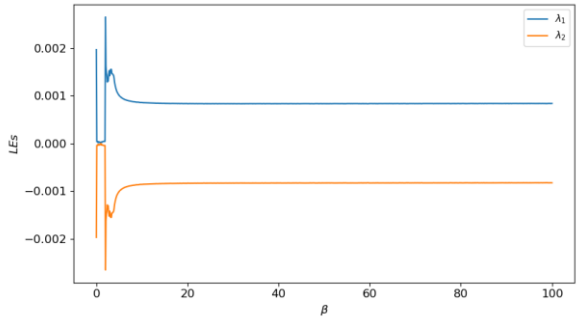

Figure 3. Lyapunov spectrum of spinor type instanton solutions (5) versus parameter β varying in the range of (0,100] for the initial points (0.5,0.5).

Looking at the trajectories in the phase diagram in Figure 1, it is not possible to reach a definite conclusion about the chaoticity. When we look at the Lyapunov spectrum in Figure 3, it is seen that the Lyapunov exponents become to 0 after a while from the beginning. Then a sharp increase occurs. Afterwards, the largest Lyapunov exponents (λ_1) proceed in a positive constant number. The largest Lyapunov exponent is $\lambda_1 \approx 0.003$. Also, since the largest Lyapunov exponents are 0 at the value close to the beginning, it is seen to be periodic. Afterwards, the trajectories can be interpreted as chaotic since they are always positive.

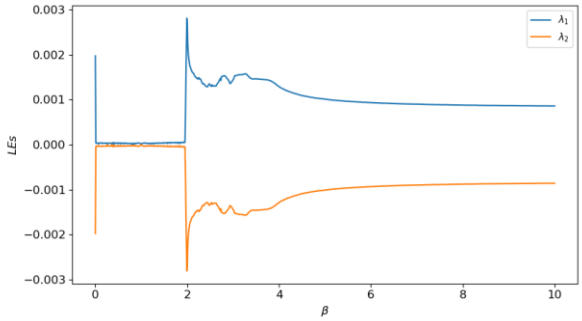

Figure 4. Lyapunov spectrum of spinor type instanton solutions (5) versus parameter β varying in the range of (0,10] for the initial points (0.5,0.5).

In order to observe the changes in the Lyapunov spectrum in more detail, a narrower area was chosen and the Lyapunov spectrum in Figure 4 is plotted. As seen in this spectrum, since largest Lyapunov exponents are 0 around β = 1 and β = 2, they are observed as periodic orbits. It increases sharply around β = 2 and then progresses positively.

Compared with the results obtained by the scale index method in Figure 2 [6], the chaotic situation in the Lyapunov spectrum for the value of β =2 has been determined. In the scale index method, values other than around β =1 are slightly above 0 [6]. When this situation is interpreted together with the Lyapunov spectrum, values slightly above 0 can be interpreted as a weak chaotic state or a quasi-periodic state.

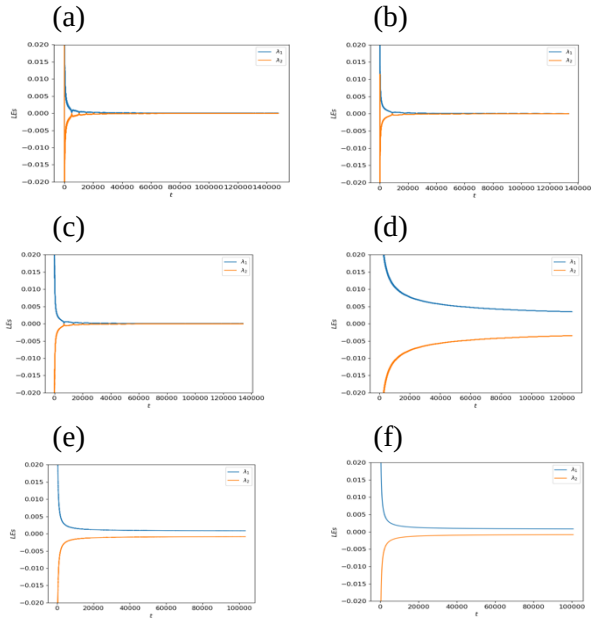

Figure 5. The time evolution of Lyapunov exponents (LEs) of the spinor type instanton solutions (5) for t = 10^5 time units with (a) β =0.1, (b) β =0.5, (c) β =1.5, (d) β =2.0, (e) β =10.0 (f) β =50.0 for initial conditions (q, p) =(0.5, 0.5) fixed.

The time evolution of Lyapunov exponents of the spinor type instanton solutions at t=10^5 time units is investigated in Figure 5. With the iteration number t=10^5, 1000 points are sampled from each trajectory studied in Figure 5. to evaluate the time evolution of the Lyapunov exponents with respect to the initial conditions at different values for the parameter value with (a) β =0.1, (b) β =0.5, (c) β =1.5, (d) β =2.0, (e) β =10.0 (f) β =50.0 for initial conditions (q, p) =(0.5, 0.5) fixed.

In Figure 5, it is seen that the Lyapunov exponents of the system (5) for (a) β =0.1, (b) β =0.5, (c) β =1.5 converge to 0. However, in Figure 5, it is seen that the Lyapunov exponents of the system (5) for (a) β =2, (b) β =10.0, (c) β =50.0 converge towards λ = ± 0.005 (β =2) and λ = ± 0, 002 (β =10.0 and 50.0). According to Figure 5, the time evolution of LEs are very small and zero indicates that the system has periodic and semi-periodic orbits in β< 2. Moreover, positive Lyapunov exponents do not have large values at β>2 values, it can be concluded that they have weak chaotic orbits.

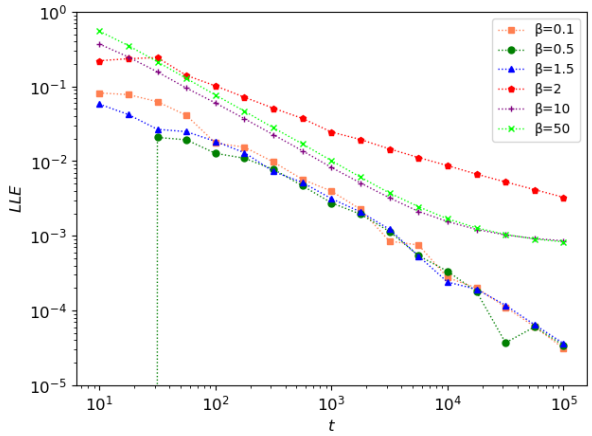

Figure 6. The time evolution of the largest Lyapunov exponents (LLEs) of the spinor type instanton solutions (5) with respect to different 6 different parameters β for t = 10^5 time units and initial conditional (q, p)=(0.5, 0.5) fixed. Parameter values: β =0.1(coral, square), β =0.5(green, circle), β =1.5 (blue, triangle), β =2.0 (red, pentagon), β =10.0 (purple, +), β =50.0 (lime, X). The axes are chosen according to the logarithmic base.

Here, only the largest Lyapunov exponent (LLE) is taken into account, as it determines the predictability of the system [12]. A positive LLE is generally accepted as an indication that the system is chaotic. The time evolution of the largest Lyapunov exponents (LLEs) of the spinor type instanton solutions Eq. (5) is investigated up to $t = 10^5$ time units. To evaluate the time evolution of the LLE, 1000 points are sampled from each trajectory. The time evolution of the LLE with 1000 test points; dots and lines represent linear regression with respect to the median in Figure 6. $t = 10^5$ is the final integration time of the simulations.

The time evolution of the LLEs of the spinor type instanton solutions with different the parameter value β and keeping the initial condition (q, p)=(0.5, 0.5) is ploted in Figure 6 (LLEs for β values; β =0.1(coral, square), β =0.5(green, circle), β =1.5 (blue, triangle), β =2.0 (red, pentagon), β =10.0 (purple, +), β =50.0 (lime, X)). In Figure 6 . In the case of β =0.1(coral, square), β =0.5(green, circle), β =1.5 (blue, triangle), LLEs tend to zero following the power law, i.e. orbits are in regular state. The other cases β =10.0 (purple, +), β =50.0 (lime, X), the LEEs begin to deviate from the $\lambda_1 \propto t^{-1}$ decrease denoting regular behavior when $t = 10^3$ time and the chaotic nature of the orbits. In Figure 6 , it is clearly seen that there is a convergence of around λ_1=10^{-3} at β =2 and values greater than β =2.

Considering the time evolution of the LLEs according to varying β values in the initial conditions (q, p)=(0.5, 0.5) fixed in Figure 6, it is seen that the fermion-like instanton solutions exhibit weak chaotic behavior.

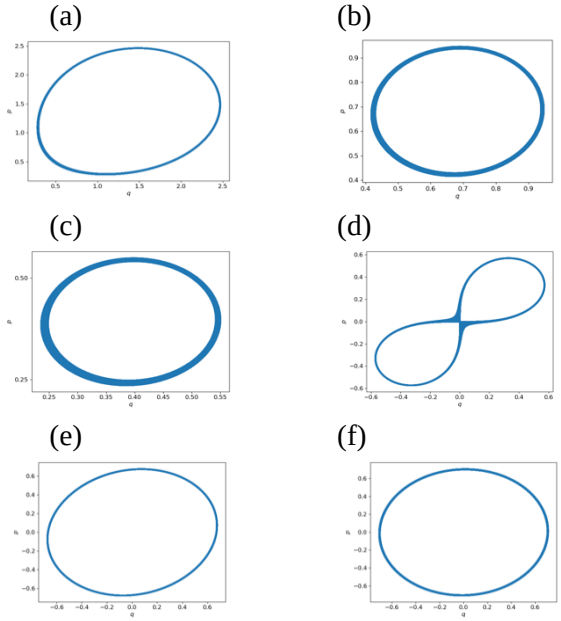

Figure 7. The phase space of the spinor type instanton solutions (5) for t = 10^5 time units with (a) β =0.1, (b) β =0.5, (c) β =1.5, (d) β =2.0, (e) β =10.0 (f) β =50.0 for initial conditions (q, p) =(0.5, 0.5) fixed.

The phase spaces of the system (5) were examined for random selected six points. In Figure 7 d), it is seen that the point (0,0) is an unstable point for β =2, which is the chaotic state, and bifurcation occurs in the phase diagram. In Figure 7. (a) β =0.1, (b) β =0.5, (c) β =1.5, values β<2, regular states appears around a single attractor. In Figure 7. (e) β =10.0 (f) β =50.0 values β>2, the system is periodic around the two attractors.

Although the phase spaces give information about the general states of the orbits, they do not give enough information about the chaotic states. For parameter value β = 2 in the system (6), the phase space and Lyapunov spectrum show a chaotic state. However, there is no chaotic situation in phase space for other parameter values. At β <2 values, the Lyapunov exponents approach zero and decrease proportionally with $\lambda_1(t) \propto t^{-1}$. The fact that the

Lyapunov exponents are very small and zero indicates that the system has periodic or semi-periodic orbits in these intervals. Since positive Lyapunov exponents do not have large values at β>2 values and according to power law (9) LLEs tends to a non-zero positive value, the orbits can be concluded that they have weakly chaotic states.

4. Conclusion and Suggestions

In quantum gauge theory, instantons have an important place in response to tunneling events between vacuums. In this study, the existence of chaos in spinor type instanton solutions found by the Heisenberg approach to the 2D conformal invariant Thirring model was investigated. The phase space and stable equilibrium points, which were found before and corresponding to the Thirring instantons, were taken as Ref. [5]. According to these values, the time evolution of the Lyapunov exponents, the time evolution of largest Lyapunov exponents of the spinor type instanton solutions (5) were plotted. Moreover Lyapunov spectrum of the system (5) was plotted. In addition, phase diagrams were examined for some critical situations.

The Lyapunov exponent is one of the most effective methods of detecting chaos [23]. According to the results found in this study, the fact that the largest Lyapunov exponent is greater than zero shows that the spinor type instanton solutions exhibit chaotic behavior. When the Lyapunov spectrum is also examined, it shows that spinor type instantons have regular orbit when the parameter value is β =α(AB)=1. In general, values less than β<2 indicate that it has regular or quasi-periodic orbits. Lyapunov spectrum, time evolution of LEs, phase space and scale index method [6] show that spinor type instanton solutions exhibit chaotic state at β =2. It is seen that there is a weakly chaotic states when the parameter values are from β>2. These results are consistent with the results found by the GALI method [7] that the orbits of spinor-type instanton solutions are regular around the fixed point, and the orbits become chaotic as they move away from the fixed point. The fact that spinor-type instanton solutions have both periodic orbits and chaotic orbits is an important sign of the existence of chaos in spinor-type instanton solutions. In the Gursey model, which is also a model with spinor type instanton solutions, research on Lyapunov exponents can be done and more information can be learned about the behavior of spinor type instanton solutions[24, 25].

Acknowledgment

I would like to thank K. Gediz Akdeniz for his support during the preparation of this study.

Statement of Research and Publication Ethics

The study is complied with research and publication ethics

References

[1] M. Dunajski, *Solitons, Instantons, and Twistors*, Oxford University Press, New York, 2010.
[2] W. E. Thirring, "A Soluble. Relativistic Field Theory," *Anal. Phys*., vol. 3, pp. 91, 1958.
[3] K. G. Akdeniz and A. Smailagić, "Classical solutions for fermionic models," *Il Nuovo Cimento A,* vol. 51, pp. 345– 357, 1979.
[4] K. G. Akdenizand M. Hortacsu, "Functional determinant for the Thirring model with instanton," *II Nuovo Cimento A*, vol. 59, pp. 181-188, 1980.
[5] B. Canbaz, C. Onem, F. Aydogmus and K. G. Akdeniz, "From Heisenberg ansatz to attractor of Thirring Instanton," *Chaos, Solitons & Fractals*, vol. 45, no. 2, pp. 188–191, 2012.
[6] N. Yılmaz, B. Canbaz, M. Akıllı and C. Onem, 2018. "Study of the stability of the fermionic instanton solutions by the scale index method," *Physics Letters A*, vol. 382, no. 32, pp. 2118-2121, 2012.
[7] B. Canbaz, "Genel Hizalama İndeksi Yöntemiyle 2 Boyutlu Saf Fermiyonik Modelde Kaosun İncelenmesi," *Avrupa Bilim ve Teknoloji Dergisi*. vol. 33, pp. 161-166, 2022.
[8] J. Greick, *Chaos: making a new science*, Oxford Sciences Publications, 19-26. Oxford, England, 1987.

[9] T. P. Shimizu, K. A. Takeuchi, "Measuring Lyapunov exponents of large chaotic systems with global coupling by time series analysis," *Chaos: An Interdisciplinary Journal of Nonlinear Science*, vol. 28, no. 12, pp. 121103, 2018.
[10] R. L. Devaney, *An Introduction to Chaotic Dynamical Systems. 3rd Edition*, CRC Press, 2021.
[11] D. Feldman, *Chaos and Dynamical Systems (Primers in Complex Systems, 7)*, Princeton University Press, 2019.
[12] C. Skokos, "The Lyapunov Characteristic Exponents and Their Computation," in *Dynamics of Small Solar System Bodies and Exoplanets*, Springer: Berlin/Heidelberg, Germany, pp. 63–135, 2010.
[13] W. Heisenberg, Zs. Naturforsch., 9a, 292, 1954.
[14] W. Siegert, 2009. *Local Lyapunov Exponents*, Springer, Berlin, pp. 143-229, 1954.
[15] A. M. Lyapunov, "General problem of stability of motion. Annals of the Faculty of Sciences of Toulouse" *Mathematics, Series 2*, vol. 9, pp. 203-474, 1947.
[16] V. I. Oseledec, "A multiplicative ergodic theorem. Lyapunov characteristic number for dynamical systems," *Trans. Moscow Math. Soc.*, vol. 19, pp. 197-231, 1968.
[17] G. Benettin, L. Galgani, A. Giorgilli and J. Strelcyn, "Lyapunov Characteristic Exponents for smooth dynamical systems and for Hamiltonian systems; a method for computing all of them. Part 1," *Theory. Meccanica*, vol. 15, pp. 9–20, 1980.
[18] G. Benettin, L. Galgani, A. Giorgilli and J. Strelcyn, "Lyapunov Characteristic Exponents for smooth dynamical systems and for Hamiltonian systems; a method for computing all of them. Part 2: Numerical application," *Meccanica*, vol. 15 pp. 21–30, 1980.
[19] J. P. Singh and B. K. Roy, "The nature of Lyapunov exponents is (+,+,−,−). Is it a hyperchaotic system?," *Chaos, Solitons Fractals*, vol. 92, pp. 73–85, 2016.
[20] J. H. Verner, "Numerically optimal Runge–Kutta pairs with interpolants," *Numer Algor*, vol. 53, pp. 383–396, 2010.
[21] G. Datseris, 2018 "Dynamical Systems. jl: A Julia software library for chaos and non- linear dynamics," *J. Open Source Softw*. vol. 3, pp. 598, 2010.
[22] C. Rackauckas and Q. Nie, 2017. "Differential Equations. jl—A performant and feature-rich ecosystem for solving differential equations Julia," *J. Open Res. Softw.*, vol. 5, pp. 15, 2010.
[23] C. Skokos, G. A. Gottwald and J. Laskar, *Chaos Detection and Predictability*, Springer, 2016.
[24] M. Ak, "Investigation of Chaos in 4D Fermionic Model by the Generalized Alignment Index Method," *Journal of the Institute of Science and Technology*, vol. 12, no. 2, pp. 726-734, 2022.
[25] F. Aydogmus, B. Canbaz, C. Onem and K. G. Akdeniz, "The Behaviours of Gursey Instantons in Phase Space," *Acta Physica Polonica B*, vol. 44, pp. 1837-1845, 2013.

Bitlis Eren Üniversitesi Fen Bilimleri Dergisi
BİTLİS EREN UNIVERSITY JOURNAL OF SCIENCE
ISSN: 2147-3129/e-ISSN: 2147-3188
VOLUME: 11 NO: 2 PAGE: 537-543 YEAR: 2022
DOI: 10.17798/bitlisfen.1052403

Optimal Location Determination of Electric Vehicle Charging Stations: A Case Study on Turkey's Most Preferred Highway

Muhammed SÜTÇÜ[1*], İbrahim Tümay GÜLBAHAR[1]

[1]*Abdullah Gül University, Faculty of Engineering, Department of Industrial Engineering (ORCID: 0000-0002-8523-9103) (ORCID: 0000-0001-9192-0782)*

Keywords: Electric vehicle charging station, Facility location, Location allocation models, Decision making in GIS.

Abstract

Today, electric vehicles are seen as one of the most suitable and environmentally friendly alternatives to internal combustion engine vehicles. An important issue related to the dissemination of electric vehicles is the location of the vehicle charging network and specifically the optimum location selection of the charging stations. Generally, most of the studies focus on popular destinations such as city centers, shopping areas, bus stations, and airports. Although these places are often used in normal life, they can usually provide an adequate solution for daily charging needs due to the number of alternative charging stations. However, finding adequate charging stations is not possible in intercity travels especially in highways. In this paper, we proposed a decision model to determine the location of electric car charging stations in highways. We create an optimization model to decide the optimum locations for the charging stations that can meet the customer demands on the Istanbul-Ankara highway. The proposed model determines optimum charging stations that enable passengers traveling with their electric vehicles to travel in Istanbul-Ankara highway in the shortest time.

1. Introduction

People prefer to use a wide variety of tools to make everyday life easier. From the first human to nowadays, people have used many vehicles such as feet, domestic horses, and bicycles to move from one location to another for different reasons such as finding food, meeting, and doing business. However, in the last two centuries, more technological means of transportation have been invented and more usage has gained popularity. One of these means of transportation is the traditional fossil fuel-dependent cars, which are used for many things.

The technology of internal combustion engine vehicles that have been on the streets since the 19th century, which we have been using almost every day of our lives, is developing day by day and the number of uses is constantly increasing with an exponential acceleration. However, with the effect of air pollution and global warming, the place of vehicles using fossil fuels in our lives is questioned [1], [2]. According to The World Bank, as of 2014, transportation has more than 20% proportion of CO2 emission in the world [3]. These adverse situations brought different opportunities, one of which is the increase in alternative energy vehicle usage trend [4]. As examples to this trend Figures 1 and 2 are shared below. This trend not only increased vehicle sales, but also supported the development of the necessary infrastructure and by-products. For more sustainable fossil energy usage in transportation industry, vehicles that energized with alternative-fuel, especially electric vehicles (EVs), are seen more logical and suitable way [5].

*Corresponding author: muhammed.sutcu@agu.edu.tr
Received: 02.01.2022, Accepted: 22.02.2022

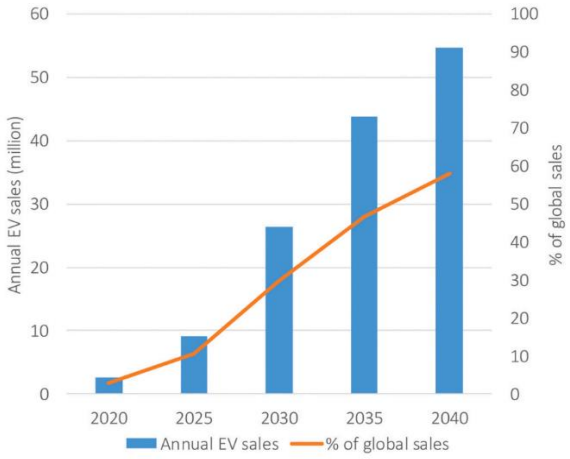

Figure 1. EV Sales' Forecast (Adopted From [17])

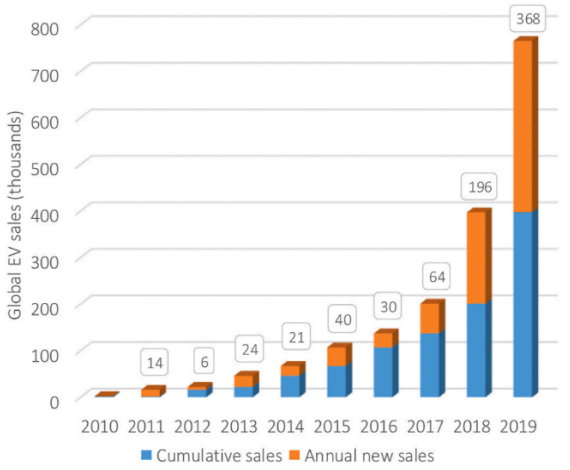

Figure 2. Global EV Sales (Adopted From [17])

The most important infrastructure requirement is undoubtedly charging stations in order to provide the maintenance and support of electric vehicles. However, it is important to understand that the infrastructure has just begun to be established, therefore the priorities and requirements are needed to be determined and an action plan must be created in the consumption of the related necessary resources. On account of the fact that, an important issue for extensive usage of EV is lack of charging stations which barrier to alternative fuel vehicles popularity [6, 7, 8]. To have an effective and useful plan for determining sites, several cases from different aspects are analyzed and various methods hold out.

The only way to increase EV (Electric Vehicle) drivers' service satisfaction is not to place new charging stations, but the regulate the schedules and places of the charging stations is a proper way to observe more satisfaction [9]. To be able to deal with that, waiting times are analyzed and revision of the locations of the charging stations is offered by Qin and Zhang, 2011 [9]. On the other hand, having broad service network is inevitable and sine qua non for the EV industry founders and customers. Therefore, in the literature new studies are seen frequently like implementation offerings in South Korea. One of the dramatic technological improvements still being observed in the South Korea, and that leads to EV network's proliferation. That give a raise to studies that focuses on to locating new EV charging stations like conducted case study by Chung and Kwon, 2015 [8]. They proposed a case study based on the actual traffic flow data of the Korean Expressway network. Three different methods are used to offer solution and comparison as multi-rotation optimization, forward myopic and backward myopic optimization. At the end, outcomes of the multi-rotation optimization model were observed as the most suitable method for large scale network problems.

Considering the traffic density and the capacity of the charging stations, another alternative study was conducted to reduce the time lost by electric vehicle drivers while reaching the charging stations [10]. The region is divided into nine different sub-regions using the Genetic Algorithm to find the best locations and successfully propose a solution to satisfy customers with EV drivers.

Another approach to deal with charging station siting problem is proposed by Erbaş et al., 2018 [11]. The approach in this study is Geographic Information System (GIS) based Multi Criteria Decision Analysis to choose places to implant charging stations. For criteria prioritization fuzzy analytical hierarchy process (AHP), for ranking between potential places technique for order preference by similarity to ideal solution (TOPSIS) are used. These approaches are applied for the inner-city of Ankara, and alternative site places are suggested as the result of the study.

The problem investigated in this paper is not just a theoretically created problem but also a globally discussed affair as mentioned. This widespread issue is taking place in actions of companies working on this related industries, non-governmental organizations, even statesmen of the countries. Recently, Scotland hosted the United Nations Climate Change Conference (COP26) between the 31st of October and the 12th of November 2021. The main focus of these conferences were the climate change and the global warming. Declaration about the zero emission cars and vans till 2035 is signed by 33 countries, 40 cities, 11 automotive manufacturers and 27 fleet owners [12].

One another motivation of this study is that the investment of TOGG (Turkey's Automobile Joint Venture Group) on the EV technology and

manufacturing in Turkey. The manufacturing process is expected to start in 2022 [13]. Therefore, burst of demand will be observed for the charging station in the region. On the other hand, when the literature checked, there exist not much study on this topic that covers possible optimum locations for charging stations in Turkey especially on highways. This study is going to be offering optimum locations for the charging stations that can meet the customer demands on the given highway.

Our main motivation in this study is the use of electric vehicles in Turkey is increasing exponentially. Especially, considering the TOGG investment and Turkey signed the agreement to come out of diesel and gasoline vehicles in Turkey by 2035, the infrastructure of charging stations is of great importance. So, based on the future progress on electric cars in Turkey, a suitable and environmentally friendly model is needed to build proper infrastructure for the electric car vehicle.

Charging is not a big problem in urban transportation. In daily life, people can usually provide an adequate solution for daily charging needs due to the number of alternative charging stations in urban areas and the range that they travel is limited. However, when traveling between cities, considering the distance to be traveled, it is not possible for electric vehicles to complete their travel with a single charge. Electric vehicle battery technology currently has a range of approximately 200 km. For this reason, vehicles may need to be charged twice in a trip of approximately 500 km, such as İstanbul – Ankara. Our contribution in this study is to create an optimization model to decide the optimum locations for the charging stations that can meet the customer demands. The proposed model determines optimum charging stations that enable passengers traveling with their electric vehicles to travel in İstanbul – Ankara highway in the shortest time.

The remainder of this article is structured as follows: In section 2, used methodology is presented and in the 3rd section basic notations and definitions in the article is given. Formulation of the mathematical model is also covered in the section 3. In section 4, the outputs of the applied methodology and the explanation of them are given. In section 5, conclusion of the article is done and suggestions for future studies is expressed.

2. Methodology

Our main focus in this study is meeting the customer demand, which is reaching the intercity EV charging services. For that purpose, a place should be selected for analyzing. Therefore, Ankara-İstanbul highway was chosen and the reason behind is that network was one of the well-fitting routes because, it is one of the most used interurban highways in Turkey. Therefore, passenger data can be collected easily on this highway.

The chosen route, Ankara – İstanbul Highway, includes 23 different entrances to the highway for drivers. Candidate places are selected, the idea was very similar to the case study that has been done by Chung and Kwon, 2015 [8]. Stopovers and the mostly known gas stations are candidate places of the study. The reason that the inner-city places were not chosen is the ranges of the EVs are generally enough to recharge in any place in a city like houses, offices and so on.

Coordinates of the stopovers and gas stations were extracted from "Google Maps". Purpose of using these places is that they have suitable infrastructure to implant charging stations and customers willing to wait and rest there. At the end, combined number of the stopovers and gas stations were determined. These places are shown in Figure 3 below. In the Figure, pins are representing toll booths and the gas stations. On the other hand, data is received from Directorate of Highways of Ankara – İstanbul, and with 23 entrance the highway divided into the 24 parts. The traffic density information of those parts is obtained from the highway traffic volume map of 2016.

Other must have information for the study is ranges of the existing EVs. Without consideration of the ranges, mathematical model and its outcomes will only be irrelevant and useless. Thus, the ranges are gathered and shown in the Table 1, also while solving the problem, inevitably, ranges were one of

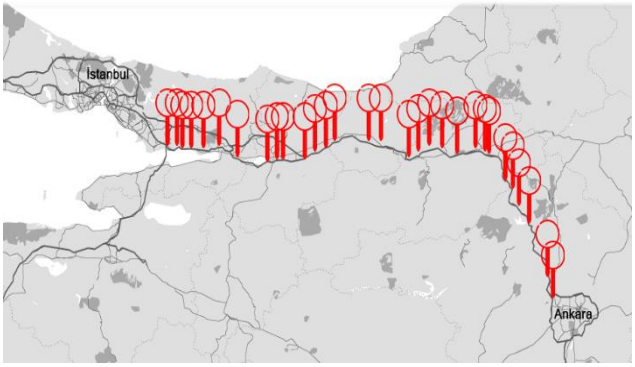

Figure 3. Toll Booths, Stopovers and Gas Stations

the limitations.

Brands have different strategies for the battery of an EV. Some seek for the long-distance coverage, however, several of them aim to offer lighter vehicle. Even the same brand can have different market plan for its models. Therefore,

different brands and models should have been considered. In the Table below, its seen that the ranges alter within each brand and models. Ranges have a non-negligible effect on the results, they change the constraints status which also directly affects the satisfaction level of the customers.

Table 1. Ranges of the Various EVs

Brand	Model (year of 2017)	Range (Kilometers)
BMW	i3	183.4
Chevrolet	Bold EV	238
Fiat	500e	135.2
Ford	Focus Electric	185
Hyundai	Ioniq Electric	199.5
Kia	Soul EV	149.7
Mercedes	B250e	120
Mitsubishi	i-MiEV	160
Nissan	Leaf	172.2
Tesla	Model S	337.9
Tesla	Model X	383.1
Volkswagen	e-Golf	201
BYD	E6	300

The least range is considered as the standard range of an EV, the reason behind, if the least range EV user can be satisfied with the given service others also can be satisfied. With this way, one of the goals of the study will be reached as desired and the customer satisfaction will be improved. On the other hand, for each model year of 2017 is selected as seen in Table 1. The reason behind is to have more affordable EVs for people and it's not logical to consider only brand-new cars.

3. Mathematical Modelling

In this section, we are going to give mathematical model that solves the current problem. Following content is basically explanation of the data, made assumptions before running the mathematical model to handle reasonable model, notations and their definition, and lastly the formulation part.

3.1. Data

The considered highway, which is İstanbul – Ankara Highway, is divided into 24 parts according to entrances as mentioned. Parts that contain stopovers and gas stations are used as candidate areas for implementation. In the mathematical modelling part, it is desired to match minimum range coverage for each model of EVs. The idea behind is to achieve maximum satisfaction of customers.

3.2. Assumptions of the Mathematical Model

A model is a representation of the real world to have better understanding on the actual situations [14]. Therefore, to solve a real-world problem, it is needed to be made some key assumptions. In this study, to make the problem able to be solved several assumptions have been made. Those assumptions are as followings:

- The drivers do not have extraordinary driving style,
- Driving ranges of the EVs are constant and invariable,
- The least range of the included EV models is applicable for every customer,
- Batteries of the EVs linearly run out,
- Neither electric-truck nor electric-motorcycle is existing in the system,
- Electricity in the charging system is not finite and not interruptible,
- No queue forms in front of the charging stations,
- The first and the last stopovers are not adequate to implant any chargers.

3.3. Modelling Sets/Indices

i *parts of the İstanbul – Ankara Highway i = {1, 2, 3, …, 24},*

j *parts of the İstanbul – Ankara Highway j = i = {1, 2, 3, …, 24};*

Data/Parameters

R_{ij} *Distance between parts of the İstanbul – Ankara Highway i and j,*

D_i *Expected demand of the İstanbul – Ankara Highway part i,*

M_i *Number of station (stopover or gas station) on the İstanbul – Ankara Highway part i;*

Decision Variables

X_i = *Capacity of the station on the İstanbul – Ankara Highway part i,*

Y_i = *{1, if the station (stopover or gas station) is selected to locate charger(s) on to the İstanbul – Ankara Highway part i; 0, otherwise},*

N_i = *Not satisfied demand of the customers on the İstanbul – Ankara Highway part i;*

3.4. Formulation Objective Function Constraints

$$z^* = min\ \Sigma_i N_i \qquad (1)$$

$$99 \times Y_i \geq X_i \qquad \forall i, \qquad (2)$$

$$X_i \geq Y_i \qquad \forall i, \qquad (3)$$

$$M_i \geq Y_i \qquad \forall i, \qquad (4)$$

$$N_i = D_i - (99 \times X_i) \qquad \forall i, \qquad (5)$$

$$Y_3 \geq 1, \qquad (6)$$

$$Y_3 \leq Y_4 + Y_5 + Y_6 + Y_7 + Y_8, \qquad (7)$$

$$X_i \in N \qquad \forall i, \qquad (8)$$

$$Y_i \in \{0,1\} \qquad \forall i, \qquad (9)$$

Decision variable X_i is defined as capacity of the station i, which means that outcome of the model as the number of chargers in the given station. On the other hand, Y_i is binary variable that determines whether the station will have charger or not. Another decision variable N_i is defined to check the demand amount that is expected to observe but not met. With this way, model and the outcomes of it are being more persuasive for the counter party of this study.

Objective function (1) is minimizing the not satisfied demand of the customers on the İstanbul – Ankara Highway. Ordinarily, the most desired outcome is to have maximum customer satisfaction, which is the first necessity of the study. Constraint (2) defined for that the chargers are not located, if there exist no station on the highway part *i*. The reason of this constraint is any charger cannot be established onto not selected station intuitively. Also, this constraint prevents model to locate more than 99 chargers on any station. Constraint (3) prevents the model to not select any place as charging station which does not have any charger capacity. Constraint (3) also ensures decision variable Y_i to take value of 1, if the chargers are located at there. On the other hand, it archives and lists the chosen locations. Constraint (4) ensures that place can be selected to implement charging station(s) if there exist at least a stopover in that part of highway. Constraint (5) works as database to keep not satisfied customer numbers in a part. In the model 1st and the 2nd parts are entrance and the exit of the İstanbul – Ankara Highway. Therefore, in the Constraint (6) it set to be locate a charging station to the 3rd station which is the first stop for the highway users. This guarantees to start with a fully charged battery to the trip. Constraint (7) ensures that on the stations from 4 to 8 there should be at least one more station which is needed for the range of the model that offers least km range capacity. Constraint (8) and (9) are to define variable X as natural number and variable Y as a binary variable.

4. Results

Given model in section 2 is examined by using GAMS software as optimization tool. Formulation and constraints are coded properly to the platform and after running the model obtained results are as follows:

- Seven places are chosen as the charging station implementation area,
- Totally, 7 stations and 15 chargers are enough to meet the demand of the customers,
- One charger for 3rd station, one charger for 8th station, one charger for 9th station, two chargers for 14th station, four chargers four 17th station, four chargers for 19th station and two chargers in 22nd station is enough to satisfy the demands on those locations is seen as an outcome of the model,
- These outcomes are shared, as a bunch, in the Table 2 below.

Table 2. Outcomes of the Mathematical Model (Selected Sites and Number of Chargers on Them)

Station:	***2***	***3***	***4***	***5***	***6***	***7***	***8***	***9***	***10***	***11***	***12***	***13***	***14***	***15***	***16***	***17***	***18***	***19***	***20***	***21***	***22***	***23***
Y_i	0	1	0	0	0	0	1	1	0	0	0	0	1	0	0	1	0	1	0	0	1	0
X_i	0	1	0	0	0	0	1	1	0	0	0	0	2	0	0	4	0	4	0	0	2	0

In the Table 2, 1st and the 24th sites are not existed. The reason behind, they are the entrance and the exit parts of the İstanbul – Ankara Highway. In the row 2, Y_i values are seen as 0 and 1. What it means that, if the value is one then it's offered to select this site as a station. On the other hand, X_i values are the offered number of chargers at the station to put on the site. For example, station 19 is selected as a station (Y_i = 1), and because of the expected EV density in that place, it's offered to establish 4 chargers (X_i = 4) to meet the demand of the customers.

Number of sites and total number of chargers in these sites were the main expected outcomes of the study. Therefore, results written above are illustrated with the Figure 4 for better understanding. Charger icons in the Figure 4 are representing the sites that can optimally meet the customer demands. To travel between İstanbul and Ankara by an EV on the highway, these offered places are meet the requirements while minimizing the unsatisfied number of customers.

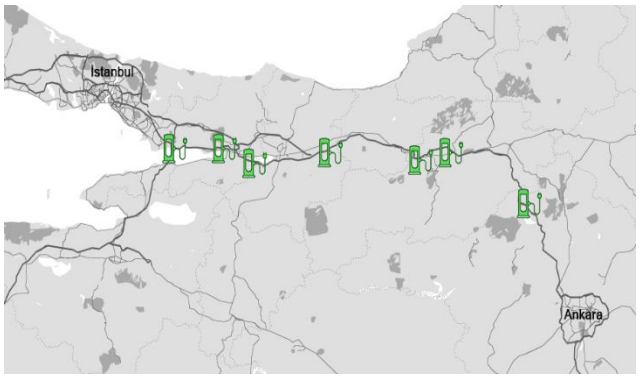

Figure 1. Charger Locations - Outcome of the Model

5. Conclusion and the Future Works

With the technological improvements, new tools are used to make life easier. Undoubtedly, the tools that are in our daily life have the most impact on establishing infrastructure network. Nowadays, EVs are one of the trending technologies to be used over the world and which is getting widely used in Turkey. The study done is born because of this necessity. Also, according to statement given by Fatih Dönmez, who is Minister of Energy and Natural Resources Ministry, shows that charging stations are going to be one of the critical infrastructure necessities. It is indicated by Minister; projections show that there is going to be more than 1 million EVs in Turkey until the 2030 [15]. However, Turkey is in the beginning of this EV era. In the first half of the 2021, only 894 EVs and 186 PHEVs (Plug-in Hybrid Electric Vehicle) are sold officially [16]. Recently, some encouragements are proposed by the government, but still the number of EVs in Turkey is very low to be appreciated by the Turkish community. Regulations and situation of infrastructure need to be supportive and satisfactory to stimulate EV usage.

One of the most used highways in Turkey, İstanbul – Ankara Highway, is selected and accordingly to traffic density potential charging station locations are determined by a mathematical modelling approach. As a result of the work done, its seen that the demand of the EV drivers can be satisfied by implementing 7 stations and 15 chargers through İstanbul – Ankara Highway.

This study had some assumptions as EVs are evenly distributed to the traditional combustion engine cars and they are using one of the most crowded highways in Turkey. For the coming studies its planned to forecast number of EVs in Turkey extending to years and their distribution. With the outcomes of forecasting approach, highways are going to be selected to work on and data will be up to date. Also, different scenarios like various charge status of EVs are going to be considered and analysis will be based on them. Lastly, the offered solution will not be stationary, it is going to be giving recommendations for several sequential years. This will help to cover real world more closely.

Acknowledgments

The authors would like to thank the anonymous reviewers and editor for their comments and suggestions.

Authors' Contribution

In this study, Author 1 contributed to literature review, evaluation of the data, building the mathematical model, analyzing the result of the mathematical model, article writing, while Author 2 contributed to formation of ideas, collection of the data, building the mathematical model, article writing and editing.

Statement of Conflicts of Interest

There is no conflict of interest between the authors.

Statement of Research and Publication Ethics

The authors declare that this study complies with Research and Publication Ethics.

References

[1] Y. He, K. M. Kockelman, and K. A. Perrine, "Optimal locations of U.S. fast charging stations for long-distance trip completion by battery electric vehicles," *Journal of Cleaner Production*, vol. 214, pp. 452–461, Mar. 2019, doi: 10.1016/j.jclepro.2018.12.188.

[2] M. Sutcu, "Effects of total cost of ownership on automobile purchasing decisions," *Transportation Letters*, vol. 12, no. 1, pp. 18–24, Jan. 2020, doi: 10.1080/19427867.2018.1501964.

[3] World Bank, "CO2 emissions from transport (% of total fuel combustion)," *World Bank*, 2014. https://data.worldbank.org/indicator/EN.CO2.TRAN.ZS?most_recent_year_desc=false (accessed Dec. 30, 2021).

[4] O. Ceylan, "Armoni Araması Yöntemi ile Elektrik Dağıtım Sistemlerinin Yeniden Yapılandırılması: Elektrikli Araçların Etkisi," Jul. 2019.

[5] K. Kieckhäfer, K. Wachter, and T. S. Spengler, "Analyzing manufacturers' impact on green products' market diffusion – the case of electric vehicles," *Journal of Cleaner Production*, vol. 162, pp. S11–S25, Sep. 2017, doi: 10.1016/j.jclepro.2016.05.021.

[6] Y. Li, C. Zhan, M. de Jong, and Z. Lukszo, "Business innovation and government regulation for the promotion of electric vehicle use: lessons from Shenzhen, China," *Journal of Cleaner Production*, vol. 134, pp. 371–383, Oct. 2016, doi: 10.1016/j.jclepro.2015.10.013.

[7] S. Lim and M. Kuby, "Heuristic algorithms for siting alternative-fuel stations using the Flow-Refueling Location Model," *European Journal of Operational Research*, vol. 204, no. 1, pp. 51–61, Jul. 2010, doi: 10.1016/j.ejor.2009.09.032.

[8] S. H. Chung and C. Kwon, "Multi-period planning for electric car charging station locations: A case of Korean expressways," *European Journal of Operational Research*, vol. 242, no. 2, pp. 677–687, Apr. 2015, doi: 10.1016/j.ejor.2014.10.029.

[9] H. Qin and Wensheng. Zhang, "Charging Scheduling with Minimal Waiting in A Network of Electric Vehicles and Charging Stations," *VANET '11: Proceedings of the Eighth ACM international workshop on Vehicular inter-networking*, pp. 51–60, Sep. 2011, doi: 10.1145/2030698.2030706.

[10] S. Ge, L. Feng, and H. Liu, "The planning of electric vehicle charging station based on Grid partition method," in *2011 International Conference on Electrical and Control Engineering, ICECE 2011 - Proceedings*, 2011, pp. 2726–2730. doi: 10.1109/ICECENG.2011.6057636.

[11] M. Erbaş, M. Kabak, E. Özceylan, and C. Çetinkaya, "Optimal siting of electric vehicle charging stations: A GIS-based fuzzy Multi-Criteria Decision Analysis," *Energy*, vol. 163, pp. 1017–1031, Nov. 2018, doi: 10.1016/j.energy.2018.08.140.

[12] E. & I. S. Department for Business and Department for Transport, "COP26 declaration on accelerating the transition to 100% zero emission cars and vans," *Policy paper*, Dec. 06, 2021.

[13] TOGG, "Turkey's Automobile featured 'New League' journey started," *Auto World*, Dec. 27, 2019. https://www.autoworlddergisi.com/turkeys-automobile-featured-new-league-journey-started/ (accessed Dec. 25, 2021).

[14] W. Winston, *Operation Research: Applications and Algorithms*, 4th ed., vol. 1. California, USA: Curt Hinrichs, 2004.

[15] Murat Temizer, Nuran Erkul Kaya, and Firdevs Yüksel, "Bakan Dönmez: 2030'da Türkiye'de 1 milyonun üzerinde elektrikli otomobil olacağını öngörüyoruz," *Anadolu Ajansı*, Jan. 16, 2020.

[16] Berkan Bayram, "2021 ilk 6 ayında satılan Elektrikli ve Hibrid araç rakamları belli oldu," *TEHAD*, Jul. 10, 2021. https://www.tehad.org/2021/07/10/2021-ilk-6-ayinda-satilan-elektrikli-ve-hibrid-arac-rakamlari-belli-oldu/ (accessed Dec. 30, 2021).

[17] Ö. Gönül, A. C. Duman, and Ö. Güler, "Electric vehicles and charging infrastructure in Turkey: An overview," *Renewable and Sustainable Energy Reviews*, vol. 143. Elsevier Ltd, Jun. 01, 2021. doi: 10.1016/j.rser.2021.110913.

Bitlis Eren Üniversitesi Fen Bilimleri Dergisi
BİTLİS EREN UNIVERSITY JOURNAL OF SCIENCE
ISSN: 2147-3129/e-ISSN: 2147-3188
VOLUME: 11 NO: 2 PAGE: 544-552 YEAR: 2022
DOI: 10.17798/bitlisfen.1054623

Determination of Gasoline Atomization Quality under the Sinusoidal Inertial Forces with Image Processing Method

Burak TANYERİ[1], Orhan ATİLA[2], Ukbe Usame UÇAR[3*], Cengiz ÖNER[4]

[1,3]*Civil Aviation High School, Aircraft Airframe-Engine Maintenance, Fırat University, TURKEY*
[2]*Dept. of Elec. and Elec. Eng., Faculty of Technology, Fırat University, TURKEY*
[4]*Automotive Engineering, Faculty of Technology, Bingöl University, TURKEY*
(ORCID: 0000-0002-3517-9755) (ORCID: 0000-0001-7211-913X) (ORCID: 0000-0002-9872-2890) (ORCID: 0000-0002-3278-2831)

Keywords: Atomization quality, Droplet size, Sinusoidal intertial forces, Gasoline direction injection

Abstract

The atomization quality has gained importance with the used of injection systems in internal combustion engines. The atomization quality has been increased by raising spray pressures by the way advances in the production technologies of high-pressure pumps and injectors. In the current situation, the spray pressures in Gasoline Direct Injection (GDI) technology have been reached bar levels between 200 and 800. When the pressure level is raised higher than the specified pressure value, the atomization quality is not provided a significant improvement and the production cost increase due to the technology required for high pressure. In this paper, the fuel has been atomized by using Sinusoidal Inertial Forces (SIF) as another method to improve the atomization quality. In the literature, there is no any study regarding the suitability of using by atomized under SIF of the gasoline fuel used in internal combustion engines. In the application study, the gasoline fuel has been atomized without the pressure by manufactured SIF generator and the droplet images obtained analysis result has been examined by using the image processing method. According to analysis results, it has been observed that the droplets sizes (around 11 µm) produced with SIF method were similar results to the droplet sizes (8-14 µm) founded using the GDI method. In addition, it was determined that the amount of atomized through the piezoelectric ceramic material in one minute was 380 ml/h. It has been determined that the smaller droplet sizes can be obtained with lower costs without using pressure thanks to this method and the method can be applied efficiently in internal combustion engines.

1. Introduction

In the internal combustion engines (ICEs), spray quality is one of the most important parameters. If it considered that it is used to aircraft, vehicles, and sea vehicles, it can be seen to play an important role in the solve the problems of the energy crisis and environmental pollution [1]. Nowadays in the used spray methods which the latest technology, the fuel is injected as primary atomization and secondary atomization process into the cylinder [2]. The secondary atomization is very effective on combustion efficiency and emission performance since it determines of droplet size, spray penetration, distribution of droplet, air-fuel rate, homogenous of the mixture, and evaporation rate of fuel [3]. Therefore, it is very important to understand the mechanism of the secondary atomization for the energy-saving and emission reduction of the ICEs. There are many studies on the development of secondary atomization in the literature. These studies are mainly attributed to the instability of gas-liquid interface decay waves, including Kelvin-Helmholz (KH) instability and Rayleigh-Taylor (RT) instability

*Corresponding author: uuucar@firat.edu.tr
Received: 07.01.2022, Accepted: 22.03.2022

[4]–[6]. As we know, any periodic function can be represented by the sine and cosine series through the Fourier transform. Therefore, it is important to study the droplet as the first step in illuminating a drop's secondary atomization mechanism under time-dependent acceleration. Faraday instability is used in the field of Hydrodynamics to explain the deformation and atomization process under the sinusoidal inertia force and observes the vibrations caused by vertical waves on the horizontal liquid layer surface [7]. Ultrasonic atomization with a high applied frequency is a typical application of the Faraday technique, and the effects of frequency on liquid have been experimentally studied by Lang [8], Rajan, et al [9]. Sinusoidal intertial forces used in many technical operations such as a clinical nebulizer, surface coating, humidifier of ambiance, liquid fuel sprays in the industry. Firstly, ultrasonic atomization discovered by Wood and Loomis was researched for many decades. Nevertheless, there is no general consensus on the underlying mechanism of droplet formation. There are currently two hypotheses [8]. The first hypothesis is the cavitation hypothesis. In this hypothesis, ultrasonic energy creates numerous microbubbles from nucleation, growth, and subsequent explosion in the liquid layer on the vibrating surface. Due to the cavitation randomly, mist size in the liquid column occurs randomly. The second hypothesis is capillary wave hypothesis. In this hypothesis, mist generation occurs when unstable oscillations tear the peaks of capillary waves away from the bulk liquid. Therefore, the droplet size of the generated mist depends on the wavelength of the capillary waves [10]. Faraday technique is a new research method used in the literature to explain the mechanism underlying atomization formation in this field. Although there is a limited number of research on this subject, Fushui Liu et al. Revealed an experimental study [11]. In the study, they revealed the effects of frequency, liquid amount, surface tension, and liquid density on atomization. The most important parameter used to evaluate air/fuel mixture quality is the Equivalence Ratio (ER) in internal combustion engine. The higher fuel injection pressure is both more uniform ER and faster evaporation of fuel droplets in the cylinder [12-14]. When the GDI technique is used beginning, the operating pressure of fuel injection was 50-100 bar [15]. Over the last decade, the injection pressure of the GDI technique is increased up to 250-800 bar due to recruitment better of fuel atomization [16]. The fuel injection pressure is expected that will increase to 1000 bar by 2025, as the reduction in the size of the fuel droplets increases the surface area required for the oxygen reaction [17]. To increase the pressure a lot of costly mechanical operations are required (smaller nozzle holes, higher pressure pump technology) [18].

Sinusoidal inertial force effect, which is used as an atomization method without requiring high pressure, it can create a new solution in this field to reduce both droplet size and engine production costs. There are no researches about the effect on engines of sinusoidal inertial forces approaches that will be alternative for fuel injection systems used jet nozzle in an internal combustion engine in literature. This study will contribute to the literature by determining the atomization quality of gasoline under sinusoidal inertial forces. In this paper, includes an experimental study to atomize gasoline fuel, which is a petroleum based fuel, under sinusoidal intertial forces and to determine the atomization quality by image processing method.

2. Experimental Setup and Method

In this experiment, a frequency generator circuit was set up to generate sinusoidal intertial forces, and vibration was obtained by sending a frequency of 400 kHz to piezoelectric transducers through these circuits. An imaging system was set up and an experimental setup was set up to ensure that the micron-sized droplets to be formed later were displayed.

2.1. Ultrasonic Generator Circuit

The ultrasonic generator (figure 1) is primarily designed in the experimental setup. “12-V 72A” a battery (which can be used in automobiles), switching circuits, amplifiers, and frequency circuits were manufactured for a 180 W generator capable of producing 400kHz frequency.

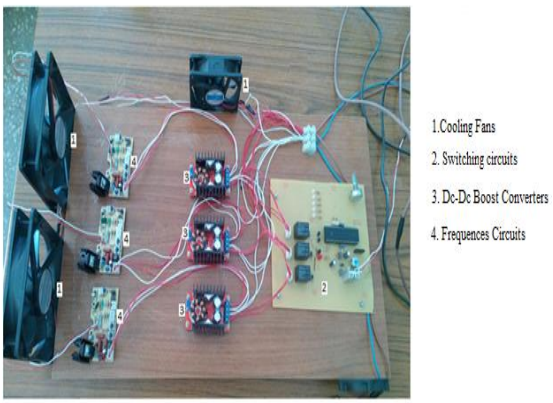

Figure 1. Ultrasonic generator circuit components

12V Dc voltage was applied to the system from the input socket, with the switching circuit of the system ready for an operation soon after. This actuating process is performed by a microprocessor directing the switching circuit, functioning the on-off switch to the open position. For this process, a relay circuit controls the voltage of the accumulator battery. The activated relay applies the battery voltage to the input socket of the converter circuit. The converter circuit voltage is raised to 30v (as previously adjusted) and sent to the pre-set frequency circuits. In the frequency circuits, the 30 V Dc voltage converts to 400 kHz signals. In the studies conducted in the literature, the effects of frequency values between 200 kHz and 2400 kHz on the droplet diameter were investigated and it was observed that the droplet diameter decreased as the frequency increased. In this study, the frequency value that can produce the same droplet diameter was chosen based on the droplet diameter of the compared GDI injector [25].This signal is also sent to the piezoelectric ceramic transducers. So these transducers generators mechanic vibrations that are converted into sinusoidal waves.

2.2. Photographing Elements and Experiment Setup

The photographing experiment setup developed for this paper has been shown figure 2 and 3. According to this setup, a high-resolution digital microscope has been used to determine the size and distribution of the droplets produced by the ultrasonic atomizer. A microscope with 20x50x200 magnification can easily view micron-sized droplets. Then the images taken are analyzed using an image processing method and droplet sizes can be calculated.

After atomization is formed in the experiment set up with gasoline fuel in a closed volume, the droplets in the liquid-gas interface move at a speed of almost zero in an environment where there is no air circulation. Droplets are displayed with ambient lighting and microscopic video capture, and the droplet size is measured by processing photo frames taken from the video.

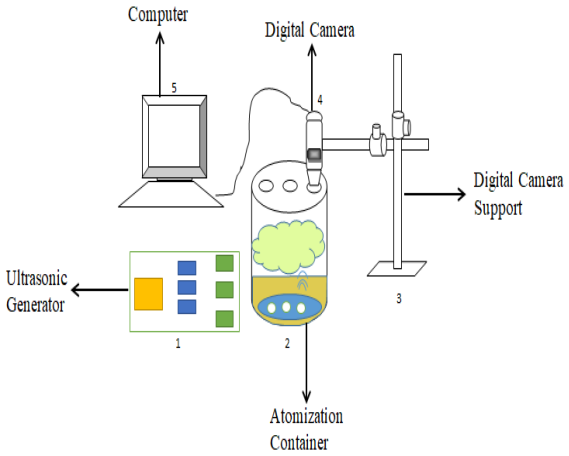

Figure 2. Schematic imagine of photographing experiment setup

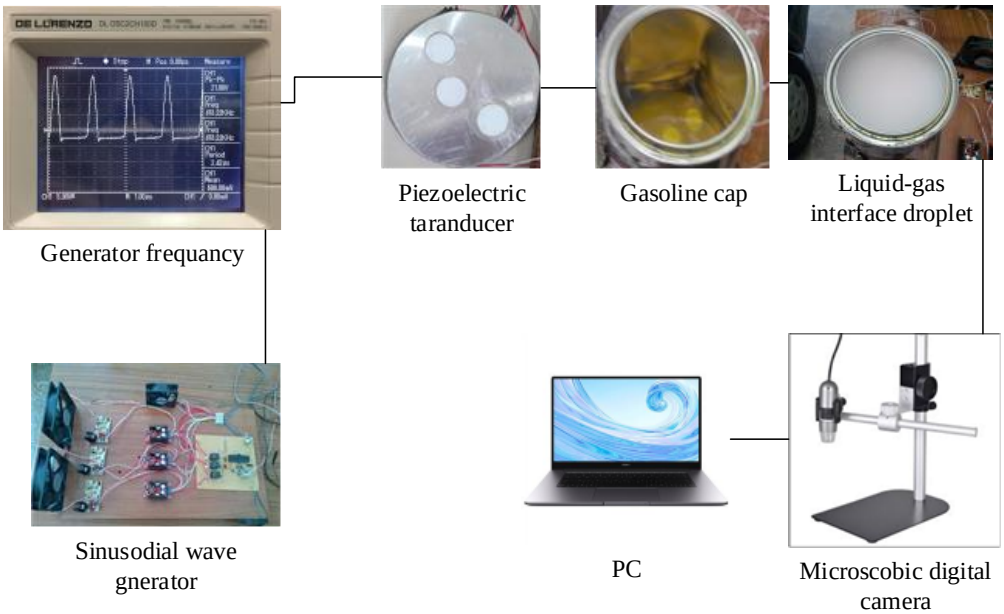

Figure 3. The photographing experiment setup

2.3. Image Processing

Image processing includes converting an image to digital and filtering enhancement, segmentation, pattern extraction, pattern recognition, feature extraction etc. on this image. Digital image processing methods have two main goals. These purposes are to improve the image so that the image can be interpreted better and to analyze the image so that the computer can interpret the image. In this paper, all image processing and feature extraction operations were conducted in a MATLAB environment.

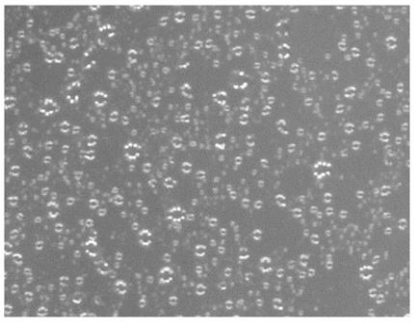

Figure 4. Original Image

The photograph in figure 4 shows image obtained from the microscope in the experiment setup that is shown in figure 2. The sound waves piezoelectric ceramic transducer produce cause the breaking of the droplets from the surface of the liquid fuel. The broken droplets fill the empty volume of the atomization container and move with a speed close to zero. Meanwhile, the digital microscope cameras immersed from three different points in fog cloud display the droplets by taking photograph and video. The obtained image has been analyzed using the flow chart in figure 5. Afterwards, this picture has been transformed to a black-white image (figure 6) by the way image program.

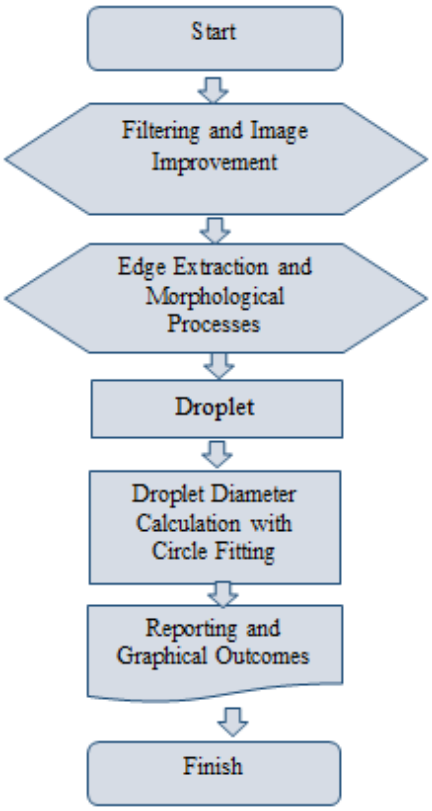

Figure 5. Image Processing Flow Chart

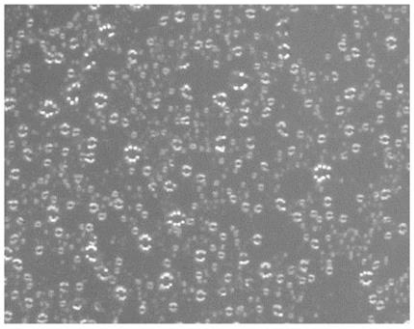

Figure 6. Improved image.

Image enhancement process has been applied on the raw image using the edge reinforcement filter for distinguish from the background more easily and to make a more accurate segmentation of the patterns in image before segmentation. Then the image has been segmented through morphological processes and edge removal methods. The Canny Edge Detection Method was used to segment the droplet images taken from the microscopic camera. The Canny Edge Detection that is a method we used utilizes as a threshold level. The Canny Algorithm preserves all edges that are above the threshold level while ignoring all the edges whose edge strength is below the threshold level. In this study, we used the regional optimum thresholding method (otsu) to determine the edge threshold level. The optimum threshold value method calculates a value called in-class (foreground

and background pixels) variance for all possible thresholds and finds the index at which this value is the lowest [19].

In the proposed algorithm, firstly G_x and G_y spatial gradients are calculated and an edge strength matrix [G] is found. Then, the edge pixels E are determined according to the threshold level(th_level) obtained previously.

$$G_x = \begin{bmatrix} -1 & 0 & 1 \\ -1 & 0 & 1 \\ -1 & 0 & 1 \end{bmatrix}$$

$$G_y = \begin{bmatrix} -1 & -2 & -1 \\ 0 & 0 & 0 \\ 1 & 2 & 1 \end{bmatrix}$$

$$[G] = \sqrt{G_x^2 + G_y^2} \qquad \text{Eq. 1.}$$

$$E = [G] > th\_level \qquad \text{Eq. 2.}$$

After the segmentation process, it is performed labelling process which each droplet pattern has an identity. Later size information of each droplet pattern is calculated and it is saved in its own label. The segmented image and labelled droplet patterns are shown in figure 7.

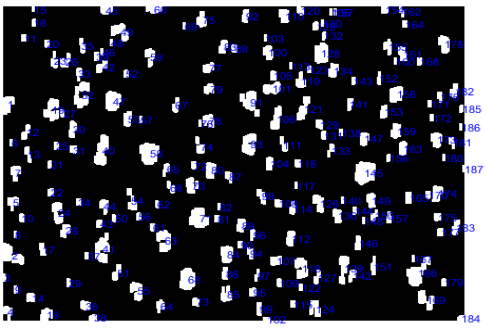

Figure 7. Segmented and labelled Image

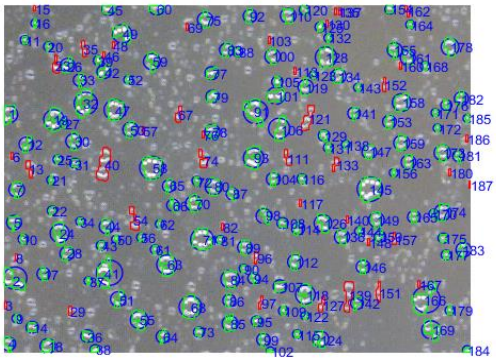

Figure 8. Calculation of droplet diameter with circle fitting method

As a result of atomization, the circle fitting method has been used to calculate the size of the fuel droplets that take a shape similar to water spheres. Fuel droplets cannot take a full circle shape due to discontinuities and incorrect mergers in the patterns obtained as a result of edge extraction and segmentation processes. On the other hand, when obtained images with a digital camera have been examined, it has been observed that a light ring has consisted around the droplets due to reflection of the LED light source in the camera. These situations cause incorrect calculations of the sizes of the droplets. In this study, we propose the circle fitting method to deal with this situation. Thus, the best circle that fits the boundaries of the existing droplet patterns will provide us with the actual size of the droplet. When this method is applied to all droplet patterns in the image taken from the camera, the sizes of all droplets can be calculated. Patterns that cannot be obtained as droplet shape as a result of incorrect segmentation are ignored and not included in the size calculation process.

According to Figure 8, patterns that have been marked with red colour have been ignored for giving false information because they are not segmented correctly.

2.3.1. Morphological Operations

Morphological image processing is non-linear operations related to the shape or morphology of features in an image. Morphological operations scan an image with a template called a structuring element. The structuring element is positioned at all possible locations in the image and it is compared with the corresponding neighbourhood of pixels. Erosion and dilation are among the most commonly used techniques from morphological operations. The erosion operation test whether the element fits within the neighbourhood, while the dilation operation test whether it hits the neighbourhood[20].

The binary dilation of F by S, denoted F⊕S, is defined as the set operation:

$$F \oplus S = \{z | \hat{S}_z \cap F \neq \emptyset\} \qquad \text{Eq. 3.}$$

where $\hat{S}$ is the reflection of the structuring element S. In other words, it is the set of pixel locations z, where the reflected structuring element overlaps with foreground pixels in F when translated to z.

The binary erosion of F by S, denoted F Θ S, is defined as the set operation.

$$F \ominus S = \{z|S_z \subseteq F\} \quad \text{Eq. 4.}$$

It is the set of pixel locations z, where the structuring element translated to location z overlaps only with foreground pixels in F. n this study, 4x2 rectangular and 2x2 square structural elements were used respectively for dilatation and erosion operations.

2.3.2. Circle Fitting

Consider n sample points (x_i, y_i). (i=1,…,n) which are fitted by a circle of radius R at the center (x_o, y_o). The geometric distance of a sample points from the center of the circle is indicated as,

$$R^2 = \sqrt{(x-x_o)^2 + (y-y_o)^2}$$
$$x^2 - 2xx_o + x_o^2 + y^2 - 2yy_o + y_o^2 \quad \text{Eq. 5.}$$

If the equation is converted to matrix format

$$[-2x \quad -2y \quad 1][x_o \quad y_o \quad -R^2 + x_o^2 + y_o^2]' = -[x^2 + y^2] \quad \text{Eq. 6.}$$

The expression is to be rearranged

$$A=[-2x \quad -2y \quad 1], B=-[x^2 + y^2]$$
$$D = A^{-1}B \quad \text{Eq. 7.}$$

to obtain x_0, y_0 and R

$$x_0 = D_{11}, y_0 = D_{21} \; and \; R = \sqrt{{x_0}^2 + {y_o}^2 - D_{31}} \quad \text{Eq. 8.}$$

2.3.3. Elimination of Incorrectly Measured Droplets

As seen in the microscope images, some droplets are very close and overlapped. This causes incorrect segmentation when separating the droplets. As a result, droplet sizes are measured incorrectly. The areas of the droplets calculated after the segmentation process and the areas of the calculated droplets after the circle fitting process are different. The difference between these areas calculated for each segment was controlled with a certain threshold level, and the droplets that were measured incorrectly were eliminated.

$$err_1 < \frac{|A_s - A_c|}{A_s} < err_2$$
$$A_s = S_i \quad \text{Eq. 9.}$$
$$A_c = \pi R_i^2$$

where A_s is droplet area calculated after segmentation S_i, $A_c$is droplet area obtained by fitting the circle after segmentation and err_1 and err_2 are threshold levels. err_1 and err_2 values were accepted as 0.2 and 2 respectively in this study.

3. Results and Discussions

This study was carried out to determine whether there is an alternative atomization method to the fuel injection system in spark-ignition engines by atomizing the gasoline fuel used in internal combustion engines under sinusoidal intertial forces and by measuring the atomization quality by image processing method.

Lang [21], who conducted research on ultrasonic atomization, presented an equation that calculates the change in the average droplet diameter depending on the frequency by making a correlation.

$$d_m = C.2\pi\left(\frac{\sigma}{\rho}\right)^{\frac{1}{3}}.\left(\frac{2}{2\pi f}\right)^{\frac{2}{3}} \quad \text{Eq. 10.}$$

Here C = 0.35 ± 0.03 constant number, σ is surface tension constant and ρ is the fluid density. σ and ρ are constants for a given fluid. In Equation 10, it can be seen that the 2/3 power of the independent variable *f* is a power function. The density of the gasoline used in the fixed frequency experiment was 737.5 kg / m^3 [22] and the surface tension of 2.21x10-2 N/m^1 was found to be 5.76 μm when applied to the Lang equation. Considering that there is a measurement coefficient in the Lang equation, it is concluded that the experimental results are close to the theoretical calculations.

The droplet size and volumetric distribution of atomization in gasoline experiments conducted at a frequency of 413 kHz have been indicated in figure 9.

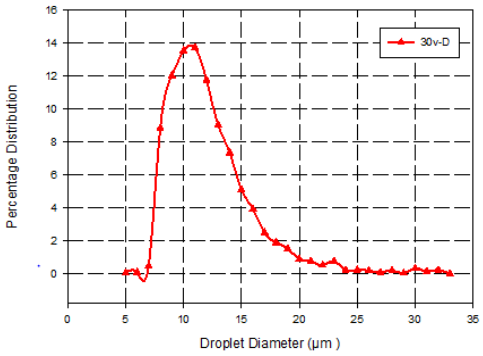

Figure 9. The volumetric distribution of droplet size

When figure 9 is examined, it is seen that the diameter of the droplets formed in the ultrasonic atomizer varies in the range of 5-33µm. In terms of volume, the most obtained droplet diameter is between 11-12 µm. When the examination of figure 10, the droplet performance of a piezo-driven injector with 200 bar spray pressure are similar to the droplet size of ultrasonic atomization examined in this study [24].

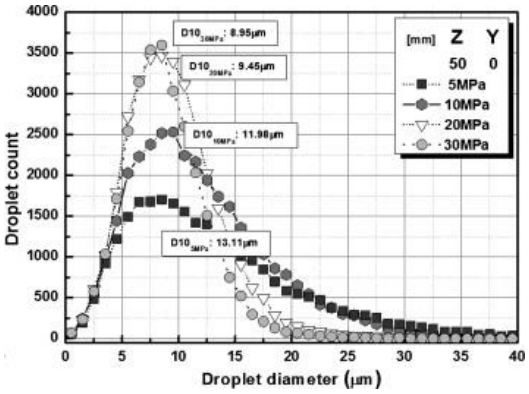

Figure 10. GDI Injector atomization quality[24]

Wadekar et al. [17] conducted a numerical study and studied the change of droplet size with pressure on a jet nozzle in Fig. 11. According to the results of the study, as the pressure increases, the droplet sizes within the determined volume decrease. When the droplet size-volumetric distribution graphs of both experimental jet nozzle studies and numerical jet nozzle studies are examined, it is seen that their tendencies are similar. In this study, a similar graphic was observed too. Therefore, it is thought that this atomization method can be used in internal combustion engines.

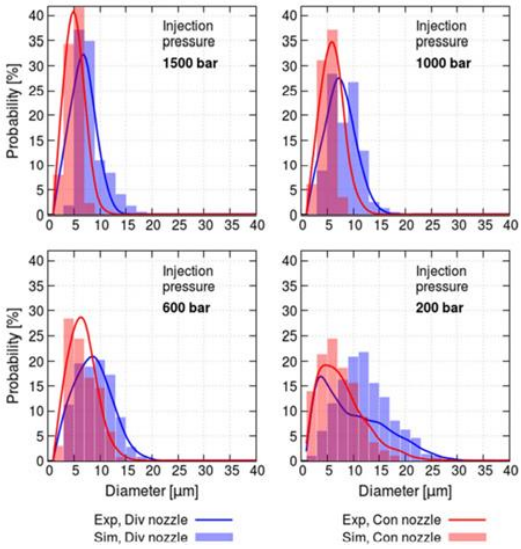

Figure 11. Comparison between measured and calculated droplet size distribution for the divergent and the convergent nozzle at 200, 600, 1000 and 1500 bar injection pressure [17].

In this paper performed under sinusoidal intertial forces, both the size of the droplet and the trend of the graph have shown similar results with the jet nozzle. According to the pressure increase in numerical and experimental studies realized on the jet nozzle, it is found that dwindling in droplet size is not remarkable. Besides, pressure increase methods have serious manufacturing difficulties and costs. In the method of atomization of the droplets with sinusoidal intertial forces, it has been determined that droplet sizes can be reduced to nano sizes without using pressure. In this respect, it has been observed that the atomization method with sinusoidal intertial forces is superior to pressure systems in terms of both production cost-manufacturing ease and operating performance.

4. Conclusions

In this paper, atomization has been performed using piezoelectric ceramic disc material and creating a sinusoidal inertial force on gasoline fuel. This atomization has been processed with image processing method by photographing through microscopic cameras and the sizes of droplets have been calculated. The sizes of droplets and their distribution have given similar results to GDI injector used in spark ignition engines. In the literature, it is seen that the droplet size distribution formed by the GDI injector at different pressures varies between 1-40 µm, and the volume of the highest amount of droplets is in the range of 8-14 µm depending on the pressure. This paper, in the results of the experiments

conducted under sinisodial intertial forces, it is seen that the droplet sizes vary between 1-35 μm and the highest volume of droplets is around 11 μm at unpressurised. Therefore, it can be said that the quality of the atomization made without using any pressure is sufficient. Since the SIF method is independent of pressure, it does not need a pressure pump, allows the droplet diameter to be controlled depending on the frequency of the sinusoidal wave formed, and is less costly than a pressure pump. As a disadvantage, the pressure pump cannot be deactivated since the ignition is provided by injection in compression ignition engines.

Also, the amount that a piezo electric ceramic material atomizes in per minute has been measured as 380 ml/h. This value is important to calculate how many sinusoidal wave generators should be used for fuel injection system of internal combustion engines. It has been found that gasoline atomization quality is suitable for spark ignition engines when both droplet distribution and size of droplet are considered. An alternative injection system to the fuel injection system of internal combustion engines can be produced using sufficient sinusoidal wave generators and it can be done scientific researches on fuel consumption and emission values of this system.

In future studies, using optimization methods, engine performance experiments can be performed by determining the ideal fuel amount required by the engine according to cycle and load conditions and creating a sufficient number of piezoelectric ceramic transducer modules.

Contributions of the authors

Dr. Lecturer Burak TANYERİ:	Conceptualization, Methodology, Software, Application
Res. Ass. Orhan Atila :	Methodology, Software, Application
Dr. Ukbe UÇAR:	Writing – Literature Review & Editing, Visualization
Prof. Dr. Cengiz: ÖNER	Writing – Literature Review & Editing, Visualization

Conflict of Interest Statement

There is no conflict of interest between the authors.

Statement of Research and Publication Ethics

The study is complied with research and publication ethics

References

[1] S. Sakai and D. Rothamer, "Effect of ethanol blending on particulate formation from premixed combustion in spark-ignition engines," in *Fuel,* 196, 154–168, 2017.

[2] D. Zuzio, J. L. Estivalezes, P. Villedieu, and G. Blanchard, "Numerical simulation of primary and secondary atomization," in *Comptes Rendus Mécanique,* 341(1–2), 15–25, 2013.

[3] S. M. Mousavi, R. K. Saray, K. Poorghasemi, and A. Maghbouli, "A numerical investigation on combustion and emission characteristics of a dual fuel engine at part load condition," in *Fuel,* 166, 309–319, 2016.

[4] C. D. Rakopoulos, G. M. Kosmadakis, and E. G. Pariotis, "Evaluation of a new computational fluid dynamics model for internal combustion engines using hydrogen under motoring conditions," in *Energy,* 34(12), 2158–2166, 2009.

[5] J. Benajes, P. Olmeda, J. Martín, D. Blanco-Cavero, and A. Warey, "Evaluation of swirl effect on the global energy balance of a HSDI diesel engine," in *Energy,* 122, 168–181, 2017.

[6] C. Habchi, D. Verhoeven, C. Huynh Huu, L. Lambert, J. L. Vanhemelryck, and T. Baritaud, "Modeling atomization and break up in high-pressure diesel sprays" in *SAE Transactions,* 106, 1391–1406, 1997.

[7] K. Takagi and T. Matsumoto, "Numerical simulation of two-dimensional faraday waves with phase-field modelling," in *Journal of Fluid Mechanics,* 686, 409–25, 2011.

[8] T. Kudo, K. Sekiguchi, K. Sankoda, N. Namiki, and S. Nii, "Effect of ultrasonic frequency on size distributions of nanosized mist generated by ultrasonic atomization," in U*ltrason Sonochemistry*, 37, 16–22, 2017.

[9] R. Rajan and A. B. Pandit, "Correlations to predict droplet size in ultrasonic atomisation" *Ultrasonics*, 39(4), 235–255, 2001.

[10] Y. Zhang, S. Yuan, and L. Wang, "Investigation of capillary wave, cavitation and droplet diameter distribution during ultrasonic atomization," in *Experimental Thermal and Fluid Science*, 120, 110219, 2021.
[11] F. Liu, N. Kang, Y. Li and Q. Wu, "Experimental investigation on the spray characteristics of a droplet under sinusoidal inertial force," in *Fuel*, 226, 156-162, 2018.
[12] W. F. Piock, B. Befrui, A. Berndorfer and G. Hoffmann, "Fuel pressure and charge motion effects on GDI engine particulate emissions," in *SAE International Journal of Engines*, 8(2), 464-473, 2015.
[13] S. K. Addepalli and J. M. Mallikarjuna, "Parametric analysis of a 4-Stroke GDI engine using CFD," in *Alexandria Engineering Journal*, 57(1), 23-34, 2018.
[14] A. A. Reddy and J. M. Mallikarjuna, "Parametric study on a gasoline direct injection engine-a CFD analysis (No. 2017-26-0039)," in *SAE Technical Paper*, 2017.
[15] T. O. Jones, "Assessment of technologies for improving light duty vehicle fuel economy: Letter report," in *The National Academies Press*, 2010. https://doi.org/10.17226/12163
[16] A. Waltner, P. Lueckert, U. Schaupp, E. Rau, R. Kemmler and R. Weller, "Future technology of the sparkignition engine: Spray-guided direct injection with piezo injector," *in: 27th Vienna Motor Symposium (2006)*, 2006.
[17] S. Wadekar, A. Yamaguchi and M. Oevermann, "Large-Eddy simulation study of ultra-high fuel ınjection pressure on gasoline sprays," in *Flow, Turbulence and Combustion*, 107(1), 149-174, 2021.
[18] F. Duronioa, A. D. Vitaa, A. Montanaro and Carlo Villantea, C, "Gasoline direct injection engines – a review of latest technologies and trends," in *Part 2. Fuel*, 265, 116947, 2020.
[19] Ganesan, P., Rajini, V., and Rajkumar, R. I., "Segmentation and edge detection of color ımages using CIELAB color space and edge detectors," *in INTERACT-2010 (pp. 393-397), IEEE*, 2010.
[20] R. M. Haralick, S. R. Sternberg, X. Zhuang, "Image analysis using mathematical morphology," in *IEEE Transactions on Pattern Analysis and Machine İntelligence*, (4), 532-550, 1987.
[21] R. J. Lang, "Ultrasonic atomization of liquids," *The Journal of the Acoustical Society of America*, 34(1), 6-8, 1962.
[22] S. No, 'Ürün Kodu: Opet – 220 Kurşunsuz Benzin 95 Oktan Ürün Spesifikasyonu', 2019.
[23] J. Hu, B. Liu, C. Zhang, H. Gao, Z. Zhao, F. Zhang, and Y. Wang, "Experimental study on the spray characteristics of an air-assisted fuel injection system using Kerosene and Gasoline," in *Fuel*, 235, 782-794, 2019.
[24] S. Lee and S. Park, "Experimental study on spray break-up and atomization processes from GDI injector using high injection pressure up to 30 MPa," in *International Journal of Heat and Fluid Flow*, 45, 14-22, 2014.
[25] T. Kudo, K. Sekiguchi, K. Sankoda, N. Namiki, and S. Nii, "Effect of ultrasonic frequency on size distributions of nanosized mist generated by ultrasonic atomization," in *Ultrasonics sonochemistry, 37*, 16-22, 2017.

Bitlis Eren Üniversitesi Fen Bilimleri Dergisi
BİTLİS EREN UNIVERSITY JOURNAL OF SCIENCE
ISSN: 2147-3129/e-ISSN: 2147-3188
VOLUME: 11 NO: 2 PAGE: 553-563 YEAR: 2022
DOI: 10.17798/bitlisfen.1056963

Mobile user type aware load balancing algorithm in SD-RAN

Müge EREL-ÖZÇEVİK[1*]

[1]*Manisa Celal Bayar University, Department of Software Engineering, TR-45400, Manisa, Turkey (ORCID: 0000-0003-3077-160X)*

Keywords: Software defined network, Radio access network, Queuing theory, iOS, Android.

Abstract

Under extreme increase on video contents in eMBB applications; the 5G requirements cannot be handled by the conventional self-organizing in 4G infrastructure. While executing load balancing in 5G RAN, mobile user type for eMBB applications should be considered. Nowadays, eMBB has been carried by QUIC and HTTP2.0 protocol for Android and iOS users, respectively. In mobile user aware load balancing, Deep Packet Inspection (DPI) up to application layer for packet routing is required. This can be only handled by Software-Defined Network (SDN) without any hardware expenditure in physical infrastructure. Therefore, this paper proposed Software-Defined Radio Access Network (SD-RAN) with two novel functions: Waiting Time Function (WTF) and Load Balancing Function (LBF). In WTF; the queuing inspired approach is proposed for the low complex implementation of the mobile user aware load balancing in 5G-RAN. Waiting Time parameters for iOS and Android users are analytically defined by M/G/1 and G/G/1 Markov queues. It is also executed by M/M/c/K Markov model SD-RAN topology. In LBF; a novel Mixed Integer Linear Problem is defined for waiting time optimization. To overcome NP hardness, a local search for the eMBB load threshold analysis is performed and determined as 0.79 and 0.94 for UMas and UMis. A low complex load balancing algorithm is proposed in the light of these thresholds. According to performance results; SD-RAN outperforms nearly 40% QoS than the conventional SON according to received packet count. It can serve 40% more users than the conventional one without any extra expenditure on physical infrastructure. As a result, it can handle eMBB flows with an acceptable waiting time under 2 milliseconds level.

1. Introduction

In today's Covid process; the main reason for the increase in data traffic is online-video contents in mobile applications, which is newly called as enhanced Mobile BroadBand (eMBB) service of 5G new radio [1,2]. It is estimated that this content in mobile applications is accounted for 74 percent of all data traffic in 2024 [3]. According to International Mobile Communications (IMT-2020), eMBB service should be served in under a few milliseconds. To handle this requirement, it is inevitable that Radio Access Network (RAN) should meet a 100-fold traffic load as compared to the 4G infrastructure [4]. It is believed that the 5G requirements can be only handled by a centralized load balancing instead of the self-organizing in 4G.

EMBB has been carrying by UDP-based QUIC (HTTP3) protocol in the application layer of 5G network stack. It outputs zero latency for connection setup and it overcomes possible packet losses caused by UDP-based connections by multiplying such connection packets. This provides us to serve mobile users with lower latency than conventional TCP-based HTTP2.0; however, it increases traffic load much more than conventional ones. QUIC protocol has been implemented in Android applications; whereas, there has been no library for iOS ones, yet. Therefore; iOS users are still using HTTP2.0 for eMBB applications. However, the legacy network cannot differentiate users as iOS or

*Corresponding author: muge.ozcevik@cbu.edu.tr
Received: 12.01.2022, Accepted: 01.04.2022

Android without the aforementioned application layer details. This motivates to consider mobile user type as iOS or Android while executing load balancing in 5G RAN [5,6].

In mobile user aware load balancing, the deep packet inspection (DPI) up to the application layer for packet routing is required [7]. However, it needs extra computing resource in the control plane due to the dynamic changes in the signature of the application. Moreover, it is hard to manage because of its complex implementation in both the control and data planes [8,9]. To handle low complex execution of DPI, Software Defined Network (SDN) has been used in the literature [10,11]. However, DPI is not supported in even the standard OpenFlow library [12,13]. Therefore, the queuing inspired approach is proposed for the low complex implementation of the mobile user aware load balancing in this paper. Thanks to the analytical model of iOS and Android users, the mobile user awareness would extremely decreases the complexity of proposed load balancing algorithm. Moreover, the Waiting Time parameter of eMBB contents varying as iOS and Android would be easily calculated in the control plane without any hardware implementation in the data plane. As a result; the Software-Defined Radio Access Network (SD-RAN) is proposed, which has an easy implementation on 5G protocol stack. It has two new functions in the control plane: Waiting Time Function (WTF) and Load Balancing Function (LBF) where the whole contributions are given below:

- WTF:
  - iOS and Android mobile users are modeled by M/G/1 and G/G/1 Markov models by considering application layer protocols such as HTTP2.0 and QUIC, respectively.
  - A Waiting Time parameter per SD-RAN is modeled by M/M/c/K Markov model and it is extracted by Jackson theorem.
- LBF:
  - A novel Mixed Integer Linear Problem is defined for the Waiting Time optimization.
  - A local search for load threshold analysis is performed to overcome NP hardness of the optimization problem.
  - A novel Load Balancing Algorithm is proposed in the light of load thresholds and optimization constraints.

The rest of paper is organized as follows. In section 2, the proposed network architecture and protocol stack of SD-RAN are given. In section 3, the proposed system architecture models Waiting Time by using Queuing Theory. Here, the implementation details of the Waiting Time optimization problem and the Load Balancing Algorithm which executes it are defined. In section 4, the performance of the proposed SD-RAN is evaluated and the paper is finalized in section 5.

2. Network Architecture

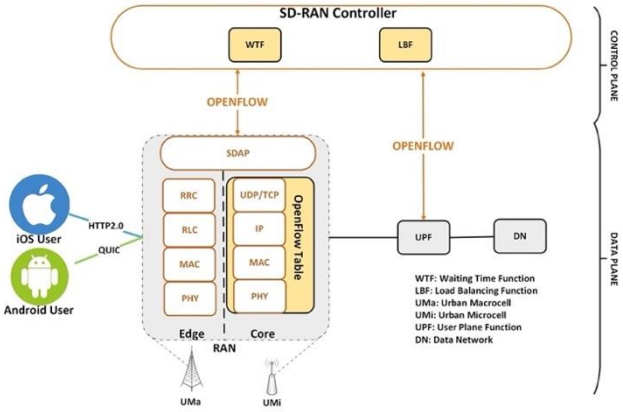

Figure 1. Network architecture of SD-RAN.

The proposed network architecture of SD-RAN is shown in Figure 1. It is decoupled as Data and Control planes. In the data plane, there are 5G components named as User Plane Function (UPF) and Data Network (DN) on the core side and there are Software Defined - Radio Access Networks (SD-RAN); i.e. base stations varying in terms of coverage area such as Urban Macrocell and Urban Microcell in the edge side. Here, a traffic flow is routed over SD-RAN, UPF and DN through to Internet Service Providers (ISP). To handle traffic flows in core, SD-RAN has an OpenFlow table where the IP-protocol stack can be managed up to the transport layer, i.e UDP/TCP. To handle traffic flow in edge, it has also a 5G protocol stack where the layers are physical (PHY), medium access control (MAC), radio link control (RLC), radio resource control (RRC). By using protocol stacks of edge side; SD-RAN manages wireless traffic in random access procedure, admission control, resource management etc. By using protocol stack of core side, it dynamically routes a traffic flow through ISP. In the core side, each device are dummy and controlled by SD-RAN controller in Control plane thanks to OpenFlow 1.5.1. protocol [13]. However, deep packet inspections are not supported in legacy and in OpenFlow switches [14]. To handle application awareness in this paper, deep packet inspection is performed by Service Data Adaptation Protocol (SDAP) layer in SD-RAN. Therefore, the proposed SD-RAN can differentiate the mobile user type such as iOS and Android. The mobile application sends this data to SD-RAN via SDAP service as exemplified in Table 1.

Table 1. Proposed OpenFlow stack and matching fields of SD-RAN.

MATCH FIELDS				ACTION	STATISTICS
IN_ PORT	ETH_ TYPE	IP_ PROTO	USER_ TYPE	Output	TX_ Packets
Port1	0x800	6 (HTTP2)	iOS	Port3	15535
Port2	0x800	17 (QUIC)	Android	Port4	17760

The OpenFlow stack of the proposed SD-RAN by considering different user types and different protocols of eMBB applications, is given in Table 1. EMBB applications such as Youtube, Spotify etc. in Android device has been newly implemented over UDP based QUIC (HTTP3) protocol. While comparing it with HTTP2.0, it provides low latency in connection setup (0-RTT), secure transmission by QUIC handshake, and easy implementation due to handling in user space instead of core space in a mobile device. However, the iOS operating system has no support for QUIC protocol. Therefore, it still uses HTTP2.0 for eMBB applications in a mobile device. In the proposed architecture, the load caused by the iOS/Android mobile applications in edge network is dynamically balanced by the SD-RAN controller. To meet this contribution, there are two newly defined functions in the control plane. They are named as Waiting Time Function (WTF) and Load Balancing Function (LBF), and they are detailed in the following section.

3. The System Architecture of the Proposed SD-RAN

The SD-RAN controller periodically takes statistics from OpenFlow switches in the data plane and dynamically creates forwarding rule to optimize load in UMa and UMi. It calculates analytically defined Waiting Time (W) per mobile user and per SD-RAN by Waiting Time Function (WTF). Then, it runs the Load Balancing Algorithm which dynamically changes the route of iOS/Android traffic flows by Load Balancing Function (LBF). The Markov model of W per user and per SD-RAN are detailed in subsection 3.1., and then the optimization formula and implementation of its in an LBF are given in subsection 3.2.

3.1. Waiting Time Function (WTF)

This function in the control plane periodically calculates Waiting Time per mobile user and per UMa and UMi RANs. The analytical definition of the Markov models are given below:

3.1.1. W model for mobile user

Table 2. Queuing models of eMBB applications and protocol details.

User Type	Application Layer protocol	Transport Layer Protocol	Queuing Model
iOS	HTTP2.0	TCP	M/G/1
ANDROID	QUIC (HTTP3)	UDP	G/G/1

In this paper, we consider two mobile operating systems such as iOS and Android. They are also called as the mobile user types in SD-RAN. EMBB applications in iOS and Android systems use different protocols such as HTTP2.0 and QUIC. The proposed queuing models of them and the protocol details are defined as in Table 2. EMBB applications in iOS uses HTTP2.0 as an application layer protocol which is carried on TCP as a transport layer protocol; whereas, such applications in Android newly uses QUIC (HTTP3) over UDP which extremely reduces RTT to meet the eMBB requests in 5G. However, there has been no implementation library of QUIC protocol in iOS yet, then, EMBB applications in iOS are carried on TCP-based HTTP2.0.

According to these protocol details of the iOS and Android systems, the Waiting Time W_{ij} of $user_i$ on SD-RAN_j are modeled by M/G/1 and G/G/1, respectively. For G/G/1, the Waiting Time is defined as follows:

$$W_{\{ij\}}(t) = \frac{C_A^2 + C_B^2}{2} \cdot \frac{\rho_j(t)}{1-\rho_j(t)} \cdot \frac{1}{\mu_j} \quad (1)$$

where as ρ_j is load of SD-RAN_j and calculated as λ_j/μ_j. Here, λ_j is the average arrival rate and defined as $\sum \lambda_i / M_j$ and μ_j is serving rate of SD-RAN_j which varies according to Urban Macrocell or Urban Microcell. They are modeled by General distribution. Therefore, C_A^2 and C_B^2 are coefficients of arrival rate as follows:

$$\boldsymbol{C_A^2 = \frac{Var\,[T]}{E^2[T]} = \lambda_i^2(t)\sigma_A^2} \quad (2)$$

$$\boldsymbol{C_B^2 = \frac{Var\,[S]}{E^2[S]} = \mu_i^2(t)\sigma_B^2} \quad (3)$$

By combining eqs.1,2, and 3, the Waiting Time of $user_i$ in SD-RAN_j is calculated as follows:

$$\boldsymbol{W_{\{ij\}}(t) = \frac{\lambda_i^2(t)\sigma_A^2 + \mu_i^2(t)\sigma_B^2}{2} \cdot \frac{\rho_j(t)}{1-\rho_j(t)} \cdot \frac{1}{\mu_j}} \quad (4)$$

For iOS users, due to handing eMBB application over TCP, the arrival rate is modeled by Poisson Distribution. Therefore, the queuing model of

iOS users is M/G/1. Because of arrival rate characteristics of this protocol, $\lambda_i^2(t)\sigma_A^2$ equals to 1. The final version of waiting time can be found below:

$$W_{\{ij\}}(t) = \frac{\rho_j(t)}{1-\rho_j(t)}.\frac{1}{2\mu_j}.\begin{cases} \frac{1+\mu_j(t)\sigma_B^2}{2} & ,i \in iOS \\ \frac{\lambda_i^2(t)\sigma_A^2+\mu_i^2(t)\sigma_B^2}{2} & ,i \in Android \end{cases} \quad (5)$$

As shown in eq. 5, the load of SD-RANs directly affects waiting time, and therefore, to handle 5G requirements for eMBB applications the load of UMa and UMi should be dynamically balanced. Here, Waiting Time for SD-RAN should be also modeled which is detailed in following sub-section.

3.2.1. W model for SD-RANs

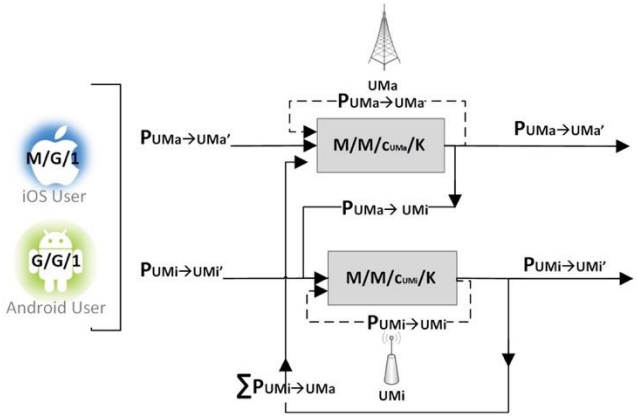

Figure 2. Proposed queuing model of SD-RAN data plane.

In SD-RAN, there are Urban Macrocells (UMa) and Urban Microcells (UMi) as the outdoor service types of SD-RANs. Therefore, the data plane of SD-RAN is analytically modelled by using Jackson's network as shown in Figure 2. Here, there are multiple definitions for the transition probabilities where the general version of the probability is defined as $P_{x\to y}$. For example; if a traffic flow of user$_i$ is transferred from UMa to UMi, it is shown by $P_{UMa\to UMi}$. For the case (x=y), it defines the remaining probability in the same SD-RAN. For the case $(x \to x')$, it shows the handover probability for UMa or UMi within itself. These probabilities dynamically changes the load per SD-RAN (ρ_j).Therefore, loads per UMa and UMi are calculated by using Jackson's network as follows:

$$\rho_j = \frac{1}{c_j\mu_j}.[\lambda_{\{j'\}}P_{\{j\to j'\}} + \lambda_j P_{\{j\to j\}} + \begin{cases} \sum\lambda_{\{UMi\}}P_{\{UMi\to j\}}\,], j \in UMa \\ \lambda_{\{UMa\}}P_{\{UMa\to j\}}\,] \;, j \in UMi \end{cases} \quad (6)$$

Moreover, W_j per SD-RAN is modelled by using M/M/c/K Markov queue. The reason to prefer M/M/c/K instead of the M/M/c queuing model is related to computational implementation. In M/M/c/K, the arrival rate is in both Poisson and Geometric series for different cases. These are finite series in M/M/c/K model; and therefore, there is no constraint such as $\rho < 1$ [15]. Then, the computation can be easily performed for overload cases $\rho \geq 1$. Thanks to that, the waiting time for also overload cases can be also analytically calculated. While working on Dense Urban topology of 5G, this case should be also considered. Therefore; each SD-RAN which serves as UMa or UMi is modeled by M/M/c/K queuing model. The details are given in Appendix A and the full formula is given below:

$$W_{\{ij\}}(t) = \frac{\rho_j c_j\left(1-\frac{(\rho_j c_j)^K}{c_j^{K-c_j}c_j!}P_0\right)+\frac{P_0(\rho_j c_j)^{c_j}\rho_j}{c_j!(1-\rho_j)^2}.\left[1-\rho_j^{K-c_j+1}-(1-\rho_j).(K-c_j+1)\left(\rho_j^{K-c_j}\right)\right]}{\lambda_j\left(1-\frac{(\rho_j c_j)^K}{c_j^{K-c_j}c_j!}P_0\right)} \quad (7)$$

3.2. Load Balancing Function (LBF)

This function in the control plane dynamically changes the route of iOS/Android traffic flow to balance the load between UMa and UMi. Therefore; the proposed optimization problem executed in LBF is defined as follows:

$$\min\left\{\sum_{i\in iOS} W_{ij}, \sum_{i\in Android} W_{ij}\right\} \; s.t. \begin{cases} P_{UMa\to UMi} = P_{UMi} | \, \rho_{UMa} > \rho_{UMa}^t \;, under\ coverage \\ P_{UMi\to UMa} = P_{UMa} | \, \rho_{UMi} > \rho_{UMi}^t \;, under\ coverage \\ P_{UMa\to UMa} + (\sum P_{UMa\to UMi}) + P_{UMa\to UMa'} = 1 \\ P_{UMi\to UMi} + P_{UMi\to UMa} + P_{UMi\to UMi'} = 1 \\ \sum_i \lambda_{ij} \leq \psi_j \\ \sum_{i\in iOS} W_{ij} < \phi_{iOS} \;, j \in \{UMa, UMi\} \\ \sum_{i\in Android} W_{ij} < \phi_{Android} \end{cases} \quad (8)$$

where the objective function is minimizing both totals waiting time for iOS and for Android traffic flows. This problem has seven constraints in total. The first two constraints define the transition between UMa and UMi when the SD-RAN is overloaded by considering load thresholds $\rho_{UMa}^t, \rho_{UMi}^t$. The third and fourth constraints are related to the general theorem such that the total probability of incoming and outcoming flows in a node should be equal to 1. The fifth constraint defines that the resource capacity ψ_j should meet the total arrival of users. Therefore,

the first five constraints are directly related to load balancing for an optimization problem. Because of including both discrete and continuous variables in these constraints, it is performed by a Mixed Integer Linear optimization problem, and the optimal solution is normally executed by using the Branch and Bound algorithm. However, such a solution results in NP-hard complexity which is not acceptable for 5G requirements. Therefore, the constraints seven and eight are also added to this optimization problem. They defines the acceptable 5G requirements ϕ for iOS and Android users. To handle it, this problem is solved by a greedy algorithm. The expected result is negligible serving time in the SD-RAN control plane with a greedy algorithm in low complexity. The threshold analysis is detailed in subsection 3.2.1 and the proposed algorithm is given in subsection 3.2.2.

3.2.1. Local Search for ρ Thresholds

In this subsection, the load thresholds are analyzed by using a local search of transition probabilities between UMa and UMi [16]. These thresholds enable to focus of much more small search space on an optimization problem, and therefore, it extremely decreases the complexity of the proposed load balancing algorithm. Thanks to this contribution, the control plane meet one of the 5G requirement defined as giving response to the data plane in 1 second.

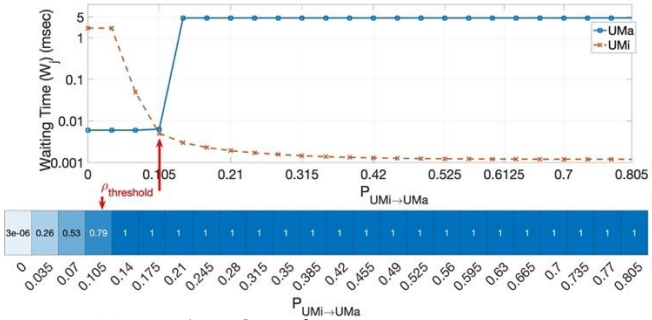

(a) $\rho_{UMa}{}^{t}$ analysis for UMa to UMi transition.

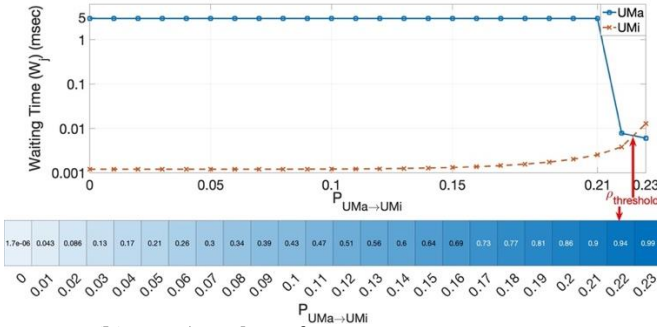

(b) $\rho_{UMi}{}^{t}$ analysis for UMa to UMi transition.

Figure 3. Threshold analysis for each transitions.

In Figure 3, there are two subfigures for $\rho_{UMa}^{t}, \rho_{UMi}^{t}$ analysis, respectively. In each subfigure, there is a line-graph for Waiting Time and there is a colormap for the load per SD-RAN. Each graphs are executed according to x-axis which shows the increased transition probabilities for UMa and UMi. The analyses depend the parameters given in a Figure 4.

- ρ_{UMa}^{t} analysis: In figure 3a, x-axis shows the transition probability between UMi to UMa where there is no assigned user in UMa initially. As the probability increases; i.e. as the load is balanced by transfering from UMi to UMa layers, the Waiting Time in UMa increases, whereas it decreases in UMi according to eqs. 6 and 7. There is one optimum point and the local search defines the optimum threshold as 0.79 when the transition probability from UMi to UMa is 0.105.
- ρ_{UMi}^{t} analysis: In figure 3b, x-axis shows the transition probability between UMa to UMi where there is no assigned user in UMis initially. As the probability increases; i.e. as the load is balanced by transfering from UMa to UMis, the optimum threshold is found as 0.94 when the transition probability from UMa and UMi is 0.22.

3.2.2. Proposed Load Balancing Algorithm

Algorithm 1 Load Balancing Algorithm

Require: $P_{UMa \rightarrow UMa'}$,$P_{UMi \rightarrow UMi'}$, OpenFlow statistics
Ensure: $P_{UMa \rightarrow UMi}$, $P_{UMi \rightarrow UMa}$
1: **for all** UMa in a topology do in parallel **do**
2: **if** $\rho_{UMa} \geq \rho^t_{UMa}$**(0.79) then**
3: Call Transition(UMa,UMi)
4: **end if**
5: **end for**
6: **for all** UMi in a topology do in parallel **do**
7: **if** $\rho_{UMi} \geq \rho^t_{UMi}$ **(0.95) then**
8: Call Transition(UMi,UMa)
9: **end if**
10: **end for**
11: **function** TRANSITION(x,y)
12: **while** W_{ix} for iOS is not acceptable || W_{ix} for Android is not acceptable **do**
13: **if** There is an Android flow in OpenFlow table of x **then**
14: Find an Android flow that would be transmitted to y
15: Check y is available
16: **if** $\rho_y < \rho^t_y$ **then**
17: Embed OpenFlow rules to x and y to meet this transition
18: Increase $P_{x \rightarrow y}$
19: **end if**
20: **else**There is an iOS flow in OpenFlow table of x
21: Find an iOS flow that would be transmitted to y
22: Check y is available
23: **if** $\rho_y < \rho^t_y$ **then**
24: Embed OpenFlow rules to x and y to meet this transition
25: Increase $P_{x \rightarrow y}$
26: **end if**
27: **end if**
28: Calculate new W_{iy} for iOS and Android
29: Calculate new ρ_x and ρ_y
30: **end while**
31: **return** $P_{x \rightarrow y}$
32: **end function**

The pseudo code of the proposed Load Balancing algorithm is given in Algorithm 1. It requires transition probabilities within UMa and UMis and OpenFlow statistics from the data plane. The main part is defined between lines 1-10. Lines between 1 and 5 check the threshold of UMa which is theoretically defined threshold 0.79 in the previous subsection. Lines between 6 and 10 also check the threshold of UMi which is theoretically defined threshold 0.95. If the SD-RANs are overloaded according to these thresholds, the transition functions are executed for load balancing from x to y. For lines 1-5, x equals to UMa and y equals to UMi; whereas for lines 6-10, they are in the opposite cases. Between lines 11-32, the transition function from x to y is defined. It checks the constraints of the proposed optimization formula in eq.8. Between lines 12-30, there is a loop that runs until all waiting times of iOS and Android users are acceptable. The algorithm firstly tries to find an Android flow to change destination SD-RAN by checking OpenFlow statistics. The reason of it, the Android applications newly use UDP-based QUIC protocol which does not need the whole connection setup as iOS applications need. This characteristic of QUIC protocol makes the route of a flow changeable without any packet loss. While balancing the load in an SD-RAN, firstly the Android flows are tried to be transmitted through other SD-RANs. If there are no suitable Android flows, in order to balance load the route of iOS flows is taken into consideration. If there is neither Android nor iOS flows in topology, this proposed algorithm does not perform load balancing.

4. Performance Evaluation

As given in Figure 5, the MATLAB R2019b is used for the simulation environment of SD-RAN. The Simulink builds a topology where there are two UMas and four UMis in total. It is divided into the data and control planes. In the control plane, there is SD-RAN controller where the proposed load balancing algorithm as given in Algorithm 1 is implemented by Stateflow library of MATLAB. In the data plane, there are two user types. One has eMBB flow from remote server in core to Android user in the edge that is carried by QUIC protocol; the other one has also eMBB flow of which the destination is the iOS user and it is carried by HTTP2.0 protocol. These users are shown in blue and red blocks respectively. They are generated at the same rate such as 50% Android and 50% iOS users in a topology. These flows are routed over either UMas or UMis where they are colored by gray and yellow blocks, respectively. The other elements in this environment are for measuring the elapsed time, and generating arrivals of M/G/1 and G/G/1 flows. The arrival rate of eMBB flow varies between 33333 and 8333333 packets/sec in a whole topology where the eMBB load per UMa is in range [0,1.5]. The total number of users is increased up to 36300 while performing an evaluation. The physical layer parameters for UMa and UMi are also found in Table 3. Uma has a 4GHz spectrum with 200MHz bandwidth usage; whereas UMi has 30 GHz spectrum

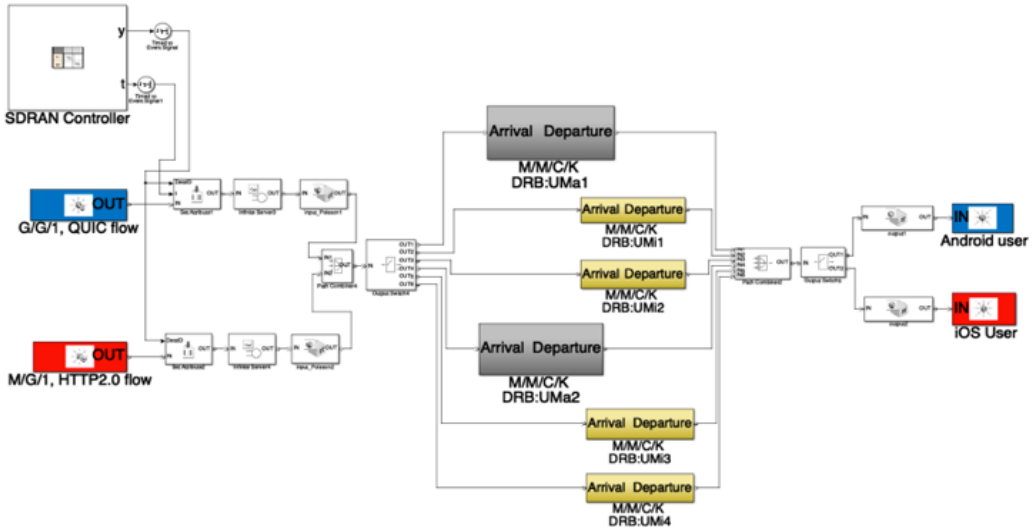

Figure 4. Performance evaluation scenario.

with 1000MHz bandwith usage. The serving rates are taken as 6e-5 and 1.2e-5 in Matlab with 10000 queue size.

Table 3. Experimental setup details.

	Spectrum, Bandwidth	Cell range	Channel	Serving Rate	Queue size
UMa	4GHz, 200MHz	1000m	20	6e-5 secs/packet	10000
UMi	30GHz, 1000MHz	400m	7	1.2e-5 secs/packet	10000

In Figure 5, the waiting time analysis is given for the proposed SD-RAN and the conventional SON for different user types such as iOS and Android via their protocols named HTTP2 and QUIC. There are four different eMBB loads as the arrival rate for UMa in the topology. As eMBB load is increased from 0.005 to 0.5, it can be served under an acceptable level (4 milliseconds) in both SD-RAN and the conventional SON. However; as it is increased from 1 to 1.5, the utilization of UMas (ρ_{UMa}) in the conventional SON goes up to 1, which means the queue becomes full and the packet drops start. In other words, the received packets by iOS or Android users is less than generated in the eMBB server. This extremely damages the QoS of both iOS and Android users because of not having centralized load balancing and user type awareness in the conventional SON. On the other hand; in the proposed SD-RAN, this eMBB load can be dynamically distributed through suitable UMis according to predetermined thresholds in sub-section 3.2.1. When eMBB load is increased up to 1.5, SD-RAN can serve all eMBB flows under 2 milliseconds level; unfortunately, the waiting time extremely exceeds 4 milliseconds level in the conventional SON. Moreover; the utilization of UMas and UMis are balanced in SD-RAN, and therefore, the received packets are nearly the same as generated in the eMBB server during simulation time. It is important to emphasize that the proposed Algorithm 1 firstly transfers QUIC based eMBB flows (Android users) through other RANs not to cause an unnecessary interruption in TCP based HTTP2 flows of iOS users. Because; switching TCP based HTTP2 flows unnecessarily, can make the QoS worse than an unbalanced case in the topology when it tries to balance. Therefore, the waiting time of HTTP based eMBB flows is higher than QUIC ones in the proposed SD-RAN, but all are under the acceptable level where there is no quality damage visible to the user.

The analysis for the received packet count is also shown in Figure 6. When the eMBB load is 0.005 and 0.5, there is no packet drop in the proposed SD-RAN for iOS users; whereas, the QoS in other cases are over 90% level according to the received packet count. When the eMBB load is 1, the received packet count is nearly 19500 for both iOS and Android users in SD-RAN; whereas, it outputs as 17125 for Android and 15825 for iOS users. Namely; the proposed SD-RAN serves the mobile users with 97.5% QoS; whereas, the QoS decreases 80% level with the conventional SON. Here, SD-RAN outperforms 17.5% QoS than the conventional one. When the load is 1.5, the received packet count is nearly 30000 in the proposed SD-RAN by 85.7% QoS; whereas, the conventional one receives only 17760 and 15535 packets for Android and iOS users respectively, which outputs 44% QoS. Here, SD-RAN outperforms nearly 40% QoS than the conventional SON according to the received packet count.

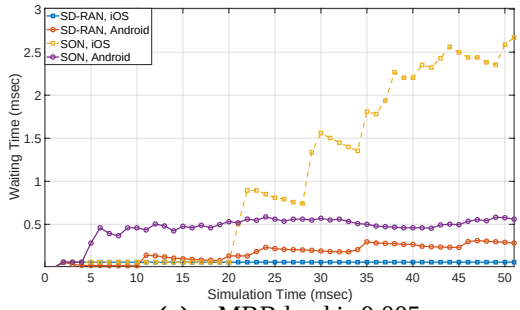

(a) eMBB load is 0.005.

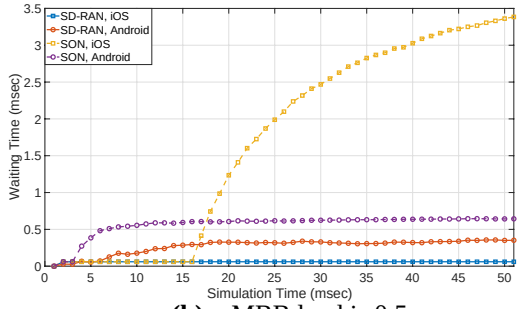

(b) eMBB load is 0.5.

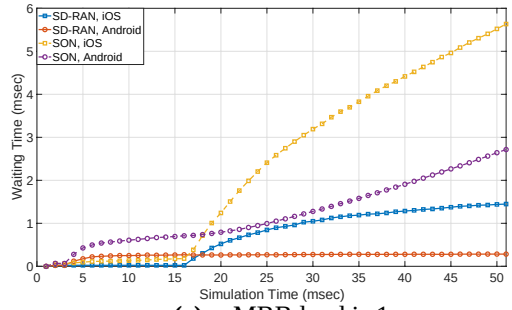

(c) eMBB load is 1.

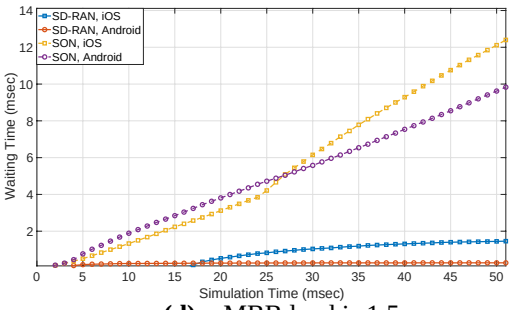

(d) eMBB load is 1.5.

Figure 5. Waiting Time analysis of the proposed SD-RAN and the conventional SON for different user types such as iOS and Android.

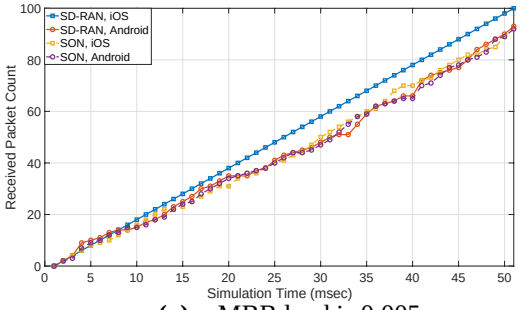

(a) eMBB load is 0.005.

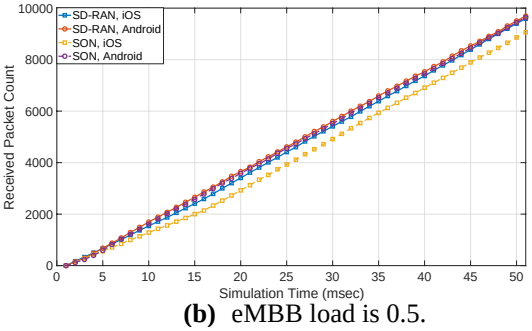

(b) eMBB load is 0.5.

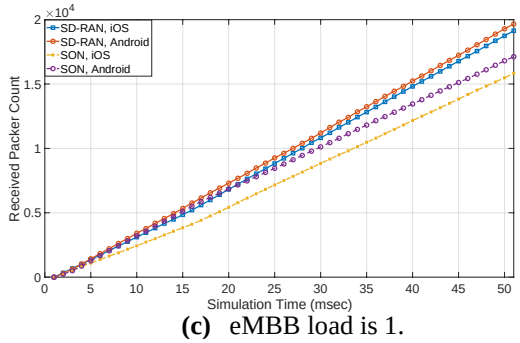

(c) eMBB load is 1.

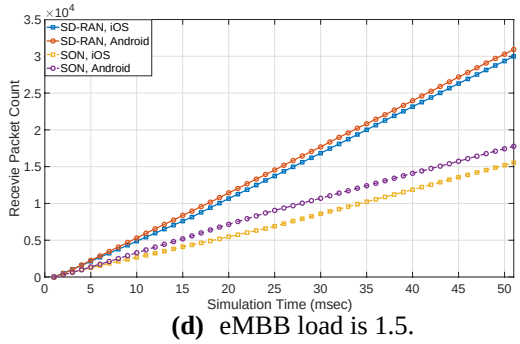

(d) eMBB load is 1.5.

Figure 6. Received Packet Count analysis of the proposed SD-RAN and the conventional SON for different user types such as iOS and Android.

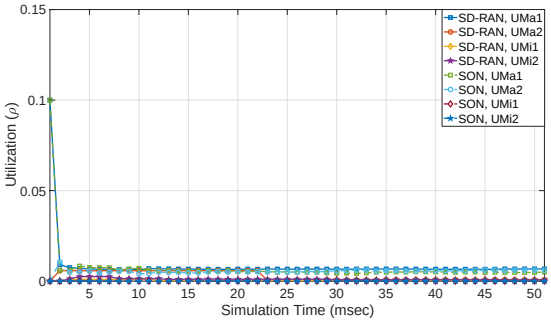

(a) eMBB load is 0.005.

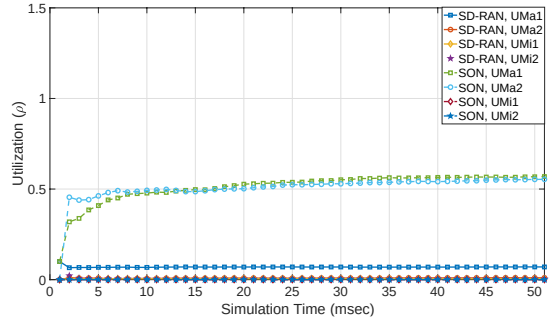

(b) eMBB load is 0.5.

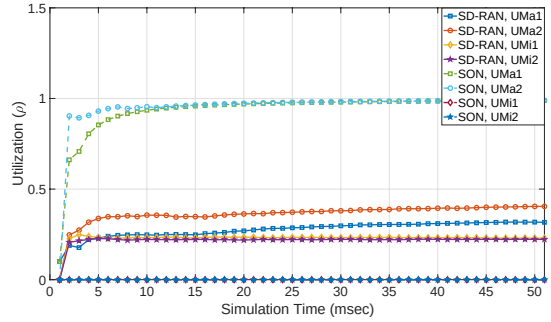

(c) eMBB load is 1.

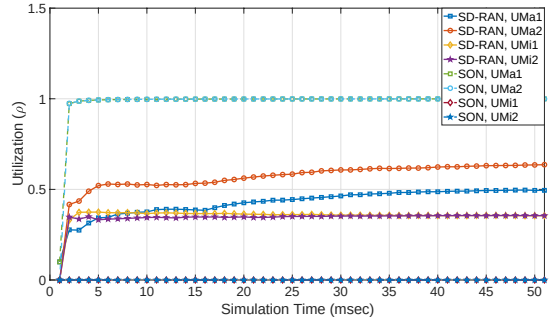

(d) eMBB load is 1.5.

Figure 7. Utilization analysis of UMas and UMis for the proposed SD-RAN and the conventional SON.

The analysis for the utilization (ρ_{UMa}, ρ_{UMi}) is also shown in Figure 7. When the eMBB load is less than 0.5, the utilization of UMas and UMis are also under 0.5 for both the conventional and proposed schemes which also means each can serve eMBB flows under the acceptable level (4 milliseconds) with at most 0.5 utilization ratio. However; when the eMBB load is 1 and 1.5; the utilization of UMas in the conventional SON quickly becomes 1 during the simulation. Here, the utilization of UMis is at too low level. Due to not having a global view, it cannot balance load in optimal on the topology. On the other hand, the utilization of UMas and UMis are in nearly 0.6 and 0.4 levels in the proposed SD-RAN, which clearly results in the optimal load balancing on the whole topology. While doing this, it also considers the user type as iOS and Android. As a result, it can serve 40% more users than the conventional one without any extra expenditure on physical infrastructure.

5. Conclusion

In this paper, a novel mobile user type aware load balancing in SD-RAN is proposed. It has two new functions: Waiting Time Function (WTF) and Load Balancing Function (LBF). In WTF; by considering mobile user type, it differentiates users such as iOS and Android which commonly use HTTP2.0 and QUIC protocol for eMBB flows. Thanks to a novel analytical model of waiting time parameter (M/M/c/K) for iOS (M/G/1) and Android (G/G/1) users, the proposed load balancing algorithm is easily performed in the control plane without any hardware implementation in the data plane. In LBF; to balance eMBB load by considering the user types, DPI in SDN is also handled by queuing inspired approach without any expenditure in OpenFlow standard library. A novel Mixed Integer Linear Problem is defined for the waiting time optimization. To overcome NP hardness of this problem, the load thresholds for UMa and UMis are preliminary analyzed and determined as 0.79 and 0.94, respectively. According to performance results; SD-RAN outperforms nearly 40% QoS than the conventional SON according to received packet count and it can serve 40% more users than the conventional one without any extra expenditure on physical infrastructure. When eMBB load is extremely high, SD-RAN can serve mobile users under a 2 milliseconds level.

Appendix A. M/M/c/K model

In M/M/c/K queuing model, the probability density function of arrival rate has different distributions for $0 \leq n < c$ and $c \leq n < K$ cases. It is in Poisson and Geometric distributions for these cases, respectively. The probability density function P_n is defined as follows:

$$P_n = \begin{cases} \frac{r^n}{n!} P_0 & , \ 0 \le n < c \\ \frac{r^n}{c^{n-c} c!} P_0 & , \ c \le n \le K \end{cases} \quad \text{(A.1)}$$

where $r = \lambda \backslash \mu$, and c is the number of server and K-c is the length of queue. By executing $\sum P_n = 1$ theorem, P_0 is calculated below:

$$P_0 = \begin{cases} \frac{1}{\frac{r^c}{c!}\left(\frac{1-\rho^{K-c+1}}{1-\rho}\right)+\sum_{n=0}^{c-1}\frac{r^n}{n!}} & , \ \rho \neq 1 \\ \frac{1}{\frac{r^c}{c!}(K-c+1)+\sum_{n=0}^{c-1}\frac{r^n}{n!}} & , \ \rho = 1 \end{cases} \quad \text{(A.2)}$$

By executing L'Hospital rule on $\sum nP_n$, the number of packets waiting in a queue (Lq) is calculated. Then, the number of packets in the whole system (L) is found as follows:

$$L = L_q + r(1 - P_k) \quad \text{(A.3)}$$

where P_k is the blocking probability. As a result, the total waiting time (W) for M/M/c/K model is calculated by using eqs.A.1,A.2, and A.3 as follows[15]:

$$W = \frac{L}{\lambda(1-P_k)} \quad \text{(A.4)}$$

Statement of Research and Publication Ethics

The authors declare that this study complies with Research and Publication Ethics.

References

[1] Ericsson, “Update 2020 Ericsson Mobility Report”, *Ericsson Technical Report*, Uen, Stockholm, Sweden, EAB-20:006745, 2020.

[2] S. E. Elayoubi, S. B. Jemaa, Z. Altman and A. Galindo-Serrano, "5G RAN Slicing for Verticals: Enablers and Challenges," *IEEE Communications Magazine*, vol. 57, no. 1, pp. 28-34, January 2019, doi: 10.1109/MCOM.2018.1701319.

[3] Ericsson, “Ericsson Mobility Report”, *Ericsson Technical Report*, Uen, Revision B, Stockholm, Sweden, EAB-18:012366, 2018.

[4] E. Hossain and M. Hasan, "5G cellular: key enabling technologies and research challenges," *IEEE Instrumentation & Measurement Magazine*, vol. 18, no. 3, pp. 11-21, June 2015, doi: 10.1109/MIM.2015.7108393.

[5] Apple, “Apple os deployement quide for the enterprise”, *Apple*, 2022. Available: https://support.apple.com/en-us/HT202944. [Accessed: 01.2022].

[6] W3Techs, “Web technology surveys”, *Q-success*, 2022. Available: https://w3techs.com [Access Date: 01.2022].

[7] C. Xu, S. Chen, J. Su, S. M. Yiu and L. C. K. Hui, "A Survey on Regular Expression Matching for Deep Packet Inspection: Applications, Algorithms, and Hardware Platforms," *IEEE Communications Surveys & Tutorials*, vol. 18, no. 4, pp. 2991-3029, Fourth quarter 2016, doi: 10.1109/COMST.2016.2566669.

[8] M. A. Ashraf, H. Jamal, S. A. Khan, Z. Ahmed and M. I. Baig, "A Heterogeneous Service-Oriented Deep Packet Inspection and Analysis Framework for Traffic-Aware Network Management and Security Systems," *IEEE Access*, vol. 4, pp. 5918-5936, 2016, doi: 10.1109/ACCESS.2016.2609398.

[9] P. Orosz, T. Tóthfalusi and P. Varga, "FPGA-Assisted DPI Systems: 100 Gbit/s and Beyond," *IEEE Communications Surveys & Tutorials*, vol. 21, no. 2, pp. 2015-2040, Second quarter 2019, doi: 10.1109/COMST.2018.2876196.

[10] J. H. Cox et al., "Advancing Software-Defined Networks: A Survey," *IEEE Access*, vol. 5, pp. 25487-25526, 2017, doi: 10.1109/ACCESS.2017.2762291.

[11] S. Sun, M. Kadoch, L. Gong and B. Rong, "Integrating network function virtualization with SDR and SDN for 4G/5G networks," *IEEE Network*, vol. 29, no. 3, pp. 54-59, May-June 2015, doi: 10.1109/MNET.2015.7113226.

[12] M. Jarschel, F. Wamser, T. Hohn, T. Zinner and P. Tran-Gia, "SDN-Based Application-Aware Networking on the Example of YouTube Video Streaming," *2013 Second European Workshop on Software Defined Networks*, 2013, pp. 87-92, doi: 10.1109/EWSDN.2013.21.

[13] Calvin Hue, Yu-Jia Chen and Li-Chun Wang, "Traffic-aware networking for video streaming service using SDN," *2015 IEEE 34th International Performance Computing and Communications Conference (IPCCC)*, 2015, pp. 1-5, doi: 10.1109/PCCC.2015.7410288.

[14] R. Udechukwu and R. Dutta, "Extending Openflow for Service Insertion and Payload Inspection," *2014 IEEE 22nd International Conference on Network Protocols*, 2014, pp. 589-595, doi: 10.1109/ICNP.2014.94.

[15] D. Gross, J.F. Shortle, J.M. Thompson, C.M. Harris, *Fundamentals of Queuing Theory*, Wiley-Interscience, 4th edition, New York, NY, USA, 2008.

[16] F. Hillier, G. Lieberman, *Introduction to Operations Research*, McGraw-Hill International Editions, 2001.

Bitlis Eren Üniversitesi Fen Bilimleri Dergisi
BİTLİS EREN UNIVERSITY JOURNAL OF SCIENCE
ISSN: 2147-3129/e-ISSN: 2147-3188
VOLUME: 11 NO: 2 PAGE: 564-573 YEAR: 2022
DOI: 10.17798/bitlisfen.1059772

Order Demand Forecast Using a Combined Approach of Stepwise Linear Regression Coefficients and Artificial Neural Network

Serdar GÜNDOĞDU[1*]

[1]*Department of Computer Technologies, Bergama Vocational School, Dokuz Eylül University, İzmir (ORCID: 0000-0003-2549-5284)*

Keywords: Feature selection, Forecast, Linear regression, Neural network.

Abstract

Nowadays, businesses' forecasts to meet the demands have become more critical. This study aimed to predict the fifteen-day order demand for an order fulfillment center using a Multilayer Perceptron Neural Network (MLPNN). The dataset used in the study was created from a real database of a large Brazilian logistics company and thirteen variables. Linear Regression Coefficients (LRC) were used as a feature selection method to reduce estimation errors. The study showed that among the variables, order type_A (A5), order type_B (A6), and order type_C (A7) had the most significant impact on total order forecasting. The effect of A6 was found to be greater than the effect of A7 and A5. The performance of the proposed model was evaluated using the mean absolute percent error (MAPE). LRC-MLPNN provided a MAPE of 2.97%. The results showed that better forecasting performance was obtained by selecting the independent variables to be used as input to the forecasting model with LRC. The proposed model can also be applied to different estimation problems.

1. Introduction

Companies operate in a business world where globalization, increased competition, and technology are rapidly developing. The agility of consumer responsiveness, key to the company's success, is critical for forecasting demands, effective supply chain management, and managing customer needs [1], [2]. Obtaining price and demand information has always been the most important commercial purpose. Demand and sales information affects production scheduling, inventory control, and delivery plans. It is an important factor in inventory management, with the objective of better matching supply and demand to reduce inventory costs and stock out [2]. Forecasting demands accurately is truly a challenging task for the supply chain [3]. Predicting using historical data is an important auxiliary tool for decision-making. In particular, the purpose of prediction in time series is to predict the behavior of complex systems by looking at past models of the phenomenon [4]. There is extensive literature on sales forecasting in commercial industries such as books [5], electronics [6], and textiles and clothing fashion [7], [8]. However, few studies focus on demand forecasting in the industrial valve sector, which is characterized by a combination of manufacturers and manufacturing industries [9].

Demand forecasting methods can be linear and nonlinear [10], [11]. Linear methods use univariate time series analysis, such as autoregressive integrated moving averages (ARIMA), multi-linear regression methods (MLR), and exponential smoothing [12], [13], [14]. Nonlinear methods use multiple nonlinear regression (MNLR), artificial neural networks (ANNs) [12], [15], [16], [17], fuzzy logic (FL) [18], [19], support vector machine (SVM) [20], genetic algorithm (GA), expert systems [21] and hybrid methods.

ANNs, widely used as forecasting tools, offer a way to make smart decisions today [22]. ANN algorithms are essential methods for demand forecasting due to their capabilities in nonlinear data and their superior forecasting performance [3], [23]. Many researchers' studies indicate the need for a demand forecast. Kuo and Xue [24] studied the ANN demand forecasting application in a beverage company [9]. The results of this study showed that the

*Corresponding author: serdar.gundogdu@deu.edu.tr
Received: 18.01.2022, Accepted: 03.06.2022

predictive ability of ANNs is better than ARIMA. Law used ANNs to demand forecasts in the tourism industry [25]. Ying and Hanbin [26] studied demand forecasting based on ANN and developed a three-layer ANN model for forecasting market demand [27]. Several examples of ANNs-based applications: financial failure [28], wind speed [29], foreign exchange rates [30], intraday electricity demand [31], and ATM cash demand [32], orders treatment center [33], semiconductor supply chain[34], heat demand forecasting at city level [35].

Feature selection (FS) plays an essential role in neural network (NN) based approaches. It is commonly associated with feature size, affecting machine learning and optimization problems run by backward induction. FS is a data preprocessing method that speeds up the learning process by reducing the number of features of the data set and facilitating the understanding and management of the data set, see [36]. It has been proven to be an effective initial step for different machine learning and data mining problems. FS aims to create simpler and more understandable models, improve data mining performance, and prepare clean data [37]. Acquiring different features requires additional costs such as money, time, and other resources. Too many features mean a high cost. Therefore, it is an important indicator in terms of reducing the number of selected features [38]. The advantages of FS can be summarized as follows: improving the prediction performance of the predictors and selecting faster and more efficient predictors. SVD (single value decomposition), PCA (principal component analysis), and Sammon's mapping are examples of size reduction methods [39].

This study aims to remove irrelevant features from the high-dimensional data set, identify the most relevant features, improve the accuracy of ANN estimation, and reduce the computational cost with LRC feature selection in daily order demand forecasting.

2. Material and Method

The dataset used was accessed from the UCI machine learning repository [40]. It was donated by Ricardo Pinto Ferreira et al. [33], Brazil. The purpose of the dataset is to predict daily demand orders for a company. The dataset consists of twelve predictors and a target (total orders) variable. Attributes are as follows (Table 1):

Table 1. Data used in the study

Attributes	Labels
Total orders (Target)	**A13**
Week of the month	**A1**
Day of the week	**A2**
Non-urgent order	**A3**
Urgent order	**A4**
Order type_A	**A5**
Order type_B	**A6**
Order type_C	**A7**
Fiscal sector orders	**A8**
Order from the traffic controller	**A9**
(1) Banking orders	**A10**
(2) Banking orders	**A11**
(3) Banking orders	**A12**

The proposed approach consists of three stages.

- Nine feature subsets (X1 to X9) were created for the DDFO (daily demand forecasting orders) dataset to construct the prediction model (Table 4). The LRC method was used for feature selection, and features (X9) were reduced to sizes smaller than twelve.
- Daily treatment orders were estimated by applying nine different input variations to the MLPNN system.
- The results were compared according to different inputs.

The block diagram of the proposed approach is shown in Figure 1.

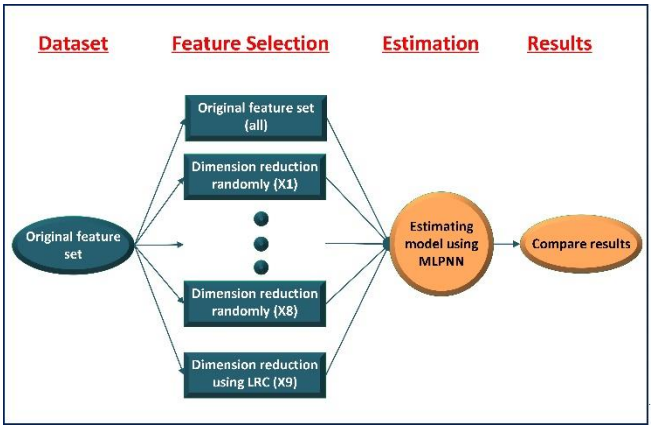

Figure 1. The block diagram of the proposed system

2.1. Multiple linear regression (MLR)

Multiple linear regression is a statistical technique that attempts to model the correlation between independent and dependent variables that depend on a linear equation [41]. The MLR model is:

$$y = c_0 + c_1x_1 + c_2x_2 + \ldots + c_kx_k + e \quad (1)$$

Here, y, c_0, x_k, c_k, and e denote the dependent variable, intersection point, independent variable, regression coefficients, and randomly measured errors.

Regression analysis evaluates the relationship of independent variables with a dependent variable. A linear regression equation with a stepwise method is sensitive to outliers to avoid inefficient measurement values. It is an extension of multiple linear regression analysis to estimate causal relationships that have been predetermined based on theory [42]. One of the methods used to find the correlation with the independent variables is the multicollinearity (MCL) test. MCL can be evaluated with variance inflation factors (VIFs), which determine the strength of the relationship between independent variables. Statistical software calculates a VIF value for each independent variable. VIF values higher than 4 indicate that there may be a problem [43].

Evaluating the regression beta coefficients (βs) is invaluable. These coefficients can be positive or negative, and a t-value associated with each can be calculated. The β is the degree of change in the dependent variable for changes in the independent variable. The t-test evaluates whether the β is different from zero. If the β is not statistically significant (if the t value is not significant), the relevant variable cannot significantly predict the outcome. If the β is significant, its sign is examined. If the coefficient is positive, there is an increase in the dependent variable as much as the β value for each unit increases in the independent variable [44].

The interactions of dependent and independent variables were analyzed and investigated using linear regression analysis by the IBM SPSS Statics 24 program.

2.2. Multiple-layer perceptron neural network

A typical MLPNN architecture consists of the input, hidden, and output layers. The output layer is fully connected to the hidden layers, and the hidden layers are fully connected to the input layer. Each layer has a weight matrix (w), a bias vector (b), and an output vector (y). If we examine the equation in Equation 2 used in problem-solving with ANNs; x_1, x_2,…..x_n, input data, w_1, w_2,… w_i, weights, the number of b is a bias, and σ is the activation function.

$$y = \sigma(\sum_{i=0}^{n} x_i \bullet w_i + b) \quad (2)$$

The neural network exposes the training data and calculates errors based on its outputs. These errors are used to adjust the biases and weights [45].

2.2.1. Design of MLP neural network

MLR aims to model the linear relationship between the independent variables and a dependent variable. The MLR equation can be written in terms of the independent variables (A1, A2,…A12) and dependent variable (A13) used in the study as follows (Equation 3).

$$A_{13} = c_0 + c_1A_1 + c_2A_2 + \ldots + c_{12}A_{12} + e \quad (3)$$

The MLR stepwise regression is a simple and popular feature selection method. It determines the suitable features used as input features to train the neural network [46].

Predictors of total orders (A13) were assessed using stepwise linear regression analysis. All independent variables listed in Table 1 were entered into the model as potential predictors (A1, A2,.....A12). A value of $p < .001$ was considered statistically significant. After stepwise linear regression analysis, A5 (Order type_A), A6 (Order type_B), and A7 (Order type_C) were found to be three independent predictors of the dependent variable (β_{A5}, β_{A6}, β_{A7}=0.566, 0.463, 0.210; $p<0.001$). A new formula (Equation 4) has emerged by updating Equation 3 between the three significant independent and dependent variables.

$$A_{13} = c_0 + c_5A_5 + c_6A_6 + c_7A_7 + e \quad (4)$$

The proposed method determined the most accurate model inputs to get the best performance. The resulting three-input ANN equation is presented below (Equation 5).

$$A_{13} = \sigma(\sum_{i=5}^{7} A_i \bullet w_i + b) \quad (5)$$

The ANN in the study is a fully connected multilayer perceptron neural network (MLPNN), whose structure is shown in Figure 2. The proposed model is constructed to forecast total orders (A13) using the MatLab R2021a. The research model of this study consists of a structure with three hidden layers with LRC-selected feature subsets in a network.

Figure 2 shows the interconnections between the input and output parameters of the MLPNN to predict the fifteen-day order demand for an order fulfillment center. Neurons present in the input and

output layers equal the number of input and output parameters, respectively [47]. Finding the optimum number of hidden layers and neurons helps design the best architecture [48]. The training datasets are used to obtain the optimum architecture of the model with the appropriate number of hidden layers, neurons in the hidden layers, momentum term, learning rate, and the number of iterations. The dataset is split into training, validation, and test datasets to perform model training. Training continues until the Sum Squared Error (SSE) value reaches the minimum value. The necessary steps during model training are as follows: (i) selection of hidden layers and neurons in the hidden layers, (ii) selection of learning rate and momentum constant, and (iii) selection of iteration numbers.

The data used to test the models was obtained from an order fulfillment center. The parameters optimization of the proposed MLPNN model was performed using a random search and trial and error approach. The result showed that the architecture of the best MLPNN model has an optimal parameter on a momentum constant of 0.99, a learning rate of 0.95, and three hidden layers. The training dataset is divided into 70%, 15%, and 15%, respectively, for each model's training, validation, and testing data. There are 30, 60, and 15 neurons in the created network structure for the first, second, and third hidden layers. Neural networks were trained using the Levenberg-Marquardt algorithm. The trained MLPNN's validity was evaluated using SSE. It has been shown that the smallest error gives more accurate results in the estimation, especially helping the senior manager to make an effective decision for the operation of the business by considering the orders.

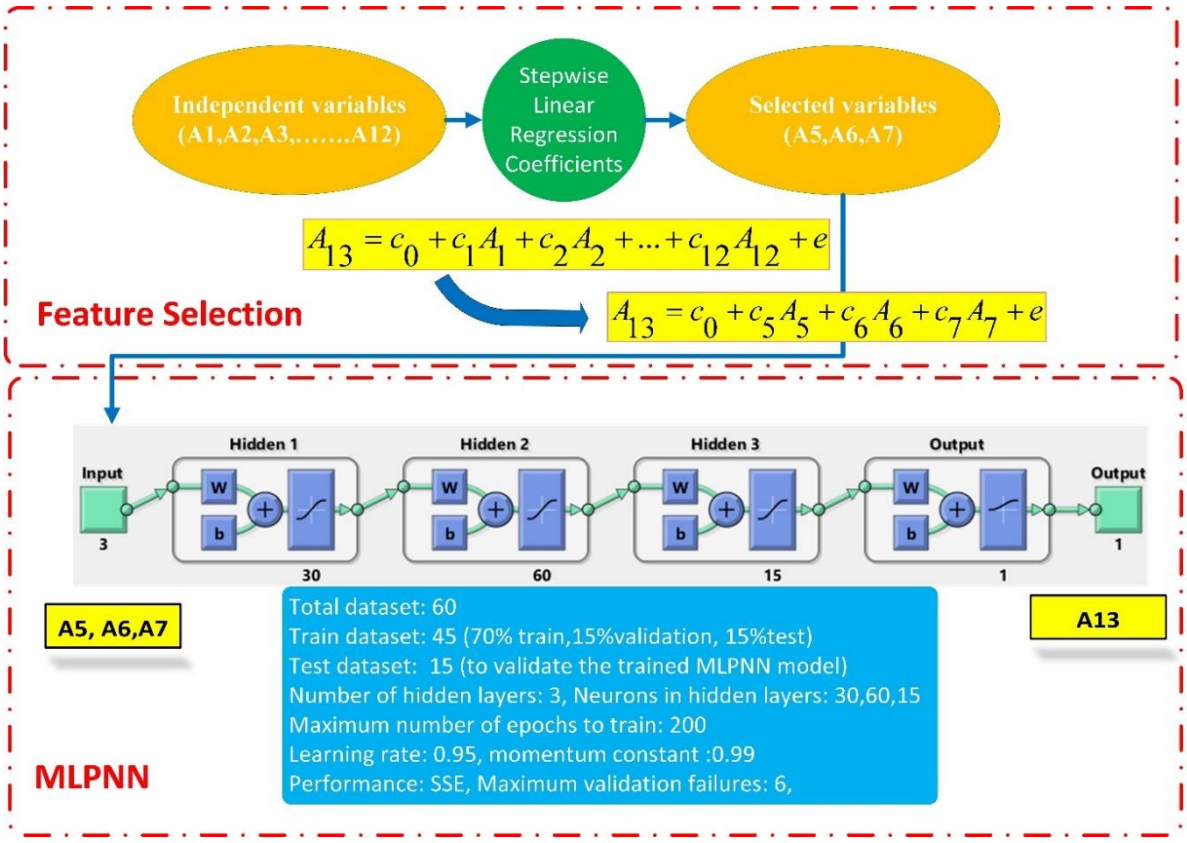

Figure 2. Schematics of the proposed MLP neural network

During the design of the MLPNN model, the data were divided into two sets of training and test subsets. While the training dataset was used to develop the MLPNN model, the test dataset not included in the training group was used to validate and examine the performance of the trained MLPNN model. This model has been proven that it can be used to predict future demand based on historical data.

To check the performance of the MLPNN model with different input sets, the mean absolute percentage error (MAPE) was measured. Using the NN approach, this performance criterion was used to measure how close the measured values were to the predicted values. This criterion helps evaluate the model's capabilities with different input sets for the A13. MAPE is computed as follows (Equation 6):

$$MAPE = \frac{100\%}{N}\sum_{i=1}^{N}\left|\frac{y_i - \hat{y}_i}{y_i}\right| \quad (6)$$

where y_i and $\hat{y}_i$ are the predicted values and the observed A13 values based on the proposed model and N is the number of days in the test data, respectively.

Model performances for each input set were compared based on the estimation of 15 samples (days).

3. Results and Discussions

Using the stepwise method, multiple linear regression was conducted to compare the independent influences of A1, A2, A3, A4…A11, and A12 on the A13.

Descriptive statistics are used to summarize and describe the basic features of data. Table 2 shows descriptive statistics for variables of interest.

Table 2. Descriptive statistics for variables of interest

	Descriptive Statistics		
	Type of Variables	**Mean**	**Std. Deviation**
A13	Dependent	300.87	89.60
A1	Independent	3.02	1.28
A2	Independent	4.03	1.40
A3	Independent	172555	69.51
A4	Independent	118921	27.17
A5	Independent	52112	18.83
A6	Independent	109.230	50.74
A7	Independent	139.53	41.44
A8	Independent	77.40	186.50
A9	Independent	44504.35	12197.91
A10	Independent	46640.83	45220.74
A11	Independent	79401.48	40504.42
A12	Independent	23114.63	13148.04

The stepwise regression procedure selects variables in a step-by-step manner [49]. This method adds or subtracts independent variables one by one by evaluating the statistical significance of the variable. It removes the least significant variable to reduce the size of the features. When the algorithm ends, a single regression model is produced. While the t statistical test is used to determine the importance of each independent variable, beta coefficients are used to determine the significance level for each independent variable. The dependent variable will increase by the number of beta coefficients [44]. Table 3 shows the results of the stepwise regression analysis.

Unstandardized regression coefficients estimated from linear regression are presented in the second column of Table 3. Standardized coefficients, also called Beta coefficients, are given in the fourth column of the same table. Based on the descriptive statistics above, it is seen how each of the independent variables affects the dependent variable (A13) while keeping all other variables constant. Beta coefficients can be used to evaluate the sensitivity of the factors [50]. A higher absolute value of the standardized coefficient indicates a stronger effect on the dependent variable (A13). As Table 3 shows, the A5, A6, and A7 have the most important effect on the A13. The effect of A6 (Beta = 0.566, $p<0.001$) is greater than the effects of A7 (Beta=0.463, $p<0.001$) and A5 (Beta=0.210, $p<0.001$).

The dimensions of attributes were reduced to 10 (A3-A12), 7 (A3, A4, A8-A12), 5 (A3, A4, A6, A7, A11), 5 (A3-A7), 4 (A3, A5-A7), 4 (A5-A8), 3 (A3, A6, A7) predictive attributes from 12, randomly. In addition, the dimensions of attributes of datasets were reduced to three (A5, A6, A7) from twelve using the LRC method. Thus, nine feature subsets (X1 to X9) for the DDFO dataset were constructed to build the forecasting model (Table 4).

Table 3. Stepwise linear regression analysis for the effect of independent variables on A13 (Target-Total orders)

Coefficients							
	Unstandardized Coefficients		Standardized Coefficients			Collinearity Statistics	
	B	Std. Error	Beta	t statistic	p	Tolerance	VIF
Cons.	5.05E-13	.000		.000	1.000		
A3	1.49E-14	.000	.000	.000	1.000	.078	12.816
A4	1.29E-14	.000	.000	.000	1.000	.219	4.570
A6	1.000	.000	.566	75.09E+6	<0.001	.208	4.811
A7	1.000	.000	.463	44.91E+6	<0.001	.111	8.971
A5	1.000	.000	.210	35.91E+6	<0.001	.345	2.897
Cons.	6.47E-13	.000		.000	1.000		
A3	9.74E-15	.000	.000	.000	1.000	.124	8.072
A6	1.000	.000	.566	88.63E+6	<0.001	.284	3.517
A7	1.000	.000	.463	78.78E+6	<0.001	.337	2.969
A5	1.000	.000	.210	46.62E+6	<0.001	.571	1.751
Cons.	1.99E-13	.000		.000	1.000		
A6	1.000	.000	.566	13.16E+7	<0.001	.615	1.625
A7	1.000	.000	.463	11.67E+7	<0.001	.726	1.378
A5	1.000	.000	.210	55.93E+6	<0.001	.807	1.239

Table 4. The nine feature subsets for DDFO dataset

Feature Subset	No of selected features	Features
X1	1	A1,A2,A3,A4,A5,A6,A7,A8,A9,A10,A11,A12
X2	2	A3,A4,A5,A6,A7,A8,A9,A10,A11,A12
X3	3	A3,A4,A8,A9,A10,A11,A12
X4	4	A3,A4,A6,A7,A11
X5	5	A3,A4,A5,A6,A7
X6	6	A3,A5,A6,A7
X7	7	A5,A6,A7,A8
X8	8	A3,A6,A7
X9*	9	A5,A6,A7

* *Obtained subset by feature selection using LRC*

The MAPE values of models for the prediction of A13 with different inputs (subsets) are shown in Figure 3a. As a result, better model performances were obtained with the X9 feature subset (Figure 3a and Figure 4f). Figure 3b illustrates the regression performance of the proposed model obtained using the X9 feature subset. A strong relationship was found between the predicted and the observed variable. According to the results, the correlation coefficient (R^2) is approximately 0.992, and this value is quite high.

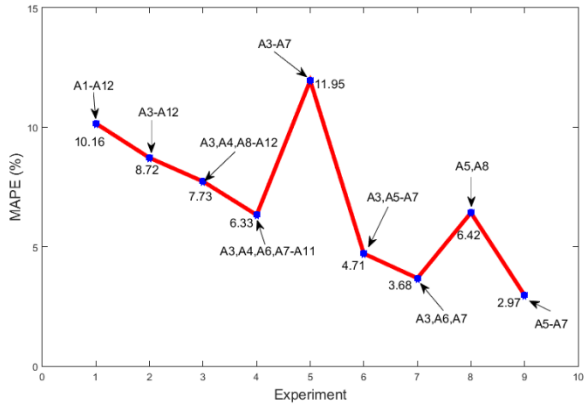

a)

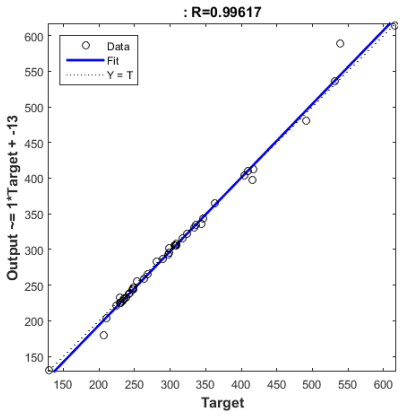

b)

Figure 3. a) Mean absolute percentage error on demand forecast with different subsets of selected attributes **b)** Regression performance of the model for X9 feature subset.

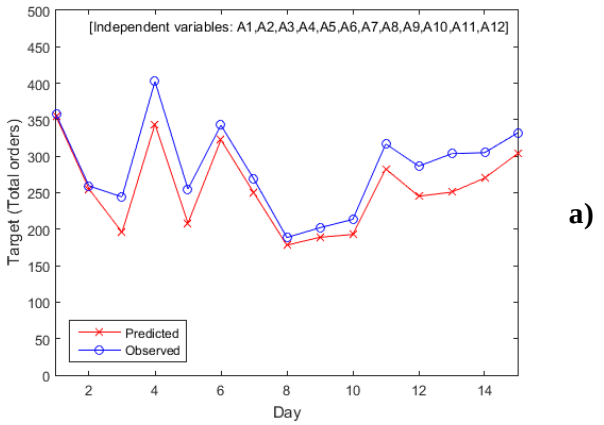

a)

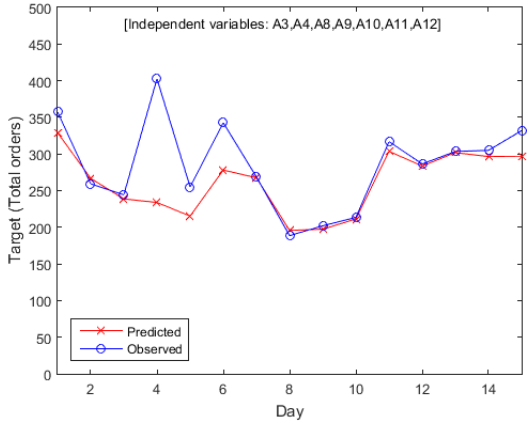

b)

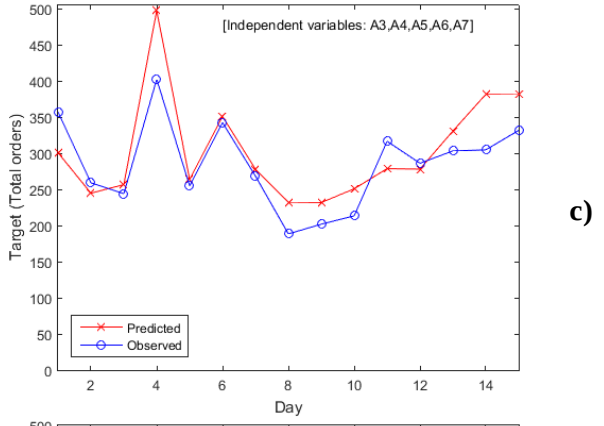

c)

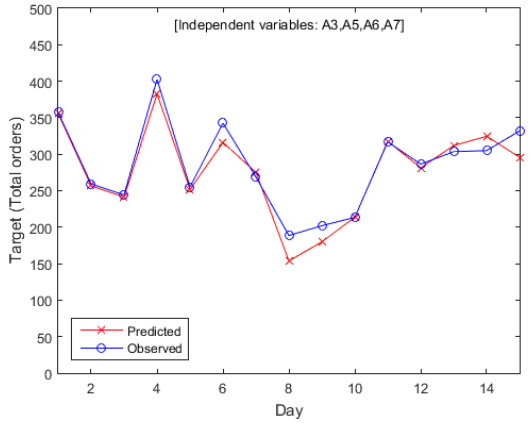

d)

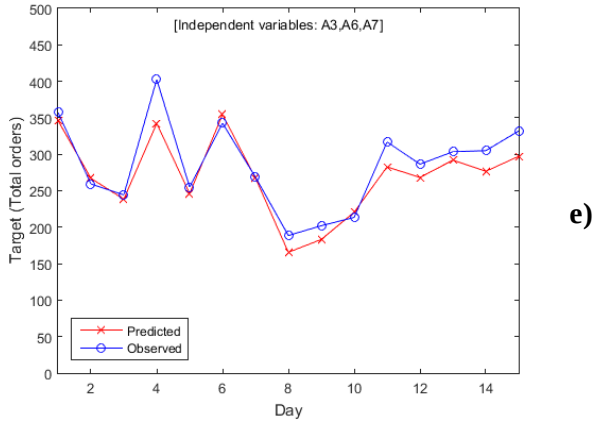

e)

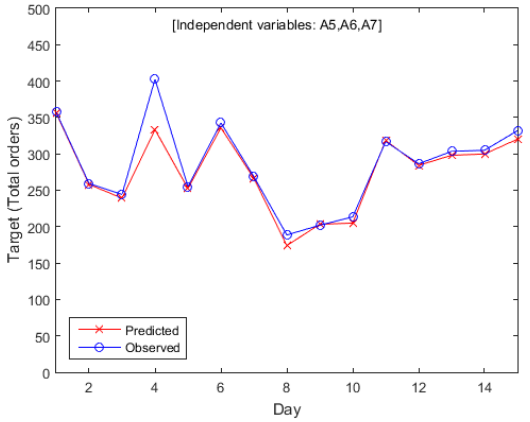

f)

Figure 4. Comparison of predictions with observed orders according to **a)** X1 **b)** X3 **c)** X5 **d)** X6 **e)** X7 **f)** X9 feature subsets

Figure 4 shows the performance of the models (different subsets of attributes selected) over the test data. The experimental results are shown in Figures 4a, 4b, 4c, 4d, 4e, and 4f; the marker curve (circle) represents observed data, and the marker curve (cross) represents the output of MLPNN. Figures 4a, 4b, 4c, 4d, and 4e were obtained using randomly selected features as model input. Figure 4f shows the performance of the proposed 3-input model. Compared to the others, the graph obtained for the proposed model shows a strong correlation between the predicted and observed values.

The data set used in this study was also used by Ferreira et al. in a previous study. Ferreira et al. found valuable results by using 12 variables in artificial neural network inputs. This study obtained successful results (R^2 with 0.992, MAPE with 2.97%) using only three variables, including order type_A (A5), order type_B (A6), and order type_C.

4. Conclusion

Demand forecasting is the field of predictive analytics dedicated to understanding consumer demand. This process needs to be accurate and timely in a trading company. This paper aims to forecast the daily demand orders of a valve manufacturing industry using the MLP neural network model and reduce the forecast error using LRC-based feature selection. The goal of feature selection is to reduce the number of attributes in the dataset. Using the linear regression coefficients and their significance, features decreased from twelve to three (A5, A6, A7). The MAPE value for the model was found to be less than 3%. The best results were obtained with the A5 (order type_A), A6 (order type_B), and A7 (order type_C) attributes. The proposed feature selection method can be considered as a good tool to improve forecast accuracy and shorten forecast time in forecasting daily demand. In future research, the feature selection technique using linear regression coefficients will be tested in many different sectors.

The Declaration of Publishing Ethics

The author declares that this study complies with Research and Publication Ethics.

References

[1] E. Eckhaus, “Consumer Demand Forecasting: Popular Techniques, Part 1: Weighted and Unweighted Moving Average,” 2010. [Online]. Available: http://www.purchasesmarter.com/articles/118. (Accessed: Nov. 22, 2021).

[2] S. P. Sethi, H. Yan, and H. Zhang, *Inventory and Supply Chain Management with Forecast Updates*. Chapter 1. New York: USA/Springer, 2005.

[3] R. Fildes, K. Nikolopoulos, S. F. Crone, and A. A. Syntetos, “Forecasting and operational research: a review,” *Journal of the Operational Research Society*, vol. 59 (9), pp. 1150–1172, September 2008.

[4] J. P. Donate, P. Cortez, G. G. Sánchez, and A.S. Miguela, “Time series forecasting using a weighted cross-validation evolutionary artificial neural network ensemble,” *Neurocomputing*, vol. 109, pp. 27–32, June 2013.

[5] K. Tanaka, “A sales forecasting model for new-released and nonlinear sales trend products,” *Expert Systems with Applications*,” vol. 37, pp. 7387–7393, November 2010.

[6] P. C. Chang, and Y.W. Wang, “Fuzzy Delphi and backpropagation model for sales forecasting in PCB industry,” *Expert Systems with Applications*, vol. 30, pp. 715–726, May 2006.

[7] Y. Ni, and F. Fan, “A two-stage dynamic sales forecasting model for the fashion retail,” *Expert Systems with Applications*, vol.38, pp. 1529–1536, March 2011.

[8] Z. L. Sun, T. M. Choi, K. F. Au, and Y. Yu, “Sales forecasting using extreme learning machine with applications in fashion retailing,” *Decision Support Systems*, vol. 46, pp. 411–419, December 2008.

[9] P. Kumar, M. Herbert, and S. Rao, “Demand forecasting using Artificial Neural Network Based on Different Learning Methods: Comparative Analysis", *IJRASET*, vol. 2, pp. 364-374, April 2014.

[10] G. S. Groppo, M. A. Costa, and M. Libânio, “Predicting water demand: a review of the methods employed and future possibilities”, *Water supply*, vol. 19, pp. 2179-2198, August 2019.

[11] G. P. Zhang, “An investigation of neural networks for linear time-series forecasting,” *Computers&Operations Research*, vol. 28, pp. 1183–1202, October 2001.

[12] J. Adamowski, and C. Karapataki, “Comparison of multivariate regression and artificial neural networks for peak urban water-demand forecasting: evaluation of different ANN learning algorithms," *Journal of Hydrologic Engineering*, vol. 15, pp. 729–743, October 2010.

[13] J. Caiado, "Performance of combined double seasonal univariate time series models for forecasting water demand," *Journal of Hydrologic Engineering*, vol. 15, pp. 215–222, March 2010.
[14] J. Adamowski, H. F. Chan, S. O. Prasher, B. Ozga-Zielinski, and A. Sliusarieva, "Comparison of multiple linear and nonlinear regression, autoregressive integrated moving average, artificial neural network, and wavelet artificial neural network methods for urban water demand forecasting in Montreal, Canada," *Water Resources Research*, vol. 48, pp. 1-14, January 2012.
[15] M. Ghiassi, D. K. Zimbra, and H. Saidane, "Urban water demand forecasting with a dynamic artificial neural network model", *Journal of Water Resources Planning and Management*, vol. 134, pp. 138–146, March 2008.
[16] M. Fırat, M. A. Yurdusev, and M. E. Turan, "Evaluation of artificial neural network techniques for municipal water consumption modeling," *Water Resources Management*, vol. 23, pp. 617–632, March 2009.
[17] M. Fırat, M .E. Turan, and M. A. Yurdusev, "Comparative analysis of neural network techniques for predicting water consumption time series," *Journal of Hydrology*, vol. 384, pp. 46–51, April 2010.
[18] A. Altunkaynak, M. Özger, and M. Çakmakcı, "Water consumption prediction of Istanbul city by using fuzzy logic approach," *Water Resources Management*, vol. 19, pp. 641–654, October 2005.
[19] M. Fırat, M. E. Turan, and M. A. Yurdusev, "Comparative analysis of fuzzy inference systems for water consumption time series prediction," *Journal of Hydrology*, vol. 374, pp. 235–241, August 2009.
[20] C. Peña-Guzmán, J. Melgarejo, and D. Prats, "Forecasting water demand in residential, commercial, and industrial zones in Bogotá, Colombia, using Least-Squares Support Vector Machines," *Mathematical Problems in Engineering*, vol. 2016, pp. 1-10, December 2016.
[21] M. Nasseri, A. Moeini, and M. Tabesh, "Forecasting monthly urban water demand using Extended Kalman Filter and Genetic Programming," *Expert Systems with Applications*, vol. 38, pp. 7387–7395, June 2011.
[22] A. Chawla, A. Singh, A. Lamba, N. Gangwani, and U. Soni, "Demand Forecasting using Artificial Neural Networks – A case study of American Retail Corporation," *in Advances in Intelligent Systems and Computing: Applications of Artificial Intelligence Techniques in Engineering*, H. Malik, S. Srivastava, Y. Sood., A. Ahmad, Eds. Singapore: Springer, 2019. pp. 79-89.
[23] A. Öztekin, R. Kizilaslan, S. Freund, and A. Iseri "A data analytic approach to forecasting daily stock returns in an emerging market," *European Journal of Operational Research*, vol. 253, pp. 697-710, September 2016.
[24] R. J. Kuo, and K. C. Xue, "A decision support system for sales forecasting through fuzzy neural networks with asymmetric fuzzy weights," *Decision Support Systems*, vol. 24, pp. 105–126, December 1998.
[25] R. Law, "Backpropagation learning in improving the accuracy of neural network-based tourism demand forecasting," *Tourism Management*, vol. 21, pp. 331–340, August 2000.
[26] Z. Ying, and X. Hanbin, "Study on the model of demand forecasting based on artificial neural network," in *2010 Ninth International Symposium on Distributed Computing and Applications to Business, Engineering and Science, Hong Kong, China, August 10-12, 2010*, pp. 382-386.
[27] S. Bhadouria, and A. Jayant, "Development of ANN Models for Demand Forecasting," *American Journal of Engineering Research (AJER)*, vol. 6, pp. 142-147, December 2017.
[28] P. du Jardin, and E. Séverin, "Forecasting financial failure using a Kohonen map: A comparative study to improve model stability over time," *European Journal of Operational Research*, vol. 221, pp. 378-396, September 2012.
[29] Q. Cao, B. T. Ewing, and M. A. Thompson, "Forecasting wind speed with recurrent neural networks," *European Journal of Operational Research*, vol. 221, pp. 148-154, August 2012.
[30] G. Sermpinis, K. Theofilatos, A. Karathanasopoulos, E. F. Georgopoulos, and C. Dunis, "Forecasting foreign exchange rates with adaptive neural networks using radial-basis functions and particle swarm optimization", *European Journal of Operational Research*, vol. 225, pp. 528-540, March 2013.
[31] M. S. Kim, "Modeling special-day effects for forecasting intraday electricity demand," *European Journal of Operational Research*, vol. 230, pp. 170-180, October 2013.
[32] K. Venkatesh, V. Ravi, A. Prinzie, and D. V. Poel, "Cash demand forecasting in ATMs by clustering and neural networks," *European Journal of Operational Research*, vol. 232, pp. 383-392, January 2014.
[33] R. P. Ferreira, A. Martiniano, A. Ferreira, A. Ferreira, and R. J. Sassi, "Study on Daily Demand Forecasting Orders using Artificial Neural Network," *IEEE Latin America Transactions*, vol. 14, pp. 1519-1525, March 2016.

[34] W. Fu, C.- F. Chien, and Z.- H. Lin, "A hybrid forecasting framework with neural network and time-series method for intermittent demand in semiconductor supply chain," in *Advances in Production Management Systems*: *IFIP WG 5.7 International Conference, APMS 2018, Seoul, Korea, August 26-30, 2018*, I. Moon, G. M. Lee, J. Park, D. Kiritsis G. Cieminski, Eds. Springer, Cham., 2018. pp. 65-72.

[35] P. Hietaharju, M. Ruusunen, and K. Leiviska, "Enabling Demand Side Management: Heat Demand Forecasting at City Level," *Materials*, vol. 12, pp. 1-17, January 2019.

[36] H. Peng, C. Ding, and F. Long, "Minimum redundancy maximum relevance feature selection," *IEEE Intelligent Systems*, vol. 20, pp. 70–71, December 2015.

[37] J. Li, K. Cheng, S. Wang, F. Morstatter, R. P. Trevino, J. Tang, and H. Liu, "Feature Selection: A Data Perspective," *ACM Computing Surveys*, vol. 50, pp. 1-45, November 2018.

[38] Y. Zhang, D. Gong, X. Gao, T. Tian, and X. Sun, "Binary differential evolution with self-learning for multi-objective feature selection," *Information Sciences*, vol. 507, pp. 67-85, January 2020.

[39] R.A. Chinnathambi, M. Campion, A. S. Nair, and P. Ranganathan, "Investigation of Price-Feature Selection Algorithms for the Day-Ahead Electricity Markets," in *2018 IEEE Electrical Power and Energy Conference (EPEC), Toronto, ON, Canada, October 10-11, 2018*, pp. 1-6.

[40] UCI Machine Learning Repository, "Daily Demand Forecasting Orders Data Set," 2017. [Online]. Available: https://archive.ics.uci.edu/ml/datasets/Daily+Demand+Forecasting+Orders (Accessed: Nov. 22, 2021).

[41] K. Abrougui, K. Gabsi, B. Mercatoris, C. Khemis, R. Amami, and S. Chehaibi, "Prediction of organic potato yield using tillage systems and soil properties by artificial neural network (ANN) and multiple linear regressions (MLR)," *Soil and Tillage Research*, vol. 190, pp. 202-208, July 2019.

[42] N. Susijawati, A. Setiawan, G. M. Putri, S. Maryam, A. Firasati, and M. Alwi, "The Effect of Organizational Commitment and Organizational Support as Intervening Variables to Turnover Intention of Employees," in *International Symposium on Social Sciences, Education, and Humanities (ISSEH 2018),* in Advances in Social Science, Education and Humanities Research, vol. 306, March 2019, pp. 283-285.

[43] J. F. Hair, W. C. Black, B. J. Babin, and R. E. Anderson, *Multivariate Data Analysis A Global Perspective*. England/Pearson Education Limited, 2010.

[44] Statistics Solutions website, "Regression". [Online]. Available: https://www.statisticssolutions.com/directory-of-statistical-analyses-regression-analysis/regression/. [Accessed: Dec. 05, 2021).

[45] M. Elbisy, and F. Osra, "Application of Group Method of Data Handling Type Neural Network for Significant Wave Height Prediction," *American Journal of Neural Networks and Applications*, vol. 5, pp. 51-57, November 2019.

[46] R. J. Kuo, M. C. Shieh, J.W. Zhang, and K.Y. Chen, "The application of an artificial immune system-based backpropagation neural network with feature selection to an RFID positioning system," *Robotics and Computer-Integrated Manufacturing*, vol. 29, pp. 431-438, December 2013.

[47] M. Lashkarbolooki, B. Vaferi, A. Shariati, and A. Z. Hezave, "Investigating vapor–liquid equilibria of binary mixtures containing supercritical or near-critical carbon dioxide and a cyclic compound using cascade neural network," *Fluid Phase Equilibria*, vol. 343, pp. 24-29, April 2013.

[48] P. L. Narayana, J. H. Kim, A. K. Maurya, C. H. Park, J.- K. Hong, J.- T. Yeom, and N. S. Reddy, "Modeling Mechanical Properties of 25Cr-20Ni-0.4C Steels over a Wide Range of Temperatures by Neural Networks," *Metals*, 10, pp. 1-12, February 2020.

[49] J. FrosT, "Guide to Stepwise Regression and Best Subsets Regression," 2020. [Online]. Available: https://statisticsbyjim.com/regression/curve-fitting-linear-nonlinear-regression/. (Accessed: Dec. 05, 2021).

[50] S. B. Zhou, L. Shengjie, and X. Yiming, "Effects of Filler Characteristics on the Performance of Asphalt Mastic: A Statistical Analysis of the Laboratory Testing Results," *International Journal of Civil Engineering*, vol. 16, pp. 1175–1183, September 2018.

Bitlis Eren Üniversitesi Fen Bilimleri Dergisi
BİTLİS EREN UNIVERSITY JOURNAL OF SCIENCE
ISSN: 2147-3129/e-ISSN: 2147-3188
VOLUME: 11 NO: 2 PAGE: 574-585 YEAR: 2022
DOI: 10.17798/bitlisfen.1061984

Investigation of Biological and Chemical Effects of Extracts from *Arum rupicola* Boiss. var. *rupicola*

Mehmet Rıza KIVANÇ[1*]

[1]*Van Sağlık Hizmetleri Meslek Yüksekokulu, Orta Öğretim Fen Ve Matematik Alanları Eğitimi Bölümü Kimya Eğitimi Anabilim Dalı*
(ORCID: 0000-0002-9667-1225)

Keywords: *Arum rupicola*, Fatty acids, Antioxidant activity, Phenolics compound, Antibacterial activity.

Abstract

The present study aimed to evaluate the fatty acid and phenolic profiles, and antioxidant and antibacterial activities of *A. rupicola*. For this purpose, For this purpose, the chemical content of the methanol extract was first determined using the HPLC-TOF/MS method. Thereafter, five extracts having different polarities (hexane-hexane, hexane-chloroform, methanol-hexane, methanol-chloroform and methanol-butanol) were obtained using the partitioning method, and the chemical contents of these extracts were determined by the GC-MS method. According to these data, various fatty acids and phenolic contents were observed. Furthermore, the antioxidant studies were performed with total phenolic compounds and ABTS, while antibacterial studies were performed with the microdilution test and the disc diffusion test using three bacteria, one gram-positive and two gram-negative bacteria. The antioxidant and antibacterial tests revealed that *A. rupicola* is both an antioxidant and an antibacterial plant. According to the obtained results, the microdilution test was shown to be more effective than the disc diffusion test. On the other hand, the inhibition percent vs. extract concentration graph showed that the MH was the most effective inhibitor. In this study, it was revealed that the methanol extract and five extracts from *A. rupicola* had a variety of phenolic compositions and fatty acids, respectively, and these five extracts also possess antioxidant effects and antibacterial activities.

1. Introduction

There has been a strong relationship between humans and plants throughout history. Today, this occurs in a variety of forms, in particular, use of plants for nutrition, fiber, drugs, and energy for humans and animals. Plants are a very important part of our lives, religion, and wealth, as well as our nourishment [1]. Plants and humans are a part of the whole which is survival for lives. They cannot be concerned to be a differ part of each other.

Arum L. is a part of the Araceae family in the flowering plants. It includes 29 species and covers a wide area of the world, from North Africa, Europe, and west and central Asia to China [2-4]. *Arum* genus plants contain many phytochemicals such as polyphenols, alkaloids, glycosides, proanthocyanidins, 2-heptanone, indoles, p-cresol, (E)-caryophyllene, monoterpenes, two sesquiterpenes, and lectin [5]. In Turkey, *Arum* genus includes a total of 18 taxa, 14 species, and 4 varieties, and its cosmopolitan species cover Turkey [6-8]. Palestinian folkloric medicine used *Arum* genus leaves in the treatment of cancer, cough, worms, constipation, hemorrhoids and urinary tract infections

*Corresponding author: mr.kivanc@yyu.edu.tr
Received: 23.01.2022, Accepted: 07.05.2022

[9-11]. It is known only for the treatment of hemorrhoids in Turkey [12].

The isolation of pure compounds from natural products, namely plants, is very important. However, this cannot be easy and need to more time for studding of natural products. After the extraction process, a couple separation techniques come. One of the separation techniques is the solvent partitioning method. This method usually involves the use of two insoluble solvents in a separating funnel. Natural products are dispersed in solvents depending on the solvents different partition coefficients. This technique is very effective as a first step in separating large amounts of compounds from the crude extract [13].

Some extracts from the plant and its metabolites biologically exhibited antibacterial [14], antimicrobial [15], antifungal [16], and antioxidant activities [17]. The bioactive components that block pathogens and have low toxicity to host cells should be considered for designing new antimicrobial drugs [18]. These compounds exist in many parts of plants such as stems, roots, leaves, barks, flowers, fruits, and seeds [19]. Alkaloids, tannins, flavonoids, phenolics [20], and fatty acids [21-23] are medicinally the most important among these compounds.

Several subspecies of *Arum* species have been studied in the past, including *'Arum elongatum* Steven' and *'Arum rupicola* Boiss. var. *virescens'*. These studies focused on the different chemical and medical properties of isolates of the *Arum* subspecies. In a survey by Özok and Güneş, the antidiabetic effect of *A. rupicola* was investigated. For this purpose, the dried form of *Arum rupicola* Boiss. var. *virescens* was extracted in water, and then its antidiabetic activity was observed in vivo [24]. In another study by Alan, the antimicrobial and antioxidant effects of ethanol and purified water extracts of the *Arum elongatum* Steven plant and their role in preventing DNA damage were investigated [25]. In this study, the antimicrobial and antioxidant effects of "*'Arum rupicola* Boiss. var. *rupicola'*" extracts obtained with different solvents and their combinations were studied for the first time. For the purpose, five extracts (hexane-hexane (HH), hexane-chloroform (HC), methanol-hexane (MH), methanol-chloroform (MC), and methanol-butanol (MB)) from *A. rupicola* collected from mountains of the Gevas district were obtained using the partition method with polar and nonpolar solvents. The antibacterial activity of these extracts was studied on *Staphylococcus aureus* and *Bacillus subtilis*, gram-positive bacterial strains, and *Escherichia coli*, gram-negative bacterial strain. Also, the fatty acid contents of these extracts were detected by GC-MS analysis.

2. Material and Methods

2.1. Material

In brief, all organic solvents, tryptic soy broth (TSB) and tryptic soy agar (TSA) were obtained from Merck. *Arum rupicola* Boiss. var. *rupicola* (*A. rupicola)* was collected from mountains of the Gevas district (Van province, Turkey) in May 2019. It was identified by Dr. Suleyman Mesut Pinar and then updated by Dr. Mehmet Fırat in a previous study [26].

2.2. Extraction protocol

Extractions of *A. rupicola* were prepared as presented in Scheme 1. This procedure was performed with minor modification and configuration [13]. Five extracts were obtained, and these were coded as hexane-hexane (HH), hexane-chloroform (HC), methanol-hexane (MH), methanol-chloroform (MC), and methanol-butanol (MB).

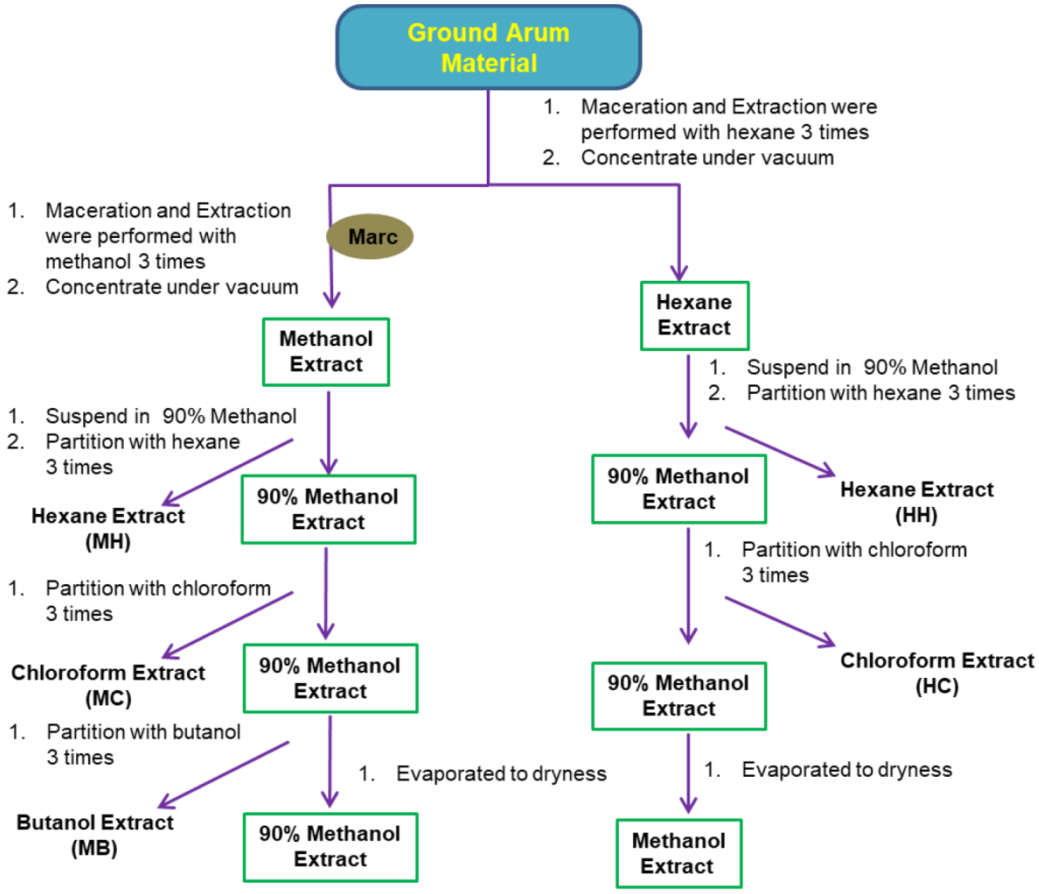

Scheme 1. The extraction and sub-fraction protocol for *A. rupicola*

2.3. HPLC-TOF/MS analysis for phenolic content of the *A. rupicola* methanol extract

Phenolic components data for polar extracts from *A. rupicola* were detected by HPLC-TOF/MS (Agilent 1260 infinity LC, 6210 TOF-MS with column Zorbax SB-C18) analysis, as described in the literature [27]. For this, the methanol extract obtained from the extraction protocol was used. The spectrum obtained from this method is given in Figure 1.

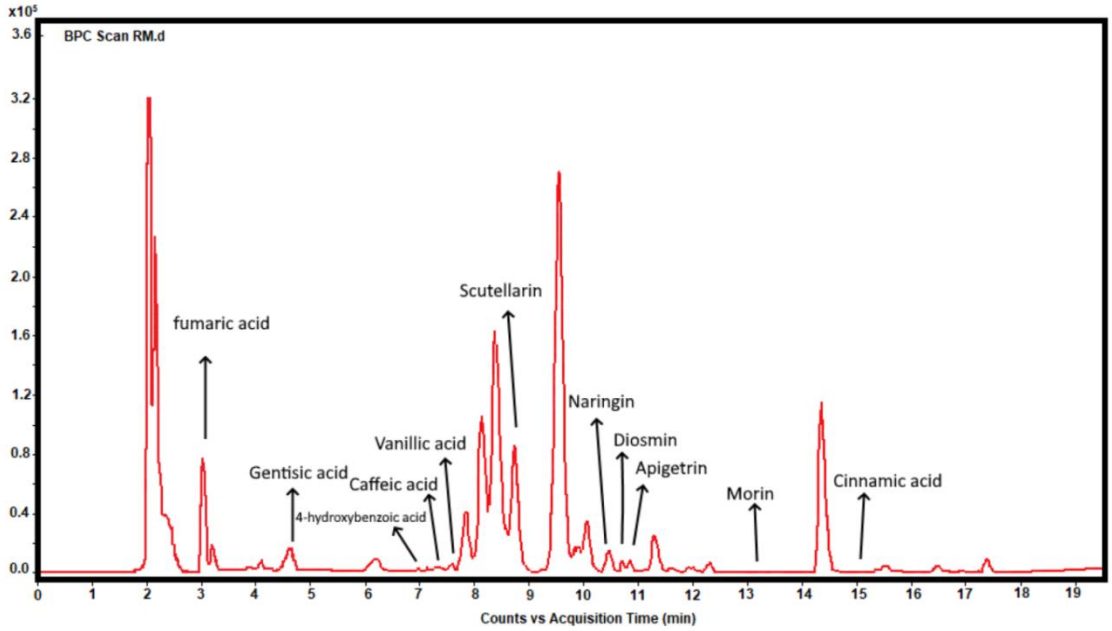

Figure 1. HPLC-TOF analysis spectrum for methanol extract of *A. rupicola*

2.4. GC-MS analysis for fatty acid profiling

The fatty acid content of the *A. rupicola* extracts was determined using GC-MS (Thermo ITQ 900 with column Thermo TR-5ms SQC) analysis. For this purpose, the five extracts were firstly removed from their solvent and then 20-30 mg of these extracts was dissolved in 3 ml of 2M KOH solution in methanol. This mixture was combined with 3 ml of hexane and these were vigorously shaken using a vortex for 20 minutes. After all experimental processes, two different phases were obtained. These were esterified and hexane solutions were added. The hexane solution was carefully extracted from the lower phase and added into the vial to determine fatty acid content [27]. The GC-MS spectrum for the MB extract is presented in Figure 2.

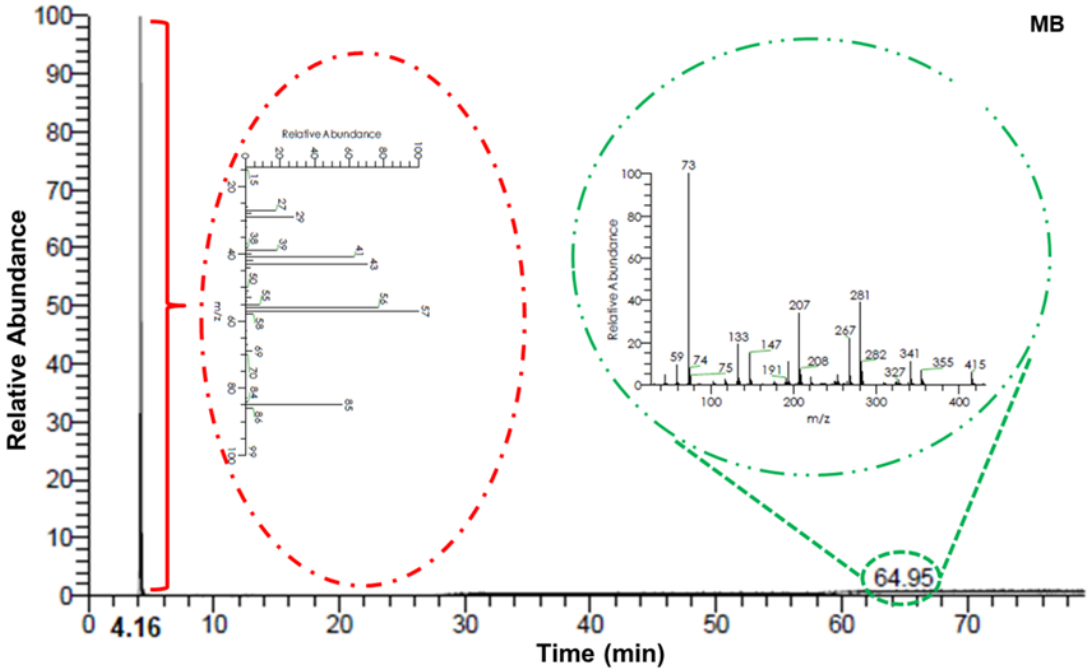

Figure 2. The GC-MS spectrum for the MB extract

2.5. Trolox equivalent antioxidant capacity (TEAC)

$ABTS^{\bullet+}$, a radical cation and a reagent, is obtained from oxidation of the ABTS reactive with persulfate to determine the antioxidant activity of different materials. This assay was carried out according to the literature [28-30] and was used for the activity of extracts from *A. rupicola*. In brief, to obtain the $ABTS^{\bullet+}$ solution, the ABTS solution was firstly prepared in water at 7 mM concentration, and then potassium persulfate with final concentration of 2.45 mM was created by using the ABTS stock solution. This mixture was placed in the dark at room temperature for 16 h to complete the reaction. For the antioxidant capacity study of *A. rupicola* extracts, the spectrophotometric value of the $ABTS^{\bullet+}$ solution should be in the range of 0.700 ± 0.02 (A_s) at $\lambda = 734$ nm before starting measurements. For this, dilution was performed using ethanol. Different concentrations (from 12.5 mL to 100 mL) of *Arum* extracts were mixed with 2.0 mL ABTS•+ solution and the spectrophotometric values were read in the 6th minute (A_f). These values were applied to the following equation and the radical scavenging activities were found.

$$inhibition\% = \left[{\left(A_s - A_f\right)}/{A_s} \right] \times 100 \qquad (1)$$

The Trolox graph was drawn by using the concentration of Trolox vs inhibition%. The TEAC value for *Arum* extracts at different concentrations was calculated from this Trolox standard graph.

2.6. Determination of total phenolic contents for *Arum* extracts

This assay was carried out according to Velioglu et al. and used the Folin-Ciocalteu reagent as standard. All extracts were prepared in DMSO at a concentration of 1 mg/mL. For this, 100 µL concentration of the extracts and 0.75 mL of Folin-Ciocalteu reagent diluted 10 times using deionized water were mixed and vortexed in a test tube. The mixture was incubated at room temperature for 5 min. A triple mixture was obtained to adding 0.75 mL of sodium carbonate (6% w/v) and then vortexed gently. After these steps, the mixture was incubated at room temperature for 90 min, and then spectrophotometric data were obtained at 725 nm using an UV−Vis spectrophotometer (T80+ UV/VIS Spectrometer, PG Ins. Ltd.). A variety of concentrations (0.1−0.01 mg/mL) of gallic acid as standard were used to draw the standard calibration graph. The total phenolic content was mean gallic acid equivalent in milligram per 100 g of each extract. The phenolic content analysis of each extract was performed in triplicate [31-32].

2.7. Antibacterial activities of the extracts

To determine the antibacterial activities of extracts from *A. rupicola*, all extracts were dissolved in DMSO (dimethyl sulfoxide) and these concentrations were prepared to 1 mg/mL. The gram-negative bacteria strain used was *Escherichia coli* (ATCC-8739) and two gram-positive bacteria strains of *Bacillus subtilis* (DSM-347) and *Staphylococcus aureus* (ATCC-6538) were used. The antibacterial activities of extracts were evaluated by the disc diffusion test and micro-dilution assay. These were performed as mentioned in the literature [33]. Firstly, bacteria were inoculated on TSB medium independently and grown overnight at 37 ℃. For the disc diffusion test, 10 µL of bacterial culture was spread on the surface of agar plates separately. Then, 30 µL of extract was dropped on agar plates individually and finally incubated at 37 ℃ overnight. For the micro-dilution assay, 100 µL of bacterial culture was added to a tube containing 20 ml of TSB liquid medium. Then, 30 µL of extract was added to this tube. Finally, tubes were incubated at 37 ℃ overnight. These tubes were spectrophotometrically assayed at 600 nm and compared to control tubes that only contained bacteria.

3. Results and Discussion

3.1. Phenolic contents in the plant

Phenolic content of the methanol extract of *A. rupicola* was examined with HPLC-TOF/MS analysis. According to this analysis, 11 types of phenolic compounds were found and these were fumaric acid, scutellarin, gentisic acid, naringin, 4-hydroxybenzoic acid, diosmin, caffeic acid, apigenin, vanillic acid, morin and cinnamic acid, given in Table 1. Among these, fumaric acid had the highest amount, followed by scutellarin and diosmin. In a previous study about phenolic contents in the plant, the phenolic content of ethanol and pure water extracts of *A. elongatum* were investigated with HPLC analysis [25]. Caffeic acid, vanillic acid, and cinnamic acid were the same, while the other components were different in this paper. As a result, *A. rupicola* contains more phenolic compounds. Some of them were found with developed instrumental techniques, HPLC-TOF/MS analyses, and methods.

Table 1. Phenolic compounds in methanol extract

Phenolic	Retention time	Results mg phenolic/kg plant
Fumaric acid	**3.29**	**277.2**
Gentisic acid	**4.50**	**1.13**
4-hydroxybenzoic acid	**6.96**	**13.6**
Caffeic acid	**7.45**	**1.12**
Vanillic acid	**7.87**	**1.14**
Scutellarin	**9.73**	**19.46**
Naringin	**10.50**	**0.7**
Diosmin	**10.62**	**17.16**
Apigenin	**10.79**	**2.75**
Morin	**13.01**	**1.69**
Cinnamic acid	**15.16**	**1.44**

3.2. Fatty acid contents in the plant

Fatty acids in five different extracts from *A. rupicola* were detected using GC-MS analysis and these are listed in Table 2. There are many different studies about the fatty acid contents of *A. rupicola* and other *Arum* varieties. The fatty acids in these were analyzed by GC-MS in seeds of *A. maculatum* [34], diethyl ether fraction of *A. palaestinum* [35], methanol extract of *A. dioscoridis* [36], acetone extract of *A. cyrinaicum* [37], methanolic and acetone extracts of *A. dioscoridis* [38], and sub-fractions of hexane extract from *A. rupicola* [26]. In this study, the fatty acids in *A. rupicola* were researched and traced more widely compared to the previous studies.

Table 2: Fatty acid content for each extract from *A. rupicola*

Sample Code	Fatty acid[a]	RT*	Area %	Molecular Formula	Molecular Weight
HH	Butane, 2,2,3-trimethyl-	4.47	19.27	C7H16	100
	2-tert-Butyl-4-isopropyl-5-methylphenol	13.61	0.11	C14H22O	206
	Dimethoxyglycerol docosyl ether	17.31	0.02	C27H56O5	460
	Spirost-8-en-11-one,3-hydroxy, (3á,5à,14á,20á,22á,25R)	20.12	0.01	C27H40O4	428
	2-Pentadecanone, 6,10,14-trimethyl-	20.85	0.10	C18H36O	268
	Hexadecanoic acid, methyl ester	24.04	0.98	C17H34O2	270
	Octadecanal,2-Bromo-	29.30	79.52	C18H35BrO	346
HC	Hexane, 2-methyl-	4.18	21.59	C7H16	100
	1,1,3,3,5,5,7,7,9,9,11, 11-dodecamethylhexasiloxane	75.51	78.41	C12H38O5Si6	430
MH	Hexane, 2-methyl-	4.31	92.41	C7H16	100
	Pregnane-3,11,20,21-tetrol, cyclic 20,21-(butylboronate), (3à,5á,11á,20R)-	23.66	0.13	C25H43BO4	418
	Stigmast-5-en-3-ol, (3á)-	40.08	7.46	C29H50O	414
MB	Butane, 2,2,3-trimethyl-	4.16	21.81	C7H16	100
	1,1,3,3,5,5,7,7,9,9,11,11-dodecamethylhexasiloxane	67.29	78.19	C12H38O5Si6	430
MC	Cyclopentane, methyl-	4.0	0.22	C6H12	84
	1,1,3,3,5,5,7,7,9,9,11, 11,13,13,15,15-hexadecamethyloctasiloxane	74.36	99.78	C16H50O7Si8	578

[a] Names of fatty acids were taken from Wiley GC-MS library
*Retention Time

3.3. The evaluation of the phenolic amount and antioxidant activity

As summarized in Table 3, the total phenolic content and the antioxidant activity of five extracts from *A. rupicola* generally increased when the polarity of these extracts increased. Also, the highest antioxidant activity and total phenolic content in the extracts was for MB. All results are found in Table 3. In a study performed by Alan (2018), although the antioxidant activities of only ethanolic and pure water extracts from *A. elongatum* were measured by ABTS, but the total phenolic content of both extracts was not researched. In this paper, both the antioxidant activities and the total phenolic content of five different extracts, which were both polar and apolar phases from *A. rupicola,* were investigated. In other studies with various species from this plant family, the total phenolic content and the antioxidant activity were researched; for example, only polar phase extracts of *A. maculatum* [5], ethanol, methanol, acetone, and water extracts of *A. dioscoridis* [39], and methanol extracts of *A. dioscoridis*, *A. elongatum*, *A. hygrophilum* and *A. palaestinum* [40].

Table 3. Antioxidant activity for five extracts of *A. rupicola* by ABTS assay

	Extracts				
	HH	**HC**	**MH**	**MB**	**MC**
(mM/mg)[a]	**0.51±0,02**	**0.52±0,02**	**1,27±0,01**	**4,87±0,03**	**3,54±0,04**
(mg/ml)[b]	**0.0227**	**0.0038**	**0.1415**	**1.1347**	**0.3119**

[a]Trolox equivalent
[b]Gallic acid equivalent

3.4. Inhibition results for plant extracts

Inhibition% vs. concentration graphs were drawn for the five extracts from *A. rupicola*. These are given in Figure 3. Of these extracts, the concentrations of HH, HC, and MH were 0.25 mg/mL while the other concentrations of the others, MC and MB, were 0.5 and 0.1 mg/mL, respectively. This graph was very detailed in the previous study [40]. That study drew the graph for a single extract, ethanol, of *A. elongatum* but this study drew the graph for five extracts of *A. rupicola*. Also, the values for inhibition% of HH, HC, MH, MC, and MB were found using Trolox equivalent as 61, 65, 75, 66, and 66%, respectively. As understood from both the graph and these values, MH had the biggest value. In the other studies, the value of inhibition% for extracts of pure water and ethanol from *A. elongatum* were 96.63 and 94.15, respectively [25]. Both values were higher than the ones in this paper and these were obtained using BHA and BHT standard compounds. However, the value of inhibition% for methanol extract from *A. elongatum* was between 50-60% using Trolox standard compounds [40]. This value is lower than the ones in this study.

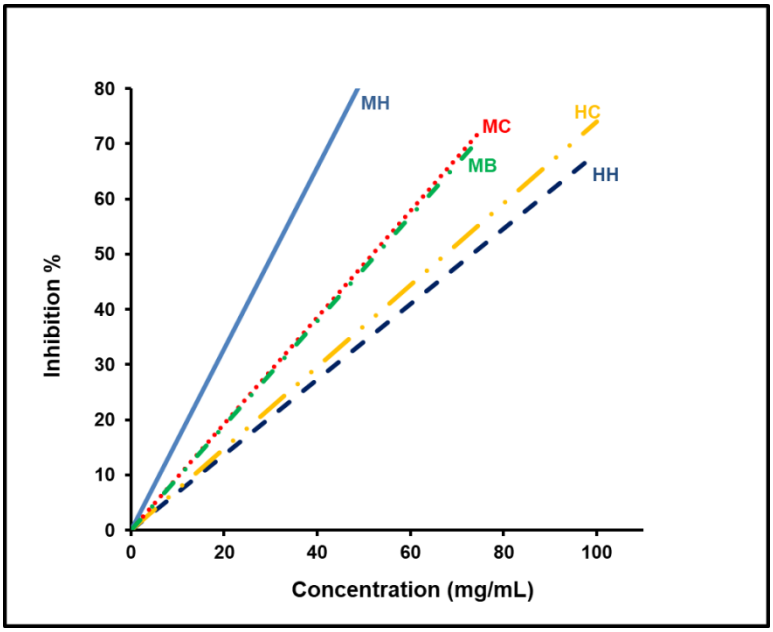

Figure 3. Relation between inhibition determined by ABTS method for five extracts of *A. rupicola*

3.5. Antimicrobial tests for plant extracts

The antimicrobial effects of the five extracts from *A. rupicola* were determined using both disc diffusion and micro-dilution assay methods. According to the disc diffusion assay, these extracts affected gram-negative bacterial strains more the gram-positive bacterial strains. The results of both antibacterial methods are given in Figure 4. Four of the five extracts except MC inhibited *E. coli* while only HH extract inhibited *B. subtilis*. The zone diameters calculated for *E. coli* using HH, HC, MH, and MB were 10.0, 10.0, 13.0, and 10.0 mm, respectively, while the value for *B. subtilis* using HH was about 6 mm. The results of the micro-dilution assay were better than the disc diffusion assay, according to the data obtained. These results are summarized in Table 4. For these microorganisms, only *S. aureus* was inhibited by all extracts. Alan investigated the antimicrobial effects of ethanol and pure water extracts obtained from *A. elongatum*. *E. coli* was inhibited only by the ethanol extract, while both extracts inhibited *S. aureus*, and, *B. subtilus* [25]. The values obtained for both extracts are similar to this paper as shown by the diameters. Both extract and the assay variety are discussed more extensively in this study. Moreover, in some studies about the different species of *Arum*, the antimicrobial activity of a variety of extracts from *A. maculatum* [5] and *A. hygrophilum* [41] were examined using both assays and disc diffusion, respectively.

Table 4. Antimicrobial activity for five extracts from *A. rupicola*

Extracts	Disc Diffusion Assay (mm)			Micro-Dilution Assay (SR %)		
	E. coli	***S. aureus***	***B. subtilis***	***E. coli***	***S. aureus***	***B. subtilis***
HH	**10.0**	**0.0**	**6.0**	**83.25**	**66.88**	**100.0**
HC	**10.0**	**0.0**	**0.0**	**100.0**	**100.0**	**100.0**
MH	**13.0**	**0.0**	**0.0**	**100.0**	**43.41**	**68.50**
MC	**0.0**	**0.0**	**0.0**	**99.69**	**68.41**	**81.76**
MB	**10.0**	**0.0**	**0.0**	**71.37**	**90.04**	**86.32**

SR % **:** survival rate percentage of microorganism

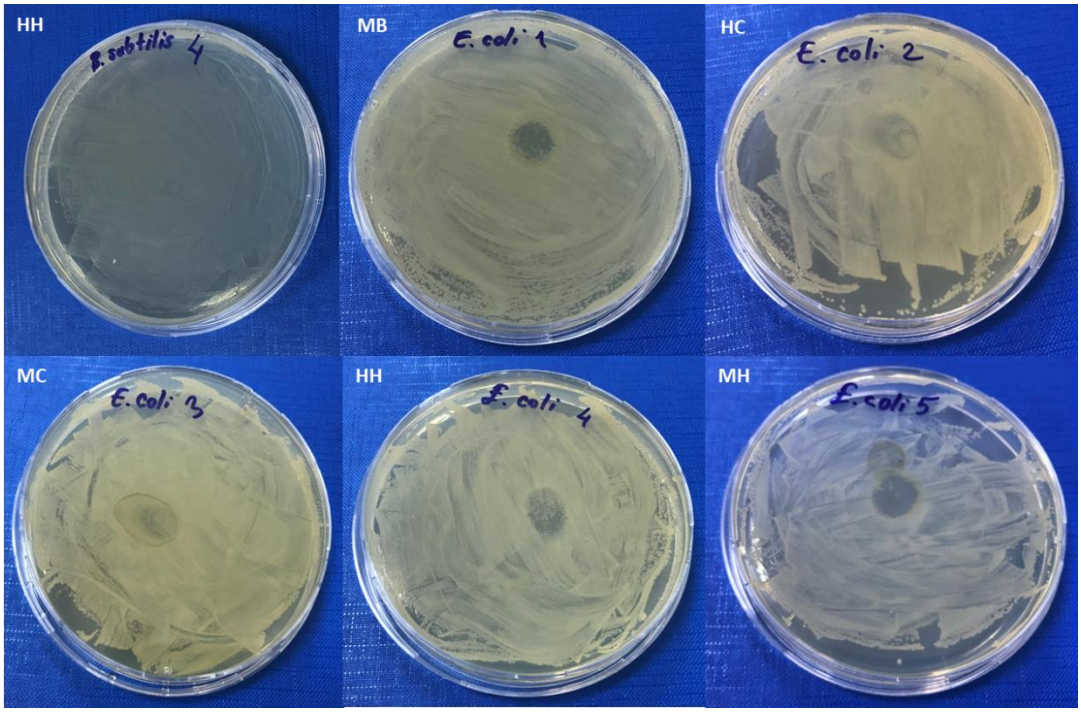

Figure 4. Antimicrobial activity of the five extracts from *A. rupicola*

4. Conclusion

A. rupicola is a plant that is not consumed because of its toxicity when fresh. However, it can be consumed after it is dried or boiled. There are many publications about this herb and similar species. With this study, five extracts of *A. rupicola* were obtained using the Scheme 1 protocol and a variety of solvents that were polar and apolar. From these extracts, methanol and hexane were the main extracts, while the others were sub-extracts. Different extracts, including different polarity compounds, were obtained. These compounds in the five extracts were analyzed by GC-MS, HPLC-TOF/MS, and UV spectrophotometry, and their antioxidant and antibacterial activities were determined. The contribution of this study is that it provides more comprehensive information about *A. rupicola*.

Statement of Research and Publication Ethics

The study is complied with research and publication ethics.

Acknowledgments

The current study was supported by the Van Yuzuncu Yil University Scientific Research Projects Unit under Grant (FHD-2020-8956).

Abbreviations: ABTS, 2,2-azinobis (3-ethylbenzothiazoline 6-sulfonate); GC-MS, Gas chromatography-mass spectrometry; DMSO, dimethyl sulfoxide; HPLC-TOF/MS, High-performance liquid chromatography-time-of-flight mass spectrometry; HPLC, High-performance liquid chromatography; BHA, Butylatedhydroxyanisole; BHT, Butylhydroxytoluene.

References

[1] B. Schaal, "Plants and people: Our shared history and future," *Plants People Planet*, vol. 1, pp. 14–19, 2019. https://doi.org/10.1002/ppp3.12

[2] P. C. Boyce, "*Arum* - A Decade of Change," *Aroideana*, vol. 29, pp. 132-137, 2006.

[3] R. Govaerts and D. G. Frodin, *World checklist and bibliography of Araceae (and Acoraceae). Kew: The Board of Trustees of the Royal Botanic Gardens* 2002.

[4] W. Lobin, M. Neumann, J. Bogner and P. C. Boyce, "A new *Arum* species (Areae, Araceae) from NE Turkey and Georgia," *Willdenowia*, vol. 37 pp. 445, 2007. https://doi.org/10.3372/wi.37.37206

[5] R. Farahmandfar, R. Esmaeilzadeh Kenari, M. Asnaashari, D. Shahrampour and T. Bakhshandeh, "Bioactive compounds, antioxidant and antimicrobial activities of *Arum maculatum* leaves extracts as

affected by various solvents and extraction methods," *Food Sci Nutr* vol. 7 pp. 465–475, 2019. https://doi.org/10.1002/fsn3.815

[6] K. Alpınar, A. Güner, S. Aslan, T. Ekim, M. Vural and M. T. Babaç, *Türkiye Bitkileri Listesi (Damarlı Bitkiler)*, İstanbul, 2012.

[7] H. Yıldırım and Y. Altıoğlu, "Türkiye için yeni bir takson kaydı: *Arum sintenisii* (Engl.) P.C.Boyce (Araceae)," *Bağbahçe Bilim Dergisi*, vol. 3, pp. 47–54, 2016.

[8] T. Baytop, *Türkçe bitki adlari sözlüğü (14th ed.)*, Ankara, 2015.

[9] G. Ágoston and B. A. Masters, *Encyclopedia of the Ottoman Empire*, New York, NY., 2009.

[10] B. Kimmerling and J. S. Migdal, *The palestinian people: A history*, Harvard University Press, 2003.

[11] R. Al-Ramahi, N. Jaradat, A. N. Zaid, F. F. Vincieri and M. Asmaa, "Medicinal herbs and methodologies for their pharmaceutical compounding in the west bank/Palestine," *Complement Ther Clin Pract*, vol. 20, no. 4, pp. 280-284, 2014. https://doi.org/10.1016/j.ctcp.2014.06.001

[12] E. Tuzlacı, P. Eryaşar-Aymaz, "Turkish folk medicinal plants, part IV: Gonen (Balıkesir)," *Fitoterapia* vol. 72, no. 4, pp. 323–343, 2001. https://doi.org/10.1016/S0367-326X(00) 00277-X

[13] D. Satyajit, Z. Sarker, A. Latif and I. Gray, *Natural product isolation. Second edition*, Humana Press, 2006. https://doi.org/10.1021/np078142v

[14] S. R. Kanatt, R. Chander and A. Sharma, "Chitosan and mint mixture: A new preservative for meat and meat products," *Food Chem*, vol. 107, pp. 845–852, 2008. https://doi.org/10.1016/j.foodchem.2007.08.088

[15] G. Işcan, N. Kirimer, M. Kürkcüoğlu, K. H. C. Başer and F. Demirci,. "Antimicrobial screening of *Mentha piperita* essential oils," *J Agric Food Chem* vol. 50, pp. 3943–3946, 2002. https://doi.org/10.1021/jf011476k

[16] M. D. Soković, J. Vukojević, P. D. Marin, D. D. Brkić, V. Vajs, L. J. L. D. van Griensven, "Chemical composition of essential oils of *Thymus* and *Mentha* species and their antifungal activities," *Molecules* vol. 14, pp. 238–249. https://doi.org/10.3390/molecules14010238

[17] S. A. Yang, S. K. Jeon, E. J. Lee, C. H. Shim and I. S. Lee, Comparative study of the chemical composition and antioxidant activity of six essential oils and their components," *Nat Prod Res*, vol. 24, pp. 140–151. https://doi.org/10.1080/14786410802496598

[18] M. Bajpai, A. Pande, S. K. Tewari, D. Prakash, "Phenolic contents and antioxidant activity of some food and medicinal plants," *Int J Food Sci Nutr*, vol. 56, pp. 287–291, 2005. https://doi.org/10.1080/09637480500146606

[19] C. N. Cutter, "Antimicrobial effect of herb extracts against *Escherichia coli* O157:H7, *Listeria monocytogenes*, and *Salmonella typhimurium* associated with beef," *J Food Prot* vol. 63pp. 601–607, 2000. https://doi.org/10.4315/0362-028x-63.5.601

[20] A. Amal, A. Ashraf and E. S. Hossam, "Chemical compositions and antioxidant/antimicrobial activities of kaffmaryam (*Anastatica hierochuntica*) and doum palm (*Hyphaene thebaica*) cultivated in Egypt," *Biyoloji Bilimleri Arastirma Dergisi*, vol. 2, no. 2, pp. 71–79, 2009. https://doi.org/10.3989/gya.064509

[21] A. P. Desbois and V. J. Smith, "Antibacterial free fatty acids: activities, mechanisms of action and biotechnological potential," *Appl Microbiol Biotechnol*, vol. 85, pp. 1629–1642, 2010. https://doi.org/10.1007/s00253-009-2355-3

[22] C. L. Fischer, D. R. Drake, D. V. Dawson, D. R. Blanchette, K. A. Brogden and P. W. Wertz, "Antibacterial activity of sphingoid bases and fatty acids against Gram-positive and Gram-negative bacteria," *Antimicrob Agents Chemother*, vol. 56 pp. 1157–1161, 2012. https://doi.org/10.1128/AAC.05151-11

[23] E. Karimi, H. Z. Jaafar, A. Ghasemzadeh and M. Ebrahimi, Fatty acid composition, antioxidant and antibacterial properties of the microwave aqueous extract of three varieties of *Labisia pumila* Benth.," *Biol Res*, vol. 48, no. 1, pp. 9, 2015. https://doi.org/10.1186/0717-6287-48-9

[24] N. Özok, and I. Güneş, "Streptozotosin kaynaklı diyabetik sıçanlarda Arum rupicola'nın in vivo antioksidan potansiyeli," *Bitlis Eren Üniversitesi Fen Bilimleri Dergisi*, vol. 8, no. 3, pp. 866-874, 2019.

[25] Y. Alan, "*Arum elongatum* Steven Ekstraktlarının Fenolik Madde Miktarı ve Biyolojik Aktivitelerinin İncelenmesi," *Bitlis Eren Üniversitesi Fen Bilimleri Dergisi*, vol. 7, no. 2, pp. 370-379, 2018.

[26] M. R. Kıvanç and V. Türkoglu, "Investigation of the effects of natural compounds isolated from *Arum rupicola* var. *rupicola* on glutathione reductase enzyme purified from bovine liver," *Biomed Chromatogr*, vol. 33, pp. e4560, 2019. https://doi.org/10.1002/bmc.4560

[27] A. Tüfekçi, H. Akşit, F. Gül and İ. Demirtaş, "Determination of Phenolic Profile of *Cirsium arvense* (L.) Scop. Subsp. *vestitum* (Wimmer et Grab.) Petrak Plant," *Eurasian J Bio Chem Sci*, vol. 1, no. 2, pp. 33-36, 2018.

[28] R. Re, N. Pellegrini, A. Proteggente, A. Pannala, M. Yang and C. Rice-Evans, "Antioxidant activity applying an improved ABTS radical cation decolorization assay," *Free Rad Bio Med*, vol. 26, pp. 1231–7, 1999. https://doi.org/10.1016/s0891-5849(98)00315-3

[29] K. Kalia, K. Sharma, H. P. Singh and B. Singh, "Effects of extraction methods on phenolic contents and antioxidant activity in aerial parts of *Potentilla atrosanguinea* Lodd. and quantification of its phenolic constituents by RP-HPLC," *J Agric Food Chem*, vol. 56, pp. 10129–10134, 2008. https://doi.org/10.1021/jf802188b

[30] F. Cömert Önder, N. Doğrular, E. Güzdüzalp, S. Barlak and M. Ay, "A Comparative Study of Three Brassicaceae Vegetables Grown in Canakkale: Determination of Total Phenolic Content and Antioxidant Activity of Pulp and Juice Samples of Radish (*Raphanus sativus* L.), Cabbage (*Brassica oleracea* L. var capitata L) and Cauliflower (*Brassica oleracea* L.)," *Çanakkale Onsekiz Mart Üniversitesi Fen Bilimleri Enstitüsü Dergisi*, vol. 6, pp. 30-38, 2020. https://doi.org/10.28979/comufbed.633456

[31] Y. S. Velioglu, G. Mazza, L. Gao and B. D. Oomah, "Antioxidant Activity and Total Phenolics in Selected Fruits, Vegetables, and Grain Products," *J Agric Food Chem*, vol. 46, pp. 4113–4117, 1998. https://doi.org/10.1021/jf9801973

[32] F. Cömert Önder, M. Ay and S. D. Sarker, "Comparative study of antioxidant properties and total phenolic content of the extracts of *Humulus lupulus* L. and quantification of bioactive components by LC−MS/MS and GC−MS," *J Agric Food Chem*, vol. 61, pp. 10498−10506, 2013. https://doi.org/10.1021/jf4031508

[33] O. Ozay, P. Ilgin, H. Ozay, Z. Gungor, B. Yılmaz and M. R. Kıvanç, "The preparation of various shapes and porosities of hydroxyethyl starch/p(HEMA-co-NVP) IPN hydrogels as programmable carrier for drug delivery," *J Macromol Sci A*, vol. 57, pp. 379–387, 2020. https://doi.org/10.1080/10601325.2019.1700803

[34] W. W. Christie, "13-Phenyltridec-9-enoic and 15-phenylpentadec-9-enoic acids in *Arum maculatum* seed oil," *Eur J Lipid Sci Technol*, vol. 105, pp. 779–780, 2013. https://doi.org/10.1002/ejlt.200300865

[35] M. M. Farid, S. R. Hussein, L. F. İbrahim, M. A. El Desouky, A. M. Elsayed, A. A. El Oqlah and M. M. Saker, "Cytotoxic activity and phytochemical analysis of *Arum palaestinum* Boiss," *Asian Paci J Trop Biomed*, vol. 5, pp. 944–947, 2015. https://doi.org/10.1016/j.apjtb.2015.07.019

[36] E. Yabalak, "Antioxidant Activity and Chemical Composition of Methanolic Extract from *Arum Dioscoridis* SM. var. *Dioscoridis* and Determination of Mineral and Trace Elements," *Journal of the Turkish Chemical Society, Section A: Chemistry*, pp. 205–218, 2017. https://doi.org/10.18596/jotcsa.350370

[37] A. Zargoun, A. Mohammed, K. Abdelshafeek, A. Ibansharrada and A. Alomari, "GC/MS Analysis of Lipid Constituents and Antimicrobial Activity of *Arum cyrinaicum* Extracts," *Egypt J Chem*, vol. 63, no. 12, pp. 4889-4910, 2020. https://doi.org/10.21608/ejchem.2020.30199.2647

[38] H. Uguzlar, E. Maltas and S. Yildiz, "Antioxidant Activity and Fatty Acid Compositions of *Arum dioscoridis* Extracts," *Biosci Biotechnol Res Asia*, vol. 8, pp. 75–82, 2011. https://doi.org/10.13005/bbra/825

[39] F. Karahan, M. Kulak, E. Urlu, H. G. Gözüacik, T. Böyümez, N. Şekeroğlu and I. H. Doğantürk, "Total phenolic content, ferric reducing and DPPH scavenging activity of *Arum dioscoridis*," *Nat Prod Res*, vol. 29, pp. 1678–1683, 2015. https://doi.org/10.1080/14786419.2014.991320

[40] N. Jaradat and M. Abualhasan, "Comparison of Phytoconstituents, Total Phenol Contents and Free Radical Scavenging Capacities between Four *Arum* Species from Jerusalem and Bethlehem," *Pharm Sci*, vol. 22, pp. 120–125, 2016. https://doi.org/10.15171/PS.2016.19

[41] H. M. Jaber, K. D. Al-Hamaideh, H. I. Al-Daghistani, N. H. Amer, M. N. Nassar, S. M. Abd Al-Latif and A. H. Al-Nuaimi, "Antibacterial Activity and Chemical Composition of *Arum hygrophilum* Boiss Crude Extracts," *JJBS*, vol. 13, no. 2, pp. 159–164, 2020. https://doi.org/10.13140/RG.2.2.30662.42562

Bitlis Eren Üniversitesi Fen Bilimleri Dergisi
BİTLİS EREN UNIVERSITY JOURNAL OF SCIENCE
ISSN: 2147-3129/e-ISSN: 2147-3188
VOLUME: 11 NO: 2 PAGE: 586-593 YEAR: 2022
DOI: 10.17798/bitlisfen.1063550

Algebraic Construction for Dual Quaternions with $\mathcal{GCN}$

Gülsüm Yeliz ŞENTÜRK[1*], Nurten GÜRSES[2], Salim YÜCE[2]

[1]*Department of Computer Engineering, Faculty of Engineering and Architecture, Istanbul Gelisim University, 34310, Istanbul, Turkey*
[2]*Department of Mathematics, Faculty of Arts and Sciences, Yildiz Technical University, 34220, Istanbul, Turkey*
(ORCID: 0000-0002-8647-1801) (ORCID: 0000-0001-8407-854X) (ORCID: 0000-0002-8296-6495)

Keywords:
Generalized complex number, Dual quaternion, Matrix form.

Abstract
In this paper, we explain how dual quaternion theory can be extended to dual quaternions with generalized complex number $(\mathcal{GCN})$ components. More specifically, we algebraically examine this new type dual quaternion and give several matrix representations both as a dual quaternion and as a $\mathcal{GCN}$.

1. Introduction

A real quaternion, as an extension of complex number in four dimensions, is defined as

$$q = a_0 + a_1 e_1 + a_2 e_2 + a_3 e_3,$$

where a_0, a_1, a_2, a_3 are real components and e_1, e_2, e_3 are non-real quaternionic units with the following multiplication schema [1-3]:

$$\begin{aligned} e_1^2 = e_2^2 = e_3^2 = -1,\\ e_1 e_2 = -e_2 e_1 = e_3,\\ e_2 e_3 = -e_3 e_2 = e_1,\\ e_3 e_1 = -e_1 e_3 = e_2. \end{aligned}$$

The set of real quaternions, which is isomorphic to Euclidean 4-space, forms a non-commutative and an associative algebra under addition and multiplication. The real quaternions have many applications such as describing rotations in robotics and computer animation with rotation axis and angle.

A dual quaternion, as an extension of dual number in four dimensions, is defined by the same form with different multiplication conditions for quaternionic units as [4-10]:

$$\begin{aligned} \mathbf{i}^2 = \mathbf{j}^2 = \mathbf{k}^2 = 0,\\ \mathbf{ij} = \mathbf{ji} = \mathbf{jk} = \mathbf{kj} = \mathbf{ki} = \mathbf{ik} = 0. \end{aligned} \quad (1)$$

The set of dual quaternions $\mathcal{Q}_{\mathcal{D}}$, which is isomorphic to Galilean 4-space, forms a commutative division algebra under addition and multiplication [7]. Furthermore, using the dual quaternions, one can express the Galilean transformation in one quaternionic equation.

From a different viewpoint, the set of generalized complex numbers ($\mathcal{GCN}$), the general bidimensional hypercomplex system, is denoted by $\mathbb{C}_{q,p}$ and defined by the ring [11-16]:

$$\frac{\mathbb{R}[X]}{\langle X^2 - qX - p \rangle} \cong \left\{ \begin{array}{c} z = x_1 + x_2 I : I^2 = Iq + p, I \notin \mathbb{R}, \\ p, q, x_1, x_2 \in \mathbb{R} \end{array} \right\},$$

where I is the generalized complex unit. It is isomorphic (as ring) to the following types considering the sign of $\Delta = q^2 + 4p$: for $\Delta > 0$ *hyperbolic system*, for $\Delta < 0$ *elliptic system* and for

*Corresponding author: gysenturk@gelisim.edu.tr
Received: 26.01.2022, Accepted: 26.06.2022

$\Delta = 0$ *parabolic system*. The canonical forms of these systems are given by, respectively,

- hyperbolic (perplex, split complex, double) numbers $\mathbb{C}_{0,1}$ [17-20],
- complex (ordinary) numbers $\mathbb{C}_{0,-1}$ [20, 21],
- dual numbers $\mathbb{C}_{0,0}$ [20, 22, 23].

Specially, dual numbers have been widely used for the search of closed form solutions in the fields of displacement analysis, kinematic synthesis, and dynamic analysis of spatial mechanisms.

In $\mathbb{C}_{\mathfrak{q},\mathfrak{p}}$, the value

$$\mathcal{D}_z = z\bar{z} = (x_1 + x_2 I)(x_1 - x_2 I) = x_1^2 - \mathfrak{p}x_2^2 + \mathfrak{q}x_1x_2$$

is referred to as the characteristic determinant of z. Considering this characteristic value, z is called timelike for $\mathcal{D}_z < 0$, spacelike for $\mathcal{D}_z > 0$ and null for $\mathcal{D}_z = 0$ [12].

Number systems play a special role in defining different types of quaternions. Combining fundamental properties of numbers and quaternions enables to determine new features. Considering the numbers mentioned above, the quaternions with different number components have been studied by several authors in many points of view [24-30]. One can see the combination of the dual numbers and the real quaternions in the studies [27, 28, 30]. Moreover, as an application, the representational method based on quaternions with dual number coefficients related to electromagnetism can be seen in [31, 32].

In this paper, we are interested in the combination of dual quaternions and $\mathcal{GCN}$. In Section 2, we extend definitions and some universal known results of dual quaternions to dual quaternions with $\mathcal{GCN}$ components. Finally, we provide a complete classification in conclusion.

2. Dual Quaternions with $\mathcal{GCN}$ Components

This original section discusses an algebraic behavior of dual quaternions with $\mathcal{GCN}$ components. Also it proceeds with the examination of several matrix representations.

Definition 1. The dual quaternion with $\mathcal{GCN}$ components is of the form:

$$\tilde{q} = a_0 + a_1\mathbf{i} + a_2\mathbf{j} + a_3\mathbf{k},$$

where the dual quaternion units satisfy equations in (1). The set of these quaternions is denoted by $\tilde{\mathcal{Q}}_{\mathcal{D}}$.

Here, I commutes with the three dual quaternion units. One can see that, the usual dual operator distinct from the dual quaternion units for $\mathfrak{q} = 0, \mathfrak{p} = 0$.

Throughout the paper, $\tilde{q} = a_0 + a_1\mathbf{i} + a_2\mathbf{j} + a_3\mathbf{k}$, $\tilde{p} = b_0 + b_1\mathbf{i} + b_2\mathbf{j} + b_3\mathbf{k}$ and $\tilde{r} = c_0 + c_1\mathbf{i} + c_2\mathbf{j} + c_3\mathbf{k} \in \tilde{\mathcal{Q}}_{\mathcal{D}}$ are taken.

We firstly define the basic algebraic operations on dual quaternions with $\mathcal{GCN}$ components. For any $\tilde{q} \in \tilde{\mathcal{Q}}_{\mathcal{D}}$, $S_{\tilde{q}} = a_0$ is the scalar part and $V_{\tilde{q}} = a_1\mathbf{i} + a_2\mathbf{j} + a_3\mathbf{k}$ is the vector part. Equality is as follows: $\tilde{p} = \tilde{q} \Leftrightarrow S_{\tilde{p}} = S_{\tilde{q}},\ V_{\tilde{p}} = V_{\tilde{q}}$. The addition of $\tilde{q}$ and $\tilde{p}$ is defined as:

$$\begin{aligned}\tilde{q} + \tilde{p} &= (a_0 + b_0) + (a_1 + b_1)\mathbf{i} \\ &\quad + (a_2 + b_2)\mathbf{j} + (a_3 + b_3)\mathbf{k} \\ &= S_{\tilde{p}} + S_{\tilde{q}} + V_{\tilde{p}} + V_{\tilde{q}} \\ &= S_{\tilde{p}+\tilde{q}} + V_{\tilde{p}+\tilde{q}}.\end{aligned}$$

The quaternion $\bar{\tilde{q}} = a_0 - a_1\mathbf{i} - a_2\mathbf{j} - a_3\mathbf{k} = S_{\tilde{q}} - V_{\tilde{q}}$ is called the conjugate of $\tilde{q}$. Furthermore, for $c \in \mathbb{C}_{\mathfrak{q},\mathfrak{p}}$, the scalar multiplication of c and $\tilde{q}$ is defined as:

$$\begin{aligned}c\tilde{q} &= ca_0 + ca_1\mathbf{i} + ca_2\mathbf{j} + ca_3\mathbf{k} \\ &= cS_{\tilde{q}} + cV_{\tilde{q}}.\end{aligned}$$

The multiplication of $\tilde{q}$ and $\tilde{p}$ is defined as:

$$\begin{aligned}\tilde{q}\tilde{p} &= a_0b_0 + (a_0b_1 + a_1b_0)\mathbf{i} \\ &\quad + (a_0b_2 + a_2b_0)\mathbf{j} + (a_0b_3 + a_3b_0)\mathbf{k} \\ &= S_{\tilde{q}}S_{\tilde{p}} + S_{\tilde{q}}V_{\tilde{p}} + S_{\tilde{p}}V_{\tilde{q}} \\ &= \tilde{p}\tilde{q}.\end{aligned} \tag{2}$$

Additionally, $N_{\tilde{q}} = \tilde{q}\bar{\tilde{q}} = \bar{\tilde{q}}\tilde{q} = a_0^2$ is called the norm of $\tilde{q}$. Hence, the quaternion $(\tilde{q})^{-1} = \dfrac{\bar{\tilde{q}}}{N_{\tilde{q}}}$ is called the inverse of $\tilde{q}$ for non-null $N_{\tilde{q}}$ that is $\mathcal{D}_{N_{\tilde{q}}} \neq 0$. As it is seen many properties of dual quaternions with $\mathcal{GCN}$ components are familiar with the usual dual quaternions.

Standard elementary conjugate properties establish the following proposition.

Proposition 1. For any $\tilde{q}, \tilde{p} \in \tilde{\mathcal{Q}}_{\mathcal{D}}$ and $c_1, c_2 \in \mathbb{R}$, the followings hold:

i) $\overline{\overline{\tilde{q}}} = \tilde{q}$,

ii) $\overline{c_1\tilde{p} + c_2\tilde{q}} = c_1\overline{\tilde{p}} + c_2\overline{\tilde{q}}$,

iii) $\overline{\tilde{q}\tilde{p}} = \overline{\tilde{p}}\,\overline{\tilde{q}} = \overline{\tilde{q}}\,\overline{\tilde{p}}$,

iv) $N_{c_1\tilde{q}} = c_1^2 N_{\tilde{q}}$,

v) $N_{\tilde{q}\tilde{p}} = N_{\tilde{q}} N_{\tilde{p}} = N_{\tilde{p}} N_{\tilde{q}}$.

Proof: Considering the conjugate, properties i) and ii) are quickly obvious.

iii) By using equation (2), we have:

$$\overline{\tilde{q}\tilde{p}} = a_0 b_0 - (a_0 b_1 + a_1 b_0)\mathbf{i} - (a_0 b_2 + a_2 b_0)\mathbf{j} - (a_0 b_3 + a_3 b_0)\mathbf{k}.$$

So, it is verified that $\overline{\tilde{q}\tilde{p}} = \overline{\tilde{p}}\,\overline{\tilde{q}} = \overline{\tilde{q}}\,\overline{\tilde{p}}$.

iv) By having property ii) and the norm, we have: $N_{c_1\tilde{q}} = (c_1\tilde{q})\overline{(c_1\tilde{q})} = c_1^2 N_{\tilde{q}}$.

v) From property iii), we get: $N_{\tilde{q}\tilde{p}} = (\tilde{q}\tilde{p})\overline{(\tilde{q}\tilde{p})} = \tilde{q}\tilde{p}\,\overline{\tilde{p}}\,\overline{\tilde{q}} = N_{\tilde{q}} N_{\tilde{p}} = N_{\tilde{p}} N_{\tilde{q}}$.

Proposition 2. $\tilde{\mathcal{Q}}_{\mathcal{D}}$ is a 4-dimensional module over $\mathbb{C}_{\mathfrak{q},\mathfrak{p}}$ and an 8-dimensional vector space over $\mathbb{R}$ with bases $\{1, \mathbf{i}, \mathbf{j}, \mathbf{k}\}$ and $\{1, I, \mathbf{i}, I\mathbf{i}, \mathbf{j}, I\mathbf{j}, \mathbf{k}, I\mathbf{k}\}$, respectively.

Definition 2. For any $\tilde{q}, \tilde{p} \in \tilde{\mathcal{Q}}_{\mathcal{D}}$, the scalar product is given by:

$$\tilde{\mathcal{Q}}_{\mathcal{D}} \times \tilde{\mathcal{Q}}_{\mathcal{D}} \to \mathbb{C}_{\mathfrak{q},\mathfrak{p}}$$
$$(\tilde{q}, \tilde{p}) \mapsto \langle \tilde{q}, \tilde{p} \rangle = S_{\tilde{q}} S_{\tilde{p}} = a_0 b_0 = S_{\tilde{p}\tilde{q}}$$

and the vector product is defined by:

$$\tilde{\mathcal{Q}}_{\mathcal{D}} \times \tilde{\mathcal{Q}}_{\mathcal{D}} \to \tilde{\mathcal{Q}}_{\mathcal{D}}$$
$$(\tilde{q}, \tilde{p}) \mapsto \tilde{q} \times \tilde{p} = S_{\tilde{q}} V_{\overline{\tilde{p}}} + S_{\overline{\tilde{p}}} V_{\tilde{q}} = V_{\tilde{q}\overline{\tilde{p}}}.$$

More specially, we examine some identities for the scalar product.

Proposition 3. For any $\tilde{q}, \tilde{p}$ and $\tilde{r} \in \tilde{\mathcal{Q}}_{\mathcal{D}}$, the followings hold:

i) $\langle \tilde{q}\tilde{r}, \tilde{p}\tilde{r} \rangle = \langle \tilde{r}\tilde{q}, \tilde{r}\tilde{p} \rangle = \langle \tilde{r}\tilde{q}, \tilde{p}\tilde{r} \rangle = \langle \tilde{q}\tilde{r}, \tilde{r}\tilde{p} \rangle$,
$= N_{\tilde{r}} \langle \tilde{q}, \tilde{p} \rangle$,

ii) $\langle \tilde{r}\tilde{q}, \tilde{p} \rangle = \langle \tilde{q}, \overline{\tilde{r}}\tilde{p} \rangle = \langle \tilde{q}, \tilde{r}\tilde{p} \rangle$.

Proof: Considering the scalar product and the norm, the following proofs can be conducted:

i) $\langle \tilde{q}\tilde{r}, \tilde{p}\tilde{r} \rangle = (a_0 c_0)(b_0 c_0) = (c_0^2)(a_0 b_0)$
$= N_{\tilde{r}} \langle \tilde{q}, \tilde{p} \rangle$,

ii) $\langle \tilde{q}\tilde{r}, \tilde{p} \rangle = (a_0 c_0) b_0 = a_0 (b_0 c_0) = \langle \tilde{q}, \tilde{p}\overline{\tilde{r}} \rangle$.

We are now ready to prove the results based on matrix approach.

Theorem 1. Every element $\tilde{q}$ of $\tilde{\mathcal{Q}}_{\mathcal{D}}$ can be represented by a quaternionic matrix:

$$\mathsf{E}_{\tilde{q}} = \begin{bmatrix} a_0 + a_3\mathbf{k} & a_1\mathbf{i} + a_2\mathbf{j} \\ a_1\mathbf{i} + a_2\mathbf{j} & a_0 + a_3\mathbf{k} \end{bmatrix}. \qquad (3)$$

Hence $\tilde{\mathcal{Q}}_{\mathcal{D}} \subseteq \mathbb{M}_2(\tilde{\mathcal{Q}}_{\mathcal{D}})$.

Proof: For $\tilde{q} \in \tilde{\mathcal{Q}}_{\mathcal{D}}$, $\mathcal{L} : \tilde{\mathcal{Q}}_{\mathcal{D}} \to \mathcal{E}$, $\tilde{q} \mapsto \mathsf{E}_{\tilde{q}}$ is a linear map, where

$$\mathcal{E} := \left\{ \mathsf{E}_{\tilde{q}} \in \mathbb{M}_2(\tilde{\mathcal{Q}}_{\mathcal{D}}) : \mathsf{E}_{\tilde{q}} = \begin{bmatrix} a_0 + a_3\mathbf{k} & a_1\mathbf{i} + a_2\mathbf{j} \\ a_1\mathbf{i} + a_2\mathbf{j} & a_0 + a_3\mathbf{k} \end{bmatrix} \right\}$$

is a subset of $\mathbb{M}_2(\tilde{\mathcal{Q}}_{\mathcal{D}})$. So, one can realize the correspondence between $\tilde{\mathcal{Q}}_{\mathcal{D}}$ and $\mathcal{E}$ by the map $\mathcal{L}$. So it is no surprised that 2×2 representation of $\tilde{q}$ is $\mathsf{E}_{\tilde{q}}$. The proof is completed.

Corollary 1. For all $\tilde{q} \in \tilde{\mathcal{Q}}_{\mathcal{D}}$, $\mathcal{L}(\tilde{q})$ can also be written as follows:

$$\mathcal{L}(\tilde{q}) = a_0 I_2 + a_1 \mathsf{I} + a_2 \mathsf{J} + a_3 \mathsf{K},$$

where $\mathcal{L}(\mathbf{i}) = \mathsf{I}$, $\mathcal{L}(\mathbf{j}) = \mathsf{J}$, $\mathcal{L}(\mathbf{k}) = \mathsf{K}$ satisfy equations in (1).

Theorem 2. For $\tilde{q}, \tilde{p} \in \tilde{\mathcal{Q}}_{\mathcal{D}}$ and $\lambda \in \mathbb{R}$, then the followings hold:

i) $\tilde{q} = \tilde{p} \Leftrightarrow \mathsf{E}_{\tilde{q}} = \mathsf{E}_{\tilde{p}}$,

ii) $\mathsf{E}_{\tilde{q}+\tilde{p}} = \mathsf{E}_{\tilde{q}} + \mathsf{E}_{\tilde{p}}$,

iii) $\mathsf{E}_{\lambda\tilde{q}} = \lambda\left(\mathsf{E}_{\tilde{q}}\right)$,

iv) $\mathsf{E}_{\tilde{q}\tilde{p}} = \mathsf{E}_{\tilde{q}}\mathsf{E}_{\tilde{p}}$.

Proof: iv) For $\tilde{q}, \tilde{p} \in \tilde{\mathcal{Q}}_{\mathcal{D}}$, using equations (2) and (3), we can write:

$$\mathsf{E}_{\tilde{q}\tilde{p}} = \begin{bmatrix} a_0b_0 + (a_0b_3 + a_3b_0)\mathbf{k} & (a_0b_1 + a_1b_0)\mathbf{i} + (a_0b_2 + a_2b_0)\mathbf{j} \\ (a_0b_1 + a_1b_0)\mathbf{i} + (a_0b_2 + a_2b_0)\mathbf{j} & a_0b_0 + (a_0b_3 + a_3b_0)\mathbf{k} \end{bmatrix}$$

Moreover, we obtain:

$$\mathsf{E}_{\tilde{q}}\mathsf{E}_{\tilde{p}} = \begin{bmatrix} a_0 + a_3\mathbf{k} & a_1\mathbf{i} + a_2\mathbf{j} \\ a_1\mathbf{i} + a_2\mathbf{j} & a_0 + a_3\mathbf{k} \end{bmatrix}\begin{bmatrix} b_0 + b_3\mathbf{k} & b_1\mathbf{i} + b_2\mathbf{j} \\ b_1\mathbf{i} + b_2\mathbf{j} & b_0 + b_3\mathbf{k} \end{bmatrix}$$
$$= \begin{bmatrix} a_0b_0 + (a_0b_3 + a_3b_0)\mathbf{k} & (a_0b_1 + a_1b_0)\mathbf{i} + (a_0b_2 + a_2b_0)\mathbf{j} \\ (a_0b_1 + a_1b_0)\mathbf{i} + (a_0b_2 + a_2b_0)\mathbf{j} & a_0b_0 + (a_0b_3 + a_3b_0)\mathbf{k} \end{bmatrix}.$$

It is clear that $\mathsf{E}_{\tilde{q}\tilde{p}} = \mathsf{E}_{\tilde{q}}\mathsf{E}_{\tilde{p}}$. The other properties can be proved similarly.

Theorem 3. Every element $\tilde{q}$ of $\tilde{\mathcal{Q}}_{\mathcal{D}}$ can be represented by the following matrix:

$$\mathcal{F}_{\tilde{q}} = \begin{bmatrix} a_0 & 0 & 0 & 0 \\ a_1 & a_0 & 0 & 0 \\ a_2 & 0 & a_0 & 0 \\ a_3 & 0 & 0 & a_0 \end{bmatrix}. \qquad (4)$$

So, $\tilde{\mathcal{Q}}_{\mathcal{D}}$ is subset of $\mathbb{M}_4(\mathbb{C}_{\mathfrak{q},\mathfrak{p}})$. Moreover, for $\tilde{q}, \tilde{p} \in \tilde{\mathcal{Q}}_{\mathcal{D}}$ and $\lambda \in \mathbb{R}$,

i) $\tilde{p} = \tilde{q} = \Leftrightarrow \mathcal{F}_{\tilde{p}} = \mathcal{F}_{\tilde{q}}$,

ii) $\mathcal{F}_{\tilde{p}+\tilde{q}} = \mathcal{F}_{\tilde{p}} + \mathcal{F}_{\tilde{q}}$,

iii) $\mathcal{F}_{\lambda\tilde{p}} = \lambda(\mathcal{F}_{\tilde{p}})$,

iv) $\mathcal{F}_{\tilde{p}\tilde{q}} = \mathcal{F}_{\tilde{p}}\mathcal{F}_{\tilde{q}} = \mathcal{F}_{\tilde{q}}\mathcal{F}_{\tilde{p}}$,

v) $\delta\mathcal{F}_{\tilde{p}}\delta = \mathcal{F}_{\bar{\tilde{p}}}$ where $\delta = \mathrm{diag}(1,-1,-1,-1)$,

and $\det(\mathcal{F}_{\tilde{p}}) = N_{\tilde{p}}^2$.

Proof: iv) For $\tilde{q}, \tilde{p} \in \tilde{\mathcal{Q}}_{\mathcal{D}}$, using equations (2) and (4), we obtain:

$$\mathcal{F}_{\tilde{q}\tilde{p}} = \begin{bmatrix} a_0b_0 & 0 & 0 & 0 \\ a_0b_1 + a_1b_0 & a_0b_0 & 0 & 0 \\ a_0b_2 + a_2b_0 & 0 & a_0b_0 & 0 \\ a_0b_3 + a_3b_0 & 0 & 0 & a_0b_0 \end{bmatrix}.$$

Also, we have:

$$\mathcal{F}_{\tilde{q}}\mathcal{F}_{\tilde{p}} = \begin{bmatrix} a_0 & 0 & 0 & 0 \\ a_1 & a_0 & 0 & 0 \\ a_2 & 0 & a_0 & 0 \\ a_3 & 0 & 0 & a_0 \end{bmatrix}\begin{bmatrix} b_0 & 0 & 0 & 0 \\ b_1 & b_0 & 0 & 0 \\ b_2 & 0 & b_0 & 0 \\ b_3 & 0 & 0 & b_0 \end{bmatrix}$$
$$= \begin{bmatrix} a_0b_0 & 0 & 0 & 0 \\ a_0b_1 + a_1b_0 & a_0b_0 & 0 & 0 \\ a_0b_2 + a_2b_0 & 0 & a_0b_0 & 0 \\ a_0b_3 + a_3b_0 & 0 & 0 & a_0b_0 \end{bmatrix}$$
$$= \mathcal{F}_{\tilde{p}}\mathcal{F}_{\tilde{q}}.$$

It is obvious that $\mathcal{F}_{\tilde{q}\tilde{p}} = \mathcal{F}_{\tilde{p}}\mathcal{F}_{\tilde{q}} = \mathcal{F}_{\tilde{q}}\mathcal{F}_{\tilde{p}}$.

v) Considering equation (4) and $\delta = \mathrm{diag}(1,-1,-1,-1)$, we get:

$$\delta\mathcal{F}_{\tilde{p}}\delta = \begin{bmatrix} 1 & 0 & 0 & 0 \\ 0 & -1 & 0 & 0 \\ 0 & 0 & -1 & 0 \\ 0 & 0 & 0 & -1 \end{bmatrix}\begin{bmatrix} b_0 & 0 & 0 & 0 \\ b_1 & b_0 & 0 & 0 \\ b_2 & 0 & b_0 & 0 \\ b_3 & 0 & 0 & b_0 \end{bmatrix}\begin{bmatrix} 1 & 0 & 0 & 0 \\ 0 & -1 & 0 & 0 \\ 0 & 0 & -1 & 0 \\ 0 & 0 & 0 & -1 \end{bmatrix},$$
$$= \begin{bmatrix} b_0 & 0 & 0 & 0 \\ -b_1 & b_0 & 0 & 0 \\ -b_2 & 0 & b_0 & 0 \\ -b_3 & 0 & 0 & b_0 \end{bmatrix}.$$

One can see that the final matrix is the matrix $\mathcal{F}_{\bar{\tilde{p}}}$, so we can write $\delta\mathcal{F}_{\tilde{p}}\delta = \mathcal{F}_{\bar{\tilde{p}}}$.

The proofs of the other properties are straightforward by considering 4×4 real matrix representation of the dual quaternions.

Definition 3. The column matrix form of $\tilde{p}$ with respect to $\{1, \mathbf{i}, \mathbf{j}, \mathbf{k}\}$ is $\tilde{p} = \begin{bmatrix} b_0 & b_1 & b_2 & b_3 \end{bmatrix}^T$.

Corollary 2. Using the above definition, the multiplication of $\tilde{q}$ and $\tilde{p}$ is also calculated as: $\tilde{q}\tilde{p} = \mathcal{F}_{\tilde{q}}\,\tilde{p} = \tilde{p}\tilde{q}$.

Corollary 3. For $\tilde{q} \in \tilde{\mathcal{Q}}_{\mathcal{D}}$,

$$\mathcal{F}_{\tilde{q}} = a_0 I_4 + a_1 \Im + a_2 \xi + a_3 \Re,$$

where

$$\Im = \begin{bmatrix} 0 & 0 & 0 & 0 \\ 1 & 0 & 0 & 0 \\ 0 & 0 & 0 & 0 \\ 0 & 0 & 0 & 0 \end{bmatrix}, \xi = \begin{bmatrix} 0 & 0 & 0 & 0 \\ 0 & 0 & 0 & 0 \\ 1 & 0 & 0 & 0 \\ 0 & 0 & 0 & 0 \end{bmatrix}, \Re = \begin{bmatrix} 0 & 0 & 0 & 0 \\ 0 & 0 & 0 & 0 \\ 0 & 0 & 0 & 0 \\ 1 & 0 & 0 & 0 \end{bmatrix}.$$

The following theorem indicates how to calculate the formula for matrix representation of the inverse of $\tilde{q} \in \tilde{\mathcal{Q}}_{\mathcal{D}}$.

Theorem 4. Let $\tilde{q} \in \tilde{\mathcal{Q}}_{\mathcal{D}}$ and $\tilde{q}^{-1}$ be the inverse of $\tilde{q}$. Then, $\mathcal{F}_{\tilde{q}^{-1}} = \dfrac{1}{\sqrt{\det(\mathcal{F}_{\tilde{q}})}} \mathcal{F}_{\bar{\tilde{q}}}$ for non-null $\det\left(\mathcal{F}_{\tilde{q}}\right)$ that is $\mathcal{D}_{\det\left(\mathcal{F}_{\tilde{q}}\right)} \neq 0$.

Theorem 5. According to $\{1, I, \mathbf{i}, I\mathbf{i}, \mathbf{j}, I\mathbf{j}, \mathbf{k}, I\mathbf{k}\}$, the real matrix representation of $\tilde{q} = a_0 + a_1\mathbf{i} + a_2\mathbf{j} + a_3\mathbf{k}$ is:

$$\mathcal{G}_{\tilde{q}} = \begin{bmatrix} x_{01} & \mathfrak{p}x_{02} & 0 & 0 & 0 & 0 & 0 & 0 \\ x_{02} & x_{01} + \mathfrak{q}x_{02} & 0 & 0 & 0 & 0 & 0 & 0 \\ x_{11} & \mathfrak{p}x_{12} & x_{01} & \mathfrak{p}x_{02} & 0 & 0 & 0 & 0 \\ x_{12} & x_{11} + \mathfrak{q}x_{12} & x_{02} & x_{01} + \mathfrak{q}x_{02} & 0 & 0 & 0 & 0 \\ x_{21} & \mathfrak{p}x_{22} & 0 & 0 & x_{01} & \mathfrak{p}x_{02} & 0 & 0 \\ x_{22} & x_{21} + \mathfrak{q}x_{22} & 0 & 0 & x_{02} & x_{01} + \mathfrak{q}x_{02} & 0 & 0 \\ x_{31} & \mathfrak{p}x_{32} & 0 & 0 & 0 & 0 & x_{01} & \mathfrak{p}x_{02} \\ x_{32} & x_{31} + \mathfrak{q}x_{32} & 0 & 0 & 0 & 0 & x_{02} & x_{01} + \mathfrak{q}x_{02} \end{bmatrix}, \quad (5)$$

where $a_i = x_{i1} + x_{i2} I \in \mathbb{C}_{\mathfrak{q},\mathfrak{p}}$, $0 \le i \le 3$. Moreover, for $\tilde{q}, \tilde{p} \in \tilde{\mathcal{Q}}_{\mathcal{D}}$ and $\lambda \in \mathbb{R}$,

i) $\tilde{p} = \tilde{q} \Leftrightarrow \mathcal{G}_{\tilde{p}} = \mathcal{G}_{\tilde{q}}$,

ii) $\mathcal{G}_{\tilde{p}+\tilde{q}} = \mathcal{G}_{\tilde{p}} + \mathcal{G}_{\tilde{q}}$,

iii) $\mathcal{G}_{\lambda\tilde{p}} = \lambda(\mathcal{G}_{\tilde{p}})$,

iv) $\mathcal{G}_{\tilde{q}\tilde{p}} = \mathcal{G}_{\tilde{q}}\mathcal{G}_{\tilde{p}}$.

Proof: Let us define the linear map $f_{\tilde{q}}$ from $\tilde{\mathcal{Q}}_{\mathcal{D}}$ to subset of $\mathbb{M}_8(\mathbb{R})$ such that $f_{\tilde{q}}\left(\tilde{p}\right) = \tilde{q}\tilde{p}$ for every $\tilde{p} \in \tilde{\mathcal{Q}}_{\mathcal{D}}$. By taking $a_i = x_{i1} + x_{i2} I \in \mathbb{C}_{\mathfrak{q},\mathfrak{p}}, 0 \le i \le 3$, we have the following equations:

$$\begin{aligned}
f_{\tilde{q}}(1) &= \tilde{q} = x_{01} + x_{02} I + x_{11}\mathbf{i} + x_{12} I\mathbf{i} + x_{21}\mathbf{j} \\
&\quad + x_{22} I\mathbf{j} + x_{31}\mathbf{k} + x_{32} I\mathbf{k}, \\
f_{\tilde{q}}(I) &= \tilde{q}I = \mathfrak{p}x_{02} + (x_{01} + \mathfrak{q}x_{02}) I + \mathfrak{p}x_{12}\mathbf{i} + \left(x_{11} + \mathfrak{q}x_{12}\right) I\mathbf{i} + \mathfrak{p}x_{22}\mathbf{j} \\
&\quad + \left(x_{21} + \mathfrak{q}x_{22}\right) I\mathbf{j} + \mathfrak{p}x_{32}\mathbf{k} + \left(x_{31} + \mathfrak{q}x_{32}\right) I\mathbf{k}, \\
f_{\tilde{q}}(\mathbf{i}) &= \tilde{q}\mathbf{i} = x_{01}\mathbf{i} + x_{02} I\mathbf{i}, \\
f_{\tilde{q}}(I\mathbf{i}) &= \tilde{q}I\mathbf{i} = \mathfrak{p}x_{02}\mathbf{i} + (x_{01} + \mathfrak{q}x_{02}) I\mathbf{i}, \\
f_{\tilde{q}}(\mathbf{j}) &= \tilde{q}\mathbf{j} = x_{01}\mathbf{j} + x_{02} I\mathbf{j}, \\
f_{\tilde{q}}(I\mathbf{j}) &= \tilde{q}I\mathbf{j} = \mathfrak{p}x_{02}\mathbf{j} + (x_{01} + \mathfrak{q}x_{02}) I\mathbf{j}, \\
f_{\tilde{q}}(\mathbf{k}) &= \tilde{q}\mathbf{k} = x_{01}\mathbf{k} + x_{02} I\mathbf{k}, \\
f_{\tilde{q}}(I\mathbf{k}) &= \tilde{q}I\mathbf{k} = \mathfrak{p}x_{02}\mathbf{k} + (x_{01} + \mathfrak{q}x_{02}) I\mathbf{k}.
\end{aligned}$$

Hence, by concerning the standard basis $\{1, I, \mathbf{i}, I\mathbf{i}, \mathbf{j}, I\mathbf{j}, \mathbf{k}, I\mathbf{k}\}$, we have 8×8 real matrix representation of $\tilde{q} \in \tilde{\mathcal{Q}}_{\mathcal{D}}$ is calculated as in equation (5). The proof of the properties can be conducted by considering the above linear map. Specially, for property iv), by taking

$$a_i = x_{i1} + x_{i2} I,\ b_i = y_{i1} + y_{i2} I \in \mathbb{C}_{\mathfrak{q},\mathfrak{p}},\ 0 \le i \le 3$$

for $\tilde{q}, \tilde{p} \in \tilde{\mathcal{Q}}_{\mathcal{D}}$ and using equations (2) and (5), the multiplication of $\mathcal{G}_{\tilde{q}}$ and $\mathcal{G}_{\tilde{p}}$ gives the matrix $\mathcal{G}_{\tilde{q}\tilde{p}}$ quickly.

With an alternative thought, $\tilde{q} = a_0 + a_1\mathbf{i} + a_2\mathbf{j} + a_3\mathbf{k}$, $a_i = x_{i1} + x_{i2} I \in \mathbb{C}_{\mathfrak{q},\mathfrak{p}}$, can be written as $\tilde{q} = q_0 + q_1 I$ in $\tilde{\mathcal{Q}}_{\mathcal{D}}$ where $q_{j-1} = x_{0j} + x_{1j}\mathbf{i} + x_{2j}\mathbf{j} + x_{3j}\mathbf{k} \in \mathcal{Q}_{\mathcal{D}}$ for $0 \le i \le 3$, $1 \le j \le 2$. So, $\tilde{\mathcal{Q}}_{\mathcal{D}}$ is a 2-dimensional module over $\mathcal{Q}_{\mathcal{D}}$ with base $\{1, I\}$. This consideration provides a reformulation of the previous results.

Theorem 6. Let $\tilde{q} = q_0 + q_1 I, \tilde{p} = p_0 + p_1 I \in \tilde{\mathcal{Q}}_{\mathcal{D}}$ and $\lambda \in \mathbb{R}$. Every element of $\tilde{\mathcal{Q}}_{\mathcal{D}}$ is written by a 2×2 dual quaternion matrix:

$$\mathcal{H}_{\tilde{q}} = \begin{bmatrix} q_0 & \mathfrak{p}q_1 \\ q_1 & q_0 + \mathfrak{q}q_1 \end{bmatrix}.$$

It means that $\tilde{\mathcal{Q}}_{\mathcal{D}}$ is subset of $\mathbb{M}_2(\mathcal{Q}_{\mathcal{D}})$. So, we have:

i) $\tilde{p} = \tilde{q} \Leftrightarrow \mathcal{H}_{\tilde{p}} = \mathcal{H}_{\tilde{q}}$,

ii) $\mathcal{H}_{\tilde{p}+\tilde{q}} = \mathcal{H}_{\tilde{p}} + \mathcal{H}_{\tilde{q}}$,

iii) $\mathcal{H}_{\lambda\tilde{p}} = \lambda(\mathcal{H}_{\tilde{p}})$,

iv) $\mathcal{H}_{\tilde{p}\tilde{q}} = \mathcal{H}_{\tilde{p}}\mathcal{H}_{\tilde{q}}$,

and $\det(\mathcal{H}_{\tilde{q}}) = q_0^2 + \mathfrak{q}q_0q_1 - \mathfrak{p}q_1^2$, where det corresponds the determinant of the quaternion matrix[2]. Moreover, $\mathcal{H}_{\tilde{q}} = q_0 I_2 + q_1 \mathsf{I}$, where $\mathsf{I} = \begin{bmatrix} 0 & \mathfrak{p} \\ 1 & \mathfrak{q} \end{bmatrix}$. (It is worth noting that there exists different ways to take I, for instance: $\mathsf{I} = \begin{bmatrix} \mathfrak{q} & 1 \\ \mathfrak{p} & 0 \end{bmatrix}$, see in [34]).

Definition 4. The column matrix form of $\tilde{p}$ with respect to $\{1, I\}$ is $\tilde{p} = \begin{bmatrix} p_0 & p_1 \end{bmatrix}^T$.

Corollary 4. By using above definition, we obtain $\tilde{q}\tilde{p} = \mathcal{H}_{\tilde{q}}\tilde{p} = \tilde{p}\tilde{q}$.

Definition 5. The matrix

$$\vec{\tilde{q}} = \begin{bmatrix} \vec{q}_0^T & \vec{q}_1^T \end{bmatrix}^T = \begin{bmatrix} \vec{q}_0 \\ \vec{q}_1 \end{bmatrix} \in \mathbb{M}_{8\times 1}(\mathbb{R})$$

is called as the vector form of $\tilde{q}$, where

$$q_{j-1} = x_{0i} + x_{1j}\mathbf{i} + x_{2j}\mathbf{j} + x_{3j}\mathbf{k} \in \mathcal{Q}_{\mathcal{D}}$$

and $\vec{q}_{j-1} = \left(x_{0j}, x_{1j}, x_{2j}, x_{3j}\right)^T = \begin{bmatrix} x_{0j} & x_{1j} & x_{2j} & x_{3j} \end{bmatrix}^T$ are vectors (matrices) for $1 \le j \le 2$.

4. Conclusion

Quaternions ([1-3]) have a deep mathematical meaning with a long history dating back and are used in physics to clarify the formulation of physical laws. A milestone moment in the use of quaternions in theoretical physic is the creation of special relativity, which unifies space and time to form a 4-dimensional space-time. By replacing real quaternions with complex ones offers a valuable tool in creating classical physical laws. Complex quaternions having several properties allow the desirable theorems of modern algebra to be applied. Furthermore, an important extension of real quaternions are the hyperbolic quaternions and the dual quaternions. Using the different types of quaternions are the way to description of the classical and quantum fields and reasonable to express space-time transformations. In terms of the hyperbolic quaternion, the general Lorentz space-time transformation can be discussed. With similar thought, the dual quaternions can be expressed for discussing the Galilean transformation. In terms of the dual quaternions this transformation with underlying algebraic features enables an efficient form [7-9].

With the leading of the above discussions, considering $\mathcal{GCN}$ as components of dual quaternions is the main motivation of this study. For this purpose, we construct dual quaternions with $\mathcal{GCN}$ coefficients for real $\mathfrak{p}, \mathfrak{q}$. Moreover, we examine the basic structures and algebraic properties by writing them in two forms: a $\mathcal{GCN}$ and a quaternion. Additionally, we established 2×2, 4×4 and 8×8 matrix representations.

With this approach, we can easily write the dual quaternions with elliptic, parabolic and hyperbolic number components considering $\Delta < 0$, $\Delta = 0$ and $\Delta > 0$, respectively, where $\Delta = \mathfrak{q}^2 + 4\mathfrak{p}$. Bearing in mind the special values $\mathfrak{p}$ and $\mathfrak{q}$, we have several types of dual quaternions with $\mathcal{GCN}$ components. For $\mathfrak{q} = 0$, $\mathfrak{p} = -1$ dual quaternions with complex number components, for $\mathfrak{q} = \mathfrak{p} = 0$ dual quaternions with dual number components and for $\mathfrak{q} = 0$, $\mathfrak{p} = 1$ dual quaternions with hyperbolic number components are obtained.

Contributions of the authors

Every author contributed equally to this work.

Conflict of Interest Statement

There is no conflict of interest between the authors.

Statement of Research and Publication Ethics

The author declares that this study complies with Research and Publication Ethics.

[2] $\det\left(\begin{bmatrix} a & b \\ c & d \end{bmatrix}\right) = da - cb$, [35].

References

[1] W. R. Hamilton, *Elements of quaternions*. New York: Chelsea Pub. Com.,1969.

[2] W. R. Hamilton, *Lectures on quaternions*. Dublin: Hodges and Smith, 1853.

[3] W. R. Hamilton, "On quaternions; or on a new system of imaginaries in algebra," *The London, Edinburgh and Dublin Philosophical Magazine and Journal of Science* (3rd Series), xxv-xxxvi, 1844–1850.

[4] W. K. Clifford, "Preliminary sketch of bi-quaternions," *Proceedings of the London Mathematical Society*, vol. s1–4, no. 1, pp. 381–395, 1873.

[5] J. D. Jr. Edmonds, *Relativistic reality: A modern view*. Singapore: World Scientific, 1997.

[6] Z. Ercan and S. Yüce, "On properties of the dual quaternions," *European Journal of Pure and Applied Mathematics*, vol. 4, no. 2, pp. 142–146, 2011.

[7] V. Majernik, "Quaternion formulation of the Galilean space-time transformation," *Acta Physica Slovaca*, vol. 56, pp. 9–14, 2006.

[8] V. Majernik and M. Nagy, "Quaternionic form of Maxwell's equations with sources," *Lettere al Nuovo Cimento*, vol. 16, pp. 165–169, 1976.

[9] V. Majernik, "Galilean transformation expressed by the dual four-component numbers," *Acta Physica Polonica*, vol. 87, no. 6, pp. 919–923, 1995.

[10] Y. Yaylı and E. E. Tutuncu, "Generalized Galilean transformations and dual quaternions," *Scientia Magna*, vol. 5, no. 1, pp. 94–100, 2009.

[11] I. Kantor and A. Solodovnikov, *Hypercomplex numbers*. New York: Springer-Verlag, 1989.

[12] F. Catoni, D. Boccaletti, R. Cannata, V. Catoni, E. Nichelatti and P. Zampetti, *The mathematics of Minkowski space-time and an introduction to commutative hypercomplex numbers*. Birkhäuser Basel, 2008.

[13] F. Catoni, R. Cannata, V. Catoni and P. Zampetti, "Two-dimensional hypercomplex numbers and related trigonometries and geometries," *Advances in Applied Clifford Algebras*, vol. 14, pp. 47–68, 2004.

[14] F. Catoni, R. Cannata, V. Catoni and P. Zampetti, "N-dimensional geometries generated by hypercomplex numbers," *Advances in Applied Clifford Algebras*, vol. 15, no. 1, 1–25, 2005.

[15] A. A. Harkin and J. B. Harkin, "Geometry of generalized complex numbers," *Mathematics Magazine*, vol. 77, no. 2, pp. 118–129, 2004.

[16] S. Veldsman, "Generalized complex numbers over near-fields," *Quaestiones Mathematicae*, vol. 42, no. 2, pp.181–200, 2019.

[17] W. K. Clifford, *Mathematical papers*, R. Tucker, Ed., New York: Chelsea Pub. Co., Bronx, 1968.

[18] P. Fjelstad, "Extending special relativity via the perplex numbers," *American Journal of Physics*, vol. 54, no. 5, pp. 416–422, 1986.

[19] G. Sobczyk, "The hyperbolic number plane," *The College Mathematics Journal*, vol. 26, no. 4, pp. 268–280, 1995.

[20] I. M. Yaglom, *A simple non-Euclidean geometry and its physical basis*. New York: Springer-Verlag, 1979.

[21] I. M. Yaglom, *Complex numbers in geometry*. New York: Academic Press, 1968.

[22] E. Pennestrì and R. Stefanelli, "Linear algebra and numerical algorithms using dual numbers," *Multibody System Dynamics*, vol. 18, no. 3, pp. 323–344, 2007.

[23] E. Study, *Geometrie der dynamen*. Leibzig: Mathematiker Deutschland Publisher, 1903.

[24] W.R. Hamilton, "On the geometrical interpretation of some results obtained by calculation with biquaternions", In *Proceedings of the Royal Irish Academy*, vol. 5, pp. 388–390, 1853.

[25] Y. Tian, "Biquaternions and their complex matrix representations," *Beiträge zur Algebra und Geometrie/Contributions to Algebra and Geometry*, vol. 54, no. 2, pp. 575–592, 2013.

[26] E. Karaca, F. Yılmaz and M. Çalışkan, "A unified approach: split quaternions with quaternion coefficients and quaternions with dual coefficients," *Mathematics*, vol. 8, no. 12, 2149, 2020.

[27] A. P. Kotelnikov, *Screw calculus and some applications to geometry and mechanics*. Kazan: Annal. Imp. Univ., 1895.

[28] A. McAulay, *Octonions: a development of Clifford's biquaternions*. University Press, 1898.

[29] M. Jafari, "On the properties of quasi-quaternion algebra," *Communications Faculty of Sciences University of Ankara Series A1 Mathematics and Statistics*, vol. 63, no. 1, pp. 1-10, 2014.

[30] L. Qi, C. Ling and H. Yan, "Dual quaternions and dual quaternion vectors," *Communications on Applied Mathematics and Computation*, pp. 1–15, 2022
[31] S. Demir and K. Özdas, "Dual quaternionic reformulation of electromagnetism," *Acta Physica Slovaca*, vol. 53, no. 6, pp. 429–436, 2003.
[32] S. Demir, "Matrix realization of dual quaternionic electromagnetism," *Central European Journal of Physics*, vol. 5, no. 4, pp. 487–506, 2007.
[33] F. Zhang, "Quaternions and matrices of quaternions," *Linear algebra and its Applications*, vol. 251, pp. 21–57, 1997.
[34] F. Messelmi, "Generalized numbers and their holomorphic functions," *International Journal of Open Problems in Complex Analysis*, vol. 7, no. 1, pp. 35–47, 2015.

Bitlis Eren Üniversitesi Fen Bilimleri Dergisi
BİTLİS EREN UNIVERSITY JOURNAL OF SCIENCE
ISSN: 2147-3129/e-ISSN: 2147-3188
VOLUME: 11 NO: 2 PAGE: 594-603 YEAR: 2022
DOI: 10.17798/bitlisfen.1065685

Breast Cancer Diagnosis with Machine Learning Techniques

Halime DOĞAN[1], Ahmet Burak TATAR[2], Alper Kadir TANYILDIZI[1], Beyda TAŞAR[1*]

[1]*Mechatronics Engineering Department, Fırat University, Elazığ, Türkiye*
[2]*Mechanical Engineering Department, Adıyaman University, Adıyaman, Türkiye*
(ORCID: 0000-0002-2825-7479) (ORCID: 0000-0001-5848-443X) (ORCID: 0000-0003-3324-5445) (ORCID: 0000-0002-4689-8579)

Keywords: Machine Learning, Breast Cancer, Wisconsin Data Set, Classification.

Abstract

Cancer deaths are one of the highest rates of death. Although breast cancer is commonly associated with women, it is sometimes seen in men, and the mortality rate for men with breast cancer may be higher. The importance of early detection and treatment of breast cancer cannot be overstated. Cancer is diagnosed at an early stage thanks to expert systems, artificial intelligence, and machine learning approaches, and data analysis makes life easier for healthcare professionals. The nearest neighbor method, principal component analysis (PCA), and neighborhood component method (NCA) approaches were employed to detect breast cancer in this study. "Breast Cancer Wisconsin Diagnostic" database was used to create and test the approach. According to the results obtained, the highest success rate with 99.42% was obtained by using neighborhood component analysis and the nearest neighbor classification algorithm method.

1. Introduction

Machine learning applications have been used in education, agriculture, health, etc. in recent years. It is widely used in studies in different fields such as Predictive analytical methods using machine learning algorithms to increase the efficiency of studies. Gummadi [1] conducted an analysis to improve students' success rates by using machine learning algorithms. Jagwani [2] stated that machine learning algorithms should be used in education to increase the communication performance between teacher and student and to provide real-time feedback advantage. However, different studies have been carried out using machine learning algorithms in many areas, from the estimation of the bacterial population in agricultural ponds [3] to the analysis and formatting of airline ticket prices in the aviation sector [4]. In addition, machine learning algorithms have been used in the early diagnosis of many diseases in the health sector. Studies have been conducted for the early detection of Alzheimer's disease using machine learning algorithms [5,6].

The International Agency for Research on Cancer (IARC) published its most recent report on worldwide cancer data on December 15, 2020 [7]. The IARC report was prepared in light of the information on 36 cancer types and the frequency and mortality rates of cancer types from 185 countries in the GLOBOCAN 2020 dataset. According to this report, 19.3 million new cases were seen in 2020 and 10.0 million people died due to cancer. Cancer affects one-fifth of the world's population at some point in their lives. Men had a mortality rate of 1/8 and women had a mortality rate of 1/11. The number of cancer patients who survive 5 years following diagnosis has been estimated to reach 50.6 million worldwide. Breast cancer diagnoses will account for around 1/8 of all cancer cases in 2020, or about 2.3 million. Breast cancer claimed the lives of 685,000 persons in 2020. Breast cancer ranks fifth among all cancer types in terms of fatality rate. [8].

*Corresponding author: btasar04@hotmail.com
Received: 31.01.2022, Accepted: 20.04.2022

The first way to reduce deaths due to breast cancer is through early diagnosis of the disease. Breast cancer diagnosis by specialists is a time-consuming procedure that demands numerous tests. (mammography and magnetic resonance imaging). The use of machine learning techniques in medicine has become common thanks to advancements in software and imaging technology. Thus, computerized analysis and diagnostic artificial intelligence applications are developed to support doctors. Early detection of cancer allows for more treatment options and a higher survival probability, particularly for breast cancer patients [9,10]. In addition, artificial intelligence, machine learning, and deep learning techniques have achieved successful results in the last 20 years, not only on cancer but also on many diseases (Stroke, Alzheimer's, etc.). This has made the use of artificial intelligence, machine learning, and deep learning algorithms in medical image processing even more important [11,12].

In recent years, many studies have focused on breast cancer diagnosis utilizing machine learning-based methodologies. Gupta P. (2020) [13] used the (WBCD) (357 benign, 212 malignant) dataset. They diagnosed it with 6 different methods: KNN, LR, DT, RF, SVM, Deep learning using Adam Gradient Descent Learning. They used these hyperparameters in their models: Number of trees in RF: 100, Max. depth in DT: 4, k neighbor value in KNN is, 6. The regularization parameter (C value) for SVM is 100, and the Coefficient Value(C)for LR is 1. Epoch value is 150 in DL. They reported the most successful method is deep learning using the gradient descent method with 98.24% accuracy rates. Chaurasia V. (2018) [14] used NB, RBF Neural Network, and J48 algorithms to classify breast cancer diagnosis. They tested their method on the WBCD dataset and they obtained this method's accuracy rates respectively, 97.36%, 96.77%, and 93.41%. They used 10-fold cross-validation for ML methods. Tafish M. [15] used the KNN, ANN, and SVM methods to solve this problem. And firstly they applied to data scaling and normalization then feature selection methods. He reported that the SVM method is the most successful than other methods with a 77.63% accuracy rate on the Breast Cancer Data in Gaza Strip (BCDG) dataset. Gopal V.N., [16] used PCA for the feature selection method and three different classification methods LR, RF, and MLP. In the study of Gopal et al. [16], the properties of the MLP classifier; It was determined as "learning rate: 0.001, max iteration: 200, tol: 0.0001, 10 cross-fold validation". These method accuracy rates were 79%, 95%, and 98% respectively. Sawssen et.al. [17] used the PCA dimension reduction method and Differential Evolution (DE) algorithm of Radial-Based Function Kernel Extreme Learning Machines (RBF-KELM) in the classification of breast cancer in their study. The results of the algorithm were tested on the WBCD and MIAS databases and compared. Algorithms accuracy rates were 98.18%, 72.7%, 94.54%, 90.9% for KELM, Poly-KELM, Wav-KELM, SVM respectively. Ismaili et.al. [18] using the MIAS data set, achieved 86.96% and 95.15% accuracy rates as a result of the SVM and ANN methods. Ateş et.al. [19] using the WBCD data set, achieved 96.5%, 92.4%, and 96.5% classification accuracy rates as a result of the NB, DT, and MLP methods. Selvi et.al. [20] using SVM, NB, RF, and KNN methods and tested that performance on the WBCD data set, achieved 93.865%, 94.74%, 96.49%, 91.23%, and 98.24% accuracy rates. Rahman et al [21] created an ANN classification model for the classification of breast cancer. They determined the number of neurons in a single hidden layer of the ANN as 15 using the Taguchi method. The success of the developed model was tested on the Wisconsin Diagnostic Breast Cancer Dataset. It was stated that the proposed model reached 98.8% accuracy in breast cancer classification. Akay et al. [22] proposed an SVM-based method with grid search and combined with feature selection for the diagnosis of breast cancer. They tested their method on different training-test sections of the Wisconsin breast cancer dataset (WBCD). The highest classification accuracy (98.53% for 70-30% training test partition) was obtained with the SVM model with five features. İbrahim et.al. [23] in their study, before passing the features to the classification step, made feature selection using the variance of the input features and correlation analysis. An ensemble method was selected from seven classification algorithms to improve breast cancer classification. They tested performance on the WBCD data set, achieving 99% accuracy rates. Memon, M. H. [24] used the linear SVM method to solve the breast cancer classification problem. They used preprocessing methods such as missing value detection, standard scalar, and min-max scalar. They selected the most relevant features with the REF method. They split the dataset into 70% for training and 30% for testing. Memon and his team [24], which has the closest accuracy to their study, used c=1, γ= 0.0001, time: 0.03 s parameter values in the SVM classifier and achieved 99% accuracy on the WBCD dataset. Bayrak, E.Y. [25] used the multiclass SVM and MLP methods and reported that the both SVM and MLP method accuracy was 95.37% for 66-33% train test splits. Kumar, P.P. [26] proposed a random decision tree algorithm. The weighting of the features according to the feature importance was carried out by the Core Neutrophic C-Means

Clustering method. Larger weights are assigned to applicable features and smaller weights to less applicable features. Performance analysis was tested on the Wisconsin Breast Cancer dataset with a 70%-30% training-test rate. SVM method test accuracy was 80% for the WBCD dataset.

Although there are many applications in the literature for the detection of breast cancer, research on this subject is still continuing since the desired level of success has not been achieved. Considering the methodological approach and results of this study, its contributions to the literature are summarized in articles.

- Unlike the studies summarized above, in this study, first of all, the feature set in the data set was analyzed. The local outlier method was applied for radius mean and tissue mean values, and outliers were removed. Thus, the success of the classification algorithm is increased.
- In the analysis of the WBCD data set used in the study, it was determined that the data in the feature set did not show a natural distribution. For this reason, a standardization process was applied to the data set in order to increase the classification success.
- The train test segmentation rate of 70%-30%, which was reported to have the highest success when the literature was analyzed, was also adopted in this study.
- In this study, two different feature reduction/selection methods (PCA and NCA) were applied to the data set separately, and the performances of the KNN classifier trained with the selected data feature vector were compared.
- Five different performance metrics (Accuracy Sensitivity Specificity Precision F1 MCC Kappa) were used to analyze the experimental results.
- The obtained results proved that the NCA feature selection and KNN classification algorithm reached a 99.42% accuracy rate and a 0.42% higher performance was obtained than the closest high-performance study in the literature.

The organization of the paper consists of three main parts. In Section 2, features of Breast Cancer in Wisconsin dataset, outlier detection, standardization and separation of the dataset, designed feature selected methods: PCA, NCA, and classification method: KNN method. And also performance metrics are included in Section 2. Section 3 includes experimental results and discussion. In that part, the confusion matrix and performance table are presented for all methods. In addition, the results of previous studies and the performance of the proposed method are compared in this section. All the important results of the study are summarized in the conclusion section.

2. Material and Method

This section offers details on the dataset and machine learning methods used to construct computerized algorithms for breast cancer detection.

2.1. Dataset for Breast Cancer in Wisconsin

The dataset [27], which is available in the UCI machine learning repository, was used in this study. There are 569 samples in this data collection, each with 32 characteristics (Figure 1). These are ID, diagnostic, and 30 real-valued input properties. The data collection contains 569 samples, 357 of which are benign and 212 of which are malignant. There are no situations where information is missing. To calculate features, a digitized picture of a fine needle aspirate (FNA) of a breast mass was used by Dua et al [27]. Features indicate the characteristics of the cell nuclei in the image. Ten real-valued features are determined for each cell nucleus: Radius, environment, area, evenness (local variation in radius lengths), compactness (perimeter^2 / area - 1.0), concave points, symmetry, fractal dimension ("coastline approximation" - 1) [27].

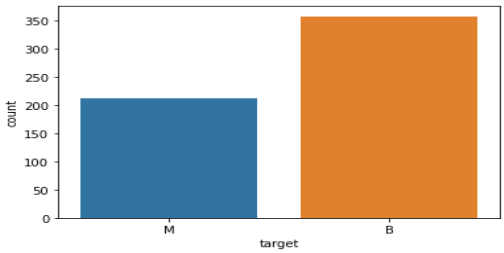

Figure 1. Benign (B) and malignant (M) data distribution

This listed feature set is presented as an input to the classification algorithm proposed in the study and a two-class problem is solved.

2.2. Outlier Detection

Many statistical testing and machine learning algorithms are susceptible to outliers. Outliers reduce classification success. The outlier value may be caused by the error made in the measurements, and for a good performance, these values should be detected in the dataset and taken before the classification step. Within the scope of this study, the local outlier method was applied for radius mean and tissue mean values, and outliers were removed (Figure 2).

The boxplot in Figure 2 provides a visualization of the statistics for the two features. The bottom and top of each rectangular box represent the border of the 25th and 75th percentiles of the data for

that sample, respectively, and the data in this range in the rate. The red line in the middle of the box is the median value of that feature. The dashes at the top and bottom of the box and the horizontal line at the end represent the normally distributed maximum and minimum values of the data. The red '+' symbols outside this horizontal line indicate the outliner values.

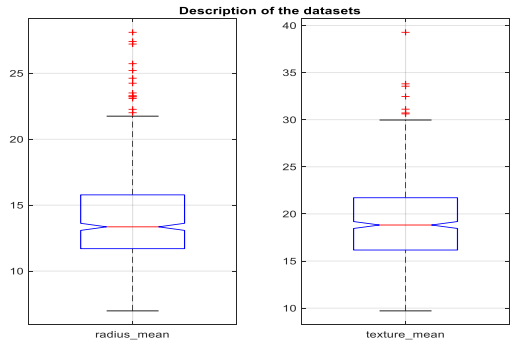

Figure 2. Display of radius mean, tissue mean values, and outliers

2.3. Standardization and Separation of Dataset

If the data set features do not resemble naturally distributed data, the classification may not work properly (such as gaussian with zero mean and unit variance) [28]. As a result, adopting the data standardization method is advantageous. Many machine learning estimators in scikit-learn require dataset standardization. The data is rescaled using a mean of 0 and a standard deviation of 1. The distribution approaches normal. The mean value is subtracted from the obtained value and divided by the standard deviation value and is shown in Eq. (1). Here x is the value in the data. μ is the mean. σ is the standard deviation of the data.

$$z = \frac{x-\mu}{\sigma} \quad (1)$$

Before beginning the model's training phase, the data set was separated into two clusters after standardization. On the training set, the model was trained, and the model's success was tested on the test set. As our training set grows, our model will learn better. As our test set grows, evaluation metrics will produce more reliable test accuracy results. Rahman et.al. [21] Wisconsin dataset was used in their study and they studied the dataset with 60%-40%, 70%-30%, and 80%-20% training-test rates. The highest success was achieved in the application where they divided 70%-30% with an accuracy of 98.5%. In the application where they divided it by 80%-20%, the success decreased to 94.7%. Akay [22], on the other hand, found an accuracy rate of 98.19% when he chose the training-test partition ratio of 50%-50%. The accuracy rate is 99.24% when he chose 70%-30%. The accuracy rate is 98.8% when he chose 80%-20% in his study.

2.4. Principal Components Analysis

Principal Components Analysis (PCA) is a multivariate size reduction technique that uses orthogonal transformations to condense a large number of linked variables into a smaller set. [29,30]. The equations used to calculate the principal components are presented in Equations (2-5). *For t= (1,2, ..., n)*, *{x(t)}* represents *a* random dataset containing zero-mean features. In this case, the covariance matrix is R;

$$R = \frac{1}{n-1}\sum_{t=1}^{n}[x(t)x(t)^T] \quad (2)$$

It has been calculated as (3) was used to calculate linear combinations of variables in the original data, namely the linear transformation from x(t) to y(t).

$$y(t) = M^T x(t) \quad (3)$$

M is an orthogonal matrix of size n × n. Column, *i*. is equal to the eigenvector. In this case, at the point, the eigenvalue problem can be written as in (4). q_i denotes the eigenvector and R an eigenvalue of the covariance matrix. ($\lambda_1>\lambda_2>\cdots>\lambda_n$).

$$\lambda_i q_i = R q_i \quad (4)$$

The principal components were calculated with the help of (5). Here $y_i(t)$, *i*. symbolizes the basic component [29,30].

$$y_i(t) = {q_i}^T x(t), i = 1,2,3,\dots,n \quad (5)$$

2.5. Neighborhood Components Analysis

Neighborhood component analysis (NCA) is a supervised learning method that uses a distance measure to classify multivariate data [31]. It is a metric learning machine learning algorithm. It learns a supervised linear transformation to improve the stochastic nearest neighbors' rule's classification accuracy in the modified space [32]. NCA is a statistical method that is used to improve accuracy. NCA's goal is to create an optimal objective function by utilizing a gradient-based optimizer. NCA selects a neighbor at random and returns the predicted decision for each class in which each point *i* selects a neighboring *j* point with *a* distance d_{ij} between points *i* and *j* and a probability of P_{ij} as Eq. (7) [33].

The sum of the absolute differences between the feature vectors given in Eq. (6) is multiplied by the weight of the vector to find the distance between them. The distance between x_i and x_j is d_{ij}.

$$d_{ij} = \sum_{l=1}^{p} w_l^2 |x_{il} - x_{jl}| \quad (6)$$

The weight of the first feature is represented by w_l. Unlike the K-Nearest Neighbor algorithm, the NCA selects a random neighbor for each class and makes the predicted judgment. Here, each point x_i chooses a neighboring point x_j with probability P_{ij}.

$$P_{ij} = \frac{k(d_{ij})}{\sum_{k=i} k(d_{ik})};\ P_{ij} = 0 \quad (7)$$

$k(z) = \exp(-z/\sigma)$ is a kernel function. The possibility of each point being chosen as the reference point is influenced by the kernel width *d*. The predicted fraction of time is represented by Probability Pi. The point *i* will be labeled in the correct class (Eq. 8) denoting the set of points in the same class as *i*. To maximize the objective function, (Eq. 9) is applied.

$$P_i = \sum_{j \in C_i} P_{ij} \quad (8)$$

$$f(w) = \frac{1}{n} \sum_{i=1}^{n} P_i \quad (9)$$

2.6. k-Nearest Neighbor Classification Method

Because of its simplicity and efficiency, the k-Nearest Neighbor Classification Method (KNN) is a commonly used pattern classification technique. It is one of the effective classification algorithms among supervised learning methods [34]. Also, KNN, a powerful multivariate statistical method that uses distance and assesses differentiating features [35], employs distance and analyzes distinguishing features. It makes no assumptions about the data's statistical properties. KNN predicts the class attribute based on the k nearest training instances in the feature space. It selects the class by taking into account the most representative samples given a data set, using the k closest samples from the classified training data. The Euclidean distance similarity metric was employed to pick neighbors in this study. The calculation of Euclidean distances is done as in Eq. (10) [36].

$$Euclidean\ Distance = \sqrt{\sum_{i=1}^{n} (x_i - y_i)^2} \quad (10)$$

In this case, x_i and y_i are two Euclidean n-space points. The classification accuracy was evaluated by dividing the number of successfully classified samples by the total number of samples after all test samples were categorized by KNN. Eq. (11) is used to calculate the mean absolute error (MAE) [36].

$$Mean\ Absolute\ Error = \frac{1}{n} \sum_{i=1}^{n} |y_i - x_i| \quad (11)$$

In this study, the design model type of KNN is Fine. The distance metric is Euclidean. The number of neighbors (*k*) is 3. Distance weight is equal.

Table 1. Performance Evaluation metrics

Performance Metric	Acronym	Equation	Explanation
Precision *(Positive Prediction Value)*	PPV	$\frac{TP}{TP + FP}$	From all samples projected to be positive, the proportion of accurately predicted positive samples.
Negative Prediction Value	NPV	$\frac{TN}{TN + FN}$	From all samples projected to be negative, the proportion of accurately predicted negative samples.
Sensitivity –Recall *(True Positive)*	TPR	$\frac{TP}{TP + FN}$	The ratio of TP results in the total number of true positive samples.
Specificity *(True Negative)*	TNR	$\frac{TN}{TN + FP}$	The ratio of TP results to the total number of true negative samples.
Accuracy	ACC	$\frac{TP + TN}{TP + TN + FP + FN}$	The ratio of the number of correct guesses made by the method to the total number of guesses made.
F-Score	F-Score	$\frac{2 \times precision \times recall}{precision + recall}$	The F-Score value shows us the harmonic average of the Sensitivity and Recall values.
MCC-Matthews correlation coefficient	MCC	$\max([(TP * TN) - FP * FN)/((TP + FP) * P * N * (TN + FN))\text{^}0.5],\ [((TP + FP) * P * N * (TN + FN))\text{^}0.5])$	
Cohen's Kappa	Kappa	$\text{po} = \text{ACC}$ $\text{pe} = ((\text{P} * (\text{TP} + \text{FP}) + (\text{FN} + \text{TN}))/(\text{TP} + \text{TN} + \text{FP} + \text{FN})\text{^}2$ $\text{kappa} = \max(\left[\frac{\text{po} - \text{pe}}{1 - \text{pe}}; \frac{\text{pe} - \text{po}}{1 - \text{po}}\right])$	

2.7. Performance Evaluation Methods

A range of performance criteria was used to compare the performance of early detection of breast cancer using machine learning techniques [37-39]. In Table 1, TP is actual value positive and prediction positive. FP is actual value negative and prediction positive. TN is actual value negative and prediction negative. FN is actual value positive and prediction negative. The terms recall, sensitivity, precision, and specificity values are described and all these metrics' formulas are in Table 1 [37-40]. The most frequently used performance criteria in machine learning applications, F1 score, MCC, Kappa, and Percentage accuracy values are calculated with the formulas in Table 1 and presented in the results section. Table 1 also includes the theoretical explanation and abbreviation of each criterion.

3. Results and Discussion

Figure 3 shows the confusion matrices obtained for the application of breast cancer detection using the KNN, PCA+KNN, and NCA+KNN methods. As can be seen, the approach with the highest TP and FP rates is the combined use of NCA+ KNN.

At the end of the study, 108 of 109 benign cells were predicted correctly and 1 was incorrectly predicted by the KNN method. Out of 62 malignant cells, 55 were predicted correctly and 7 were incorrectly predicted. With the PCA+ KNN method, 103 of 109 benign cells were correct and 6 were incorrect; Out of 62 malignant cells, 55 were predicted correctly and 7 were incorrectly predicted. By the NCA + KNN method, 108 of 109 benign cells were predicted correctly and 1 was predicted incorrectly. Table 2 shows the performance metric table. After feature selection with PCA, the use of the KNN classifier has a 92.39% accuracy rate, although it reduces the success. In the application where only the KNN algorithm was used, an accuracy rate of 95.32% was achieved. The highest success was obtained in feature selection with NCA and classification with KNN, and the accuracy rate was 99.42%. The F1 score performance values of these three methods are 0.9643, 0.9406, and 0.9954, respectively. Sensitivity, Specificity, Precision, Kappa, and MCC values are also included in the table.

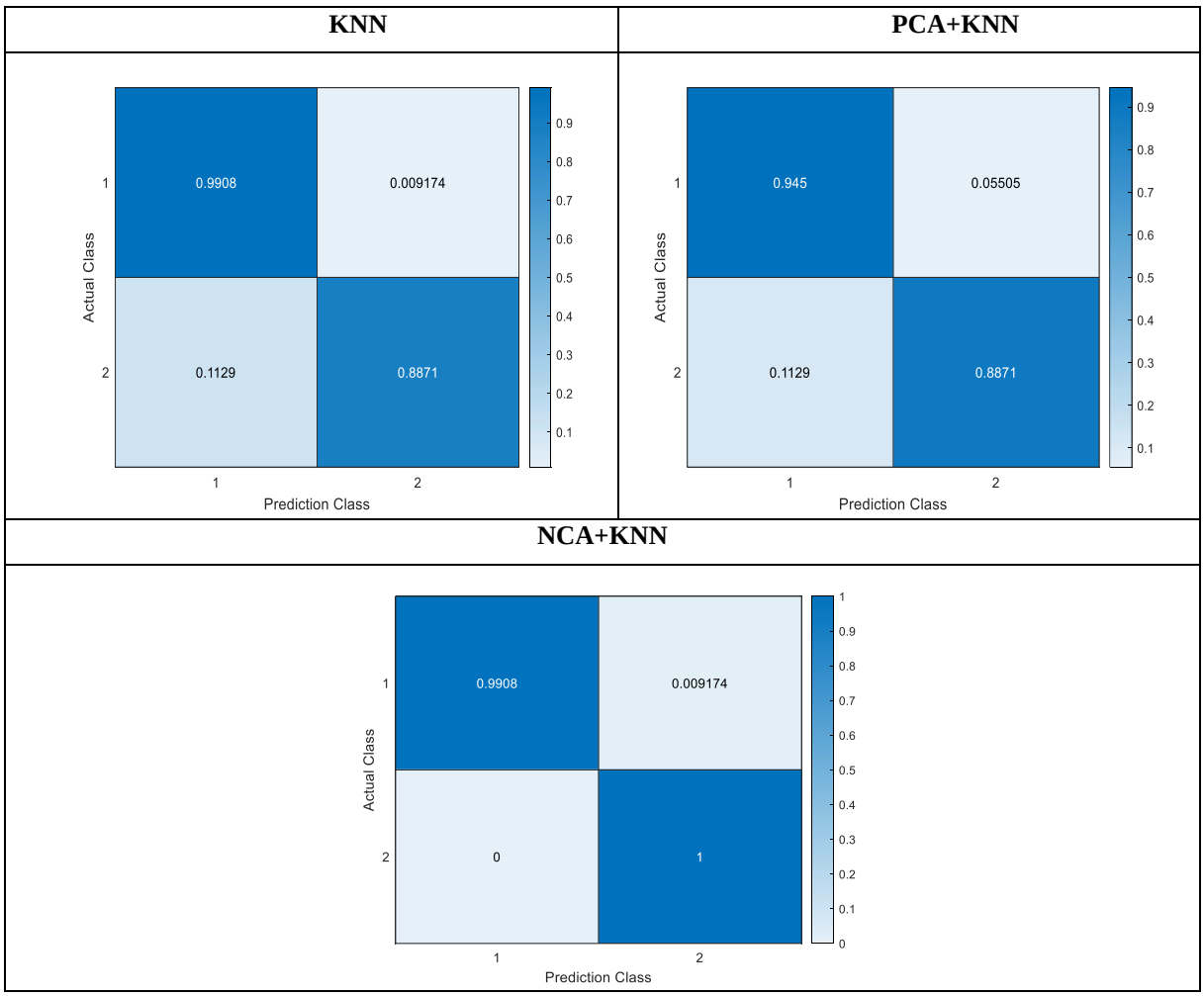

Figure 3. Confusion matrices of classification methods

Table 2. Performances of classification methods

Classifier	Accuracy	Sensitivity	Specificity	Precision	F1	MCC	Kappa
KNN	0.9532	0.9908	0.8871	0.93.91	0.9643	0.8966	0.8966
PCA + KNN	0.9240	0.9450	0.8871	0.9364	0.9406	0.8350	0.8350
NCA + KNN	0.9942	0.9908	1	1	0.9954	0.9875	0.9874

Table 3 summarizes the results of chest cancer detection studies using the WDBC dataset. It is seen that the classification accuracies of the existing studies in the literature vary between 72% and 99%, the precision value varies between 78% and 100%, the recall value varies between 79% and 99.24%, and F1 scores vary between 75% and 99%. In this study, the 99.42% accuracy, 100% precision, 99.08% recall, and 99.54% F1 score values obtained with the NCA + KNN method are relatively higher than the studies in the literature.

Table 3. Comparison of the results of some breast cancer diagnosis studies using the WBCD dataset

Study	Outliner Detection	Data selection	Classification Algorithms	Accuracy (%)	Precision	Recall / Sensitivity	F1-Score
Gupta (2020)[13]	X	√	*KNN*	95.8	93.5	93.5	93
			LR	95.8	96.5	95	95.5
			DT	95.8	96.5	95	95.5
			RF	97.2	97	97.5	97
			SVM	97.2	97.5	97	97
			DLL	98.24	98	98	98
Chaurasia (2018) [14]	X	X	*NB*	97.36	-	97.4	-
			RBF Neural Network	96.77	-	97.07	-
			J48 Algorithm	93.41	-	93.4	-
Gopal (2021) [16]	X	√	*LR*	79	78	79	78
			RF	95	90	94	92
			MLP	98	98	97	96
Sawssen (2022) [17]	X	√	PCA+KELM	98.18	-	94.83	92.80
			PCA+Poly-KELM	72.7	-	93.82	90.51
			PCA+Wav-KELM	94.54	-	100	91.26
			PCA+SVM	90.9	-	85.91	91.04
Ateş (2021) [19]	X	X	*NB*	96.5	96.70	93.70	95.20
			DT	92.4	87.90	92.10	89.90
			MLP	96.5	95.20	95.20	95.20
Sevli (2019) [20]	X	X	*SVM*	93.86	97.37	86.05	-
			NB	94.74	100	86.06	-
			RF	96.49	95.35	95.35	-
			KNN	91.23	94.59	81.39	-
			LR	98.24	100	95.35	-
Rahman (2020) [21]	X	X	*ANN*	98.8	98.40	99.10	98.80
Akay (2009) [22]	X	√	*SVM*	98.53	99.55	99.24	-
Ibrahim (2021) [23]	X	√	*Ensemble based*	99.00	99.29	96.00	97.51
Memon (2019) [24]	√	√	*SVM-linear*	99.00	99	98	99
Bayrak (2019) [25]	X	X	*SVM*	95.37	95.40	95.40	-
			MLP	95.37	95.50	95.40	-
Kumar (2021) [26]	X	X	*GA-SVM*	80.00	92.50	80.00	75.00
This Study	√	√	KNN	95.32	93.91	99.08	96.43
			PCA + KNN	92.40	93.64	94.50	94.06
			NCA + KNN	**99.42**	**100**	**99.08**	**99.54**

******* k-Nearest Neighbor (*KNN*), Logistic Regression (LR), Decision Tree (DT), Random Forest (RF), Support Vector Machine (SVM), Artificial Neural Network (ANN), Naive Bayes Algorithm (NB), RBF Neural Network, Kernel Extreme Learning Machine (KELM)

As can be seen in Table 3, studies have been conducted in the literature on the prediction of breast cancer diagnosis by many different machine learning techniques. Although similar machine learning classification methods are used in the literature, the reason for achieving success in different accuracy ranges is the pre-processing and feature selection/reduction methods applied to the data before the classification step. In order to design an effective machine learning model, it is necessary to analyze the data well, detect and remove outliers, and select the most effective features. In this study, unlike previous studies, the step of detection and exclusion of outliers was added to the data set. When the table is examined, it is seen that the results of the studies with feature selection [13,16-17,22-24] are considerably higher than the results of the studies without feature selection [14,16-21,25-26]. PCA, KPCA, etc. in the literature. Although these methods were used, the feature selection method with NCA was applied to WBCD data for the first time in this study. And the obtained results showed that feature selection with NCA is much more efficient than feature selection with PCA.

4. Conclusion

In this study, three models for the diagnosis of breast cancer with machine learning methods have been developed. The dataset was used for training and testing the developed method. According to the results obtained, it was seen that the highest classification success was obtained by using the NCA+KNN technique with 99.42%.

It is thought that this method can be used as an assistive system for physicians in the early-stage detection of breast cancer, which is an important problem of our time, with high accuracy. Early diagnosis and treatment of breast cancer prolong patient survival. It also shortens the treatment process with early diagnosis, which significantly reduces healthcare costs.

Acknowledgment

This study was supported by Firat University within the scope of the MF 21.14 Graduate BAP Project.

Contribution of Authors

Every author contributed equally to this work.

Conflict of Interest

There is no conflict of interest between the authors.

Statement of Research and Publication Ethics

Research and publication ethics complied with the study.

References

[1] P. Gummadi, “Analysis of machine learning in education sector”, 1-5, 2020.

[2] A. Jagwani, “A review of machine learning in education”, *Journal of Emerging Technologies and Innovative Research (JETIR)*, 6(5), 384-386, 2019.

[3] G. Buyrukoğlu, S. Buyrukoğlu, Z. Topalcengiz, “Comparing regression models with count data to artificial neural network and ensemble models for prediction of generic escherichia coli population in agricultural ponds based on weather station measurements”, *Microbal Risk Analysis*, 19, 100171, 2021.

[4] S. Buyrukoğlu, Y. Yılmaz, “An approach for airfare prices analysis with penalized regression methods”, *Data Science*, 4(2), 57-61, 2021.

[5] S. Buyrukoğlu, “Early detection of Alzheimer’s disease using data mining: comparison of ensemble feature selection approaches”, *Konya Journal of Engineering Sciences*, 9(1), 50-61, 2021.

[6] S. Buyrukoğlu, “Improvement of machine learning models’ performances based on ensemble learning for the detection of Alzheimer Disease”, *6th International Conference on Computer Science and Engineering*, 102-106, 2021.

[7] World Health Organzation, “International agency for research on cancer-iarc”, 2020, https://gco.iarc.fr/today/home.

[8] L. Çelik, “Meme kanseri taramasinda yapay zeka”, 2020, https://www.drozdogan.com/turkiye-kanser-istatistikleri-2020/

[9] C. Eyupoglu, “Breast cancer classification using k-nearest neighbors’ algorithm”, *The Online Journal of Science and Technology*, 8(3), 29-34, 2018.

[10] Ł. Jeleń, A. Krzyżak, T. Fevens, M. Jeleń, “Influence of feature set reduction on breast cancer malignancy classification of fine needle aspiration biopsies”, *Computers in Biology and Medicine*, 79, 80- 91, 2016.

[11] S. Savaş, "Detecting the stages of Alzheimer's disease with pre-trained deep learning architectures", *Arabian Journal for Science and Engineering*, 47, 2201-2218, 2022.
[12] S. Savaş, N. Topaloğlu, Ö. Kazcı, P. Koşar, "Comparison of deep learning models in carotid artery intima-media thickness ultrasound images: CAIMTUSNet", *Journal of Information Technologies*, 15(1), 1-12, 2022.
[13] P. Gupta, S. Garg, "Breast cancer prediction using varying parameters of machine learning models", *Procedia Computer Science*, vol. 171, pp. 593–601, 2020.
[14] V. Chaurasia, S. Pal, B. Tiwari, "Prediction of benign and malignant breast cancer using data mining techniques", *Journal of Algorithms & Computational Technology*, vol. 12, no. 2, pp. 119–126, 2018.
[15] M.H. Tafish, A.M. El-Halees, "Breast cancer severity degree predication using data mining techniques in the gaza strip", *in 2018 International conference on promising electronic technologies (ICPET), Deir El-Balah*, pp. 124–128, 2018.
[16] V.N. Gopal, F.A. Turjman, L. Anand, M. Rajesh, "Feature selection and classification in breast cancer prediction using IoT and machine learning", *Measurement*, 178, 109442, 2021.
[17] B. Sawssen, T. Okba, "A novel machine learning approach for breast cancer diagnosis", *Measurement*, 187, 110233, 2022.
[18] F. Ismaili, L. Shabani, B. Raufi, J. Adjari, X. Zenuni, "Enhancing breast cancer detection using data mining classification techniques", *Press Academia Procedia, 2nd World Conference on Technology, Innovation and Enterpreunership, 2017, İstanbul, Turkey*, 2017.
[19] İ. Ateş, T.T. Bilgin, "The investigation of the success of different machine learning methods in breast cancer diagnosis", *Konuralp Medical Journal*, 13(2), 347-356, 2021.
[20] O. Sevli, "Performance Comparison of Different Machine Learning Techniques in Diagnosis of Breast Cancer", *European Journal of Science and Technology*, 16, 176-185, 2019.
[21] A. Rahman, R.C. Muniyandi, D. Albashish, M. Rahman, O.L. Usman, "Artificial neural network with taguchi method for robust classification model to improve classification accuracy of breast cancer", *PeerJ Computer Science*, 2-27, 2020.
[22] M.F. Akay, "Support vector machines combined with feature selection for breast cancer diagnosis", *Expert Systems with Applications*, 36, 3240-3247, 2009.
[23] S. Ibrahim, S. Nazir, S.A. Velastin, "Feature selection using correlation analysis and principal component analysis for accurate breast cancer diagnosis", *Journal of Imaging*, 7(225), 3-16, 2021.
[24] M.H. Memon, J.P. Li, A.U. Haq, M.H. Memon, W. Zhou, "Breast cancer detection in the IOT health environment using modified recursive feature selection", *Hindawi Wireless Communication and Mobile Computing*, 1-19, 2019.
[25] E.Y. Bayrak, P. Kırcı, T. Ensari, "Comparison of machine learning methods for breast cancer diagnosis", *2019 Scientific Meeting on Electrical-Electronics & Biomedical Engineering and Computer Science (EBBT)*, 2019.
[26] P.P. Kumar, M.A.V. Bai, G.G. Nair, "An efficient classification framework for breast cancer using hyperparameter tuned random decision forest classifier and Bayesian optimization", *Biomedical Signal Processing and Control*, 68, 102682, 2021.
[27] D. Dua, C. Graff, "UCI machine learning repository", *Irvine, CA: University of California, School of Information and Computer Science*, 2019 http://archive.ics.uci.edu/ml
[28] A. Zang, A. Casari, "Feature engineering for machine learning: principles and techniques for data scientist", *O'Relly Media Publishing, Sebastopol, USA*, 2018.
[29] F. Salo, A.B. Nassif, A. Essex," Dimensionality reduction with IG-PCA and ensemble classifier for network intrusion detection", *Computer Networks*, 148, 164-175, 2019.
[30] H.J. Chiu, T.H.S. Li, P.H. Kuo, "Breast cancer–detection system using PCA, multilayer perceptron, transfer learning, and support vector machine", *IEEE Access*, 8, 204309-204324, 2020.
[31] S. Laghmati, B. Cherradi, A. Tmiri, O. Daanouni, S. Hamida, "Classification of patients with breast cancer using neighborhood component analysis and supervised machine learning techniques", *In 2020 3rd International conference on advanced communication technologies and networking (CommNet), IEEE* pp. 1-6, 2020.
[32] S.F. Khorshid, A.M. Abdulazeez, "Breast cancer diagnosis based on k-nearest neighbors: a review", *PalArch's Journal of the archaeology of Egypt/Egyptology*, 18(4), 1927-1951, 2021.

[33] R. Massafra, A. Latorre, A. Fanizzi, R. Bellotti, V. Didonna, V. Giotta, V. Lorusso, "A clinical decision support system for predicting invasive breast cancer recurrence: preliminary results", *Frontiers in Oncology,* 11, 284, 2021.

[34] T. Savaş, S. Savaş, "Feature-based performance comparison of machine learning algorithms for phishing detection through uniform resource locator", *Journal of Polytechnic, early access,* 2021.

[35] T.A. Assegie, "An optimized k-nearest neighbor-based breast cancer detection", *Journal of robotics and control (JRC),* 2(3), 115-118, 2021.

[36] C.J. Willmott, K. Matsuura, "Advantages of the mean absolute error (MAE) over the root mean square error (RMSE)", *in assessing average model performance. Climate Research,* 30, 79-82, 2005.

[37] G. Kou, Y. Peng, G. Wang, "Evaluation of clustering algorithms for financial risk analysis using MCDM methods", *Inf Sci (Ny),* 275, 1–12, 2014

[38] H. Xiao, K. Yi, R. Peng, G. Kou, "Reliability of a Distributed Computing System with Performance Sharing", *IEEE Trans Reliab*, 1–12, 2021.

[39] G. Kou, H. Xiao, M. Cao, L.H. Lee, "Optimal computing budget allocation for the vector evaluated genetic algorithm in multi-objective simulation optimization", *Automatica*, 129, 109599, 2021.

[40] H. Xiao, Y. Yan, G. Kou, S. Wu, "Optimal Inspection Policy for a Single-Unit System Considering Two Failure Modes and Production Wait Time", *IEEE Trans Reliab,* pp:1–13, 2021.

Bitlis Eren Üniversitesi Fen Bilimleri Dergisi
BİTLİS EREN UNIVERSITY JOURNAL OF SCIENCE
ISSN: 2147-3129/e-ISSN: 2147-3188
VOLUME: 11 NO: 2 PAGE: 604-612 YEAR: 2022
DOI: 10.17798/bitlisfen.1068022

Some Algebraic Structure on Figurate Numbers

Ahmet EMİN[1*]

[1]*Ministry of National Education, 10662 Karesi, Balıkesir, Turkey*
(ORCID: 0000-0001-7791-7181)

Keywords: Figurate numbers, Centered polygonal numbers, Algebraic structure, Binary operation.

Abstract
In this study, some information about figurate numbers and centered polygonal numbers is given. Also, a general binary operator that includes all centered polygonal numbers is defined, and it is investigated whether the algebraic structures defined with the general binary operator specify a groupoid and semigroup or not. And finally, some examples are given on the subject.

1. Introduction

Figurate numbers are natural numbers that can be represented by regular geometric patterns with equally spaced points. The theory of figurate numbers is not one of the main subjects of mathematics, but the charm of these numbers has raised awareness among scientists for thousands of years. Many special numbers have been created by being inspired from figurate numbers. Pythagoras triples, Perfect numbers, Mersenne numbers, Cullen numbers, Woodall numbers, Fermat numbers, Fibonacci numbers, Pell numbers, Lucas numbers, Thabit numbers, etc. are examples of such numbers.

These special number classes which are derived from Figurate numbers have a long and rich history dating back to ancient Greek times. They were first introduced in the Pythagorean school in the 6th century BC to enable the connection between geometry and arithmetic. It is possible to give some of the mathematicians who worked in this field and whose works are still center of interest today; "Pythagoras of Samos (ca. 582 BC–ca. 507 BC), Diophantus of Alexandria (ca. 210–ca. 290), Leonardo of Pisa who was also known as Leonardo Fibonacci (ca. 1170–ca. 1250), Gerolamo Cardano (1501–1576), Pierre de Fermat (1601–1665), John Pell (1611–1685), Blaise Pascal (1623–1662), Leonhard Euler (1707–1783), Joseph Louis Lagrange (1736–1813), Carl Friedrich Gauss (1777–1855), Augustin-Louis Cauchy (1789–1857)." [1].

Figurate numbers have different names according to their form of shapes on the plane. If the geometric pattern is arranged with a regular polygon, then the figurate number is called a polygonal number. If the geometric pattern is arranged with a regular polyhedron, then the figurate number is called a polyhedral number. Also, there are many different forms of figurate numbers such as centered polygonal, pronic, oblong, L-shape, cross, pyramidal numbers, etc.

Polygonal numbers are examples of figurate numbers and are probably the most well-known. Polygonal numbers start from a fixed point and increase in numbers by constructing larger and larger regular polygons. In particular, triangular and square numbers are examples of polygonal numbers. Triangular numbers can be obtained by adding to a fixed point two, three, four, five etc. points and arranging them in the form of an equilateral triangle.

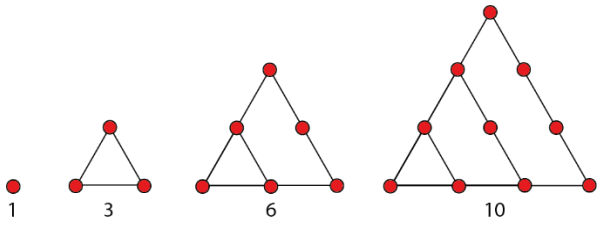

Figure 1. Some triangular numbers.

Similarly, square numbers can be obtained by adding to a fixed point three, five, seven, nine etc. points and arranging them in the form of a square.

*Corresponding author: drahmetemin@gmail.com
Received: 03.02.2022, Accepted: 08.06.2022

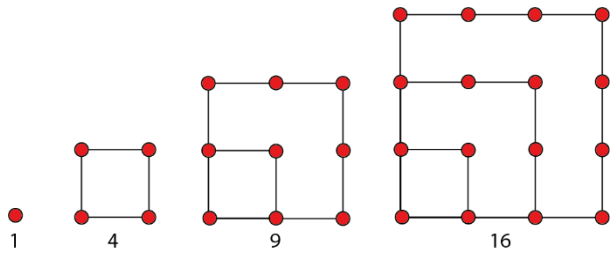

Figure 2. Some square numbers.

Mathematicians have worked on triangular and square numbers since ancient times. But studies on this field have been intensified for the last three centuries especially in this century. For example, in 1638, the famous mathematician Pierre de Fermat came up with Polygonal Number Theory but without proof. That is, "every positive integer can be written as the sum of three or fewer triangular numbers, and as the sum of four or fewer square numbers." In 1770 Joseph Louis Lagrange proved that polygonal number theory is valid for square case, Carl Friedrich Gauss proved the triangular case in 1796. And finally in 1818, Cauchy became the first person who proved the most general case of this problem that is, "every positive integer can be written as the sum of *n* or fewer *n*-gonal numbers." [2].

The other example of figurate numbers is Centered polygonal numbers. Centered polygonal numbers are regular polygons that are surrounded around a fixed point. By adding a point in the center in the plane, polygonal layers with a constant number of sides are constructed around this point. The number of points in these sides of the polygonal layers increases one more than the previous layer. Thus, the number of points in each polygonal layer of a centered *m*-gonal numbers increases *m* more points than the previous layer. For more detailed information on the subject, see [1], [2].

2. Material and Method

Binary operators have played an important role in many algebraic structures. It takes various names according to the binary operation defined on algebraic structures. Groupoid, semigroup and monoid are some of them. Specifically, it was proven by Sparavigna that it is a groupoid with binary operators defined on some polygonal numbers in [3]-[5]. Also, Emin studied semigroup construction on polygonal numbers in [6]. By using methods similar to those in these papers, we will give a general binary operator that includes all centered polygonal numbers. In addition, it will be investigated whether the algebraic structures defined with the general operator specify a groupoid and semigroup or not. By the way, maybe other algebraic properties, such as the studies in [7]-[10], can be studied by other mathematicians with the binary operation defined on this new algebraic structure.

The concept of groupoid, semigroup, monoid, and centered polygonal numbers will be explained and also their definitions and properties were given in this part of the study.

Definition 2.1. A groupoid (G, ∇) is defined as a non-empty set G on which a binary operation ∇ (by which we mean a map $\nabla: G \times G \longrightarrow G$) is defined. In other words, groupoid is an algebraic structure on a set with a binary operator. The only restriction on the operator is closure. It means that applying the binary operator on two elements of given set G returns with a value in which itself is a member of G. For more information, see [11], [12]. We say that (G, ∇) is a semigroup if the operation ∇ is associative, that is to say, if, for all $x, y, z \in G$

$$(x \nabla y) \nabla z = x \nabla (y \nabla z) \tag{1}$$

A semigroup is an associative groupoid; a semigroup with an identity is called a monoid.

Definition 2.2. For $m = 3, 4, 5, \ldots$ and $n \in \mathbb{N}, n-th$ centered m-gonal number formula is as follows [1];

$$CS_m(n) := \frac{mn^2 - mn + 2}{2} \tag{2}$$

Algebraically, for $n \in \mathbb{N}$ and $m \geq 3, n-th$ centered m-gonal number $CS_m(n)$ is obtained as the sum of the first n elements of the arithmetic progression $1, m, 2m, 3m, \ldots, (n-1)m$. So, it holds [1];

$$\begin{aligned} CS_m(n) &= 1 + m + 2m + 3m + \cdots + (n-1)m \\ &= 1 + m\big(1 + 2 + 3 + \cdots + (n-1)\big) \\ &= 1 + m\frac{(n-1)n}{2} \\ &= \frac{mn^2 - mn + 2}{2}. \end{aligned} \tag{3}$$

Example 2.1. In particular, for $m = 3, 4, 5, 6$ and $n \in \mathbb{N}, n-th$ centered m-gonal number formulas are as follows;

$$
\begin{aligned}
CS_3(n) &= 1 + 3\frac{n(n-1)}{2} = \frac{3n^2 - 3n + 2}{2}, \\
CS_4(n) &= 1 + 4\frac{n(n-1)}{2} = 2n^2 - 2n + 1, \\
CS_5(n) &= 1 + 5\frac{n(n-1)}{2} = \frac{5n^2 - 5n + 2}{2}, \\
CS_6(n) &= 1 + 6\frac{n(n-1)}{2} = 3n^2 - 3n + 1.
\end{aligned} \tag{4}
$$

The expression above implies the following recurrence formula for centered m-gonal numbers:

$$CS_m(n+1) = CS_m(n) + mn\,. \tag{5}$$

In particular, the result is;

$$
\begin{aligned}
CS_3(n+1) &= CS_3(n) + 3n, \\
CS_4(n+1) &= CS_4(n) + 4n, \\
CS_5(n+1) &= CS_5(n) + 5n, \\
CS_6(n+1) &= CS_6(n) + 6n, \\
CS_7(n+1) &= CS_7(n) + 7n, \\
CS_8(n+1) &= CS_8(n) + 8n.
\end{aligned} \tag{6}
$$

For some situations the value $CS_m(0) = 0$ can be accepted, where necessary, see [1], [6].

Example 2.2. For $n = 1, 2, 3, 4, 5$, and $m = 3, 4, 5, 6$ some centered polygonal numbers are as follows [13, A005448, A001844, A005891, A003215];

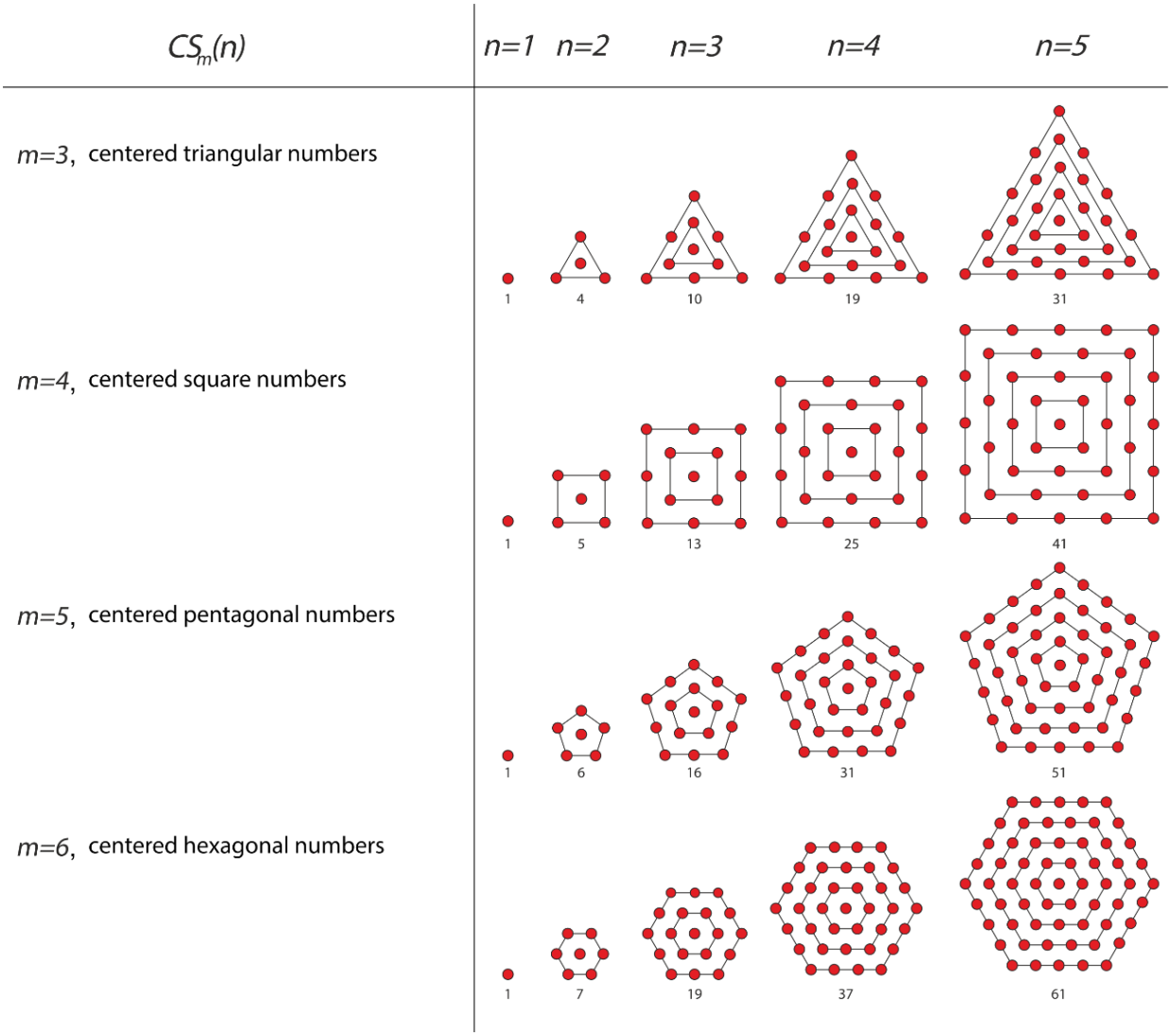

Figure 3. Some centered polygonal numbers

3. Findings and Discussion

In this section, we create a set consisting of elements of all centered polygonal numbers sequence $CS_m(n)$. After that we obtain an algebraic structure by defining binary operation on the defined set. And finally, we give a theorem and a corollary that show necessary conditions for this algebraic structure to be semigroup and monoid.

3.1. Construction of Algebraic Structure on Centered Polygonal Numbers

Before we can construct the theorem that yields the main result of this paper, we need to define a set and a binary operation on that set. So, let C denote the sequence of numbers $CS_m(n)$. That is, let

$$C = \left\{1, 1+m, 1+3m, 1+6m, 1+10m, \dots, 1+m\frac{n(n-1)}{2}, \dots\right\}. \quad (7)$$

Now we can find a binary operation of given set of C since

$$\begin{aligned}\left(CS_m(n)-\frac{8-m}{8}\right)^{\frac{1}{2}} &= \left(\frac{mn^2-mn+2}{2}-\frac{8-m}{8}\right)^{\frac{1}{2}}\\ &= \left(\frac{4mn^2-4mn+m}{8}\right)^{\frac{1}{2}}\\ &= \left(\frac{m}{2}\left(\frac{4n^2-4n+1}{4}\right)\right)^{\frac{1}{2}}\\ &= \sqrt{\frac{m}{2}}\left(\left(\frac{2n-1}{2}\right)^2\right)^{\frac{1}{2}}\\ &= \sqrt{\frac{m}{2}}\left(n-\frac{1}{2}\right). \quad (8)\end{aligned}$$

We define

$$\begin{aligned}M_n &= \left(CS_m(n)-\frac{8-m}{8}\right)^{\frac{1}{2}} = \sqrt{\frac{m}{2}}\left(n-\frac{1}{2}\right),\\ M_k &= \left(CS_m(k)-\frac{8-m}{8}\right)^{\frac{1}{2}} = \sqrt{\frac{m}{2}}\left(k-\frac{1}{2}\right),\\ M_{n+k} &= \left(CS_m(n+k)-\frac{8-m}{8}\right)^{\frac{1}{2}} = \sqrt{\frac{m}{2}}\left(n+k-\frac{1}{2}\right). \quad (9)\end{aligned}$$

We use M_n for definition of binary operation.

$$\begin{aligned}M_{n+k} &= M_n \nabla M_k = M_n + M_k + \sqrt{\frac{m}{8}}\\ &= \sqrt{\frac{m}{2}}\left(n-\frac{1}{2}\right)+\sqrt{\frac{m}{2}}\left(k-\frac{1}{2}\right)+\sqrt{\frac{m}{8}}\\ &= \sqrt{\frac{m}{2}}\left(n+k-\frac{1}{2}\right). \quad (10)\end{aligned}$$

Therefore, we have the binary operation:

$$\begin{aligned}&\left(CS_m(n+k)-\frac{8-m}{8}\right)^{\frac{1}{2}} = M_{n+k}\\ &= M_n \nabla M_k = M_n + M_k + \sqrt{\frac{m}{8}}\\ &= \left(CS_m(n)-\frac{8-m}{8}\right)^{\frac{1}{2}}+\left(CS_m(k)-\frac{8-m}{8}\right)^{\frac{1}{2}}+\frac{\sqrt{m}}{2\sqrt{2}}. \quad (11)\end{aligned}$$

As a result, from (11), we can rewrite the defined binary operation as follows:

$$\begin{aligned}&CS_m(n)\nabla CS_m(k) = CS_m(n+k)\\ &= CS_m(n)+CS_m(k)+\frac{m}{4}-1\\ &+2\left(CS_m(n)-\frac{8-m}{8}\right)^{\frac{1}{2}}\left(CS_m(k)-\frac{8-m}{8}\right)^{\frac{1}{2}}\\ &+\frac{\sqrt{m}}{\sqrt{2}}\left(CS_m(n)-\frac{8-m}{8}\right)^{\frac{1}{2}}+\frac{\sqrt{m}}{\sqrt{2}}\left(CS_m(k)-\frac{8-m}{8}\right)^{\frac{1}{2}}.\end{aligned}$$

In the following lemma, we give a necessary condition for the algebraic structure (C, ∇) to be a groupoid.

Lemma 3.1.1. Let C be the set of sequence of numbers $CS_m(n)$, that is, let

$$C = \left\{1, 1+m, 1+3m, 1+6m, 1+10m, \dots, 1+m\frac{n(n-1)}{2}, \dots\right\}.$$

Also let ∇ be a binary operation on C such that

$$\begin{aligned}&CS_m(n)\nabla CS_m(k) = CS_m(n+k)\\ &= CS_m(n)+CS_m(k)+\frac{m}{4}-1\\ &+2\left(CS_m(n)-\frac{8-m}{8}\right)^{\frac{1}{2}}\left(CS_m(k)-\frac{8-m}{8}\right)^{\frac{1}{2}}\\ &+\frac{\sqrt{m}}{\sqrt{2}}\left(CS_m(n)-\frac{8-m}{8}\right)^{\frac{1}{2}}+\frac{\sqrt{m}}{\sqrt{2}}\left(CS_m(k)-\frac{8-m}{8}\right)^{\frac{1}{2}}. \quad (12)\end{aligned}$$

where $n, k \in \mathbb{N}$ and $m \geq 3$. Then the algebraic structure (C, ∇) is a groupoid.

Proof. From binary operation (12), we can have recursive relation for $k = 1$:

$$CS_m(n)\nabla CS_m(1) = CS_m(n+1)$$
$$= CS_m(n) + CS_m(1) + \frac{m}{4} - 1$$
$$+2\left(CS_m(n) - \frac{8-m}{8}\right)^{\frac{1}{2}}\left(CS_m(1) - \frac{8-m}{8}\right)^{\frac{1}{2}}$$
$$+ \frac{\sqrt{m}}{\sqrt{2}}\left(CS_m(n) - \frac{8-m}{8}\right)^{\frac{1}{2}} + \frac{\sqrt{m}}{\sqrt{2}}\left(CS_m(1) - \frac{8-m}{8}\right)^{\frac{1}{2}}.$$

Thus, $CS_m(n+1) = CS_m(n)\nabla CS_m(1)$

$$= CS_m(n) + \frac{m}{2} + \sqrt{2m}\left(CS_m(n) - \frac{8-m}{8}\right)^{\frac{1}{2}}.$$

And so, we have

$$CS_m(n+1) = CS_m(n) + \sqrt{2m}\left(CS_m(n) - \frac{8-m}{8}\right)^{\frac{1}{2}} + \frac{m}{2}. \quad (13)$$

We prove this part of the lemma using the method of mathematical induction on n. For $n = 2, 3, 4, 5$ and starting from number $CS_m(1) = 1$, we have $1 + m, 1 + 3m, 1 + 6m, 1 + 10m$ which are the elements of the set of C. Indeed, for $m \geq 3$,

$$CS_m(2) = CS_m(1) + \sqrt{2m}\left(CS_m(1) - \frac{8-m}{8}\right)^{\frac{1}{2}} + \frac{m}{2}$$
$$= 1 + \sqrt{2m}\left(1 - \frac{8-m}{8}\right)^{\frac{1}{2}} + \frac{m}{2}$$
$$= 1 + \sqrt{2m}\frac{\sqrt{m}}{2\sqrt{2}} + \frac{m}{2} = 1 + m.$$

$$CS_m(3) = CS_m(2) + \sqrt{2m}\left(CS_m(2) - \frac{8-m}{8}\right)^{\frac{1}{2}} + \frac{m}{2}$$
$$= 1 + m + \sqrt{2m}\left(1 + m - \frac{8-m}{8}\right)^{\frac{1}{2}} + \frac{m}{2}$$
$$= 1 + m + \sqrt{2m}\frac{\sqrt{9m}}{2\sqrt{2}} + \frac{m}{2} = 1 + 3m.$$

$$CS_m(4) = CS_m(3) + \sqrt{2m}\left(CS_m(3) - \frac{8-m}{8}\right)^{\frac{1}{2}} + \frac{m}{2}$$
$$= 1 + 3m + \sqrt{2m}\left(1 + 3m - \frac{8-m}{8}\right)^{\frac{1}{2}} + \frac{m}{2}$$
$$= 1 + 3m + \sqrt{2m}\frac{\sqrt{25m}}{2\sqrt{2}} + \frac{m}{2}$$
$$= 1 + 3m + \frac{6m}{2} = 1 + 6m.$$

$$CS_m(5) = CS_m(4) + \sqrt{2m}\left(CS_m(4) - \frac{8-m}{8}\right)^{\frac{1}{2}} + \frac{m}{2}$$
$$= 1 + 6m + \sqrt{2m}\left(1 + 6m - \frac{8-m}{8}\right)^{\frac{1}{2}} + \frac{m}{2}$$
$$= 1 + 6m + \sqrt{2m}\frac{\sqrt{49m}}{2\sqrt{2}} + \frac{m}{2}$$
$$= 1 + 6m + \frac{8m}{2} = 1 + 10m.$$

Now we suppose that the recursive formula (13) is true for n. That is, for $m \geq 3$,

$$CS_m(n) = CS_m(n-1) + \sqrt{2m}\left(CS_m(n-1) - \frac{8-m}{8}\right)^{\frac{1}{2}} + \frac{m}{2}$$
$$= \frac{m(n-1)^2 - m(n-1) + 2}{2}$$
$$+ \sqrt{2m}\left(\frac{m(n-1)^2 - m(n-1) + 2}{2} - \frac{8-m}{8}\right)^{\frac{1}{2}} + \frac{m}{2}$$
$$= \frac{mn^2 - 3mn + 2m + 2}{2}$$
$$+ \sqrt{2m}\left(\frac{mn^2 - 3mn + 2m + 2}{2} - \frac{8-m}{8}\right)^{\frac{1}{2}} + \frac{m}{2}$$
$$= \frac{mn^2 - 3mn + 2m + 2}{2} + \frac{m(2n-3)}{2} + \frac{m}{2}$$

$$= \frac{mn^2 - mn + 2}{2}$$

is the element of the set of C. Also, from (3) and (9), we have

$$CS_m(n) = CS_m(n-1) + \sqrt{2m}\left(CS_m(n-1) - \frac{8-m}{8}\right)^{\frac{1}{2}} + \frac{m}{2}$$
$$= 1 + m + 2m + 3m + \cdots + (n-3)m + (n-2)m$$
$$+\sqrt{2m}\sqrt{\frac{m}{2}}\left(n - 1 - \frac{1}{2}\right) + \frac{m}{2}$$
$$= 1 + m + 2m + 3m + \cdots + (n-3)m + (n-2)m$$
$$+(n-1)m - \frac{m}{2} + \frac{m}{2}$$
$$= 1 + m + 2m + 3m + \cdots + (n-3)m + (n-2)m$$
$$+(n-1)m. \quad (14)$$

We need to show that the recursive formula (13) is true for $n + 1$. From (9) and (14),

$$CS_m(n) + \sqrt{2m}\left(CS_m(n) - \frac{8-m}{8}\right)^{\frac{1}{2}} + \frac{m}{2}$$
$$= 1 + m + 2m + 3m + \cdots + (n-3)m + (n-2)m$$
$$+(n-1)m + \sqrt{2m}\sqrt{\frac{m}{2}}\left(n - \frac{1}{2}\right) + \frac{m}{2}$$
$$= 1 + m + 2m + 3m + \cdots + (n-3)m + (n-2)m$$
$$+(n-1)m + nm - \frac{m}{2} + \frac{m}{2}$$

$$= 1 + m + 2m + 3m + \cdots + (n-3)m + (n-2)m + (n-1)m + nm$$
$$= 1 + m(1 + 2 + 3 + \cdots + (n-2) + (n-1) + n)$$
$$= 1 + m\frac{n(n+1)}{2}$$
$$= \frac{mn^2 + mn + 2}{2}$$
$$= CS_m(n+1).$$

Therefore $CS_m(n+1)$ is element of the set of C. That means, the algebraic structure (C, ∇) satisfies the properties of closure which gives us the lemma 3.1.1. that (C, ∇) is a groupoid. Hence the result.

In the following theorem, we give a necessary condition for the algebraic structure (C, ∇) to be a semigroup which is the main conclusion of this study.

Theorem 3.1.1. Let C be the set of sequence of numbers $CS_m(n)$, that is, let

$$C = \left\{1, 1+m, 1+3m, 1+6m, 1+10m, \dots, 1 + m\frac{n(n-1)}{2}, \dots\right\}.$$

Also let ∇ be a binary operation on C such that

$$CS_m(n)\nabla CS_m(k) = CS_m(n+k)$$
$$= CS_m(n) + CS_m(k) + \frac{m}{4} - 1$$
$$+2\left(CS_m(n) - \frac{8-m}{8}\right)^{\frac{1}{2}}\left(CS_m(k) - \frac{8-m}{8}\right)^{\frac{1}{2}}$$
$$+ \frac{\sqrt{m}}{\sqrt{2}}\left(CS_m(n) - \frac{8-m}{8}\right)^{\frac{1}{2}} + \frac{\sqrt{m}}{\sqrt{2}}\left(CS_m(k) - \frac{8-m}{8}\right)^{\frac{1}{2}}.$$

where $n, k \in \mathbb{N}$ and $m \geq 3$. Then the algebraic structure (C, ∇) is a semigroup.

Proof. From lemma 3.1.1. the algebraic structure (C, ∇) is a groupoid. Now we need to show that (C, ∇) satisfies the properties of associativity. From (9) and (10), we know

$M_{n+k} = M_n \nabla M_k = M_n + M_k + \sqrt{\frac{m}{8}}$ where $n, k \in \mathbb{N}$, $m \geq 3$ and

$$M_n = \left(CS_m(n) - \frac{8-m}{8}\right)^{\frac{1}{2}} = \sqrt{\frac{m}{2}}\left(n - \frac{1}{2}\right),$$
$$M_k = \left(CS_m(k) - \frac{8-m}{8}\right)^{\frac{1}{2}} = \sqrt{\frac{m}{2}}\left(k - \frac{1}{2}\right),$$
$$M_{n+k} = \left(CS_m(n+k) - \frac{8-m}{8}\right)^{\frac{1}{2}} = \sqrt{\frac{m}{2}}\left(n + k - \frac{1}{2}\right).$$

For $n, k, p \in \mathbb{N}$ and $m \geq 3$,

$$(M_n \nabla M_k)\nabla M_p = M_{n+k} + M_p + \sqrt{\frac{m}{8}}$$
$$= \sqrt{\frac{m}{2}}\left(n + k - \frac{8-m}{8}\right) + \sqrt{\frac{m}{2}}\left(p - \frac{8-m}{8}\right) + \sqrt{\frac{m}{8}}$$
$$= \sqrt{\frac{m}{2}}\left(n + k + p - \frac{8-m}{4}\right) + \sqrt{\frac{m}{8}} \quad (15)$$

And

$$M_n \nabla (M_k \nabla M_p) = M_n + M_{k+p} + \sqrt{\frac{m}{8}}$$
$$= \sqrt{\frac{m}{2}}\left(n - \frac{8-m}{8}\right) + \sqrt{\frac{m}{2}}\left(k + p - \frac{8-m}{8}\right) + \sqrt{\frac{m}{8}}$$
$$= \sqrt{\frac{m}{2}}\left(n + k + p - \frac{8-m}{4}\right) + \sqrt{\frac{m}{8}} \quad (16)$$

So, with the results of equations (15) and (16), we obtain, $(M_n \nabla M_k)\nabla M_p = M_n \nabla (M_k \nabla M_p)$ which gives us the theorem 3.1.1. that (C, ∇) satisfies the properties of associativity. Hence the result.

As seen in Figure 3, centered polygonal numbers start from $CS_m(1) = 1$. However, in some studies, as you can see in [1] and [6], centered polygonal numbers start from the number $CS_m(0) = 0$. Now by considering the start point as the number $CS_m(0) = 0$ and theorem 3.1.1., we can give the following corollary which gives the conditions for (C, ∇) to be a monoid.

Corollary 3.1.1. Let C be the set of sequence of numbers $CS_m(n)$ and let ∇ be a binary operation on C(defined in (7)) such that,

$$CS_m(n)\nabla CS_m(k) = CS_m(n+k)$$
$$= CS_m(n) + CS_m(k) + \frac{m}{4} - 1$$
$$+2\left(CS_m(n) - \frac{8-m}{8}\right)^{\frac{1}{2}}\left(CS_m(k) - \frac{8-m}{8}\right)^{\frac{1}{2}}$$
$$+ \frac{\sqrt{m}}{\sqrt{2}}\left(CS_m(n) - \frac{8-m}{8}\right)^{\frac{1}{2}} + \frac{\sqrt{m}}{\sqrt{2}}\left(CS_m(k) - \frac{8-m}{8}\right)^{\frac{1}{2}}.$$

where $n, k \in \mathbb{N}$ and $m \geq 3$. If $CS_m(0) = 0 \in C$, then the algebraic structure (C, ∇) is a monoid.

Proof. In theorem 3.1.1., we have proved that (C, ∇) is a semigroup. To show that the algebraic structure (C, ∇) is a monoid, it must be shown that it has an

identity element. Let $CS_m(0) = 0 \in C$, then, from the binary operation ∇ we have,

$$CS_m(n) \nabla\, CS_m(0) = CS_m(n+0) = CS_m(n)$$

and

$$CS_m(0) \nabla\, CS_m(n) = CS_m(0+n) = CS_m(n).$$

Thus, we have,

$CS_m(n) \nabla\, CS_m(0) = CS_m(0) \nabla\, CS_m(n) = CS_m(n)$ which gives us the corollary 3.1.1. that (C, ∇) satisfies the properties of identity. Hence the result.

Example 3.1.1. [13, A005448] known as centered triangular numbers. Centered triangular numbers are integer having the following form below:

$$\begin{aligned} CS_3(n) &= 1 + 3 + 6 + 9 + 12 + \cdots + 3(n-1) \\ &= 1 + 3\big(1 + 2 + 3 + 4 + \cdots + (n-1)\big) \\ &= 1 + 3\frac{(n-1)n}{2} \\ &= \frac{3n^2 - 3n + 2}{2}. \end{aligned}$$

Let A denote the sequence of numbers $CS_3(n)$. That is, let

$$A = \{1,4,10,19,31,46,64,85,109,136,166,199,235,\ 274,316, \ldots\}$$

Now we can find a binary operation of given set of A. Since

$$\begin{aligned} \left(CS_3(n) - \frac{5}{8}\right)^{\frac{1}{2}} &= \left(\frac{3n^2 - 3n + 2}{2} - \frac{5}{8}\right)^{\frac{1}{2}} \\ &= \left(\frac{12n^2 - 12n + 3}{8}\right)^{\frac{1}{2}} \\ &= \left(\frac{3}{2}\left(\frac{4n^2 - 4n + 1}{4}\right)\right)^{\frac{1}{2}} \\ &= \sqrt{\frac{3}{2}}\left(\left(\frac{2n-1}{2}\right)^2\right)^{\frac{1}{2}} \\ &= \sqrt{\frac{3}{2}}\left(n - \frac{1}{2}\right). \end{aligned}$$

we define:

$$T_n = \left(CS_3(n) - \frac{5}{8}\right)^{\frac{1}{2}} = \sqrt{\frac{3}{2}}\left(n - \frac{1}{2}\right),$$

$$T_k = \left(CS_3(k) - \frac{5}{8}\right)^{\frac{1}{2}} = \sqrt{\frac{3}{2}}\left(k - \frac{1}{2}\right),$$

$$T_{n+k} = \left(CS_3(n+k) - \frac{5}{8}\right)^{\frac{1}{2}} = \sqrt{\frac{3}{2}}\left(n + k - \frac{1}{8}\right).$$

We use T_n for definition of binary operation:

$$\begin{aligned} T_{n+k} = T_n \nabla T_k &= T_n + T_k + \frac{\sqrt{3}}{2\sqrt{2}} \\ &= \sqrt{\frac{3}{2}}\left(n - \frac{1}{2}\right) + \sqrt{\frac{3}{2}}\left(k - \frac{1}{2}\right) + \frac{\sqrt{3}}{2\sqrt{2}} \\ &= \sqrt{\frac{3}{2}}\left(n + k - \frac{1}{2}\right). \end{aligned}$$

As a result, we can rewrite the defined binary operation as follows:

$$\begin{aligned} &CS_3(n) \nabla CS_3(k) = CS_3(n+k) \\ &= CS_3(n) + CS_3(k) - \frac{1}{4} \\ &+2\left(CS_3(n) - \frac{5}{8}\right)^{\frac{1}{2}}\left(CS_3(k) - \frac{5}{8}\right)^{\frac{1}{2}} \\ &+\sqrt{\frac{3}{2}}\left(CS_3(n) - \frac{5}{8}\right)^{\frac{1}{2}} + \sqrt{\frac{3}{2}}\left(CS_3(k) - \frac{5}{8}\right)^{\frac{1}{2}} \end{aligned} \tag{17}$$

From binary operation (17), we can have recursive relation for $k = 1$:

$$\begin{aligned} CS_3(n+1) &= CS_3(n) \nabla CS_3(1) \\ &= CS_3(n) + 2\sqrt{\frac{3}{2}}\left(CS_3(n) - \frac{5}{8}\right)^{\frac{1}{2}} + \frac{3}{2}. \end{aligned}$$

And so, we obtain

$$CS_3(n+1) = CS_3(n) + \frac{2\sqrt{3}}{\sqrt{2}}\left(CS_3(n) - \frac{5}{8}\right)^{\frac{1}{2}} + \frac{3}{2}.$$

Starting from number $CS_3(1) = 1$, we have $4, 10, 19, 31, 46, 64, 85, 109, 136, 166, 199, 235,\ 274, 316, \ldots$ which are the elements of the set of A. From lemma 3.1.1. and theorem 3.1.1., one can say that the algebraic structure (A, ∇) is a groupoid and semigroup. Also, if the $CS_3(0) = 0 \in A$ then the algebraic structure (A, ∇) is a monoid from corollary 3.1.1.

Example 3.1.2. [13, A005891] known as centered pentagonal numbers. Centered pentagonal numbers are integer having the following form below:

$$\begin{aligned} CS_5(n) &= 1+5+10+15+20+\cdots+5(n-1) \\ &= 1+5\big(1+2+3+4+\cdots+(n-1)\big) \\ &= 1+5\frac{(n-1)n}{2} \\ &= \frac{5n^2-5n+2}{2}. \end{aligned}$$

Let B denote the sequence of numbers $CS_5(n)$. That is, let

$B = \{1, 6, 16, 31, 51, 76, 91, 106, 141, 181, 226, 276, 331, 391, \dots\}$

Now we can find a binary operation of given set of B. Since

$$\begin{aligned} \left(CS_5(n)-\frac{3}{8}\right)^{\frac{1}{2}} &= \left(\frac{5n^2-5n+2}{2}-\frac{3}{8}\right)^{\frac{1}{2}} \\ &= \left(\frac{20n^2-20n+5}{8}\right)^{\frac{1}{2}} \\ &= \left(\frac{5}{2}\left(\frac{4n^2-4n+1}{4}\right)\right)^{\frac{1}{2}} \\ &= \sqrt{\frac{5}{2}}\left(\left(\frac{2n-1}{2}\right)^2\right)^{\frac{1}{2}} \\ &= \sqrt{\frac{5}{2}}\left(n-\frac{1}{2}\right). \end{aligned}$$

we define:

$$P_n = \left(CS_5(n)-\frac{3}{8}\right)^{\frac{1}{2}} = \sqrt{\frac{5}{2}}\left(n-\frac{1}{2}\right),$$

$$P_k = \left(CS_5(k)-\frac{3}{8}\right)^{\frac{1}{2}} = \sqrt{\frac{5}{2}}\left(k-\frac{1}{2}\right),$$

$$P_{n+k} = \left(CS_5(n+k)-\frac{3}{8}\right)^{\frac{1}{2}} = \sqrt{\frac{5}{2}}\left(n+k-\frac{1}{2}\right).$$

We use P_n for definition of binary operation:

$$P_{n+k} = P_n \nabla P_k = P_n + P_k + \frac{\sqrt{5}}{2\sqrt{2}}$$

$$= \sqrt{\frac{5}{2}}\left(n-\frac{1}{2}\right) + \sqrt{\frac{5}{2}}\left(k-\frac{1}{2}\right) + \frac{\sqrt{5}}{2\sqrt{2}}$$

$$= \sqrt{\frac{5}{2}}\left(n+k-\frac{1}{2}\right).$$

As a result, we can rewrite the defined binary operation as follows:

$$\begin{aligned} &CS_5(n)\nabla CS_5(k) = CS_5(n+k) \\ &= CS_5(n) + CS_5(k) + \frac{1}{4} \\ &+2\left(CS_5(n)-\frac{3}{8}\right)^{\frac{1}{2}}\left(CS_5(k)-\frac{3}{8}\right)^{\frac{1}{2}} \\ &+\sqrt{\frac{5}{2}}\left(CS_5(n)-\frac{3}{8}\right)^{\frac{1}{2}} + \sqrt{\frac{5}{2}}\left(CS_5(k)-\frac{3}{8}\right)^{\frac{1}{2}}. \end{aligned} \quad (18)$$

From binary operation (18), we can have recursive relation for $k = 1$:

$$\begin{aligned} CS_5(n+1) &= CS_5(n)\nabla CS_5(1) \\ &= CS_5(n) + \frac{2\sqrt{5}}{\sqrt{2}}\left(CS_5(n)-\frac{3}{8}\right)^{\frac{1}{2}} + \frac{5}{2}. \end{aligned}$$

And so, we obtain

$$CS_5(n+1) = CS_5(n) + \frac{2\sqrt{5}}{\sqrt{2}}\left(CS_5(n)-\frac{3}{8}\right)^{\frac{1}{2}} + \frac{5}{2}.$$

Starting from number $CS_5(1) = 1$, we have $6, 16, 31, 51, 76, 91, 106, 141, 181, 226, 276, 331, 391, \dots$ which are the elements of the set of B. From lemma 3.1.1. and theorem 3.1.1., one can say that the algebraic structure (B, ∇) is a groupoid and semigroup. Also, if the $CS_5(0) = 0 \in B$, then the algebraic structure (B, ∇) is a monoid from Corollary 3.1.1.

4. Conclusion and Suggestions

Firstly, in this paper, the definition of algebraic structure and, in particular, the definitions of groupoid, semigroup, and monoid were made. Also, figurate numbers and centered polygonal numbers were introduced. Later, the algebraic structure was proved to be a groupoid and a semigroup with the binary operation defined on centered polygonal numbers. And finally, some examples were given on the subject.

Acknowledgement

I would like to thank the referees for their important suggestions and comments that improve the study.

Statement of Research and Publication Ethics

In this paper, research and publication ethics were followed.

References

[1] E. Deza and M. M. Deza, *Figurate Numbers;* World Scientific Publishing Company, Singapore, 2014.
[2] T.L. Heath, *Diophantus of Alexandria: A study in the History of Greek Algebra;* CUP Archive, 1910.
[3] A. C. Sparavigna, "Groupoids of OEIS A003154 Numbers (star numbers or centered dodecagonal numbers)," *Zenodo*, doi: 10.5281/zenodo.3387054, 2019.
[4] A. C. Sparavigna, "Groupoids of OEIS A093112 and A093069 Numbers (oblong and odd square numbers)," *Zenodo*, doi: 10.5281/zenodo.3247003, 2019.
[5] A. C. Sparavigna, "On a generalized sum of the Mersenne Numbers," *Zenodo*, doi: 10.5281/zenodo.2634312, 2018.
[6] A. Emin, "Semigroup Construction On Polygonal Numbers," *Journal of Engineering Technology and Applied Sciences.*, 2021.
[7] A. Emin, F. Ateş, "Some New Results on the Orthodox, Strongly π- Inverse and π- regularity of Some Monoids," *Bulletin of The Society of Mathematicians Banja Luka*, vol. 11, no. 3, 2021.
[8] A. Emin, F. Ateş, S. Ikikardeş, and I. N. Cangül, "A new monoid construction under crossed products," *Journal of Inequalities and Applications.*, vol. 2013, no. 1, 2013.
[9] F. Ateş, "Some new monoid and group constructions under semidirect products," *Ars. Combinatoria*, vol. 2009, no. 1, 2009.
[10] E. K. Cetinalp, "Regularity of Iterated Crossed Product of Some Monoids," *Bulletin of The Society of Mathematicians Banja Luka*, vol. 12, no. 1, 2022.
[11] J. M. Howie, *Fundamentals of semigroup theory*. Oxford, England: Clarendon Press, 1995.
[12] E. W. Weisstein, "Groupoid," *https://mathworld.wolfram.com/*. [Accessed: 24-Mar-2022].
[13] "The on-line encyclopedia of integer sequences® (OEIS®)," *Oeis.org*. [Online]. Available: http://oeis.org. [Accessed: 24-Mar-2022].

Bitlis Eren Üniversitesi Fen Bilimleri Dergisi
BİTLİS EREN UNIVERSITY JOURNAL OF SCIENCE
ISSN: 2147-3129/e-ISSN: 2147-3188
VOLUME: 11 NO: 2 PAGE: 613-619 YEAR: 2022
DOI: 10.17798/bitlisfen.1068508

Genipin Crosslinked Human Serum Albumin Nanoparticles

Emine Dila KURTUL[1], Merve ÇAPKIN YURTSEVER[1*]

[1]*Adana Alparslan Türkeş Science and Technology University, Faculty of Engineering, Department of Bioengineering, Adana, Turkey*
(ORCID: 0000-0001-5172-8710) (ORCID: 0000-0001-7874-4016)

Keywords: HSA, Genipin, Nanoparticle, Desolvation

Abstract
The use of human serum albumin (HSA) nanoparticles as drug delivery systems in controlled drug release studies has gained importance today. Albumin nanoparticles are biocompatible, biodegradable and provide sustained release. To maintain long-term drug delivery, HSA nanoparticles need to be cross-linked. A chemical crosslinker, glutaraldehyde is generally used in the literature and has some toxic effects on the cells. In this study, a biological crosslinker, genipin, was used for the production of HSA nanoparticles by desolvation technique. Two different temperatures and genipin concentrations were studied in order to decrease crosslinking time. The nanoparticles were characterized by Scanning Electron Microscopy (SEM) and Dynamic Light Scattering (DLS). The crosslinking time was reduced from 8-24 hours to 2 hours by raising the temperature to 37°C from room temperature. HSA nanoparticles which are crosslinked by genipin may have potential use in drug delivery system and may be applied in personalized medicine applications.

1. Introduction

Nanoparticles are structures with sizes ranging from 1 to 100 nm, according to the description of NNI (National Nanotechnology Initiative). The small size of nanoparticles provides them unique physicochemical and biological features; thus, they are more readily taken up by cells which gives them the ability of delivering drugs to the desired target organ [1]. Drug delivery systems play an important role for the controlled release of a drug molecule or its transport to the targeted organ [2]. Particle size and surface properties are main factors that affect the potential of drug carrier system [3]. Toxicity, distribution in living organism and targeting ability of nanoparticle heavily depend on particle size [4]. Nanoparticles are removed from the body by renal, lymphatic or reticuloendothelial system according to their sizes [5]. In a study, accumulation of nanoparticles in the spleen with diameters higher than 230 nm was shown [6]. Studies have shown that nanoparticles smaller than 100 nm is expected not to activate the lymphatic system however, particles with 200 nm and larger size tend to activate the lymphatic system [7]. The surface charge properties of the nanoparticles are described by zeta potential that represents the electrical potential of particles. Zeta potential is affected by parameters such as the particle composition and the medium in which it is dispersed. Nanoparticles with a zeta potential greater than (±) 30 mV form more stable suspensions, which means prevention of aggregate formation [4].

Different types of materials such as synthetic and natural polymers can be used for nanoparticle formation. Human serum albumin (HSA) is a remarkably soluble protein abundant in human blood plasma and has a molecular weight of 66.5 kDa and shows an average half-life of 19 days [8], [9]. The HSA protein acts as a carrier for endogenous and exogenous compounds with a high ligand binding capacity. Thanks to this feature, it carries out various functions in human body such as carrying hormones and fatty acids with low water solubility, making some toxins harmless and regulating pharmacokinetic

Corresponding author: mcyurtsever@atu.edu.tr
Received: 07.02.2022, Accepted: 21.04.2022

properties of many drugs such as sulfonamides, penicillin etc. [10]. In addition to these compounds, HSA binds to various heavy metals to control their concentration in blood. Also, the major function of HSA is to regulate the colloid osmotic pressure of blood which facilitates water and water-soluble substances to pass from capillary vessels to tissues [11]. It is stable in the 4-9 pH range and at 60°C for 10h. It is primarily uptake by inflamed tissues and tumor cells that makes it a good candidate to be used as a directed drug carrier. When it is degraded, amino acids as degradation products supply nutrition to peripheral tissue [9]. In brief, nanoparticles manufactured using HSA for drug delivery systems exhibit many advantages: having functional groups such as amino and carboxylic groups on the nanoparticle surface which allow binding of albumin nanoparticles with drug targeting ligands, providing sustained release, biodegradability and prevention of toxicity [8], [9], [12].

Desolvation, emulsion, coacervation, nanospray drying, self-assembly, and nanoparticle albumin bound technology are some of the techniques which can be applied to obtain albumin nanoparticles. Desolvation and emulsification are the most preferred methods in the production of protein nanoparticles [13]. In desolvation technique, proteins in aqueous solutions are dehydrated by addition of desolvating agent, such as ethanol, and gain spherical shape to produce nanoparticles. The desolvation technique has been improved as an alternative to emulsification because it is a more robust and reproducible technique which minimizes possible denaturation and triggering self-assembly of proteins in the presence of desolvating agent [12], [14]. After nanoparticle production by desolvation technique, the protein nanoparticles are generally crosslinked with chemical cross-linking agents like glutaraldehyde, however this agent may lead to some toxic effects both *in vitro* and *in vivo* studies [15].

Genipin is a natural crosslinking agent that can be used to crosslink various polymeric materials including primary amine groups, such as chitosan, collagen, gelatin, and proteins. The mechanism of genipin crosslinking is based on crosslinking of free amino groups which are present in lysine, hydroxylysine, and arginine amino acids [16]. The biocompatibility of materials crosslinked with genipin is higher than that of materials crosslinked with glutaraldehyde or any other epoxy compound [17]–[19]. In the literature, Shahgholian et al. conducted studies on crosslinking of bovine serum albumin (BSA) nanoparticles with genipin instead of glutaraldehyde crosslinker by desolvation technique, which is the main method of albumin nanoparticle production. They have shown that genipin could crosslink BSA nanoparticles after 24 h incubation at 25ºC. In another experimental study [20], Luo et al. worked on tannic acid coating of genipin-crosslinked HSA nanoparticles and they showed that genipin was able to crosslink HSA nanoparticles at room temperature (RT) after 16 h, keep them stable and enhance their encapsulation efficiency [21]. Lin et al. have shown that sugar beet pectin-BSA nanoparticles with diameter ~180 nm was obtained by ultrasonication in the presence of genipin after 24 h at RT [22].

In this study, it was aimed to obtain genipin crosslinked HSA nanoparticles and to decrease crosslinking time with increasing crosslinking temperature. Nanoparticles obtained by desolvation technique were crosslinked with genipin. Optimization studies were carried out by changing the genipin concentration and temperature during crosslinking.

2. Material and Method

Albumin, Human Fraction V Powder was purchased from Sigma-Aldrich, USA. Genipin with 98% purity was obtained from Challenge Bioproducts, Taiwan. Ethanol Absolute with 99.9 % purity was purchased from Isolab, Germany.

2.1. Synthesis of genipin crosslinked HSA nanoparticles

HSA nanoparticles were synthesized by desolvation method [3] as illustrated in Fig 1. 10 mg HSA was dissolved in 500 µl ultra-pure water. For nanoparticle formation, 2 ml of desolvating agent, ethanol, was added (1 ml/min) dropwise by using a syringe-pump under constant stirring (600 rpm) at RT. After desolvation process, nanoparticles were crosslinked by addition of genipin with 0.2% and 2.2% w/w of HSA solution under constant stirring in an incubator set at 37°C and at RT. After crosslinking process, HSA nanoparticles suspension was recovered by centrifugation at 15000 rpm, 4°C for 20 min. Nanoparticles were washed with ultra-pure water three times. Finally, nanoparticles were resuspended in ultra-pure water.

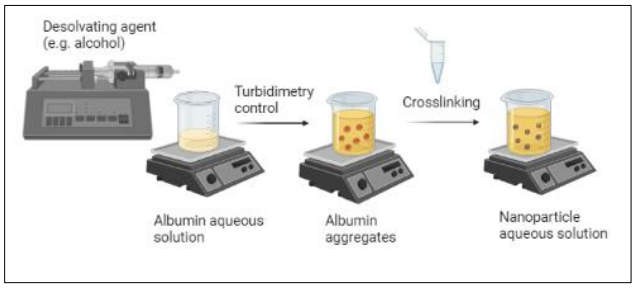

Figure 1. The schematic illustration of the HSA nanoparticle production via desolvation method

2.2. Characterization of HSA nanoparticles

The morphology of nanoparticles and particle size were investigated by Scanning Electron Microscopy SEM (FEI – Quanta 650 Field Emission SEM, Çukurova University Central Research Laboratory) analysis. One droplet of diluted suspension was deposited on carbon tapes and dried at RT. Then the sample was sputter-coated with gold and then investigated by SEM. To compare the change in particle size and their distribution, the diameter of nanoparticles was measured by ImageJ (NIH, Bethesda, MD) software.

Dynamic Light Scattering (DLS) analysis was carried out to determine the average particle size, size distribution and zeta-potential of the nanoparticles. The sample was taken from the nanoparticle suspension after homogenization by sonication, and the final nanoparticle concentration was adjusted to 0.1 mg/ml by adding ultra-pure water at different pH values (7, 8 and 9) and PBS. Diluted and homogenized nanoparticle suspension was added into the device-specific cuvette and the measurement was done by a Malvern Zetasizer (Nano-ZS, Malvern, Mersin University (MEITAM)) at RT.

3. Results and Discussion

3.1. The effect of temperature and genipin concentration on the nanoparticle properties

In this study, we aimed to decrease the crosslinking time with changing genipin concentration and temperature. Favorable crosslinking condition of genipin is in the range of temperature between 25-45°C [17]. In this study, to decrease crosslinking time of the HSA nanoparticles, they were immediately placed into 37ºC-incubator soon after genipin addition and stirred at 600 rpm for different durations. Crosslinking of HSA nanoparticles at 0.2 w/w genipin concentration at RT for 24 h resulted significant aggregation of the nanoparticles on the interface of the solution and glass beaker as seen in Fig. 2a. However, there were not any aggregation in the nanoparticle suspension when they were crosslinked at 37ºC for 2 h at the same genipin concentration. Further studies were carried out at 37ºC. In the literature, HSA or BSA nanoparticles which were obtained by desolvation technique were generally crosslinked with glutaraldehyde for 24 hours at 25°C [3], [12]. In a study conducted by Shahgolian et al., glutaraldehyde as covalent crosslinker was used to obtain BSA nanoparticles. Genipin solution (0.1, 0.2, 0.3% w/w of BSA) is used to crosslink BSA nanoparticles for 24h at 25°C [20]. Here, genipin crosslinking time was reduced to 2 h with increased temperature.

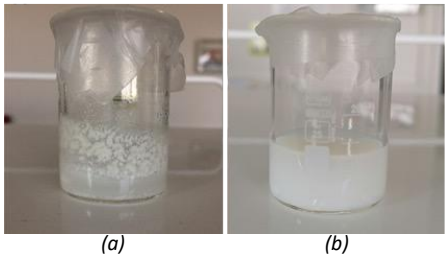

(a) *(b)*

Figure 2. a) Genipin crosslinked HSA nanoparticles at RT for 24h **b)** Genipin crosslinked HSA nanoparticles at 37°C for 2 hours

3.2. Morphology of the nanoparticles

To determine the effect of genipin concentration and crosslinking time on HSA nanoparticles they were crosslinked with genipin concentrations (0.2% w/w and 2.2% w/w of HSA) for 2, 3 and 4 h at 37°C at 600 rpm. SEM images of these nanoparticles were given in Fig. 3. It was observed that uniform, spherical and nanometer range nanoparticles were synthesized successfully.

The particle size distribution of the nanoparticles was determined by ImageJ software (NIH, USA) from the SEM images (Fig. 4). The average diameter of the nanoparticles was not affected by increasing crosslinking time for 0.2% w/w genipin crosslinked HSA nanoparticles (Fig. 4a, b and c). On the other hand, there was a slight increase in the diameters of HSA nanoparticles which were crosslinked at 2.2% w/w genipin concentration (Fig. 4d, e and f). The average diameter of the nanoparticles slightly increased from ≈20 nm to ≈22 nm for 2 and 4 h crosslinking time, respectively. The diameter of the nanoparticle is important for drug delivery studies. Nanoparticles up to 200 nm are simultaneously taken into the cell by multiple endocytosis pathways [23]. In the literature, the size of nanoparticles crosslinked with glutaraldehyde is ranging from 150-300 nm [3], [12]. Here, genipin crosslinked HSA nanoparticles with very small diameter were obtained. Crosslinking

of HSA nanoparticles with 0.2 w/w genipin at 37ºC for 2 h resulted in a significant decrease in nanoparticle size. For further studies, 2h of crosslinking time was chosen.

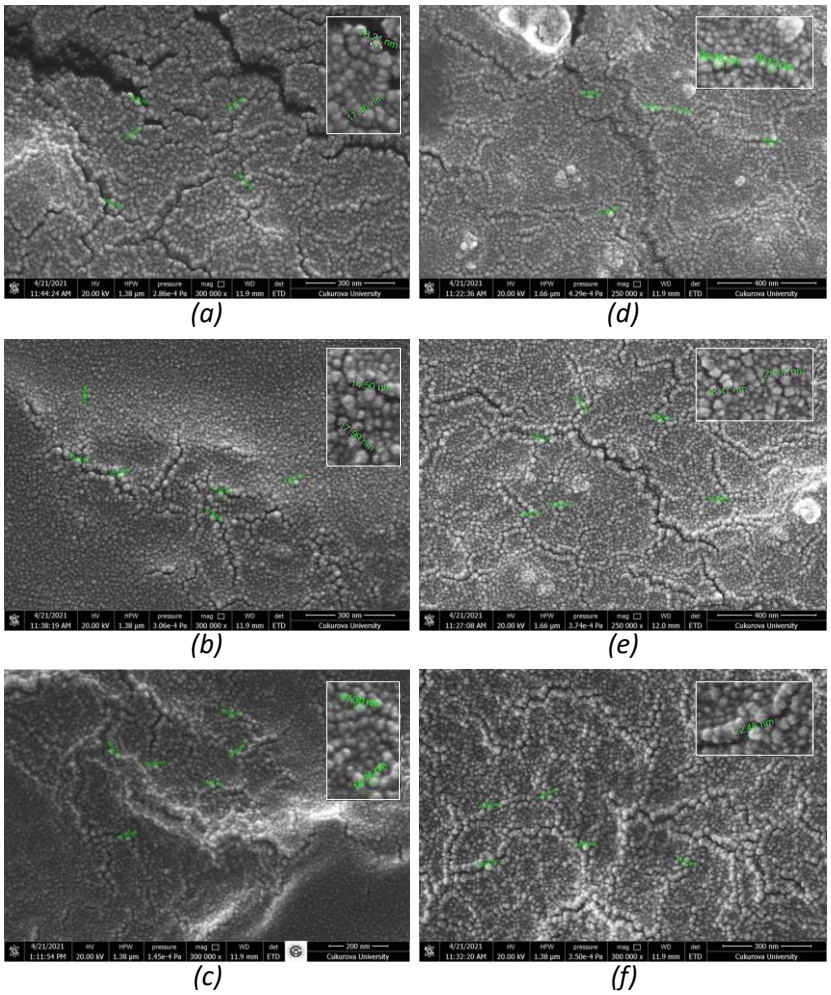

Figure 3. SEM images of 0.2% w/w genipin crosslinked HSA nanoparticles for **a)** 2 h, **b)** 3 h and **c)** 4 h; 2.2% w/w genipin crosslinked HSA nanoparticles **d)** 2 h; **e)** 3 h and **f)** 4 h

3.3. Particle size and size distribution of the nanoparticles by DLS

Particle sizes and size distributions of genipin crosslinked HSA nanoparticles by DLS analysis are summarized in Table 1. According to our results, the Z-average values were not correlated with the diameters of the nanoparticles as seen in SEM images. Due to the accumulation problem of the nanoparticles which were directly dispersed in ultra-pure water, it was difficult to measure the exact Z-average values of nanoparticles. However, it was clearly seen that, this accumulation problem was much more significant for 2.2% w/w genipin crosslinked HSA nanoparticles which may be due to high crosslinker concentration.

Zeta-potential of the nanoparticles is a very important parameter which describes the colloidal stability of the nanoparticles. Zeta-potential is a measure of repulsion between nanoparticles. Nanoparticles with charge other than -30 mV to +30 mV form more stable suspensions, which means prevention of aggregate formation [6]. The ideal formulation of nanoparticles has the smallest size and the zeta potential value other than -30 mV to +30 mV zeta potential, and the lowest polydispersity [24]. Due to the aggregation behavior of the nanoparticles here, zeta-potential values were out of this range.

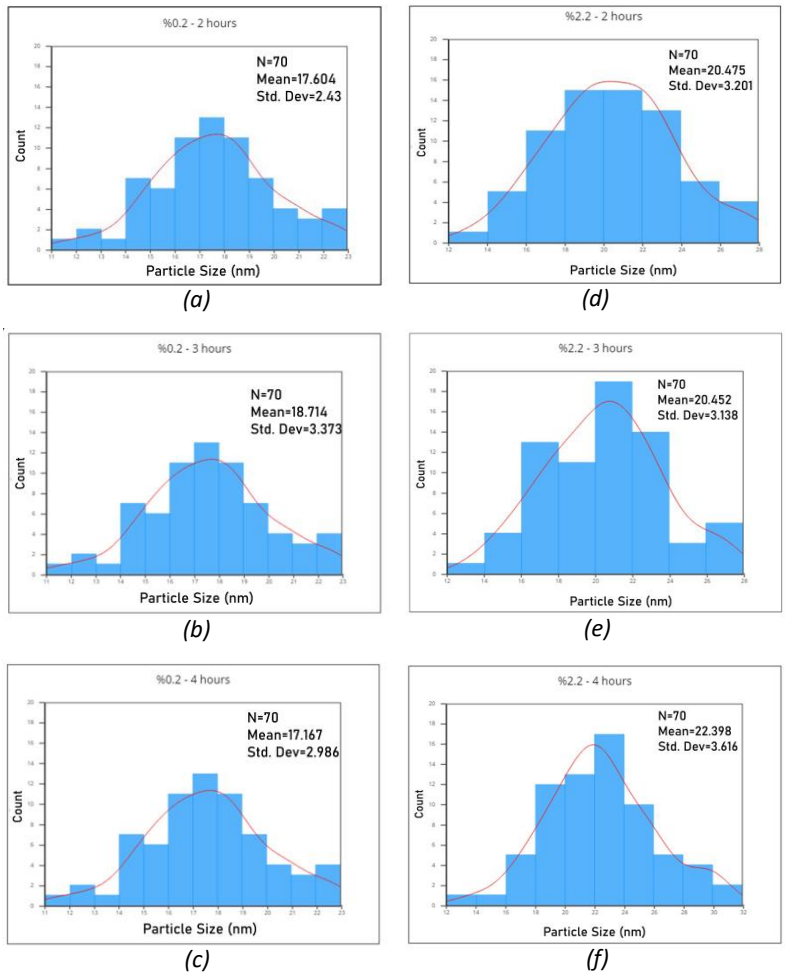

Figure 4. Size distribution curves of 0.2% w/w genipin crosslinked HSA nanoparticles for **a)** 2 h, **b)** 3 h and **c)** 4h; 2.2% w/w genipin crosslinked HSA nanoparticles **d)** 2 h; **e)** 3 h and **f)** 4 h.

Table 1. Z-average, zeta potential and PDI values of HSA nanoparticles

Genipin concentration (w/w)	Z-average (intensity, d.nm)	PDI	Zeta-potential (mV)
0.2%	323.5	0.668	-18.2
2.2%	1700	0.396	-1.21

To decrease the accumulation behavior the nanoparticles (0.2% w/w genipin crosslinked for 2 h) were diluted in PBS and in ultra-pure water with different pH values such as 8 and 9. The results are shown in Table 2. The accumulation tendency of the nanoparticles decreased when they were diluted in PBS environment and in ultra-pure water with increased pH. Z-average was decreased from 323.5 to 50.72 (intensity, d.nm) by increasing the pH from 7 to 9. PDI also was decreased from 0.668 to 0.227.

Protonation of carboxyl and amino groups of HSA protein below its isoelectronic point which is pH 4.7, results net positive charge and above its isoelectronic point results net negative charge. These differences in charges can alter protein electrostatic repulsion and trigger aggregation, which results in larger nanoparticles. This finding reveals that it is possible to modify the colloidal characteristics of HSA nanoparticles by varying the experimental parameters [24].

Table 2. Z-average and PDI values of HSA nanoparticles at different pH values.

Crosslinking condition	pH	Z-average (intensity, d.nm)	PDI
0.2% (w/w) genipin – 2h at 37°C	PBS (7.4)	144.6	0.278
	8	56.14	0.473
	9	50.72	0.227

4. Conclusion and Suggestions

Desolvation method is an efficient and simple method to produce human serum albumin nanoparticles. In this study, genipin crosslinked HSA nanoparticles with diameters smaller than 50 nm were successfully produced after 2 hours incubation at 37°C under stirring by desolvation technique. There was no significant morphological change between nanoparticles crosslinked at 0.2 or 2.2 w/w genipin concentrations. However, it was just observed that tendency of nanoparticles to coagulate increase as the genipin concentration increase. In conclusion, these genipin crosslinked HSA nanoparticles with diameters smaller than 50 nm may have potential to be used as drug carriers in drug delivery systems.

Acknowledgment

This study was supported by the Scientific Research Projects Coordination Unit of Adana Alparslan Türkeş Science and Technology University (BAP) with the project number 20332001. Dila Kurtul was supported by the TÜBİTAK-BİDEB 2210-C National Scholarship in Priority Fields in Science Program for MSc students.

Contributions of the authors

This study was conducted as MSc thesis of Emine Dila Kurtul and she contributed to the literature review, experiments, evaluation of data and article writing, while Merve Çapkın Yurtsever contributed to the formation of ideas, evaluation of the data, article writing and editing.

Conflict of Interest Statement

There is no conflict of interest between the authors.

Statement of Research and Publication Ethics

The study is complied with research and publication ethics.

References

[1] A. Z. Wilczewska, K. Niemirowicz, K. H. Markiewicz, and H. Car, "Nanoparticles as drug delivery systems," *Pharmacological Reports*, vol. 64, no. 5. Elsevier B.V., pp. 1020–1037, 2012. doi: 10.1016/S1734-1140(12)70901-5.

[2] J. K. Patra *et al.*, "Nano based drug delivery systems: Recent developments and future prospects" *Journal of Nanobiotechnology*, vol. 16, no. 1. BioMed Central Ltd., Sep. 19, 2018. doi: 10.1186/s12951-018-0392-8.

[3] K. Langer, S. Balthasar, V. Vogel, N. Dinauer, H. von Briesen, and D. Schubert, "Optimization of the preparation process for human serum albumin (HSA) nanoparticles," *International Journal of Pharmaceutics*, vol. 257, no. 1–2, pp. 169–180, May 2003, doi: 10.1016/S0378-5173(03)00134-0.

[4] R. Singh and J. W. Lillard, "Nanoparticle-based targeted drug delivery," *Experimental and Molecular Pathology*, vol. 86, no. 3. pp. 215–223, Jun. 2009. doi: 10.1016/j.yexmp.2008.12.004.

[5] Y. G. Roh *et al.*, "Protein Nanoparticle Fabrication for Optimized Reticuloendothelial System Evasion and Tumor Accumulation," *Langmuir*, vol. 35, no. 11, pp. 3992–3998, Mar. 2019, doi: 10.1021/acs.langmuir.8b03776.

[6] S. Hong, D. W. Choi, H. N. Kim, C. G. Park, W. Lee, and H. H. Park, "Protein-based nanoparticles as drug delivery systems," *Pharmaceutics*, vol. 12, no. 7. MDPI AG, pp. 1–28, Jul. 01, 2020. doi: 10.3390/pharmaceutics12070604.

[7] S. A. A. Rizvi and A. M. Saleh, "Applications of nanoparticle systems in drug delivery technology," *Saudi Pharmaceutical Journal*, vol. 26, no. 1. Elsevier B.V., pp. 64–70, Jan. 01, 2018. doi: 10.1016/j.jsps.2017.10.012.

[8] F. Kratz, "A clinical update of using albumin as a drug vehicle - A commentary," *Journal of Controlled Release*, vol. 190. Elsevier, pp. 331–336, Sep. 28, 2014. doi: 10.1016/j.jconrel.2014.03.013.

[9] F. Kratz, "Albumin as a drug carrier: Design of prodrugs, drug conjugates and nanoparticles," *Journal of Controlled Release*, vol. 132, no. 3, pp. 171–183, Dec. 2008, doi: 10.1016/j.jconrel.2008.05.010.

[10] T. Pappa and S. Refetoff, "Thyroid hormone transport proteins: Thyroxine-binding globulin, transthyretin, and albumin," in *The Curated Reference Collection in Neuroscience and Biobehavioral Psychology*, Elsevier Science Ltd., 2016, pp. 483–490. doi: 10.1016/B978-0-12-809324-5.03494-5.

[11] P. Lee and X. Wu, "Review: Modifications of Human Serum Albumin and Their Binding Effect," 2015. doi: 10.2174/1381612821666150302115025.

[12] A. O. Elzoghby, W. M. Samy, and N. A. Elgindy, "Albumin-based nanoparticles as potential controlled release drug delivery systems," *Journal of Controlled Release*, vol. 157, no. 2. pp. 168–182, Jan. 30, 2012. doi: 10.1016/j.jconrel.2011.07.031.

[13] M. Tarhini, H. Greige-Gerges, and A. Elaissari, "Protein-based nanoparticles: From preparation to encapsulation of active molecules," *International Journal of Pharmaceutics*, vol. 522, no. 1–2. Elsevier B.V., pp. 172–197, Apr. 30, 2017. doi: 10.1016/j.ijpharm.2017.01.067.

[14] T. K. Giri, "Alginate Containing Nanoarchitectonics for Improved Cancer Therapy," in *Nanoarchitectonics for Smart Delivery and Drug Targeting*, Elsevier Inc., 2016, pp. 565–588. doi: 10.1016/B978-0-323-47347-7.00020-3.

[15] S. Zhao, W. Wang, Y. Huang, Y. Fu, and Y. Cheng, "Paclitaxel loaded human serum albumin nanoparticles stabilized with intermolecular disulfide bonds," *Medchemcomm*, vol. 5, no. 11, pp. 1658–1663, Nov. 2014, doi: 10.1039/c4md00200h.

[16] A. O. Elzoghby, M. M. Elgohary, and N. M. Kamel, "Implications of Protein- and Peptide-Based Nanoparticles as Potential Vehicles for Anticancer Drugs," in *Advances in Protein Chemistry and Structural Biology*, vol. 98, Academic Press Inc., 2015, pp. 169–221. doi: 10.1016/bs.apcsb.2014.12.002.

[17] B. Manickam, R. Sreedharan, and M. Elumalai, "'Genipin'-The Natural Water Soluble Cross-linking Agent and Its Importance in the Modified Drug Delivery Systems: An Overview," 2014. doi: 10.2174/1567201813106660059.

[18] J. Y. Lai, "Biocompatibility of genipin and glutaraldehyde cross-linked chitosan materials in the anterior chamber of the eye," *International Journal of Molecular Sciences*, vol. 13, no. 9, pp. 10970–10985, Sep. 2012, doi: 10.3390/ijms130910970.

[19] G. Yang *et al.*, "Assessment of the characteristics and biocompatibility of gelatin sponge scaffolds prepared by various crosslinking methods," *Scientific Reports*, vol. 8, no. 1, Dec. 2018, doi: 10.1038/s41598-018-20006-y.

[20] N. Shahgholian, G. Rajabzadeh, and B. Malaekeh-Nikouei, "Preparation and evaluation of BSA-based hydrosol nanoparticles cross-linked with genipin for oral administration of poorly water-soluble curcumin," *International Journal of Biological Macromolecules*, vol. 104, pp. 788–798, Nov. 2017, doi: 10.1016/j.ijbiomac.2017.06.083.

[21] R. Luo *et al.*, "Genipin-crosslinked human serum albumin coating using a tannic acid layer for enhanced oral administration of curcumin in the treatment of ulcerative colitis," *Food Chemistry*, vol. 330, Nov. 2020, doi: 10.1016/j.foodchem.2020.127241.

[22] J. Lin *et al.*, "Genipin-crosslinked sugar beet pectin-bovine serum albumin nanoparticles as novel pickering stabilizer," *Food Hydrocolloids*, vol. 112, Mar. 2021, doi: 10.1016/j.foodhyd.2020.106306.

[23] H. J. Lee *et al.*, "Enzyme delivery using the 30Kc19 protein and human serum albumin nanoparticles," *Biomaterials*, vol. 35, no. 5, pp. 1696–1704, Feb. 2014, doi: 10.1016/j.biomaterials.2013.11.001.

[24] M. Tarhini *et al.*, "Human serum albumin nanoparticles as nanovector carriers for proteins: Application to the antibacterial proteins 'neutrophil elastase' and 'secretory leukocyte protease inhibitor,'" *International Journal of Pharmaceutics*, vol. 579, Apr. 2020, doi: 10.1016/j.ijpharm.2020.119150.

Bitlis Eren Üniversitesi Fen Bilimleri Dergisi
BİTLİS EREN UNIVERSITY JOURNAL OF SCIENCE
ISSN: 2147-3129/e-ISSN: 2147-3188
VOLUME: 11 NO: 2 PAGE: 620-629 YEAR: 2022
DOI: 10.17798/bitlisfen.1071340

Implementation of Fuzzy Expert System as a Decision Support System in the Personnel Development Processes

Fulya ASLAY[1*]

[1]*Computer Engineering Department, Erzincan Binali Yildirim University, Erzincan, Turkey (ORCID: 0000-0001-5212-6017)*

Keywords: Fuzzy expert system, Decision support system, Personnel improving, Personnel evaluation.

Abstract

In this day where quality personnel employment is also important for the production of quality products and services, the organizations evaluate the performances by their performance management systems within the organization and try to achieve their targeted business performance by determining appropriate training and development programs. The development activities are spread over a longer period, as they are individual and continuous, and require the implementation of individual development activities. When the studies in the literature are examined, it is observed that standardized development activities are generally applied to the employees in this process and mostly socio-psychological factors are not taken into consideration. In this study, a decision support system, in which the employees' knowledge and skills, psychological status, communication skills, job satisfaction and demographic characteristics can be evaluated, has been developed in order to assist managers in their decision-making during the job placement and development processes of the employees. It will be possible to obtain the maximum efficiency and work performance with minor cost and time by planning the development activities in accordance with the needs and situation of each personnel thanks to the system developed in the study.

1. Introduction

In a globalizing world, the conditions of competition are constantly increasing and forcing businesses to be better in every respect. Accordingly, the employment of qualified personnel for the production of quality products and services is gaining importance gradually. The phenomenon of development and change, which is already the return of the modern era, requires the restructuring of each organization and thus the determination and development of the employee needs. In this context, the organizations evaluate performance by their performance management systems within the organization and try to achieve their targeted business performance by determining appropriate training and development programs [1].

For increasing the performance in the organizations, on one hand, the training activities are performed in order to allow the personnel to have technical and professional knowledge that he needs in daily business life and on the other hand, development activities are performed in order to allow the personnel to develop his knowledge, skills and behaviors that he will need for doing his job better [2], [3]. These development activities require a longer process as they are individual and continuous.

In the literature and in practice, there are many methods especially for personnel selection and these methods are mostly applied to the candidates in recruitment processes. However, as much as the personnel selection, it is also very important that the personnel is placed in the right position and then trained [4]. When the studies in the literature are examined, it is observed that mostly socio-psychological factors are not taken into consideration in this process [5]. However, the employees encounter many socio-psychological phenomenon both in their

*Corresponding author: faslay@erzincan.edu.tr
Received: 10.02.2022, Accepted: 24.03.2022

workplaces and in their daily lives, and these factors directly affect the work performance of employees [6].

In this study, a decision support system, in which the employees' knowledge and skills, psychological status, communication skills, job satisfaction and demographic characteristics can be evaluated, has been developed in order to assist managers in their decision-making during the job placement and development processes of the employees. In this way, it is aimed to enable the employees to work in job positions where they can be most productive and to benefit from the development programs just for themselves by identifying the shortcomings of each employee. In addition, by means of the system developed in this study, it is possible to support the managers regarding the evaluation of employees' existing job positions, their promotions, their dismissals or their assignment to another job position. On the other hand, it's also possible to evaluate the shortcomings of the employees and therefore to obtain maximum efficiency and work performance by implementing a special development program only for that employee and especially by saving cost and time.

This study consists of five parts. In the second part, detailed information about personnel development is given and a summary of the studies in the literature is presented. In the third part, the performance criteria determined for this study (stress and anxiety, anger, job satisfaction, communication and business knowledge) is discussed. In the fourth part, the expert systems and fuzzy expert systems are described and in the fifth part, the fuzzy expert system and the user interface of this system developed by taking into consideration the professional and technical information of the employees as well as the socio-psychological and demographic characteristics have been introduced. The study concludes with the conclusion and discussion part.

2. Personal Improving

The development consists of implementing and developing strategy and plans to improve the performance of individuals and groups in order to improve the long-term competitiveness potential of an organization; implementing the performance plan and revision processes; promoting education, long-term personal development and team development to increase the capacity of individuals [7], [8].

Organizations can achieve targeted corporate performance only if the employees perform their activities in a quality way. In order to achieve organizational goals, it is important that the employees are motivated to develop individual performance skills, to understand the relationship between institutional goals and individual goals [9]. However, the employees of an organization may not always perform the desired or expected performance from them in their existing job positions. While the performance of the employee may be below the expected performance, it is another reason that the actual performance of the employee may be higher than the performance required by the job. [10]. The first problem is considered as a problem and it's tried to be solved by improvement and development efforts, and the second problem is mostly ignored. The second issue, which we encounter, should be emphasized especially in terms of evaluation of the possible opportunities by the company, verification of employee's job satisfaction and employee's efficiency. In this way, in case that a balanced match between job positions and employee capacity is achieved, it will be possible for the enterprise to achieve a higher performance than the average and to gain a competitive advantage that can compete with its competitors.

In case that the employee doesn't provide the qualifications required by the job position, the enterprises may perform development methods for the employees. This development process depends on four factors. These are organization, human resources department, employer and the individual himself. If any negativity is experienced due to any of these factors, the benefit of development may decrease [11]. In addition, performance development should not only be a study that is aiming the unsuccessful personnel but at the same time it should be aiming the performance development of the successful employees [12]. In this context, there may be various motivations for development. For example, while the subordinate focuses on an upward mobility by asking "What can I do to get promoted", the manager may want to increase the motivation and productivity of the employees by asking "What can I do to encourage my employees to do their best". On the other hand, a senior executive may address issues like what it takes to keep and develop the most talented ones in order to make them support leading the company in the future by asking "What shall we do in order to ensure that the most skilled people in our company are in the right positions" [13].

On the job trainings are usually provided to increase the job performance of employees in organizations. The aim of these trainings is to enable the personnel to have the knowledge, skills and behaviors that they may need in their daily work life.

Unlike Training, the development is the activities that will help the personnel to upgrade his existing skills and thus to perform and to be productive at the desired level, in addition to the knowledge and skills that the personnel needs in order to do his job better. The development can't be considered as a short-term activity like training. The development is individual and continuous. However, it must be known that there won't be any development without training. Training and development are integral parts of a process. The training is performed in order to add new ones to the ones previously learned by an individual. And in the development, it's aimed to make full use of the capacity of the employees and to increase this capacity further [14].

Development activities are carried out especially in order to increase the performance. In the study in [15], it has evaluated the components affecting performance improvement in the following six dimensions;

- ✓ Information (information) development is ensuring that the employee has sufficient information about the quality and quantity of the performance expected from him.
- ✓ Knowledge (knowledge) and skills development means developing the knowledge and skills required for the expected performance of the employee.
- ✓ Motivation development is providing sufficient motivation to the employee in order to make him realize what is expected from him.
- ✓ Structure and process development is the arrangement of the structure and processes in which the employee takes part in such a way that will facilitate the performance expected from him.
- ✓ Development of working tools and conditions is improving the working tools and conditions in a way that will support employee's performance.
- ✓ Health development means supporting the employee if the employee's mental, physical and mental health prevents the employee from performing the expected performance from him.

Personnel development has two dimensions, both individual and organizational. Personnel development programs let people learn, be open to new ideas and receive feedback from their colleagues, take decisions on their own and perform them, self-assess, create goals for development and improve their power of analysis. Personnel development program is developed in the organization in order to meet the objectives, improve the quality of relationships for developing group effectiveness, develop a professional working climate, developed a structure that facilitates development, eliminate the structures and factors that fail to perform their tasks and create processes that provide feedback for continuous regeneration [16].

In the study in [16] it is conducted a study on the development of managers and teachers working in primary schools. According to the findings, he emphasized that in the personnel development program to be organized for administrators and teachers, it's necessary to give importance to emotional, mental and physical development especially for female staff, and also to consider the characteristics such as gender, seniority, duty, level of education while organizing personnel development programs. In the study in [17] it is researched the status of training activities for the development of human resources in small and medium-sized enterprises by a survey and it has been emphasized that training activities were carried out in a way that was inconsistent with the program development perspective, the activities for the determination of the requirements were not performed sufficiently or the educational institutions were sending their own personnel to the training programs that they suggested through notification. In the study in [18] it is examined the effect of employee satisfaction on employee performance by training and development activities in the companies. Because of his survey, he stated that the training and development granted to company employees had a positive effect on employee satisfaction and performance. In the study in [19] it is examined the evaluation of the effects of training and development provided by human resources in the companies on employee performance, and also the positive and negative effects of training and development on employees. According to this, he stated that in the light of the career, material, productivity, positivity and psychological effects of the employee, the trainings provided within the institution have positive results. In addition, he reached the conclusion that training and development activities within the company satisfied the employees averagely. In the study in [20] it has been comprehensively addressed the issues of performance, learning and development, guidance-based learning and development conceptually, and has proposed a model for development-oriented performance management by taking expert and practitioner views on the subject. The model is based on one-to-one training and development process, such as mentoring or coaching. In the study in [21] it has

been researched the relationship between the human resources management and job satisfaction. According to this, he has defended that increasing the level of success in the human resources management functions of enterprises will make a significant contribution to achieving their organizational goals and increase the performance of their employees. Especially, he emphasized that the enterprises should review and improve continuously their overall functions such as personnel selection and placement, performance evaluation, remuneration and rewarding, career management, training and development, and their level in occupational health and safety function. In the study in [22] it is tried to determine the effect of performance empowerment on performance and efficiency with the survey that he conducted on bank employees by emphasizing that empowerment is one of the most important elements of human resources development. According to this, he stated that performance strengthening has no effect on performance but it has an impact on efficiency.

On the other hand, there are decision support systems in the literature that use various techniques developed to evaluate personnel for personnel development or recruitment. In the study in [23] it is proposed a fuzzy Analytic Hierarchy Process (AHP) based model that can be used to select the personnel by using general and personal criteria such as education, foreign language, experience, age, physical appearance, effective time use, and teamwork skills. In the study in [24] it is used Gray Relational Analysis (GRA) and Technique for Order of Preference by Similarity to Ideal Solution (TOPSIS) methods to select research and development personnel. In the study, the benchmark weights and linguistic variables showing the qualities of the candidates were expressed in gray numbers, and the ranking was made according to the gray relationship degrees. In the study in [25] it is evaluated the degree of adaptation between the characteristics of the employees and the needs of the employer by taking into account factors such as foreign language skills, computer skills, experience, age, military service, gender, non-smoking personnel, driver's license and education graded by 3 different authorities in an enterprise by combining Matlab fuzzy tool and Preference Ranking Organization Method for Enrichment of Evaluations (PROMETHEE) method which is one of the multi-criteria decision making methods. In the study in [26] it is proposed a TOPSIS based approach for the selection of senior executives and considered the fuzzy TOPSIS method with veto thresholds. In the study in [27] it is addressed the problem of personnel selection for an institution providing training services by using GRA and Gray Analytical Network Process (GANP) in an integrated way to solve group decision making problems involving both subjective and objective criteria. In the study in [28] it is proposed an intuitive fuzzy multiple criteria group decision-making method with GRA in the selection of the appropriate one among four candidates for the system engineering position in a software company.

3. Personnel Improving Performance Critters

The performance criteria required by any business position in the enterprises refer to the criteria required for the successful performance of that business. These criteria can be listed as the knowledge and skills required by the job, personal characteristics and expected results/outputs. In addition, productivity, self-development effort, management skill, cooperation and communication skill is also the recommended elements to be considered as general performance criteria [29]. After the determination of main performance criteria, the important sub-criteria can be determined for each criteria according to the quality of the job and employee.

When the studies conducted on personnel development and presented in the second part are examined; in the studies it is observed that the performances of people are mostly evaluated with traditional performance evaluation scales or behavioral expectation scales such as quantity and quality of work, knowledge level, cooperation and communication skills, undertaking etc.

In this study, demographic, psychological, personal and professional characteristics of the employees were evaluated together in order to enable employees to benefit more effectively from personnel development programs. According to this, “stress and anxiety”, “anger”, “job satisfaction”, “communication level”, “professional knowledge level” criteria are evaluated according to the following methods.

Stress and anxiety level of the employees have been evaluated by a scale developed in [30]. According to this, at this scale, which is developed to measure job stress, psychological and psychosomatic symptoms related to the stress experienced by the employee at work are measured. On the scale consisting of 7 questions, answers are measured with 5-point Likert scale.

The anger states of the employees are measured by the Multidimensional Anger Scale developed in [31]. On this scale, people's feelings, thoughts and attitudes about anger are determined.

The questions on the scale consisting of 5 parts are being scored between 1 to 5 as Likert type.

For the evaluation of employees' job satisfaction, a four point Likert type scale has been used consisting of 10 items developed in [32]. Items in the scale are scored between 1 and 4. Here, the lowest and highest scores in the scale will be between 10 and 40 and 20 and higher scores will be considered as job satisfaction.

And the communicational skill of employees is being evaluated in [33]. It's a five point likert scale and it consists of 25 statements. The excess score obtained from the scale without the contrary items means that individuals evaluate their own communication skills positively.

Occupational knowledge of the employees is measured by the questions prepared by the managers and experts determined within the institution according to the employees' area of specialization. Here, each point received by the employees according to five different criteria is calculated according to the rating level from 1 to 10 (1 is the lowest and 10 is the highest) and it is provided that all points taken from the criteria are evaluated on the same scale.

4. Fuzzy Logic and Fuzzy Expert Systems

4.1 Fuzzy Logic

Fuzzy logic, based on fuzzy sets, helps in modeling uncertain and imprecise data in the real world by enabling the realization of the processes similar to human thought in [34]. In the classical set concept, an element is either an element of a set or it is not, and a there can never be a partial membership to a set. If the element's membership value is 1, then it is the complete element of the set, if it is 0, then it is not the element of the set. In other words, the membership of the elements can only have [0, 1] values in the classical sets. Unlike classical sets, membership degrees of the elements in the fuzzy sets can have an infinite number in the range of [0, 1] as shown in Figure 1.

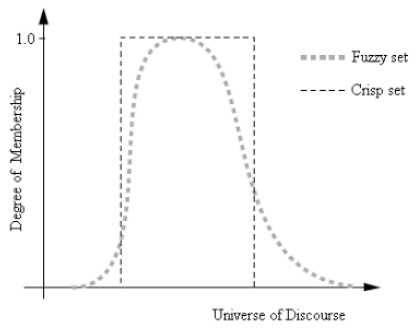

Figure 1. Illustration of a crisp and a fuzzy set.

4.2 Fuzzy Expert Systems

The experts, who specialize in tasks that require expertise, make logical inferences and reach conclusions based on the information in their fields. In cases where adequate specialists cannot be reached or where the employment of specialist is expensive or limited, the systems used to make conclusions by transferring the opinions of experts to an informatics system and making inferences are called expert systems. Expert systems consist of the following components [35];

- ✓ Database that contains facts, rules and information about a certain problem;
- ✓ Inference Mechanism that uses the information stored expertly to find solutions to problems;
- ✓ User Interface that ensures communication with the user;
- ✓ Information Acquisition Module that helps to improve the database

Fuzzy expert systems are expert systems consisting of blurring, inference, knowledge base (rule base and database) and defuzzification subsystems, which use fuzzy logic instead of classical logic in data processing [36]. By applying the fuzzy logic developed by Lotfi A. The definitive statements on the input and output of the expert systems are expanded to fuzzy expressions sets and these developed expert systems may exhibit closer expertise to the human justice system [37]. In this way, expert systems that adapt better to real life problems can be developed by eliminating small errors and small uncertainties in the input data and the sharp limits in the logic of inference. The structure of a fuzzy expert system is shown is Figure 2 [38].

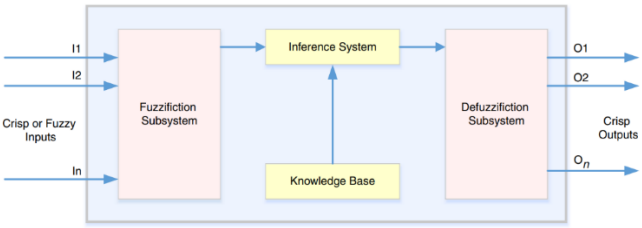

Figure 2. Structure of a fuzzy expert system.

In a fuzzy expert system, the inputs are taken as crisps and the input values are blurred by using the input membership functions whose boundaries and shapes are defined by the actual experts of the job. The inference mechanism in the fuzzy expert system, evaluates the data coming from the blurring block with the rules in the rule base and produces fuzzy output data appropriate to input data. The fuzzy data

in the output of this block are also presented to the output as definite values by using the output membership functions and the defuzzification method whose boundaries and the shapes are determined by the experts. All this process can be monitored comprehensibly by a prepared user interface and the parameters can be changed.

5. Developed Decision Support System

Expert knowledge, incomplete and uncertain information and situations can be modeled by using artificial intelligence techniques such as expert systems, fuzzy logic, artificial neural networks in decision support systems. Decision support systems using these techniques are called intelligent decision support systems. Since intelligent decision support systems give successful results, a decision support system has been developed with the fuzzy expert system in this study. The block diagram of the personnel assessment decision support system developed within the scope of the study is given in Figure 3.

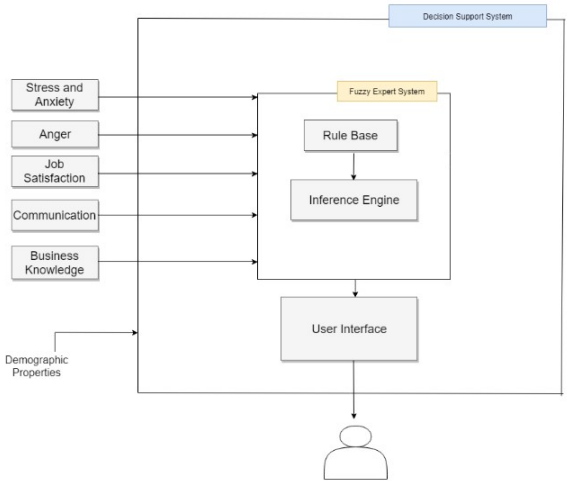

Figure 3. Structure of the decision support system.

In this context, first of all, each personnel, who is wanted to be evaluated, has been evaluated by stress & anxiety, anger, job satisfaction, communication and business knowledge scales that were presented in the previous chapters. The indicators of scales are different from each other and each of these are between 0-10 and each personnel gets a definite point between 0-10 for each of this criteria in the system. Also, according to the professional knowledge, a definite point is obtained again between 0-10 by performing measurements with a professional test according to employee's professional field. For each criteria, definite values are entered in the fuzzy expert system as an input. The membership function, which is prepared thanks to the opinion of the experts and used to blur "low, medium, high" linguistic values of all inputs, is shown in Figure 4.

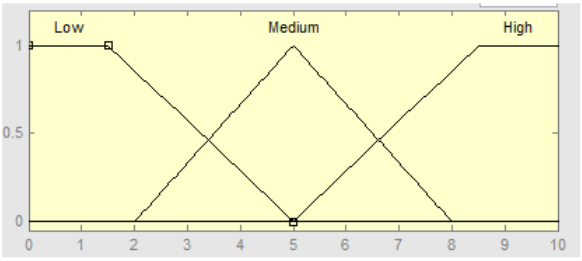

Figure 4. Membership function regarding all input criteria.

In the developed system, two-stage inference mechanism has been applied. In the first stage, Max-Min inference mechanism developed in [39] has been used for inference. In this model, the premise (rule's "if" part) and final part (rule's "then" part) consist of fuzzy propositions. The weighted average method is used for defuzzification. The inference mechanism consists of 35 rules because there are 5 criteria in the system and each criteria has 3 fuzzy sets. The rules are created with the knowledge and experience of a group of experts consisting of a manager, a human resources personnel and a psychologist. The weight of all rules is equal. The fuzzy values obtained as a result of inference mechanism are defuzzied by the membership function shown in Figure 5 and consisting of five sets determined also by the experts as "very low", "low", "medium", "high", "very high". After the defuzzification, "Result" intermediate output, where employee status assessment is performed in the system, is produced.

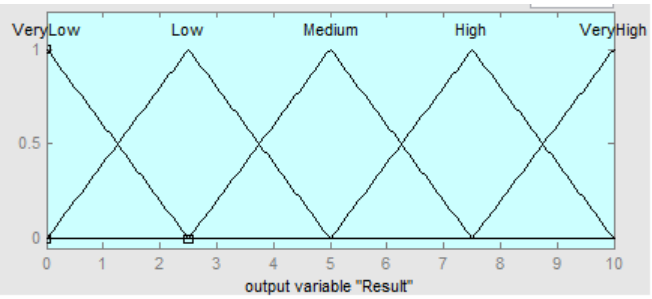

Figure 5. Membership function regarding result.

In the second stage, Takagi-Sugeno mechanism produced in [40] is used for inference. In this model, while the premise of the rule is defined as

a fuzzy, the final part contains definite values and it is defined as a linear function of input variables. In the system, the status of the employees according to all their input criteria is evaluated by Sugeno and "Action To Be Done" output.

According to the linguistic values, in compliance with five sample employees' criteria, "Result" output determined by mandami and the development program output that is necessary to be applied to the employee determined by sugeno is shown in Table 1.

Owing to the created rules, each criteria is evaluated jointly and an inference is made for the operation which is necessary to be applied to each employee accordingly. There will be no training and development for those in very good condition. For the ones in a very bad situation, no training will be given and they can be dismissed after their demographic characteristics in the decision support system are also evaluated.

For the decision support system developed in the study, demographic characteristics are defined as indispensable criteria or a preferable criterion according to the job position. Thus, by considering the demographic characteristics required from the employees, their positions in the work place can be reassessed. All criteria used for decision support system is shown in the following Table 2.

Table 1. Evaluation of employees according to the criteria and development program to be implemented.

No	Stress & Anxiety	Anger	Job Satisfaction	Communication	Business Knowledge	Result	Action
1	High	High	Medium	Low	Low	Very Low	No operation (Very Bad)
2	Medium	High	High	Low	Medium	Low	Intense Anger and communication, medium business knowledge
3	High	High	Medium	Medium	Medium	Low	Intense Stress and Intense Anger Training
4	High	Low	High	High	Medium	Medium	Intense Stress and Medium Business Knowledge Training
5	Low	Medium	Low	Medium	High	Medium	Organizing Business Conditions
6	Low	Low	Medium	Low	High	High	Intense Communication Training
7	Low	Medium	High	High	High	Very High	No operation (Very Good)

Table 2. Criteria used for decision support system.

Features	Performance Scales	Measurement Value
Psychological	Stress and Anxiety	Fuzzy Categorical (Low, Medium, High)
	Anger	Fuzzy Categorical (Low, Medium, High)
	Job Satisfaction	Fuzzy Categorical (Low, Medium, High)
	Business Knowledge	Fuzzy Categorical (Low, Medium, High)
	Communication Skill	Fuzzy Categorical (Low, Medium, High)
Demographic	Gender	Binary (Men, Women)
	Age	Categorical (18-25, 26-35, 36-45, 46-55, 56-70)
	Educational Level	Categorical (High School, Bachelor's, Master's, Doctorate)
	Marital Status	Binary (Single, Married)
	Driving License	Binary (Yes, No)
	Military Service	Binary (Related, No Connection)
	Language Skill	Categorical (0-20, 21-40, 41-60, 61-80, 81-100)
	Computer Skill	Categorical (0-20, 21-40, 41-60, 61-80, 81-100)

The user interface of the developed application is shown in Figure 6. Here; Questioning by ID number, the department where employees work and demographic characteristics are displayed. In the interface, the assessment of employee no.6 is presented in Table 1. In the third part of the study, the results of tests conducted according to the detailed performance criteria are entered in scale 1-10. After clicking "Evaluate" button, first of all, the assessment is performed between the ranges of Very Low - Very High related to the overall result of the employee that has mamdani output (Overall Result). In addition, according to the employee's information, advice of the programs that can be applied for personnel development (Improving Advice) and advice of the position change (lower level, promotion, management position, etc.) (Position Advice) that may be in the institution, if any, is given.

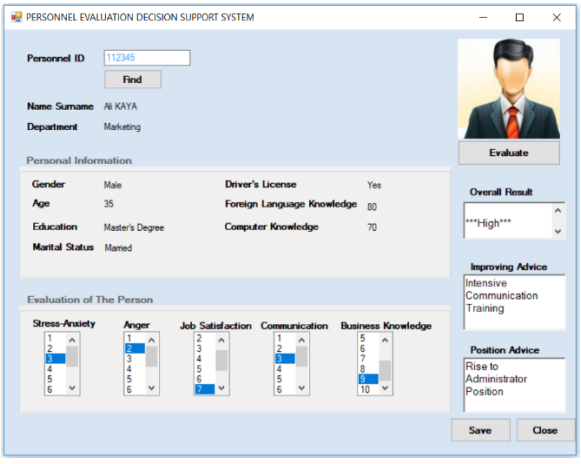

Figure 6. The User interface.

6. Conclusion and Discussion

In this study, a decision support system has been developed in order to assist managers in their decision-making during the job placement and development processes of the employees. This system has two stages; at the first stage, the employees were evaluated in terms of the performance criteria determined in the third part, which are "stress and anxiety", "anger", "job satisfaction", "communication". In addition, for "business knowledge" criteria, occupational success levels of individuals are determined in the range of 1-10 points by applying a test with professional questions appropriate to their work areas. With the developed fuzzy expert system, the crisp values obtained from these tests are blurred in three categories as "low", "medium" and "high". And this way, according to these criteria, a status detection is performed for each employee at five different levels: "very low", "low", "medium", "high", "very high".

At the second stage, a decision support system is applied in which the people's demographic characteristics are assessed in order to assign the most appropriate person to a job position or determine if the existing employees are suitable for their jobs and also plan appropriate individual development programs for the employee. The compliance of the characteristics such as gender, age, education level, computer skills, and years of work with the job position is evaluated.

Finally, considering both stages and the demographic characteristics of the personnel who is in a bad position both psychologically and professionally, his compliance with the job can be assessed and he can be left out of the staff before any investment is made. On the other hand, a better level

can be achieved with the related training and development methods which will be applied to the personnel at a low, medium and high level psychologically and professionally. The personnel in the best status in terms of all characteristics can be promoted to a manager position or they can be considered as ready to take additional responsibility.

With the system developed in the study, it will be possible to plan the development activities in accordance with the needs and status of each personnel and to obtain maximum efficiency and work performance with less cost and time. In addition, the employees who need to be dismissed are determined and it's provided that the most appropriate employees are chosen for the job positions. The advantage of other studies is that the effects of psychological factors on employees are included in the decision support system.

Finally, the outputs of the developed system are compared with the opinions of an expert team consisting of a senior executive, a department manager and a psychologist and the success of the system has been %100 confirmed by experts.

Statement of Research and Publication Ethics

The study is complied with research and publication ethics.

References

[1] C. Akinci, and E. S. Smith, "Collective Intuition: Implications for Improved Decision Making and Organizational Learning," *British Journal of Management*, vol. 30, pp. 558-577, 2019.

[2] O. Tregaskis, and P. Almond, "Multinationals and Skills Policy Networks: HRM as a Player in Economic and Social Concerns," *British Journal of Management*, vol. 30, pp. 593-609, 2019.

[3] C. B. Uyargil, A. C. Acar, A. O. Özçelik, G. İ. Dündar, V. L. Tüzüner, and Ö. Z. Sadullah, *Human Resources Management*, Beta Publishing, Istanbul, 2015.

[4] I. Findikci, *Human Resources Management*. 7. Edition, Alfa Publishing, Istanbul, 2019.

[5] M. Cetin, "Development of Public Relations from Organizational Theories Perspective," *Gazi University Journal of Communication Theory and Research*, vol. 18, pp. 33-44, 2003.

[6] F. J. Froese, V. Peltokorpi, A. Varma, and A. H. Hansel, "Multinationals and Skills Policy Networks: HRM as a Player in Economic and Social Concerns," *British Journal of Management*, vol. 30, pp. 610-623, 2019.

[7] T. Gruenberg, "Performance Improvement - A Method to Support Performance Improvement in Industrial Operations," Ph.D. Thesis, Department of Production Engineering Royal Institute of Technology, Stochkolm, 2007.

[8] T. C. Kassaneh, V. Havinal, "Investigation of Company-wide Performance Factors in Ethiopian Leather Footwear Industry," *Research Journal of Social Science and Management*, vol. 7, pp. 13-22, 2017.

[9] I. Barutcugil, *Performance Management*. Kariyer Publishing, Istanbul, 2002.

[10] M. Gursoy, "Human performance technology model in improving employee performance and performance technology situation and attitude survey," M.S. Thesis, Marmara University Social Sciences Institute, Istanbul, 2003.

[11] K. Eroglu, "Development and Function of the Human Resources Department in Enterprises," *Kurgu Journal*, vol. 16, pp. 255-270, 1999.

[12] C. Uyargil, *Performance Evaluation*. Human Resources Management, Beta Publications, Istanbul, 2013.

[13] M. Inan, Çalışanları Geliştirmek, Hergün Karşılaştığınız Sorunlara Uzman Çözümler. Harvard Business School Publishing, Istanbul, 2009.

[14] R. Kasımov, "The Importance of Training and Development in Human Resources Management: An Application in Large-Scale Enterprises Operating in Azerbaijan," M.S. Thesis, Nigde University Social Sciences Institute, Nigde, 2006.

[15] E. Sanders, S. Thiagarajan, *Performance Intervention Maps*. American Society for Training and Development, USA, 2001.

[16] I. Aydogan, "Views of MEB Primary School Administrators and Teachers on Personnel Development," Ph.D. Thesis, Ankara University Institute of Education Sciences, Ankara.

[17] I. Sokmen, "An analysis of human resources development activities conducted in small to medium sized enterprizes (SMEs)," M.S. Thesis, Anadolu University Educational Sciences Institute, Eskisehir, 2010.

[18] N. Ozyurt, "Training and Development in Human Resources," M.S. Thesis, Beykent University Social Sciences Institute, Istanbul, 2013.
[19] S. Hatay, "The Importance of Education Development Function in terms of Performance Management System and a Research," M.S. Thesis, Istanbul Arel University Social Sciences Institute, Istanbul, 2014.
[20] G. O. Cavusoglu, "Guidance based learning and development processes for high performance in organization and a model suggestion," M.S. Thesis, Maltepe University Social Sciences Institute, Istanbul, 2015.
[21] G. Demirkaya, "The relationship between human resources management functions and business satisfaction: A research on alumni of Kocaeli University aerospace and space sciences faculty," M.S. Thesis, Kocaeli University Social Sciences Institute, Kocaeli, 2015.
[22] E. Merdan, "Investigation of Effect of Personnel Improvement on Performance and Efficiency: An Application in the Banking Sector," M.S. Thesis, Gumushane University Social Sciences Institute, Gumushane, 2018.
[23] Z. Gungor, G. Serhadlioglu, and S. E. Kesen, "A Fuzzy AHP Approach to Personnel Selection Problem," *Applied Soft Computing*, vol. 9, pp. 641-646, 2009.
[24] D. Wang, "Extension of TOPSIS Method for R&D Personnel Selection Problem with Interval Grey Number," International Conference on Management and Service Science, Beijing, China, Sept. 20-22, 2009, 1-4.
[25] T. Dereli, A. Durmusoglu, S. U. Seckiner, and N. Avlanmaz, "A Fuzzy Approach for Personnel Selection Process," *Turkish Journal of Fuzzy Systems*, vol. 1, pp. 126-140, 2010.
[26] A. Kelemenis, and D. Askounis, "A New TOPSIS-Based Multi-Criteria Approach to Personnel Selection," *Expert Systems with Applications*, vol. 37, pp. 4999-5008, 2010.
[27] E. Kose, H. S. Aplak, and M. Kabak, "An Integrated Approach Based on Grey System Theory for Personnel Selection," *Ege Academic Review*, vol. 13, pp. 461-471, 2013.
[28] S. F. Zhang, and S. Y. Liu, "A GRA-Based İntuitionistic Fuzzy Multi-Criteria Group Decision Making Method for Personnel Selection," *Expert Systems with Applications*, vol. 38, pp. 11401-11405, 2011.
[29] E. Isigicok, "Performance Measurement, Management and Statistical Analysis," *Econometrics and Statistics e-Journal*, vol. 7, pp. 1-23, 2008.
[30] R. J. House, and J. R. Rizzo, "Role Conflict and Ambiguity as Critical Variables in a Model of Organizational Behaviour," *Organizational Behaviour & Human Performance*, vol. 7, pp. 467-505, 1972.
[31] J. M. Siegel, "The Multidimensional Anger Inventory," *Journal of Personality and Social Psychology*, vol. 5, pp. 191-200, 1986.
[32] E. Tezer, "Job Satisfaction Scale," *Hacettepe University School of Social Services Journal*, vol. 9, pp. 55-76, 1991.
[33] F. Korkut, "Development of the Communication Skills Evaluation Scale: Reliability and Validity Studies," *Turkish Psychological Counseling and Guidance Journal*, vol. 2, pp. 18-23, 1996.
[34] V. Nabiyev, *Artificial Intelligence-Problems-Methods-Algorithms*. Seckin Publishing, Ankara, 2003.
[35] P. Jackson, *Introduction to Expert Systems*, 2nd Edition, Workingham: Addison-Wesley, 1990.
[36] T. W. Liao, "Classification of Welding Flaw Types with Fuzzy Expert Systems," *Expert Systems with Applications*, vol. 25, pp. 101-111, 2003.
[37] L. A. Zadeh, "Fuzzy Sets," *Information and Control*, vol. 2, pp. 338-353, 1965.
[38] J. R. Llata, E. G. Sarabia, and J. P. Oria, "Fuzzy Expert System with Double Knowledge Base for Ultrasonic Classification," *Expert Systems with Applications*, vol. 20, pp. 347-355, 2001.
[39] E. H. Mamdani, "Application of fuzzy algorithms for control of simple dynamic plant," *Proceedings of the Institution of Electrical Engineers*, vol. 121, pp. 1585 – 1588, 1974.
[40] M. Sugeno, Industrial Applications of Fuzzy Control, Elsevier Science Publishing, New York, USA, 1985.

Bitlis Eren Üniversitesi Fen Bilimleri Dergisi
BİTLİS EREN UNIVERSITY JOURNAL OF SCIENCE
ISSN: 2147-3129/e-ISSN: 2147-3188
VOLUME: 11 NO: 2 PAGE: 630-639 YEAR: 2022
DOI: 10.17798/bitlisfen.1071785

Isolation and Characterization of Alkane Hydrocarbons-Degrading *Enterobacter ludwigii* strain D8 from Petroleum-Contaminated Soils

Ayşe EREN[1], Kemal GÜVEN[1*]

[1]*Dicle University, Faculty of Science, Department of Molecular Biology and Genetics, TR21280 Diyarbakir, Turkey.*
(ORCID: 0000-0002-5601-6808) (ORCID: 0000-0002-0181-3746)

Keywords: Oil pollution, Bacterial characterization, 16S rRNA gene sequence analysis, GC-MS analysis, Bioremediation.

Abstract
A bacterial strain has been isolated from petroleum contaminated soil with in southeastern Turkey. This isolated strain was characterized to determine its hydrocarbon biodegradation potential. Phenotypic features and 16 S gene sequence analysis of rRNA revealed that strain D8 belongs to the *Enterobacter* genus and most closely resembles *Enterobacter ludwigii* (100%). The optimum temperature and pH values for the growth of *E. ludwigii* D8 were found to be 30°C and 5.0, respectively. This bacterial strain grew in long and medium chain hydrocarbons such as 1% decane, pentadecane and squalene separately at the end of 3 days incubation in the basal medium (BM) under optimum conditions. It was shown that *E. ludwigii strain* D8 degraded about 27% of crude oil incubated for 5 days, while it degraded 29% of pentadecane after 3 days of incubation determined by Gas chromatography-MS analysis. The biodegradation potential of petroleum hydrocarbons of *E. ludwigii* strain D8 isolated and characterized in this study indicates that this strain may play a role in the bioremediation process.

1. Introduction

The most common environmental pollutants are petroleum hydrocarbons [1]. Oil spill can cause serious environmental pollution and harm all organisms including plants, animals, aquatic animals and humans [2]. Although oil is a very important resource in the world economy, the operation, transportation and manipulation of oil may result in spills that damage the ecosystem [3]. The accidental discharge and leakage may happen during the extraction, refining and distribution of petrochemical products as well as due to the accidents such as damaged pipes, blasting wells and fire, broken tanks, sinking ships, and wars. Crude oil spills and fires can also pollute ground water and air. Thus, the pollution caused should be treated and cleaned for a safe environment [4]. To clean up crude oil-contaminated sites is an important and preferential task for the maintenance of the nature and mainly succeeded by physical and chemical methods. On the other hand, the uses of these methods are known to be very expensive and need site restoration [5]. There have been many physicochemical and biological methods to assess treatment of environments contaminated with petroleum. However, biological treatment methods are mostly preferred rather than physico-chemical methods using chemical agents, because it is more reliable, capable of succeeding high remediation levels and cost-effective, as well as being simple for low-energy design, setting-up and operation [6,7].

Bioremediation using biological tools is well known to be an efficient, economical and environmentally friendly approach for treatment of oil-contaminated sites [8, 9]. Recently, although a wide variety of microorganisms including archaea, bacteria and fungi that can degrade hydrocarbons within petroleum have been isolated from contaminated soils, bacterial strains are the most

*Corresponding author: kemalg@dicle.edu.tr
Received: 11.02.2022, Accepted: 22.03.2022

plentiful and significant in microbial ecosystems [10-12]. Recent research has identified more than 79 bacterial species capable of degrading petroleum hydrocarbons [13]; *Bacillus* sp., *Acinetobacter* sp., *Alcanivorax* sp., *Achromobacter* sp., *Enterobacter* sp., *Pseudomonas* sp., *Stenotrophomonas* sp., *Ochrobactrum* sp., *Cronobacter* sp., *Nocardia* sp., *Micrococcus s*p., *Pantoea* sp., *Klebsiella* sp. [14-19]. *Enterobacter* genus is Gram-negative, facultative aerobic, rod-shaped, non-spore-forming, which belongs to the family *Enterobacteriaceae*. *Enterobacter* species are universal bacteria that live in various aquatic and terrestrial environments (soil, water, food and sewage), as well as being important human opportunistic pathogens. *Enterobacter ludwigii* belongs to the *Enterobacter cloacae* complex [20-22]. There have been a few reports on *E. cloacae* strains degrading hydrocarbons. *E. cloacae strain* S1:CND1 isolated from oil-contaminated soil has been found to degrade alkanes, such as n-hexane and n-hexadecane, polyaromatic naphthalene, as well as diesel and crude oil [23,24]. Moreover, *E. cloacae* was found to degrade highly hexadecane, heptadecane, tridecane, and docosane in diesel oil after two-week incubation by 99.71%, 99.23%, 99.66%, and 98.34% respectively [25].

This study aims to investigate and characterize the bacterium *Enterobacter ludwigii* strain D8 isolated from petroleum-contaminated soils and to determine its potential of petroleum hydrocarbon biodegradation.

2. Material and Method

2.1. Sample Collection and Bacterial Isolation

For the isolation of bacterial strain that degrade petroleum hydrocarbons, a soil sample was taken from oil-contaminated soil around the oil well in Southern Raman (South Raman, petrol station1, Batman) region.

The Basal medium (BM) consisted, per liter: 5.0 mL phosphate buffer, 1.0 mL solution of calcium chloride, 3.0 mL solution of magnesium sulfate, 1.0 mL solution of ferric chloride, as well as 1.0 mL mineral elements at trace levels which contain $ZnSO_4.H_2O$, $MnSO_4$ and $(NH_4)_6MoO_{24}.4H_2O$. 1% of Crude oil was filtered (0.2 mm pore size) and transferred into the medium for determination of the bacterial biodegradation of the hydrocarbons in petroleum. Crude oil used in the experiments was provided from oil refinery in Batman. Contaminated soil (1 g) was transferred into 100 mL BM with1% crude oil and samples were placed in a shaker water bath for incubation at 120 rpm at 30 °C for 5 days. After incubation, 1 mL aliquots were taken from each sample and transferred to freshly prepared BM with crude oil (1%). Following two subculture cycles, the bacterial cells were grown on nutrient agar (NA) at optimum temperature for 5 days. Colonies differed phenotypically on the plates were transferred to NA, and then pure cultures were transferred to BM in the absence or presence of crude oil to determine degradation.

2.2. Morphological, Biochemical and Physiological Characteristics

Gram staining was carried out following the method of Dussault [26]. For growth in liquid medium, the temperature used was in the range between 10 °C and 45 °C, while the pH range was between 4.0 and 12.0. The initial pH of media was calibrated using acidic and basic solutions. Urease test was carried out according to Lanyi [27]. Procedures described within Bergey et al. [28] and Claus and Berkeley [29] were followed to determine different biochemical properties such as indole, oxidase, citrate, catalase and urease activity as well as motility of the studied isolate.

2.3. Antibiotic Resistance

Antibiotic susceptibility of D8 strain was determined using disk diffusion method. Antibiotic multidisc ampicillin (10 µg), lincomycin (15 µg), neomycin (10 µg), novobiocin (5 µg), kanamycin (5 µg), chloramphenicol (30 µg), fucidic acid (10 µg), gentamicin (10 µg), tilmicosin (15 µg), streptomycin (10 µg), penicillin (2-10 units), bacitracin (10 units), nystatin (100 units), tetracycline (30 µg). After the bacterial strain D8 was inoculated on NA, antibiotic discs were placed on NA. Agar plates were placed in an incubator for 48 hours at 30 °C. After incubation, results were obtained by measuring of inhibition zone diameters.

2.4. Phylogenetic Analysis

Identification of the strain D8 was carried out by 16S rRNA gene sequencing. 16S rRNA sequence analysis of the strain was performed by BMLabosis (Ankara). The 16S rRNA gene sequence for strain D8 was determined (D8: 1413). A BLAST search GenBank database to compare sequences (http://www.ncbi.nlm.nih.gov/blast/) was used. 16S rRNA gene similarities were retrieved from the database by identifying the most closely related strains. The phylogenetic tree was built using the Mega X software package.

2.5. Growth of Bacterial Cells in Crude Oil and Single Hydrocarbons

A fresh culture was obtained, which was grown in NB liquid medium for 24 hours. Then it was centrifuged to recover from NB and the pellet was washed with BM. This process was repeated 3 times. Bacteria were incubated in crude oil for 5 days and in single hydrocarbons (1% hexane, heptane, octane, decane, pentadecane, hexadecane, squalene and toluene) for 3 days at 30°C at 120 rpm under optimum growth conditions. Following incubation, the bacterial growth was measured at OD 600 nm. All of these hydrocarbons were obtained from (Sigma-Aldrich, USA).

2.6. GC-MS Analyses of crude oil and hydrocarbon degradation by strain D8

The degradation activities of crude oil and single n-alkanes by the strain were analysed using Gas Chromatography-Mass Spectrometry (GC-MS). The bacterial strain was pre-cultured in Nutrient broth overnight at 30°C. They were then replaced in to 100 mL flasks comprising 25 mL of BM plus 1% single hydrocarbon (pentadecane) or crude oil and incubated under optimum conditions. After incubation, the cells were removed, and the remaining hydrocarbons in NB medium were used for calculating degradation ratio of crude oil and hydrocarbons tested.

3. Result and Discussion

3.1. Collection of Samples and Bacterial Isolation

Oil-contaminated soil sample was taken from near oil well in South Raman (South Raman petrol station1, Batman) area. Soil samples was transferred to BM with 1% filtered-crude oil and incubated for 5 days. After serial dilutions and growth observations on both BM and NB media, one bacterial strain was found to use and grow within crude oil. Figure 1 shows the strain degrades and grow in crude oil (decreasing petroleum layer and increasing bacterial density compared to control).

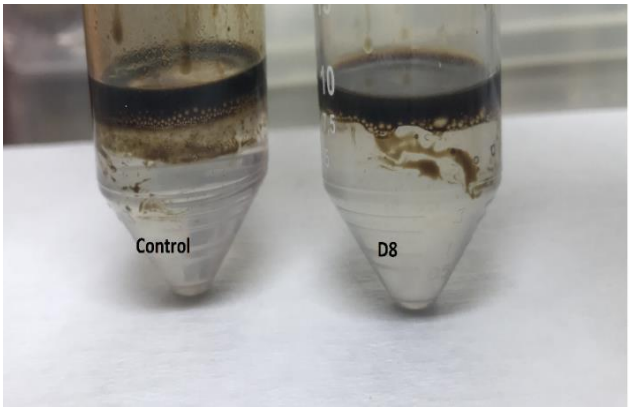

Figure 1. Demonstration of growth of strain D8 at 1% crude oil as carbon source, compared to control.

3.2. Morphological, Biochemical and Physiological Characteristics

The results of the biochemical and morphological tests of isolated strain D8 can be seen in Table 1.

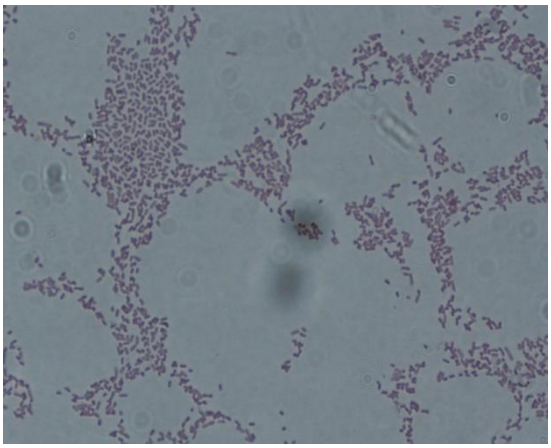

Figure 2. The Gram-staining of the strain D8 observed under light microscope (×1000 magnification).

As seen in Figure 2, the cells are rod-shaped and gram negative. Strain D8 was aerobic, spore forming, motility and starch hydrolysis, catalase, citrate, urease positive and gelatine, oxidase and indole negative (Table 1).

Table 1. The phenotypical characteristics of the *E. ludwigii* strain D8 compared to other related species.

Characteristics	1	2	3	4	5	6
Cell shape	R	NDA	R	R	NDA	R
Gram staining	(-)	(-)	(-)	(-)	(-)	(-)
Spore	(+)	NDA	NDA	(+)	NDA	(-)
Motility	(+)	NDA	NDA	NDA	(+)	(+)
Growth pH	3.0-11.0	NDA	5.0-8.0	6.0-10.0	NDA	NDA
Optimum growth pH	5.0	NDA	6.0	7.0	7.0	NDA
Growth temperature (°C)	20-40	NDA	25-40	28-44	NDA	NDA
Optimum Growth temperature (°C)	30	NDA	30	37	40	NDA
Oxygen requirement	A	NDA	NDA	NDA	NDA	A
Gelatin hydrolysis	(-)	NDA	(-)	(+)	(-)	NDA
Starch hydrolysis	(+)	NDA	(+)	(-)	(+)	(+)
Oxidase	(-)	(-)	(-)	NDA	NDA	NDA
Urease	(+)	(-)	(+)	NDA	NDA	NDA
Citrate	(+)	(+)	(+)	(+)	(+)	NDA
Catalase	(+)	(+)	(+)	NDA	(+)	(+)
Indole	(-)	(-)	(-)	NDA	(-)	(-)
NaCl resistance	7	NDA	NDA	4-12	NDA	NDA

+ = positive; - = negative; NDA= no data available; R=Rod; A= aerobic.

1. *E. ludwigii* strain D8, 2. *E. hormaechei* strain KA6 [30], 3. *Enterobacter* species strain ALK-23 [31], 4. *Enterobacter* sp. strain F3 [32], 5. *E. ludwigii* strain LY-62 [33], 6. *E. ludwigii* strain MS32 [34].

In a similar study, *E. ludwigii* strain LY-62 was gram negative and motile, the starch hydrolysis, catalase, citrate were positive, while gelatin hydrolysis and indole was found to be negative [33]. In addition, studies on most *Enterobacter* strains have shown that they are gram-negative, rod-shaped and motile. It was also found that catalase positive while oxidase was negative in isolated strains studied [30-34].

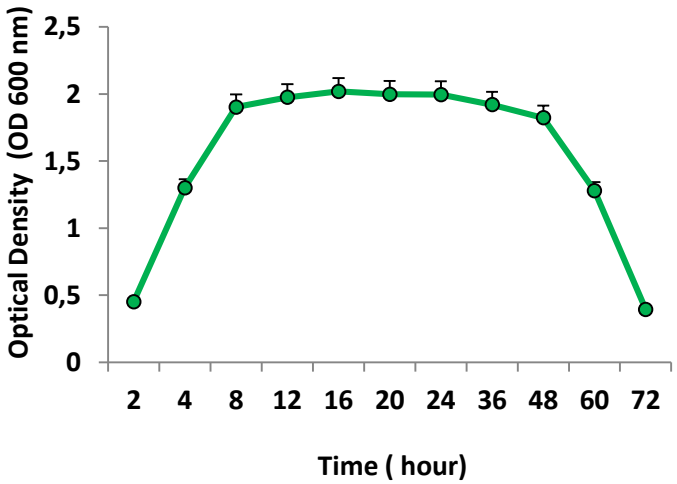

Figure 3. Effect of cultivation time on the strain growth.
Bacterial cells were grown at optimum temperature and pH for 72 hrs.

It was observed that the growth of the D8 strain was maximum between 8 to 24 hours. The growth was then found to decrease up to 72 hours (Figure 3).

a)

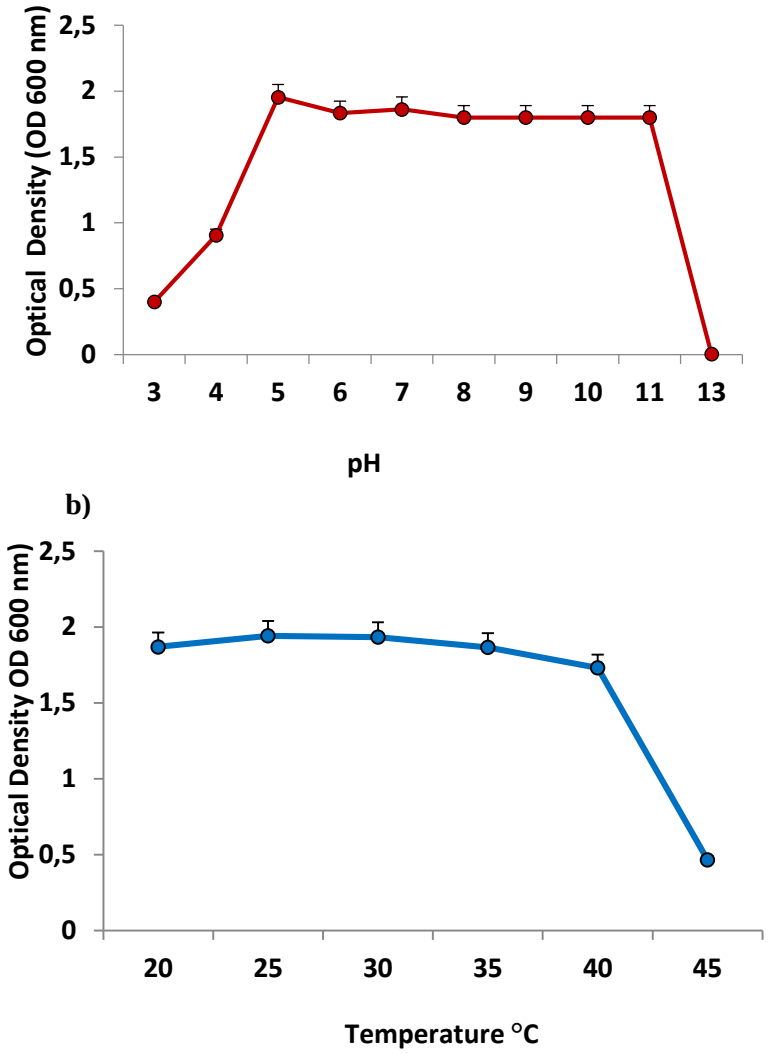

Figure 4. Effects of pH (a) and temperature (b) on the bacterial growth.

For strain D8, the growth range was determined to be between 20-40°C with optimum of 30°C (Figure 4b). In addition, the strain was found to grow in the pH range between 3.0-11.0 (Figure 4a) with optimum value of 5.0. The strain D8 was also found to tolerate up to 7% of NaCl. In a previous study, *Enterobacter* species strain ALK-23 was found to grow at an optimum 30°C in the range of 25-40°C. Also, the pH range in which the strain grows was 5.0 to 8.0 with an optimum pH of 6.0. [31].

3.3. Antibiotic Resistance

D8 was found to be ampicillin, fucidic acid, novobiosin, bacitracin, streptomycin, lincomycin, penicillin, neomycin, kanamycin, nystatin resistant, gentamicin, tilmicosin semi-susceptible, chloramphenicol, tetracycline sensitive (Table 2). *E. ludwigii* CCUG 51323^T strain was also found to be sensitive to gentamicin, but resistant to ampicillin [35].

Table 2. Antibiogram results of D8 (mm: zone of inhibition).

Antibiotics	D8

Novobicin (5 µg)	0
Fucidic acid (10 µg)	0
Kanamycin (5 µg)	12
Bacitracin (10 units)	0
Gentamicin (10 µg)	15
Tilmicosin (15 µg)	18
Ampicillin (10 µg)	0
Streptomycin (10 µg)	12
Chloramphenicol (30 µg)	30
Lincomycin (15µg)	0
Penicillin G (2 units)	0
Tetracycline (30 µg)	33
Neomycin (10 µg)	6
Penicillin G (10 units)	0
Nystatin (100 units)	0

3.4. Phylogenetic Analysis

The gene sequence analysis of 16 S rRNA showed that isolated strain D8 was a member of *Enterobacter* genus. After phylogenetic analysis, phylogenetic dendrogram was drawn, as seen in Figure 5. The bacterial strain designated as D8 was found to be most similar to *E. ludwigii* strain LY-62 (100%). GenBank accession number: MT374261.

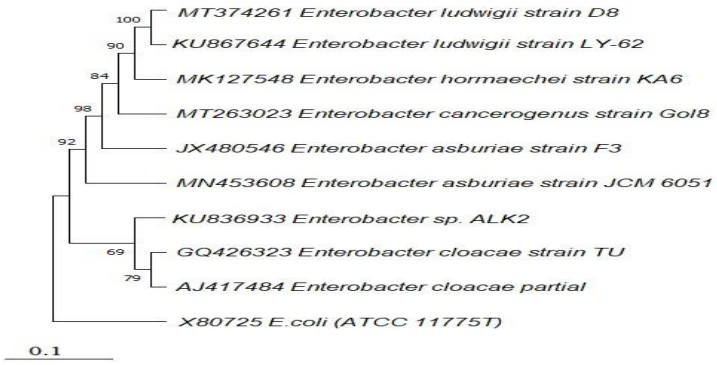

Figure 5. The 16S gene sequence analysis of the strain D8.

3.5. Growth of the Bacterial Strain in Various Hydrocarbons

Figure 6 shows that strain D8 uses alkane hydrocarbons to meet carbon and energy needs. Bacterial strain D8 was found to grow and degrade both medium and long chain alkanes such as decane, pentadecane, hexadecane and squalene instead of short chain alkanes. It was found to degrade pentadecane mostly for effective growth.

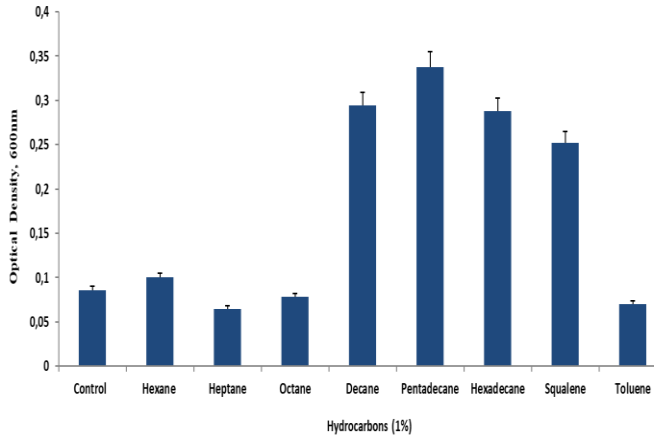

Figure 6. Growth of strain D8 at 1% single hydrocarbon concentrations. Each data represents the mean of at least 3 different experiments.

3.6. GC-MS Analyses of Degradation of Crude Oil and Single Hydrocarbons by the strain D8

Figure 7(A, B) shows gas chromatography-mass spectroscopy and degradation of n-alkanes (C_{11}-C_{33}) by strain D8 in 1%crude oil. GC-MS analysis showed that after 5 days of incubation, strain D8 degraded about 27 % hydrocarbons in crude oil. The total petroleum hydrocarbon degradation values were calculated by using decreased values, compared to abiotic control (Figure 7).

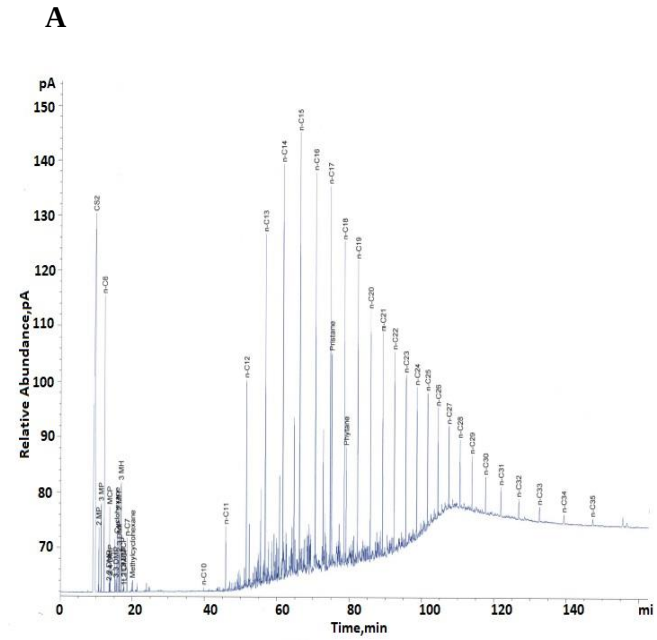

Figure 7. GC profiles of crude oil A) Abiotic control B) After degradation by strain D8. C_{11}-C_{33} represents n-alkanes.

In the present study, it was found that the strain grew better in 1% pentadecane in the basal medium. As seen in Figure 8A and B, the strain also degraded single pentadecane as much as 29% using the gas chromatographic analysis after 3 days of short incubation time.

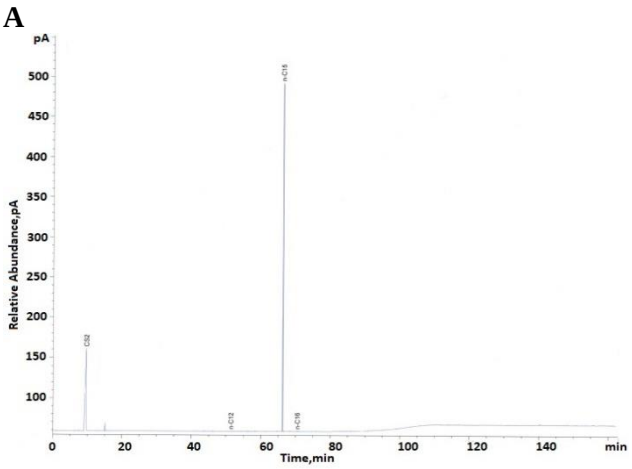

B

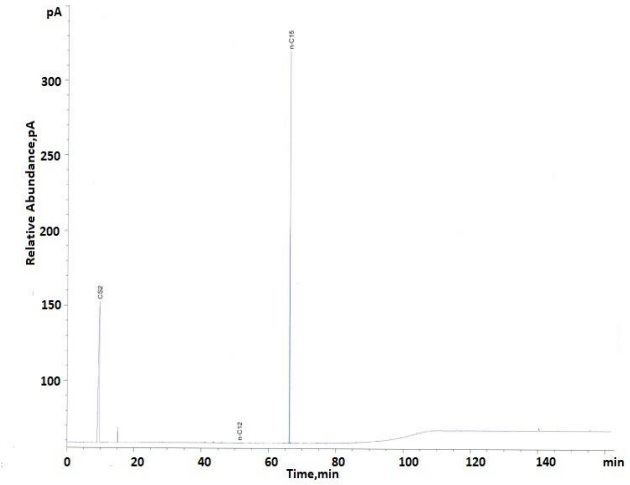

Figure 8. GC-MS Analysis of pentadecane degradation. A) Abiotic control of 1% pentadecane. B) After degradation of 1% pentadecane by strain D8.

Acinetobacter spp. is known that n-alkanes with different chain lengths (C_{10}-C_{40}) are used as the sole carbon source [36]. *Acinetobacter baumannii* MKS2 was found to degrade about 43 % of crude oil after 7 days [37]. In a recent study, GC-MS analysis of the hydrocarbon compounds indicated that the studied crude oil possessed alkanes in the range of C_{20}-C_{44} and *Enterobacter* ALK-23, *B. methylotrophicus* ALK16 and *Alcaligenes* ALK-14 were found to degrade maximum 5.59%, 8.11% and 11.65%, respectively [31]. *Pseudomonas aeruginosa* found 49.93% degradation of 0.5% diesel oil after 20 day incubation period [4]. They found that *P. aeruginosa* showed 34.4% degradation in diesel oil within 10 days [38]. *E. cloacae* TU was found to use n-hexadecane as sole carbon source [23]. However, studies on members of *Enterobacter* sp are mainly focused on degradation of aromatic hydrocarbons rather than n-alkanes degradation. *Enterobacter* sp. strain F3 was used to evaluate naphthalene degradation in petroleum-contaminated soil and a reduction of 61.11% in initial concentration was observed [32]. Kafilzadeh and Khezri [39] revealed that *E. ludwigii* KH-A5 showed highest degradation rate (96%) which is likely to be due to high levels of enzyme production responsible for aniline biodegradation under favourable growth conditions, similar to those of other bacteria reported previously [40,41].

4. Conclusion and Recommendations

Different microorganisms, including bacteria that can break down hydrocarbons in petroleum or single hydrocarbons, have been isolated from soils contaminated with petroleum. Bacteria are most dominant microorganisms in microbial ecology, degrading petroleum hydrocarbons. In the present study, 16S rRNA gene sequence analysis and phenotypic characteristics of the isolated strain D8 from oil-contaminated soil showed that it most closely resembles *Enterobacter ludwigii*. The strain D8 was found to degrade 27% of 1% crude oil incubated for 5 days, whereas it degraded 29% of 1% pentadecane after 3 days of incubation. The strain D8 in the current work appears to break down both crude oil and single hydrocarbons in shorter incubation times, and further microbial consortium studies with the strain of interest may have a good advantage in bioremediation of petroleum-contaminated soils.

Acknowledgements

This study, a part of Ayse EREN's Ph.D project, was supported by Coordination Unit for Scientific Research Projects in Dicle University (Project number: FEN.19.014).

Authors' Contributions

AE: Conceptualization, Data Curation, Formal Analysis, Visualization and Writing-original draft; KG: Funding Acquisition, Project Administration, Resources, Data Curation, Formal Analysis, Investigation, Methodology, Writing-review and editing.

Conflicts of Interest

The authors declare no conflict of interest.

Statement of Research and Publication Ethics

The study is complied with research and publication ethics.

References

[1] Ö. Acer, K. Güven, F. Matpan Bekler and R. Gül-Güven, ''Isolation and characterization of long chain alkane-degrading *Acinetobacter* sp. BT1A from oil contaminated soil in Diyarbakır, in the Southeast of Turkey,'' *Bioremediation Journal*, vol.20, no.1, 2016.

[2] J. Alikhani, J. Shayegan, A. Akbari,''Risk assessment of hydrocarbon contaminant transport in vadose zone as it travels to groundwater table: A case study, *''Advances in environmental technology*, pp.77-84, 2015.

[3] D. Cerqueda-García, J.Q. García-Maldonado, L. Aguirre-Macedo, U.García-Cruza,''A succession of marine bacterial communities in batch reactor experiments during the degradation of five different petroleum types*,'' Marine Pollution Bulletin*, vol.150, pp.110775, 2020.

[4] S.K. Panda, R.N. Kar, and C.R. Panda, ''Isolation and identification of petroleum hydrocarbon degrading microorganisms from oil contaminated environment*,'' International journal of environmental sciences*, vol.3, no.5, pp.1314-1321, 2013.

[5] U.E. Ezeji ,S.O. Anyadoh, and V.I. Ibekwe,'' Clean up of crude oil-contaminated soil,'' *Terr. Aquat. Environ. Toxicol*, vo.1,no.2, pp.54-59, 2007.

[6] G.H. Liu, Z.Yea, K.Tong, Y.Y. Zhang, ''Biotreatment of heavy oil wastewater by combined upflow anaer sludge blanket and immobilized biological aerated filter in a pilot-scale test,'' *Biochem. Eng. J*, vol.72,pp. 48-53,2013.

[7] G. Moussavi, M. Ghorbanian,''The biodegradation of petroleum hydrocarbons in an upflow sludge-blanket/fixedfilm hybrid bioreactor under nitrate-reducing conditions: Performance evaluation and microbial identification,'' *Chem. Eng. J*, vol.280, pp. 121-131, 2015.

[8] M.K. Awasthi, A.Selvam, M. T.Chana, J.W.C.Wong,''Bio-degradation of oily food waste employing thermophilic bacterial strains,'' Bioresour. Technol, vol. 248,pp.141-147, 2018.

[9] Y. Huang ,H. Pana Q. Wang, Y. Ge, W. Liu, P. Christie,'' Enrichment of the soil microbial community in the bioremediation of a petroleum-contaminated soil amended with rice straw or sawdust,'' *Chemosphere*, vol. 224, pp.265-271,2019.

[10] Ö. Acer, K. Güven, A. Poli, P. D. Donato, L. Leone, L. Buono, R. Gül Güven, B. Nicolaus and I. Finore,''*Acinetobacter mesopotamicus* sp. nov., petroleum-degrading bacterium, isolated from petroleum-contaminated soil in Diyarbakir, in the Southeast of Turkey. Current Microbiology, vol. 77, no.2, pp.3192-3200, 2020.

[11] K. Jyothi, K. Surendra Babu, K. Nancy Clara, A Kashyap,''Identification and isolation of hydrocarbon degrading bacteria by molecular characterization,'' *Helix*, vol.2,pp.105-111, 2012.

[12] M. Mahjoubi, A. Jaouani, A. Guesmi, S. Ben Amor, A. Jouini, H. Cherif, A. Najjari, A. Boudabous, N. Koubaa,, A. Cherif,'' Hydrocarbonoclastic bacteria isolated from petroleum contaminated sites in Tunisia: isolation, identification and characterization of the biotechnological potential. *New Biotechnol*, vol.30, no.6, 723-733, 2013.

[13] X. Xu, W. Liu, S. Tian, W. Wang, Q. Qi, P. Jiang, X. Gao, F. Li, H. Li and H. Yu,''Petroleum hydrocarbon-degrading bacteria for the remediation of oil pollution under aerobic conditions: A Perspective Analysis,''*Front. Microbiol*, 9:2885, 2018.

[14] K. V. Sajna, R. K. Sukumaran, L. D. Gottumukkala, A, Pandey,''Crude oil biodegradation aided by biosurfactants from *Pseudozyma* sp. NII 08165 or its culture broth,'' *Bioresour. Technol*, vol.191, pp.133-139, 2015.

[15] H. Wilkes, W. Buckel, B.T. Golding, R. Rabus,'' Metabolism of hydrocarbons in n alkane utilizing anaerobic bacteria,'' *J. Mol. Microbiol. Biotechnol*, 26, 138-151. 2016.

[16] A. Ledezma-Villanueva et al,''Biodegradation kinetic rates of diesel-contaminated sandy soil samples by two different microbial consortia,''*Ann. Microbiol*, vol. 66, pp.197-206, 2016.

[17] C. Rizzo, A.C. Rappazzo, L. Michaud, E.D. Domenico, C. Rochera, A. Camacho, A. L. Giudice,'' Efficiency in hydrocarbon degradation and biosurfactant production by *Joostella* sp. A8 when grown in pure culture and consortia, *J. Environ. Sci*, vol.67, pp. 115-126, 2018.

[18] S. Kumari, R.K. Regar, N. Manickam,''Improved polycyclic aromatic hydrocarbon degradation in a crude oil by individual and a consortium of bacteria,'' *Bioresour. Technol*, vol. 254, pp.174-179, 2018.

[19] P. Wanapaisan et al,'' Synergistic degradation of pyrene by five culturable bacteria in a mangrovesediment-derived bacterial consortium,'' *J. Hazard Mater*, vol. 342,pp. 561-570, 2018.

[20] H. Hoffmann et al, ''Description of *Enterobacter ludwigii* sp. Nov., a novel *Enterobacter* species of clinical relevance,'' *Systematic and Applied Microbiology*, vol. 28, pp.206-212, 2005.

[21] T. Y. Kwon, S. M. Shim, M. Y. Heo, D. H An, K. S Shin, J. H. Lee,''Isolation and characterization of exopolysaccharide-producing bacteria from Korean fermented vegetables,'' *Korean Journal of Microbiology and Biotechnology*, vol. 35, pp.191-195, 2007.

[22] A. Paauw, M. Caspers, F. Schuren, M. Leverstein-van Hall, A. Delétoile, R . Montijn, J. Verhoef, A. C. Fluit'' Genomic diversity within the *Enterobacter cloacae* complex,'' PLoS ONE, vol.3, pp. 3018-3028, 2008.

[23] X. Hua, Z .Wu, H. Zhang, D. Lu, M. Wang, Y. Liu, Z. Liu,'' Degradation of hexadecane by *Enterobacter cloacae* strain TU that secretes an exopolysaccharide as a bioemulsifier,'' *Chemosphere,* vol. 80, pp. 951-956, 2010.

[24] A. Mukherjee, B. Chettri, J. S. Langpoklakpam, A. K. Singh, D. Chattopadhyay,''Draft genome sequence of hydrocarbon-degrading *Enterobacter cloacae* strain S1: CND1, isolated from crude oil-contaminated soil from the Noonmati oil refinery, Guwahati, Assam, India,'' Genome Announcements, vol.4, no.3, 2016.

[25] S. Ramsey, A. Arumugam, P. Chandran,'' Optimization of *Enterobacter cloacae* (KU923381) for diesel oil degradation using response surface methodology (RSM),*''Journal of Microbiology*, vol.55, no.2, pp.104-111, 2017.

[26] H. P. Dussault,''An improved technique for staining red halophilic bacteria,'' Journal of Bacteriol, vol.70, pp. 484-485,1955.

[27] B. Lányi,''1 Classical and rapid identification methods for medically important bacteria,''. *Method Microbiol*, vol.19, pp.1-67,1988.

[28] Bergey D.H., Krieg N.R., Holt J.G. 1989. Bergey's manual of systematic bacteriology. Williams & Wilkins Co, Baltimore, ISBN:0-683-04108-8.

[29] D. Claus and C.W. Berkeley,''The genus *Bacillus* in: Bergey's manual of systematic bacteriology,''vol.2: 1105, 1986.

[30] H. Abtahi et al,'' Effect of competition between petroleum-degrading bacteria and indigenous compost microorganisms on the efficiency of petroleum sludge bioremediation: Field application of mineral-based culture in the composting process,'' *Journal of Environmental Management*, vol. 258, pp.110013, 2020.

[31] A. Dwivedi, S. Chitranshi, A. Gupta, A. Kumar, J. Lal Bhat,'' Assessment of the Petroleum Oil Degradation Capacity of Indigenous Bacterial Species Isolated from Petroleum Oil-Contaminated Soil,'' *International Journal of Environmental Research* ,vol.13,pp.735-746, 2019.

[32] B. Gupta, A. Rajor K, J Kaur,'' Isolation, Characterisation of Novel *Pseudomonas* and *Enterobacter* sp. from contaminated soil of chandigarh for naphthalene degradation,'' *In book: Utilization and Management of Bioresources*, pp.175-186, 2018.

[33] J. Zhang, T.Cui, X. Li,''2018. Screening and identification of an *Enterobacter ludwigii* strain expressing an active β-xylosidase,'' *Annals of Microbiology*, vol. 68,pp. 261-271.

[34] F.T. Wendy et al,''*Enterobacter ludwigii*, a candidate probiont from the intestine of Asian seabass,'' *Journal of Science and Technology in the Tropics*, 10: 5-14, 2014.

[35] Jerin I., et al,'' Diesel degradation efficiency of *Enterobacter sp., Acinetobacter sp*., and *Cedecea sp.* isolated from petroleum waste dumping site: a bioremediation view point. *Archives of Microbiology*, vol. 203, pp. 5075-5084, 2021.

[36] M. Throne-Holst, A .Wentzel, T.E. Ellingsen, H.K. Kotlar, S. B. Zotchev,''Identification of Novel Genes Involved in Long-Chain *n*-Alkane Degradation by *Acinetobacter* sp. Strain DSM 17874,*''Applied and Environmental Microbiology, vol.* 73.no.10,pp.3327-3332, 2007.

[37] S. Muthukamalam, S. Sivagangavathi, D. Dhrishya, S.S. Rani,'' Characterization of dioxygenases and biosurfactants produced by crude oil degrading soil bacteria,'' *Brazilian Journal of Microbiology*, vol. 48, no.4, pp.637-647, 2017.

[38] C. Simaria, G. Pant, G. Sibi,'' Characterization and evaluation of polycyclic aromatic hydrocarbon (Pah) degrading bacteria isolated from oil contaminated soil,'' *Applied Microbiology: Open Access*, 1:1, 2015.

[39] F. Kafilzadeh and A. Khezri'' Biodegraditon of aniline by *Enterobacter ludwigii* KH-A5 isolated from the soil around shiraz refinery,iran,'' *Global Nest Journal*, vol. 18,no.4, pp. 697-707, 2016.

[40] D. Wang, G. Zheng, S. Wang, D. Zhang., L. Zhou,'' Biodegradation of aniline by Candida tropicalis AN1 isolated from aerobic granular sludge,'' *J Environ Sci*, vol. 23,no.12,pp. 2063-2068, 2011.

[41] V.Sarwade and K. Gawai,'' Biodegradation of aniline by alkaliphilic strain *Bacillus badius* D1,''IOSR J Environ Sci Toxicol Food Technol, 8(5): 71-78, 2014.

Bitlis Eren Üniversitesi Fen Bilimleri Dergisi
BİTLİS EREN UNIVERSITY JOURNAL OF SCIENCE
ISSN: 2147-3129/e-ISSN: 2147-3188
VOLUME: 11 NO: 2 PAGE: 640-648 YEAR: 2022
DOI: 10.17798/bitlisfen.1077833

An Analysis of the Turkish Railway Transport by Comparison with European Countries

Burçin PAÇACI[1*], Mustafa Kürşat ÇUBUK[1], Kürşat YILDIZ[2], Fatih KARAÇOR[1]

[1]*Gazi Üniversitesi, Mühendislik Fakültesi, İnşaat Mühendisliği Bölümü, ANKARA*
[2] *Gazi Üniversitesi, Teknoloji Fakültesi, İnşaat Mühendisliği Bölümü, ANKARA*
(ORCID: 0000-0001-6053-0458) (ORCID: 0000-0001-8155-7123) (ORCID: 0000-0003-2205-9997) (ORCID: 0000-0003-1201-7857)

Keywords: Transportation, Railway, Economy.

Abstract
The fact that transportation infrastructure has a great impact on economic development reveals the necessity of more economical, comfortable, and environmentally friendly transportation between transportation systems. With the rapid development of technology, the importance of the railway transportation system, which can carry high-capacity, economical and safe cargo, in the transportation sector is increasing. Although railway transportation has been used for many years in our country, it is not at the desired level in terms of both freight and passenger transportation. For a more balanced and systematic distribution of transportation infrastructure, transportation systems should be analyzed. In this study, the development of railway transport in Turkey, its ratio among other types in terms of freight and passenger transport, and its status in railway transport compared to European countries have been analyzed. In line with this information, the deficiencies in rail transport and the investments that need to be made have been determined.

1. Introduction

Transportation is defined as the transportation of cargo or passengers from one place to another and has developed depending on the needs and infrastructure technologies from the past to the present [1]. Transport, which has a close relationship with other sectors, shows the level of economy and welfare level of a country. With the increasing population, rapid urbanization, and industrialization, the demand for transportation is increasing. While meeting this demand, the most reliable, comfortable, fast, and environmentally friendly transportation systems should be preferred for the sustainability of economies. When these priorities were taken into consideration, railway transportation is far ahead of all transportation systems. In terms of price, it is known that railway transportation is 40-50% cheaper in passenger transportation and 70% cheaper in freight transportation compared to other transport modes [2].

Railway transportation is a clean, quiet system with very high energy efficiency, which requires less land use in cities and between cities. The fact that the rail systems are less affected by the climate and fast and have the ability to transfer high volumes in urban and intercity transportation make railways the most convenient transportation mode [3]. Being cheap and fixed price is among the advantages of the railway, while the disadvantages are that it is not appropriate for slope lands, cannot deliver from door to door, and has lots of handlings [4]. Although the railway seems expensive in terms of infrastructure and operation, it is a transportation system that can be profitable even in a short time [5]. With the increasing number of wagons, transportation capacity in terms of passengers and freight can increase. Moreover, when the transport system increases its shipping capacity, its average cost will decrease too. Railway transportation, which is generally used low-value products, decreases waiting time because of the absence of traffic. In this way, more accurate

*Corresponding author: burcinpcc@gmail.com:
Received: 23.02.2022, Accepted: 13.05.2022

information about transportation time can be obtained [6].

2. The Railway Systems in the World

Railways are environmentally friendly transportation systems, and for this reason, the mode of the railway will be in more demand in the next coming years, since railway CO_2 emissions are quite low compared to the road. Transportation activities are the only sector in the European Union where greenhouse gas emissions have increased since 1990 and road transport emissions account for 25% of total CO_2 [7].

CO_2 emission values of roads and railways are given in Figure 1 [8]. According to this figure, While the CO_2 emission value of road is the highest, the CO_2 emissions value of rail (electric) is the lowest. CO_2 emission value has increased by rail (diesel). The European Green Deal was developed to reduce emissions by 90% by 2050 and aims to significantly improve the sustainability of transport and promote zero and low emission vehicles and alternative fuels [7].

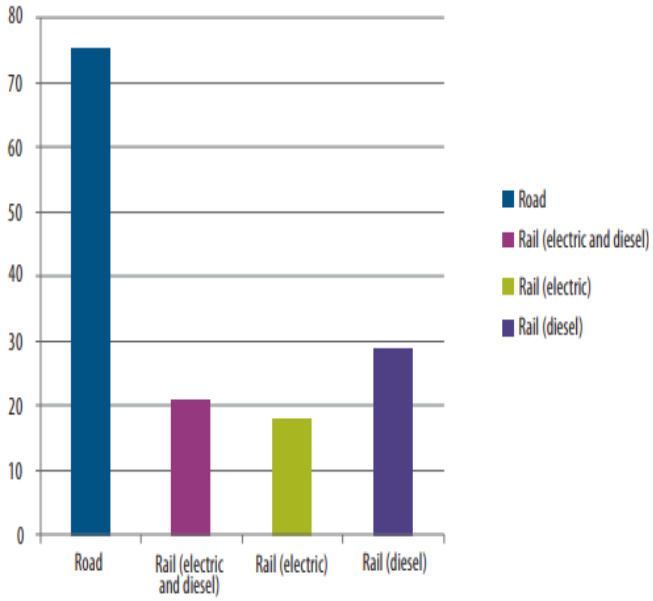

Figure 1: CO_2 emissions per tonne-kilometer in the EU in 2012 [8]

When the European railway system is studied properly, it is obvious that there are some deficiencies in its infrastructure capacity and quality, and there are also some difficulties in speed and loading due to these deficiencies. Infrastructure usage and pricing system implementations are needed to reorganize. t-This reorganization may increase the earnings of the railways to ensure fair competition with other modes and to have easy access between the modes. In other words, high-speed rail transport should be encouraged with financial incentives. For this reason, strong actions are needed to open market forces to railways [9].

The liberalization of the European rail freight market creates more competition and foresees a reduction in costs by transferring transportation from road to rail [10].

In order to meet the demand for railway transport in Europe better, network management is also required to be re-regulated. Passenger lines among railway operators, diversification of services, and further expansion of EU rail transport may create great opportunities for rail transport in the long run. Network management should be better regulated in order to better meeting of the demand for transport in Europe [11]. Europe went through many reforms to improve the railway. These reforms are shown in Figure 2 [12]. Although these reforms have been created in many places in the world such as the USA, Latin America and Asia, they have not been implemented so consistently anywhere [10].

When the transportation activities in Europe are evaluated, it is seen in Table 1 that automobile and bus transportation is ahead of the railroad [13]. According to Table 1, Austria has the highest rate with 12.9% and the lowest rate belongs to Greece with 0.9% in terms of railway usage by passengers. In Turkey, this rate is calculated as 2.7%. In the Americas, on the other hand, transportation by automobile and bus, which belongs to road transportation, has a large proportion and this rate is 99.6% in total. Passenger transportation by rail in the USA is 0.4%.

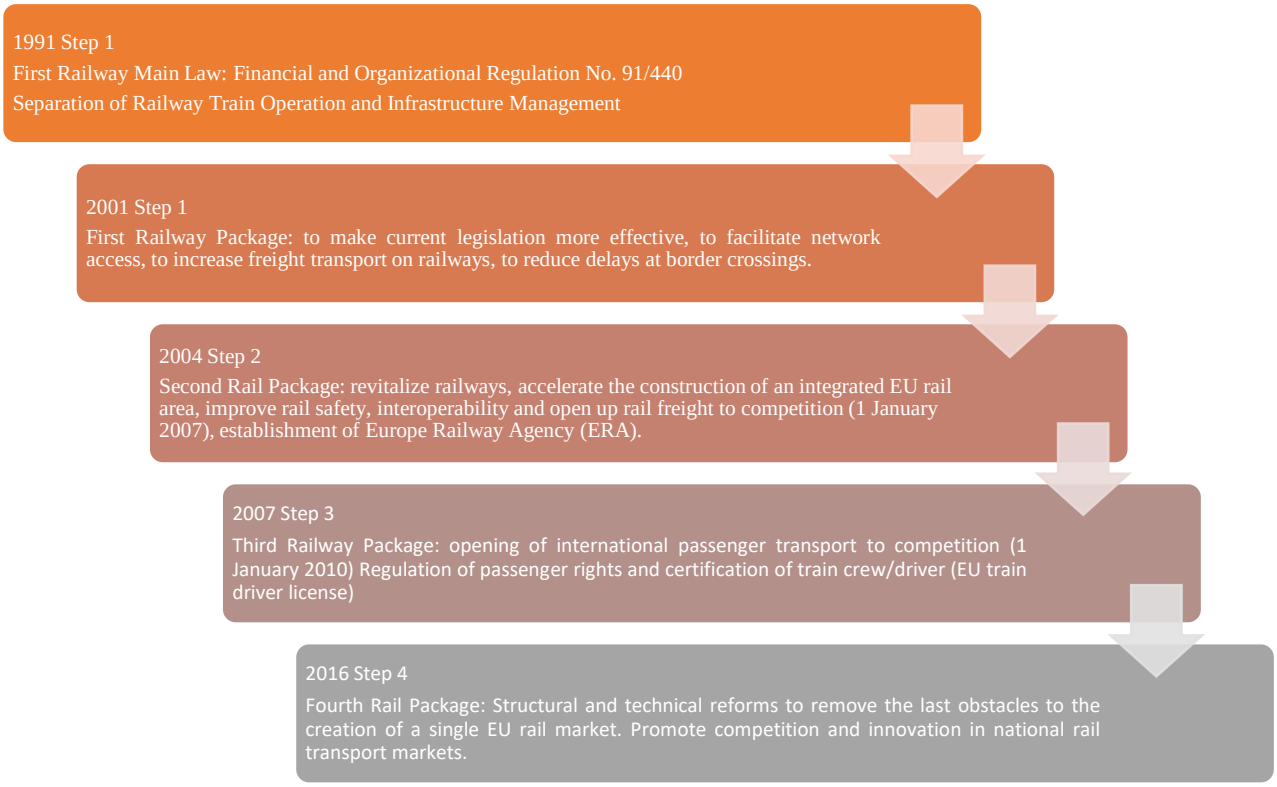

Figure 2: EU railway legislations

Table 1: Passenger transport by countries and transport systems (Passenger-Km) [13]

	Railway		**Passenger Car**		**Bus**		**Total**
	Billion	**%**	**Billion**	**%**	**Billion**	**%**	**Billion**
Turkey	**8.9**	**2.7**	**229.4**	**70.2**	**88.3**	**27.0**	**326.6**
England	69.7	8.9	672.7	86.3	36.8	4.7	779.2
Greece	1.1	0.9	103.4	82.7	20.5	16.4	125
Germany	98.1	9.1	920.2	85.1	62.5	5.8	1080.8
Italy	55.5	6.3	722.9	82.0	103	11.7	881.4
Spain	28.4	7.1	340.6	84.9	32.2	8.0	401.2
France	97.1	10.6	757.1	83.0	57.6	6.3	911.8
Austria	13.2	12.9	78.5	77.0	10.3	10.1	102
Czech Republic	10.2	9.6	78	73.4	18.1	17.0	106.3
Poland	21	7.8	212.4	79.3	34.5	12.9	267.9
Hungary	7.8	8.6	63.9	70.5	18.9	20.9	90.6
Bulgaria	1.5	2.2	57.2	83.4	9.9	14.4	68.6
Netherlands	18.9	11.2	144.7	85.7	5.3	3.1	168.9
Romania	5.6	4.3	103.8	80.3	19.9	15.4	129.3
European Union	476.9	8.1	4916.5	83.3	511.4	8.7	5904.8
USA	37.5	0.4	7804.1	92.2	624.7	7.4	8466.3

Since transportation is of a great importance in EU Economy, freight transportation activities related to transportation constitute 9% of the total gross value added and create 11 million jobs [14]. In Table 2, freight transport rates of countries by rail, road, inland waterway and oil line are given [13]. The share of freight transport in rail is higher than the share of passenger transport. According to this table, the country with the highest rate of freight transport by rail is Russia with 61.4%. According to the table, the country with the lowest share in rail freight transport is Greece with 2.1%. Among the transportation types in Table 2, the rate of freight transportation by rail in Turkey was found to be 4.5%.

Table 2: Freight transports by countries and transportation systems (Ton-Km)

	Railway		Road		Inland Waterways		Oil Pipeline		Total
	Billion	**%**	**Billion**	**%**	**Billion**	**%**	**Billion**	**%**	**Billion**
Turkey	**14.48**	**4.5**	**266.5**	**83.4**			**38.65**	**12.1**	**319.6**
England	17.21	8.9	165.3	85.8	0.10	0.1	9.97	5.2	192.6
Greece	0.41	2.1	19.4	97.8			0.03	0.2	19.8
Germany	124.62	19.3	458.6	70.8	46.90	7.2	17.23	2.7	647.3
Italy	22.07	12.4	146.1	81.8	0.10	0.1	10.33	5.8	178.6
Spain	10.70	4.8	203.6	90.9			9.70	4.3	224.0
France	32.04	9.6	283.4	84.5	7.30	2.2	12.45	3.7	335.2
Austria	22.00	28.1	46.3	59.1	1.50	1.9	8.58	11.0	78.4
Czech Republic	16.56	26.7	43.5	69.9			2.11	3,4	62.1
Poland	59.39	24.5	161.9	66.7	0.10	0.04	21.31	8.8	242.7
Hungary	10.58	25.4	27.0	64.8	1.60	3.8	2.50	6.0	41.7
Bulgaria	3.82	18.6	11.1	54.3	4.90	23.9	0.67	3.3	20.5
Netherlands	7.02	6.1	55.1	48.0	47.20	41.1	5.54	4.8	114.9
Romania	13.08	28.2	20.0	43.0	12.30	26.5	1.08	2.3	46.4
European Union	440.53	17.2	1874,2	73.1	135.10	5.3	114.01	4.4	2563,9
USA	2525.22	34.2	2969.5	40.2	463.00	6.3	1429.81	19.4	7387.5
China	2882.10	14.1	7124,9	34.9	9905.20	48.5	530.07	2.6	20442.3
Russia	2597.78	61.4	241.2	5.7	61,00	1.4	1331.62	31.5	4231.6

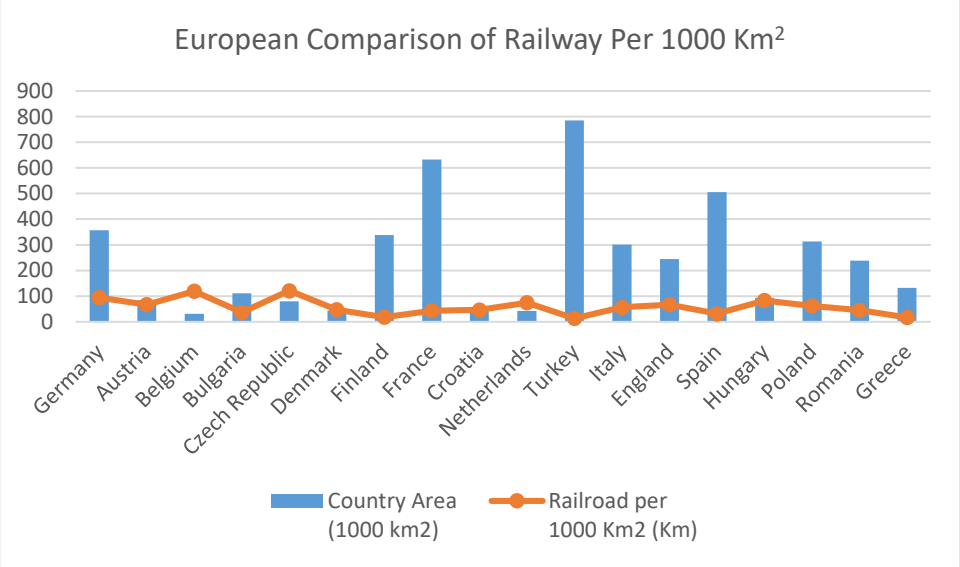

Figure 3: Comparison of rail length decreased to 1000 km^2

In Figure 3, the area values of the countries and the railway lengths per 1000 km^2 are given [13]. According to the figure, the Czech Republic has the highest rate, with 121 km of railways per 1000 km^2. In Turkey, on the other hand, there is 13 km of railways per 1000 km^2.

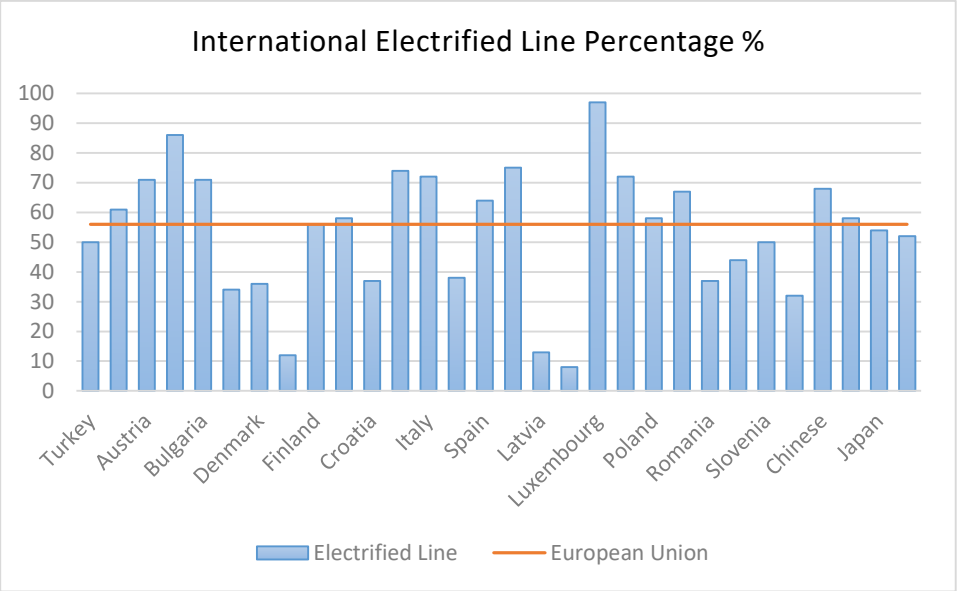

Figure 4: Percentage of international electric lines

Figure 4 shows the percentages of electrified lines owned by countries and the European Union [13]. According to this figure, Luxembourg has the highest share with 97%. Lithuania has the lowest share with 8%. Turkey's electrified line (electric rail system) rate is shown as 50%. In the European Union, this rate was detected as 54%.

3. Railway Systems in Turkey

Almost every person uses railways in European countries especially in Switzerland[6]. However, in Turkey, the share of railways in passenger transportation is very low. The shares of transportation systems in passenger transportation in Turkey by years is shown in Figure 5 [15].

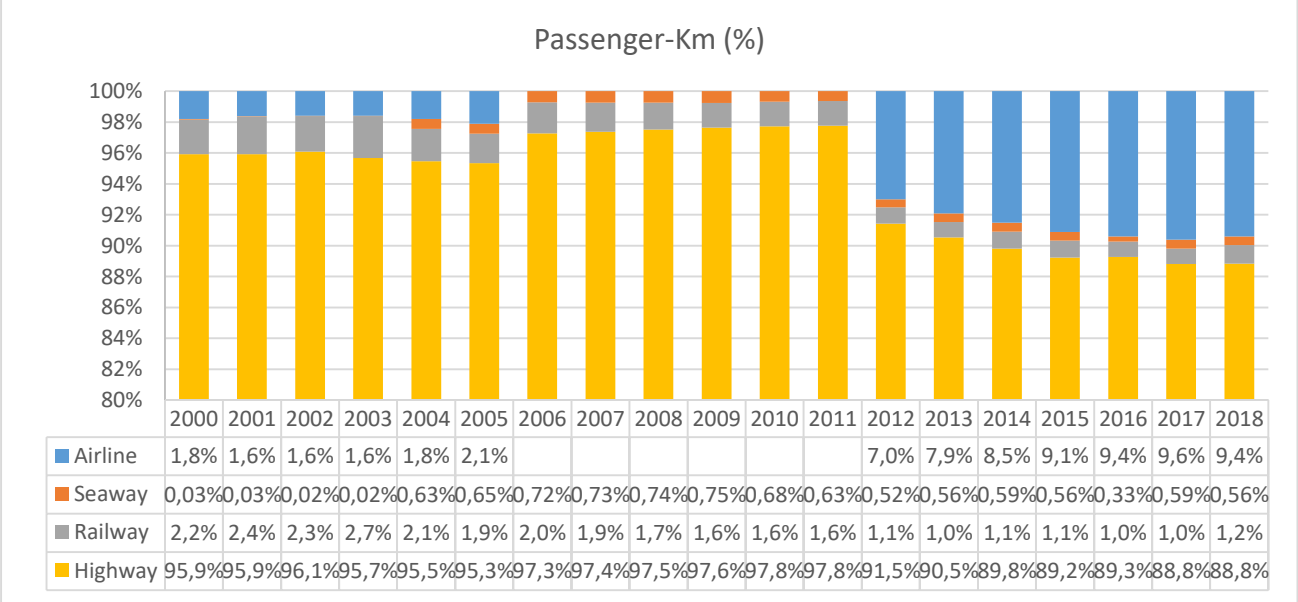

	2000	2001	2002	2003	2004	2005	2006	2007	2008	2009	2010	2011	2012	2013	2014	2015	2016	2017	2018
Airline	1,8%	1,6%	1,6%	1,6%	1,8%	2,1%							7,0%	7,9%	8,5%	9,1%	9,4%	9,6%	9,4%
Seaway	0,03%	0,03%	0,02%	0,02%	0,63%	0,65%	0,72%	0,73%	0,74%	0,75%	0,68%	0,63%	0,52%	0,56%	0,59%	0,56%	0,33%	0,59%	0,56%
Railway	2,2%	2,4%	2,3%	2,7%	2,1%	1,9%	2,0%	1,9%	1,7%	1,6%	1,6%	1,6%	1,1%	1,0%	1,1%	1,1%	1,0%	1,0%	1,2%
Highway	95,9%	95,9%	96,1%	95,7%	95,5%	95,3%	97,3%	97,4%	97,5%	97,6%	97,8%	97,8%	91,5%	90,5%	89,8%	89,2%	89,3%	88,8%	88,8%

Figure 5. Passenger transportation (Passenger-Km) by transportation systems in Turkey

When Figure 5 is examined, there is a remarkable increase in air transport, while road transport is at the forefront of passenger transport in all years. In maritime transport, the change has been fluctuating over the years. However, decreasing trend may easily be observed in the share of railways in passenger transport.

Nevertheless, according the recent studies, the rail share of passenger transportation has been increasing in recent years by high-speed train (HST). In HST Enterprises, better railway service can be provided by providing the best design and shortening the travel time. HST systems have been developed to increase the railway shipping capacity, thus its competitiveness against other modes will also be strengthened too [16]. In Table 3, the number of passengers by years is given [13]. High speed train usage rate is given in Figure 6.

Table 3: Main line and HST quantities (Passenger-Km Million)

	2009	**2010**	**2011**	**2012**	**2013**	**2014**	**2015**	**2016**	**2017**	**2018**	**2019**	**2020**
Main Line	3232	3017	3257	2035	1790	1833	1812	1397	1426	1762	2163	495
HST	237	476	665	914	1186	1555	1847	1871	2218	2551	2678	941
Total	3469	3493	3922	2949	2976	3388	3659	3268	3644	4313	4841	1436

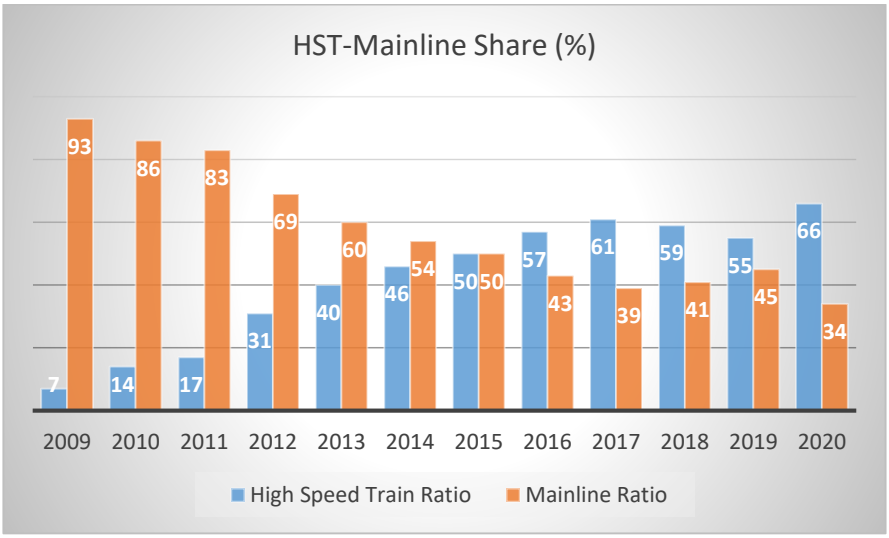

Figure 6: HST and mainline share

The most important thing about a transportation system is the providing of an environmentally friendly and efficient service without energy waste and without external dependency. An efficient transportation system requires swift operational and administrative activities, adequate planning, and qualified and sufficient personnel. There is an unbalanced distribution among the transportation modes in Turkey. In order to re-balance this distribution, it is necessary to decrease density of road transport and increase density of other transportation systems. By investing in high-speed train, Turkey tries to transfer its road passenger traffic to the railways, since density of road transport makes Turkey dependent on oil [17]. This situation can be avoided only by rail transport. In Figure 7, the amount of freight transport between transportation systems is given [15].

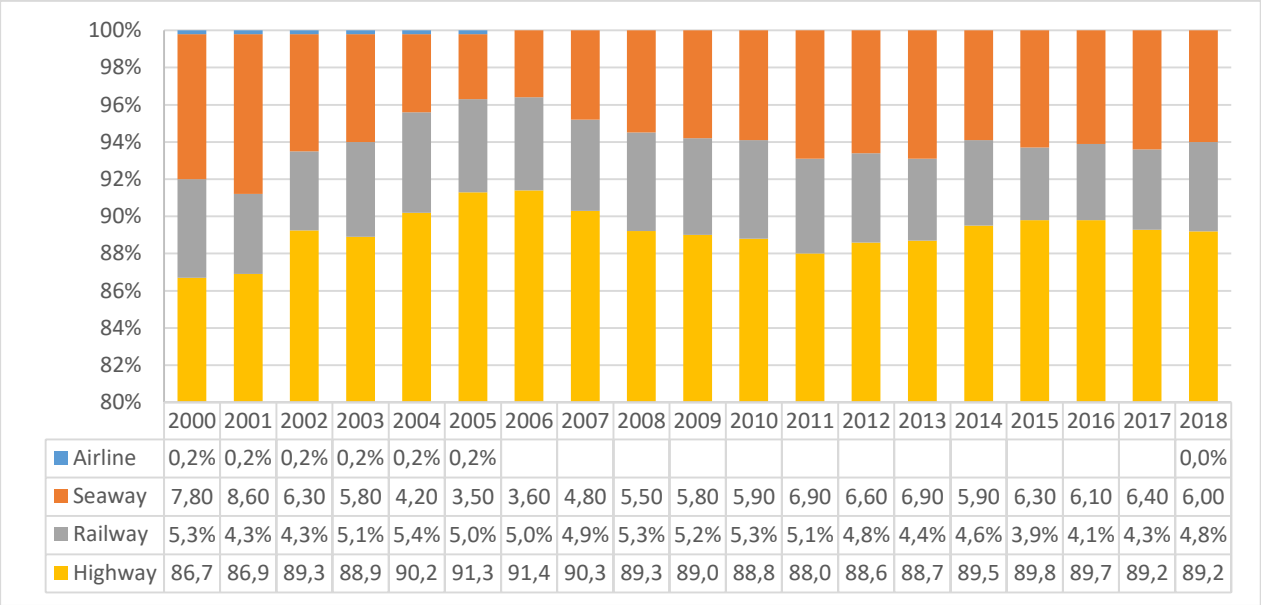

	2000	2001	2002	2003	2004	2005	2006	2007	2008	2009	2010	2011	2012	2013	2014	2015	2016	2017	2018
Airline	0,2%	0,2%	0,2%	0,2%	0,2%	0,2%													0,0%
Seaway	7,80	8,60	6,30	5,80	4,20	3,50	3,60	4,80	5,50	5,80	5,90	6,90	6,60	6,90	5,90	6,30	6,10	6,40	6,00
Railway	5,3%	4,3%	4,3%	5,1%	5,4%	5,0%	5,0%	4,9%	5,3%	5,2%	5,3%	5,1%	4,8%	4,4%	4,6%	3,9%	4,1%	4,3%	4,8%
Highway	86,7	86,9	89,3	88,9	90,2	91,3	91,4	90,3	89,3	89,0	88,8	88,0	88,6	88,7	89,5	89,8	89,7	89,2	89,2

Figure 7: Freight carriage by transportation systems in Turkey (Tonne -Km)

According to Figure 7, highway has the largest share in freight transportation and its rank is the first. Airline, on the other hand, is not a system that has an important share in freight transportation and most importantly there has been no significant change in rail freight transport. In seaway, the rate freight of transportation has a higher rate than its share in passenger transportation, and there have been small increases and decreases in freight transportation over the years.

Railway transportation within the territory of today's Turkey can be splitted to three main periods. These periods are; The Ottoman Empire Period, New-republic period (1923-1950) and present period (1950-2022).

Since 1963, some development plans have been implemented in Turkey. These devolopment plans comprise of activities which are setting highway network which is complement to railway, making regulations that will increase its contribution to the economy, setting transportation which is contemporary and appropriate to neccesserities [5]. The target of Turkey's development plan is to increase the share of rail freight transport to 15% and the share of passenger transport to 10%. In the long term, the target is to increase the share of freight transport to 20% and the share of passenger transport to 15%. With a well-planned transportation system, the cities will grow in a balanced way and the demand for the railway transportation system will increase. As this demand increases, railway systems will provide more effective transportation service. In Figure 8, the railway length by years is shown. Increasing our railway network to 31,000 km is targeted in the long-term development plan [13].

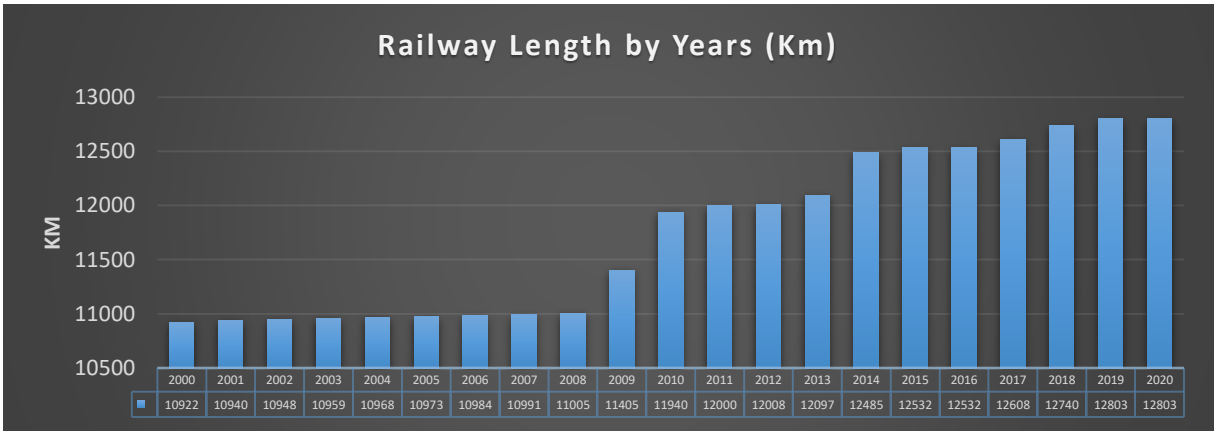

	2000	2001	2002	2003	2004	2005	2006	2007	2008	2009	2010	2011	2012	2013	2014	2015	2016	2017	2018	2019	2020
	10922	10940	10948	10959	10968	10973	10984	10991	11005	11405	11940	12000	12008	12097	12485	12532	12532	12608	12740	12803	12803

Figure 8: Railway length by years

4. Conclusion and Evaluation

Rail transport, which improves the quality of life of people, paves the way for modern, fast and economical transport. With the technological developments, the distances between countries have shortened and countries have become closer to each other. In this context, the implementation of high-speed railway projects, the modernization of existing roads and terminals, the development of the railway industries will strengthen Turkey's position as a logistical base of its region [18].

The general reason of being less developed in railway system is so simple. There has been no enough investments for the railways since 1950. This negligence is being tried to be covered by the use of high-speed trains in passenger transportation. In line with this information obtained in both freight and passenger transportation, in order to ensure the balance between transportation modes, these actions should be taken:

- Infrastructure investments should be prioritized
- Necessary investments should be prioritized
- The deficiencies should be analyzed fully and accurately after that these deficiencies should be eliminated.
- High-speed train lines are constantly being updated and growing. It is obvious that the current situation is improving day by day and the line lengths are increasing.
- Rail transport investments should be more active in terms of modal balance
- In freight transportation, the number of wagons and the length of the main line should be increased.
- However, the necessary importance is not given to the freight transport lines in Turkey. As a result, the share of rail freight transport decreases, therefore, road freight transport and CO_2 emissions increase.
- In this regard, the length of the lines should be increased by increasing the maintenance and repair of freight transport lines and the construction of connection roads that do not exist.

However, although the railway is a sustainable mode of transportation, especially in developing countries, railway enterprises or companies need to strive to improve their performance in terms of sustainability [19].

Since Turkey is at a crossroads in providing the transition from Asia to Europe, it should renew and optimize its transportation systems. With a balanced and strong transportation system, the country's economy will switch its traffic from road transportation to the railway transportation. It is an important issue for Turkey's economical sustainability because road transportation makes the country dependent on oil imports. All in all, investments and regulations for railway mode is of great importance for the future of Turkish economy.

Contribution of the Authors

The article was produced with the joint contributions of the authors.

Conflict of Interest Statement

There is no conflict of interest between the authors.

Statement of Research and Publication Ethics

Research and publication ethics were complied with in the study.

References

[1] B. Erkayman, "Lojistikte taşıma şekillerinin belirlenmesi," M.S. thesis, Dept. Industrial Eng., Yıldız Teknik Univ., İstanbul, Turkey, 2007.

[2] A. Kabasakal and A.O. Solak, "Demiryolu ve karayolu ulaştırma sistemlerinin ekonomik etkinlik analizi," in Anadolu University Journal of Social Sciences, no.10, vol. 1, pp. 123-126, 2010.

[3] T. Alataş and E. T. Somunkıran. "Türkiye'de demiryolu ulaşımının sorunları ve çözüm önerileri." [Online]. Available: https://docplayer.biz.tr/55032223-Turkiye-de-demiryolu-ulasiminin-sorunlari-ve-cozum-onerileri.html [Accessed:Feb.15, 2022].

[4] S. Usluer, "Kısa ve orta mesafeli hatlarda kapıdan kapıya yolcu taşımacılığında ulaştırma şekillerinin incelenmesi, en etkin ulaştırma şekli için bir karar destek modeli önerilmesi," Ph.D. dissertation, Dept. Civil Aviation Management, Anadolu Üniversitesi, Eskişehir, Turkey, 2016.

[5] İ. Atmaca, "Demiryolu ulaşımının kentsel gelişim üzerindeki etkileri ve Isparta kenti örneklemesi," M.S. thesis, Dept. City and Regional Planning, Süleyman Demirel Üniversitesi, Isparta, Turkey, 2009.

[6] "Demiryolu Taşımacılığının Avantajları ve Dezavantajları." [Online]. Available: https://rayhaber.com/2018/04/demiryolu-tasimaciliginin-avantajlari-ve-dezavantajlari/ [Accessed: May. 31, 2019].
[7] B. Djordjević, A.S. Mane and E. Krmac, "Analysis of dependency and importance of key indicators for railway sustainability monitoring: A new integrated approach with DEA and Pearson correlation,"in Research in Transportation Business & Management, no.41. 2021.
[8] "Rail freight transport in the EU: still not on the right track." [Online]. Available: https://www.eca.europa.eu/Lists/ECADocuments/SR16_08/SR_RAIL_FREIGHT_EN.pdf [Accessed: Feb. 15, 2022].
[9] C. Nash and C. Rivera-Trujillo, "Rail regulatory reform in Europe–principles and practice," presented at STELLA Focus Group 5 synthesis meeting, Athens, 1-26, 2004.
[10] G. Esposito, L. Cicatiello, S. Ercolano, "Reforming railways in the EU: An empirical assessment of liberalization policies in the European rail freight market," in Transportation Research Part A, no.132, pp.606-613, 2020.
[11] L. Di Pietrantonio, J. Pelkmans, "The economics of EU railway reform," in Journal of Network Industries, no.3, vol.4, pp.295-346, 2004.
[12] Y. Uğurlu, "Avrupa Birliği'nde Demiryolları," in Railway Engineering Association, no.7, pp. 37-44, 2018.
[13] TCDD, Republic of Turkey State Railways General Directorate 2016-2020 Statistics Yearbook, Ankara.
[14] X.L. Fernández, J. Gundelfinger and P. Coto-Millán, "The impact of logistics and intermodality on airport efficiency," in Transport Policy, Article in Press, 2021.
[15] "Ulaştırma Türlerine Göre Taşınan Yolcu ve Yük Miktarı." [Online]. Available: https://cevreselgostergeler.csb.gov.tr/ulastirma-turlerine-gore-tasinan-yolcu-ve-yuk-miktari-i-85789 [Accessed: Feb. 15, 2022].
[16] M. Givoni, "Development and impact of the modern high-speed train: A review," in Transport reviews, no.26, vol.5, pp.593-611, 2006.
[17] TMMOB, "Ulaşımda Demiryolu Gerçeği." pp:1-82, Ankara, 2012.
[18] T.C. Ulaştırma ve Altyapı Bakanlığı, "Ulaşan ve Erişen Türkiye 2018,", Working Report, Ankara, Türkiye, 2018.
[19] M. Ilıcalı, A. Öngel, M. Ç. Kızıltaş, "Sürdürülebilir Bir Ulaştırma Sistemi ve Demiryolu Yatırımları." [Online]. Available: https://ww4.ticaret.edu.tr/ulastirma/wp-content/uploads/sites/85/2016/05/B%C4%B0LD%C4%B0R%C4%B0-S%C3%BCrd%C3%BCr%C3%BClebilir-Bir-Ula%C5%9Ft%C4%B1rma-Sistemi-ve-Demiryolu-Yat%C4%B1r%C4%B1mlar%C4%B1.pdf [Accessed: Feb. 15, 2022].

Bitlis Eren Üniversitesi Fen Bilimleri Dergisi
BİTLİS EREN UNIVERSITY JOURNAL OF SCIENCE
ISSN: 2147-3129/e-ISSN: 2147-3188
VOLUME: 11 NO: 2 PAGE: 649-659YEAR: 2022
DOI: 10.17798/bitlisfen.1082417

Forms and Vertical and Lateral Load Capacities of Columns in Mimar Sinan's Mosques

Rabia İZOL[1*], Okan TÜRKMEN[1], M. Arif GÜREL[1], Paki TURĞUT[2]

[1]*Department of Civil Engineering, Faculty of Engineering, Harran University, Sanliurfa, Turkey,*
[2]*Department of Civil Engineering, Faculty of Engineering, İnönü University, Malatya, Turkey*
(ORCID: 0000-0002-7568-3817) (ORCID: 0000-0001-7230-815X) (ORCID: 0000-0002-1046-4410) (ORCID: 0000-0002-3711-4605)

Keywords: Mimar Sinan, Mosque, Column, Vertical and lateral load capacity, Abaqus software.

Abstract
Along with the walls, columns are the main load-bearing elements in carrying vertical and horizontal loads in most historic masonry buildings. When the mosques of Mimar Sinan, the great Ottoman architect, are examined, it is seen that there is a wide variety in column forms. In this study, the column forms in Sinan's a few mosques were investigated, their geometric dimensions were measured, and the vertical and lateral load carrying capacities of them were determined. The columns examined are the columns of Sinan Pasha, Kılıç Ali Pasha, Üsküdar Mihrimah Sultan, Selimiye, Şehzade and Süleymaniye mosques. Initially, the vertical capacities of the columns were calculated with both the classical stress equation and the Abaqus program, and very close results were obtained with the two calculation methods. Then, lateral load carrying capacities were calculated only by using of the Abaqus software. It has been once again seen and emphasized that height is also important, together with other relevant factors, on the lateral load capacities of the columns.

1. Introduction

There are many great architects and engineers in the history of world architecture and engineering. One of these names is undoubtedly Mimar Sinan, who was the chief architect of the Ottoman Empire for fifty years between 1538 and 1588. Most of the great Ottoman structures of the second half of the 16th century are the work of Sinan. He, along with his assistants, designed and oversaw the construction of buildings, bridges, aqueducts etc. throughout the empire [1]. The great architect died in 1588, when he was about a hundred years old, leaving behind an unprecedented number and quality of works [2].

Nearly 400 of Sinan's works have survived to the present day. Mosques are undoubtedly among his most striking works with their magnificence. Sinan's mosques have been the subject of numerous studies for today's architects and engineers. The examinations, measurements and analyses made within the scope of this study are on the columns of some mosques of the great architect.

As it is known, columns in historical masonry buildings can be divided into two groups as 'pillars' and 'piers'. Pillars are formed either from a single specially shaped stone or from several specially shaped stones. Piers, on the other hand, are formed by laying a large number of stones or bricks (sometimes both together) with a mortar. The main piers of some large mosques are gigantic and are called as 'elephant leg'. For example, the piers of the Süleymaniye and Sultan Ahmet mosques are like this. Columns within the scope of this study are "piers" only, and hereinafter referred to as "columns"

2. Some related previous works

The load-bearing elements of historical masonry mosques and similar structures are walls, columns,

*Corresponding author: izolrabia1@gmail.com
Received: 03.03.2022, Accepted: 15.04.2022

buttresses, arches, domes and foundations. Columns are of vital importance in carrying vertical and horizontal loads together with the walls. It is seen that many studies have been performed in the technical literature on these elements. Yokel [3] investigated the stability and load bearing capacity of rectangular cross-sectional elements made of no-tension material under the effect of eccentric vertical load. Frisch-Fay [4] studied the stability of eccentrically loaded masonry rectangular columns analytically and using the matrix-displacement approach. Ahunbay [5] discussed the construction techniques and materials used in Mimar Sinan structures.

La Mendola and Papia [6] investigated the stability of masonry piers numerically by considering both their own weight and the effect of eccentric vertical load. De Falco and Lucchesi [7] extended Yokel' s [3] work to the stability analysis of columns made of materials that do not have tensile strength but also have limited compressive strength and deformation capacity. Arıoğlu and Arıoğlu [8] conducted a comprehensive study on the physical and mechanical properties of a limestone (Küfeki stone) that Mimar Sinan used extensively in his structures. Gurel et al. [9] investigated the lateral stiffness of masonry rectangular columns using a numerical model capable of capturing the cracking and second-order effects. Gurel et al. [10] tried to determine the lateral load capacity of cylindrical masonry columns for seismic transverse forces. In his PhD thesis, Şeker [11] examined the behavior of Mimar Sinan mosques under static and dynamic loads. In this context, he discussed the mosque construction techniques, materials used and their properties, and finally performed static and dynamic analyses on three-dimensional models of Sinan's 28 mosques. Gurel [12] studied the stability of slender circular masonry columns under their own weight and eccentric vertical load. Crespi et al. [13] performed seismic assessment of the Santa Maria di Collemaggio Basilica in L'Aquila (Italy) focusing the attention on the behavior of the octagonal stone columns of the naves. Çaktı et al. [14] studied the seismic behaviour of the Mihrimah Sultan Mosque in Edirnekapı, one of the most elegant works of the Sinan. Broseghini et al. [15] analysed several aspects of the instability of homogeneous masonry circular columns loaded with a vertical eccentric load.

It is seen that, in the technical literature, various studies have been carried out on masonry columns, and Mimar Sinan mosques have been examined in terms of some technical and material properties. However, no special study was found about the forms and load capacities of columns in Sinan's mosques. In the context of this study, the columns in Mimar Sinan's some mosques were examined in situ, their geometric dimensions were measured, and their vertical and horizontal load carrying capacities were determined. Thus, some more information was obtained about the columns, one of the most vital elements, in the buildings of the great architect.

3. Materials and Method

When his works are examined, it is immediately seen that Sinan added something "different" to each of his designs. Namely, "innovation" is one of the most outstanding features of the master architect. This search for innovation is also evident in the columns of his building-type structures such as mosques. The authors examined many mosques of the Mimar Sinan on site and clearly observed this fact. It has been observed that there are many different column types, from classical rectangular and circular columns to hexagonal and octagonal columns, and to the columns with special geometric shaped cross-sections having protrusions to provide supports to the arches. Here, the columns of only six mosques are considered. These mosques are Sinan Pasha (Beşiktaş), Kılıç Ali Pasha, Mihrimah Sultan (Üsküdar), Selimiye, Şehzade and Süleymaniye mosques. Column dimensions of the buildings were determined by the authors by in situ measurements. Figure 1 presents a general view of the columns, their cross-sectional shapes and dimensions.

Although this study is on column forms in Sinan mosques, it should be noted that determining how form affects the vertical and horizontal capacities of columns is not the main purpose of this first study on the subject. This issue can be explored in another study in the future.

The materials used in the construction of Mimar Sinan mosques are as important as their rational and innovative designs. When looked at the materials used by Sinan in his buildings, it is seen that he used stone, brick and wood as the main materials, Khorasan mortar and lime as the binder, as well as nails, clamps and tenons of various sizes. His buildings are completely stone or stone-brick mixed structures. Among the mosques we examined, it is seen that Marmara marble had been used in the

columns of Kılıç Ali Pasha Mosque and limestone (Küfeki) had been used in the columns of all other mosques. As the mortar, generally Khorasan mortar had been used in all mosques.

It is known that masonry structures can be modeled by detailed micro modeling, simplified micro modeling or macro modeling technique. The details of these techniques will not be discussed here, as they are included in relevant studies. In this study, macro modeling technique (homogeneous material approach) has been preferred. According to this approach, masonry texture is considered as a homogeneous continuum that incorporates the properties of the masonry units and the mortar. By adopting this approach, the compressive strength values were calculated with the $f_c = 0.45 {f_s}^{0.7} {f_m}^{0.3}$ expression, [16]. In the expression, f_s and f_m indicate the compressive strength of the stone and mortar. The characteristic values provided by this equation have been multiplied by a factor of 1.2 to obtain the average values. While determining the elastic modulus, E, of the homogeneous texture, the formula $E = 750 f_c$ has been used, [17]. The Poisson's ratio, ν, has been taken as 0.20, which is commonly used for brittle materials. The physical and mechanical properties of the materials (Küfeki stone, Marmara marble and Khorosan mortar) of the columns have been taken from the studies of Şeker [11], Korkmaz [18], Arioğlu and Arioğlu [8]. The f_c and E values for the columns have been obtained by the two expressions given above and are presented in Table 1. The tensile strength value, f_t, for the material of all columns has been taken simply as 1 MPa. The columns have been modeled and analyzed in the Abaqus [19]. The Concrete Damaged Plasticity model in the program has been used to consider degradation in modulus of elasticity of the material due to damage. Stress-strain relations for the texture of the columns were obtained using the diagrams proposed by Hognestad [20] in compression and by Massicotte et al. [21] in tension, Fig. 2. Damaged plasticity parameters used in the analyses were taken from Abaqus's user manuel and the related study of the Valente and Milani [22], (Table 2).

Static analyses have been performed in the Abaqus program to determine both the vertical and horizontal load capacities of the columns. Vertical load capacities were also determined using the classical $\sigma = N/A$ expression in Strength of Materials. The "displacement control method" was used to determine the vertical load capacities of the columns with the Abaqus program. As for the horizontal load capacities, they were determined by applying firstly a vertical load equal to their own weight to the columns, and then imposing horizontal displacement using again the displacement control method. The C3D8R finite element type has been used in the finite element models of the columns. Finite element models of the columns are given in Fig. 3. All freedoms of all nodes at the base cross-sections of the columns were restrained, i.e. the columns were taken as fixed at their bases.

4. Analyses, obtained results and discussions

In this part of the study, the vertical and lateral load carrying capacities of the columns have been calculated. The values of the vertical capacities obtained from the classical formula and the Abaqus are presented in Table 3. The results are quite close to each other. Compared to the formula, the program gave higher capacity values for the columns, except the Kılıç Ali Paşa Mosque column. It is rather normal to have some difference between the formula and the Abaqus results. Because, the formula is based on simply not exceeding the strength without any damage to the columns, whereas Abaqus, by considering many parameters, takes into account the damage to the columns as the calculation progresses. On the other hand, it is needless to say that, the vertical capacity increases from the columns with small cross-sectional area to the larger ones. With a value of approximately 460000 kN, column of the Süleymaniye Mosque has the highest vertical load capacity.

In the analyses with the Abaqus program, vertical displacement was imposed to the upper cross-sections of the columns and the total axial (vertical) reaction forces were calculated at the nodes in the base sections of the columns. Vertical displacement - base axial reaction graphs obtained with the program are given in Fig. 4.

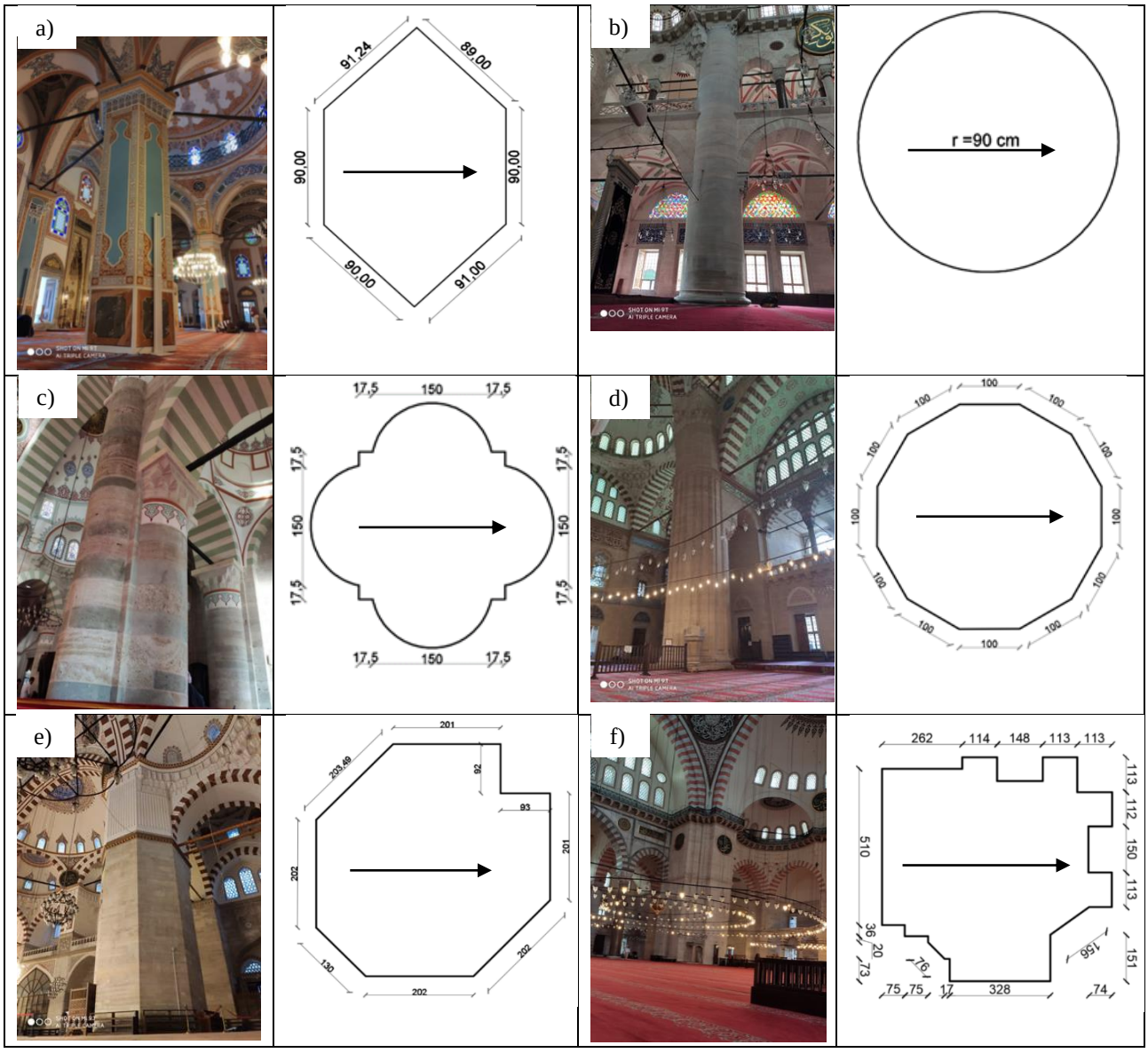

Figure 1. Columns, their sections and dimensions in the examined mosques of Mimar Sinan: a) Sinan Pasha Mosque, b) Kılıç Ali Pasha Mosque, c) Mihrimah Sultan Mosque (Üsküdar), d) Selimiye Mosque, e) Şehzade Mosque, f) Süleymaniye Mosque (dimensions are in cm and drawings are not to scale)

Table 1. Material properties used in calculations for the columns

Material	Unit weight, γ (kN/m^3)	Modulus of elasticity, E (MPa)	Compressive strength, f_c (MPa)	Tensile strength, f_t (MPa)	Poisson's ratio, ν
Küfeki stone + Khorasan mortar	19.7	8630	11.5	1	0.20
M. marble + Khorasan mortar	26.5	10656	14.25	1	0.20

From the graphs, the behavior of the columns under increasing axial displacement, hence increasing axial load, can be clearly seen. With the analyses made with Abaqus, it is as if axial loading tests were performed on the columns in the laboratory. In this way, resistance to the increased load, reaching the maximum resistance, then

decrease in resistance with increasing damage in the body, and eventually the complete crushing of the columns could be observed. This is just one of the numerous examples that illustrate the possibilities that an advanced software like Abaqus provides for engineers.

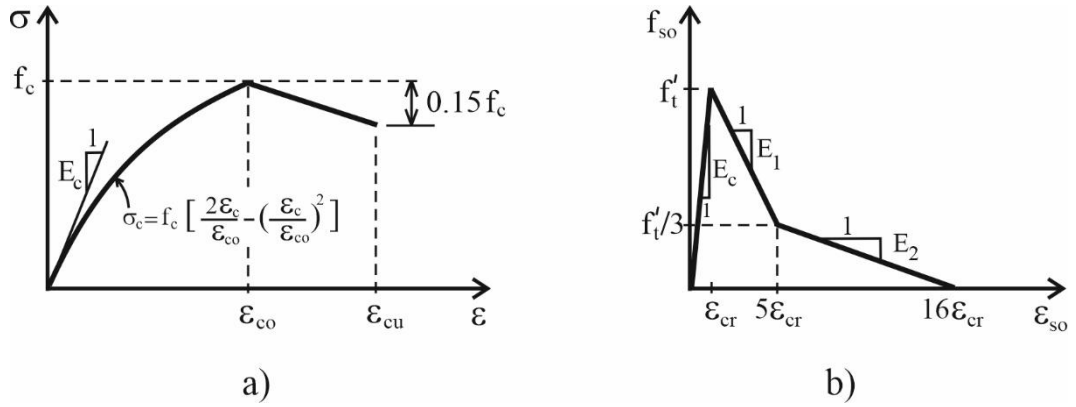

Figure 2. Stress-strain diagrams for the texture of the columns: a) in compression (Hognestad [20]), b) in tension (Massicotte et al. [21])

Table 2. Damaged plasticity parameters used in the analyses, [22]

Dilatation angle	Strength ratio	Eccentricity	*K* par.	Viscosity par.
10°	1.16	0.1	0.667	0.002

Table 3. Geometric properties of the columns and the vertical load carrying capacities obtained for them

Mosque	Column height, *h*(m)	Cross-sect. area, *A* (m^2)	N_{max}, Class. cal. (kN)	N_{max}, Abaqus (kN)
Sinan Pasha	5.8	1.93	22200	24891
Kılıc Ali Pasha	11.3	2.46	35600	34331
Mihrimah Sultan	10.3	6.84	78700	79900
Selimiye	19.2	10.87	125000	135606
Şehzade	15.2	15.39	177000	190007
Süleymaniye	18.65	36	414000	458734

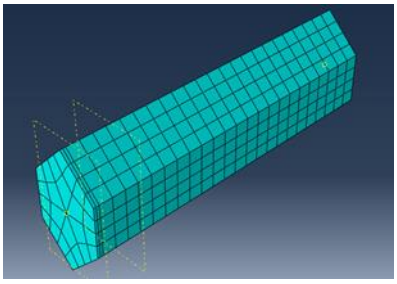

a) Column of Sinan Pasha Mosque,
Number of elements: 600
Number of nodes: 962

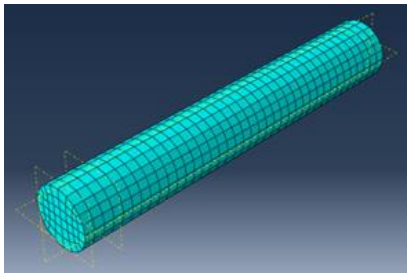

b) Column of Kılıç Ali Pasha Mosque,
Number of elements: 1672,
Number of nodes: 2145

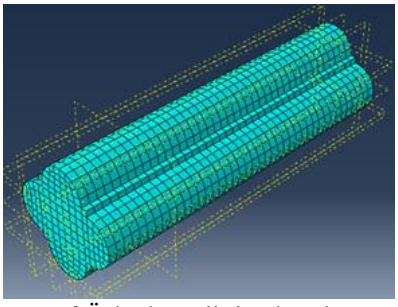

c) Column of Üsküdar Mihrimah Sultan Mosque,
Number of elements: 6232
Number of nodes: 7434

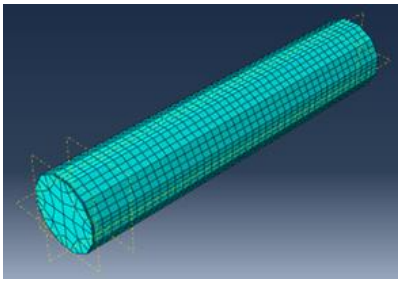

d) Column of Selimiye Mosque,
Number of elements: 1760
Number of nodes: 2745

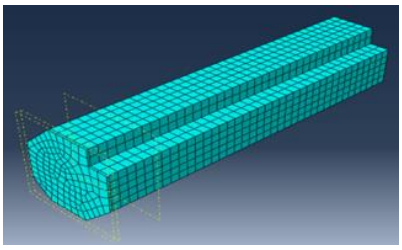

e) Column of Şehzade Mosque,
Number of elements: 4797
Number of nodes: 5720

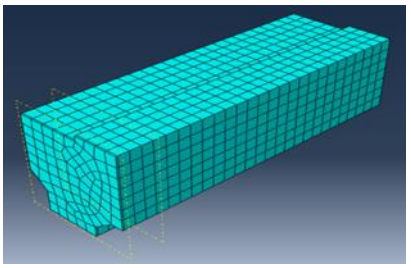

f) Column of Süleymaniye Mosque,
Number of elements: 2241
Number of nodes: 2856

Figure 3. Finite element meshes of the columns

When an approximate superstructure weight is calculated for any of the mosques, taking into account the dome, main arches, pendentives and weight towers (if any), and the force per column is determined (see reference [10]), it is seen that the value obtained is well below the capacity of the column. It is well known that this is the case in the vast majority of historical buildings, that is, the load-bearing elements in these buildings had been "overdesigned" against vertical loads. Here, we saw that Sinan also adhered to the tradition and designed and built the columns in his mosques in a rather safe way against vertical loads. The fact that he was the chief architect in the most powerful period of the Ottoman Empire is undoubtedly another important factor that enabled Sinan to be more generous in his designs.

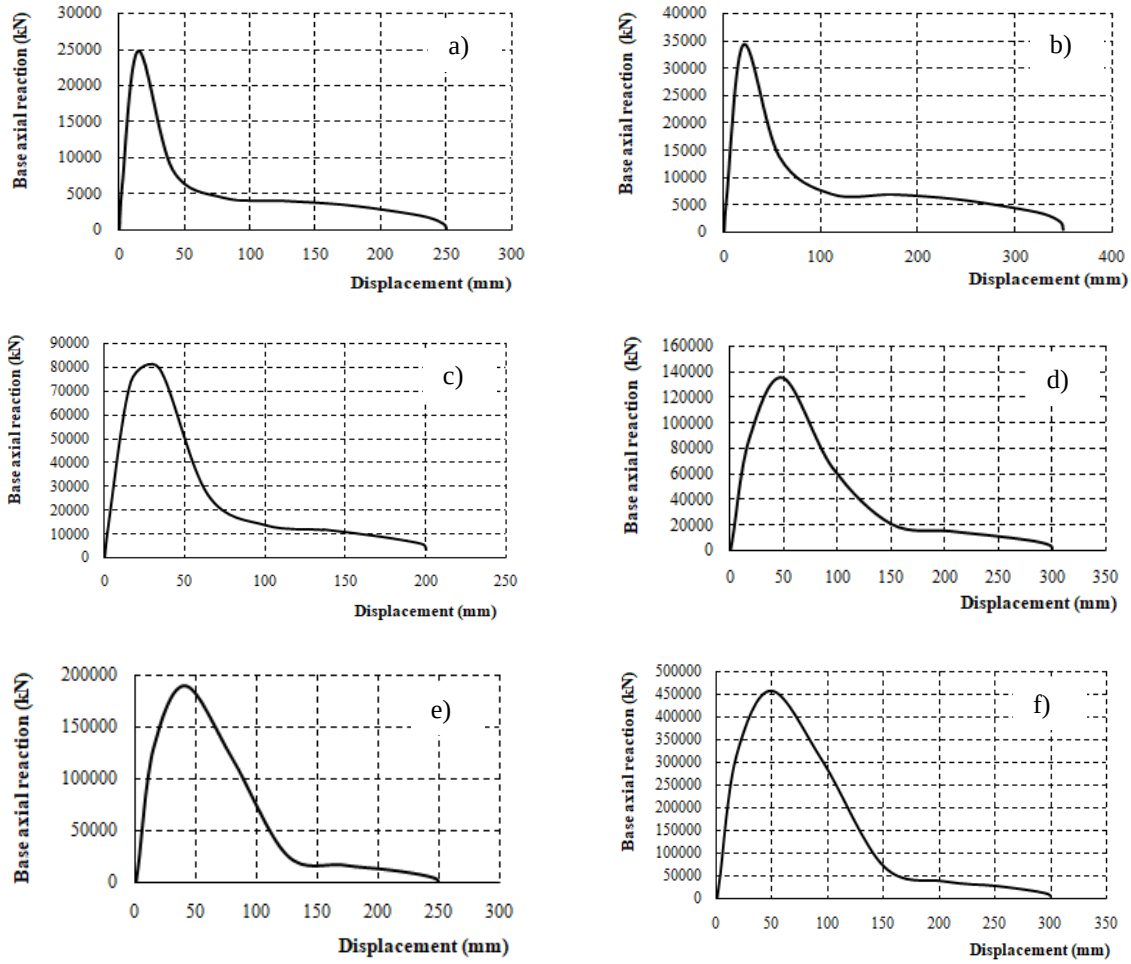

Figure 4. Vertical displacement – base axial reaction graphics for the columns: a) Sinan Pasha Mosque, b) Kılıç Ali Pasha Mosque, c) Üsküdar Mihrimah Sultan Mosque, d) Selimiye Mosque, e) Şehzade Mosque, and f) Süleymaniye Mosque

To determine the horizontal load capacities of the columns, initially an axial load equal to self-weight of the column was applied to the top of each column in the Abaqus program. Then, gradually increasing horizontal displacements were imposed on the upper section of the column and the shear forces at the base cross-section were calculated. The directions in which the horizontal displacement is applied to the columns are indicated in Fig. 1 on the column cross-sections. Top cross-section horizontal displacement versus base shear force relationships obtained in this way are presented in Fig. 5. The values determined for the horizontal load capacities of the columns are given in Table 4. If desired, by considering various values of the axial load applied to the top sections of the columns, it can also be determined how this load affects the horizontal capacities.

The cross-section shape, which does not all that come to the fore when calculating vertical capacities, shows itself in the horizontal capacities. This can be noticed when Fig. 4 and Fig. 5 are compared. Indeed, while the graphs in Fig. 4 are more similar among themselves, the similarity of the graphs in Fig. 5 is less. Of course, the fact that column heights are important when calculating horizontal capacities also has influence on this situation. When Table 3 and Table 4 are examined together, this can be seen immediately. For example, let' s compare the columns of Mihrimah Sultan and Şehzade Mosques. For this comparison to be meaningful, it is worth remembering that identical material properties (Küfeki stone + Khorasan mortar) were taken into account for the two columns, Table 1. The cross-sectional area of the Şehzade Mosque' s column is bigger than that of the Mihrimah Sultan Mosque, and therefore its vertical load capacity is higher, Table 3. However, the column of the Şehzade Mosque has a slightly lower horizontal load capacity due to its greater height, Table 4. This simple comparison

shows once again how important the column length is on the lateral load capacities of the columns, a fact well known to structural engineers.

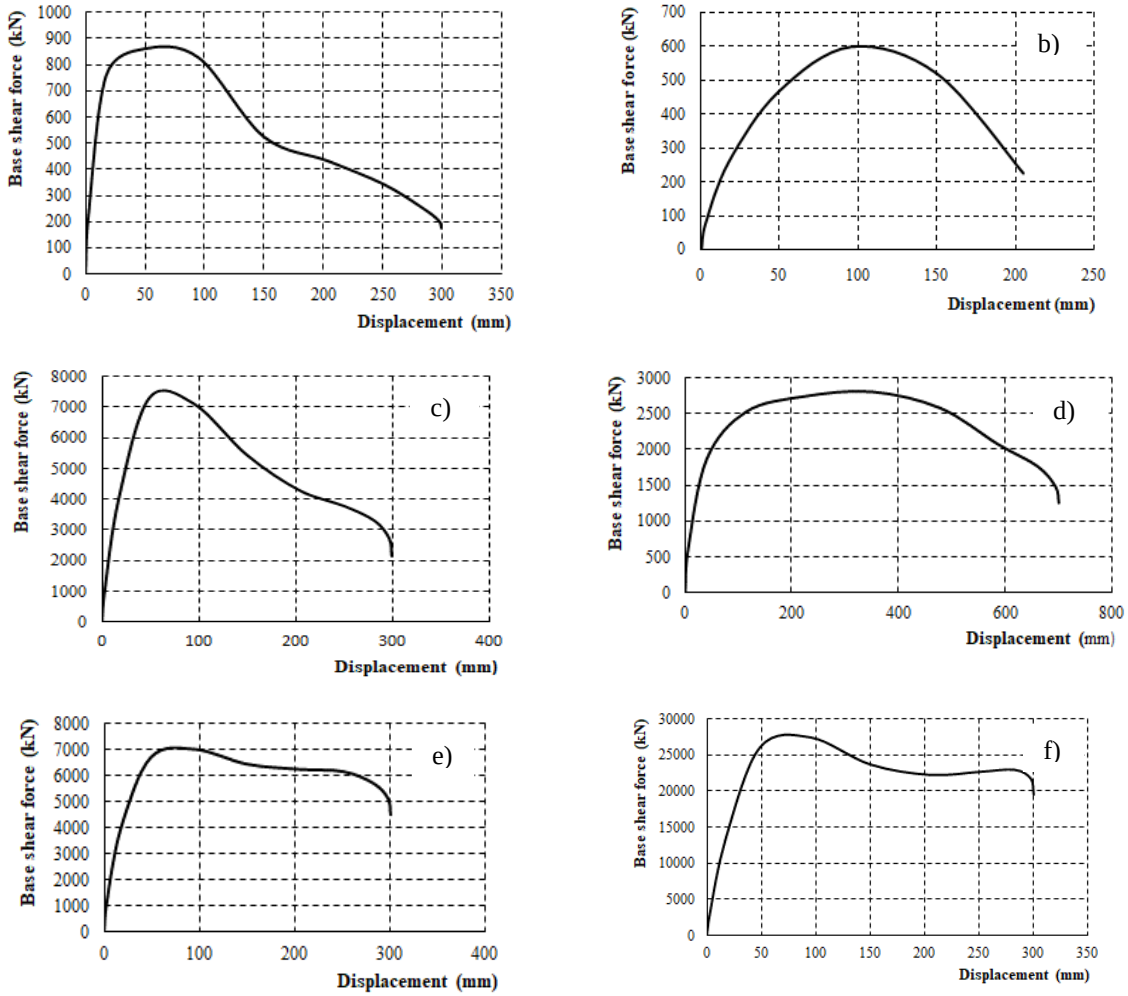

Figure 5. Top section horizontal displacement – base shear force graphics for the columns: a) Sinan Pasha Mosque, b) Kılıç Ali Pasha Mosque, c) Üsküdar Mihrimah Sultan Mosque, d) Selimiye Mosque, e) Şehzade Mosque, and f) Süleymaniye Mosque

Table 4. The results obtained for the horizontal load carrying capacities of the columns

Mosque	H_{max} **(kN)**
Sinan Pasha	857
Kılıç Ali Pasha	600
Mihrimah Sultan	7279
Selimiye	2740
Şehzade	6997
Süleymaniye	27526

If the horizontal load capacities of all columns are compared, it is seen that, despite its great height, the column of the Süleymaniye Mosque is well ahead, as in its vertical load capacity, due to its colossal cross-sectional area. From here, it is seen that, as is the common opinion of all experts on the subject, Sinan designed and built the Süleymaniye in a privileged way in terms of "strength" as well as in other aspects. As for the columns of other mosques, the values obtained show that, they also have lateral load capacities at significant levels. Therefore, it is obvious that, together with the walls, they will provide significant lateral resistance to the buildings

they belong to under horizontal effects such as earthquakes and winds.

5. Some further remarks

In this study, in particular, the column forms, and vertical and lateral load capacities of Mimar Sinan mosques are discussed. As mentioned earlier, there are many other studies on Sinan's mosques. On the other hand, when we look at the literature, it is seen that there are innumerable works about historical structures and historical mosques in general. A few such works are given in [23-29] for the sake of sample. Investigation of historical buildings in every aspect and comprehensively will guide us in understanding these structures better and transferring them to future generations with confidence. Therefore, future studies in this direction will also certainly be valuable.

6. Conclusions

The great Ottoman architect Sinan is one of the most prominent figures in the history of world architecture, "whose works are worth examining elaborately and in all aspects". Numerous studies (scientific articles, theses, etc.) have been made on his works. This study aimed to determine the vertical and horizontal load capacities of the columns of some mosques of the great architect. Mosques considered are Sinan Pasha, Kılıç Ali Pasha, Üsküdar Mihrimah Sultan, Selimiye, Şehzade and Süleymaniye Mosques. The columns of these structures have different geometric shapes. Their dimensions were measured in situ, and the material properties were taken from studies related to the subject. The vertical load capacities of the columns were determined both with the classical stress expression and with the Abaqus program, and the lateral load capacities were determined only with Abaqus. The vertical load capacities determined by the two methods are rather close. Very high vertical load capacity values were calculated for all columns. It has been determined that the horizontal load capacities are also generally quite good, especially the column of the Süleymaniye Mosque, which has a very large cross-section. Hence, it is understood that Sinan designed and built the columns in his buildings to withstand vertical loads very well and to have substantial resistance to horizontal loads. He almost always kept the outer walls thick in his buildings and did not leave the columns alone against horizontal loads.

Acknowledgment

The authors would like to express their gratitude to Çağrı Mollamahmutoğlu, an academic member of Yıldız Technical University Civil Engineering Department, for his invaluable help about Abaqus program.

Contribution of the Authors

The article was produced with the joint contributions of the authors.

Conflict of Interest Statement

There is no conflict of interest between the authors.

Statement of Research and Publication Ethics

Research and publication ethics were complied with in the study.

References

[1] D. Macaulay, *Mosque*, Houghton Mifflin Company, Boston, USA, 2003.
[2] P. Rabb, *We are all servants here! Mimar Sinan - architect of the Ottoman Empire*, Periodica Polytechnica Architecture, 44(1), pp. 17-37, 2013.
[3] F.Y. Yokel, *Stability and load capacity of members with no tensile strength*, Journal of the Structural Division, Proceed. ASCE, 97-ST7, pp. 1913-1926, 1971. https://doi.org/10.1061/JSDEAG.0002954
[4] R. Frisch-Fay, *Stability of masonry piers*, International Journal of Solids and Structures", 11, pp. 187-198, 1975.
[5] Z. Ahunbay, *Construction techniques and materials used in Mimar Sinan structures* (in Turkish), Mimarbaşı Koca Sinan: His Age and Works, T. C. General Directorate of Foundations, İstanbul, 1988.
[6] L. La Mendola, and M. Papia, *Stability of masonry piers under their own weight and eccentric load*,

Journal of Structural Engineering, ASCE, 119(6), pp. 1678 1693, 1993.
[7] A. De Falco, and M. Lucchesi, *Stability of columns with no tension strength and bounded compressive strength and deformability. Part I: Large eccentricity*, International Journal of Solids and Structures, 39, pp. 6191-6210, 2002.
[8] N. Arioğlu, E. Arioğlu, *Engineering mystery of Master Architect Sinan's "Küfeki" shell limestone*, Architectural Science Review, 48, pp. 163-172, 2005.
[9] M. A. Gurel, A. Senocak, R. K. Pekgokgoz, and M. Gumuscu, *Numerical assessment of the lateral stiffness of unreinforced masonry rectangular columns,* International Journal of Architectural Heritage, 5:6, pp. 559-585, 2011.
[10] M. A. Gurel, R. K. Pekgokgoz, F. Cili, *Strength capacity of unreinforced masonry cylindrical columns under seismic transverse forces*, Bull Earthquake Eng., 10, pp. 587–613, 2012.
[11] B. S. Seker, *Investigation of the behavior of Mimar Sinan mosques under static and dynamic loads*, Karadeniz Technical University, Institute of Science, PhD Thesis, Trabzon, 340 page (In Turkish), 2011.
[12] M. A. Gurel, *Stability of slender masonry columns with circular cross-section under their own weight and eccentric vertical load*, International Journal of Architectural Heritage, 10:8, pp. 1008-1024, 2016.
[13] P. Crespi, A. Franchi, N. Giordano, M. Scamardo, P. Ronca, *Structural analysis of stone masonry columns of the Basilica S. Maria di Collemaggio,* Engineering Structures, 129, pp. 81-90, 2016. https://doi.org/10.1016/j.engstruct.2016.05.045
[14] E. Çaktı, Ö. Saygılı, E. Dar, and T. Ercan, *Seismic Behavior of The Edirnekapı Mihrimah Sultan Mosque in Istanbul*, 6th ECCOMAS Thematic Conference on Computational Methods in Structural Dynamics and Earthquake Engineering, 2017.
[15] M. Broseghini, P. Zanetti, A.D. Jefferson, M. Gei, *Progressive instability in circular masonry columns*, Engineering Structures, 157, pp. 96-104, 2018.
[16] R. Illampas, I. Ioannou, P. B. Lourenço, *Seismic appraisal of heritage ruins: The case study of the St. Mary of Carmel church in Cyprus,* Engineering Structures, 224, Article 111209, 2020.
[17] M. Tomaževič, *Earthquake-Resistant Design of Masonry Buildings*, Imperial College Press, London, 268 pages, 1999.
[18] Ş. Korkmaz, *Determination of thermal conductivity, physical and mechanical properties of brick materials used in historical buildings*, Dep. of Civil Eng., Graduate School of Natural and Applied Sciences, Süleyman Demirel University, Isparta, 241 pages, (in Turkish), 2019.
[19] Abaqus, Theory manual. Version 6.14-5; 2014.
[20] E. Hognestad. *A study of combined bending and axial load in reinforced concrete members*, University of Illinois Bulletin, Vol. 49, No. 22, Urbana, Illinois, 128 pages, 1951.
[21] B. Massicotte, A.E. Elwi, J.G. MacGregor, *Tension stiffening model for planar reinforced concrete members*, ASCE Journal of Structural Engineering 116 (11), pp. 3039–3058, 1990.
[22] M. Valente, and G. Milani, *Effects of geometrical features on the seismic response of historical masonry towers*, Journal of Earthquake Engineering, 2017.
[23] A. E. Akan, G. Ç. Başok, A. Er, H. T. Örmecioğlu, S. Z. Koçak, T. Cosgun, O. Uzdil, B. Sayin, *Seismic evaluation of a renovated wooden hypostyle structure: A case study on a mosque designed with the combination of Asian and Byzantine styles in the Seljuk era (14th century AD)*, Journal of Building Engineering, 43, 103112, 2021.
[24] E. Isik, B. Antep, A. Buyuksarac, M.F. Isik, *Observation of behavior of the Ahlat Gravestones (TURKEY) at seismic risk and their recognition by QR code*, Structural Engineering and Mechanics, 72(5), 643–652, 2019.
[25] T. Cosgun, B. Sayin, B. Gunes, A.O. Avşar, R. Şengün, Gümüşdağ, G. *Rehabilitation of historical ruined castles based on field study and laboratory analyses: The case of Bigalı Castle in Turkey*, Revista de la Construcción, 19(1), 52–67, 2020.
[26] H. Bilgin, F. Ramadani, *Numerical study to assess the structural behavior of the Bajrakli Mosque (Western Kosovo)*, Hindawi, Advances in Civil Engineering, 2021, 4620916, 2021.
[27] E. Işık, E. Harirchian, E. Arkan, F. Avcil, and M. Günay, *Structural Analysis of Five Historical Minarets in Bitlis (Turkey)*, Buildings, 12, 159, 2022.
[28] R. İzol, M. A. Gürel, R. K. Pekgökgöz, F. Avcil, *Out-of-plane seismic resistance of high masonry walls having rectangular buttresses*, Journal of the Faculty of Engineering and Architecture of Gazi University- 34:2 (2019) 1007-1023. 2019.

[29] M. A. Gürel, R. İzol, B. İpekyüz, H. A. Büyüktaşkın, and R.K. Pekgökgöz, *Comparison of Buckling Loads of Masonry Slender Columns with Rectangular and Circular Cross-Section*, Journal of Polytechnic, 2021; 24(1) : 131-142. 2021. (In Turkish).

Bitlis Eren Üniversitesi Fen Bilimleri Dergisi
BİTLİS EREN UNIVERSITY JOURNAL OF SCIENCE
ISSN: 2147-3129/e-ISSN: 2147-3188
VOLUME: 11 NO: 2 PAGE: 660-665 YEAR: 2022
DOI: 10.17798/bitlisfen.1083043

Double and Type (3,0) Minkowski Pythagorean Hodograph Curves

Aziz YAZLA[1], Muhammed Talat SARIAYDIN[1*]

[1]*Selcuk University, Faculty of Sceince, Department of Mathematics, 42130, Konya, TÜRKİYE (ORCID: 0000-0003-3720-9716) (ORCID: 0000-0002-3613-4276)*

Keywords: Double Minkowski Pythagorean hodograph curve, Minkowski-Hopf map, Type (n,m) curve.

Abstract

In present paper, Double Minkowski Pythagorean Hodograph (DMPH) curves and type (3,0) Minkowski Pythagorean Hodograph (MPH) curves are studied. Firstly, we obtained the conditions for a MPH curve to be a DMPH curve. Then, we examined these conditions in split quaternion form. Finally, a special class of seventh degree MPH curves is characterized and illustrative examples are given.

1. Introduction

Polynomials are symbolic objects that are frequently used, especially in computer science and computational algebra. Consisting of polynomial components, polynomial curves are one of the curves studied extensively in computational geometry. These curves have application areas such as computer aided geometric design, robotics, navigation, and motion control, therefore they maintain their importance today. Pythagorean hodograph curves, simply PH curves, are polynomial curves that provide the equality called the Pythagorean condition. This condition is satisfied by the hodograph of these curves and a distinguishing property for them among the polynomial curves. For planar PH curves, this condition can be expressed using the conformal map $\mathbb{C} \to \mathbb{C}$ defined by $z \to z^2$ and taking z as a complex polynomial [4]. For spatial PH curves, this condition can be given using quaternion polynomials. The quaternion formulation gives a very elegant and concise description of this structure which contributes to the development of basic algorithms to construct and analyze the PH curves [5]. Alternatively, using complex polynomials, the construction of spatial PH curves can be given with the Hopf map $\mathbb{C}^2 \to \mathbb{R}^3$. This transformation associates points $P \in \mathbb{R}^3$ with complex number pairs α, β such that $P = H(\alpha, \beta)$. Taking α and β as complex polynomials, the Pythagorean condition can be obtained [6].

In computer aided design and manufacturing, PH curves play an important role, as rational representations of shapes are important in fields such as robotics, animation, computer graphic design, and motion control. Considering the applications mentioned above, orthonormal frames are needed to describe the direction of the particle moving along a path. One of the most commonly used orthonormal frames is the Frenet frame. However, this frame is not very suitable for practical applications because it is not defined at points where the second derivative of the curve is zero and because the normal plane vectors rotate unnecessarily about the tangent. To overcome this problem, rotation minimizing orthonormal frames (RMF) are used [7]. Using this, RRMF-PH curves of type (n, m) is defined by Dospra [2]. In this study, some special type (n, m) curves are examined. For further information on PH curves and applications, see [3], [9-11].

In this paper, we describe DMPH curves as a new concept that will be helpful for Lorentzian geometry and its physical applications in Minkowski 3-space. We express the conditions provided by such curves using split quaternion polynomials. Also, we study MPH curves of type $(3,0)$ which are a class of MPH curves with degree 7. We give illustrative examples for both MPH curves of type $(3,0)$ and DMPH curves that support the constructed theories that will find applications.

*Corresponding author: talatsariaydin@gmail.com
Received: 04.03.2022, Accepted: 27.05.2022

2. Preliminaries

The set

$$\widetilde{\mathbb{H}} = \{\varepsilon = \varepsilon_0 + \varepsilon_1 \boldsymbol{i} + \varepsilon_2 \boldsymbol{j} + \varepsilon_3 \boldsymbol{k} : \varepsilon_0, \varepsilon_1, \varepsilon_2, \varepsilon_3 \in \mathbb{R}, \boldsymbol{i}^2 = \boldsymbol{j}^2 = 1, \boldsymbol{k}^2 = -1, \boldsymbol{ijk} = 1\}$$

which is defined in $(-,+,+,-)$ signed $\mathbb{R}_2^4$ semi-Euclidean space is called the ring of split quaternions. We present the classification of split quaternions according to their semi-Euclidean scalar product with themselves in $\mathbb{R}_2^4$. Let $\varepsilon = \varepsilon_0 + \varepsilon_1 \boldsymbol{i} + \varepsilon_2 \boldsymbol{j} + \varepsilon_3 \boldsymbol{k} \in \widetilde{\mathbb{H}}$. In this case, if

i. $\langle \varepsilon, \varepsilon \rangle_{\mathbb{R}_2^4} = -\varepsilon_0^2 + \varepsilon_1^2 + \varepsilon_2^2 - \varepsilon_3^2 > 0$,
ii. $\langle \varepsilon, \varepsilon \rangle_{\mathbb{R}_2^4} = -\varepsilon_0^2 + \varepsilon_1^2 + \varepsilon_2^2 - \varepsilon_3^2 < 0$,
iii. $\langle \varepsilon, \varepsilon \rangle_{\mathbb{R}_2^4} = -\varepsilon_0^2 + \varepsilon_1^2 + \varepsilon_2^2 - \varepsilon_3^2 = 0$,

then ε is called spacelike, timelike or lightlike split quaternion, respectively [8].

Let $\omega(t) = (\alpha(t), \beta(t), \gamma(t))$ be a PH curve in $\mathbb{R}^3$. If the components of the hodograph of ω are relatively prime, there exist polynomials $k(t), l(t), m(t), q(t)$ such that

$$\begin{aligned}
\alpha'(t) &= k^2(t) + l^2(t) - m^2(t) - q^2(t) \\
\beta'(t) &= 2[k(t)q(t) + l(t)l(t)] \\
\gamma'(t) &= 2[l(t)q(t) - k(t)m(t)] \\
\sigma(t) &= k^2(t) + l^2(t) + m^2(t) + q^2(t).
\end{aligned}$$

where,

$$[\alpha'(t)]^2 + [\beta'(t)]^2 + [\gamma'(t)]^2 = \sigma^2(t).$$

This kind of hodographs are called primitive hodographs [5].

Spatial PH curves can be generated by quaternion polynomials. Let $\boldsymbol{K}(t) = k(t) + l(t)\boldsymbol{i} + m(t)\boldsymbol{j} + q(t)\boldsymbol{k}$ be a quaternion polynomial. The quaternion product

$$\begin{aligned}
\omega'(t) &= \boldsymbol{K}(t)\boldsymbol{i}\boldsymbol{K}^*(t) \\
&= [k^2(t) + l^2(t) - m^2(t) - q^2(t)]\,\boldsymbol{i} \\
&\quad +2[k(t)q(t) + l(t)m(t)]\,\boldsymbol{j} \\
&\quad +2[l(t)q(t) - k(t)m(t)]\,\boldsymbol{k}
\end{aligned}$$

gives the hodograph of the PH curve, so generates the PH curve [1].

3. DMPH Curves and Type (3,0) Curves

In this section, we give the definition of DMPH curve. We construct DMPH conditions in Minkowski-Hopf map form and split quaternion form. Then, we give illustrative examples. Also, we characterize type (3,0) MPH curves and give an example.

First of all, we present some basic concepts on MPH curves. Since all null curves in $\mathbb{R}_1^3$ are MPH curves and there is no timelike MPH curve, we consider regular spacelike MPH curves.

The characterization of planar MPH curves can be given with hyperbolic polynomials. If $\omega(t) = (\alpha(t), \beta(t))$ is a MPH curve in $\mathbb{R}_1^2$, the hodograph of ω is expressed with the hyperbolic polynomial $\gamma(t) = k(t) + l(t)\boldsymbol{e}$ such that $\omega'(t) = \gamma^2(t)$. On the otherhand, spatial MPH curves are characterized by split quaternion polynomials. If $\omega(t) = (\alpha(t), \beta(t), \gamma(t))$ is a MPH curve in $\mathbb{R}_1^3$, the hodograph of ω is expressed with the split quaternion polynomial $\boldsymbol{T}(t) = k(t) + l(t)\boldsymbol{i} + m(t)\boldsymbol{j} + q(t)\boldsymbol{k}$ such that $\omega'(t) = \boldsymbol{T}(t)\boldsymbol{i}\boldsymbol{T}^*(t)$ [9].

Definition.3.1. For a regular polynomial curve $\omega(t)$ in $\mathbb{R}_1^3$ Minkowski space, if both $\|\omega'(t)\|_L$ and $\|\omega'(t) \times_L \omega''(t)\|_L$ are polynomials of t, then $\omega(t)$ is called a Double Minkowski Pythagorean Hodograph (DMPH) curve [12].

Theorem.3.1. Let $\omega(t)$ be a regular MPH curve given in Minkowski-Hopf map form with hyperbolic polynomials $f_1(t)$ and $f_2(t)$. $\omega(t)$ with timelike normal is a DMPH curve iff the proportionality polynomial of $f_1(t)$ and $f_2(t)$ defines a planar MPH curve.

Proof. The DMPH condition given in [12] is expressed as

$$f_1(t)f_2'(t) - f_1'(t)f_2(t) = \delta(t)\boldsymbol{\mu}^2(t) \qquad (3.1)$$

where $\delta(t)$ is a real polynomial and $\mu(t) = a(t) + b(t)\boldsymbol{e}$ is a hyperbolic polynomial such that the polynomials $a(t)$ and $b(t)$ are relatively prime.

Identifying the set of hyperbolic numbers H with $\mathbb{R}_1^2$, since the right side of the equality (3.1) defines a planar MPH curve, we can consider the proportionality polynomial of $f_1(t)$ and $f_2(t)$ as the hodograph of a planar MPH curve.

Minkowski-Hopf map forms of DMPH conditions can be derived by direct calculations. Differentiating the equalities

$$\alpha'(t) = f_1(t)\overline{f_1}(t) - f_2(t)\overline{f_2}(t), \quad \beta'(t) - \gamma'(t)\boldsymbol{e} = 2f_1(t)\overline{f_2}(t)$$

we get

$$\alpha''(t) = f_1'(t)\overline{f_1}(t) + f_1(t)\overline{f_1}'(t) - f_2'(t)\overline{f_2}(t) - f_2(t)\overline{f_2}'(t)$$

and

$$\beta''(t) - \gamma''(t)\boldsymbol{e} = 2\left(f_1'(t)\overline{f_2}(t) + f_1(t)\overline{f_2}'(t)\right).$$

Then, we can write

$$\beta'(t)\gamma''(t) - \beta''(t)\gamma'(t) = \frac{1}{2}\boldsymbol{e}[(\beta'(t) - \gamma'(t)\boldsymbol{e})(\beta''(t) + \gamma''(t)\boldsymbol{e}) + (\beta'(t) + \gamma'(t)\boldsymbol{e})(\beta''(t) - \gamma''(t)\boldsymbol{e})$$

and

$$(\beta'(t)x''(t) - \beta''(t)\gamma'(t)) + (\gamma'(t)\alpha''(t) - \gamma''(t)\alpha'(t))\boldsymbol{e} = \alpha''(t)(\beta'(t) + \gamma'(t)\boldsymbol{e}) - \alpha'(t)(\beta''(t) + \gamma''(t)\boldsymbol{e}).$$

Denoting

$$\eta(t) = f_1(t)f_2'(t) - f'_1(t)f_2(t),$$

we find

$$\beta'(t)\gamma''(t) - \beta''(t)\gamma'(t) = 2\boldsymbol{e}(\overline{f_1}(t)\overline{f_2}(t)\eta(t) - f_1(t)f_2(t)\bar{\eta}(t))$$

and

$$(\beta'(t)\alpha''(t) - \beta''(t)\gamma'(t)) + (\gamma'(t)\alpha''(t) - \gamma''(t)\alpha'(t))\boldsymbol{e} = -2\left(\overline{f_1}^{\,2}(t)\eta(t) + f_2^2(t)\bar{\eta}(t)\right).$$

Thus, if N is timelike,

$$\|\omega' \times_L \omega''\|_L^{\,2} = \left(\beta'(t)\gamma''(t) - \beta''(t)\gamma'(t)\right)^2 + \left(\gamma'(t)\alpha''(t) - \gamma''(t)\alpha'(t)\right)^2 - \left(\beta'(t)\alpha''(t) - \beta''(t)\alpha'(t)\right)^2$$

$$= -4\sigma^2(t)|\eta(t)|$$

we obtain

$$\rho(t) = -4|\eta(t)| = 4|\boldsymbol{e}\eta(t)|.$$

If N is spacelike, we obtain

$$\rho(t) = 4|\eta(t)|.$$

Example.3.1. Consider the curve

$$\omega(t) = \left(t, \frac{2}{3}t^3, -t^2\right)$$

in $\mathbb{R}_1^3$ Minkowski space. The curve $\omega(t)$ is a DMPH curve and Frenet vectors and curvatures of $\omega(t)$ are

$$T(t) = \frac{1}{2t^2-1}(1, 2t^2, -2t),$$
$$N(t) = \frac{2}{(2t^2-1)^2}(-2t(t^2-1), 2t^3 - t, 1 - 2t^4),$$
$$B(t) = \frac{2}{2t^2-1}(t^2, 1, -t)$$

and

$$\kappa(t) = \frac{2}{(2t^2-1)^2}, \tau(t) = \frac{2}{(2t^2-1)^2}.$$

Since $\langle \omega'(t), \omega'(t)\rangle_L = (2t^2-1)^2$, $\omega(t)$ is a spacelike curve for $t \neq \pm\frac{1}{\sqrt{2}}$. Hence, for all $t \in \mathbb{R} \setminus (-\frac{1}{\sqrt{2}}, \frac{1}{\sqrt{2}})$, $\|\omega'(t)\|_L = 2t^2 - 1$, so $\omega(t)$ is a MPH curve. On the other hand, since $\langle \omega'(t) \times_L \omega''(t), \omega'(t) \times_L \omega''(t)\rangle_L = 4(2t^2-1)^2$ for $t \neq \pm\frac{1}{\sqrt{2}}$, $\omega'(t) \times_L \omega''(t)$ and so $B(t)$ is spacelike and $N(t)$ is timelike. Hence, for all $t \in \mathbb{R} \setminus (-\frac{1}{\sqrt{2}}, \frac{1}{\sqrt{2}})$, $\|\omega'(t) \times_L \omega''(t)\|_L = 2(2t^2-1)$, so $\omega(t)$ is a DMPH curve.

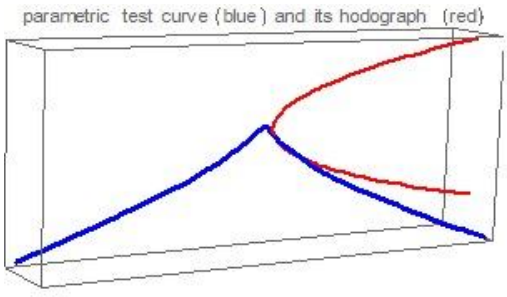

(1.a)

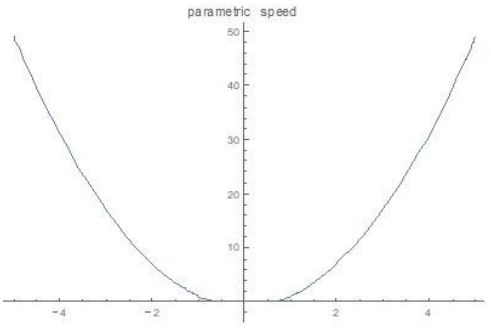

(1.b)

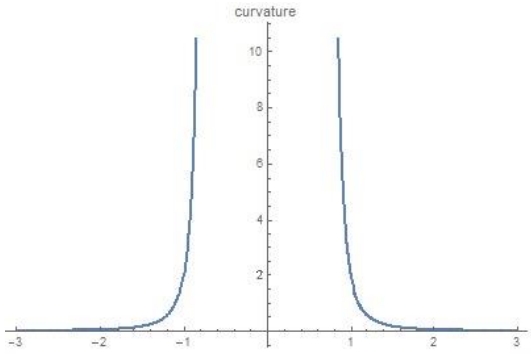

(1.c)

Figure 1. DMPH curve interpolator

Example.3.2. Consider the curve

$$\omega(t)=\left(\frac{3}{2}\left(\frac{t^3}{3}-t\right),\frac{3}{2}t^2,\frac{1}{2}\left(\frac{t^3}{3}+t\right)\right)$$

in $\mathbb{R}_1^3$ Minkowski space. The curve $\omega(t)$ is a DMPH curve and Frenet vectors and curvatures of $\omega(t)$ are

$$T(t)=\frac{1}{2\sqrt{2}(t^2+1)}(3t^2-3{,}6t,t^2+1),$$
$$N(t)=\left(\frac{2t}{t^2+1},-\frac{t^2+1}{t^2-1},0\right),$$
$$B(t)=\frac{1}{2\sqrt{2}(t^2+1)}(1-t^2,-2t,-3(t^2+1)),$$

and

$$\kappa(t)=\frac{3}{2(t^2+1)^2},\tau(t)=\frac{1}{2(t^2+1)^2}.$$

Since $\langle\omega'(t),\omega'(t)\rangle_L=2(t^2+1)^2$, $\omega(t)$ is a spacelike curve for every $t\in\mathbb{R}$. Hence, for every $t\in\mathbb{R}$, $\|\omega'(t)\|_L=\sqrt{2}(t^2+1)$, so $\omega(t)$ is a MPH curve. On the other hand, since $\langle\omega'(t)\times_L\omega''(t),\omega'(t)\times_L\omega''(t)\rangle_L=-18(t^2+1)^2$ for all $t\in\mathbb{R}$, $\omega'(t)\times_L\omega''(t)$ and so $B(t)$ is timelike and $N(t)$ is spacelike. Hence, for all $t\in\mathbb{R}$, $\|\omega'(t)\times_L\omega''(t)\|_L=3\sqrt{2}(t^2+1)$, so $\omega(t)$ is a DMPH curve.

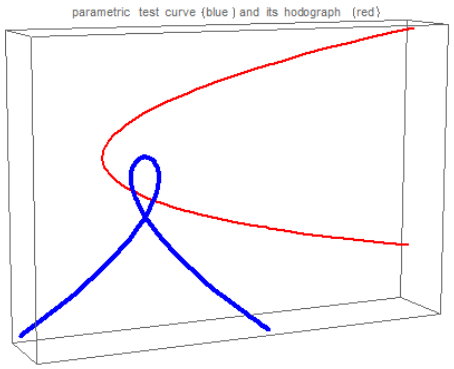

(2.a)

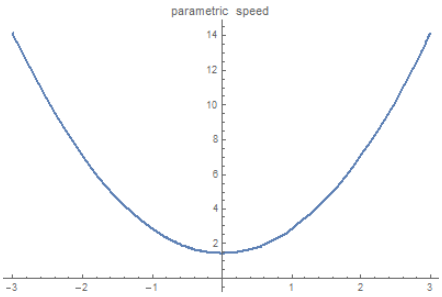

(2.b)

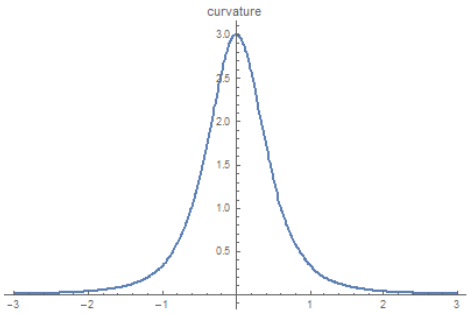

(2.c)

Figure 2. DMPH curve interpolator

Let $\omega(t)$ be a seventh degree MPH curve constructed by a cubic split quaternion polynomial $\boldsymbol{T}(t)=k(t)+l(t)\boldsymbol{i}+m(t)\boldsymbol{j}+q(t)\boldsymbol{k}$ in normal form. For $i=0,1,2$, $k_i,l_i,m_i,q_i\in\mathbb{R}$ and we can write

$$k(t)=t^3+k_2t^2+k_1t+k_0,l(t)$$
$$=l_2t^2+l_1t+l_0,$$
$$m(t)=m_2t^2+m_1t+m_0,q(t)$$
$$=q_2t^2+q_1t+q_0.$$

We suppose that $|\boldsymbol{T}(t)| \neq 0$, since we study non-null MPH curves. A MPH curve of degree 7 is of type (3,0) iff

$$l_1 = l_2 = 0,$$
$$3l_0 = m_2q_1 - m_1q_2,$$
$$3m_0 = m_1k_2 - m_2k_1,$$
$$3q_0 = k_2q_1 - k_1q_2.$$

If $\alpha(t)$ is a non-planar MPH space curve of type (3,0), then

$$l_1 = l_2 = 0, l_0 = \frac{1}{3}(m_2q_1 - m_1q_2), k_2 = 3\frac{m_2q_0 - m_0q_2}{m_2q_1 - m_1q_2}, k_1 = 3\frac{m_1q_0 - m_0q_1}{m_2q_1 - m_1q_2}, [12].$$

Example.3.3. Let $k_0 = -2, m_0 = -1, m_1 = -2, m_2 = 1, q_0 = -3, q_1 = 4, q_2 = 1$. In this case, since

$$l_0 = \frac{1}{3}(m_2q_1 - m_1q_2) = 2,$$
$$k_1 = 3\frac{m_1q_0 - m_0q_1}{m_2q_1 - m_1q_2} = 5,$$
$$k_2 = 3\frac{m_2q_0 - m_0q_2}{m_2q_1 - m_1q_2} = -1$$

we find

$$k(t) = t^3 - t^2 + 5t - 2,$$
$$l(t) = 2,$$
$$m(t) = t^2 - 2t - 1,$$
$$q(t) = t^2 + 4t - 3.$$

Since

$$\alpha'(t) = k^2(t) - l^2(t) + m^2(t) - q^2(t) = t^6 - 2t^5 - 3t^4 - 2t^3 + 3t^2 - 2t,$$
$$\beta'(t) = 2[k(t)q(t) - l(t)m(t)] = 2t^5 + 2t^4 - 8t^3 - 10t^2 + 2t - 2,$$
$$\gamma'(t) = 2[k(t)m(t) - l(t)q(t)] = 2t^5 - 4t^4 - 8t,$$
$$|\boldsymbol{T}(t)| = k^2(t) - l^2(t) - m^2(t) + q^2(t) = t^6 - 2t^5 - 3t^4 + 10t^3 + 5t^2 + 2t - 2$$

and

$$[\alpha'(t)]^2 + [\beta'(t)]^2 - [\gamma'(t)]^2 = |\boldsymbol{T}(t)|^2$$

the curve

$$\omega(t) = (\frac{1}{7}t^7 - \frac{1}{3}t^6 + \frac{11}{5}t^5 - \frac{13}{2}t^4 + 7t^3 + 4t^2 - 8t, \frac{1}{3}t^6 + \frac{6}{5}t^5 - t^4 + \frac{38}{3}t^3 - 19t^2 + 16t, \frac{1}{3}t^6 - \frac{6}{5}t^5 + 3t^4 - \frac{26}{3}t^3 - 9t^2 + 16t)$$

is a non-planar MPH space curve of type (3,0) such that $\omega(0) = (0,0,0)$. For all $t \in \mathbb{R}$ such that $|\boldsymbol{T}(t)| \neq 0$, Euler-Rodrigues frame of $\omega(t)$ is obtained as

$$\boldsymbol{e}_1(t) = \Omega(t^6 - 2t^5 + 11t^4 - 26t^3 + 21t^2 + 8t - 8{,}2t^5 + 6t^4 - 4t^3 + 38t^2 - 38t + 16{,}2t^5 - 6t^4 + 12t^3 - 26t^2 - 18t + 16),$$
$$\boldsymbol{e}_2(t) = \Omega(-2t^5 - 6t^4 + 4t^3 - 46t^2 + 54t - 8, t^6 - 2t^5 + 9t^4 - 18t^3 + 17t^2 - 2, -2t^4 - 8t^3 + 28t^2 - 24t + 2),$$
$$\boldsymbol{e}_3(t) = \Omega(2t^5 - 6t^4 + 12t^3 - 18t^2 + 14t - 8{,}2t^4 - 20t^2 - 16t + 14, t^6 - 2t^5 + 13t^4 - 10t^3 + 41t^2 - 40t + 18).$$

where $\Omega = (t^6 - 2t^5 + 11t^4 - 2t^3 + 37t^2 - 48t + 8)^{-1}$. Since $\omega(t)$ is of type (3,0), its ERF is a RRMF.

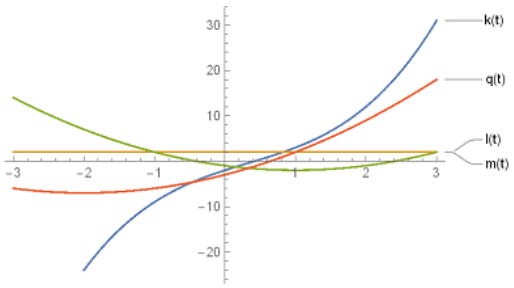

Figure 3. The condition of ERF to be RRMF

4. DMPH Curves and Type (3,0) Curves

In this study, DMPH curves are discussed as a new model of MPH curves. This model is based on rational forms of Frenet frame and curvatures of MPH curves. Considering the importance of rational representations of curves in applications, this study will also be beneficial in practice. It is obvious that by associating DMPH curves with split quaternion polynomials and Minkowski-Hopf map, it will contribute to the theory of interpolation and

approximation in Minkowski 3-space, as well as physical applications. DMPH curve conditions are investigated according to the normal vector of the curve. Thus, two examples are given for timelike and spacelike cases of the normal vector.

On the other hand, type (3,0) MPH curves are examined in this work. This special type of seventh degree MPH curves is characterized by a cubic split quaternion polynomial which is in normal form. The conditions satisfied by non-planar type (3,0) curves are given and an example is constructed by means of these properties. Type (3,0) MPH curves have a rotation minimizing ERF, so ERF is more useful than the Frenet frame in applications of these curves.

Contributions of the Authors

All authors contributed equally to this manuscript.

Conflict of Interest Statement

There is no conflict of interest between the authors.

Statement of Research and Publication Ethics

The study is complied with research and publication ethics.

References

[1] H. I. Choi, D. S. Lee, H. P. Moon, "Clifford Algebra, Spin Representation and Rational Parameterization of Curves and Surfaces," *in Advances in Computational Mathematics*, 17(1-2), 5-48, 2002.

[2] P. Dospra, "Quaternion Polynomials and Rational Rotation-Minimizing Frame Curves. Ph.D. Thesis," in *Agricultural University of Athens*, 2015.

[3] R. T. Farouki, T. Sakkalis, "Pythagorean Hodographs," in *IBM Journal of Research and Development*, 34(5), 736-752, 1990.

[4] R. T. Farouki, "The Conformal Map $z \rightarrow z^2$ of the Hodograph Plane," in *Computer Aided Geometric Design*, 11(4), 363-390, 1994.

[5] R. T. Farouki, T. Sakkalis, "Pythagorean-Hodograph Space Curves," in *Advances in Computational Mathematics*, 2(1), 41-66, 1994.

[6] R. T Farouki, "Pythagorean-Hodograph Curves," in *Springer*. 2008.

[7] C. Y. Han, "Nonexistence of Rational Rotation-Minimizing Frames on Cubic Curves," in *Computer Aided Geometric Design*, 25(4-5), 298-304, 2008.

[8] J. I. Inoguchi, "Timelike Surfaces of Constant Mean Curvature in Minkowski 3-Space," in *Tokyo Journal of Mathematics*, 21(1), 141-152 1998.

[9] Ç. Ramis, "PH Curves and Applications. M.S. Thesis," in *Ankara University*, 2013.

[10] A. Yazla, M. T. Sariaydin, "Applications of the Fermi-Walker derivative." in *Journal of Science and Arts*, 19(3), 545-560, 2019.

[11] A.Yazla, M. T. Sariaydin, "On Surfaces Constructed by Evolution According to Quasi Frame," in *Facta Universitatis, Series: Mathematics and Informatics*, 605-619, 2020.

[12] A. Yazla, M. T. Sariaydin, "Modeling with Double Minkowski Pythagorean Hodograph Curves," (Submitted).

Bitlis Eren Üniversitesi Fen Bilimleri Dergisi
BİTLİS EREN UNIVERSITY JOURNAL OF SCIENCE
ISSN: 2147-3129/e-ISSN: 2147-3188
VOLUME:11 NO: 2 PAGE: 666-677 YEAR: 2022
DOI: 10.17798/bitlisfen.1080973

Stress-Controlled Dynamic Triaxial Experiments to Examine the Liquefaction Response of Clean Sand

Abdülhakim ZEYBEK[1*]

[1]*Muş Alparslan University, Faculty of Engineering-Architecture, Department of Architecture, Muş (ORCID: 0000-0001-7096-5770)*

Keywords: Dynamic triaxial testing, Stress-controlled tests, Liquefaction, Clean sand.

Abstract

Loosely packed cohesionless soils may suffer partial or complete liquefaction during seismic loading, causing significant structural damage. The dynamic behavior of liquefiable soils is widely investigated through element testing under controlled cyclic loading in undrained conditions. In this work, a total of 20 stress-controlled dynamic triaxial experiments were conducted to investigate the influence of loading frequency and relative density on the liquefaction behavior of clean sand. The triaxial specimens were prepared at different relative densities in the range of 38 to 90% and subjected to varying cyclic stress ratios (CSR) with loading frequencies of 0.1 and/or 1 Hz. The experimental results indicated that under similar test conditions, the number of cycles needed for liquefaction was greater at 1 Hz than at 0.1 Hz, revealing that sand specimens exhibited higher liquefaction strength at higher loading frequencies. Furthermore, regardless of the cyclic loading frequency, the liquefaction resistance of sand increased with increasing densities.

1. Introduction

Historical records indicate that soil liquefaction resulted in significant damage in many past earthquake events [1]. Extensive liquefaction-induced deformations (i.e., sand boils, landslides, lateral spreading, bridge, and shallow foundation failure) were observed in the 1964 Alaska-USA earthquake [2] and the Niigata-Japan earthquake [3], which captivated the interest of researchers and engineers. Since the 1964 earthquakes, a concentrated research effort has been devoted to liquefaction-related problems, and these studies have provided important knowledge on different aspects of earthquake-induced liquefaction [4], [5]. Despite remarkable advances over the last half-century, a complete understanding of the liquefaction phenomenon remains incomplete due to its complex nature, and there are still some uncertainties regarding the influencing parameters. Earthquake-induced liquefaction is still threatening the safety of structures all around the world, and this fact underlines the need for further study on this topic.

Some researchers constructed fully instrumented sites to capture the in situ soil behavior during an earthquake event [6]. Although real earthquake data is ideal to correctly evaluate the in situ behavior of liquefiable soil, it is extremely challenging and economically unfeasible in many cases. Therefore, many researchers have concentrated on alternative research methodologies (i.e., physical modeling, and element testing). Amongst these, element testing (i.e., dynamic triaxial, cyclic simple shear tests) has become more popular and commonly used by geotechnical engineers as it allows studying the problem of liquefaction under controlled and repeatable test conditions, and its cost is comparatively lower.

Liquefaction is directly related to excess pore pressures developed under seismic loading, which causes substantial effective stress and shear stiffness degradation. Seed and Lee [7] performed cyclic triaxial experiments on clean sand specimens and proposed the condition of initial liquefaction in which excess pore pressures (u_e) develop and become equal to initial effective confining stress (σ_o' or σ_c'). It was

*Corresponding author: a.zeybek@alparslan.edu.tr
Received: 05.03.2022, Accepted: 21.04.2022

shown that loose sand samples suffered complete liquefaction because of the quick build-up of excess pore pressures and extensive shear strength degradation occurred over a large amplitude of strains, whereas dense samples suffered gradual softening and dilated at large strains. Ishihara [8] later proposed that a 5% double amplitude axial strain that occurred during undrained cyclic loading corresponds to the onset of liquefaction. Muhunthan and Schofield [9] suggested that besides the state of zero effective stress, the formation of cracks or micro-fissures, and high hydraulic gradients are crucial for the occurrence of liquefaction.

Liquefaction studies reveal that relative density (D_r), initial effective confining stress (σ_c'), and fines content (FC) are some of the important parameters that govern the cyclic response of liquefiable soils. Considering the field observations from the 1964 Niigata earthquake, the main focus of the earlier studies was placed on sandy soils [10], [11]. However, following numerous field observations that sands with some amount of silt and/or clay and silt can also liquefy when subjected to seismic loading, many researchers have extended their interest in elucidating the role of fines in the response of sandy soils. These studies concluded that the type and plasticity of fines and fine content were important factors influencing the liquefaction behavior of sand-silt or sand-clay mixtures [12]-[17]. The analysis of case histories and experimental studies provided conclusive evidence that loose deposits of sandy soils suffer larger volumetric compaction during cyclic loading, generating higher excess pore pressures. The tendency for volumetric strains significantly decreases as relative density increases. Researchers reached a consensus that increasing the relative density of sandy soils enhances the liquefaction resistance [18]-[21]. Through extensive laboratory studies, researchers also reached an agreement that initial effective confining stress significantly affects the liquefaction resistance of sandy soils, which reduces as confining stress increases [22]. This effect was observed to be particularly more noticeable at larger densities.

It is known that real earthquakes involve irregular shear stresses and the frequency content of seismic excitation varies (typically 0-15 Hz). Through the cyclic laboratory tests, investigators have suggested that the liquefaction behavior of sandy soils relies not only on the initial test conditions but also on the frequency of seismic loading. Due to the experimental difficulties and inherent limitations of the test devices, many of these studies have been conducted using sinusoidal loading. Some early studies showed that loading frequency has an insignificant impact on the soil's liquefaction behavior [23]-[26]. More recent studies have reported that an increase in loading frequency leads to an increase in liquefaction resistance of sandy soils [27]-[32]. On the contrary, some researchers have observed higher liquefaction resistance at lower loading frequencies [33], [34]. From this review of literature, it is obvious that, despite a large number of studies, no common consensus has been reached, and the effect of loading frequency remains unclear. Further study of this topic will be of value to draw more definite conclusions.

The current study aims to offer valuable insights into the impact of loading frequency and relative density on the cyclic behavior of liquefiable soils. With this aim, several stress-controlled dynamic triaxial experiments were conducted on clean sand from the Sile region of Istanbul. The reconstituted triaxial specimens were prepared with different relative densities ranging from 38 to 90%, and were tested under undrained cyclic loading conditions with varying cyclic stress ratios at two different loading frequencies (0.1 and 1 Hz).

2. Experimental Investigation

2.1. Materials Tested

In this work, triaxial specimens were prepared using clean silica sand (AFS 55/60). The sand was taken from a sand quarry located in the Sile-Istanbul region. Figure 1 demonstrates the particle size distribution (PSD) determined through the dry sieve analysis. Table 1 summarizes the main physical properties obtained in general accordance with ASTM standards. As per the United Soil Classification System (USCS), this type of soil is poorly graded sand (SP).

In the aftermath of the 1964 earthquakes, extensive laboratory research has been conducted on specimens of clean sand obtained from various quarries around the world. Due to their wide availability, some of the test materials (i.e., Ottawa, Toyoura, Nevada, Monterey, Hostun sand) have been highly preferred by researchers, and thus the liquefaction behavior of these sands has been firmly established in geotechnical earthquake engineering. Alternatively, due to the increased cost of imported sand, many researchers tend to use locally available soils. The grain size distribution analysis offers useful insights into the suitability of local sands for liquefaction studies. Figure 1 compares the PSD of Sile sand with the liquefaction boundaries recommended by Tsuchida [35]. It appears that Sile sand falls into the boundaries of most liquefiable soil.

It is highly liquefaction susceptible soil and suitable material for liquefaction studies [36], [37].

Table 1. Basic physical properties of sand used in this study

Properties	Value
Median particle size, D_{50} [mm]	0.296
Coefficient of uniformity, C_u	1.352
Specific gravity, G_s	2.65
Min. void ratio, e_{min}	0.574
Max. void ratio, e_{max}	0.885
USCS classification	SP

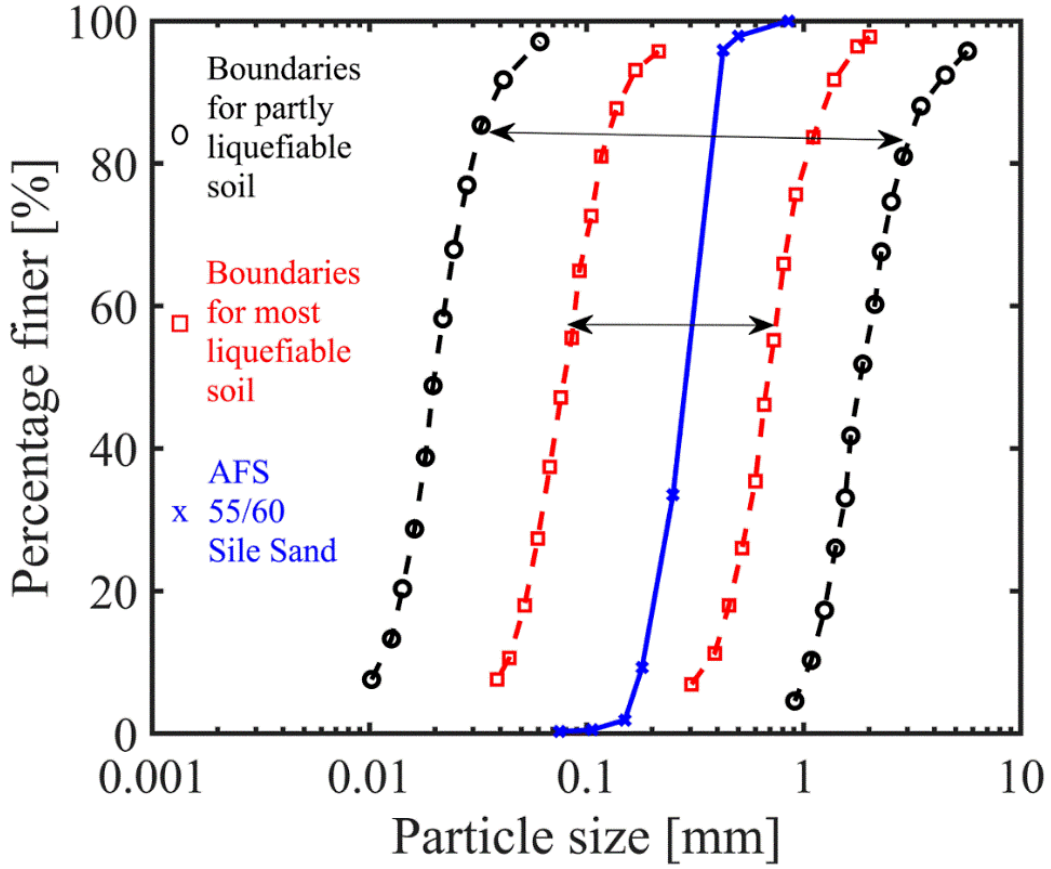

Figure 1. Particle size distribution curve for AFS 55/60 Sile sand

2.2. Testing Apparatus

The experiments were conducted using the Dynatriax EmS apparatus located in the Civil Engineering Laboratory of Mus Alparslan University. Figure 2 shows the main components of the test system.

The Dynatriax EmS system is manufactured by Wykeham Farrance-Controls Groups. It is a fully automated electromechanical apparatus that can conduct stress and/or strain-controlled dynamic triaxial experiments in drained and undrained conditions. The apparatus has a dynamic actuator that can apply loading cycles in the range of 0.01-10 Hz.

During the experiments, saturation, consolidation, and cyclic loading of triaxial specimens were automatically controlled with the assistance of the Dynatriax software and data acquisition system. The saturation of specimens was assessed by checking Skempton's B value. Once the cyclic loading ceased, the excess pore pressure dissipation was performed with the solenoid valve located on the drainage line. The cell, back and excess pore water pressures, axial load/displacements, and volume changes were measured through the monitoring sensors, including pressure transducers, submersible load cell, linear variable differential transducers, and an automatic volume change device. The instruments were periodically calibrated.

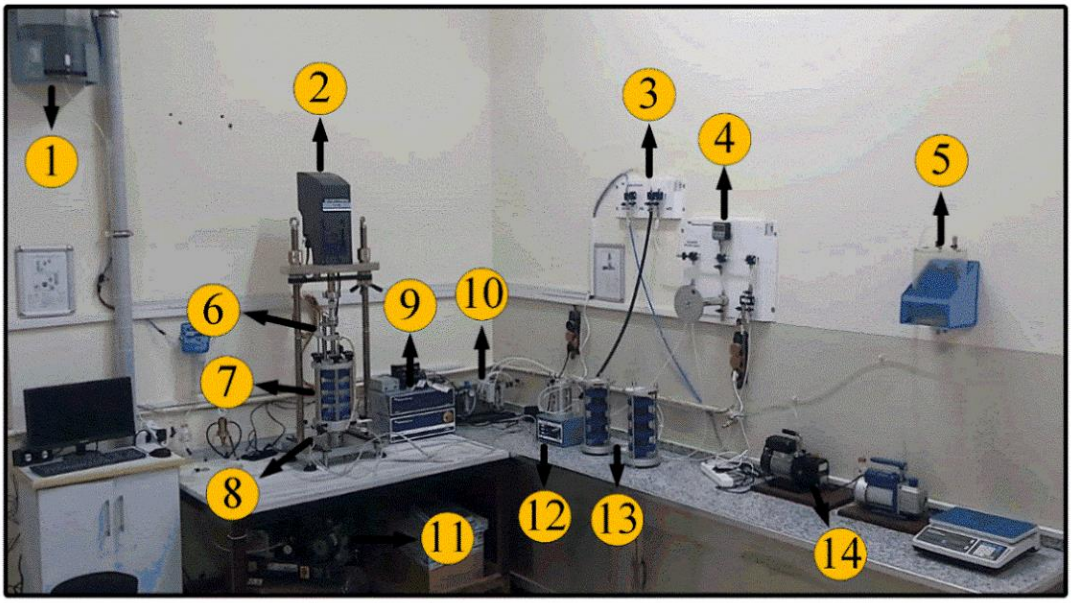

1) De-airing tank, 2) Actuator, 3) Valve panel, 4) Water distribution panel, 5) Vacuum chamber, 6) LVDT, 7) Triaxial cell and submersible load cell, 8) Pressure transducer, 9) CDC and Drive unit, 9) Air receiver, 10) Air compressor, 11) Volume change device, 12) Air/water cylinders, 13) Vacuum pumps

Figure 2. The main components of the dynamic triaxial system used during the experimental work

2.3. Testing Procedure

2.3.1. Preparation of Sand Specimens

The loose ($D_r \approx 40\%$) and medium dense specimens ($D_r \approx 55\%$) were prepared using the dry pluviation technique, while dense specimens ($D_r \approx 90\%$) were prepared using the dry tamping method. The diameter (D) of the reconstituted sand specimens was 70 mm, and the ratio of height to diameter (H/D) was approximately 2 during the tests. Figure 3 shows different stages of specimen preparation.

After flushing the drainage lines with de-aired water, a porous stone, filter paper, and latex membrane were placed over the base pedestal of the triaxial cell. This was followed by the placement of a cylindrical split mold (Figure 3a). For loose to medium dense specimens, the sand was rained into the mold utilizing a modified funnel with a sieve and maintaining a constant drop height. The opening sizes of the sieve were varied to adjust the density. For the dense specimens, sand was compacted in 10 equal layers by freely dropping a tamper from a predetermined height. The top cap, filter paper, and porous stone were positioned (Figure 3b). Vacuum pressure (20 kPa) was applied before removing the split mold, maintaining the verticality of the sand specimens (Figure 3c). The specimen heights were measured with caution.

The triaxial cell was mounted and then filled with de-aired water. Eventually, 20 kPa cell pressure was applied before the suction was released (Figure 3d).

2.3.2. Saturation, Consolidation, and Shearing of Sand Specimens

On completion of specimen preparation, the sand specimens were saturated, consolidated, and subjected to cyclic loading. Figure 4 presents a schematic of the stages of the dynamic triaxial tests.

The specimens were washed with carbon dioxide gas (CO_2) and de-aired water to expedite the saturation process. CO_2 gas was carefully applied to the specimens, giving special attention to gas pressure that remained within desirable limits (typically 10 kPa). After 20 minutes of CO_2 flushing, de-aired water was passed through the sand specimens. This was followed by a cell and back pressure ramp involving a gradual increase in cell pressure (CP or σ_3) and back pressure (BP or u_0) by maintaining a constant differential pressure ($\sigma_c' = 10$ kPa). This process ceased once the desired back pressure (u_0 =350 kPa) was accomplished. The Skempton's coefficient ($B = \frac{\Delta_u}{\Delta\sigma_3}$, where Δ_u and $\Delta\sigma_3$ correspond to pore pressure and confining stress change, respectively) was periodically measured to control the status of saturation, and the B values at the beginning of the consolidation process were ranging from 0.99 to 1.

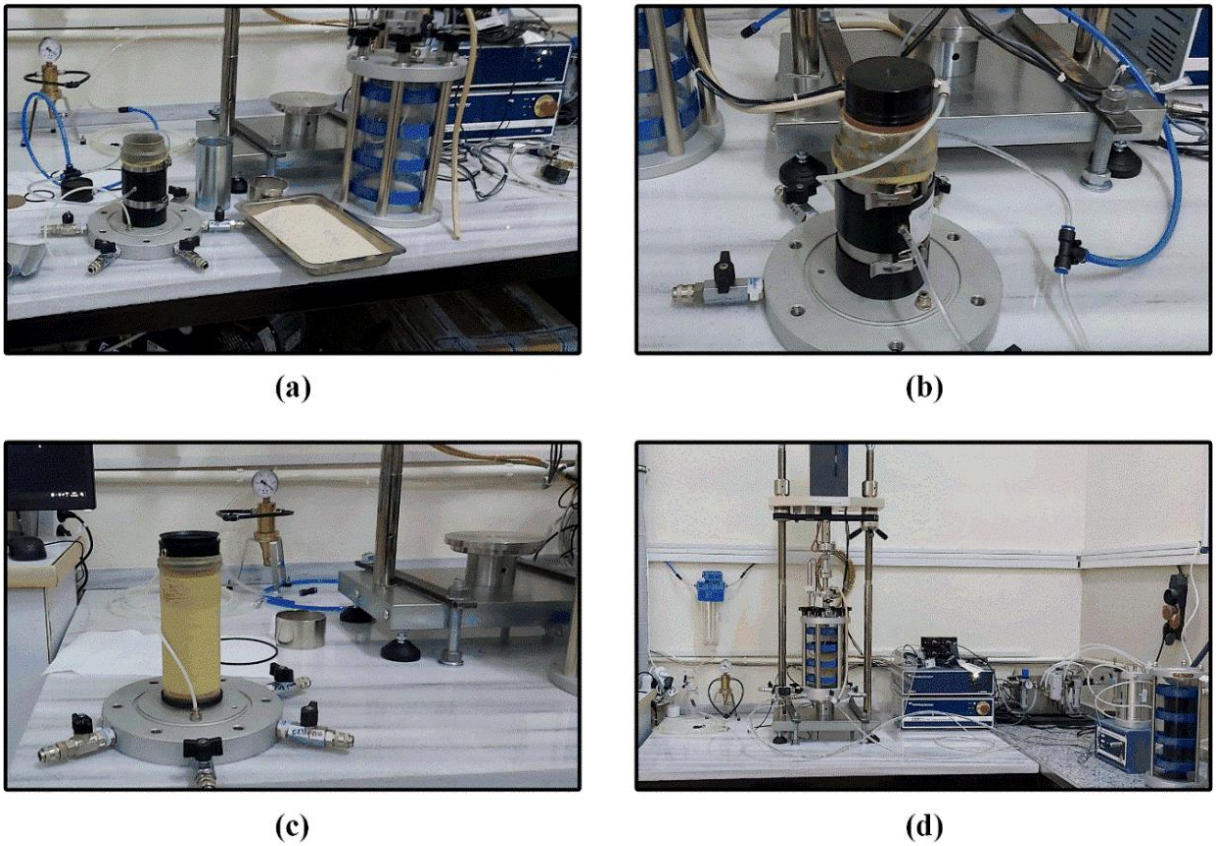

Figure 3. Preparation of triaxial specimens

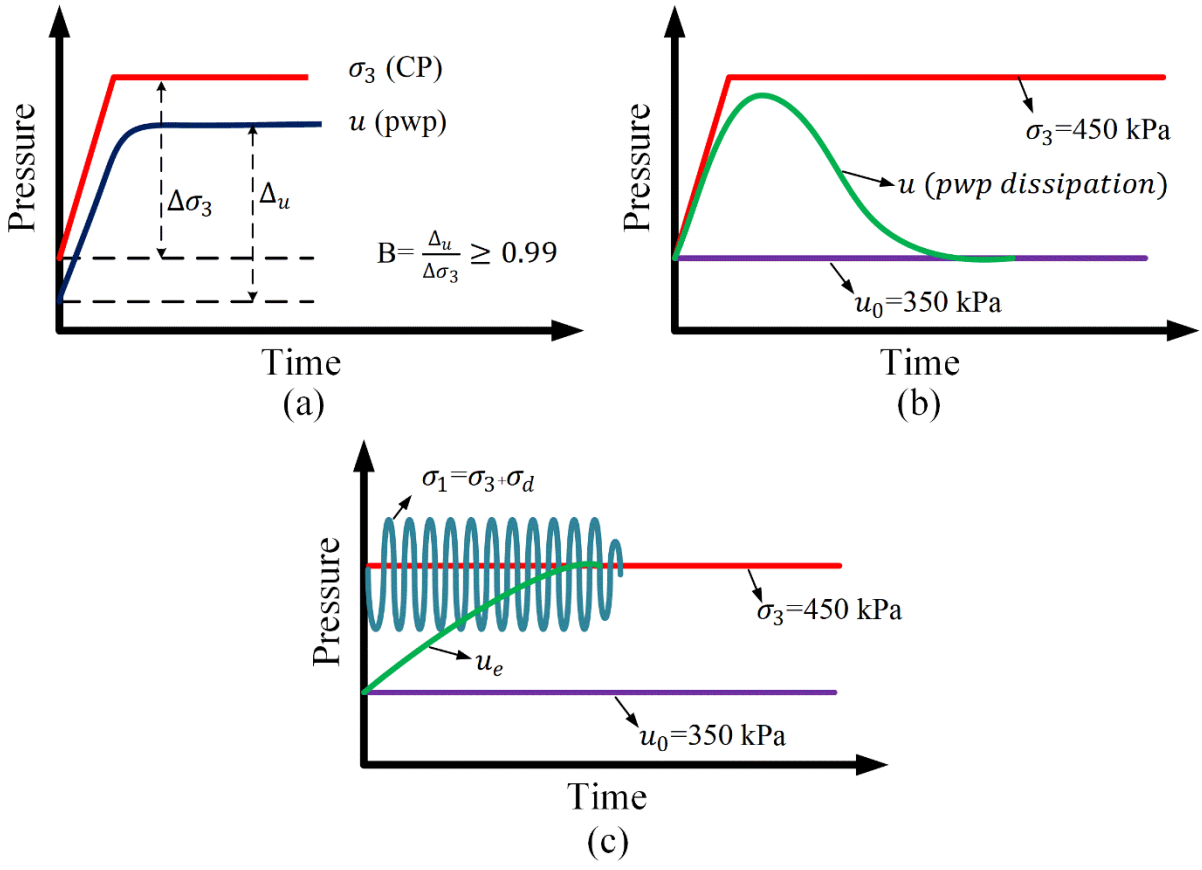

Figure 4. Saturation, consolidation, and cyclic loading of triaxial specimens

Saturated specimens were isotropically consolidated to 100 kPa ($\sigma_c' = 100$ kPa) by maintaining the back pressure at 350 kPa and increasing the cell pressure up to 450 kPa. At the end of the consolidation process, where volume changes were insignificant, the specimens were subjected to a simple harmonic (sinusoidal) loading.

A total of 20 stress-controlled dynamic triaxial experiments were carried out in undrained conditions. Table 2 gives a summary of the test program and provides typical experimental results that are representative of a larger database. The reconstituted specimens at loose, medium, and dense conditions were axially loaded at different amplitudes of cyclic stress, having two different loading frequencies, which are the most widely used in stress-controlled dynamic triaxial tests, namely 0.1 and 1 Hz. The applied cyclic stress ratios ($CSR = \frac{\sigma_d}{2\sigma_c'}$, where σ_d and σ_c' denote the deviatoric stress and effective confining stress, respectively) ranged from 0.08 to 0.3.

Table 2. Experimental program and typical test results

Test No	Test ID	Specimen Density	D_r (%)	u_0 (kPa)	σ_c' (kPa)	Frequency (Hz)	CSR	N_{liq}
1	LS1		40.0	350	100	0.1	0.08	194
2	LS2		39.0	350	100	0.1	0.10	75
3	LS3		38.0	350	100	0.1	0.13	23
4	LS4	Loose Sand	41.0	350	100	0.1	0.18	3
5	LS5		42.0	350	100	1.0	0.08	220
6	LS6		39.0	350	100	1.0	0.10	83
7	LS7		40.0	350	100	1.0	0.13	33
8	LS8		39.0	350	100	1.0	0.18	3
9	MS1		55.0	350	100	1.0	0.13	581
10	MS2	Medium	56.0	350	100	1.0	0.18	57
11	MS3	Dense Sand	55.0	350	100	1.0	0.20	27
12	MS4		54.0	350	100	1.0	0.25	1
13	DS1		89.0	350	100	0.1	0.18	670
14	DS2		88.0	350	100	0.1	0.23	102
15	DS3		88.0	350	100	0.1	0.26	35
16	DS4	Dense Sand	87.0	350	100	0.1	0.30	1
17	DS5		90.0	350	100	1.0	0.18	791
18	DS6		88.0	350	100	1.0	0.23	121
19	DS7		87.0	350	100	1.0	0.26	43
20	DS8		89.0	350	100	1.0	0.30	2

3. Results and Discussions

3.1. Behavior of Clean Sand under Undrained Cyclic Loading

Figure 5 presents typical experimental results for loose and dense specimens. The specimens having a relative density (D_r) of 41 and 88% were tested under deviatoric stress (q) of 36 kPa and 52 kPa at initial effective confining stress (σ_c') of 100 kPa, corresponding to cyclic stress ratios of 0.18 and 0.26.

It can be inferred from the figure that regardless of relative density, significant excess pore pressures (u_e) accumulated during undrained cyclic loading and caused significant effective stress and stiffness degradation. The rate of excess pore pressure accumulation was different for the loose and dense specimens. The loose sand specimen suffered a rapid development of excess pore pressure. After a few loading cycles, pore pressure reached the initial confining (total) stress, and the excess pore pressure ratio (r_u) was equal to unity, corresponding to the initiation of liquefaction. Mean effective stress (p') reduced with increasing excess pore pressure, and the stress path moved towards the critical state line, showing a flow type behavior.

In the dense sand specimen, the first cycle caused a rapid increase of excess pore pressure and a rapid reduction of p'. During the following cycles, excess pore pressure increased progressively, and the decrease in p' was more gradual. The stress path touched the critical state line after a larger number of loading cycles. The observed trends are valid for the simple harmonic loading condition and structures of sand created with reconstitution methods of dry pluviation and tamping methods.

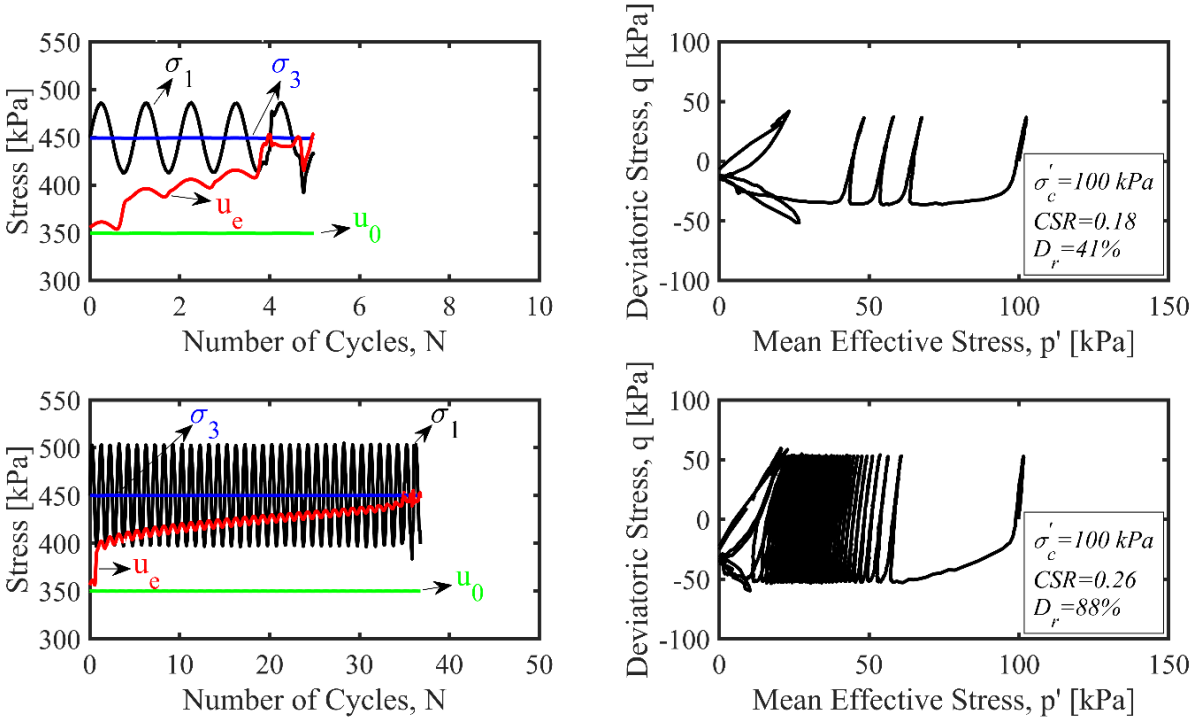

Figure 5. Typical cyclic behavior of sand specimen under undrained loading condition

3.2. Excess Pore Pressure Development

Experimental data recorded at different relative densities and loading frequencies are presented in this section to discuss the role of density and frequency in the development of excess pore pressure. For this purpose, excess pore pressure ratios (r_u) are plotted against the number of cycles (N).

Figure 6 illustrates the $r_u - N$ plots for loose, medium, and dense sand specimens tested at the same loading frequency and σ_c'. It is clear that under the same cyclic stress ratio ($CSR = 0.18$), the loose sand specimen ($D_r = 39\%$) showed a faster excess pore pressure development, causing a significant reduction in sand's stiffness and extensive soil softening.

The liquefaction criterion ($r_u = 1$) was satisfied after approximately three loading cycles. In medium dense sand ($D_r = 56\%$), excess pore pressure seems to grow relatively slowly, and sand liquefied after the application of 57 loading cycles. It seems that softening was intensified when r_u was in the vicinity of 0.70. The excess pore pressure accumulated in the dense sand was very small at 100 loading cycles, and a significant number of loading cycles were required for $r_u = 1$. The medium dense sand was observed to behave like loose sand when subjected to CSR of 0.25-0.26. The results also exhibit that dense sand liquefied when the magnitude and number of applied cyclic stresses were sufficient enough to cause liquefaction.

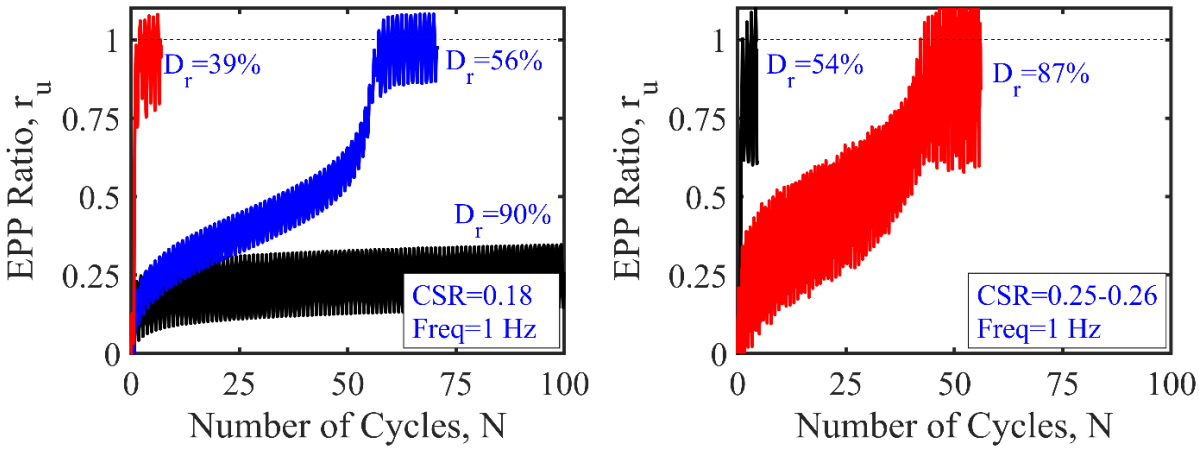

Figure 6. Typical excess pore pressure data recorded at different relative densities

Figure 7 plots the excess pore pressures captured at 0.1 and 1 Hz to provide insights into the influence of loading frequency. This analysis was conducted for loose and dense specimens tested at CSR of 0.08 and 0.23, respectively. The results exhibited that excess pore pressures increased in both cases, and ultimately reached σ_c'=100 kPa. Under analogous test conditions, the number of cycles required for liquefaction was larger at a higher loading frequency (1 Hz) than at a lower frequency (0.1 Hz). The interesting observation is that for both loose and dense sand the build-up of excess pore pressure was faster during the initial cycles, and it accumulated at a slower rate in the subsequent cycles. Moreover, for the density ranges under consideration, the rise of excess pore pressure at the early stages of the cyclic loading was faster at 0.1 Hz than at 1 Hz.

3.3. Liquefaction Resistance

The above results emphasized the role that relative density and loading frequency play in the excess pore pressure response of Sile sand. To offer further insights into this matter, cyclic resistance curves, presenting the relationship between the cyclic stress ratio (CSR) and the number of cycles for liquefaction N_{liq}, are depicted in Figures 8 and 9.

Figure 8 provides information about the influence of relative density on sand's liquefaction resistance. Regardless of the loading frequency, dense sand required much higher CSR than loose sand at the same number of cyclic loadings. This indicated that sand specimens exhibit a much higher liquefaction resistance as the density increased, as expected. This finding appears to be consistent with the results of many published studies [18]-[21].

N_{liq} values recorded during 1 Hz tests were normalized with those measured during 0.1 Hz tests. Figure 9 depicts the variation of normalized N_{liq} with CSR for loose and dense sand. In almost every test, the resistance of sand to liquefaction was much higher at 1 Hz. Irrespective of D_r and CSR, the liquefaction resistance of loose and dense sand was observed to increase as the loading frequency increased from 0.1 to 1 Hz. These observations are in agreement with many previous research studies [27]-[32]. The experiments carried out at the same CSR showed that the effect of loading frequency was more noticeable for dense sand than loose sand. It is noteworthy that this observation was made based on a limited dataset, and further research will be useful to draw a more concrete conclusion about this aspect.

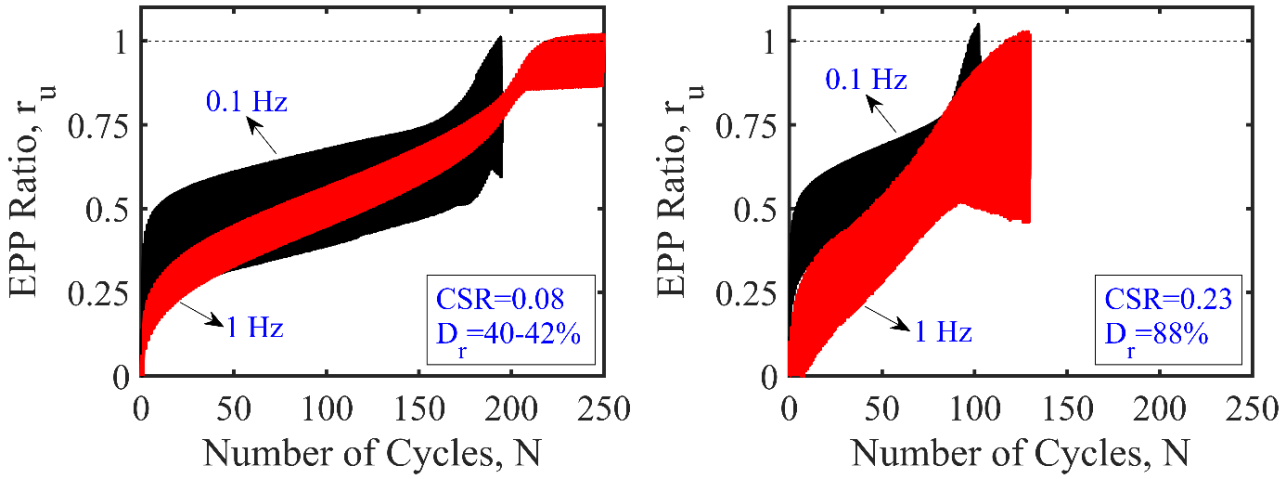

Figure 7. Typical excess pore pressure data recorded at different loading frequencies

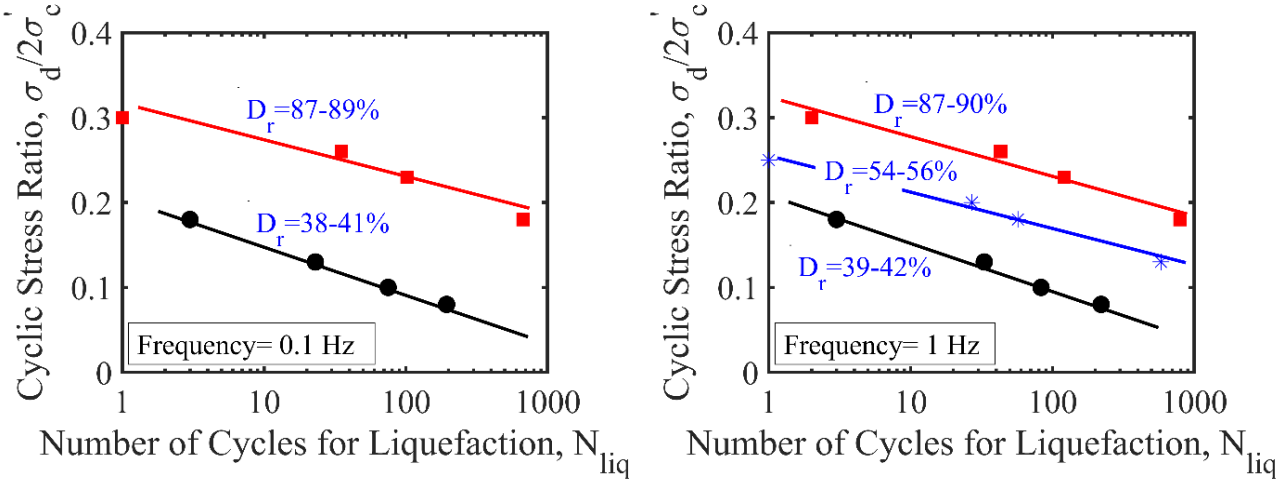

Figure 8. Influence of relative density on liquefaction resistance of sand

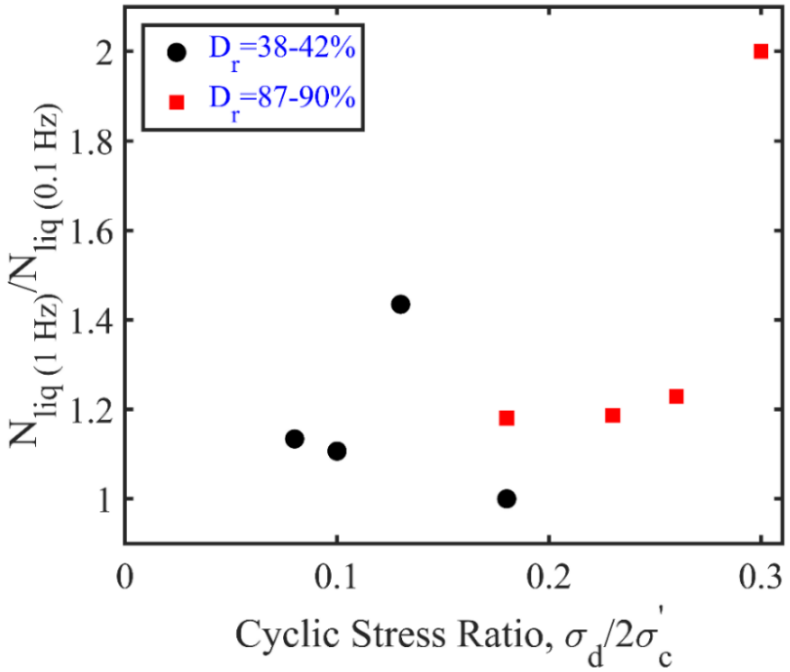

Figure 9. Influence of cyclic loading frequency on sand's liquefaction resistance

4. Conclusions

Earthquake-induced liquefaction is a complicated phenomenon. Over the years, significant research has been performed in the laboratory and/or field to improve the understanding of the liquefaction behavior of sandy soils. Despite an important amount of research effort, there are still important uncertainties and disagreements regarding some aspects of soil liquefaction. The role that some soil parameters and loading conditions play in the cyclic behavior of liquefiable soils has not been adequately understood, and the results of published studies are usually contradictory.

This work intends to provide insights into the liquefaction behavior of clean sand, paying particular attention to the impact of relative density and loading frequency on the excess pore pressure generation. With this aim, a total of 20 stress-controlled undrained dynamic triaxial experiments were conducted on saturated, clean sand specimens. The following conclusions are deduced from this work.

Under comparable test conditions (i.e., similar cyclic stress ratio and loading frequency), lower excess pore pressures were accumulated in dense specimens than in loose specimens, suggesting that the resistance of sand to liquefaction increases with an increase in relative density. These results seem to correlate well with the published studies.

Loading frequency was observed to influence the excess pore pressure behavior and liquefaction resistance of sand prepared at different relative densities. The resistance of sand to liquefaction tends to increase as the loading frequency is increased. This effect was more pronounced for dense specimens. In every case, excess pore pressures were generated faster at the early stages of the cyclic loading. The rate of excess pore pressure generation was greater at a lower frequency. These results highlight that the state of practice should appropriately account for the impacts of loading frequency to accurately assess the liquefaction behavior of sand.

This study incorporated the effects of two parameters only, and the test data was collected using a sinusoidal type of loading and effective confining stress of 100 kPa. Future tests should consider the other test parameters (i.e., stress level) and examine the combined effects of these parameters under various cyclic loading patterns that closely replicate the actual earthquake excitation.

Acknowledgment

The author thanks Murat ULU and Tahsin CALP for their technical assistance and support during the experiments.

Statement of Research and Publication Ethics

This study complies with scientific research and publication ethics and principles.

References

[1] I. Towhata, "Geotechnical Earthquake Engineering," Springer, 2008.
[2] M. Wyss and J. N. Brune, "The Alaska Earthquake of 28 march 1964: a complex multiple rupture," Bull. Seismol. Soc. Am., vol. 57, no. 5, pp. 1017-1023, Oct. 1967. [Online]. Available: https://authors.library.caltech.edu/48262/1/1017.full.pdf. [Accessed: Apr. 21, 2022].
[3] K. Ishihara and Y. Koga, "Case studies of liquefaction in the 1964 Niigata Earthquake," Soils Found., vol. 21, no. 3, pp. 35-52, Sep. 1981, doi: https://doi.org/10.3208/sandf1972.21.3_35
[4] K. Ishihara, F. Tatsuoka, and S. Yasuda, "Undrained deformation and liquefaction of sand under cyclic stresses," Soils Found., vol. 15, no. 1, pp. 29-44, Mar. 1975, doi: https://doi.org/10.3208/sandf1972.15.29
[5] F. H. Lee, "Centrifuge modelling of earthquake effects on sand embankments," Ph.D. dissertation, Dept. Civil Eng., Cambridge Univ., Cambridge, UK, 1985.
[6] T. L. Holzer, T. C. Hanks, and T. L. Youd, "Dynamics of liquefaction during the 1987 Superstition Hills, California, Earthquake," Science, vol. 244, no. 4900, pp. 56-59, Apr. 1989, doi: https://doi.org/10.1126/science.244.4900.56
[7] H. B. Seed and K. L. Lee, "Liquefaction of saturated sands during cyclic loading," J. Soil Mech. Found, vol. 92, no. 6, pp. 105-134, Nov. 1966, doi: https://doi.org/10.1061/JSFEAQ.0000913
[8] K. Ishihara, "Liquefaction and flow failure during earthquakes," Géotechnique, vol. 43, no. 3, pp. 351-451, Sep. 1993, doi: https://doi.org/10.1680/geot.1993.43.3.351
[9] B. Muhunthan and A. N. Schofield, "Liquefaction and dam failures," Slope Stability 2000, ASCE Special Publication, 266-280, Aug. 2000, doi: https://doi.org/10.1061/40512(289)20
[10] H. B. Seed and W. H. Peacock, "Test procedures for measuring soil liquefaction characteristics," J. Soil Mech. Found., vol. 97, no. 8, pp. 1099-1119, Aug. 1971, doi: https://doi.org/10.1061/JSFEAQ.0001649
[11] K. Ishihara, "Stability of natural deposits during earthquakes," in 11th Int. Conf. on Soil Mechanics and Foundation Engineering, Balkema, San Francisco, USA, Aug. 12-16, 1985, pp. 321-376. [Online]. Available: https://www.issmge.org/publications/publication/stability-of-natural-deposits-during-earthquakes. [Accessed: Apr. 21, 2022].
[12] W. Finn, R. Ledbetter, and G. Wu, "Liquefaction in silty soils: design and analysis. ground failures under seismic conditions," ASCE, pp. 51-76, 1994.

[13] S. Thevanayagam, M. Fiorillo, and J. Liang, "Effect of nonplastic fines on undrained cyclic strength of silty sands," Soil Dynamics and Liquefaction 2000, 77-91, 2000, doi: https://doi.org/10.1061/40520(295)6
[14] C. P. Polito and II J. R. Martin, "Effects of nonplastic fines on the liquefaction resistance of sands," J. Geotech. Geoenviron. Eng., vol. 127, no. 5, pp. 408-415, May 2001, doi: https://doi.org/10.1061/(ASCE)1090-0241(2001)127:5(408)
[15] D. D. Porcino and V. Diano, "The influence of non-plastic fines on pore water pressure generation and undrained shear strength of sand–silt mixtures," Soil Dyn. Earthq. Eng., vol. 101, pp. 311-321, Oct. 2017, doi: https://doi.org/10.1016/j.soildyn.2017.07.015
[16] E. E. Eseller-Bayat, M. Monkul, Ö. Akin, and S. Yenigun, "The coupled influence of relative density, CSR, plasticity and content of fines on cyclic liquefaction resistance of sands. J. Earthq. Eng., vol. 23, no. 6, pp. 909-929, 2019, doi: https://doi.org/10.1080/13632469.2017.1342297
[17] E. Karakan, N. Tanrinian, and A. Sezer, "Cyclic undrained behavior and post liquefaction settlement of a nonplastic silt," Soil Dyn. Earthq. Eng., vol. 120, pp. 214-227, May 2019, doi: https://doi.org/10.1016/j.soildyn.2019.01.040
[18] Y. P. Vaid and S. Sivathayalan, "Fundamental factors affecting liquefaction susceptibility of sands," Can. Geotech. J., vol. 37, no. 3, pp. 592-606, June 2000, doi: https://doi.org/10.1139/t00-040
[19] J. A. H. Carraro, P. Bandini, and R. Salgado, "Liquefaction resistance of clean and nonplastic silty sands based on cone penetration resistance," J. Earthq. Eng., vol. 129, no. 11, pp. 965-976, Nov. 2003, doi: https://doi.org/10.1061/(ASCE)1090-0241(2003)129:11(965)
[20] K. Adalier and A. Elgamal, "Liquefaction of over-consolidated sand: a centrifuge investigation, J. Earthq. Eng., vol. 9, no. 1, pp. 127-150, 2005, doi: https://doi.org/10.1080/13632460509350582
[21] C. Liu and J. Xu, "Experimental study on the effects of initial conditions on liquefaction of saturated and unsaturated sand, "Int. J. Geomech., vol. 15, no. 6, Dec. 2013, doi: https://doi.org/10.1061/(ASCE)GM.1943-5622.0000350
[22] Y. Vaid, J. Chern, and H. Tumi, "Confining pressure, grain angularity and liquefaction. J. Geotech. Geoenviron. Eng., vol. 111, no. 10, 1229-1235, Oct. 1985, doi: https://doi.org/10.1061/(ASCE)0733-9410(1985)111:10(1229)
[23] Y. Yoshimi and H. Oh-oka, "Influence of degree of shear stress reversal on the liquefaction potential of saturated sand," Soils Found., vol. 15, no. 3, pp. 27-40, Sep. 1975, doi: https://doi.org/10.3208/sandf1972.15.3_27
[24] F. Tatsuoka, S. Toki, S. Miura, H. Kato, M. Okamoto, S. Yamada, S. Yasuda, and F. Tanizawa, "Some factors affecting cyclic undrained triaxial strength of sand," Soils Found., 26 (3): 99-116, Sep. 1986, doi: https://doi.org/10.3208/sandf1972.26.3_99
[25] C.P. Polito, "The effects of non-plastic and plastic fines on the liquefaction of sandy soils," Ph.D. dissertation, Virginia Polytechnic Institute and State University, Blacksburg, VA, USA, 1999. [Online]. Available: https://vtechworks.lib.vt.edu/handle/10919/30243. [Accessed: Apr. 21, 2022].
[26] X. H. Wang and H. L. Zhou, "Study on dynamic steady state strength of sand soil liquefaction," J. Rock Mech. Geotech. Eng., vol. 22, pp. 96-102, 2003.
[27] K. L. Lee and J. A. Fitton, "Factors affecting the cyclic loading strength of soil," ASTM International, STP33637S: 71-95, 1969, doi: https://doi.org/10.1520/stp33637s
[28] N. Y. Chang, N. P. Hsieh, D. L. Samuelson, and M. Horita, "Effect of frequency on liquefaction potential of saturated Monterey no. o sand. in: computational methods and experimental measurements," Edited by Keramidas G.A., Brebbia C.A., Springer, Berlin, Heidelberg, pp. 433-446, 1982, doi: https://doi.org/10.1007/978-3-662-11353-0_34
[29] Y. Guo and L. He, "The influences of the vibration frequencies on liquefaction strength of saturated sands," Journal of Disaster Prevention and Mitigation Engineering, vol. 29, pp. 618-623, 2009.
[30] T. Feng and L. Zhang, "Experimental study on effect of vibration frequency on dynamic behaviors of saturated sands," J. Water Resour. Plan. Manag., vol. 11, pp. 11-14, 2013.
[31] S. Zhang, Y. F. Zhang, L. K. Zhang, and C. J. Liu, "Influence of confining pressure and vibration frequency on the liquefaction strength of the saturated gravel sand," Journal of Xinjiang Agricultural University, vol. 38, pp. 68-71, 2015.
[32] Z. Nong, S. Park, S. W. Jeong, and D. E. Lee, "Effect of cyclic loading frequency on liquefaction prediction of sand," Appl. Sci., vol. 10, no. 13, pp. 4502, June 2020, doi: https://doi.org/10.3390/app10134502

[33] J. P. Mulilis, C. K, Chan, and H. B. Seed, "The effects of method of sample preparation on the cyclic stress-strain behavior of sands (EERC report 75-18). Berkeley, CA, USA: University of California, 1975.
[34] H. K. Dash and T. G. Sithara, "Effect of frequency of cyclic loading on liquefaction and dynamic properties of saturated sand," Int. J. Geotech, vol. 10, 5, pp. 487-492, May 2016, doi: https://doi.org/10.1080/19386362.2016.1171951
[35] H. Tsuchida, "Prediction and countermeasure against liquefaction the liquefaction in sand deposits," In Abstract of the Seminar, Port and Harbour Research Institute, 3.1-3.33, 1970.
[36] A. Zeybek, "Suggested method of specimen preparation for triaxial tests on partially saturated sand," Geotech. Test. J., vol. 45, no. 2, 2022, doi: https://doi.org/10.1520/GTJ20210168
[37] E. E. Eseller-Bayat and D. B. Gulen, "Undrained dynamic response of partially saturated sands tested in a DSS-C device," J. Geotech. Geoenviron. Eng., vol. 146, no. 11, pp. 04020118, 2020, doi: https://doi.org/10.1061/(ASCE)GT.1943-5606.0002361

Bitlis Eren Üniversitesi Fen Bilimleri Dergisi
BİTLİS EREN UNIVERSITY JOURNAL OF SCIENCE
ISSN: 2147-3129/e-ISSN: 2147-3188
VOLUME: 11 NO: 2 PAGE: 678-693 YEAR: 2022
DOI: 10.17798/bitlisfen.1088988

An Integrated Fuzzy Approach Based Failure Mode and Effects Analysis for a Risk Assessment

Burak EFE[1*]

[1]*Necmettin Erbakan University, Department of Industrial Engineering, Konya, Türkiye (ORCID: 0000-0001-7092-3001)*

Keywords: Risk evaluation, mathematical model, FMEA, fuzzy TOPSIS, fuzzy extension of AHP

Abstract

This paper provides to cope with the limitations of traditional FMEA by using an integrated fuzzy multi-criteria decision making method, which considers fuzzy extension of AHP (Analytic Hierarchy Process) and fuzzy TOPSIS (Technique for Order Preference by Similarity to Ideal Solution), and a linear programming. The proposed method is shown for an application to failure mode and effects analysis (FMEA) based risk assessment of a construction firm. Firstly, fuzzy extension of AHP approach is utilized to define the weights of criteria in risk evaluation. Secondly, fuzzy TOPSIS approach is used to determine the most important failure mode in the construction firm. This work handles a sensitivity analysis and a comparison with the other methods. FMEA related papers in the literature presents only ranking of failure modes by using various methods. This study aims to handle the limited resources such as budget and time in a linear programming to establish a suitable occupational health and safety policy.

1. Introduction

Failure Mode and Effects Analysis (FMEA) is a systematic quality improvement technique to prevent any possible malfunctions that may occur in the system, design, process or services in advance [1]. The technique focuses on improving safety and increasing customer satisfaction, while eliminating defects and preventing potential errors [2]. Any undesirable situation regarding the process, such as the structural disorder of the process, the irregularity in its functioning, the irregularity in its implementation, and the output not meeting the expectations, are considered as "errors". These may be previously known events, or they may be events that have never been encountered but are likely to happen. Failure mode is a short and general statement that summarizes the physical conditions in which the failure occurs with correct adjectives. The probability of failure is a frequency of how often any error can occur. The effect of the failure is the result of a failure that will occur in a system, design, process or service. It is necessary to consider this effect not only as the consequences of the failure in the system, but also in terms of its effect on other systems and components [1]. The process to be improved with the FMEA technique is examined in detail by the FMEA team. By identifying and prioritizing improvement opportunities, it is determined where to start the work. Then, it is questioned what kind of problems may occur in the process. If there are issues that need to be taken into account, such as customer expectations, it is examined whether they can be met or not [2]. Risk priority number (RPN) is a numerical value calculated by multiplying the the probability of failure (O), severity of failure (S) and non-detection of failure (D). RPN is calculated as O*x*S*x*D. FMEA technique uses RPN value as a practical tool in order to rank the failure modes in terms of their risk [3].

The interpretation of the RPN value is made on the basis of the definition of these multipliers and the scales used. The increase in the probability of

*Corresponding author: burakefe0642@gmail.com
Received: 16.03.2022, Accepted: 13.06.2022

failure or the severity of the effect and the difficulty of determination generally mean an increased risk. If the relevant scales are prepared accordingly, a high RPN value will indicate high risk, and a low RPN will indicate low risk [1]. Table 1 presents some of FMEA based on multi-criteria decision making (MCDM) papers. The proposed method has some contributions as follows:

1. This paper ensures to reduce the loss of information by using fuzzy number instead of crisp number.
2. Each decision maker can have different judgments about a selection process due to their experience and knowledge. In group decision making environment, each decision maker presents their judgments to achieve a group judgment in evaluation process. The weights of the decision makers, which depend on characteristics of the decision makers, are important to achieve a group judgment. Inaccurate weights of the decision makers generate the mistaken group judgment. This situation generates the mistaken decision and inherently loss of cost and waste of time. This paper presents an attribute based aggregation technique (ABAT) proposed by Olcer and Odabasi [17] to cope with this limitation.

Table 1. Papers about FMEA

Methods	Authors
Fuzzy evidential reasoning and belief rule-based approach	Liu et al. [4]
DEMATEL and TODIM	Ulu and Şahin [5]
Fuzzy inference system	Jee et al. [6]
Fuzzy PROMETHEE	Efe et al. [7]
Fuzzy and grey theories	Zhou and Thai [8]
Hesitant 2-tuple linguistic term sets and an extended QUALIFLEX approach	Liu et al. [9]
Z numbers based AHP, entropy and VIKOR methods	Mohsen and Fereshteh [10]
Intuitionistic fuzzy AHP - VIKOR methods	Efe et al. [3]
Fuzzy best-worst, relative entropy, VIKOR	Tian et al. [11]
MULTIMOORA (Multi-objective Optimization By Ratio Analysis) and AHP	Fattahi and Khalilzadeh [12]
Quality function deployment and intuitionistic fuzzy VIKOR	Efe [13]
Fuzzy ANP	Yazdani et al. [14]
Intuitionistic fuzzy best-worst method	Yazdi et al. [15]
Regret theory and PROMETHEE under linguistic neutrosophic context	Zhu et al. [16]
Double upper approximated rough number, FUCOM and TOPSIS	Dhalmahapatra et al. [28]

3. This paper presents 45 different situations with regard to an occupational health and safety policy. This study uses a linear programming due to limited budget, time properties. The construction firm could select the most appropriate situation according to its conditions.

This paper aims to provide an integrated multi-criteria decision making approach to define the most important failure mode for a construction firm. Priority values of criteria, which are O, S and D, have been defined by utilizing fuzzy extension of AHP approach. The rankings of failure modes in the construction firm are defined by using fuzzy TOPSIS method based on an ABAT. The results of the proposed method are compared with results of the different methods, which are FAHP-fuzzy VIKOR and FAHP-fuzzy GRA. A sensitivity analysis can be realized under different β coefficients. A linear programming is suggested to form an occupational health and safety policy. This mathematical model is solved in GAMS software program.

2. The Proposed approach

The suggested integrated multi-criteria decision making approach is utilized to rank the failure modes in a risk assessment. Firstly, the priorities of criteria in risk evaluation will be defined by fuzzy extension of AHP. Decision makers present the pair wise comparison matrixes to acquire the priorities of O, S and D criteria so that they use the linguistic statements in Table 2.

Table 2. Linguistic terms for O, S and D

Terms	Fuzzy numbers
Absolutely strong (AS)	(7/2,4,9/2)
Very strong (VS)	(5/2,3,7/2)
Few strong (FS)	(3/2,2,5/2)
Poor (P)	(2/3,1,3/2)
Equal (E)	(1,1,1)

An ABAT is utilized to degrade to a group judgment the judgments of three decision makers. The ranking of the failure modes in the construction firm are determined by using fuzzy TOPSIS approach. Decision makers present their judgments for the values of failure modes based on criteria by using linguistic statements in Table 3.

Table 3. Linguistic terms for failure modes

Terms	Fuzzy numbers
Absolute Poor (AP)	(0,0.1,0.2)
Very Poor (VP)	(0.1,0.2,0.3)
Poor (P)	(0.1,0.3,0.5)
Fairly Poor (FP)	(0.4,0.45,0.5)
Medium (M)	(0.3,0.5,0.7)
Fairly Good (FG)	(0.5,0.55,0.6)
Good (G)	(0.5,0.7,0.9)
Very Good (VG)	(0.8,0.9,1)
Absolute Good (AG)	(0.9,1,1)

2.1. Fuzzy extension of AHP

AHP, which simultaneously considers qualitative and quantitative data, was developed by Saaty [18]. Fuzzy extension of AHP approach was developed by Chang [19]. Chang integrated fuzzy logic with Saaty's AHP. The weights of O, S and D criteria in risk assessment are calculated by utilizing fuzzy extension of AHP systematically in an uncertain environment. Fuzzy extension of AHP approach is defined in Eqs. (1)-(9) [19, 20]:

When $m_1^- \geq m_2^-, m_1 \geq m_2, m_1^+ \geq m_2^+$

The degree of the possibility is defined as one [21]:

$$V(M_1 \geq M_2) = 1 \tag{1}$$

The ordinate of the highest intersection point is determined as follows [19, 21]:

$$V(M_2 \geq M_1) = hgt(M_1 \cap M_2)$$
$$= \mu(d) = \frac{m_1^- - m_2^+}{(m_2 - m_2^+) - (m_1 - m_1^-)} \tag{2}$$

The value of the fuzzy synthetic extent can be determined as follows [19, 21]:

$$F_i = \sum_{j=1}^{m} M_{gi}^j \otimes \left[\sum_{i=1}^{n}\sum_{j=1}^{m} M_{gi}^j\right]^{-1}, \; i = 1,2,...,n \tag{3}$$

$$\sum_{j=1}^{m} M_{gi}^j = (\sum_{j=1}^{m} m_{ij}^-, \sum_{j=1}^{m} m_{ij}, \sum_{j=1}^{m} m_{ij}^+), j = 1,2,...,m \tag{4}$$

$$\left[\sum_{i=1}^{n}\sum_{j=1}^{m} M_{gi}^j\right]^{-1} = \left(\frac{1}{\sum_{i=1}^{n}\sum_{j=1}^{m} M_{ij}^+}, \frac{1}{\sum_{i=1}^{n}\sum_{j=1}^{m} M_{ij}}, \frac{1}{\sum_{i=1}^{n}\sum_{j=1}^{m} M_{ij}^-}\right) \tag{5}$$

$$V(F \geq F_1, F_2, ..., F_k) = \min V(F \geq F_i), i = 1,2,...,k \tag{6}$$

$$d(F_i) = \min V(F_i \geq F_k) = W_i' \quad k = 1,2,...,n \; and \; k \neq i \tag{7}$$

The weights of criteria are as follows after above procedure:

$$W' = (W_1', W_2', ..., W_n')^T \tag{8}$$

$$W = (W_1, W_2, ..., W_n)^T \tag{9}$$

The consistency ratio is calculated for the pair-wise comparison matrix, which shows relationship between O, S and D criteria. Fuzzy numbers of the pair-wise comparison matrix must be defuzzied into crisp numbers to calculate the consistency ratio. Crisp number is obtained from fuzzy number $\tilde{X} = (l,m,u)$ by using Eq.(10) [22]:

$$P(\tilde{X}) = \frac{1}{6}(l + 4 \times m + u) \tag{10}$$

The relative importance is calculated by using Eq.(11).

$$Aw = \lambda_{\max} w \tag{11}$$

The consistency index (*CI*) is defined as indicated in Eq. (12) [23]:

$$CI = (\lambda_{\max} - n)/(n-1) \tag{12}$$

The consistency ratio (*CR*) considers the consistency of the assessments. It must be smaller than 0.1 and is calculated by using Eq.(13). The assessment, which CR is bigger than 0.1, must be revised to correct it. (Wang and Yang, 2007).

$$CR = CI \; / \; RI \tag{13}$$

Random consistency index (*RI*) can be acquired from Table 4.

Table 4. Random consistency index.

N	1	2	3	4	5	6	7	8	9	10
RI	0	0	0.58	0.9	1.12	1.24	1.32	1.41	1.45	1.49

The additive weighted aggregation (AWA) operator is presented in Eq.(14) [24]:

$$g_i = \lambda_k \times g_{ik} \tag{14}$$

2.2. Attribute based aggregation technique

Chen [25] suggested an aggregation approach with fuzzy logic for homo/heterogeneous group of experts. Homogeneous group of experts means that the importance degree of each expert is equal. Heterogeneous group of experts means that the importance degree of each expert is not equal. This phase aims to acquire a group judgment by combining the judgments of homo/heterogeneous group f experts. Let be the relative importance of each expert $E_k(k=1,2,...,M)$ we_k, where $we_k \in [0,1]$ and $\sum_{k=1}^{M} we_k = 1$.

The aggregation method for homo/heterogeneous groups of experts is introduced below [17, 20]:

Step 1: Determine the degree of similarity of E_u expert's opinions to E_v expert's opinions as in Eq.(15) . Let U=(u_1, u_2, u_3) and V=(v_1, v_2, v_3) be two standardised triangular fuzzy numbers where $0 \le u_1 \le u_2 \le u_3 \le 1$ and $0 \le v_1 \le v_2 \le v_3 \le 1$

$$S(U,V) = 1 - \frac{|u_1 - v_1| + |u_2 - v_2| + |u_3 - v_3|}{3} \tag{15}$$

where $S(U,V) \in [0,1]$.

Step 2: Define the agreement matrix (AM).

$$AM = \begin{bmatrix} 1 & S_{12} & \dots & S_{1v} & \dots & S_{1M} \\ \dots & \dots & & \dots & & \dots \\ S_{u1} & S_{u2} & \dots & S_{uv} & \dots & S_{uM} \\ \dots & \dots & & \dots & & \dots \\ S_{M1} & S_{M2} & \dots & S_{Mv} & \dots & 1 \end{bmatrix} \tag{16}$$

where $S_{uv} = S(R_u, R_v)$, if $u \neq v$ and $S_{uv} = 1$, if $u=v$.

Step 3: Determine the average degree of similarity *AA(E_u)*.

$$AA(E_u) = \frac{1}{M-1} \sum_{v=1, v \neq u}^{M} S(R_u, R_v) \tag{17}$$

Step 4: Determine the relative importance of agreement RA (E_u).

$$RA(E_u) = \frac{AA(E_u)}{\sum_{u=1}^{M} AA(E_u)} \tag{18}$$

Step 5: Determine the consensus degree coefficient CC(E_u).

$$CC(E_u) = \beta we_u + (1-\beta) RA(E_u) \tag{19}$$

where $\beta (0 \le \beta \le 1)$. When $\beta = 0$, a homogeneous group of experts problem is considered.

Step 6: Aggregate the fuzzy opinions.

$$R_{AG} = CC(E_1) \otimes R_1 \oplus CC(E_2) \otimes R_2 \oplus \dots \oplus CC(E_M) \otimes R_M \tag{20}$$

2.3. Fuzzy TOPSIS

Hwang and Yoon suggested TOPSIS approach, which ranks alternatives. TOPSIS method aims to find solution [26]. Fuzzy TOPSIS method integrates fuzzy logic to classical TOPSIS method thus it ensures to ease a decision making process in ambiguous environment. The stages of fuzzy TOPSIS method are presented as follows [20, 27]:

Step 1: Defining the fuzzy decision matrix $\tilde{A}$: The decision maker defines $\tilde{A}_{ij}$ matrix as a beginning matrix and this matrix is shown in Eq.(21):

$$\tilde{A}_{ij} = \begin{bmatrix} \tilde{a}_{11} & \tilde{a}_{12} & \dots & \tilde{a}_{1n} \\ \tilde{a}_{21} & \tilde{a}_{22} & \dots & \tilde{a}_{2n} \\ \vdots & \vdots & \vdots & \vdots \\ \tilde{a}_{m1} & \tilde{a}_{m2} & \dots & \tilde{a}_{mn} \end{bmatrix} \tag{21}$$

Step 2: Determining the normalized fuzzy decision matrix $(\tilde{R})$: Eq.(22) is used to normalize the beginning matrix.

$$\tilde{r}_{ij} = \frac{\tilde{a}_{ij}}{\sqrt{\sum_{k=1}^{m} a_{kj}^2}} \tag{22}$$

Eq.(23) is utilized to acquire $\tilde{R}_{ij}$ matrix [20, 27]:

$$\tilde{R}_{ij} = \begin{bmatrix} \tilde{r}_{11} & \tilde{r}_{12} & \cdots & \tilde{r}_{1n} \\ \tilde{r}_{21} & \tilde{r}_{22} & \cdots & \tilde{r}_{2n} \\ \vdots & \ddots & \cdots & \vdots \\ \tilde{r}_{m1} & \tilde{r}_{m2} & \cdots & \tilde{r}_{mn} \end{bmatrix} \quad (23)$$

where

$$\tilde{r}_{ij} = \left(\frac{a_{ij}}{c_j^+}, \frac{b_{ij}}{c_j^+}, \frac{c_{ij}}{c_j^+} \right) and\, c_j^+ = \max_i c_{ij} \text{ (Benefit criteria)}$$

$$\tilde{r}_{ij} = \left(\frac{a_j^-}{c_{ij}}, \frac{a_j^-}{b_{ij}}, \frac{a_j^-}{a_{ij}} \right) and\, a_j^- = \min_i a_{ij} \text{ (Cost criteria)}$$

Step 3: Defining the weighted normalized fuzzy decision matrix $(\tilde{v})$: Eqs.(24)-(25) is employed to calculate $\tilde{v}_{ij}$ matrix which shows the multiplication of $\tilde{r}_{ij}$ matrix and the weights of assessment criteria (w_i) [27]:

$$\sum_{i=1}^{n} w_i = 1 \quad (24)$$

$$\tilde{v}_{ij} = \begin{bmatrix} w_1\tilde{r}_{11} & w_2\tilde{r}_{12} & \ldots & w_n\tilde{r}_{1n} \\ w_1\tilde{r}_{21} & w_2\tilde{r}_{22} & \ldots & w_n\tilde{r}_{2n} \\ . & & & . \\ . & & & . \\ . & & & . \\ w_1\tilde{r}_{m1} & w_2\tilde{r}_{m2} & \ldots & w_n\tilde{r}_{mn} \end{bmatrix} \quad (25)$$

$i = 1,2,...,m; j = 1,2,...,n \; where \; \tilde{v}_{ij} = \tilde{r}_{ij}(.)w_j$

$\tilde{v}_{ij}$ is expressed by $\left(\tilde{a}_{ijk}, \tilde{b}_{ijk}, \tilde{c}_{ijk}\right)$.

Step 4: Defining the fuzzy ideal solution (FPIS) and fuzzy negative ideal solution (FNIS): Eqs.(26)-(27) are utilized to compute the FPIS and FNIS of the alternatives :

$$A^+ = \tilde{v}_1^+, \tilde{v}_2^+, ..., \tilde{v}_n^+ \quad where\, \tilde{v}_j^+ = 1,1,1 \quad (26)$$

$$A^- = \tilde{v}_1^-, \tilde{v}_2^-, ..., \tilde{v}_n^- \quad where\, \tilde{v}_j^- = 0,0,0 \quad (27)$$

Step 5: Defining the separation scales of each alternative: Eqs.(28)-(29) are employed to calculate the distance measure d_i^+, d_i^- from the FPIS and the FNIS for each alternative:

$$d_i^+ = \sum_{j=1}^{n} dv(\tilde{v}_{ij}, \tilde{v}_j^+), i = 1,2,...,m \quad (28)$$

$$d_i^- = \sum_{j=1}^{n} dv(\tilde{v}_{ij}, \tilde{v}_j^-), i = 1,2,...,m \quad (29)$$

If $\tilde{v}_{ij} = \tilde{a}_{ij}, \tilde{b}_{ij}, \tilde{c}_{ij}$ and $\tilde{v}_j^+ = 1,1,1$ and $\tilde{v}_j^- = 0,0,0$:

$$dv(\tilde{v}_{ij}, \tilde{v}_j^+) = \sqrt{\frac{1}{3}\left[(\tilde{a}_{ij} - 1)^2 + (\tilde{b}_{ij} - 1)^2 + (\tilde{c}_{ij} - 1)^2 \right]},$$

$$dv(\tilde{v}_{ij}, \tilde{v}_j^-) = \sqrt{\frac{1}{3}\left[(\tilde{a}_{ij} - 0)^2 + (\tilde{b}_{ij} - 0)^2 + (\tilde{c}_{ij} - 0)^2 \right]}.$$

Step 6: Defining the closeness coefficient (CC_i) of each alternative: Eq.(30) is used to calculate CC_i for each alternative:

$$CC_i = \frac{d_i^-}{d_i^- + d_i^+} \quad (30)$$

Step 7: Rank the alternatives: CC_i values according to its increasing values are employed to rank the alternatives.

3. An application for risk evaluation

3.1. Implementation

After examining the process and identifying potential problems or areas for improvement, a risk assessment is made. Risk assessment is the scoring of failures in terms of probability of occurrence, severity of impact and determination. This scoring is done through ready-made scales or new scales to be prepared. There is no single and standardized scale to be used in FMEA applications, but low scores on the scales are attributed to low risk levels, and high scores are attributed to high risk levels. Existing information is used while scoring. If such a resource is not available, the scoring is done based on the experience and foresight of the team members. Another requirement at this stage is FMEA forms in which study-related records will be processed. These forms are also non-standard and FMEA teams can adapt these forms according to their own work. Risk assessment procedure covers determining of decision makers for risk assessment, defining failure modes, defining O, S

and D criteria that presented in assessment stage, defining the weights of the O, S and D criteria and ranking orders of failure modes, solving a mathematical model phases. A real life application in a construction firm is presented to show the efficiency of the suggested method. Fig. 1 indicates the flowchart of the suggested method. Thirty-five failure modes in the construction firm are presented in Table 5. In order to conclude a comprehensive study such as FMEA in the most effective way, consultation with others and cooperation when necessary will be needed. It is extremely beneficial to conduct FMEA with teamwork, as it will be possible for everyone to benefit from the experience and knowledge of each other in teamwork. For this reason, after the critical problems to be worked on are determined, the first thing to do is to form this team. All team members should be selected from individuals who are knowledgeable about the process to be worked on and even about group behavior, are directly or indirectly related to the problem, and are willing to participate in the study. Team members should be people who are familiar with the process to be worked on, and all of them should have been given the necessary training for this job before starting to work. This paper collected the judgments of three experts. In this study, the suggested integrated fuzzy extension of AHP-fuzzy TOPSIS approach is utilized to order the failure modes in the construction firm. The priorities of criteria in risk assessment will be defined by fuzzy extension of AHP. Pair wise comparison matrixes of decision makers' judgments are considered to acquire priorities of criteria by utilizing the linguistic variables, which is indicated in Table 2.

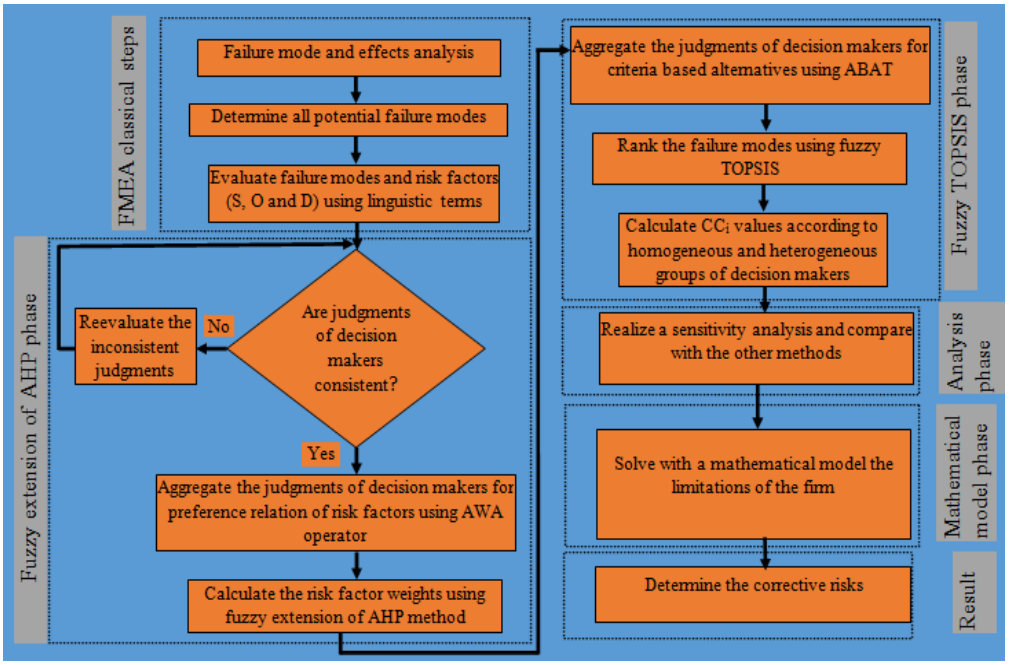

Figure 1. Flowchart of the suggested method.

Thirty-five failures based on O, S and D criteria are ranked. Fuzzy extension of AHP approach is used to define the weights of criteria and fuzzy TOPSIS approach is used to order criteria based failure modes. The three experts present the pair-wise comparison matrix of criteria as showing in Table 3.

Table 5. Failure modes in the construction firm

FM1	Working without prevention of staff in T shaft cavity
FM2	Non-running with water the pumice cutting machine during cutting
FM3	Injuring the foot of sharp materials in places
FM4	Working without prevention of staff building wall in square shaft cavity
FM5	Unsuitability of isolation and grounding of pumice grooving machine
FM6	Loss of balance
FM7	The broken stems of the mechanical hand tools
FM8	Open ends of electrical cables
FM9	Falling of the materials below when workers go from insecure places
FM10	Inappropriate utilization of pumice grooving machine
FM11	Hasty and careless working during building wall

FM12	Overthrowing the ladder in the edges of balcony and fronts of window
FM13	Holding the sharp edges of materials
FM14	Deformed railings located on the floors
FM15	Manual handling of heavy loads
FM16	Rubbish shot used to pour material and filth
FM17	Utilization of damaged and deformed cables
FM18	Utilization without protection the pumice grooving machine
FM19	Wrong utilization of pumice cutting machine
FM20	Noncovering the cavities in the ground during laying brick
FM21	Loading over material to the scaffolding
FM22	Absence of emergency stop button of the pumice cutting machine
FM23	Overthrowing the material from palet
FM24	Utilization of nonstandart scaffolding
FM25	Noncovering the cavities after building wall
FM26	Irritation of the skin
FM27	Utilization without protection the pumice cutting machine
FM28	Attempting to break the material with hands
FM29	Noncovering the shaft cavities in downstairs operations
FM30	Entering plaster to eye
FM31	Electrical leakage in the pumice cutting machine
FM32	Staggering to the material during manual handling the material
FM33	Working without prevention of staff building wall in elevator and shaft cavity
FM34	Absence of warning signboards of the pumice cutting machine
FM35	Availability of dust in the environment

The overall weights of O, S and D criteria are calculated in fuzzy extension of AHP stage by using AWA operator, which is presented in Eq.(14). Fuzzy extension of AHP is utilized to calculate the importance degrees of O, S, and D criteria by helping of Eqs. (1)-(9). The results of computation are indicated in Tables 6.-7. The weights of criteria is calculated detailly and indicated below. The weights of criteria can be defined according to decision maker E3 below:

Table 6. Pairwise comparison matrix of O, S and D criteria.

		O	S	D	CR
	O	(1.000,1.000,1.000)	(0.667,1.000,1.493)	(0.667,1.000,1.500)	
E1	S	(0.670,1.000,1.500)	(1.000,1.000,1.000)	(1.000,1.000,1.000)	
	D	(0.667,1.000,1.500)	(1.000,1.000,1.000)	(1.000,1.000,1.000)	0.032
		O	S	D	
	O	(1.000,1.000,1.000)	(1.500,2.000,2.500)	(0.670,1.000,1.500)	
E2	S	(0.400,0.500,0.667)	(1.000,1.000,1.000)	(0.670,1.000,1.500)	
	D	(0.667,1.000,1.493)	(0.667,1.000,1.493)	(1.000,1.000,1.000)	0.084
		O	S	D	
	O	(1.000,1.000,1.000)	(0.400,0.500,0.670)	(0.667,1.000,1.500)	
E3	S	(1.493,2.000,2.500)	(1.000,1.000,1.000)	(0.667,1.000,1.500)	
	D	(0.667,1.000,1.500)	(0.667,1.000,1.500)	(1.000,1.000,1.000)	0.084

Table 7. Total weight of criteria for each decision maker.

	O	S	D	Weights of experts
E1	0,333	0,333	0,333	0,35
E2	0,451	0,225	0,323	0,25
E3	0,226	0,450	0,324	0,40
Overall weight	0,320	0,353	0,327	

$$\sum_{i=1}^{n}\sum_{j=1}^{m} M_{gi}^{j} = (1,1,1) + (0.4,0.5,0.67) + \ldots + (1,1,1)$$

$$= (7.56, 9.50, 12.17)$$

$$\left[\sum_{i=1}^{n}\sum_{j=1}^{m} M_{gi}^{j}\right]^{-1} = \left(\frac{1}{12.17}, \frac{1}{9.50}, \frac{1}{7.56}\right) = 0.082, 0.105, 0.132$$

$$\sum_{j=1}^{m} M_{g1}^{j} = (1,1,1) + (0.4,0.5,0.67) + (0.67,1,1.5) = (2.07, 2.50, 3.17)$$

$$\sum_{j=1}^{m} M_{g2}^{j} = (3.16, 4.00, 5.00) \quad \sum_{j=1}^{m} M_{g3}^{j} = (2.33, 3.00, 4.00)$$

$$F_1 = \sum_{j=1}^{m} M_{g1}^{j} \otimes \left[\sum_{i=1}^{n}\sum_{j=1}^{m} M_{gi}^{j}\right]^{-1} = (2.07, 2.50, 3.17) \otimes 0.082, 0.105, 0.132$$

$$= (0.170, 0.263, 0.419)$$

$$F_2 = \sum_{j=1}^{m} M_{g2}^{j} \otimes \left[\sum_{i=1}^{n}\sum_{j=1}^{m} M_{gi}^{j}\right]^{-1} = (0.260, 0.421, 0.661)$$

$$F_3 = \sum_{j=1}^{m} M_{g3}^{j} \otimes \left[\sum_{i=1}^{n}\sum_{j=1}^{m} M_{gi}^{j}\right]^{-1} = (0.192, 0.316, 0.529)$$

$$V(F_1 \geq F_2) = 0.503, V(F_1 \geq F_3) = 0.812,$$
$$V(F_2 \geq F_1) = 1.000, V(F_2 \geq F_3) = 1.000,$$
$$V(F_3 \geq F_1) = 1.000, \; V(F_3 \geq F_2) = 0.719,$$

The weight vectors are determined as follows.

$$d(F_1) = MinV(F_1 \geq F_2, F_3) = Min(0.503, 0.812) = 0.503$$
$$d(F_2) = MinV(F_2 \geq F_1, F_3) = Min(1.000, 1.000) = 1.000$$

$$d(F_3) = MinV(F_3 \geq F_1, F_2) = Min(1.000, 0.719) = 0.719$$

$$W' = (d(F_1), d(F_2), d(F_3))^T = (0.503, 1.000, 0.719)^T$$

$$W = (0.226, 0.450, 0.324)$$

We could say that the weights of O, S, and D criteria according to expert 3 are 0.226, 0.450 and 0.324, respectively. The CRs is smaller than 0.1 for the pair-wise comparison matrix of O, S, and D criteria. This means that judgments of three decision makers are rather consistent and are suitable to use in the next phases. The CRs, which are calculated by helping of Eqs.(10)-(13), are presented in the last column of Table 6. The weights of decision makers, which are indicated in the last column of Table 7, can be rather important while aggregating the judgments of the decision makers.

The outcomes of fuzzy extension of AHP approach are presented in Table 7 so that these results are used in next phase of risk assessment. This paper used fuzzy TOPSIS based on an ABAT to rank the failure modes in the construction firm. The judgments of three decision makers are indicated as linguistic terms in Table 8 about criteria based failure modes. Eqs.(15)-(20) are utilized to obtain the aggregated fuzzy decision matrix of the criteria based failure modes and the results according to homogeneous and heterogeneous groups of decision makers are in Table 9 and Table 10, respectively. β that shows the moderator's dominance in the ABAT, is considered as 0.4 in fuzzy TOPSIS calculation. For example, aggregation calculations for occurrence criteria are indicated in Table 11 detailly. Degree of agreement (S), average degree of agreement (AA), relative degree of agreement (RA), consensus degree coefficient (CC) are introduced in Table 11.

Table 8. The criteria based failure modes with linguistic variables

	E1			E2			E3		
	O	O	O	O	S	D	O	S	D
FM1	M	G	FP	VG	FG	P	G	FP	AP
FM2	M	G	FP	FG	M	FP	M	FP	FG
FM3	M	FP	G	FP	FP	M	VP	P	FG
FM4	M	AG	VP	FP	AG	AP	FP	VG	AP
FM5	G	FP	G	VG	FP	M	M	P	FG
FM6	M	G	M	G	FG	G	G	AG	FG
FM7	G	FP	G	VG	FP	VG	P	VP	AG
FM8	G	FP	G	G	FP	FG	G	VP	G
FM9	G	FP	G	VG	FP	FG	M	M	AG
FM10	M	FG	FG	VP	G	G	FP	M	VP
FM11	G	FP	G	FG	VP	M	FG	FP	FP
FM12	M	M	M	VG	G	G	VG	FP	FP
FM13	G	FP	G	P	FP	VG	M	AP	G
FM14	G	FP	G	VG	VP	FG	VG	FP	FP
FM15	G	FP	G	FP	VP	M	M	FP	FG
FM16	G	FP	G	VG	FP	VG	FG	M	AG
FM17	G	FP	G	VG	FP	G	FG	FP	VG
FM18	M	G	FG	M	FG	VG	VP	G	VP
FM19	M	G	FG	P	FG	FP	FP	G	M
FM20	M	G	M	FP	VG	G	G	FG	VP
FM21	M	G	FG	M	M	P	FP	AG	M
FM22	FG	G	M	P	FG	FP	P	G	FG
FM23	M	G	G	VG	VP	FP	FG	FP	AG
FM24	M	FP	FG	VP	G	P	M	FP	FG
FM25	FG	G	M	FP	M	M	M	M	P
FM26	M	FP	G	VP	P	G	FP	VP	FG
FM27	M	G	M	FG	FG	FP	P	FG	FG
FM28	M	VP	FG	FG	P	FP	FG	AP	FP
FM29	M	FG	M	VG	M	VG	G	FP	FG
FM30	FG	FG	M	FP	G	FG	FP	M	P
FM31	M	M	FP	VP	FG	VP	VP	P	FG
FM32	M	M	G	FG	M	FG	FP	M	G
FM33	FG	G	FP	FP	FG	P	P	AG	P
FM34	M	G	FP	M	M	G	M	M	FP
FM35	M	G	FP	VP	FG	VP	VP	VG	FG

Table 9. Aggregated fuzzy decision matrix with homogeneous groups of decision makers.

	O	S	D
FM1	(0.532,0.700,0.868)	(0.467,0.565,0.663)	(0.166,0.286,0.405)
FM2	(0.364,0.516,0.668)	(0.397,0.547,0.697)	(0.432,0.482,0.532)
FM3	(0.273,0.389,0.506)	(0.306,0.403,0.500)	(0.434,0.582,0.731)
FM4	(0.368,0.466,0.564)	(0.867,0.967,1.000)	(0.032,0.132,0.232)
FM5	(0.532,0.700,0.868)	(0.306,0.403,0.500)	(0.434,0.582,0.731)
FM6	(0.438,0.638,0.838)	(0.622,0.742,0.831)	(0.434,0.582,0.731)
FM7	(0.489,0.656,0.822)	(0.310,0.375,0.440)	(0.741,0.872,0.969)
FM8	(0.500,0.700,0.900)	(0.310,0.375,0.440)	(0.500,0.653,0.806)
FM9	(0.532,0.700,0.868)	(0.368,0.466,0.564)	(0.622,0.742,0.831)
FM10	(0.273,0.389,0.506)	(0.434,0.582,0.731)	(0.385,0.500,0.615)
FM11	(0.500,0.597,0.694)	(0.310,0.375,0.440)	(0.397,0.547,0.697)
FM12	(0.664,0.791,0.918)	(0.397,0.547,0.697)	(0.397,0.547,0.697)
FM13	(0.300,0.500,0.700)	(0.287,0.351,0.415)	(0.592,0.762,0.931)
FM14	(0.708,0.838,0.969)	(0.310,0.375,0.440)	(0.467,0.565,0.663)
FM15	(0.397,0.547,0.697)	(0.310,0.375,0.440)	(0.434,0.582,0.731)
FM16	(0.595,0.714,0.834)	(0.368,0.466,0.564)	(0.741,0.872,0.969)

FM17	(0.595,0.714,0.834)	(0.400,0.450,0.500)	(0.592,0.762,0.931)
FM18	(0.242,0.413,0.583)	(0.500,0.653,0.806)	(0.470,0.550,0.630)
FM19	(0.269,0.418,0.566)	(0.500,0.653,0.806)	(0.400,0.500,0.600)
FM20	(0.397,0.547,0.697)	(0.595,0.714,0.834)	(0.305,0.475,0.645)
FM21	(0.332,0.484,0.636)	(0.558,0.727,0.866)	(0.303,0.453,0.603)
FM22	(0.220,0.375,0.530)	(0.500,0.653,0.806)	(0.400,0.500,0.600)
FM23	(0.518,0.635,0.752)	(0.338,0.450,0.563)	(0.592,0.714,0.806)
FM24	(0.242,0.413,0.583)	(0.430,0.525,0.620)	(0.380,0.475,0.570)
FM25	(0.400,0.500,0.600)	(0.362,0.562,0.762)	(0.238,0.438,0.638)
FM26	(0.273,0.389,0.506)	(0.196,0.315,0.434)	(0.500,0.653,0.806)
FM27	(0.303,0.453,0.603)	(0.500,0.597,0.694)	(0.400,0.500,0.600)
FM28	(0.436,0.534,0.632)	(0.067,0.200,0.333)	(0.432,0.482,0.532)
FM29	(0.532,0.700,0.868)	(0.400,0.500,0.600)	(0.518,0.635,0.752)
FM30	(0.432,0.482,0.532)	(0.434,0.582,0.731)	(0.303,0.453,0.603)
FM31	(0.158,0.288,0.417)	(0.303,0.453,0.603)	(0.342,0.408,0.473)
FM32	(0.400,0.500,0.600)	(0.300,0.500,0.700)	(0.500,0.653,0.806)
FM33	(0.337,0.435,0.533)	(0.622,0.742,0.831)	(0.194,0.347,0.500)
FM34	(0.300,0.500,0.700)	(0.362,0.562,0.762)	(0.430,0.525,0.620)
FM35	(0.158,0.288,0.417)	(0.595,0.714,0.834)	(0.342,0.408,0.473)

Table 10. Aggregated fuzzy decision matrix with heterogeneous groups of decision makers.

	O	S	D
FM1	(0.521,0.692,0.863)	(0.464,0.564,0.664)	(0.166,0.281,0.395)
FM2	(0.358,0.515,0.671)	(0.402,0.548,0.694)	(0.435,0.485,0.535)
FM3	(0.262,0.381,0.499)	(0.295,0.398,0.500)	(0.440,0.585,0.731)
FM4	(0.367,0.467,0.566)	(0.864,0.964,1.000)	(0.033,0.133,0.233)
FM5	(0.517,0.688,0.859)	(0.295,0.398,0.500)	(0.440,0.585,0.731)
FM6	(0.435,0.635,0.835)	(0.637,0.758,0.845)	(0.432,0.577,0.723)
FM7	(0.459,0.629,0.799)	(0.298,0.365,0.432)	(0.738,0.871,0.967)
FM8	(0.500,0.700,0.900)	(0.298,0.365,0.432)	(0.500,0.657,0.813)
FM9	(0.517,0.688,0.859)	(0.365,0.468,0.570)	(0.637,0.758,0.845)
FM10	(0.280,0.396,0.511)	(0.428,0.576,0.725)	(0.367,0.479,0.591)
FM11	(0.500,0.599,0.699)	(0.316,0.380,0.444)	(0.402,0.548,0.694)
FM12	(0.648,0.779,0.909)	(0.394,0.540,0.686)	(0.394,0.540,0.686)
FM13	(0.308,0.508,0.708)	(0.268,0.335,0.401)	(0.585,0.757,0.928)
FM14	(0.703,0.835,0.968)	(0.316,0.380,0.444)	(0.464,0.564,0.664)
FM15	(0.396,0.551,0.706)	(0.316,0.380,0.444)	(0.440,0.585,0.731)
FM16	(0.587,0.704,0.822)	(0.365,0.468,0.570)	(0.738,0.871,0.967)
FM17	(0.587,0.704,0.822)	(0.400,0.450,0.500)	(0.603,0.769,0.934)
FM18	(0.233,0.400,0.566)	(0.500,0.657,0.813)	(0.448,0.529,0.610)
FM19	(0.277,0.423,0.568)	(0.500,0.657,0.813)	(0.398,0.502,0.606)
FM20	(0.400,0.555,0.710)	(0.587,0.704,0.822)	(0.291,0.457,0.623)
FM21	(0.335,0.482,0.630)	(0.579,0.744,0.876)	(0.310,0.459,0.608)
FM22	(0.228,0.380,0.532)	(0.500,0.657,0.813)	(0.402,0.503,0.604)
FM23	(0.513,0.629,0.745)	(0.347,0.460,0.574)	(0.609,0.732,0.819)
FM24	(0.245,0.418,0.590)	(0.428,0.520,0.612)	(0.388,0.480,0.572)
FM25	(0.398,0.502,0.606)	(0.365,0.565,0.765)	(0.231,0.431,0.631)
FM26	(0.280,0.396,0.511)	(0.200,0.314,0.428)	(0.500,0.648,0.795)
FM27	(0.290,0.445,0.600)	(0.500,0.599,0.699)	(0.402,0.503,0.604)
FM28	(0.434,0.533,0.633)	(0.064,0.194,0.324)	(0.433,0.483,0.533)
FM29	(0.521,0.692,0.863)	(0.404,0.499,0.594)	(0.513,0.629,0.745)
FM30	(0.433,0.483,0.533)	(0.428,0.576,0.725)	(0.290,0.445,0.600)
FM31	(0.163,0.295,0.426)	(0.290,0.445,0.600)	(0.351,0.416,0.480)
FM32	(0.396,0.497,0.598)	(0.300,0.500,0.700)	(0.500,0.657,0.813)
FM33	(0.328,0.431,0.534)	(0.637,0.758,0.845)	(0.199,0.349,0.500)
FM34	(0.300,0.500,0.700)	(0.365,0.565,0.765)	(0.428,0.520,0.612)
FM35	(0.163,0.295,0.426)	(0.605,0.725,0.846)	(0.351,0.416,0.480)

Eqs.(21)-(25) are utilized to transform to the weighted normalized fuzzy decision matrix the aggregated fuzzy decision matrix. In this paper occurrence and severity criteria are the cost criteria and detection criterion is a benefit criteria. FPIS A^+ and FNIS A^- are $\tilde{v}^+ = (1,1,1)$ and $\tilde{v}^- = (0,0,0)$ for this benefit criteria, respectively. Eqs. (26)-(29) are used to measure the distance of each failure mode from FNIS and FPIS concurrently. For example, the values of FPIS and FNIS d_1^+, d_1^- for failure mode 1 are computed as follows. Eq.(30) is utilized to calculate CC_1 as an example as follows. Similarly, calculations (d_i^+, d_i^-, CC_i) can be done for the other situations.

$$d_1^+ = \sqrt{\frac{1}{3}[(0-0.1723)^2 + (0-0.2288)^2 + (0-0.2854)^2]}$$
$$+\sqrt{\frac{1}{3}[(0-0.1638)^2 + (0-0.1990)^2 + (0-0.2342)^2]}$$
$$+\sqrt{\frac{1}{3}[(1-0.0560)^2 + (1-0.0948)^2 + (1-0.1335)^2]} = 1{,}3403$$

$$d_1^- = \sqrt{\frac{1}{3}[(1-0.1723)^2 + (1-0.2288)^2 + (1-0.2854)^2]}$$
$$+\sqrt{\frac{1}{3}[(1-0.1638)^2 + (1-0.1990)^2 + (1-0.2342)^2]}$$
$$+\sqrt{\frac{1}{3}[(0-0.0560)^2 + (0-0.0948)^2 + (0-0.1335)^2]} = 1{,}6740$$

$$CC_1 = \frac{d_1^-}{d_1^+ + d_1^-} = \frac{1{,}6740}{1{,}3403 + 1{,}6740} = 0{,}5553$$

We specified thirty-five failure modes to define the most important failure mode. Distance based separation scales values d_i^+, d_i^- and closeness coefficient (CC_i) of the thirty-five failure modes are showed at Table 12.

Table 11. Aggregation calculations for occurrence criterion

	FM1	FM2	... FM34	FM35
E1	(0.3,0.5,0.7)	(0.3,0.5,0.7)	... (0.3,0.5,0.7)	(0.3,0.5,0.7)
E2	(0.8,0.9,1.0)	(0.5,0.55,0.6)	... (0.3,0.5,0.7)	(0.1,0.2,0.3)
E3	(0.5,0.7,0.9)	(0.3,0.5,0.7)	... (0.3,0.5,0.7)	(0.1,0.2,0.3)
S				
S12	0.60	0.88	... 1.00	0.70
S13	0.80	1.00	... 1.00	0.70
S23	0.80	0.88	... 1.00	1.00
AA				
AA(E1)	0.70	0.94	... 1.00	0.70
AA(E2)	0.70	0.88	... 1.00	0.85
AA(E3)	0.80	0.94	... 1.00	0.85
RA				
RA(E1)	0.318	0.340	... 0.333	0.292
RA(E2)	0.318	0.319	... 0.333	0.354
RA(E3)	0.364	0.340	... 0.333	0.354
CC				
CC(E1)	0.331	0.344	... 0.340	0.315
CC(E2)	0.291	0.292	... 0.300	0.313
CC(E3)	0.378	0.364	... 0.360	0.373
R_{AG}^{HM}	(0.532,0.700,0.868)	(0.364,0.516,0.668)	... (0.300,0.500,0.700)	(0.158,0.288,0.417)
R_{AG}^{HT}	(0.521,0.692,0.863)	(0.358,0.515,0.671)	... (0.300,0.500,0.700)	(0.163,0.295,0.426)

Table 12. The separation scales and the closeness coefficient.

	Heterogeneous				Homogeneous			
	d_i^+	d_i^-	CC_i	Rank	d_i^+	d_i^-	CC_i	Rank
FM1	1,3403	1,6740	0,5553	2	1,3410	1,6733	0,5551	2
FM2	1,2094	1,8031	0,5985	13	1,2104	1,8021	0,5982	12

FM3	1,0765	1,9367	0,6427	32	1,0818	1,9310	0,6409	32
FM4	1,4454	1,5665	0,5201	1	1,4459	1,5658	0,5199	1
FM5	1,1788	1,8358	0,6090	20	1,1850	1,8292	0,6069	19
FM6	1,2879	1,7281	0,5730	4	1,2821	1,7342	0,5749	4
FM7	1,0539	1,9565	0,6499	33	1,0652	1,9447	0,6461	33
FM8	1,1473	1,8678	0,6195	24	1,1519	1,8628	0,6179	23
FM9	1,1481	1,8632	0,6187	23	1,1562	1,8547	0,6160	22
FM10	1,1811	1,8323	0,6081	19	1,1741	1,8393	0,6104	20
FM11	1,1512	1,8579	0,6174	22	1,1491	1,8602	0,6181	24
FM12	1,2735	1,7407	0,5775	6	1,2777	1,7369	0,5762	6
FM13	1,0419	1,9759	0,6548	34	1,0435	1,9740	0,6542	34
FM14	1,2237	1,7834	0,5931	9	1,2225	1,7844	0,5934	8
FM15	1,1256	1,8867	0,6263	28	1,1233	1,8889	0,6271	29
FM16	1,1133	1,8951	0,6299	30	1,1153	1,8929	0,6293	30
FM17	1,1362	1,8728	0,6224	25	1,1420	1,8673	0,6205	25
FM18	1,1972	1,8188	0,6030	18	1,1930	1,8228	0,6044	18
FM19	1,2121	1,8027	0,5979	12	1,2099	1,8048	0,5987	13
FM20	1,2860	1,7307	0,5737	5	1,2804	1,7362	0,5755	5
FM21	1,2726	1,7444	0,5782	7	1,2701	1,7477	0,5791	7
FM22	1,1988	1,8171	0,6025	16	1,1970	1,8190	0,6031	17
FM23	1,1332	1,8759	0,6234	26	1,1372	1,8721	0,6221	26
FM24	1,1693	1,8443	0,6120	21	1,1712	1,8426	0,6114	21
FM25	1,2320	1,7929	0,5927	8	1,2275	1,7971	0,5942	9
FM26	1,0324	1,9821	0,6575	35	1,0296	1,9857	0,6586	35
FM27	1,1969	1,8151	0,6026	17	1,1993	1,8120	0,6017	15
FM28	1,0933	1,9202	0,6372	31	1,0960	1,9176	0,6363	31
FM29	1,1997	1,8118	0,6016	15	1,2007	1,8110	0,6013	14
FM30	1,2190	1,7943	0,5955	11	1,2178	1,7949	0,5958	11
FM31	1,1266	1,8890	0,6264	29	1,1294	1,8856	0,6254	28
FM32	1,1315	1,8877	0,6252	27	1,1338	1,8851	0,6244	27
FM33	1,2933	1,7202	0,5708	3	1,2898	1,7238	0,5720	3
FM34	1,2062	1,8166	0,6010	14	1,2033	1,8196	0,6019	16
FM35	1,2218	1,7896	0,5943	10	1,2181	1,7932	0,5955	10

3.2. Comparison and discussion

The most important failure mode is defined the FM4 according to the heterogeneous results of fuzzy TOPSIS in Table 10. The risk assessment process is also presented with different approaches, which are fuzzy AHP- fuzzy VIKOR and fuzzy AHP- fuzzy GRA. The ranking orders results of thirty-five failure modes are acquired by utilizing these methods and the results are shown in Table 13. FM4 is selected the most important failure mode.

Table 13. Result comparison with other methods.

	FAHP-FVIKOR	FAHP-FGRA	The proposed approach	
			Hetero geneous	Homo geneous
FM1	3	2	2	2
FM2	22	10	13	12
FM3	33	29	32	32
FM4	1	1	1	1
FM5	11	16	20	19
FM6	5	3	4	4
FM7	29	35	33	33
FM8	12	22	24	23
FM9	15	23	23	22
FM10	26	20	19	20
FM11	25	18	22	24
FM12	4	5	6	6
FM13	34	33	34	34
FM14	2	11	9	8
FM15	30	24	28	29
FM16	17	30	30	30
FM17	13	27	25	25
FM18	19	17	18	18
FM19	14	14	12	13
FM20	8	4	5	5
FM21	7	6	7	7
FM22	18	19	16	17
FM23	24	26	26	26
FM24	27	21	21	21
FM25	16	8	8	9
FM26	35	34	35	35
FM27	21	15	17	15
FM28	31	32	31	31
FM29	9	12	15	14
FM30	20	9	11	11
FM31	28	31	29	28

FM32	32	25	27	27
FM33	6	7	3	3
FM34	23	13	14	16
FM35	10	28	10	10

A sensitivity analysis is implemented to define the effect of β coefficient on the CC_i value, which defines the final ranking of the failure modes. β coefficient begins as 0.1 value and ends as 1 value with increasing 0.1 value so that β coefficient changes as in Fig. 2. It is obvious that distance measure based CC_i is not sensitive for varying β coefficient according to Fig. 2. FM4 remains the most important failure mode in all computations so the firm must consider to eliminate FM4 from work environment firstly. FM26 remains the most unimportant failure mode in all computations so the firm must consider eliminating FM26 from work environment finally.

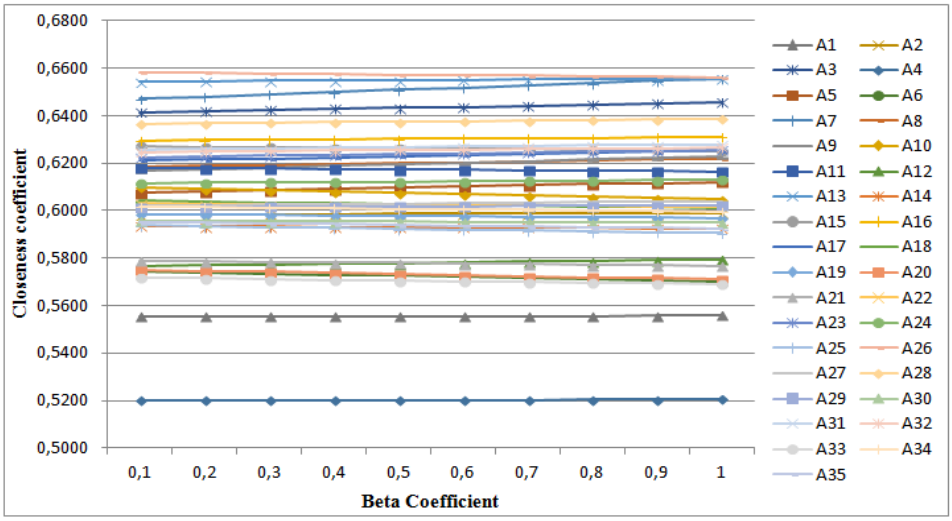

Figure 2. Sensitivity analysis due to exchanging of β value

3.3. Linear programming

The managers of the firm aim to handle limited resources such as budget and time. This study suggests a linear programming including these constraints. The firm planned to allocate 22500-27500 Turkish Liras (TL), 16-24 weeks, 11-15 correctable risks as constraints. We defined 3 different budget values, which are 22500, 25000 and 27500 TL. We defined 3 different times, which are 16, 20 and 24 weeks. We presented 11, 12, 13, 14, and 15 values for number of corrective risk. Cost and time data of failure modes in the construction firm are presented in Table 14.

Table 14. The additional data of the failure modes

FM	c_i	b_i	t_i	FM	c_i	b_i	t_i
FM1	750	1200	2	FM19	150	250	1
FM2	500	800	2	FM20	1000	1250	2
FM3	300	750	1	FM21	200	400	1
FM4	750	1200	2	FM22	250	500	1
FM5	1500	2500	3	FM23	200	400	1
FM6	1000	2000	1	FM24	1500	2500	3
FM7	150	250	1	FM25	1000	1250	2
FM8	150	250	1	FM26	150	350	1
FM9	750	1200	1	FM27	150	250	1
FM10	150	300	1	FM28	250	500	1
FM11	150	300	1	FM29	1000	1250	2
FM12	200	300	1	FM30	250	400	1
FM13	100	200	1	FM31	350	750	1
FM14	750	1000	2	FM32	200	300	1
FM15	500	750	2	FM33	750	1200	2
FM16	200	250	1	FM34	300	600	1
FM17	600	1000	1	FM35	1000	1500	3
FM18	150	250	1				

Notations

x_i : Binary variable, equal to 1 when failure mode i is corrective

c_i : Total cost after corrective action

b_i : Total cost without corrective action

t_i : Necessary time to correct failure mode i

q^* : CC value of failure mode, which has the highest CC value in Table 12

q_i : CC value of failure mode i in Table 12

$|q_i - q^*|$ defines the absolute value of difference between q_i and q^* values. Eq. (31) aim to maximize the impact values of corrective risks as possible.

$$\max \sum_{i=1}^{n} |q_i - q^*| . x_i \quad (31)$$

st.

$$\sum_{i=1}^{n} c_i . x_i + b_i . (1 - x_i) \leq budget \quad (32)$$

$$\sum_{i=1}^{n} t_i . x_i \leq time \quad (33)$$

$$\sum_{i=1}^{n} x_i \leq number\ of\ correctable\ risk \quad (34)$$

$$x_i = 0 - 1 \quad (35)$$

Eq. (32) means the limited budget. Eq. (33) presents the limited time. Eq. (34) shows maximum number of correctable risk. Eq. (35) shows binary variable.

Table 15 presents the results of linear programming in GAMS software program. Though FM12, FM14, FM20, FM25, FM33 and FM35 are one of the first ten failures according to the result of the proposed method with heterogeneous groups of decision makers. FM4 is the most important failure mode for the results of FAHP-FTOPSIS method and mathematical model.

Table 15. The results of linear programming

Budget	Time	NOCR	CR
22500	16	11	1,4,5,6,9,17,21,24,31,34
22500	16	12	3,4,5,6,9,17,21,22,24,30,34
22500	16	13	3,4,5,6,9,17,21,22,24,30,34
22500	16	14	3,4,5,6,9,17,21,22,24,30,34
22500	16	15	3,4,5,6,9,17,21,22,24,30,34
22500	20	11	1,2,4,5,6,9,12,20,21,24,33
22500	20	12	1,4,5,6,9,12,20,21,24,30,33,34
22500	20	13	1,4,5,6,9,12,20,21,24,30,33,34
22500	20	14	1,4,5,6,9,12,17,19,20,21,30,31,33,34
22500	20	15	1,4,5,6,9,12,17,19,21,22,27,30,31,33,34
22500	24	11	1,4,5,6,12,14,20,21,24,33,35
22500	24	12	1,4,5,6,12,14,20,21,24,25,33,35
22500	24	13	1,2,4,5,6,12,14,20,21,24,25,30,33
22500	24	14	1,4,5,6,12,14,19,20,21,24,25,27,30,33
22500	24	15	1,2,4,5,6,9,12,14,19,20,21,25,30,33,34
25000	16	11	1,4,6,12,14,19,20,21,27,30,33
25000	16	12	1,4,6,12,19,20,21,22,27,30,33,34
25000	16	13	1,4,6,10,12,18,19,21,22,27,30,33,34
25000	16	14	1,4,6,10,12,18,19,21,22,27,30,33,34
25000	16	15	1,4,6,10,12,18,19,21,22,27,30,33,34
25000	20	11	1,4,6,12,14,20,21,25,30,33,35
25000	20	12	1,4,6,12,14,19,20,21,25,30,33,35
25000	20	13	1,2,4,6,12,14,19,20,21,25,27,30,33
25000	20	14	1,4,6,12,14,19,20,21,22,25,27,30,33,34
25000	20	15	1,4,6,10,12,14,18,19,20,21,22,27,30,33,34
25000	24	11	1,4,6,12,14,20,21,25,30,33,35
25000	24	12	1,2,4,6,12,14,20,21,25,30,33,35
25000	24	13	1,2,4,6,12,14,19,20,21,25,30,33,35
25000	24	14	1,2,4,6,12,14,19,20,21,25,29,30,33,35
25000	24	15	1,2,4,6,12,14,19,20,21,25,27,30,33,34,35
27500	16	11	1,4,6,12,14,19,20,21,27,30,33
27500	16	12	1,4,6,12,19,20,21,22,27,30,33,34
27500	16	13	1,4,6,10,12,18,19,21,22,27,30,33,34
27500	16	14	1,4,6,10,12,18,19,21,22,27,30,33,34
27500	16	15	1,4,6,10,12,18,19,21,22,27,30,33,34
27500	20	11	1,4,6,12,14,20,21,25,30,33,35
27500	20	12	1,4,6,12,14,19,20,21,25,30,33,35
27500	20	13	1,2,4,6,12,14,19,20,21,25,27,30,33
27500	20	14	1,4,6,12,14,19,20,21,22,25,27,30,33,34
27500	20	15	1,4,6,10,12,14,18,19,20,21,22,27,30,33,34

27500	24	11	1,4,6,12,14,20,21,25,30,33,35
27500	24	12	1,2,4,6,12,14,20,21,25,30,33,35
27500	24	13	1,2,4,6,12,14,19,20,21,25,30,33,35
27500	24	14	1,2,4,6,12,14,19,20,21,25,29,30,33,35
27500	24	15	1,2,4,6,12,14,19,20,21,25,27,30,33,34,35

*Corrective risks: CR, Number of corrective risk: NOCR

The managers should ensure a safe workplace for their employess. This study presents an occupational health and safety approach by using fuzzy logic, multi criteria decision making methods and linear programming. The firms can pay compensation in the result of occupational accident. Firms should make necessary precautions by performing a risk evaluation. This study handles fuzzy logic and multi criteria decision making methods for a risk evalution. This approach can be insufficient due to budget and time constraints of the firm. This paper examines a linear programming for these constraints.

4. Conclusion

Fuzzy extension of AHP has little calculation time and is very simpler than other fuzzy AHP procedures. The weights of O, S and D criteria are calculated by utilizing fuzzy extension of AHP. The failure modes are ranked in uncertain environment by using fuzzy TOPSIS. Classical TOPSIS method uses crisp number in evaluation procedures and this situation can generate information loss in ambiguous environment. Fuzzy TOPSIS method, which uses linguistic variables in uncertain environment, is proposed to overcome this drawback in this paper.
The weights obtained from fuzzy extension of AHP are employed in fuzzy TOPSIS computations and the thirty-five failure modes are ranked for defining the most important failure mode. The suggested model is implemented within a construction firm and shows that it can be efficiently utilized in risk evaluation problem. This paper presented a linear programming due to some limitations of the firm. The most important failure mode is defined the FM4 according to the homogeneous and heterogeneous results of fuzzy TOPSIS. The proposed approach is compared with different approaches. FM4 is selected the most important failure mode according to the results of the handled methods.

Several decision makers participate to evaluate the problem in group decision making so that each decision maker can have the prejudice about the problem. This situation can cause inaccurate solutions and inherently damage to the firm. A group judgment is usually preferred to decrease the siding and to prevent the prejudice in group decision making. Each decision maker can have different judgments about a selection process due to their experience and knowledge. The weights of the decision makers, which depend on characteristics of the decision makers, are important to achieve a group judgment. Inaccurate weights of the decision makers generate the wrong group judgment and inherently damage to the firm. This study proposes an ABAT presented by Olcer and Odabasi [17] to cope with this drawback. The quality and efficiency of the proposed method is considered by helping of a sensitivity analysis and other comparision methods. The results of FMEA can't meet the demands of the firms in long period. This paper proposed a mathematical model to overcome this limitation. This mathematical model is solved in GAMS software program. The presented method needs some experts about risk evaluation area. It takes time and is very difficult. The constraints of linear programming can be insufficient to handle a comprehensive analysis. This paper handles Type 1 fuzzy numbers, which present crisp membership degrees, to define the judgments of decision makers. Interval type-2 fuzzy numbers handles more ambiguity of the real life world. In future paper, interval type 2 fuzzy numbers based multi-criteria decision making methods can be considered for the risk assessment. Furthermore, additional constraints for linear programming can be handled in future papers.

Statement of Research and Publication Ethics

The study is complied with research and publication ethics

References

[1] J.B. Bowles and C.E. Peláez, "Fuzzy logic prioritization of failures in a system failure mode, effects and criticality analysis," *Reliability Engineering & System Safety*, vol. 50, no. 2, pp. 203–213, 1995.

[2] N.R. Sankar and B. S. Prabhu, "Modified approach for prioritization of failures in a system failure mode and effects analysis," *International Journal of Quality & Reliability Management*, vol. 18, no. 3, pp. 324–336, 2001.
[3] B. Efe, M. Kurt and Ö. F. Efe, "An Integrated Intuitionistic Fuzzy Set And Mathematical Programming Approach For An Occupational Health And Safety Policy," *Gazi University Journal of Science*, vol. 30, no. 2, pp. 73-95, 2017.
[4] H. C. Liu, L. Liu and Q. L. Lin, "Fuzzy failure mode and effects analysis using fuzzy evidential reasoning and belief rule-based methodology," *IEEE Transactions on Reliability*, vol. 62, no. 1, pp. 23-36, 2013.
[5] M. Ulu and H. Şahin, "An integrated approach for fire extinguishers selection with DEMATEL and TODIM methods," *Business & Management Studies: An International Journal*, vol. 9, no. 4, pp. 1696-1707, 2021.
[6] T. L. Jee, K. M. Tay and C. P. Lim, "A New Two-Stage Fuzzy Inference System-Based Approach to Prioritize Failures in Failure Mode and Effect Analysis," *IEEE Transactions on Reliability*, vol. 64, no. 3, pp. 869-877, 2015.
[7] B. Efe, M. A. Yerlikaya and Ö. F. Efe, "İş Güvenliğinde Bulanık Promethee Yöntemiyle Hata Türleri ve Etkilerinin Analizi: Bir İnşaat Firmasında Uygulama," *Gümüşhane Üniversitesi Fen Bilimleri Enstitüsü Dergisi*, vol. 6, no. 2, pp. 126-137, 2016.
[8] Q. Zhou and V. V. Thai, "Fuzzy and grey theories in failure mode and effect analysis for tanker equipment failure prediction," *Safety Science*, vol. 83, pp. 74-79, 2016.
[9] H. C. Liu, J. X. You, P. Li and Q. Su, "Failure mode and effect analysis under uncertainty: An integrated multiple criteria decision making approach," *IEEE Transactions on Reliability*, vol. 65, no. 3, pp. 1380-1392, 2016.
[10] O. Mohsen and N. Fereshteh, "An extended VIKOR method based on entropy measure for the failure modes risk assessment – A case study of the geothermal power plant (GPP)," *Safety Science*, vol. 92, pp. 160-172, 2017.
[11] Z. P. Tian, J. Q. Wang and H. Y. Zhang, "An integrated approach for failure mode and effects analysis based on fuzzy best-worst, relative entropy, and VIKOR methods," *App. S. Comp.* vol. 72, pp. 636–646, 2018.
[12] R. Fattahi and M. Khalilzadeh, "Risk evaluation using a novel hybrid method based on FMEA, extended MULTIMOORA, and AHP methods under fuzzy environment," *Saf. Sci.* vol. 102, pp. 290–300, 2018.
[13] B. Efe, "Analysis of operational safety risks in shipbuilding using failure mode and effect analysis approach," *Ocean Engineering*. vol. 187, 106214, 2019.
[14] M. Yazdani, M. R. Abdi, N. Kumar, M. Keshavarz-Ghorabaee and F. T. Chan, "Improved decision model for evaluating risks in construction projects," *J. Cons. Eng. Man.* vol.145, no. 5, 04019024, 2019.
[15] M. Yazdi, A. Nedjati, E. Zarei and R. Abbassi, "A reliable risk analysis approach using an extension of best-worst method based on democratic-autocratic decision-making style," *Journal of Cleaner Production*, vol. *256*, 120418, 2020.
[16] J. Zhu, B. Shuai, G. Li, K. S. Chin and R. Wang, "Failure mode and effect analysis using regret theory and PROMETHEE under linguistic neutrosophic context," *Journal of Loss Prevention in the Process Industries*, 104048, 2020.
[17] A. I. Olcer and A. Y. Odabasi, "A new fuzzy multiple attributive group decision making methodology and its application to propulsion/manoeuvring system selection problem," *European Journal of Operational Research*, vol. 166, pp. 93–114, 2005.
[18] T. L. Saaty, "The analytic hierarchy process," New York: McGraw-Hill, 1980.
[19] D. Y. Chang, "Applications of the extent analysis method on fuzzy AHP," *European Journal of Operational Research*, vol. 95, no. 3, pp. 649–655, 1996.
[20] B. Efe, "An integrated fuzzy multi criteria group decision making approach for ERP system selection," *Applied Soft Computing*, vol. *38*, pp. 106-117, 2016.
[21] K. Shaw, R. Shankar, S. S. Yadav and L. S. Thakur, "Supplier selection using fuzzy AHP and fuzzy multi-objective linear programming for developing low carbon supply chain," *Expert Systems with Applications*, vol. 39, pp. 8182-8192, 2012.
[22] Y. Deng and F. T. S. Chan, "A new fuzzy dempster MCDM method and its application in supplier selection," *Expert Systems with Applications*, vol. 38, no. 8, pp. 9854–9861, 2011.

[23] J. J. Wang and D. L. Yang, "Using a hybrid multi-criteria decision aid method for information systems outsourcing," *Computers & Operations Research*, vol. 34, no. 12, pp. 3691 – 3700, 2007.
[24] Z. Xu, "An automatic approach to reaching consensus in multiple attribute group decision making," *Computers & Industrial Engineering*, vol. 56, pp. 1369–1374, 2009.
[25] S. M. Chen, "Aggregating fuzzy opinions in the group decision-making environment," *Cybernetics and Systems*, vol. 29, pp. 363–376, 1998.
[26] C. L. Hwang and K. Yoon, "Multiple attributes decision making methods and applications," Berlin: Springer, 1981.
[27] F. R. L. Junior and L. Osiro L. C. R. Carpinetti "A comparison between Fuzzy AHP and Fuzzy TOPSIS methods to supplier selection," *Applied Soft Computing*, vol. 21, pp. 194–209, 2014.
[28] K. Dhalmahapatra, A. Garg, K. Singh, N. F. Xavier and J. Maiti, "An integrated RFUCOM–RTOPSIS approach for failure modes and effects analysis: A case of manufacturing industry," *Reliability Engineering & System Safety*, 108333, 2022.

Bitlis Eren Üniversitesi Fen Bilimleri Dergisi
BİTLİS EREN UNIVERSITY JOURNAL OF SCIENCE
ISSN: 2147-3129/e-ISSN: 2147-3188
VOLUME: 11 NO: 2 PAGE: 694-705 YEAR: 2022
DOI: 10.17798/bitlisfen.1094003

Progressive Collapse Response of Reinforced Concrete Buildings Designed According to Turkish Earthquake Code

Aydın DEMİR[1*]

[1]*Department of Civil Engineering, Faculty of Engineering, Sakarya University, 54050, Sakarya, Turkey*
(ORCID: 0000-0001-8797-5078)

Keywords: Progressive collapse, Nonlinear dynamic analysis, Reinforced concrete, Government buildings occupancy class, Turkish earthquake code.

Abstract
In this study, the progressive collapse response of reinforced concrete buildings designed for the 'government buildings' occupancy class was investigated numerically. For this purpose, two reinforced concrete framed buildings were initially designed according to the Turkish Earthquake Code published in 2018. Later, those buildings' progressive collapse responses were evaluated using the Alternate Path direct design approach defined in the GSA-2016 and UFC 4-023-03 guidelines. Three different column removal scenarios were employed independently by applying the nonlinear dynamic analysis method. Nonlinear fiber hinges were used to simulate the plasticity of the structural load-bearing members. As a result of this study, it is deduced that a limited local collapse disproportioned to the initial failure was observed on the investigated buildings. In addition to the conventional seismic design methods, the buildings designed according to the Turkish Earthquake Code should also be assessed with respect to the explicit design approaches against unforeseeable extreme events to reduce their progressive collapse risk.

1. Introduction

Structures may be expose to unforeseeable events such as accidents, deliberate attacks, misuse, etc., in their service lives. They may lose some of their load-bearing members during such circumstances. For example, a car accident hitting a building or a bomb explosion due to terrorist attacks may result in severe damage and the loss of some structural elements. Because these events are generally not considered in the design process, they might lead to dramatic human casualties and economic losses. Several dramatic events have been experienced in Turkey and worldwide, specifically due to terrorist attacks targeting government buildings due to their significance [1], [2]. For example, the bombing of the Alfred P. Murrah Federal Building in Oklahoma City in 1995 was the deadliest act of terrorism in US history, resulting in 168 casualties and several hundred more injured [3]. Moreover, a terrorist attack that targeted Elazig Police Headquarters in 2016 led to the martyrization of 3 police officers and the injury of 217 people [4]. The buildings exposed to these events were severely damaged as well (Fig. 1).

An initial local failure caused by an extreme event may propagate from structural member to member and eventually might disproportionately collapse a large part of a structure or entirely. This phenomenon is called progressive collapse (PC) of structures [5]. There are quite a few direct design methods to evaluate the progressive collapse resistance of structures. The guidelines released by the US General Service Administration (GSA-2016) [6] and the US Department of Defense (UFC 4-023-03) [7] implement the direct design approaches to evaluate the PC response of new and existing government and military buildings. In these methods, the progressive collapse response of structures is evaluated by simulation of a column loss scenario in the different locations on the structure [8].

*Corresponding author: aydindemir@sakarya.edu.tr
Received: 27.03.2022, Accepted: 12.05.2022

a) Alfred P. Murrah Federal Building [3] b) Elazig Police Headquarters [4]

Figure 1. Examples of the building damage after explosions

On the other hand, conventional design codes such as Eurocode 2 [9], ASCE/SEI 7-16 [5], IBC [10], etc., do not give specific design criteria to reduce the risk of progressive collapse. Instead, they implement indirect design approaches that aim to improve the robustness of structures by providing sufficient strength, ductility, redundancy, etc. Moreover, it is a fact that proper seismic detailing as prescribed in current seismic design codes improves the resistance of structures against PC. However, it should be noted that since progressive collapse is not considered and evaluated explicitly, the PC risk of those buildings will never be abolished. Thus, special attention is still needed to design against extreme events [11]–[13].

In the literature, Tsai and Lin [11] observed the effect of the seismic design on the PC resistance of reinforced concrete (RC) structures subjected to a column failure. That behavior was also investigated by Marchis et al. [12] on the mid-rise and by Sheikh et al. [13] on the RC framed structures. Abdulsalam and Chaudhary [14] evaluated the progressive collapse of RC buildings by defining flexure-axial-shear interaction in plastic hinges. Marchis and Botez [15] researched the effect of the number of stories on the collapse resistance of RC frames.

Turkey also has one of the most modern seismic design codes. It frequently updates its seismic code depending on recent scientific advances due to being in an earthquake-prone zone [2]. However, it also has no special explicit design or evaluation methods against PC of structures built in the country. The last update of the Turkish Earthquake Code was released in 2018 (TEC2018) [16]. Like its contemporaries, it is expected to improve the structural integrity during an extreme event by providing sufficient structural robustness. Because it also does not include any explicit design prescriptions to reduce the risk of progressive collapse, the response of the buildings designed according to TEC2018 [16] should be investigated to observe their performance under any extreme event. The studies in the literature for this objective are very scarce, specifically for RC buildings. Mahad [17] investigated the global collapse response of 2-dimensional RC structures under blast loads. For that reason, in the present study, the progressive collapse response of RC buildings designed according to TEC2018 [16] was investigated numerically. The occupancy class of the buildings was selected as 'government buildings' due to their inherent high risk against extreme events.

Furthermore, several studies in the literature have investigated the seismic response of RC buildings designed according to TEC2018 [16]. Firstly, Nemutlu and Sari [18] designed two RC buildings, including different structural load-bearing systems, with respect to TEC2018 [16], ASCE/SEI 7-16 [5], and IBC [10]. Later, they evaluated the analysis results comparatively to determine the differences and causes between TEC2018 [16] and those international design codes. They determined that the base shears calculated from TEC2018 [16] are significantly higher than those obtained by international design codes. Aksoylu and Arslan [19] evaluated the empirical period calculation method of TEC2018 for RC buildings. They compared the results with the Rayleigh period formula on 2-5 story RC frame and shear wall dwellings and school buildings under different soil conditions. As a result of the study, it was suggested that the empirical formula proposed for building height classes (BHC) 6-7-8 should be re-evaluated since it yields to different shear forces for buildings having the given BHC. Similarly, Aksoylu and Arslan [20] investigated different seismic load calculation techniques defined in the 2007 and 2018 updates of the Turkish Earthquake Code for RC buildings. For this purpose, linear elastic analyses were conducted

on 3-4-5-story frame and shear wall RC buildings. It was concluded that TEC2018 increases story displacements and natural periods, and decreases base shear forces due to the new cracked section stiffness implementation.

Moreover, Isik and Demirkiran [21] observed the performance of RC structures under different ground motion levels. Four different earthquake motion levels were considered for the buildings located in four different cities under various earthquake hazards with varying probabilities of exceedance. It was deduced that the target top displacements expected from the structures were significantly changed. Lastly, the pre and post-seismic performance of RC buildings was investigated by Isik et al. [22] and Nemutlu et al. [23], respectively. The former authors performed an earthquake hazard analysis of the Eastern Anatolian Region of Turkey using a performance-based seismic evaluation approach. The latter authors investigated the structural damage that occurred on RC and masonry structures after the Elazig-Sivrice earthquake (Jan. 24, 2020). Several structural deficiencies, such as short columns, low concrete strength, strong beam-weak column mechanism, non-ductile detailing, etc., were determined on the buildings.

This study investigated numerically the progressive collapse response of RC buildings designed for the 'government buildings' occupancy class. For this purpose, two RC framed buildings were initially designed according to TEC2018 [16] by using ProtaStructures [24], which is a specialized structural engineering finite element (FE) software for the design of RC structures. Later, the progressive collapse response of those buildings was evaluated using one of the direct design approaches defined in the GSA-2016 [6] and UFC 4-023-03 [7] guidelines. Three different column removal scenarios were employed independently by applying the Nonlinear Dynamic Analysis Method of the Alternate Path direct design approach. Nonlinear fiber hinges were used to simulate the plasticity of the structural load-bearing members. Moreover, progressive collapse analyses of the buildings were conducted using SAP2000 [25], a commercial FE software for static and dynamic analysis of structures. As a result, it is deduced that a limited local collapse disproportioned to the initial failure was observed on the investigated buildings.

2. Properties of the Designed Buildings

A prototype symmetric building plan was created for the analyses, as depicted in Fig. 2. Two different building heights were selected as 10.5 m (3-story) and 24.5 m (7-story). The elevation view of the 7-story building is illustrated in Fig. 2 as well. The 'government buildings' occupancy class was selected for the buildings. They were assumed to be located in a medium soil condition. The dead, live, and snow loads on the buildings were calculated according to TS 498 [26]. The parameters used for the design of buildings according to TEC2018 [16] are reported in Table 1. Moreover, the horizontal elastic design spectrum used in the seismic analyses is shown in Fig. 3.

The compressive strength of concrete is 30 MPa (C30), and the tensile strength of reinforcing steel is 420 MPa (B420C). The columns have a square

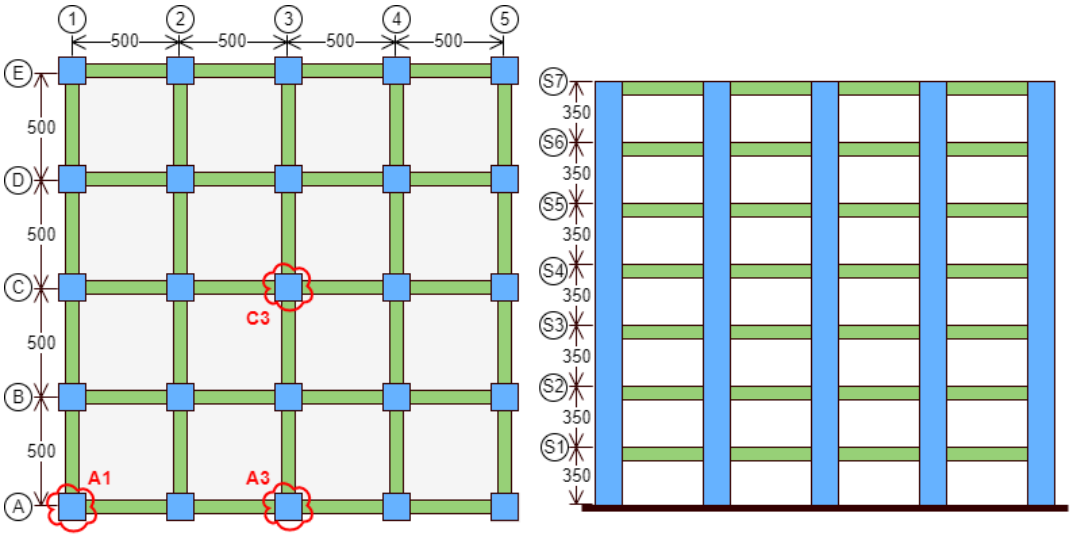

Figure 2. Plan (left) and elevation (right) views of the buildings (dimensions in cm)

section (*A*: section dimension), while the beams have a rectangular section area (*B*: section width and *H*: section height). The geometrical and reinforcing details of the members were kept constant and are reported in Tables 2 and 3. In the tables, ϕ shows the reinforcement diameter in mm, and *s* represents stirrup spacing. Moreover, typical drawings of columns and beams are illustrated in Fig. 4. The buildings were designed according to the requirements of both TEC2018 [16] and TS 500 [27]. A structural engineering finite element software, ProtaStructures [24], specialized in designing RC structures, was used to design the buildings.

Table 1. Design parameters of the buildings

Parameter		Value
Soil class	:	ZC
Soil shear velocity (m/s)	:	500
Building usage class	:	1
Building height class (for 3 & 7-Story)	:	8 & 6
Seismic design class	:	3a
Ductility level	:	High
Earthquake Ground Motion Level	:	DD-2
Design spectral response acceleration parameter at short periods (S_{DS})	:	0.413
Design spectral response acceleration parameter at the 1.0 s period (S_{D1})	:	0.114
Response modification coefficient (R)	:	8
Overstrength coefficient (D)	:	3

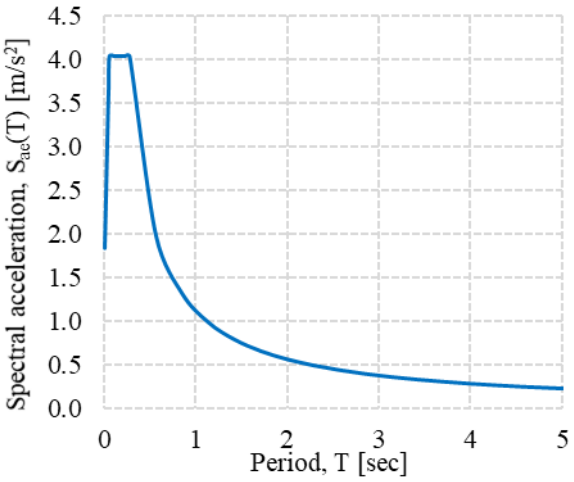

Figure 3. The horizontal elastic design spectrum

On the other hand, GSA-2016 [6] and UFC 4-023-03 [7] standards specify design recommendations to decrease the potential of PC for new and existing governmental structures that may be exposed to localized structural damage due to unforeseeable extreme events. They aim to limit the propagation of the initial damage by providing a robust and balanced structural system. All three or more-story governmental buildings must comply with these guidelines. The standards apply a threat-independent approach without explicitly considering the cause of the initial event. Three direct design approaches are employed in UFC 4-023-03 [7]: Alternate Path, Enhanced Local Resistance, and Tie Forces. However, GSA-2016 [6] uses only the Alternate Path (AP) design approach. The AP approach is common to both guidelines, and vertical structural members are notionally and independently removed at specific plan and elevation locations. It also requires that the building can bridge over that removed element. Moreover, three analysis methods are employed in the AP approach: Linear Static (LS), Nonlinear Static (NS), and Nonlinear Dynamic (ND). While there are some geometric irregularity limitations in LS and NS methods, ND can be used for buildings with irregularity [6], [7].

Table 2. Geometrical and reinforcing details of the column sections

Designed Building	*A* [cm]	Longitudinal Bars	Stirrups & Ties	# of Ties	*s* [cm]
3-story	35	8ϕ16	ϕ8	1	8
7-story	50	8ϕ20	ϕ8	1	8

Table 3. Geometrical and reinforcing details of the beam sections

Designed Building	*B* [cm]	*H* [cm]	Top bars	Bottom Bars	Stirrups	*s* [cm]
3-story	25	40	4ϕ18	3ϕ16	ϕ8	10
7-story	25	50	5ϕ14	3ϕ14	ϕ8	11

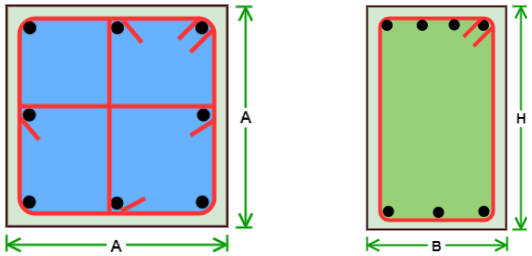

Figure 4. Typical column (left) and beam (right) sections

Additionally, primary and secondary components must be determined in the building before the analysis. The acceptance criteria for the primary members are calculated according to the given prescriptions in the guidelines, which generally refer to the acceptance criteria defined in ASCE/SEI 41-13 [28]. Afterward, locations of the removed load-bearing elements are determined as described in the guidelines: external columns at the corner of the building, near the middle of the short side and the long side, and some internal columns. Moreover, the columns at locations where the building plan

geometry changes significantly must be removed. Ultimately, the structural components of the building must not exceed the calculated acceptance criteria. If the analysis predicts these acceptance criteria are not satisfied, the building does not meet the progressive collapse requirements and must be re-designed or retrofitted to eliminate the nonconforming elements [6], [7]. The general outline of the procedure to evaluate the PC response of structures prescribed in the GSA-2016 [6] and UFC 4-023-03 [7] guidelines is summarized in Fig. 5. Further details can be found in the relevant standards.

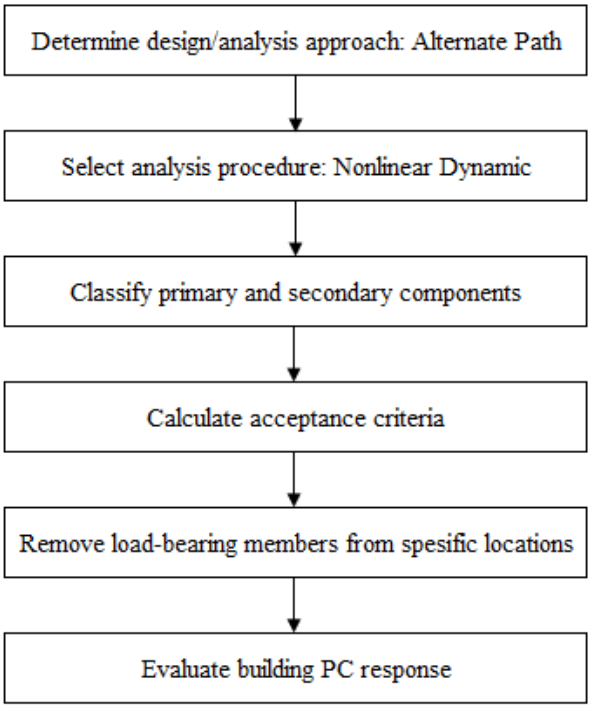

Figure 5. Analysis procedure to evaluate progressive collapse response of structures

3. Numerical Modeling of the Buildings for Progressive Collapse Analysis

The nonlinear dynamic analysis method of the Alternate Path direct design approach according to both GSA-2016 [6] and UFC 4-023-03 [7] guidelines was used for the progressive collapse evaluation of the designed buildings. A three-dimensional finite element (FE) model was created (Fig. 6) in SAP2000 [25], which is a static and dynamic FE analysis software for structures. Beams and columns were modeled using frame elements. Instead of modeling the slabs, a rigid diaphragm was assigned at every story level. The loads on the slabs were distributed and assigned to surrounding beam elements.

There are two main modeling approaches to simulate the post-yield inelastic behavior of the structural load-bearing members: concentrated (lamped) and distributed plasticity models (Fig. 7). It is assumed in the lamped plasticity model (Figs. 7a and 7b) that the deformation beyond the elastic limit occurs only in discrete locations, and the remaining part of the member stays elastic. Inelastic behavior is obtained by integrating plastic strain and curvature occurring in a predefined hinge length. Nevertheless, in a distributed plasticity model, a member's cross-section is discretized into a series of representative axial fibers extending throughout the element or along with a finite length hinge zone (fiber hinge) (Figs. 7c, 7d, and 7e). A stress-strain relationship needs to be defined for each fiber. Ultimately, axial force-deformation and biaxial moment-rotation relationships are obtained by integrating the behavior over the section and multiplying by the hinge length [29]-[31]. On the other hand, it is a fact that RC frame structures can resist the disproportionate collapse by developing two critical load-resisting mechanisms on their members: Vierendeel (arching) Action and Catenary Action. While fiber elements can successfully capture those mechanisms in addition to the flexural behavior of frame members, those features are neglected in the conventional concentrated plastic hinge approach [12], [29], [32]. Because of that reason, in this study, the nonlinear behavior of the structural load-bearing members was simulated using nonlinear fiber hinges, which are one of the methods of distributed plasticity approach (Fig. 7(c)).

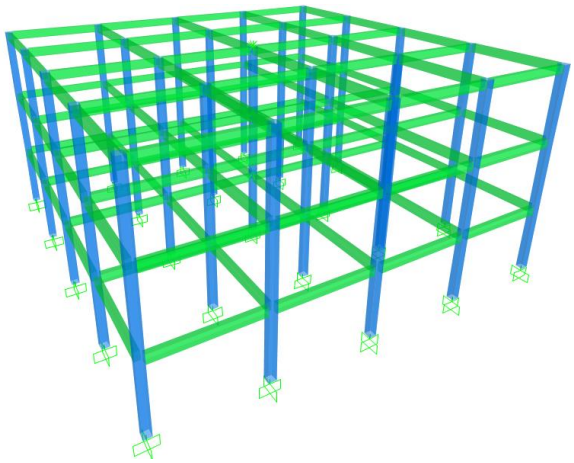

Figure 6. FE model of the 3-story building

The sections were first discretized with an optimum fiber layout to implement fiber sections in SAP2000. The program automatically assigned the fibers to the center of every reinforcement, and confined and unconfined concrete which were

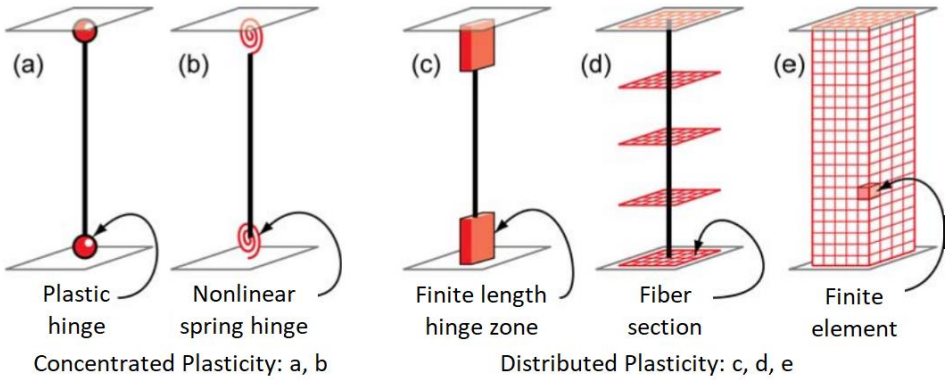

Figure 7. Nonlinear beam-column element models [29]

meshed into several square or rectangular areas. Later, the material properties of both concrete and reinforcing bars were assigned to the relevant fibers. Finally, the fiber hinges were defined at both ends of the beams and columns in a finite length hinge zone as half the section depth [16]. Moreover, the constitutive material models of both concrete and reinforcing steel were created following the material models given in TEC2018 [16].

A nonlinear static analysis case was defined first for the gravity loads combined with Eq. 1 as given in UFC 4-023-03 [7]. DL represents Dead Load, LL stands for Live Load, and S is Snow Load in the equation. That load case was used to obtain the forces present at equilibrium in each removed column. It was also considered the starting condition for the column removal analysis case. Later, the column member was omitted in the structural model, and the equivalent column loadings were applied to the node above the removed column end as a new load case. This model case simulates the condition in which the removed column exists on the building. Afterward, a new load pattern was created to include the equivalent removed column loadings with the opposite signs to simulate the column removal procedure. As depicted in Fig. 8, a ramp function was defined to apply this load pattern incrementally to the same joint above the removed column to abolish the equivalent column loadings by a nonlinear dynamic time-history load case [6], [7].

$$1.2DL + 0.5LL + 0.2S \quad (1)$$

Moreover, the ramp function's column removal duration was considered less than one-tenth of the building's fundamental response period, as suggested by UFC 4-023-03 [7] (Fig. 8). Therefore, it was taken as 0.10 s for the 3-story and 0.15 s for the 7-story building since the fundamental period of the buildings was obtained as 1.04 s and 1.56 s, respectively. The column removal was conducted on the 0.5th second after equilibrium was reached for the gravity analysis. The total duration of the removal was set to 3 seconds to see the residual vertical displacement after damping the oscillation. The Direct Integration solution algorithm was used for the nonlinear dynamic time-history load case. A Rayleigh damping with 5 % was defined depending on the buildings' fundamental first and second periods. Newmark time integration method was employed for the analysis, and its Gamma and Beta coefficients were taken as 0.50 and 0.25, respectively. Lastly, P-Delta and Large Displacements options were activated in the program to consider the geometric nonlinearity of the members and catenary behavior on the surrounding beams due to column removal [30], [33].

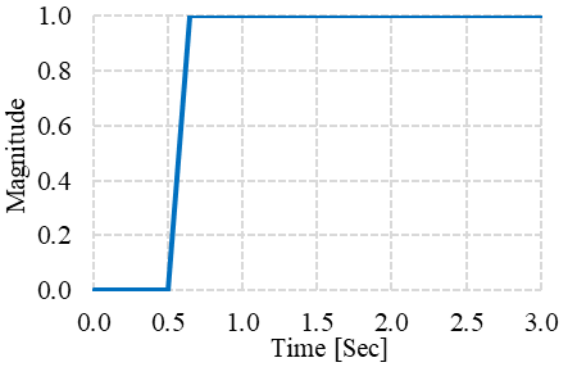

Figure 8. The defined ramp function for the 7-story building to simulate column removal

Three column removal scenarios on the first story of the buildings were implemented as suggested by GSA-2016 [6] and UFC 4-023-03 [7]. The simulations of one exterior corner column (A1), one column in the middle of an outermost axis (A3), and one column at the center of the building (C3) were conducted independently to investigate the progressive collapse response of the structures. The locations of the removed columns are shown in Fig. 2.

The acceptance criteria for the damage states of the RC members were determined according to TEC2018 [16] depending on the strain measured both in concrete and longitudinal reinforcement. Three different damage limits are prescribed in the code: Limited Damage (LD), Moderate Damage (MD), and Severe Damage (SD). The Severe Damage strain limit for concrete is defined in TEC2018 [16] as given in the following equation (Eq. 2):

$$0.0035 + 0.04\sqrt{\omega_{we}} \leq 0.018 \quad (2)$$

where, ω_{we} is the mechanical reinforcement ratio of effective confinement bars, and it can be calculated as follows (Eq. 3):

$$\omega_{we} = \alpha_{se}\rho_{sh,min}\frac{f_{ywe}}{f_{ce}} \quad (3)$$

where, α_{se} represents the efficiency coefficient of confinement reinforcement and $\rho_{sh,min}$ shows the minimum of the volumetric confinement reinforcement ratio of the section in both lateral directions. Moreover, f_{ywe} and f_{ce} are the expected tensile yield strength of lateral reinforcement, and compressive strength of concrete, respectively. The Severe Damage strain limit for reinforcing steel is defined in TEC2018 [16] as $0.4\varepsilon_{su}$, where ε_{su} is the ultimate tensile strain of reinforcement that is 0.08 for the B420C reinforcing steel. Moreover, the Moderate Damage strain limits for both concrete and reinforcing steel can be calculated by taking 75 % of the Severe Damage strain limits. Lastly, the Limited Damage strain limit is constant for both concrete and reinforcing steel as 0.0025 and 0.0075, respectively. The calculated damage state limits of the members were defined in the sections' material model and reported in Table 4.

4. Results and Discussion

The vertical displacement time-history results of the nodes above the removed columns are depicted in Fig. 9 for different column loss scenarios. The residual vertical displacement (u_r) result of those nodes is reported in Table 5. The residual displacements experienced due to the corner column (A1) loss scenario were obtained as -36.5 mm and -18.3 mm for the 3-story and 7-story buildings, respectively. It was determined that u_r is higher for the 3-story building than for the 7-story structure (Fig. 9a). Similar behavior was observed for the middle edge column removal (A3), and u_r was obtained as -57.0 mm and -23.6 mm in this scenario (Fig. 9b). It is a fact that more beams participate in load transfer from the removed column to surrounding members through Vierendeel and Catenary Actions while the number of the stories of the buildings increases. Moreover, the most severe damage case was experienced due to removing the middle column on the inner axis (C3). The residual vertical displacement increased dramatically as the number of floors decreased. The residual displacement of the 7-story building was obtained as -38.6 mm while u_r of the node above the removed columns did not stop at any point. As a result, the members above and surrounding the removed column collapsed (Fig. 9c).

The damage response of the load-bearing members was assessed according to the acceptance criteria calculated in the previous section. The fiber hinge occurrence schemes of the members are depicted in Figs. 10 and 11. Since the buildings are symmetric in their plans and the results are the same for the perpendicular axis, only elevation views of the axis on which the removed column exists are shown. The beams bridging over the removed column had limited and moderate damage at their ends upon removing the corner column A1 from the 3-story building (Fig. 10a). No damage occurred to the surrounding columns. When column A3 was removed from the building, most of the beams in the vicinity of the removed column experienced moderate damage at their hinge locations. Moreover, limited damage occurred on the surrounding top story columns' upper ends (Fig. 10b). The removal of the inner axis column C3 led to a dramatic increase in the vertical displacement of the surrounding members. They failed due to the exceedance of their load-carrying

Table 4. Acceptance criteria for the structural members

Analyzed Building	Section Type	Concrete Strain			Reinforcement Strain		
		LD	MD	SD	LD	MD	SD
3-story	Column	-0.0025	-0.0089	-0.0119	0.0075	0.0240	0.0320
	Beam	-0.0025	-0.0052	-0.0069	0.0075	0.0240	0.0320
7-story	Column	-0.0025	-0.0080	-0.0106	0.0075	0.0240	0.0320
	Beam	-0.0025	-0.0041	-0.0055	0.0075	0.0240	0.0320

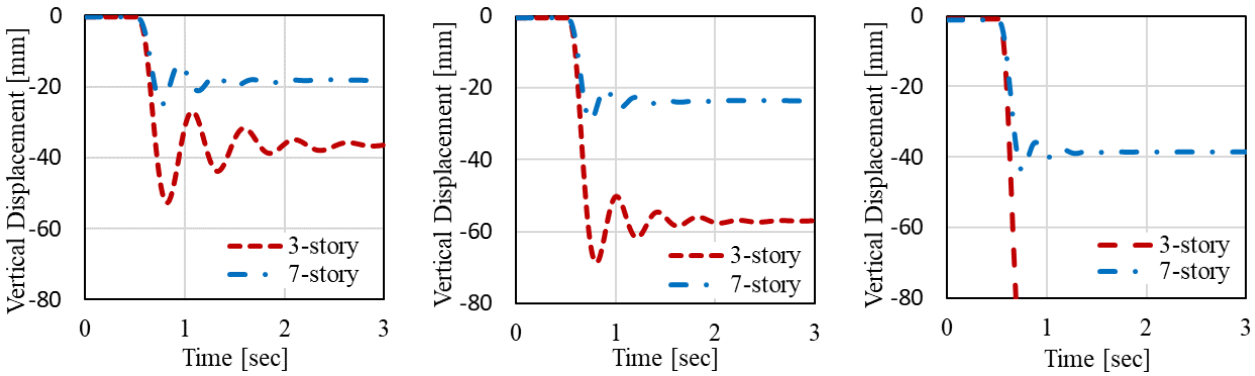

a) Removal of column A1 b) Removal of column A3 c) Removal of column C3

Figure 9. The vertical displacement time-history of the node above the removed column

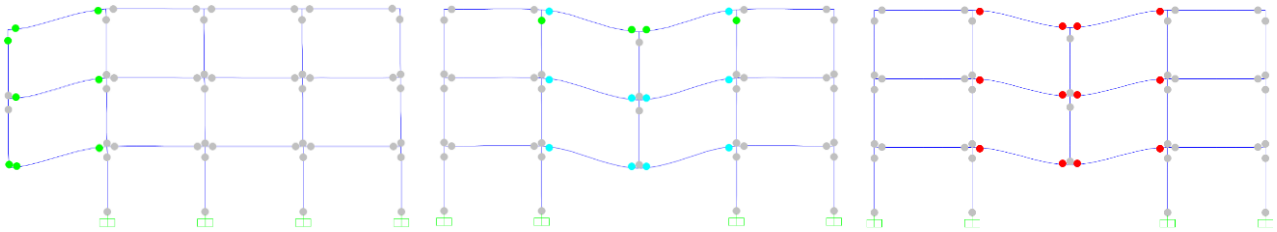

a) Removal of column A1 b) Removal of column A3 c) Removal of column C3

Figure 10. Fiber hinge damage results of the 3-story building*

*Gray: no damage, green: limited damage, cyan: moderate damage, pink: severe damage (collapse prevention), red: failure (collapse).

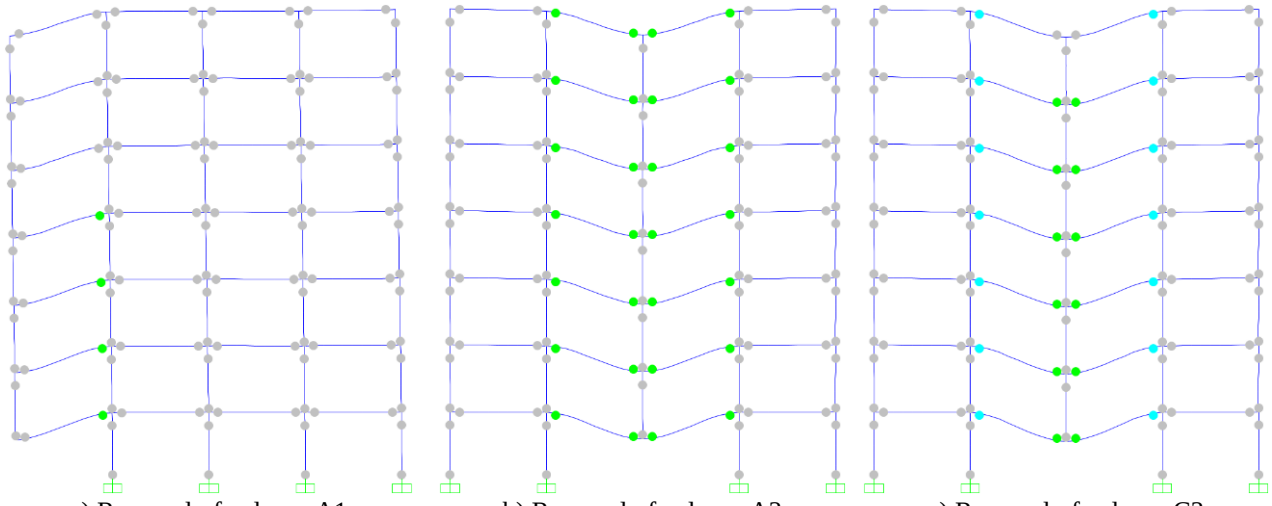

a) Removal of column A1 b) Removal of column A3 c) Removal of column C3

Figure 11. Fiber hinge damage results of the 7-story building*

*Gray: no damage, green: limited damage, cyan: moderate damage, pink: severe damage (collapse prevention), red: failure (collapse).

capacities. Ultimately, a local collapse happened on the 3-story building (Fig. 10c).

After removing the corner column A1 from the 7-story building, no significant damage was observed on the members other than limited damage that occurred only on the lower-story beam-ends joining the surrounding columns (Fig. 11a). Limited damage was experienced at both ends of beams bridging over the removed column upon removing the middle column of the outer edge axis (A3) (Fig. 11b). Lastly, when the inner axis column C3 was removed from the building, the surrounding beams experienced

limited damage at their ends above the removed column and moderate damage at their other ends connecting to the surrounding columns (Fig. 11c). Any local collapse was not observed on the 7-story building under all column removal scenarios.

The buildings experienced different damage states on their load-bearing members after losing one of their columns on their first floors. The damage was localized specifically on the members directly interacting with the removed column. The building plans showing the experienced damage zones are depicted in Fig. 12. The most severe damage occurred in the inner column loss scenario. The most likely reasons for that behavior are: i) the loads needed to be transferred to the surrounding structural members become high on the beams bridging over the removed column since the inner axis columns have a larger tributary loading area, ii) gravity loads become conservative for the outer axis columns due to having lower tributary loading areas since the same geometry and reinforcing details were considered for all inner and outer axis' columns. Nonetheless, if a more precise design were to be performed for the outer axis columns, a probable decrease in column geometry and reinforcing detail would lead to severe damage and failure on the members on those axes as well. A local collapse was observed only in the 3-story building in the case of inner column loss. No general collapse happened on any building for any column removal scenario.

Table 5. Result of the residual vertical displacement value of the node above the removed column

Analyzed Building	Removed Column	u_r [mm]
3-story	A1	-36.5
	A3	-57.0
	C3	collapse
7-story	A1	-18.3
	A3	-23.6
	C3	-38.6

Consequently, it can be deduced that the progressive collapse risk of buildings designed according to TEC2018 [16] with 'government buildings' occupancy class is high specifically due to an inner column loss. An unforeseeable initial failure may propagate to the surrounding members and lead to a disproportionate local collapse. Moreover, since there was no irregularity in the investigated buildings, it should be noted that the existence of any irregularity on a structure might further reduce its progressive collapse resistance. Therefore, in addition to the conventional seismic design methods, government buildings should also be designed according to the explicit design approaches against extreme events to reduce their PC risk. Moreover, the progressive collapse response of existing government buildings should also be evaluated accordingly.

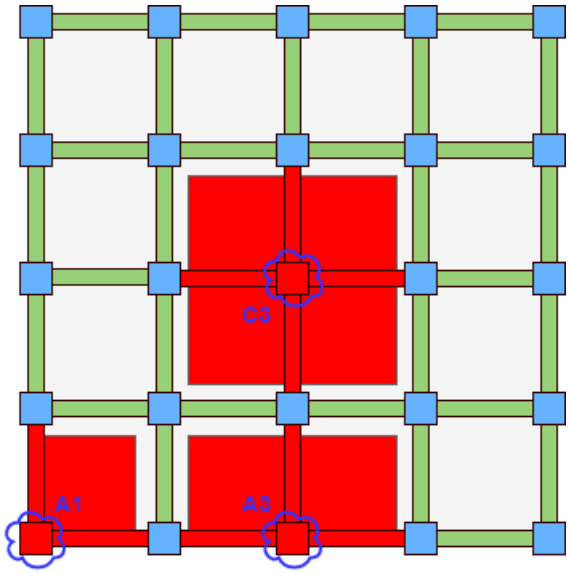

Figure 12. The experienced damage and collapse regions after a column loss

5. Conclusion and Suggestions

The objective of this study is to investigate the progressive collapse response of RC frame buildings designed according to TEC2018 [16] for the 'government buildings' occupancy class. For this purpose, one of the direct design approaches of GSA-2016 [6] and UFC 4-023-03 [7] guidelines was implemented by using the Nonlinear Dynamic Analysis Method of the Alternate Path design approach. Nonlinear fiber hinges were used to simulate the plasticity of the structural load-bearing members. The following conclusions were deduced:

- The residual vertical displacement of the node above the removed column decreases as the number of stories of the buildings increases under all column loss scenarios.
- The damage to the structural members after a column removal was localized on the members surrounding the removed column. The damage was not distributed to other members of the building. Thus, a total collapse was not observed.
- The inner column loss scenario leads to the most severe damage case for the buildings. Moreover, the damage experienced on the buildings increases while the story number decreases for all column loss scenarios.

- In addition to the conventional seismic design procedures, the structures designed for the 'government buildings' occupancy class require additional direct design considerations to improve their progressive collapse resistance against extreme events.

The structural design of the buildings was simplified in the study by generalizing their member sections similar to the common practice to reduce labor and formwork costs, and construction errors. Since corner and side columns connect to fewer load-bearing members to redistribute the loads after a column removal, their PC response could be as severe as the interior column. Therefore, a more precise design could be done for the building to more accurately observe the response of structures subjected to a corner and side column loss scenario. Moreover, the existing buildings designed and constructed before the current TEC2018 [16] may have a higher progressive collapse risk since they were built using prior engineering knowledge. Therefore, special attention should be paid to those buildings' PC resistance under likely dramatic extreme events to prevent casualties and economic losses. For this purpose, new studies can be done on the buildings with different structural systems, loads, soil properties, etc., to be able to assess in a more generalized manner the progressive collapse risk of 'government buildings' occupancy class structures designed to TEC2018 [16] or previous updates of it.

Acknowledgments

The author was supported by the 2219-International Postdoctoral Research Fellowship Program of The Scientific and Technological Research Council of Turkey (TUBITAK). The author also thanks Prof. Dr. Halil Sezen for his exceptional support and guidance.

Statement of Research and Publication Ethics

The study is complied with research and publication ethics

References

[1] B. Sevim and A. T. Toy, "Blasting response of a two-storey RC building under different charge weight of TNT explosives," *Iranian Journal of Science and Technology, Transactions of Civil Engineering*, vol. 44, no. 2, pp. 565-577, Jun 23, 2020, doi: 10.1007/s40996-019-00256-0.

[2] R. A. Oyguç, "Seismic assessment of damaged buildings after 24 January 2020 Elazığ earthquake," (in Turkish), *Bitlis Eren University Journal of Science*, vol. 11, no. 1, pp. 140-155, 2022, doi: 10.17798/bitlisfen.1000615.

[3] "Oklahoma City bombing." fbi.gov. https://www.fbi.gov/history/famous-cases/oklahoma-city-bombing (accessed Feb. 02, 2022).

[4] "Elazığ saldırısını PKK üstlendi." aljazeera.com.tr. http://www.aljazeera.com.tr/haber/elazig-saldirisini-pkk-ustlendi (accessed Feb. 02, 2022).

[5] *Minimum Design Loads and Associated Criteria for Buildings and Other Structures Minimum design loads for buildings and other structures*, ASCE/SEI 7-16, American Society of Civil Engineers, Virginia, 2016.

[6] *Alternate Path Analysis and Design Guidelines for Progressive Collapse Resistance*, GSA-2016, General Services Administration, Washington, DC, 2016.

[7] *Design of building to resist progressive collapse*, UFC 4-023-03, US Department of Defense, Washington, DC, 2016.

[8] O. Yagob, K. Galal, and N. Naumoski, "Progressive collapse of reinforced concrete structures," *Structural Engineering and Mechanics, An Int'l Journal*, vol. 32, no. 6, pp. 771-786, 2009, doi: 10.12989/sem.2009.32.6.771.

[9] *Design of Concrete Structures: Part 1-1: General Rules and Rules for Buildings*, Eurocode 2, *European Committee for Standardization*, Brussels, 2004.

[10] *International Building Code*, IBC, International Code Council, Inc, Washington, DC, 2020.

[11] M. H. Tsai and B. H. Lin, "Investigation of progressive collapse resistance and inelastic response for an earthquake-resistant RC building subjected to column failure," *Engineering Structures*, vol. 30, pp. 3619-3628, 2008, doi: 10.1016/j.engstruct.2008.05.031.

[12] A. G. Marchis, T. S. Moldovan, and A. M. Ioani, "The influence of the seismic design on the progressive collapse resistance of mid-rise RC framed structures," *Acta Technica Napocensis: Civil Engineering & Architecture*, vol. 56, no. 2, pp. 222-234, 2013.

[13] T. A. Sheikh, J. M. Banday, and M. A. Hussain, "Progressive collapse study of seismically designed low rise reinforced concrete framed structure," *Civil Engineering and Architecture*, vol. 9, no. 5, pp. 1327-1338, 2021, doi: 10.13189/cea.2021.090506.

[14] M. A. Abdulsalam and M. T. A. Chaudhary, "Progressive collapse of reinforced concrete buildings considering flexure-axial-shear interaction in plastic hinges," *Cogent Engineering*, vol. 8, no. 1:1882115, 2021, doi: 10.1080/23311916.2021.1882115.

[15] A. G. Marchisa and M. D. Botez, "A numerical assessment of the progressive collapse resistance of RC frames with respect to the number of stories," *Procedia Manufacturing*, vol. 32, pp. 136-143, 2019, doi: 10.1016/j.promfg.2019.02.194.

[16] *Specification for buildings to be built in seismic zones*, TEC2018, Disaster and Emergency Management Presidency, Government of Republic of Turkey, Ankara, 2018.

[17] M. A. A. Mahad, "Global response of 2D reinforced concrete structures under blast loads and progressive collapse," M.S. thesis, Institute of Graduate Studies, Istanbul Kultur University, Istanbul, Turkey, 2021.

[18] Ö. F. Nemutlu and A. Sarı, "Comparison of Turkish earthquake code 2018 and U.S. seismic codes in terms of earthquake calculations," (in Turkish), 5. International Conference on Earthquake Engineering and Seismology, Ankara, 8-11 Oct. 2019.

[19] C. Aksoylu and M. H. Arslan, "Empirical evaluation of periodic calculations for frame+shear wall type of reinforced concrete buildings according to TEC-2019 standard," (in Turkish), *Uludağ University Journal of The Faculty of Engineering*, vol. 24, no. 3, pp. 365-382, 2019, doi: 10.17482/uumfd.603437.

[20] C. Aksoylu and M. H. Arslan, "Comparative investigation of different earthquake load calculation methods for reinforced concrete buildings in the 2007 and 2019 codes," (in Turkish), *International Journal of Engineering Research and Development*, vol. 13, no. 2, pp. 359-374, 2021, doi: 10.29137/umagd.844186.

[21] E. Işık and E. Demirkıran, "The effect of different earthquake ground motion level on performance of reinforced-concrete structures," *Bitlis Eren University Journal of Science and Technology*, vol. 11, no. 2, pp. 29-35, 2021, doi: 10.17678/beuscitech.952812.

[22] E. Işık, E. Harirchian, A. Büyüksaraç, and Y. L. Ekinci, "Seismic and structural analyses of the Eastern Anatolian Region (Turkey) using different probabilities of exceedance," *Applied System Innovation*, vol. 4, no. 4, pp. 89, 2021, doi: 10.3390/asi4040089.

[23] O. F. Nemutlu, B. Balun, and A. Sari, "Damage assessment of buildings after 24 January 2020 Elazığ-Sivrice Earthquake," *Earthquakes and Structures*, vol. 20, no. 3, pp. 325-335, 2021, doi: 10.12989/EAS.2021.20.3.325.

[24] *Structural Engineering Software*. ProtaStructures 2021 Academic Version, Prota Eng. Comp., Besiktas, Istanbul.

[25] *Three-Dimensional Static and Dynamic Finite Element Analysis and Design of Structures*. SAP2000 V23 Academic Version, Computer and Structures, Inc., California.

[26] *Design Loads for Buildings*, TS 498, Turkish Standards Institute, Ankara, 1997.

[27] *Requirements for Design and Construction of Reinforced Concrete Structures*, TS 500, Turkish Standards Institute, Ankara, 2002.

[28] *Seismic Evaluation and Retrofit of Existing Buildings*, ASCE/SEI 41-13, American Society of Civil Engineers, Virginia, 2013.

[29] G. G. Deierlein, A. M. Reinhorn, and M. R. Willford, "NEHRP seismic design technical brief no. 4 - Nonlinear structural analysis for seismic design: A guide for practicing engineers," NIST, Maryland, Rep. 10-917-5, 2010.

[30] Computers and Structures, Inc. *CSI Technical Knowledge Base*. Accessed: Mar. 15, 2022. [Online]. Available: https://wiki.csiamerica.com

[31] R. Y. Wu and C. P. Pantelides, "Concentrated and distributed plasticity models for seismic repair of damaged RC bridge columns," *J. Compos. Constr.*, vol. 22, no. 5:04018044, 2018, doi: 10.1061/(ASCE)CC.1943-5614.0000879.

[32] F. Sadek, Y. Bao, J. A. Main, and H. S. Lew, "Evaluation and Enhancement of Robustness for Reinforced Concrete Buildings," *J. Struct. Eng.*, vol. 148, no. 1:04021248, 2022, doi: 10.1061/(ASCE)ST.1943-541X.0003226.

[33] S. Sagiroglu, "Analytical and experimental evaluation of progressive collapse resistance of reinforced concrete structures," Ph.D. Dissertation, The Department of Civil and Environmental Engineering, Northeastern University, Boston, MA, USA, 2012.

Bitlis Eren Üniversitesi Fen Bilimleri Dergisi
BİTLİS EREN UNIVERSITY JOURNAL OF SCIENCE
ISSN: 2147-3129/e-ISSN: 2147-3188
VOLUME: 11 NO: 2 PAGE: 706-714 YEAR: 2022
DOI: 10.17798/bitlisfen.1094692

Durability Analysis in Seat Components Based on Design Criteria

Hüseyin Sertan BOLU[1], Oktay ÇAVUŞOĞLU[1,2*], Çiğdem DİNDAR[1,2], Hakan AYDIN[1]

[1]*Bursa Uludağ Üniversitesi, Mühendislik Fakültesi, Makine Mühendisliği Bölümü 16059 Nilüfer/Bursa*
[2]*TOFAŞ Ar-Ge, Yeni Yalova Yolu Cad. No:574 Bursa/TÜRKİYE*
(ORCID: 0000-0001-8807-8715) (ORCID: 0000-0002-2826-1814) (ORCID: 0000-0002-4597-906X) (ORCID: 0000-0001-7364-6281)

Keywords: Durability analysis, Dynamic analysis, Crash test, Finite element analysis.

Abstract
In this study, the suitability of the M1 class vehicle rear seat according to the ECE R17 luggage retention regulation has been examined. Strength improvement studies were carried out on the seat corner component. The development studies for the seat design according to the boundary and loading conditions specified by the ECE R17 regulation were created in the finite element method pre-processing software Hyper Mesh and the analysis was carried out in the RADIOSS solver. The design of the seat, which was determined by finite element analysis results, was verified by physical tests.

1. Introduction

Nowadays, stricter emission rules, social awareness created by increasing global warming, and decreasing fossil fuel reserves have been major factors in the automotive industry's preference for lighter vehicles, engines with smaller volumes and fuel consumption. OEMs are trying to reduce their CO_2 emissions by considering these criteria day by day [1]–[4]. When we think of a passenger car, we see that seat is among the components that OEMs focus on in terms of weight. In particular, the provision of light, cheap, comfortable and safe seats by seat manufacturers is of great importance for them to be in the competitive market [5].

In the seat development process, the most important cost is the high number of prototypes and tests produced for physical tests. The use of virtual analyzes [6] to minimize the number of prototypes and repeated tests is one of the most preferred methods [7]. With a finite element model validated by physical testing, faster and less costly design processes can be managed. The vehicle seats; seat, back frame, armrest, headrest, foam and fabric. The safety conditions developed for the vehicle seat are the most important design factors to ensure the durability of the seat and passenger safety rather than the design determining factors such as aesthetics, comfort and lightness [8]–[11].

In the literature, many studies have been reported by researchers and automotive manufacturers. Kangralkar et al. [12] conducted barrier work to reduce the potentially lethal effect of luggage load during a collision. In the study, they made an improvement study on the left support bracket by making a design change on the finite element without the need for the design software with the HyperMorph tool. A more durable design has emerged by reducing the stress values on the improvement bracket. Düvenci et al. [13], in their research, performed ECE R14 seat belt pull analysis on the seat frame for DP600 steel, AA 5754 H22 aluminum alloy, Titanium grade 2 and grade 5 as the seat leg material. According to the results obtained, strength and cost analysis was performed. In here, it was determined that the seat leg made of 5 mm thick AA 5754 H22 material and the seat leg made of 2 mm thick DP 600 material showed strength under ECE R14 seat belt tension regulation forces. While the 2mm DP 600 seat leg weighs 1980 gr, it has been measured that it weighs 1640 gr with 5 mm AA 5754 H22. In addition, he calculated that while 17.17%

*Corresponding author: oktay.cavusoglu@hotmail.com
Received: 30.03.2022, Accepted: 27.05.2022

reduction was achieved with aluminum alloy material, it was 65.72% more costly.

In this study, the finite element analysis model was created in HyperMesh software in the rear seat of a passenger vehicle in accordance with the European standards ECE R17 luggage load collision regulation, and the results were obtained in the RADIOSS open code (explicit) solver. The obtained analysis results were compared with the results in the physical test conditions and verified. Strength improvement work was carried out on the seat corner bracket on the validated finite element model and the test conditions were examined with an aluminum alloy material as an alternative to steel material.

2. Material and Method

2.1. Classification of vehicle seats

Vehicles are classified into certain categories. The M-class seat category defines vehicles with at least 4 wheels that can carry passengers. The N class defines vehicles that have at least 4 wheels and are used to carry loads. In this study, we will analyze the vehicle safety conditions of an M1 class vehicle seat, which can carry a maximum of 8 passengers, excluding the driver's seat. The M1 Class Passenger Car Rear Seat is basically a 40/60 split rear seat; it consists of a back frame, seat, foam and fabric components. Optional headrest and armrest elements are also added.

2.2 Safety Requirements for Vehicle Seats (ECE R17)

In ECE R17 specification, there are many test conditions such as the durability of the backrest, the strength of the headrest, the energy dissipation, the strength of the seat attachment points and the crash resistance of the back luggage load. Within the scope of this study, the specification of the luggage load hitting the rear seat during a frontal collision will be considered for the rear seatback frame. In the luggage crash specification, the effects of the luggage loads on the seat and passenger safety are examined during the frontal impact of the vehicle. Consequences such as baggage loads exceeding the seat and reaching the passenger compartment, rupture of the seat frame, and displacement of the seat beyond a certain value are undesirable. In this specification, a frontal crash test is performed using cube-shaped objects positioned in a certain position and with certain dimensions. The acceleration-time graph of the vehicle is limited to the lower and upper values. For a 40/60 rear seat, 2 cube-shaped objects with a mass of 18 Kg are used. The dimensions of the cubes are 300mm × 300mm × 300mm. The distance between the cubes should be 50 mm. The cubes must be 200 mm behind the backrest. During the test, the acceleration to be applied should be between the curves called the acceleration corridor [14,15].

2.3 Evaluation of Test Results

During testing, the headrests in their highest position, the displacement value must not exceed a vertical plane located 150 mm from the R point. The seat assembly must not exceed 100 mm from the R point of displacement of the seat. There should be no rupture or breaking that will cause injury to the sheet metal or other parts of the seat frame. In addition, luggage loads should remain behind the seat and should not pass into the passenger area.

2.4 Seat Design

The seat model was studied as a solid model in cad design software. To create the finite element model more easily, a middle surface is also created in the sheet metal parts. In this study, a seat designed in accordance with the standards was used.

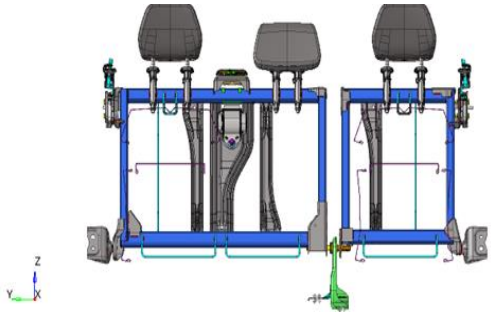

Figure 1. Seat design.

2.5 Seat Finite Element Model

The seat finite element model was created in HyperMesh and HyperCrash software. Sheet metal parts that make up the majority of the skeleton are modeled with shell elements. The shell elements were formed on the middle surface of the three-dimensional part and both surfaces were given depth to be isotropic to half the thickness of the part. The shell element size was determined to be 4 mm on average, taking into account the shortest edge dimensions of the pieces and the time step parameters. The shell model consists of square elements with four nodes and triangular elements with three nodes. The wires in the ridge frame are formed with a one-dimensional beam element. An average element size of 4 mm is taken into account. Diameter information is entered to represent the cylindrical wire geometry.

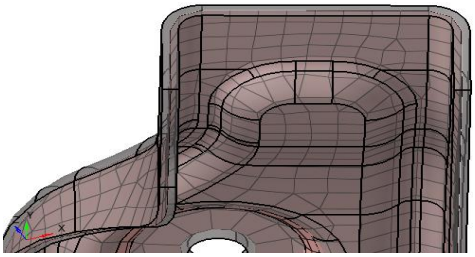

Figure 2. Use of shell elements in sheet metal parts.

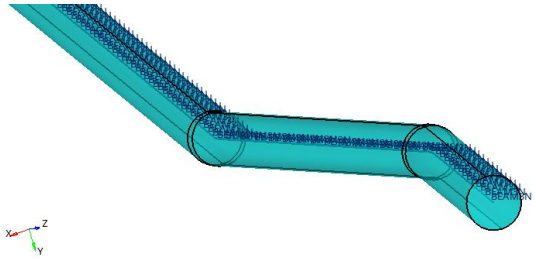

Figure 3. Use of beam elements in wire modeling.

The bolts are modeled in the Radioss solver with spring elements classified as type 13. The most important features of these spring elements are that they can simulate compression, torsion, and buckling behaviors. When the Cartesian coordinate system is taken as reference, there are six freedoms in the X, Y, Z axes, including translational and rotational freedoms. (Dx, Dy, Dx, Rx, Ry, Rz). In this study, all other rotational and translational movements are kept constant except for the rotational freedom in the longitudinal Y axis of the element to represent the bolt behavior. The foam is modeled in three dimensions, consisting of triangular prism elements. The average element size was determined as 15 mm, and attention was paid to ensure that the tetra collapse value, which is one of the element quality parameters, is greater than 0.1.

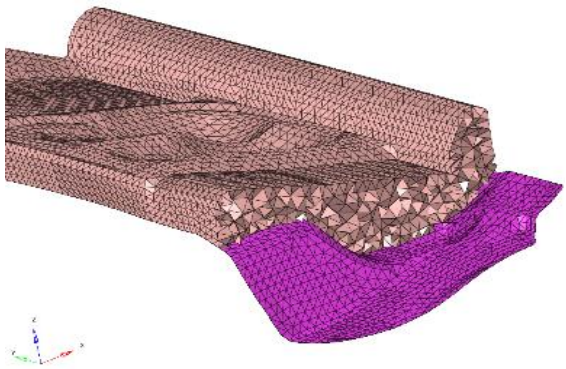

Figure 4. The use of three-dimensional elements in foam modeling.

Welds are modeled with Rbody, which is the rigid element type for arc welding, and arc elements for spot welding using the spot welding tools available in the software.

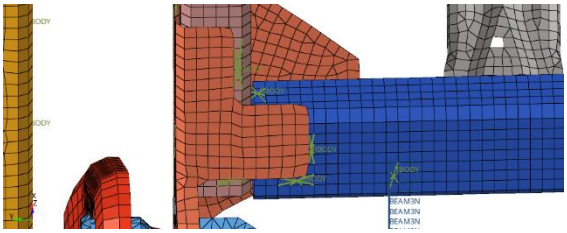

Figure 5. The use of welding modeling.

In addition, to simulate the dummy used in the test, a deformable male dummy weighing approximately 80 kg was used.

2.6 Mechanical Properties

In this study, S420 steel material was chosen for the seat frame profile and brackets. For S420 material definition; Steel density, modulus of elasticity, Poisson's ratio, as well as engineering stress-strain curves obtained from four test specimens drawn at different tensile rates were generated using the necessary formulations for actual stress-strain curves that the software takes into account. The reason for applying the tensile test at different speeds is because the analysis to be done is a dynamic analysis and the material will behave differently at different speeds, so it has been applied to increase the convergence to the physical test results. In this study, it is assumed that the part will begin to rupture after 20% plastic deformation for the S420MC material. Table 1 shows the mechanical properties of material S420MC.

Table 1. Materials Properties of S420MC

Density (kg/mm^3)	Young's Module (Gpa)	Poisson's Ratio	Yield Stress (Mpa)	Elongation (%)
$7.8*10^{-6}$	207	0.3	544	20

Table 2. Materials Properties of AA 6082

Density (kg/mm^3)	Young's Module (Gpa)	Poisson's Ratio	Yield Stress (Mpa)	Elongation (%)
$7.8*10^{-6}$	207	0.3	544	20

Table 3. Type 7 contact identification

Contact	Stiffness Definition	Contact	Minimum Gap	Friction
Node to Surface Multi Usage Contact	K=(Km+Ks)/2	Variable Gap	0.1	0.2

ECE R17 analysis was repeated with AA 6082 material from aluminum alloys for weight reduction [16]. The mechanical properties of the material used and the stress-strain curve are defined. Table 2 shows the mechanical properties of material AA 6082.

To introduce the contact between the components, type 7 and type 11 contacts from Radioss contact types are used. Type 7 is preferred for surface-to-surface contacts and type 11 is preferred for node-surface contacts. The friction coefficient is taken as μ=0.2 for metal-to-metal contacts.

After the seat finite element model is completed, boundary and loading conditions by the specification are applied. The blocks are positioned 200 mm behind the seat and 50 mm apart on a plane that will represent the trunk floor. To provide the floor boundaries moving in the X-direction under test conditions, the X-direction translation is allowed for the seat and vehicle connection points and the trunk floor plane, while translational and rotational movements in other directions are restricted. Gravity has been applied in the –Z direction, affecting the entire structure.

Maximum acceleration of 0.3518 mm⁄ms2 was applied at the 40th millisecond. In terms of speed, it reached a maximum speed of 18.05 mm/ms. Unlike the applied acceleration regulation corridor signal, the frontal impact signal is defined by the model with the mannequin.

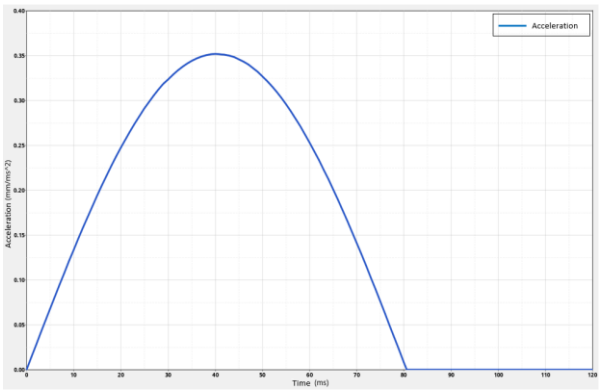

Figure 6. Acceleration curve.

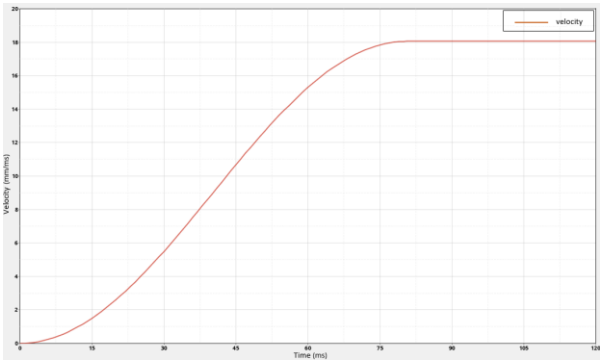

Figure 7. Velocity curve.

After the modeling was completed with the implementation of the regulation conditions, a total of 712059 elements were formed.

3. Result and Discussion

This study was concluded firstly by modeling an M1 class passenger rear seat using the finite element method, then analyzing the created model under ECE R17 baggage retention test conditions and performing the physical test, and finally evaluating the results and determining the most suitable material, thickness and design for the corner bracket.

3.1. Evaluation of the Analysis Results

3.1.1 Examination of Animation

In the model run up to 120 ms; the situation occurred at 120 ms at the initial moment, the behavior at the 85th ms when the maximum displacement occurred, and the spring back behavior that started after 85 ms were observed. When we check visually, it is seen that the blocks do not pass in front of the seats by the regulation conditions.

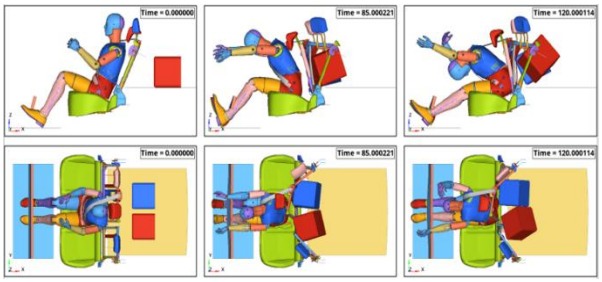

Figure 8. Animation images.

3.1.2 Examination of Plastic Deformation Results

According to the desired output plastic deformation results, it has been seen that the maximum value was 45% on the profile. This value is greater than the initial 20% rupture value we determined, but when the bending behavior of the profile is examined, it is seen that the material is exposed to compression force rather than tensile force. It is foreseen that there will be no rupture on the profile for the compression behavior.

In the inner corner bracket examined within the scope of this study, it was determined that 17.4% of plastic deformation caused by tensile forces remained below the rupture initial limit and would not pose a risk. According to these results, it is interpreted that the seat design provides the regulation conditions and that the physical test can be done.

3.2. Comparison of Analysis Results with Physical Test

As a result of the ECE R17 physical test performed on the proto-type seat frame also analyzed with the finite element produced for design verification, the rupture in the inner corner bracket was observed. However, in the finite element analysis, results were obtained that there would be no risk of rupture. To proceed with different designs, thickness and material studies are required to improve the test results, to eliminate the risk of rupture the inner corner bracket and to find the most suitable solution. To do all these studies on the finite element model before the physical test can be possible provides them can be realized in a shorter time and with less costly. Studies on the finite element model, whose accuracy is not physically ensured, will become meaningless. As a result of these findings, it is necessary to carry out correlation studies between the results of both the analysis and the physical test.

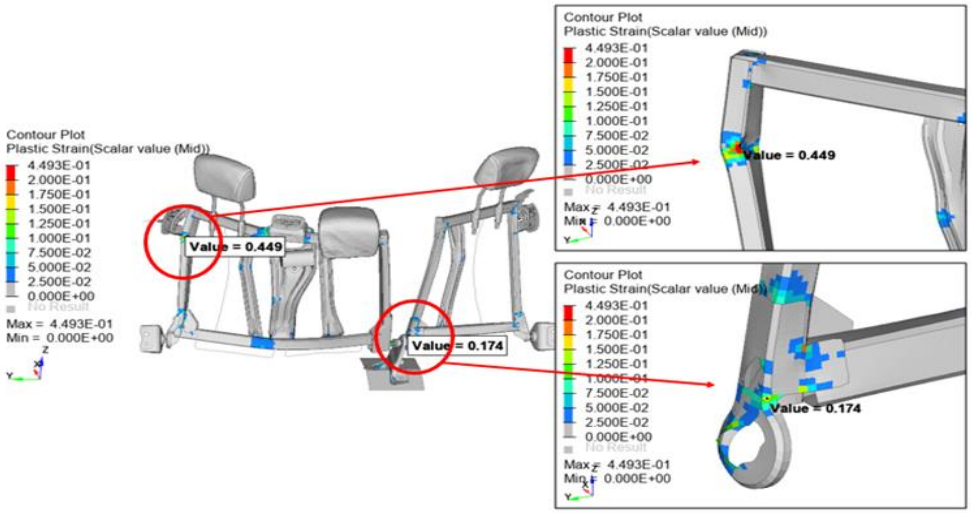

Figure 9. Plastic deformation results.

Figure 10. Rupture in the bracket that occurred during physical testing.

3.3 Increasing the Correlation of the Finite Element Model with the Test

As a result of the research, it was determined that the thickness in the area where the rupture occurred during the forming of the bracket production decreased to 1 mm locally. In line with these findings, local thickness assignment was made in the region where the thickness decreased in the finite element model and the element size was reduced from 4 mm to 2 mm to get more accurate results.

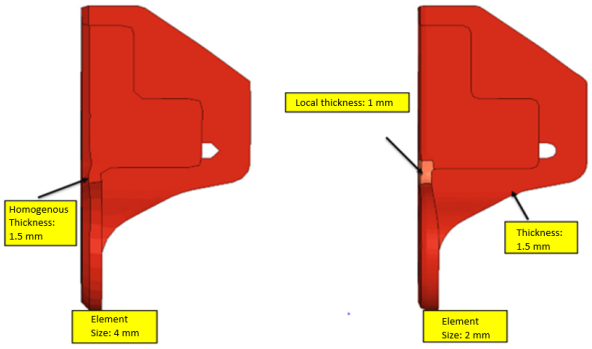

Figure 11. Bracket modeling accuracy definitions.

3.3.1. Comparison of the Analysis Results with the Test after the Thickness Change

According to the results obtained with the local thickness change in the finite element model, plastic deformation was observed at 191%. It has been observed that similar data with the physical test results were obtained from the finite element model, which was performed with a result which was greater than 20%, which we accepted as the beginning of the rupture.

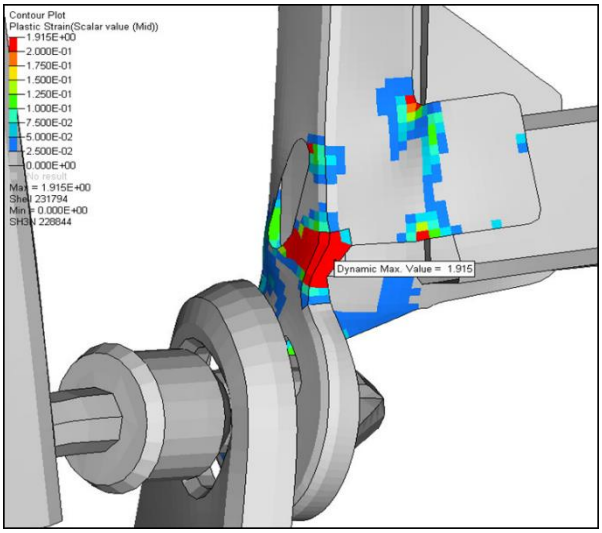

Figure 12. Bracket plastic deformation results

3.4 In case of Increased Bracket Thickness

The analysis was repeated by increasing the thickness of the bracket from 1.5 mm to 2 mm and determining that the local thickness would be 1.5 mm in the relevant region after production. It is aimed to decrease the plastic deformation value by increasing the strength of the bracket with the increase in thickness.

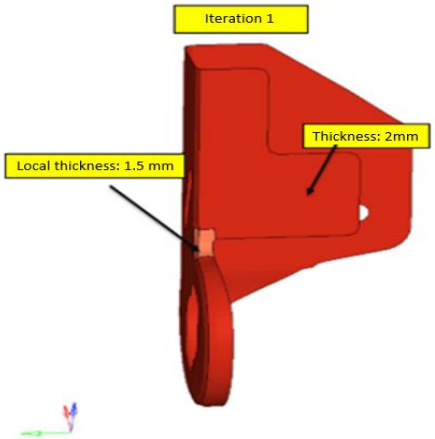

Figure 13. First iteration design change.

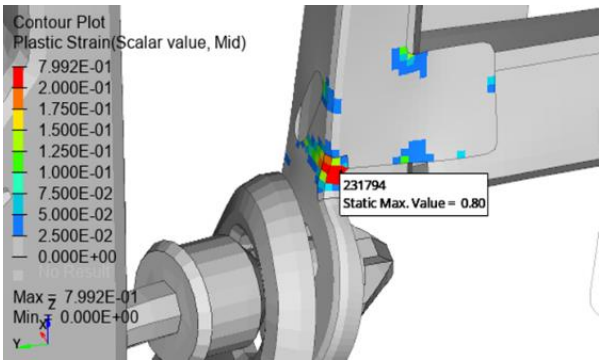

Figure 14. First iteration plastic deformation results.

According to the results, the plastic deformation value has decreased from 191% to 80%, but it is still higher than the 20% limit value.

3.5. Increasing the Cross-section Thickness

The plastic deformation result was 20.3% according to the design change realized by expanding the cross-section where the thickness was kept at 1.5 mm and rupture was observed, by preventing the local thickness from decreasing during production. Although there is a major improvement compared to the first situation, it is still seen to be higher than the limit value.

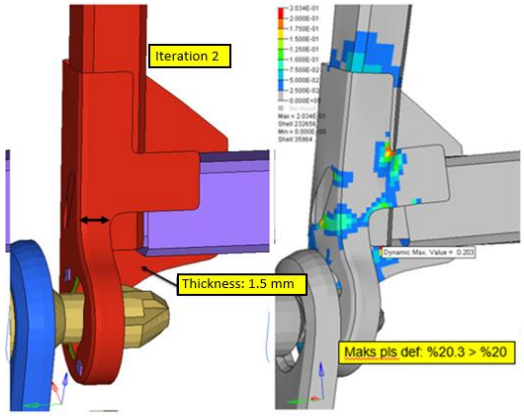

Figure 15. Second iteration results (a) Design change (b) Plastic deformation.

3.6. Adding a Support Bracket

In the third study, it was observed that the thickness was the same as the original design (1.5mm), the expanded design in the second iteration was applied, and the amount of plastic deformation in the rupture area decreased in the design to which 2 mm additional support bracket was added. With these results, the study on finite elements has been completed.

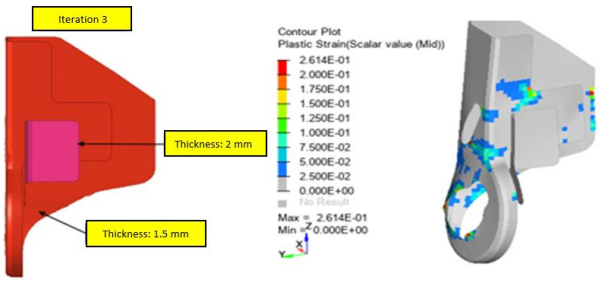

(a) **(b)**

Figure 16. Third iteration results in (a) Design change (b) Plastic deformation.

3.6.1. Verification of the Changed Design by Physical Testing

It is necessary to determine the verification of the renewed design by physical test. As a result of the test performed on the prototype seat produced according to the new design, no rupture was observed as same as in the result of the finite element analysis, and results by ECE R17 conditions were obtained with this seat design.

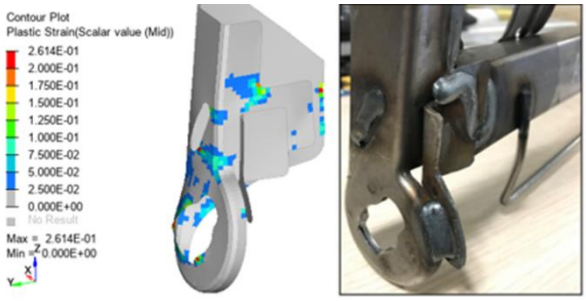

Figure 17. Third iteration analysis - test comparison.

3.7 Design Change to Reduce Production Cost

When the design in which the risk of rupture the corner bracket is eliminated is examined, it is seen that a process with many shaping, bending, and cutting processes have emerged. It is seen that this part, which can be produced by gradual sheet metal forming, has high mold investment and labor costs. As a result of the design simplification studies, a design change was made that is easier and cheaper to manufacture, as in figure 18. For the brackets to be used here, will be produced from 4 mm and 2 mm thick S420MC material. With the finite element analysis, it was seen that there is no risk in the new design and the physical test was carried out by producing the prototype seat and no risk was observed as a result of the test. Thus, the design was suspended and a seat design suitable for mass production was created.

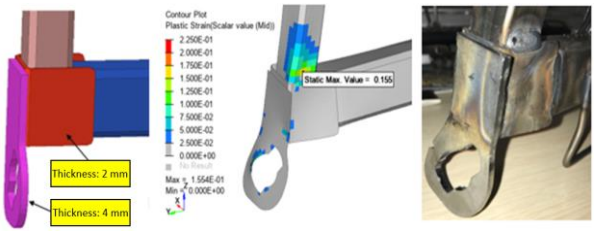

(a) **(b)** **(c)**

Figure 18. Fourth iteration (a) New design and thicknesses (b) Virtual analysis of plastic deformation results (c) An image after the physical test.

3.8 Weight Reduction Using Aluminum Material

In this study, which was carried out to reduce the weight of the seat frame, finite element analysis was performed by using AA 6082 aluminum alloy instead of S420MC steel material. Considering the weight, the skeleton, which was 7.27 kg with steel material, was decreased to 2.51 kg with aluminum material.

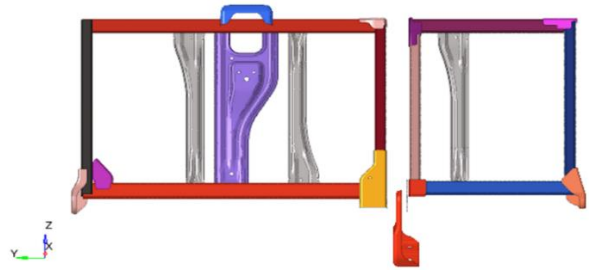

Figure 19. Components with AA 6082 material applied.

When the analysis results are examined, it is seen that the maximum plastic deformation is 138.5% and it is well above the limit value of 9% for this alloy. In addition, it also cannot provide the displacement values from other regulation conditions as well as the risk of rupture.

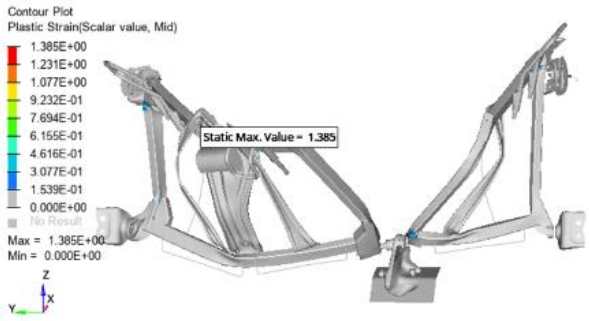

Figure 20. Plastic deformation results with AA 6082 material.

4. Conclusion

In this study, the European standard ECE R17 luggage retention test for the M1 class vehicle rear seat is simulated by the finite element method, and its accuracy was verified by physical testing. Although increasing the thickness reduced the amount of deformation, it was not a solution alone and positive results were obtained with the addition of support brackets. After the design in which the risk of rupture is removed, the optimum design was found by making a design change study that can be shortened in the production process to reduce the cost. The virtual analysis was repeated with AA 6082 material instead of S420MC steel material on the final design. When the results were examined, it was seen that the seat frame was lighter by 65.4%. It was concluded that AA 6082 was not suitable as the seat frame material, since the seat did not pass the ECE R17 test conditions.

Contribution of the Authors

The article was produced with the joint contributions of the authors.

Conflict of Interest Statement

There is no conflict of interest between the authors.

Statement of Research and Publication Ethics

The study has complied with research and publication ethics.

References

[1] S. Sharma and S. K. Ghoshal, “Hydrogen the future transportation fuel: From production to applications,” Renew. Sustain. Energy Rev., vol. 43, pp. 1151–1158, 2015, doi: 10.1016/j.rser.2014.11.093.

[2] V. Singh and S. K. Sharma, “Fuel consumption optimization in air transport: a review, classification, critique, simple meta-analysis, and future research implications,” Eur. Transp. Res. Rev., vol. 7, no. 2, 2015, doi: 10.1007/s12544-015-0160-x.

[3] M. Gonçalves, H. Monteiro, and M. Iten, “Life Cycle Assessment studies on lightweight materials for automotive applications - An overview,” Energy Reports, vol. 8, pp. 338–345, 2022, doi: 10.1016/j.egyr.2022.01.067.

[4] A. Beaudet, F. Larouche, K. Amouzegar, P. Bouchard, and K. Zaghib, “Key challenges and opportunities for recycling electric vehicle battery materials,” Sustain., vol. 12, no. 14, pp. 1–12, 2020, doi: 10.3390/su12145837.

[5] A. Mayyas, A. Qattawi, M. Omar, and D. Shan, “Design for sustainability in automotive industry: A comprehensive review,” Renew. Sustain. Energy Rev., vol. 16, no. 4, pp. 1845–1862, 2012, doi: 10.1016/j.rser.2012.01.012.

[6] Ç. Dindar, H. Beytüt, and S. Karagöz, "Effect of heat treatment and cross section on the crashworthiness of 51CrV4 spring steel," Uludağ Univ. J. Fac. Eng., vol. 24, no. 2, pp. 477–488, 2019, doi: 10.17482/uumfd.477569.

[7] B. Camburn et al., "Design prototyping methods: State of the art in strategies, techniques, and guidelines," Des. Sci., vol. 3, no. Schrage 1993, pp. 1–33, 2017, doi: 10.1017/dsj.2017.10.

[8] M. Guida, G. Lamanna, F. Marulo, and F. Caputo, "Review on the design of an aircraft crashworthy passenger seat," Prog. Aerosp. Sci., vol. 129, no. March 2021, p. 100785, 2022, doi: 10.1016/j.paerosci.2021.100785.

[9] H. Fazlollahtabar, "A subjective framework for seat comfort based on a heuristic multi criteria decision making technique and anthropometry," Appl. Ergon., vol. 42, no. 1, pp. 16–28, 2010, doi: 10.1016/j.apergo.2010.04.004.

[10] W. Karwowski, "Ergonomics and human factors: The paradigms for science, engineering, design, technology and management of human-compatible systems," Ergonomics, vol. 48, no. 5, pp. 436–463, 2005, doi: 10.1080/00140130400029167.

[11] S. Hiemstra-van Mastrigt, L. Groenesteijn, P. Vink, and L. F. M. Kuijt-Evers, "Predicting passenger seat comfort and discomfort on the basis of human, context and seat characteristics: a literature review," Ergonomics, vol. 60, no. 7, pp. 889–911, 2017, doi: 10.1080/00140139.2016.1233356.

[12] P. Kangralkar, G. Chidambaram, K. Hendre, 2015. Study of Cargo Barrier in ECE 17 test (Luggage Retention) Regulation. 2015 Altair Technology Conference, India.

[13] F. Düvenci, (2017). "Araç yolcu koltuk ayaklarında farklı malzemelerin kullanımının sonlu elemanlar yöntemi ve testler ile mekanik etkisinin karşılaştırılması, " Master's thesis, Uludağ University.

[14] K.-U. Schmitt, M. H. Muser, and P. Niederer, "a New Neck Injury Criterion Candidate for Rear-End Collisions Taking Into Account Shear Forces and Bending Moments," Technology, pp. 1–9, 2000.

[15] Corrigendum to Regulation No 17 of the Economic Commission for Europe of the United Nations (UN/ECE) — Uniform provisions concerning the approval of vehicles with regard to the seats, their anchorages and any head restraints (OJ L 373, 27.12.2006). [Online]. Available: https://eurlex.europa.eu/legalcontent/EN/TXT/. [Accessed: Mar. 28, 2022].

[16] H. Aydın, O. Tunçel, K. Yiğit, F. Balamur, O. Çavuşoğlu, and O. Düzgün, "AA6082-T6 ve Aa1035-H14 Alüminyum Alaşımlarında Haddeleme Yönünün ve Deformasyon Hızının Çekme Özellikleri Üzerindeki Etkisi," Uludağ Univ. J. Fac. Eng., vol. 22, no. 3, pp. 81–96, 2017, doi: 10.17482/uumfd.297265.

Bitlis Eren Üniversitesi Fen Bilimleri Dergisi
BİTLİS EREN UNIVERSITY JOURNAL OF SCIENCE
ISSN: 2147-3129/e-ISSN: 2147-3188
VOLUME: 11 NO: 2 PAGE: 715-726 YEAR: 2022
DOI: 10.17798/bitlisfen.1107311

Forecasting of Export Volume Using Artificial Intelligence Based Algorithms

Erdemalp ÖZDEN[1*]

[1]*Bayburt Üniversitesi, İktisadi ve İdari Bilimler Fakültesi, İktisat Bölümü, 69000, Merkez/Bayburt (ORCID: 0000-0001-5019-1675)*

Keywords: Export volume, Forecasting, SVM, ANFIS, MLR

Abstract

Technological breakthroughs have transformed communication and taken transportation, health, and commerce to an unprecedented level. In this way, sudden developments have rapidly affected all countries. In this context, analysis methods are changing compared to the past, and annual analyses fail to catch the trend even for macroeconomic indicators. In this paper, new artificial intelligence-based estimation methods were used to see the future trend of export volume, and their estimation performances were compared by adding them to the classical econometric method. Historical quarterly data from 2013 to 2021 were used in the training and testing phases of the models. For this purpose, the variables of gross domestic product, foreign direct investment, and dollar exchange rate, which affect the export volume, were determined as inputs in estimating the export volume. According to the analysis results, support vector machine model was determined as the best method for predicting export volume in Turkey. This study can provide an essential basis for policymakers to export estimation and formulate their export-enhancing policies effectively.

1. Introduction

The Covid-19 pandemic, which affected the whole world in 2019, radically changed the economy, trade, and how countries and companies do business. This change has shaken the economies profoundly, and as a result, most countries have experienced economic constriction, reaching 20% of their GDP [1]. According to this report, this economic shrinkage is the most severe recession after World War II. In terms of Turkey, there was no constriction in GDP after the pandemic. On the contrary, there was a growth of 1.8% in 2020 and 11% in 2021 [2], [3]. The most crucial driving force behind the growth in this period was Turkey's exports.

In the post-1980 neoliberal period, Turkey was in a position to import more in its trade with other countries (see Figure 1) and thus was in a situation where there was a trade deficit. The foreign trade deficit causes the current account deficit. Therefore, even if the economy continues to grow, it is compensated by increasing the current account deficit. Although this situation partially supports the growth of the country's economy, it is not sustainable. The growth provided by the increase in exports is the healthiest among others. In this respect, exports and their future trend are essential for Turkey.

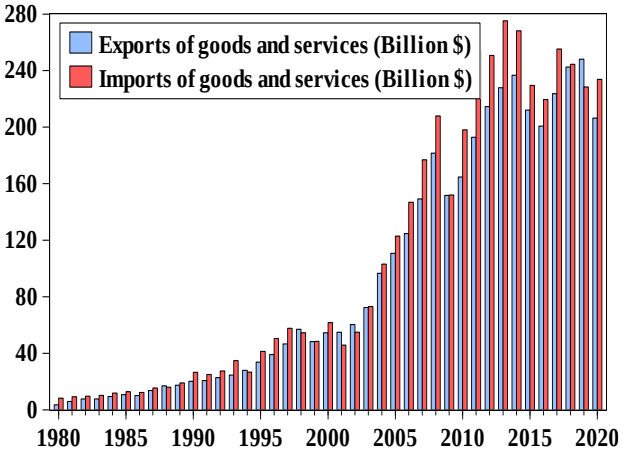

Figure 1. Turkey's exports and imports

*Corresponding author: eozden@bayburt.edu.tr
Received: 21.04.2022, Accepted: 20.06.2022

With globalization, trade between economies has increased and accelerated simultaneously. The changes are experienced rapidly, and a situation that comes into being in one country affects other countries much faster than before. Therefore, this situation should be considered when establishing prediction models. For this reason, datasets created with as short intervals as possible will be beneficial both in capturing changes quickly and predicting the future. With this motivation, this study uses quarterly data between 2013 and 2022. Then, artificial intelligence-based (AI-based) and classical multilinear regression (MLR) estimate the export volume and determine the best estimating method.

The literature about estimation and forecasting methods for export is reviewed in the second part of the study. In the third part, the dependent and independent variables and the created data set and statistics are examined, then the details of the models used in the study are discussed. Finally, the results are evaluated and compared according to the selected performance criteria in the fourth section.

2. Literature Review

The relationship between exports and the other indicators has been determined using statistical and econometric models in the previous studies. However, the prediction performance of artificial intelligence-based models draws attention in today's literature. While statistical models can adequately model linear relationships between data, they have difficulty seeing nonlinear relationships. For this reason, it is tried to eliminate this deficiency with artificial intelligence-based models [4], [5]. In particular, the kernel functions of machine learning models have effective results in responding to nonlinear relationships. Therefore, MLR and AI-based models were developed in this study, and their results were compared. The variables were determined by examining previous studies. Some studies in this area are summarized below.

Shetewy et al. (2022) evaluated the financial sector development and the effect of internet use on export volume for thirty Chinese provinces using two distinct approaches and a data set spanning 18 years. The study developed prediction models using Panel-Corrected Standard Error (PCSE), an econometric method, and Gaussian Process Regression (GPR) moles as an ML model. According to the study results, panel data analysis showed that internet usage increased exports for all provinces of China. In addition, internet usage in high-middle-developed provinces significantly affects exports. The results of the GPR model revealed that GDP, internet use, and financial development are essential indicators for predicting export growth.

Qiu (2022) developed three different models to model and predict the export value from China to the USA, considering six variables and the seasonal variations of these variables. ARIMA and AR-GARCH statistical models were compared with the artificial neural network model. Performance metrics were chosen to evaluate the estimation results of the developed models. Although there are differences in the estimation results, the estimation results in the three models were satisfactory. It has been suggested that the developed forecasting models can be used for planning to improve China's exports.

Liu (2021) developed a forecasting model using artificial neural networks and fuzzy theory for index estimation of foreign trade exports. The ANFIS model, which is used by combining the two methods, was used. In addition, the ARIMA model was also estimated to compare the results of this model. As a result, the estimation adequacy of both models is at an acceptable level. Furthermore, the study's findings show that the fuzzy neural network estimating model gives better results for export trend forecasting.

Costantiello et al. (2021) estimated the import of goods for 28 countries in their study. In the study, a data set for 2010-to 2019 was designed. The study consisted of two stages. First, analyses were made using classical statistical methods. Then, prediction models were developed using different machine learning techniques to compare the results of these analyses.

Jia et al. (2021) proposed a machine learning-based model to predict the destination of oil exports using oil shipment information. Crude oil shipment dataset covering the years 2013-2016 was created using cargo, ship, geographical, and macroeconomic variables. According to the estimation model results, it was determined that quality and cargo size were adequate for destination estimation. Furthermore, the study has shown that it effectively predicts oil trading models in microdata.

Suler et al. (2021) estimated exports from the Czech Republic to China using artificial neural networks (ANN). An ANN model with the best estimation ability was developed using historical data in the study. Models were constructed with three different scenarios. These scenarios are established with time series of data with a time delay of 1 month, five months, and ten months. As a result, it has been observed that the applied Multi-Layer Perception is the most efficient in estimating exports.

Minh Khiem et al. (2021) developed a model that predicts the price of shrimp products exported from Vietnam to the USA using ML algorithms. A

data set covering the years 1995-2019 was used in the study. Thirty-three different variables were determined as input variables. First, however, the Akaike Information Criterion (AIC) was calculated, and 15 variables that gave the most accurate result were used. Next, prediction models are developed using random forest and gradient boosting decision tree algorithms. The study's findings showed that the random forest algorithm for six-month predictions and the gradient boosting algorithm for shorter predictions perform more effectively.

Research on exports draws attention to the literature in economics and econometrics. Moreover, many studies have long examined the link between exports and the economy. In the continuation of the literature review, current studies using econometric methods were examined to set an example for this research.

Nugroho and Lakner (2022) conducted a panel data analysis using a data set covering the years 1990-2018 to examine the effect of globalization on coffee exports. The GDP and exchange rate variables positively affect coffee exports. Furthermore, the relationship between mike coffee exports with GDP, exchange rate, and commercial and political globalization index has been examined. As a result of the study, it has been seen that the commercial globalization index has a negative effect on coffee exports, while the political globalization index has a favorable impact on exports.

Lazarov (2019) applied the vector autoregression (VAR) model and Granger causality test to analyze Macedonia's export structure based on products and observe the contribution of exports to the country's development. According to the findings, exports and economic growth have a favorable and statistically significant association.

Mukhlis and Qodri (2019) used a data set spanning the years 1980 to 2017 to investigate the relationship between Indonesia's export, import, foreign direct investment, and economic development variables. The link between the variables was modeled using the vector error correction model (VECM). The study's conclusions revealed that foreign direct investment had an impact on Indonesia's economic growth.

3. Material and Method

3.1. Data Collection Process

In the study, gross domestic product (GDP), foreign direct investment (FDI), and exchange rate are used to estimate Turkey's export volume. As of the study period, the most up-to-date data were collected quarterly from different data sources. Table 1 describes variables, abbreviations, and units.

The relations between economic growth and exports and imports of countries have been discussed in detail in the economics literature. Most studies have looked at the causality between economic growth and exports. There is a causality running from exports to growth in [16]–[18] studies. In [19]–[21] studies, on the other hand, the opposite is the case. In other words, growth affects exports positively. In [22]–[25] studies, on the other hand, a two-way causality can be mentioned. Exports were chosen as the dependent variable in this study, and the predictive power of growth on exports was examined to measure the effect of change in the Turkish economy on exports.

Table 1. Definition and descriptive statistics of the variables

Variables	**Export Volume**	**Gross Domestic Products**	**Foreign Direct Investment**	**USD/TRY Exchange Rate**
Abbrivaition	EXP	GDP	FDI	ER
Unit	US Dollars, Billions - Quarterly	US Dollars, Billions - Quarterly	US Dollars, Billions - Quarterly	1 US Dollar Equivalence
Source	UN Comtrade, 2021	Turkstat	CBRT	CBRT
Mean	42.93	897.83	43.92	4.43
Std	6.31	441.47	7.35	2.34
Max	64.44	2,313.81	58.54	11.16
Min	32.40	388.66	32.07	1.78
Skewness	1.37	1.34	0.11	0.93
Kurtosis	5.54	4.61	1.89	3.17

In the economic literature, it has been shown that foreign direct investment generally positively affects economies' exports. Countries where foreign investment comes from, have developed their export supply capacity strongly over time. In this way, the export content changed, which led to the production of higher technological products. In addition, this development contributed to the structural development of exports. This contribution is not always linear. UNCTAD reported a U-shaped relationship between exports and FDI [26]. Accordingly, while FDI is beneficial for a newly developing country in exports, this relationship weakens over time. Then, the export structure continues to strengthen, and when it comes to the stage of development, the FDI-export relationship gets stronger again. [27], [28] studies also reveal a positive relationship between FDI and exports.

One of the best-known hypotheses in economics is the one that reveals the relationship between the value of money and foreign trade. For example, if the country's currency depreciates against foreign currencies, exports will increase because they will become cheaper, and imports will decrease because they will become expensive. Many studies test this hypothesis, such as [29], [30]. However, the period in which this hypothesis was put forward was when the countries' economies accepted the fixed exchange rate regime. Each country fixed the external value of its currency to the reserve currencies, and the currency of the devaluing country became cheaper, and imports decreased while exports increased. A similar situation cannot be fully mentioned in the floating exchange rate regime.

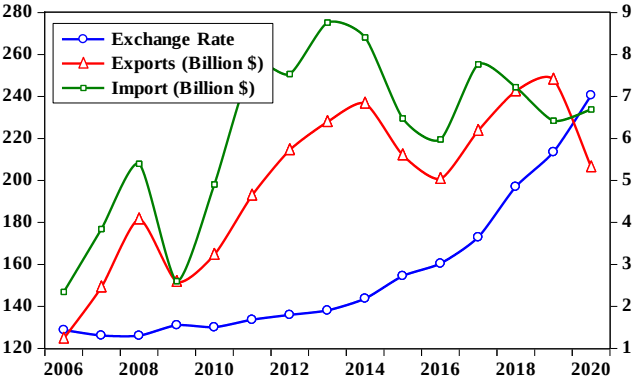

Figure 2. Export, Import and Exchange rate in Turkey

Figure 2 shows that despite the rapid depreciation of the Turkish lira against the dollar in recent years, the increase in exports remained more limited. In fact, when we look at the last period, it is seen that there has been an increase in imports, contrary to expectations. The main reason behind this situation is that after the pandemic, even though the prices for the economies of the countries to which goods are exported, the demand has decreased. On the other hand, domestic demand increased in the growing Turkish economy, which led to an increase in imports towards the end of 2020.

In this study, the pattern between these variables, which significantly impact exports, and export volume, will be investigated. Based on this pattern, it will try to find the most reliable forecasting method. Two different AI-based techniques were used in the study, and these techniques were compared with the classical econometric method. The data set was divided into 70% training and 30% test set to compare these methods.

It is seen in Figure 3 that the data used in the application are on different scales. These scale differences in terms of both econometric and artificial intelligence-based methods may cause the results to be erroneous and biased. Preprocessing is required to prevent these disruptions. In this respect, there are two most commonly used methods to scale the variables in the data set to a particular scale. One of them is to normalize the data set to a specific range. The other is standardization. In this study, the standardization method was applied. This method is represented as $X' = \frac{X-\mu}{\sigma}$. Here μ is the mean of the feature values, and σ is the standard deviation of the feature values. In this way, more meaningful comparisons can be made, and more meaningful results can be achieved.

3.2. Multilinear Regression (MLR)

One of the most frequently used tools in examining the relationship between dependent and independent variables is MLR. In its general structure, the MLR is represented as follows:

$$Y_i = \beta_1 + \beta_2 X_{2i} + \beta_3 X_{3i} + \cdots + \beta_k X_{ki} + u_i \quad (1)$$

In this equation, the variable Y is the dependent variable, the variables Xs are the explanatory variables, and u is the random term. In this study, the data set is the time series data of Turkey. For an MLR method to be made on the time series, specific preliminary tests must be made for the data set beforehand. The most important thing is to test whether the variables are stationary to avoid spurious regression. If the variables are not stationary, it is ensured that all variables are stationary at the same level so that the analysis can be performed. Another critical assumption for the MLR model is that there is no multicollinearity between the variables in the regression [31]. This problem arises when there is a high correlation between variables, which leads to

unreliable and unstable regression coefficient estimates. After these tests are done, MLR analysis can be done.

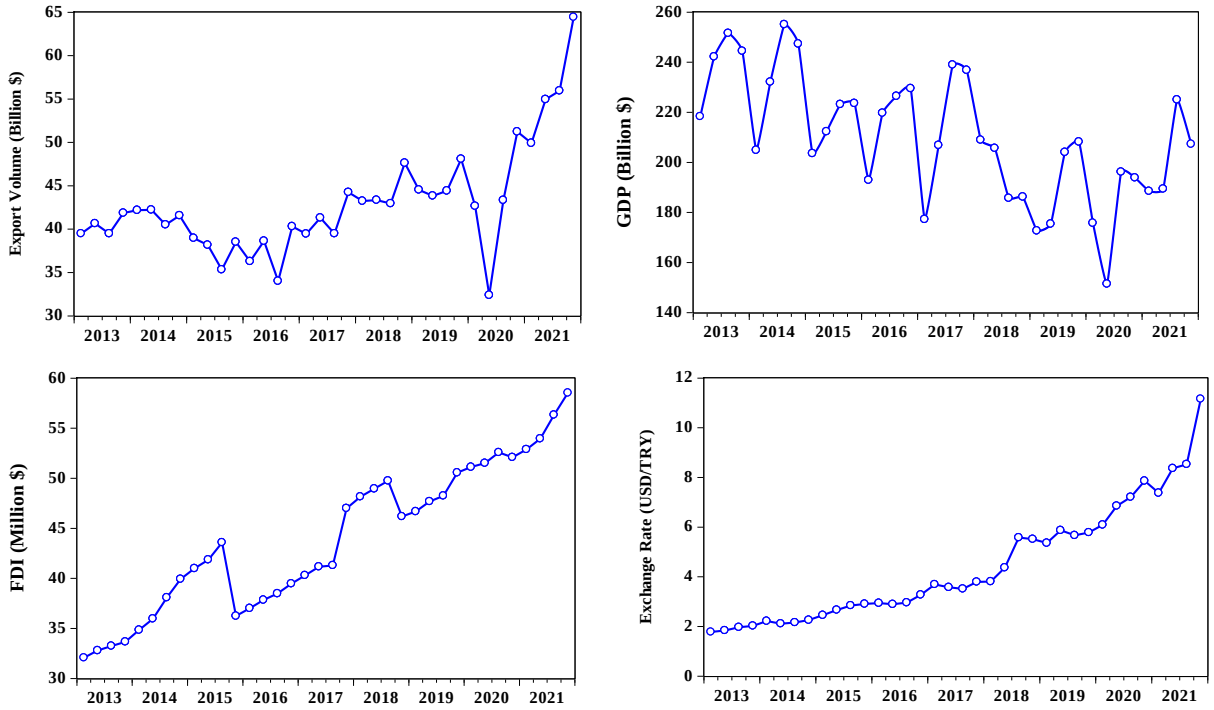

Figure 3. The change of the variables by years

3.3. Adaptive Neuro-Fuzzy Inference System (ANFIS)

By combining different methods, models can produce more effective and efficient results. New models created by different models are called hybrid models. Using the two models together will create an efficient framework, considering each model has different advantages. The Adaptive Neuro-Fuzzy Inference System (ANFIS), which was first used in 1991, is one of the best examples of hybrid models. Many applications have been made with the developed framework, and effective results have been obtained. This method allows the use of artificial neural networks and fuzzy systems together. Fuzzy systems are rule-based systems and provide results by making inferences according to the determined rules [32]–[34].

On the other hand, artificial neural networks have the ability to learn. They can learn the model's relationship between input and output thanks to their learning ability. When combined with fuzzy-based models' ability to understand verbal expressions better, this ability can produce effective results. Therefore, this study used the ANFIS method to develop a forecasting model [35].

The ANFIS architecture is made up of layers that contain nodes. The second, third, and fifth layers have fixed nodes, while the first and fourth layers have adaptive nodes. Fuzzy, product, normalized, defuzzification, and total output layers are the names of these layers [36]. ANFIS is related to the Takagi-Sugeno fuzzy inference system because of its structure. In Figure 4, the basic ANFIS structure is modeled. This structure has two inputs and one output variable.

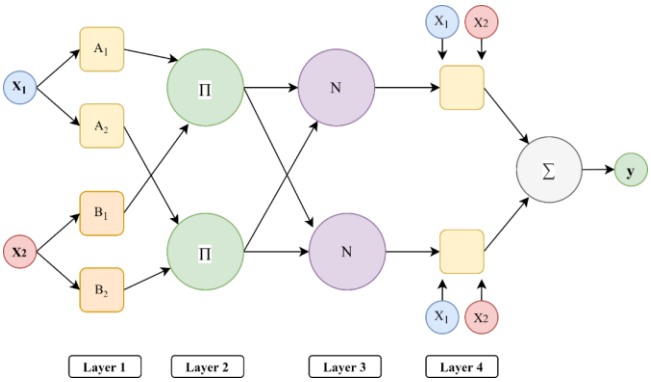

Figure 4. ANFIS framework with two inputs and one output

Layer 1 is the layer where the data becomes fuzzy. The input values are transferred to the next layer thanks to the nodes in this layer. The input value

determines the output value of the layer, and the membership degrees are determined according to the selected membership function. The rule layer is the second layer. The effect of the Sugeno-type fuzzy logic structure may be seen at each node's output.

The layer containing the normalization process is the third layer containing fixed nodes. It takes the second layer's outputs as input and ensures that the data is scaled. The layer where the fuzzy expressions are clarified is the fourth layer. Normalized rules are recalculated by multiplying them with linear functions in this layer. Finally, the fifth layer is the layer containing a single node from which the total output is calculated, known as the total output layer [34].

Fuzzy inference systems, which are similar in general structure, have different types when studies are examined. The structure of the membership function used reveals this difference. For example, Mamdani, Tsukamoto, and Sugeno inference systems are inference systems that differ according to the membership function [34], [37].

3.4. Support Vector Machine (SVM)

Support vector machines are one of the methods used to solve classification problems. There are many applications in this field, such as Chandrasekaran et al. (2019), Chong & Pu, (2006), Diao et al. (2015), Ozden & Guleryuz (2021), and Zhang et al. (2016), who proposed a forecasting model using SVM. The fact that support vector machines produce effective results for regression problems has caused the method to be used frequently in solving regression problems and is called Support Vector Regression (SVR). SVM is a supervised learning approach that is based on structural risk minimization and statistical learning theories [38], [43]. SVR carries almost all the principles of the SVM method. Since the output for the regression is a real number, there are unlimited possibilities for the outcome. The tolerance (epsilon) limitation is used to limit these possibilities. While the model can be used for linear data, it can also be used for nonlinear data through kernel functions. Therefore, effective modeling of nonlinear relationships between datasets is possible with SVR. The mathematical formulation for SVR is given in Eq (2).

$$\text{maximize}\begin{cases}\frac{1}{2}\sum_{i=1}^{j}(\omega_i-\omega_i{}^*)(\omega_i-\omega_i{}^*)\,K\langle x_i,x_j\rangle\\ -\epsilon\sum_{i=1}^{j}(\omega_i+\omega_i{}^*)+\sum_{i=1}^{j}y_i(\omega_i-\omega_i{}^*)\end{cases}$$
$$\text{s.t}\begin{cases}\sum_{i=1}^{k}(\omega_i-\omega_i{}^*)=0\ and\ \omega_i,\omega_i{}^*\in[0,C]\\ 0\le\ \omega_i,\omega_i{}^*\le\frac{C}{j}\\ i=1,2,\dots,j\end{cases}\qquad(1)$$

Eq. (2), ω_i and ω_{i*} are nonnegative multipliers, and x_i is observed data. The data size is indicated by l, and the penalty coefficient and the penalty dimension are shown by C, ϵ respectively. The kernel function is represented as K (x_i, x_j.). Eq. (3) shows the regression equation [43].

$$f(x)=\sum_{i=1}^{j}(\omega_i-\omega_i^*)\,K(\omega_i-\omega_j)+b^* \qquad (3)$$

4. Results and Discussion

4.1. Comparing the performance of models

There are different performance criteria to compare the models' performances used in the study. The most commonly used ones are mean black root error (RMSE), correlation (R^2), mean absolute percentage error (MAPE), and Mean Absolute Deviation (MAD). The formulas for these criteria are given below in Table 2.

In order to compare the performances, the data set was divided into training (70%) and testing (30%). In this way, the estimation sensitivities of the models in the study will be measured, and the best estimating method will be determined.

At this stage, there are some points to be considered while analyzing with the classical method. First of all, this method must undergo certain preliminary tests. One of them is the stationarity test, which is very important for the time series. Figure 3 shows that even without analysis, the variables are in an increasing trend. Therefore, it is essential to determine the degree of stationarity of the series. Therefore, the most commonly used Augmented Dickey-Fuller (ADF) unit root test was conducted for this purpose, and the results are shared in Table 3.

Table 2. The formulas for the metrics

$$RMSE = \sqrt{\frac{1}{n}\sum_{t=1}^{n}(EXP_t^{observed} - EXP_t^{predicted})^2} \quad (2)$$

$$R^2 = \left(\frac{\sum_{t=1}^{n}(EXP_t^{observed} - \overline{EXP_t^{observed}})\,(EXP_t^{predicted} - \overline{EXP_t^{predicted}})}{\sqrt{\sum_{t=1}^{n}(EXP_t^{observed} - \overline{EXP_t^{observed}})^2\,(EXP_t^{predicted} - \overline{EXP_t^{predicted}})^2}} \right)^2 \quad (3)$$

$$MAPE = \frac{1}{n}\sum_{t=1}^{n}\left|\frac{EXP_t^{observed} - EXP_t^{predicted}}{EXP_t^{predicted}}\right| \text{x } 100\% \quad (4)$$

$$MAD = \frac{1}{n}\sum_{t}^{n}\left|EXP_t^{observed} - EXP_t^{predicted}\right| \quad (5)$$

Table 3. The ADF and PP Unit Root Tests

ADF Unit Root Test		EXP	GDP	FDI	ER
Level	t-Stat.	-1.65	-3.66**	-2.43	0.40
	Prob.	0.75	0.04	0.36	0.99
1st Difference	t-Stat.	-6.88***	-3.83**	-5.72***	-5.29***
	Prob.	0.00	0.03	0.00	0.00

Notes: a: (*)Significant at the 10%; (**)Significant at the 5%; (***) Significant at the 1% and (no) Not Significant, b: Lag Length based on AIC, c: Prob. Based on MacKinnon's (1996) one-sided p-values.

According to Table 3, only GDP is stationary at the level, while other variables are not stationary at the level. In order to be able to perform time series analysis, all variables must be stationary at the same level. In this respect, the differences of all variables are taken, and all variables are stationary in their first order. The graphs of the stationary variables can be seen in Figure 5.

Figure 5 shows that the variables oscillate around the mean zero and do not show a particular trend. As a result, the stationary data set will be used while performing the classical econometric analysis.

Another critical challenge is the problem of multicollinearity. Again, the variance inflation factor (VIF) will be used to determine whether such a problem exists.

As shown in Table 4, the average VIF value of the model was 1.305. Some studies have pointed out that values of five and above can cause problems. Since the VIF value is below the critical value, which is five, it states that there is no multicollinearity problem [44].

Table 4. Multicollinearity Test

Variable	Coefficient Uncentered Variance	Centered VIF	VIF
GDP	3.05E-05	1.725	1.444
FDI	97328.90	1.212	1.043
Exchange Rate	1.71E+12	1.803	1.428
Mean VIF			1.305

As a result of all these tests, it can be passed to the stage of estimating with the classical method. However, there is a critical point to be mentioned at this stage. One of the most important advantages of artificial intelligence-based applications is that they do not require much pre-testing as classical econometric methods. Therefore, after the normalization or standardization of the data set, analyzes were performed for SVM and ANFIS. For this purpose, Table 5 compares the models according to their performance criteria.

Table 5. The performance of all models

	Measure	MLR	SVM	ANFIS
Training	RMSE	0.0869	0.0816	0.0302
	MAPE	0.2251	0.1830	0.0967
	MAD	0.0678	0.0557	0.0213
	R2	0.8035	0.8716	0.9746
Testing	RMSE	0.0768	0.0901	0.0934
	MAPE	0.2096	0.1614	0.2636
	MAD	0.0648	0.0648	0.0730
	R2	0.7957	0.8329	0.7163

Looking at Table 5, low MAPE, MAD, and RMSE values and high R^2 values mean that that method is a better estimator. This table should be

examined in two stages. First, the best predictive model is the ANFIS model for all performance criteria during the training phase. At this stage, SVM gave the second-best result. In the testing phase, situations have changed. At this stage, the best predictive method is SVM. MLR, on the other hand, seems to be better than the ANFIS method during the testing phase. The performance of these methods during the training and testing phases can be seen in Figure 6.

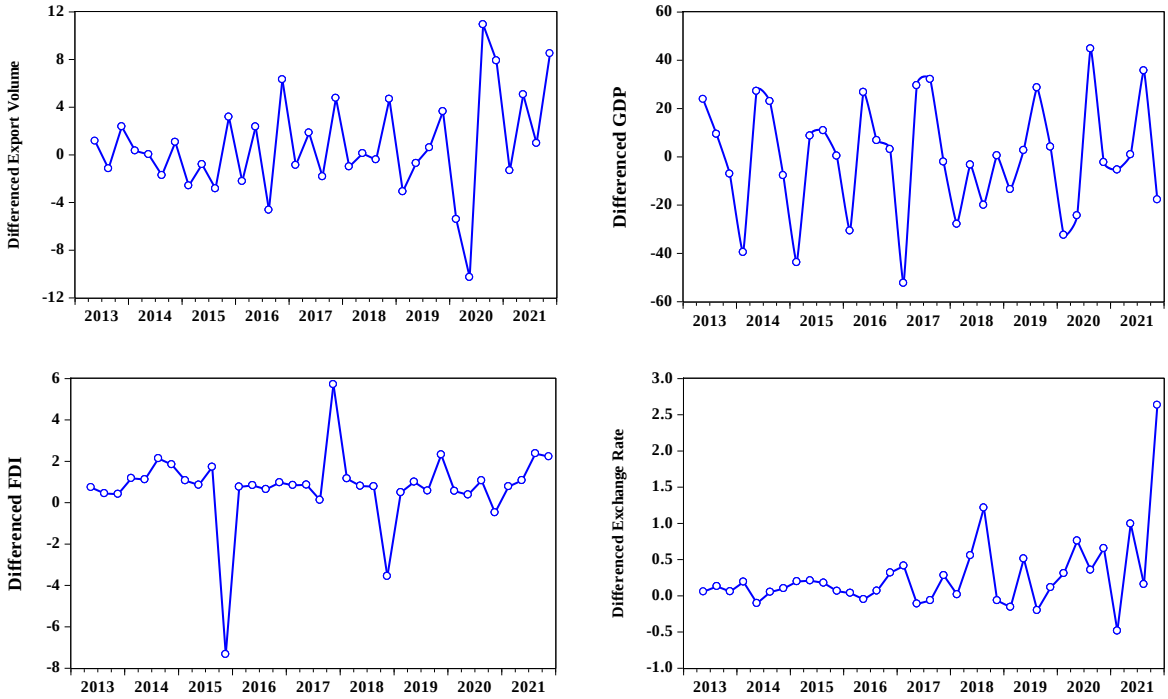

Figure 5. Change of stationary variables by years

Testing accuracy is always more important than training accuracy when comparing forecasting performances. Although ANFIS is high accuracy in the training phase, it did not give successful results in the testing phase compared to other models. In fact, it fell behind even the classical regression estimator during the testing phase. Although the ANFIS method is superior to MLR in capturing nonlinear patterns, this example observed the opposite. The main reason for this may be overfitting in the ANFIS method. Therefore, these over-learned data do not perform well in forecasting. Therefore, on the other hand, the SVM method performs much better in the testing phase than the others.

5. Conclusion and Suggestions

One of the crucial problems of the Turkish economy is the current account deficit, which has been going on for many years. The fact that the products subject to export are produced using raw materials, intermediate goods, and energy and that these final goods also carry exchange rate risk creates a serious added value problem. Despite the increase in the country's growth rate, export goods are exposed to price competition with their competitors. Therefore, Turkey's external demand elasticity is low (solid), and this may cause cost inflation due to the exchange rate and negatively affect growth. One of the most important tools to overcome this is to increase the country's exports and make them sophisticated. Therefore, policymakers need to evaluate their export estimation well.

Estimating the future trend of export volume has frequently found its place in the economic literature. These estimates were measured and evaluated by econometric methods. However, the use of econometric methods has certain limitations. First, the relationship between the variables is expected to have a structure suitable for economic theory. In addition, the variables must be stationary in terms of time series. Another significant limitation is that there is no multicollinearity between the variables. On the other hand, there are no such constraints in artificial intelligence-based forecasting methods. In addition, it gives much more reliable results in capturing the nonlinear patterns between the variables.

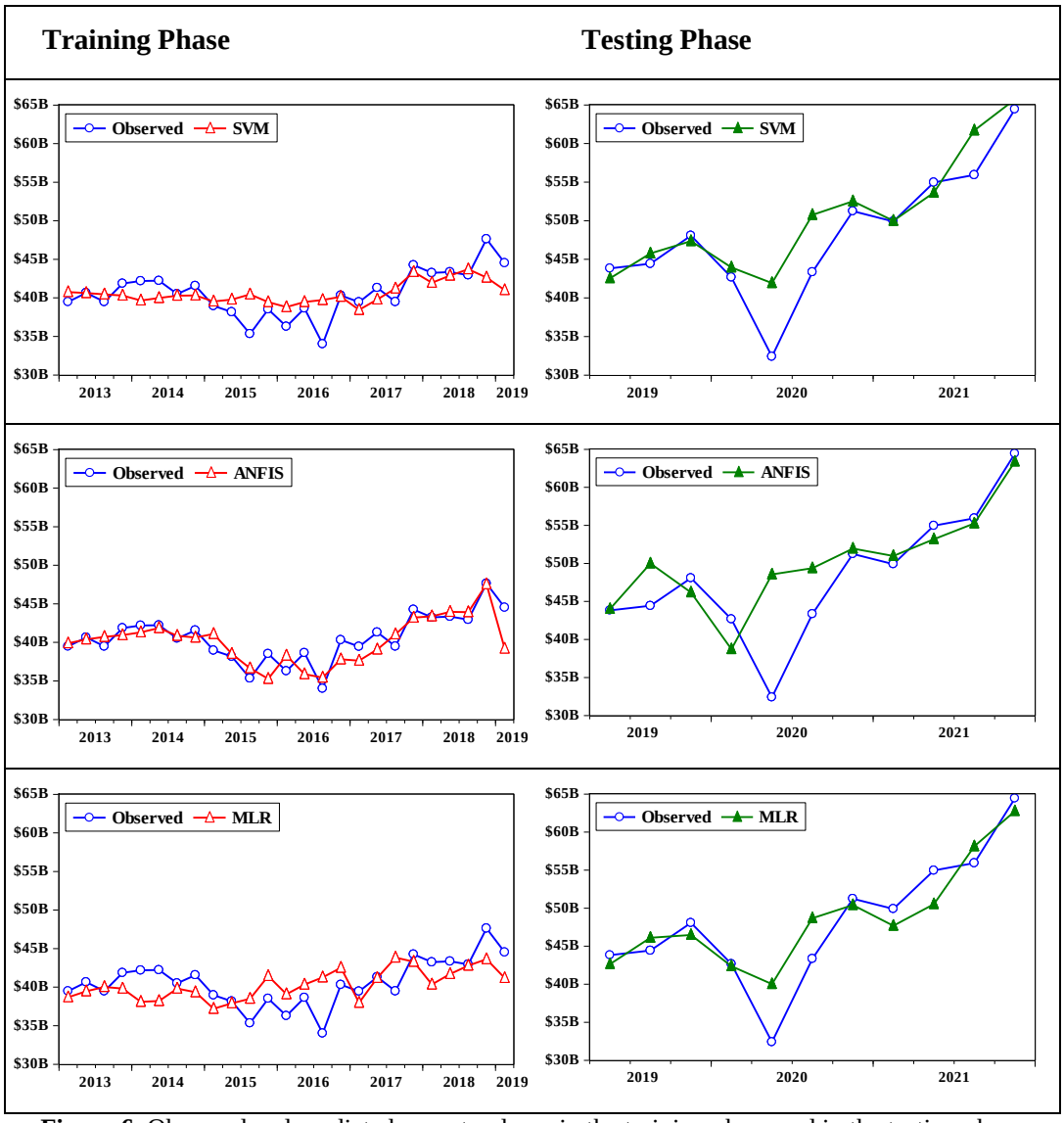

Figure 6. Observed and predicted export volume in the training phase and in the testing phase

In the light of all these, an export volume estimation was made in this study. Unlike other studies, in this study, quarterly data were used, not annual data. In this way, it has been tried to find a reliable estimation method for policymakers and sectoral managers in today's fast data flow.

The models' performances were evaluated using various well-known statistical measures such as R2, RMSE, MAPE, and MAD. As a result of the analysis, SVM was determined as the best method for export volume forecasting with R^2 = 0.8329, RMSE = 0.0901, MAPE = 0.1614, MAD = 0.0648.

In future studies, while estimating exports, other economic determinants not included in this study can be added to the model, and the forecast accuracy can be increased. Furthermore, estimates can be made with different econometric forecasting methods. Finally, predictions can be made with different AI-based methods, and it can be observed whether the prediction accuracy can be increased with hyperparameter optimization. The conclusion section should be stand alone. The aim of the study and its significant results should be given briefly in a concrete way. In addition, suggestions and opinions that are requested to be conveyed to the readers regarding the results of the study can be stated.

Statement of Research and Publication Ethics

The study is complied with research and publication ethics.

References

[1] Worldbank, "Global Economic Prospects," Washington, DC, 2022. doi: 10.1596/978-1-4648-1758-8.

[2] TURKSTAT, "Yıllık Gayrisafi Yurt İçi Hasıla, 2020," 2021. https://data.tuik.gov.tr/Bulten/Index?p=Yillik-Gayrisafi-Yurt-Ici-Hasila-2020-37184#:~:text=Yıllık verilere dayalı olarak hesaplanan,milyar 883 milyon TL oldu.

[3] Reuters, "Turkey's economy grew 11% in 2021; to cool to 3.5% in 2022," 2022. https://www.reuters.com/markets/asia/turkeys-economy-grew-11-2021-cool-35-2022-2022-02-22/

[4] D. Guleryuz, "Forecasting outbreak of COVID-19 in Turkey; Comparison of Box–Jenkins, Brown's exponential smoothing and long short-term memory models," *Process Saf. Environ. Prot.*, vol. 149, pp. 927–935, 2021, doi: https://doi.org/10.1016/j.psep.2021.03.032.

[5] B. Efe, M. Kurt, and Ö. F. Efe, "Hazard analysis using a Bayesian network and linear programming," *Int. J. Occup. Saf. Ergon.*, vol. 26, no. 3, pp. 573–588, Jul. 2020, doi: 10.1080/10803548.2018.1505805.

[6] N. Shetewy, A. I. Shahin, A. Omri, and K. Dai, "Impact of financial development and internet use on export growth: New evidence from machine learning models," *Res. Int. Bus. Financ.*, vol. 61, p. 101643, 2022, doi: https://doi.org/10.1016/j.ribaf.2022.101643.

[7] C. Qiu, "China's Economic Forecast Based on Machine Learning and Quantitative Easing," *Comput. Intell. Neurosci.*, vol. 2022, p. 2404174, 2022, doi: 10.1155/2022/2404174.

[8] Y. Liu, "Foreign Trade Export Forecast Based on Fuzzy Neural Network," *Complexity*, vol. 2021, p. 5523222, 2021, doi: 10.1155/2021/5523222.

[9] A. Costantiello, L. Laureti, and A. Leogrande, "Estimation and Machine Learning Prediction of Imports of Goods in European Countries in the Period 2010-2019," vol. 5, pp. 188–205, Jul. 2021.

[10] H. Jia, R. O. Adland, and Y. Wang, "Global Oil Export Destination Prediction: A Machine Learning Approach," *Energy J.*, vol. 42, 2021.

[11] P. Suler, Z. Rowland, and T. Krulicky, "Evaluation of the Accuracy of Machine Learning Predictions of the Czech Republic's Exports to the China," *Journal of Risk and Financial Management* , vol. 14, no. 2. 2021. doi: 10.3390/jrfm14020076.

[12] N. Minh Khiem, Y. Takahashi, K. Dong, H. Yasuma, and N. Kimura, "Predicting the price of Vietnamese shrimp products exported to the US market using machine learning," *Fish. Sci.*, vol. 87, Apr. 2021, doi: 10.1007/s12562-021-01498-6.

[13] A. D. Nugroho and Z. Lakner, "Effect of Globalization on Coffee Exports in Producing Countries : A Dynamic Panel Data Analysis," vol. 9, no. 4, pp. 419–429, 2022, doi: 10.13106/jafeb.2022.vol9.no4.0419.

[14] D. Lazarov, "Empirical analysis of export performance and economic growth: the case of Macedonia," *Int. J. Trade Glob. Mark.*, vol. 12, no. 3–4, pp. 381–393, Jan. 2019, doi: 10.1504/IJTGM.2019.101541.

[15] I. Mukhlis and L. H. Qodri, "Relationship between Export, Import, Foreign Direct Investment and Economic Growth in Indonesia BT - Proceedings of the Third Padang International Conference On Economics Education, Economics, Business and Management, Accounting and Entrepreneurship (PIC," Sep. 2019, pp. 729–737. doi: https://doi.org/10.2991/piceeba-19.2019.12.

[16] M. N. Islam, "Export expansion and economic growth: testing for cointegration and causality," *Appl. Econ.*, vol. 30, no. 3, pp. 415–425, Mar. 1998, doi: 10.1080/000368498325930.

[17] A. V Jordaan and J. H. Eita, "Export and Economic Growth in Namibia: A Granger Causality Analysis," *South African J. Econ.*, vol. 75, no. 3, pp. 540–547, Sep. 2007, doi: 10.1111/j.1813-6982.2007.00132.x.

[18] S. Abosedra and C. F. Tang, "Are exports a reliable source of economic growth in MENA countries? New evidence from the rolling Granger causality method," *Empir. Econ.*, vol. 56, no. 3, pp. 831–841, Mar. 2019, doi: 10.1007/s00181-017-1374-7.

[19] J. Ahmad and A. C. C. Kwan, "Causality between exports and economic growth," *Econ. Lett.*, vol. 37, no. 3, pp. 243–248, Nov. 1991, doi: 10.1016/0165-1765(91)90218-A.

[20] S. S. Alhakimi, "Export and Economic Growth in Saudi Arabia: The Granger Causality Test," *Asian J. Econ. Empir. Res.*, vol. 5, no. 1, pp. 29–35, 2018.

[21] S. M. R. Jahangir and B. Y. Dural, "Crude oil, natural gas, and economic growth: impact and causality analysis in Caspian Sea region," *Int. J. Manag. Econ.*, vol. 54, no. 3, pp. 169–184, Sep. 2018, doi: 10.2478/ijme-2018-0019.

[22] J. S. Mah, "Export expansion, economic growth and causality in China," *Appl. Econ. Lett.*, vol. 12, no. 2, pp. 105–107, Feb. 2005, doi: 10.1080/1350485042000314343.
[23] T. O. Awokuse, "Exports, economic growth and causality in Korea," *Appl. Econ. Lett.*, vol. 12, no. 11, pp. 693–696, Sep. 2005, doi: 10.1080/13504850500188265.
[24] R. Guntukula, "Exports, imports and economic growth in India: Evidence from cointegration and causality analysis," *Theor. Appl. Econ.*, vol. 25, no. 2, pp. 221–230, 2018.
[25] A. S. Kalaitzi and E. Cleeve, "Export-led growth in the UAE: multivariate causality between primary exports, manufactured exports and economic growth," *Eurasian Bus. Rev.*, vol. 8, no. 3, pp. 341–365, Sep. 2018, doi: 10.1007/s40821-017-0089-1.
[26] UNCTAD, "World Investment Report," 2002.
[27] F. Ahmad, M. U. Draz, and S.-C. Yang, "Causality nexus of exports, FDI and economic growth of the ASEAN5 economies: evidence from panel data analysis," *J. Int. Trade Econ. Dev.*, vol. 27, no. 6, pp. 685–700, Aug. 2018, doi: 10.1080/09638199.2018.1426035.
[28] P. Sun, Y. Tan, and G. Yang, "Export, FDI and the welfare gains from trade liberalization," *Econ. Model.*, vol. 92, pp. 230–238, 2020, doi: https://doi.org/10.1016/j.econmod.2020.01.003.
[29] K.-L. Wang and C. B. Barrett, "Estimating the Effects of Exchange Rate Volatility on Export Volumes," *J. Agric. Resour. Econ.*, vol. 32, no. 2, pp. 225–255, Apr. 2007, [Online]. Available: http://www.jstor.org/stable/40987362
[30] Y. Qian and P. Varangis, "Does exchange rate volatility hinder export growth?," *Empir. Econ.*, vol. 19, no. 3, pp. 371–396, Sep. 1994, doi: 10.1007/BF01205944.
[31] P. Das, "Analysis of Collinear Data: Multicollinearity," in *Econometrics in Theory and Practice*, Singapore: Springer Singapore, 2019, pp. 137–151. doi: 10.1007/978-981-32-9019-8_5.
[32] H. Bonakdari, H. Moeeni, I. Ebtehaj, M. Zeynoddin, A. Mahoammadian, and B. Gharabaghi, "New insights into soil temperature time series modeling: linear or nonlinear?," *Theor. Appl. Climatol.*, vol. 135, no. 3–4, pp. 1157–1177, 2019, doi: 10.1007/s00704-018-2436-2.
[33] A. Azadeh, S. M. Asadzadeh, and A. Ghanbari, "An adaptive network-based fuzzy inference system for short-term natural gas demand estimation: Uncertain and complex environments," *Energy Policy*, vol. 38, no. 3, pp. 1529–1536, 2010, doi: 10.1016/j.enpol.2009.11.036.
[34] D. Guleryuz, "Prediction of Capacity Utilization Rate for Turkey Using Adaptive Neuro-Fuzzy Inference System With Particle Swarm Optimization and Genetic Algorithm," in *Handbook of Research on Advances and Applications of Fuzzy Sets and Logic*, 1st ed., S. Broumi and B. M'Sik, Eds. IGI Global, 2022, p. 450. doi: 10.4018/978-1-7998-7979-4.
[35] D. Guleryuz, "Determination of industrial energy demand in Turkey using MLR, ANFIS and PSO-ANFIS," *J. Artif. Intell. Syst.*, vol. 3, no. 1, pp. 16–34, Jan. 2021, doi: 10.33969/AIS.2021.31002.
[36] A. Esfahanipour and W. Aghamiri, "Adapted Neuro-Fuzzy Inference System on indirect approach TSK fuzzy rule base for stock market analysis," *Expert Syst. Appl.*, vol. 37, no. 7, pp. 4742–4748, 2010, doi: 10.1016/j.eswa.2009.11.020.
[37] M. Blej and M. Azizi, "Comparison of Mamdani-type and Sugeno-type fuzzy inference systems for fuzzy real time scheduling," vol. 11, pp. 11071–11075, Jan. 2016.
[38] E. Ozden and D. Guleryuz, "Optimized Machine Learning Algorithms for Investigating the Relationship Between Economic Development and Human Capital," *Comput. Econ.*, 2021, doi: 10.1007/s10614-021-10194-7.
[39] C. Zhang, H. Wei, X. Zhao, T. Liu, and K. Zhang, "A Gaussian process regression based hybrid approach for short-term wind speed prediction," *Energy Convers. Manag.*, vol. 126, pp. 1084–1092, 2016, doi: 10.1016/j.enconman.2016.08.086.
[40] N. Chandrasekaran, Radhakhrishna Somanah, Dhirajsing Rughoo, Raj Kumar Dreepaul, Tyagaraja S. Modelly Cunden, and Mangeshkumar Demkah, *Digital Transformation from Leveraging Blockchain Technology, Artificial Intelligence, Machine Learning and Deep Learning*, vol. 863. Springer Singapore, 2019. doi: 10.1007/978-981-13-3338-5.
[41] G. Diao, L. Zhao, and Y. Yao, "A dynamic quality control approach by improving dominant factors based on improved principal component analysis," *Int. J. Prod. Res.*, vol. 53, no. 14, pp. 4287–4303, 2015, doi: 10.1080/00207543.2014.997400.
[42] W. Chong and C. Pu, "Application of support vector machines in debt to GDP ratio forecasting," *Proc. 2006 Int. Conf. Mach. Learn. Cybern.*, vol. 2006, no. August, pp. 3412–3415, 2006, doi:

10.1109/ICMLC.2006.258504.
[43] D. Güleryüz, "Predicting Health Spending in Turkey Using the GPR, SVR, and DT Models .," *Acta Infologica*, vol. 5, no. 1, pp. 155–166, 2021.
[44] R. M. O'Brien, "A Caution Regarding Rules of Thumb for Variance Inflation Factors," *Qual. Quant.*, vol. 41, no. 5, pp. 673–690, 2007, doi: 10.1007/s11135-006-9018-6.

Bitlis Eren Üniversitesi Fen Bilimleri Dergisi
BİTLİS EREN UNIVERSITY JOURNAL OF SCIENCE
ISSN: 2147-3129/e-ISSN: 2147-3188
VOLUME: 11 NO: 2 PAGE: 727-732 YEAR: 2022
DOI: 10.17798/bitlisfen.1109645

Hypersphere and the Third Laplace-Beltrami Operator

Erhan GÜLER[1*]

[1]*Bartın Üniversitesi, Fen Fakültesi, Matematik Bölümü, Geometri Anabilim Dalı*
(ORCID: 0000-0003-3264-6239)

Keywords: Euclidean space, Third Laplace-Beltrami operator, Hypersphere, Gauss map, Curvature.

Abstract
In this work, we examine the differential geometric objects of the hypersphere $\mathbf{h}$ in four dimensional Euclidean geometry $\mathbb{E}^4$. Giving some notions of four dimension, we consider the ith curvature formulas of the hypersurfaces of $\mathbb{E}^4$. In addition, we reveal the hypersphere satisfying $\Delta^{\mathbf{III}}\mathbf{h} = \mathcal{A}\mathbf{h}$ for some 4×4 matrix $\mathcal{A}$.

1. Introduction

Surfaces, hypersurfaces (hypfaces), and also sphere and hypersphere have been studied by mathematicians for centuries.

Almost sixty years ago, Obata [1] worked the conditions for a Riemannian manifold to be isometric with a sphere; Takahashi [2] gave the related Euclidean submanifold (subfold) is 1-type (1-t), if and only if it is minimal or minimal in a hypersphere in $\mathbb{E}^m$; Chern et al. [3] focused the minimal subfolds of a sphere; Cheng and Yau [4] introduced the hypfaces having constant curvature; Chen et al. [5-11] researched the subfolds of finite type (f-t) whose immersion into $\mathbb{E}^m$ (or $\mathbb{E}_v^m$) taking the finite number eigenfunctions of its Laplacian. Garay studied [12] expanded the Takahashi theorem in m-space. Chen and Piccinni [11] focused the subfolds with f-t the Gauss map ($\mathbf{G}$) in $\mathbb{E}^m$. Dursun [13] considered the hypfaces having pointwise 1-t $\mathbf{G}$ in $\mathbb{E}^{n+1}$.

In $\mathbb{E}^3$; Takahashi [2] proved the spheres, minimal surfaces are the unique supplying $\Delta r = \lambda_{\in\mathbb{R}} r$; Ferrandez et al. [14] found the surfaces holding $\Delta H = A_{\in Mat(3,3)} H$, are the right circular cylinder, or open sphere, or minimal; Choi and Kim [15] classifed the minimal helicoid having pointwise 1-t (p1-t) $\mathbf{G}$ of the first type; Garay [16] studied f-t rotational surface; Dillen et al. [17] obtained that the unique surfaces supplying $\Delta r = A_{\in Mat(3,3)} r + B_{\in Mat(3,1)}$ are the circular cylinders, minimal surfaces, spheres; Stamatakis and Zoubi [18] focused the rotational surfaces holding $\Delta^{III} x = Ax$; Senoussi and Bekkar [19] gave the helical surfaces M^2 of f-t depends on I, II and III; Kim et al. [20] introduced the Cheng-Yau operator with its $\mathbf{G}$ of the rotational surfaces.

In $\mathbb{E}^4$; Moore [21,22] considered the general rotational surfaces; Hasanis and Vlachos [23] obtained the hypfaces having harmonic mean curvature; Cheng and Wan [24] gave the complete hypfaces having CMC; Kim and Turgay [25] worked the surfaces having L_1-p1-t $\mathbf{G}$; Arslan et al. [26] studied the Vranceanu surface having p1-t $\mathbf{G}$; Arslan et al. [27] worked the generalized rotational surfaces; Güler et al. [28] introduced the helicoidal hypfaces; Güler et al. [29] worked the $\mathbf{G}$ and the third Laplace-Beltrami operator (LBo) of the rotational hypfaces.

In Minkowski geometry $\mathbb{E}_1^4$; Ganchev and Milousheva [30] studied the analogue surfaces of [21,12]; Arvanitoyeorgos et al. [31] indicated if M_1^3 has $\Delta H = \alpha_{\in\mathbb{R}} H$, then M_1^3 covers CMC; Arslan and Milousheva [32] introduced the meridian surfaces having p1-t $\mathbf{G}$; Turgay [33] considered some

*Corresponding author: eguler@bartin.edu.tr
Received: 27.04.2022, Accepted: 28.06.2022

classifications of Lorentzian surfaces f-t **G**; Dursun and Turgay [34] worked spacelike surfaces having p1-t **G**.

Do Carmo and Dajczer [35] considered the rotational hypersurfaces in spaces of constant curvature; Alias and Gürbüz [36] worked an extension theorem of Takahashi.

We introduce the hypersphere in $\mathbb{E}^4$. In Section 2, we recall the notions of $\mathbb{E}^4$. We consider the curvature formulas of a hypface of $\mathbb{E}^4$. We define the hypersphere in Section 3. Finally, we give the hypersphere satisfying $\Delta^{\mathbf{III}}\mathbf{h} = \mathcal{A}_{\in Mat(4,4)}\mathbf{h}$ in Section 4. In Section 5, we serve the results and discussion. We present the conclusion and suggestions in the last section.

2. Preliminaries

We give basic elements, definitions, etc. considered in this paper. Let $\mathbb{E}^{n+1}$ describe a Euclidean $(n+1)$-space with a Euclidean inner product defined by $\langle \vec{x}, \vec{y} \rangle = \sum_{i=1}^{n+1} x_i y_i$, where $\vec{\boldsymbol{x}} = (x_1, x_2, \dots, x_{n+1})$, $\vec{y} = (y_1, y_2, \dots, y_{n+1})$ are the vectors in $\mathbb{E}^{n+1}$.

Let $\mathbf{h}$ be an hypface in $\mathbb{E}^{n+1}$, $\mathbf{S}$ be its shape operator. The characteristic polynomial of $\mathbf{S}$ is given by

$$P_{\mathbf{s}}(\lambda) = det(\mathrm{S} - \lambda \mathfrak{T}_n) = \sum_{k=0}^{n} (-1)^k s_k \lambda^{n-k} = 0.$$

Here, $i = 0,1, \dots, n$, $\mathfrak{T}_n$ is the identity n-matrix. See [36] for details. Then, the curvature formulas of $\mathbf{h}$ are $\binom{n}{0}\mathfrak{C}_0 = s_0 = 1$ (by definition), $\binom{n}{1}\mathfrak{C}_1 = s_1$,…, $\binom{n}{n}\mathfrak{C}_n = s_n = K$. The k-th fundamental form of the hypface $\mathbf{h}$ is given by $\mathbf{I}\left(\mathbf{S}^{k-1}(X), Y\right) = \langle \mathbf{S}^{k-1}(X), Y \rangle$. Then, we obtain

$$\sum_{i=0}^{n} (-1)^i \binom{n}{i} \mathfrak{C}_i \mathbf{I}\left(\mathbf{S}^{n-i}(X), Y\right) = 0.$$

Any vector will be identified with its transpose in the paper. Considering the curve $\mathcal{C}$ as follows

$$\gamma(w) = \big(f(w), 0, 0, \varphi(w)\big),$$

where f, φ are the differentiable functions, and taking ℓ as the axis x_4, the orthogonal transformation of $\mathbb{E}^4$ has the following

$$Z(u,v) = \begin{pmatrix} \cos u \cos v & -\sin u & -\cos u \sin v & 0 \\ \sin u \cos v & \cos u & -\sin u \sin v & 0 \\ \sin v & 0 & \cos v & 0 \\ 0 & 0 & 0 & 1 \end{pmatrix}, \quad (1)$$

and $u, v \in \mathbb{R}$.

Then, the rotational hypface is stated by $\mathbf{h}(u,v,w) = Z(u,v).\gamma(w)$. Supposing $\mathbf{h}$ be the immersion $M^3 \subset \mathbb{E}^3 \to \mathbb{E}^4$, the multiple vector product is given by

$$\vec{x} \times \vec{y} \times \vec{z} = det \begin{pmatrix} e_1 & e_2 & e_3 & e_4 \\ x_1 & x_2 & x_3 & x_4 \\ y_1 & y_2 & y_3 & y_4 \\ z_1 & z_2 & z_3 & z_4 \end{pmatrix},$$

where e_i are the standart base elements, x_i, y_i, z_i are the elements of the vectors $\vec{x}, \vec{y}, \vec{z}$ respectively, of $\mathbb{E}^4$. We have

$$\mathbf{I} = \begin{pmatrix} E & F & A \\ F & G & B \\ A & B & C \end{pmatrix},$$

$$\mathbf{II} = \begin{pmatrix} L & M & P \\ M & N & T \\ P & T & V \end{pmatrix},$$

$$\mathbf{III} = \begin{pmatrix} X & Y & O \\ Y & Z & J \\ O & J & U \end{pmatrix},$$

where $\mathbf{I}, \mathbf{II}, \mathbf{III}$ are the fundamental form matrices with the following coefficients

$E = \langle \mathbf{h}_u, \mathbf{h}_u \rangle$, $F = \langle \mathbf{h}_u, \mathbf{h}_v \rangle$, $G = \langle \mathbf{h}_v, \mathbf{h}_v \rangle$,
$A = \langle \mathbf{h}_u, \mathrm{h}_w \rangle$, $B = \langle \mathbf{h}_v, \mathbf{h}_w \rangle$, $C = \langle \mathbf{h}_w, \mathbf{h}_w \rangle$,
$L = \langle \mathbf{h}_{uu}, \mathbf{G} \rangle$, $M = \langle \mathbf{h}_{uv}, \mathbf{G} \rangle$, $N = \langle \mathbf{h}_{vv}, \mathbf{G} \rangle$,

$P = \langle \mathbf{h}_{uw}, \mathbf{G} \rangle, T = \langle \mathbf{h}_{vw}, \mathbf{G} \rangle, V = \langle \mathbf{h}_{ww}, \mathbf{G} \rangle,$
$X = \langle \mathbf{G}_u, \mathbf{G}_u \rangle, Y = \langle \mathbf{G}_u, \mathbf{G}_v \rangle, Z = \langle \mathbf{G}_v, \mathbf{G}_v \rangle,$
$O = \langle \mathbf{G}_u, \mathbf{G}_w \rangle, J = \langle \mathbf{G}_v, \mathbf{G}_w \rangle, U = \langle \mathbf{G}_w, \mathbf{G}_w \rangle$

of the hypface $\mathbf{h}$. Here,

$$\mathbf{G} = \frac{\mathbf{h}_u \times \mathbf{h}_v \times \mathbf{h}_w}{\|\mathbf{h}_u \times \mathbf{h}_v \times \mathbf{h}_w\|} \tag{2}$$

is the Gauss map of the $\mathbf{h}$. Hence, $\mathbf{I}^{-1} \cdot \mathbf{II}$ holds the shape operator matrix $\mathbf{S}$. See [28,29] for details. Any hypface $\mathbf{h}$ in $\mathbb{E}^4$ has the following: $\mathfrak{C}_0 = 1$, and

$$\mathfrak{C}_1 = \frac{\begin{Bmatrix} (EN + GL - 2FM)C \\ +(EG - F^2)V - LB^2 - NA^2 \\ -2(APG - BPF - ATF + BTE - ABM) \end{Bmatrix}}{3[(EG - F^2)C - EB^2 + 2FAB - GA^2]}, \tag{3}$$

$$\mathfrak{C}_2 = \frac{\begin{Bmatrix} (EN + GL - 2FM)V \\ +(LN - M^2)C - ET^2 - GP^2 \\ -2(APN - BPM - ATM + BTL - PTF) \end{Bmatrix}}{3[(EG - F^2)C - EB^2 + 2FAB - GA^2]}, \tag{4}$$

$$\mathfrak{C}_3 = \frac{(LN - M^2)V - LT^2 + 2MPT - NP^2}{3[(EG - F^2)C - EB^2 + 2FAB - GA^2]}. \tag{5}$$

See [37] for details. The hypface $\mathbf{h}$ is *i*-minimal, when $\mathfrak{C}_i = 0$.

3. Hypersphere in 4-Space

We reveal the hypersphere, then obtain its geometric objects in $\mathbb{E}^4$. Assume $\gamma: I \subset \mathbb{R} \to \Pi$ be a curve in a plane Π, ℓ be a line on Π in $\mathbb{E}^4$.

Definition 1. A rotational hypface in $\mathbb{E}^4$ is called hypersphere, when the profile curve

$$\gamma(w) = (r\,cosw, 0, 0, r\,sinw)$$

rotates by (1) around the *axis* $\ell = (0,0,0,1)$ for $r > 0$. So, the hypersphere spanned by the vector ℓ, is defined by $\mathbf{h}(u,v,w) = Z(u,v) \cdot \gamma(w)$. Therefore, more clear form of $\mathbf{h}$ is written by

$$\mathbf{h}(u,v,w) = \begin{pmatrix} r\cos u \cos v \cos w \\ r \sin u \cos v \cos w \\ r \sin v \cos w \\ r \sin w \end{pmatrix}. \tag{6}$$

Here, $r > 0$, $0 \le u, v, w \le 2\pi$. When $w = 0$, we have the sphere in $\mathbb{E}^4$. See [38] for details.

Next, we will obtain the $\mathbf{G}$ and the $\mathfrak{C}_i$ of the hypersphere (6). The first quantities of (6) are given by

$$\mathbf{I} = diag(r^2 \cos^2 v \cos^2 w, r^2 \cos^2 w, r^2). \tag{7}$$

By (2), we obtain the $\mathbf{G}$ of the hypersphere (6) as follows

$$\mathbf{G} = \begin{pmatrix} \cos u \cos v \cos w \\ \sin u \cos v \cos w \\ \sin v \cos w \\ \sin w \end{pmatrix}. \tag{8}$$

By taking the second derivatives of (6) with respect to u, v, w, and by the $\mathbf{G}$ (8) of the hypersphere (6), we have

$$\mathbf{II} = diag(-r \cos^2 v \cos^2 w, -r \cos^2 w, -r). \tag{9}$$

Computing the shape operator matrix of the hypersphere (6): $\mathbf{S} = -\frac{1}{r}\mathfrak{T}_3$, we find the following third quantities

$$\mathbf{III} = diag(r^2 \cos^2 v \cos^2 w, r^2 \cos^2 w, 1). \tag{10}$$

Finally, by using (3), (4), (5), with (7), (9), respectively, we obtain the following.

Theorem 1. Suppose $\mathbf{h} : M^3 \subset \mathbb{E}^3 \to \mathbb{E}^4$ be the hypface given by (6). Then, the hypersphere $\mathbf{h}$ has the following curvatures

$$\mathfrak{C}_1 = -\frac{1}{r}, \quad \mathfrak{C}_2 = \frac{1}{r^2}, \quad \mathfrak{C}_3 = -\frac{1}{r^3}.$$

4. Hypersphere Satisfying $\Delta^{\mathbf{III}}\mathbf{h} = \mathcal{A}\mathbf{h}$

In this section, we give the third LBo of a function, and then calculate it by using the hypersphere (6).

Definition 2. The third LBo of $\phi = \phi(x^1, x^2, x^3)|_{D\subset\mathbb{R}^3}$ of C^3 depends on the third fundamental form is defined by

$$\Delta^{\mathbf{III}}\phi = \frac{1}{\sqrt{|t|}}\sum_{i,j=1}^{3}\frac{\partial}{\partial x^i}\left(\sqrt{|t|}t^{ij}\frac{\partial\phi}{\partial x^j}\right),$$

where $\mathbf{III} = \left(t_{ij}\right)_{3\times3}, \left(t^{ij}\right) = (t_{kl})^{-\mathbf{1}}$ and $t = det\left(t_{ij}\right)$. See [29] for details.

Therefore, the third LBo of the hypersphere (6) transforms to

$$\Delta^{\mathbf{III}}\mathbf{h} = \frac{1}{\sqrt{|det\ \mathbf{III}|}}\left(\frac{\partial}{\partial u}\Phi - \frac{\partial}{\partial v}\Omega + \frac{\partial}{\partial w}\Psi\right), \qquad (11)$$

where

$$\Phi = \frac{(OZ - J^2)\frac{\partial\mathbf{h}}{\partial u} - (JU - OY)\frac{\partial\mathbf{h}}{\partial v} + (JY - UZ)\frac{\partial\mathbf{h}}{\partial w}}{\sqrt{|det\ \mathbf{III}|}},$$

$$\Omega = \frac{(JU - OY)\frac{\partial\mathbf{h}}{\partial u} - (OX - U^2)\frac{\partial\mathbf{h}}{\partial v} + (UY - JX)\frac{\partial\mathbf{h}}{\partial w}}{\sqrt{|det\ \mathbf{III}|}},$$

$$\Psi = \frac{(JY - UZ)\frac{\partial\mathbf{h}}{\partial u} - (UY - JX)\frac{\partial\mathbf{h}}{\partial v} + (XZ - Y^2)\frac{\partial\mathbf{h}}{\partial w}}{\sqrt{|det\ \mathbf{III}|}}.$$

By using the derivatives $\frac{\partial\Phi}{\partial u}, \frac{\partial\Omega}{\partial v}, \frac{\partial\Psi}{\partial w}$, and substituting them into (11), respectively, we obtain the following.

Theorem 2. Let $\mathbf{h} : M^3 \subset \mathbb{E}^3 \to \mathbb{E}^4$ be an hypersphere (6). Then, $\mathbf{h}$ has the following

$$\Delta^{\mathbf{III}}\mathbf{h} = -3\,r\,\mathbf{G},$$

where $r > 0$.

Proof. By direct computation, it is clear.

5. Results and Discussion

Considering all findings in the previous section, we give the following results.

Corollary 1. Assume that $\mathbf{h} : M^3 \subset \mathbb{E}^3 \to \mathbb{E}^4$ be an hypersphere (6). Therefore, the hypersphere $\mathbf{h}$ has $\Delta^{\mathbf{III}}\mathbf{h} = \mathcal{A}\mathbf{h}$, where

$$\mathcal{A}_{\in Mat(4,4)} = (-1)^{i+1}3r^i\mathfrak{C}_i\mathfrak{T}_4, \qquad i = 0,1,2,3.$$

and $\mathfrak{T}_4$ is the 4×4 identity matrix.

6. Conclusion and Suggestions

In this paper, we introduce the the hypersphere $\mathbf{h}$ in four dimensional Euclidean geometry $\mathbb{E}^4$. Recalling some notions of 4-dimension, we give the ith curvature formulas of the hypersurfaces of $\mathbb{E}^4$. Moreover, we present the hypersphere supplying $\Delta^{\mathbf{III}}\mathbf{h} = \mathcal{A}\mathbf{h}$ for some 4×4 matrix $\mathcal{A}$. It can be studied in other space forms.

Statement of Research and Publication Ethics

The study is complied with research and publication ethics.

References

[1] M. Obata, "Certain conditions for a Riemannian manifold to be isometric with a sphere," *J. Math. Soc. Japan*, vol. 14, pp. 333-340, 1962.

[2] T. Takahashi, "Minimal immersions of Riemannian manifolds," *J. Math. Soc. Japan*, vol. 18, pp. 380-385, 1966.

[3] S. S. Chern, M. P. do Carmo, and S. Kobayashi, *Minimal Submanifolds of a Sphere with Second Fundamental Form of Constant Length, Functional Analysis and Related Fields*. Springer, Berlin, 1970.

[4] S. Y. Cheng and S. T. Yau, "Hypersurfaces with constant scalar curvature," *Math. Ann.*, vol. 225, pp. 195-204, 1977.
[5] B. Y. Chen, "On submanifolds of finite type," *Soochow J. Math.*, vol. 9, pp. 65-81, 1983.
[6] B. Y. Chen, *Total Mean Curvature and Submanifolds of Finite Type*, World Scientific, Singapore, 1984.
[7] B. Y. Chen, *Finite Type Submanifolds and Generalizations*, University of Rome, 1985.
[8] B. Y. Chen, "Finite type submanifolds in pseudo-Euclidean spaces and applications," *Kodai Math. J.*, vol. 8, no. 3, pp. 358-374, 1985.
[9] B. Y. Chen, "Surfaces of finite type in Euclidean 3-space," *Bull. Math. Soc. Belg.*, vol. 39, pp. 243-254, 1987.
[10] B. Y. Chen, "Null 2-type surfaces in $\mathbb{E}^3$," *Kodai Math. J.*, vol. 11, pp. 295-299, 1988.
[11] B. Y. Chen and P. Piccinni, "Submanifolds with finite type Gauss map," *Bull. Austral. Math. Soc.*, vol. 35, pp. 161-186, 1987.
[12] O. J. Garay,, "An extension of Takahashi's theorem," *Geom. Dedicata*, vol. 34, pp. 105-112, 1990.
[13] U. Dursun, "Hypersurfaces with pointwise 1-type Gauss map," *Taiwanese J. Math.*, vol. 11, no. 5, pp. 1407-1416, 2007.
[14] A. Ferrandez,, O. J. Garay and P. Lucas, *On a certain class of conformally at Euclidean hypersurfaces*, In Global Analysis and Global Differential Geometry, Springer, Berlin, 48-54. 1990.
[15] M. Choi and Y. H. Kim, Characterization of the helicoid as ruled surfaces with pointwise 1-type Gauss map, *Bull. Korean Math. Soc.*, vol. 38, pp. 753-761, 2001.
[16] O. J. Garay, "On a certain class of finite type surfaces of revolution," *Kodai Math. J.*, vol. 11, pp. 25-31, 1988.
[17] F. Dillen, J. Pas and L. Verstraelen, "On surfaces of finite type in Euclidean 3-space," *Kodai Math. J.*, vol. 13, pp. 10-21, 1990.
[18] S. Stamatakis and H. Zoubi, "Surfaces of revolution satisfying $\Delta^{\mathrm{III}}\mathrm{x} = \mathrm{Ax}$," *J. Geom. Graph.*, vol. 14, no. 2, pp. 181-186, 2010.
[19] B. Senoussi and M. Bekkar, "Helicoidal surfaces with $\Delta^{\mathrm{J}}\mathrm{r} = \mathrm{Ar}$ in 3-dimensional Euclidean space," *Stud. Univ. Babeş -Bolyai Math.*, vol. 60, no. 3, pp. 437-448, 2015.
[20] D. S. Kim, J. R. Kim and Y. H. Kim, "Cheng-Yau operator and Gauss map of surfaces of revolution," *Bull. Malays. Math. Sci. Soc.*, vol. 39, no. 4, pp. 1319-1327, 2016.
[21] C. Moore, "Surfaces of rotation in a space of four dimensions," *Ann. Math.*, vol. 21, pp. 81-93, 1919.
[22] C. Moore, "Rotation surfaces of constant curvature in space of four dimensions," *Bull. Amer. Math. Soc.*, vol. 26, pp. 454-460, 1920.
[23] Th. Hasanis, and Th. Vlachos, "Hypersurfaces in $\mathbb{E}^4$ with harmonic mean curvature vector field," *Math. Nachr.*, vol. 172, pp. 145-169, 1995.
[24] Q. M. Cheng and Q. R. Wan, "Complete hypersurfaces of $\mathbb{R}^4$ with constant mean curvature," *Monatsh. Math.*, vol. 118, pp. 171-204, 1994.
[25] Y. H. Kim and N. C. Turgay, "Surfaces in $\mathbb{E}^4$ with L_1-pointwise 1-type Gauss map," *Bull. Korean Math. Soc.*, vol. 50, no. 3, pp. 935-949, 2013.
[26] K. Arslan, B. K. Bayram, B. Bulca, Y.H. Kim, C. Murathan and G. Öztürk, "Vranceanu surface in $\mathbb{E}^4$ with pointwise 1-type Gauss map," *Indian J. Pure Appl. Math.*, vol. 42, no. 1, pp. 41-51, 2011.
[27] K. Arslan, B. K. Bayram, B. Bulca and G. Öztürk, "Generalized rotation surfaces in $\mathbb{E}^4$," *Results Math.*, vol. 61, no. 3, pp. 315-327, 2012.
[28] E. Güler, M. Magid and Y. Yaylı, "Laplace-Beltrami operator of a helicoidal hypersurface in four-space," *J. Geom. Symm. Phys.*, vol. 41, pp. 77-95, 2016.
[29] E. Güler, H. H. Hacısalihoğlu, and Y. H. Kim, "The Gauss map and the third Laplace-Beltrami operator of the rotational hypersurface in 4-space," *Symmetry*, vol. 10, no. 9, pp. 1-12, 2018.

[30] G. Ganchev and V. Milousheva, "General rotational surfaces in the 4-dimensional Minkowski space," *Turkish J. Math.*, vol. 38, pp. 883-895, 2014.

[31] A. Arvanitoyeorgos, G. Kaimakamis and M. Magid, "Lorentz hypersurfaces in $\mathbb{E}_1^4$ satisfying $\Delta H = \alpha H$," *Illinois J. Math.*, vol. 53, no. 2, pp. 581-590, 2009.

[32] K. Arslan and V. Milousheva, "Meridian surfaces of elliptic or hyperbolic type with pointwise 1-type Gauss map in Minkowski 4-space," *Taiwanese J. Math.*, vol. 20, no. 2, pp. 311-332, 2016.

[33] N. C. Turgay, "Some classifications of Lorentzian surfaces with finite type Gauss map in the Minkowski 4-space," *J. Aust. Math. Soc.*, vol. 99, no. 3, pp. 415-427, 2015.

[34] U. Dursun and N. C. Turgay, "Space-like surfaces in Minkowski space $\mathbb{E}_1^4$ with pointwise 1-type Gauss map," *Ukr. Math. J.*, vol. 71, no. 1, pp. 64-80, 2019.

[35] M. P. Do Carmo and M. Dajczer, "Rotation hypersurfaces in spaces of constant curvature," *Trans. Amer. Math. Soc.*, vol. 277, pp. 685-709, 1983.

[36] L. J. Alias and N. Gürbüz, "An extension of Takashi theorem for the linearized operators of the highest order mean curvatures," *Geom. Dedicata*, vol. 121, pp. 113-127, 2006.

[37] E. Güler, Fundamental form IV and curvature formulas of the hypersphere, *Malaya J. Mat.*, vol. 8, no. 4, pp. 2008-2011, 2020.

[38] E. Güler and K. Yılmaz, "Hypersphere satisfying $\Delta x = \mathcal{A}x$ in 4-space," *Palestine J. Math.*, vol. 11, no. 3, pp. 21-30, 2022.